THE UNIVERSITY OF TEXAS AT AUSTIN
CENTER FOR TRANSPORTATION RESEARCH

TECHNICAL REPORT 0-7089-1
TxDOT PROJECT NUMBER 0-7089

Develop and Validate Precast Column Solutions for Texas Bridges

Emmanuel Montero-Carvajal
Chakravarthi Kotha
Luke Small
Lucas Zilveti
Chunsuk Park
Hansol Jang
Elias Saqan
Zach Webb
Hwa-Ching Wang
Juan Murcia-Delso
Oguzhan Bayrak

August 2024

Published November 2024

https://library.ctr.utexas.edu/ctr-publications/0-7089-1.pdf

Technical Report Documentation Page

1. Report No. FHWA/TX-25/0-7089-1	2. Government Accession No.	3. Recipient's Catalog No.
4. Title and Subtitle Develop and Validate Precast Column Solutions for Texas Bridges		5. Report Date Submitted: July 2024
		6. Performing Organization Code
7. Author(s) Emmanuel Montero-Carvajal, Chakravarthi Kotha, Luke Small, Lucas Zilveti, Chunsuk Park, Hansol Jang, Elias Saqan, Zach Webb, Hwa-Ching Wang, Juan Murcia-Delso, Oguzhan Bayrak.		8. Performing Organization Report No. 0-7089
9. Performing Organization Name and Address Center for Transportation Research The University of Texas at Austin 3925 W. Braker Lane, 4th Floor Austin, TX 78759		10. Work Unit No. (TRAIS)
		11. Contract or Grant No. 0-7089
12. Sponsoring Agency Name and Address Texas Department of Transportation Research and Technology Implementation Division P.O. Box 5080 Austin, TX 78763-5080		13. Type of Report and Period Covered Technical Report September 2020 – July 2024
		14. Sponsoring Agency Code
15. Supplementary Notes Project performed in cooperation with the Texas Department of Transportation.		

16. Abstract

This research addresses the application of precast columns in Texas bridge construction. The project combines experimental and analytical methods to develop innovative design concepts and construction details for precast concrete columns. Key design concept includes a spun-cast precast shell filled with a cast-in-place (CIP) core and connecting reinforcement to the bent cap and the footing. The interface shear capacity between the shell and the core is also considered vital for composite action. The research involved comprehensive experimental investigations and finite element analyses into interface shear strength of small-scale specimens and into the constructability and structural performance of full-scale prototype specimens. Significant findings include the effectiveness of plastic shims for column alignment, the importance of proper vibration, and the impact of internal roughness on column placement. Regarding affecting factors on the structural performance, the developed precast column system was found to be comparable or superior compared to traditional TxDOT standard column design given that the design guidelines in this report are followed. The design guidelines were established based on extensive testing and modeling, recommending optimal dimensions, concrete strengths, reinforcement configurations, and connection details. A simplified analytical method for constructing the P-M interactive diagram was introduced. The project culminated in a set of detailed design recommendations aimed at enhancing the implementation of precast columns, improving efficiency, and ensuring structural integrity in bridge construction. This work provides valuable insights and guidelines for integrating precast columns into Texas bridge infrastructure, supporting advancements in both practical application and theoretical understanding.

17. Key Words	18. Distribution Statement
Precast columns, non-contact splice, prestressed concrete, self-reacting frame, circular column, interface shear properties, cold joint, finite element analysis, spun cast.	No restrictions

19. Security Classif. (of report)	20. Security Classif. (of this page)	21. No. of pages	22. Price
Unclassified	Unclassified	331	

Form DOT F 1700.7 (8-72) Reproduction of completed page authorized

THE UNIVERSITY OF TEXAS AT AUSTIN
CENTER FOR TRANSPORTATION RESEARCH

Develop and Validate Precast Column Solutions for Texas Bridges

Emmanuel Montero-Carvajal
Chakravarthi Kotha
Luke Small
Lucas Zilveti
Chunsuk Park
Hansol Jang
Elias Saqan
Zach Webb
Hwa-Ching Wang
Juan Murcia-Delso
Oguzhan Bayrak

CTR Technical Report:	0-7089-1
Report Date:	July, 2024
Project:	0-7089
Project Title:	Develop and Validate Precast Column Solutions for Texas Bridges
Sponsoring Agency:	Texas Department of Transportation
Performing Agency:	Center for Transportation Research at The University of Texas at Austin

Project performed in cooperation with the Texas Department of Transportation and the Federal Highway Administration.

Center for Transportation Research
The University of Texas at Austin
3925 W. Braker Lane, 4th floor
Austin, TX 78759

http://ctr.utexas.edu/

Disclaimers

Author's Disclaimer: The contents of this report reflect the views of the authors, who are responsible for the facts and the accuracy of the data presented herein. The contents do not necessarily reflect the official view or policies of the Federal Highway Administration or the Texas Department of Transportation (TxDOT). This report does not constitute a standard, specification, or regulation.

Patent Disclaimer: There was no invention or discovery conceived or first actually reduced to practice in the course of or under this contract, including any art, method, process, machine manufacture, design or composition of matter, or any new useful improvement thereof, or any variety of plant, which is or may be patentable under the patent laws of the United States of America or any foreign country.

Engineering Disclaimer

NOT INTENDED FOR CONSTRUCTION, BIDDING, OR PERMIT PURPOSES.

Project Engineer: Oguzhan Bayrak
Professional Engineer License State and Number: Texas No. 106598
P.E. Designation: Research Supervisor

Acknowledgments

The authors are grateful to the Texas Department of Transportation (TxDOT) for providing the funds to conduct this research study. The contributions of the project director Jade′ Adeiwura (RTI PM) (Bridge Division) and other members of the Project Monitoring Committee – Graham Bettis, Doug Beer, Edgar Cuellar, Jonathon Boleware, – are deeply appreciated.

Table of Contents

Chapter 1. Introduction 1
1.1. Overview 1
1.2. Project Objectives 2
1.3. Project Scope 2
1.4. Organization 3

Chapter 2. Literature Review 5
2.1. Precast Column Systems 5
2.2. Projects with Precast Column Systems 9
2.2.1. Projects with Full-height Precast RC Columns 9
2.2.2. Projects with Precast Concrete Column Shells and CIP Core 17
2.2.3. Precast Column Systems Proposed in Studies 18
2.2.4. Analytical Studies and Design Recommendations 18
2.2.5. Experimental Research 26
2.3. Characterization of Interface Shear Properties 31
2.3.1. Existing Code Expressions 31
2.3.2. Properties Affecting Interface Shear Strength 35
2.4. Development Length for Steel Reinforcement and Prestressing Strands Embedded in Concrete 41
2.4.1. Existing Code Expressions 42
2.4.2. Recent research 45
2.5. Finite Element Analysis (FEA) Parameters 47
2.5.1. Element Shapes 47
2.5.2. Mesh size 48
2.5.3. Reinforcement Bond Models 48
2.6. Summary 49

Chapter 3. Precast-CIP Interface Shear Behavior 51
3.1. Introduction 51
3.2. Experimental Program 51
3.2.1. Specimen Design and Test Matrix 51
3.2.2. Specimen Details 53
3.2.3. Fabrication of Specimens 55
3.2.4. Test Setup 62
3.2.5. Test Procedure 65
3.3. Experimental Results and Discussion 66
3.3.1. Summary of Test Results 66
3.3.2. Damage Pattern and Shear Stress-Slip Behavior 67

3.3.3. Evaluation of Test Variables 82
3.4. Evaluation of Strength using Code Design Expressions 88
3.4.1. ACI 318-19 88
3.4.2. AASHTO LRFD 2020 89
3.4.3. Modifications to AASHTO LRFD for Core-Shell Interfaces 90
3.5. Summary 92
Chapter 4. Full-Scale Experimental Program 94
4.1. Specimen Design and Test Variables 94
4.1.1. Overview of Design Concept 94
4.1.2. Test Matrix 95
4.1.3. Nomenclature 96
4.2. Specimens Fabrication and Test Setup 96
4.2.1. Components and Dimensions 96
4.2.2. Footing and Bent Cap Detailing 100
4.2.3. Construction of CIP Control Specimen 104
4.2.4. Spun Cast Precast Column Shells 112
4.2.5. Precast Foundations 116
4.2.6. Precast Bent Caps 118
4.2.7. Construction Sequence of Precast Specimens 120
4.2.8. Assembly of Specimens in the Laboratory 124
4.2.9. Instrumentation 155
4.3. Test Method 159
4.4. Laboratory Results 161
4.4.1. Specimen S1-CIP (Cast-In-Place, Specimen as Baseline) 161
4.4.2. Specimen S2-R-AASH9-45 – Intentionally Roughened 166
4.4.3. Specimen S3-S-AASH9-45 – Not Intentionally Roughened 170
4.4.4. Specimen S4-R-Tx-34 – Embedment length of 2’10’’ 175
4.4.5. Specimen S5-R-ZABORAC-28 – Embedment length of 2’4’’ 180
Chapter 5. Data Analysis from Large-Scale Testing 186
5.1. Development Length of the Rebars in the Connections 186
5.1.1. Strain Profiles 186
5.1.2. Evaluation of Development Length 188
5.2. Comparison of Load-Displacement Behavior 191
5.2.1. Load-Displacement at 6-in. eccentricity Test 191
5.2.2. Load-Displacement at 12-in. eccentricity Test 192
5.2.3. Load-Displacement at 20-in. eccentricity Test 193
5.2.4. Load-Displacement at 40.25-in. eccentricity Test 194

5.3. Damage Pattern and Opening at the Connections 201
5.3.1. Crack width associated with the applied load 201
5.3.2. Opening in the connections for precast columns 202
5.4. Capacity of the Precast Column Solution 205
5.4.1. Column Capacity Considering Stress in Prestressing Strands 205
5.4.2. P-M Curves by Various Sectional Stress Distribution Models 208
5.5. Summary 211
Chapter 6. Finite Element Analysis 213
6.1. Shear Interface Model 213
6.1.1. Interface Models Design 213
6.1.2. Material Models and Properties 215
6.1.3. Shell-Core Interface Behavior and Properties 216
6.1.4. Analysis and Results 219
6.1.5. Summary 221
6.2. Cast in place (CIP) column 3D Modeling and Analysis 221
6.2.1. Model Preparation 221
6.2.2. FE Model Validation 228
6.2.3. FE Analysis and Discussion 231
6.2.4. Influence of Mesh Size and Loading Rate on the Accuracy 244
6.2.5. Summary of CIP model 247
6.3. Precast Column 3D Modeling and Analysis 248
6.3.1. Components and Reinforcement of Experimental Specimen 248
6.3.2. Model Preparation 249
6.3.3. FE Model Validation 258
6.3.4. FE Analysis and Discussion 261
6.3.5. Parametric analysis on connections and bond model 281
6.3.6. Summary of Precast Model 285
6.4. Precast Columns with Different Interfaces and Reinforcement Length 286
6.4.1. Precast Column with Smooth Interface Analysis and Results 286
6.4.2. Precast Column with Different Lap Splice Length (2’-4”) 289
6.4.3. Summary of Precast Column Models with Different Parameters 292
6.5. Summary 293
Chapter 7. Design Guidelines and Recommendations 295
7.1. Design Assumptions for Axial and Moment Capacity 295
7.2. P-M Interaction Diagram 296
7.3. Suggested Specifications for the Precast Column Solution 297

7.3.1. Hollow Precast Shell and Sectional Dimensions 297
7.3.2. Minimum Concrete Strength 297
7.3.3. The Roughness of Internal Face for the Precast Shell 297
7.3.4. Limits on Structural Configuration 297
7.3.5. Concrete Cover 298
7.3.6. Minimum Reinforcement 298
7.3.7. Development Length Inside the Precast Shell 298
7.3.8. Void of Precast Bent Cap Connection 298
7.3.9. Mounting Shims 299
7.4. Precast Column Assembling 299
Chapter 8. Conclusions 300
Chapter 9. Value of Research 303
9.1. Introduction 303
9.2. Level of Knowledge 304
9.3. Quality of Life and Customer Satisfaction 304
9.4. System Reliability and Increased Service Life 304
9.5. Expedited Project Delivery 305
9.6. Reduced User Cost 305
9.7. Reduced Construction, Operations, and Maintenance Cost 305
9.8. Engineering Design Improvement 305
References 306
Appendix A. Design example using a layered section analysis and a parabolic shape for the concrete stress 311
Appendix B. Design example using rectangular stress block for the concrete 324
Appendix C. Drawings for the Precast Column Solution 331

List of Tables

Table 3-1. Test Matrix 52
Table 3-2. Summary of Concrete Mixtures 54
Table 3-3. Summary of Test Results 67
Table 3-4. Proposed cohesion values 91
Table 3-5. Proposed shape factors 91
Table 3-6. Proposed Shrinkage Factors 91
Table 4-1. Test Matrix 95
Table 4-2. Setup sensors 156
Table 4-3. Test load ratio according to the eccentricities 159
Table 4-4. Summary of concrete properties for Specimen S1-CIP 162
Table 4-5. Summary of rebar properties for Specimen S1-CIP 162
Table 4-6. Summary of mechanical properties for Specimen S2-R-AASH9-45 166
Table 4-7. Summary of rebar properties for Precast Column Specimens 166
Table 4-8. Summary of mechanical properties for Specimen S3-S-AASH9-45 171
Table 4-9. Summary of mechanical properties for Specimen S4-R-Tx-34 176
Table 4-10. Summary of mechanical properties for S5-R-ZABORAC-28 181
Table 5-1. Summary of development lengths 188
Table 5-2. Precast Column Capacity using the formula for development length from AASHTO 206
Table 5-3. Precast Column Capacity using the formula for development length from ACI. 208
Table 5-4. Precast column capacity prediction using different concrete models. 211
Table 6-1. Material Properties of Concrete for Shell Macroelement and Core Macroelement 215
Table 6-2. Assigned Material Parameters of Reinforcement and Load Plates 216
Table 6-3. Interface Properties for Different Types of Surfaces 219
Table 6-4. Summary of shear strength obtained from FE models 220
Table 6-5. Material Parameters of Concrete for Column-Footing and Bent Cap 222
Table 6-6. Assigned Material Parameters of Reinforcement and Load Plates 223
Table 6-7. Assigned Material Parameters of Prestressing Strand 223
Table 6-8. Parameters Defining the Bond Stress Slip Relationship of Reinforcement 224

Table 6-9. Assigned Monitors for Full-Scaled Cast-in-Place Specimen 228
Table 6-10. Horizontal Displacement Values for all the Loading Cases at the End of Test 230
Table 6-11. FEA Models with Different Parameters for 40.25-in. Eccentricity Loading-Analysis 244
Table 6-12. FEA results of Different Models at the Mid-Height of the Column 245
Table 6-13. Material Parameters of Concrete for Column Core-Footing and Bent Cap 249
Table 6-14. Material Parameters of Concrete for Precast Concrete Shell 250
Table 6-15. Assigned Material Parameters of Reinforcement and Load Plates 251
Table 6-16. Assigned Material Parameters of Prestressing Strands 251
Table 6-17. Assigned Material Properties for Shell-Core Interface 252
Table 6-18. Assigned Monitors for Full-Scaled Cast-in-Place Specimen 257
Table 6-19. Analytical and Experimental Results of Precast Column (Specimen S2-R-AASH9-45) 261
Table 6-20. Estimated Precast Shell Connection Properties 282
Table 6-21. Interface Properties for Different Types of Surfaces 286
Table 9-1. Selected Benefit Area 303

List of Figures

Figure 2-1: Main types of precast column systems 5
Figure 2-2: Summary of precast column connection details 8
Figure 2-3: Precast columns and pier caps in I-85 interchange project (Mallela et al. 2013) 10
Figure 2-4: Coupler used to splice rebar used in I-85 interchange project (Mallela et al. 2013) 11
Figure 2-5: Precast columns in casting yard in Parkview Avenue Bridge (Attanyake et al. 2012) 11
Figure 2-6: Precast bent cap being erected in Parkview Avenue Bridge (Attanyake et al. 2012) 12
Figure 2-7: Pier cap erection in Rawson Avenue Bridge (Olivia 2014) 13
Figure 2-8: Precast column in Rawson Avenue Bridge (Olivia 2014) 13
Figure 2-9: Precast column during placement, Siggelkow Road Bridge (source: www.countymaterials.com) 14
Figure 2-10: Precast column installation using grouted splice couplers in Keg Creek Bridge (Littleton 2013) 14
Figure 2-11: Precast column-to-cap beam connection in Keg Creek Bridge (Littleton 2013) 15
Figure 2-12: Precast column-to-footing connection in Keg Creek Bridge (Littleton 2013) 15
Figure 2-13: Erection of the precast column in Moore's Mill Road Bridge (City of Auburn 2019) 16
Figure 2-14: Erection of precast column in Laurel Street Overcrossing (Mellon 2018) 17
Figure 2-15: Precast column shells, LP-340 over IH-35 (Wolf 2005) 18
Figure 2-16: Precast column system proposed by Hieber et al. (2005) 19
Figure 2-17: Footing-to-column connection proposed by Hieber et al. (2005) 20
Figure 2-18: Precast column design proposed by Fouad et al. (2006) 21
Figure 2-19 Characteristics of column systems proposed by Fouad et al. (2006) 21
Figure 2-20: Column connections proposed by Fouad et al. (2006) 22
Figure 2-21: Precast column-footing connection with grouted duct/splice sleeve and socket connection proposed by Aktan and Attanayake (2013) 23
Figure 2-22: Precast column-footing connection with grouted void/pocket and shear key proposed by Atkan and Attanayake (2013) 23
Figure 2-23: Precast column to bent cap connection with grouted pocket (Restrepo et al. 2011) 24

Figure 2-24: Precast column to bent cap with grouted corrugated duct connection (Atkan and Attanayake 2013)..... 24
Figure 2-25: Vertical splice duct connection between precast column and precast bent cap (FHWA 2009) 25
Figure 2-26: SPER system using short pier panels (Ralls et al. 2005) 25
Figure 2-27: SPER system using tall pier panels (Ralls et al. 2005) 26
Figure 2-28: Precast column system developed by Pang et al. (2008) 27
Figure 2-29: Socket connections proposed by Haraldsson et al. (2013)..... 27
Figure 2-30: Socket connection between precast column and footing in U.S. 12 bridge (Khalegi et al. 2012) 28
Figure 2-31: Study on socket connections by Cheng et al. 2020. 29
Figure 2-32: Production method for specimens by Kim et al. (2016) 30
Figure 2-33: Test setup used by Kim et al. (2016) 31
Figure 2-34: Illustration of Shear Friction Hypothesis proposed by Birkeland and Birkeland (1966)..... 36
Figure 2-35: Shear strength for various conditions from Santos et al. (2014). 37
Figure 2-36: Test specimens prepared and tested by Aziz 2010. The number listed in the middle denotes the number of specimens made for each case. 37
Figure 2-37: Strength and Slip for various push-off tests as performed by Hanson (1960)..... 38
Figure 2-38: Differences in Young's Modulus vs Number of Cohesive Failures (Santos et al. 2011)..... 39
Figure 2-39: Depiction of variation of normal and shear stresses across an interface due to shrinkage of added concrete (Birkeland 1960) 40
Figure 2-40 Element types used in ATENA 3D software (Atena Theory)..... 47
Figure 2-41 Analytical Bond Stress-Slip Relationship (CEB-FIP, 2010). 48
Figure 2-42 Bond Model for Reinforcement (Bigaj, 1999)..... 49
Figure 3-1: Schematic Specimen and test method..... 52
Figure 3-2 Nomenclature of push-off specimens..... 53
Figure 3-3: Typical specimen 53
Figure 3-4: Completed rebar cage..... 55
Figure 3-5: Exterior formwork used for all specimens..... 55
Figure 3-6: 1/8" steel void, 1/4" steel void, sonotube void..... 56
Figure 3-7: Initial square steel void form 56
Figure 3-8: Wooden form and fabrication 57
Figure 3-9: First round of precasting 58
Figure 3-10: Second round of precasting..... 58

Figure 3-11: Formwork blow out due to missing screws connecting sidewall to base 59
Figure 3-12: Example of finished shell and interface 59
Figure 3-13: Finished shell for square cores 60
Figure 3-14: Roughened interface after sandblasting 60
Figure 3-15: Specimens with filled void 61
Figure 3-16: Cast of phase-two specimens 61
Figure 3-17: Load frame 63
Figure 3-18: Vibrating wire strain gauge locations 64
Figure 3-19: Arrangement of potentiometers for slip measurement 65
Figure 3-20: Load vs average slip for Group I-C-S 68
Figure 3-21: Pure slip failure as seen on the top and bottom of Group I-C-S 69
Figure 3-22: Load vs average slip for Group I-C-S-SR 69
Figure 3-23: Interface slip failure as observed in top and bottom of Group I-C-S-SR 70
Figure 3-24: Length change of monitored companion prisms 71
Figure 3-25: Load vs average slip for Group I-C-T 72
Figure 3-26: Slip failure as observed on the top of specimens in Group I-C-T 72
Figure 3-27: Representative examples of shell cracking observed in Group I-C-T 73
Figure 3-28: Load vs average slip for Group I-C-T-SR 73
Figure 3-29: Slip failure as observed on the top of Group I-C-T-SR 74
Figure 3-30: Shell cracking representative of Group I-C-T-SR 74
Figure 3-31: Load vs average slip for Group I-Sq-S 75
Figure 3-32: Group I-Sq-S after failure 76
Figure 3-33: Load vs average slip for Group I-Sq-T 76
Figure 3-34: Interface failure modes at the top of Group I-Sq-T 77
Figure 3-35: Shell cracking seen in Group I-Sq-T 77
Figure 3-36: Load vs Average Slip for Group II-C-S 78
Figure 3-37: Group II-C-S after failure. 78
Figure 3-38: Group II-C-S exhibiting a partial bearing failure on the surface 79
Figure 3-39: Group II-Sq-S after failure showing side face cracking 79
Figure 3-40: Group II-Sq-S after failure 80
Figure 3-41: Load vs average slip for Group II-Sq-S 80
Figure 3-42: Pure slip failures as seen on the top of Group II-C-T 81
Figure 3-43: Representative examples of cracking in Group II-C-T 81

Figure 3-44: Load vs average slip for Group II-C-T 82
Figure 3-45: Effect of shape on peak interface shear stress in Series I 83
Figure 3-46: Effect of shape on peak interface shear stress in Series II 84
Figure 3-47: Effect of SRC on peak interface shear stress 85
Figure 3-48: Effect of roughness on peak interface shear stress in Series I 86
Figure 3-49: Effect of roughness on peak interface shear stress in Series II 86
Figure 3-50: Effect of the sequence of cast on peak interface shear stress for round interface 87
Figure 3-51 Effect of the sequence of cast on peak interface shear stress for square interface 88
Figure 3-52: Test interface shear capacity versus calculated interface shear capacity per AASHTO LRFD 90
Figure 3-53: Test interface shear capacity versus calculated interface shear capacity per the proposed method 92
Figure 4-1: Schematic design of the specimens used in the study. 94
Figure 4-2: Specimen's nomenclature. 96
Figure 4-3: Testing Setup for Specimen S1-CIP 97
Figure 4-4: 3D representation of the Test Setup for the Specimen S1-CIP 97
Figure 4-5: Test Setup Footing Top View for Specimen S1-CIP 98
Figure 4-6: Testing Setup for Precast Specimens 99
Figure 4-7: 3D representation of the Test Setup for Precast Specimens 99
Figure 4-8: Test Setup Footing Top View for Precast Specimens 100
Figure 4-9: Final Rebar Layout for Specimen S1-CIP. 101
Figure 4-10: Final Footing Extending Bars for Specimen S1-CIP. 101
Figure 4-11: Final Precast Footing Rebar Layout 102
Figure 4-12: Final Precast Footing Extending Bars (length of extending bars is variable) 102
Figure 4-13: Final Precast Bent Cap Rebar Layout 103
Figure 4-14: Bent Cap connecting bars detail 104
Figure 4-15: CIP Footing Formwork 105
Figure 4-16: CIP Footing Rebar Cage 106
Figure 4-17: Finished CIP Footing 106
Figure 4-18: As-built hole location in the CIP Foundation 107
Figure 4-19: CIP Column Cage Construction 108
Figure 4-20: CIP Column "X" Bars 109
Figure 4-21: CIP Column Final Cage and Pre-Bracing 109
Figure 4-22: CIP Column Bracing Design 110
Figure 4-23: Casting of CIP Column 111
Figure 4-24: Slump measurement and cylinder samples for CIP Column 111

Figure 4-25: CIP Column after removing formwork. 112
Figure 4-26: Precast hollow column details..... 112
Figure 4-27: Precast Columns Reinforcing Spiral 113
Figure 4-28: Precast Column Strain Gauge Installation 113
Figure 4-29: Precast Column Placing into Formwork 114
Figure 4-30: Precast Column Pour Preparation and Pour 115
Figure 4-31: Final Precast Column Elements 115
Figure 4-32: Inspection of the foundations at Valley Prestress 116
Figure 4-33: Steel cage of the foundations at Valley Prestress 117
Figure 4-34: Precast foundations in the FSEL yard..... 117
Figure 4-35: Precast bent caps prepared in Valley Prestress 118
Figure 4-36: Corrugated steel pipes used in the bent caps..... 119
Figure 4-37: Steel cage and corrugated steel pipe in the bent caps. 119
Figure 4-38: Inspection of the PVC sleeves in the bent caps. 120
Figure 4-39: Spacers used to warranty spacing in the top spirals. 120
Figure 4-40: Construction sequence: Step 1 to Step 4 122
Figure 4-41: Construction sequence: Step 5 to Step 8 123
Figure 4-42: Construction sequence: Step 9 124
Figure 4-43: HDPE shims located on the top of the column 125
Figure 4-44: Installation of the bent cap. 125
Figure 4-45 Alignment of the bent cap with the marks using a laser level 126
Figure 4-46: Placement of steel form between the bent cap and the column 126
Figure 4-47: Casting of concrete in the void and vibration close to the edges 127
Figure 4-48: State of the void after removing the formwork. 127
Figure 4-49: Cast-in-Place Specimen after casting the void. 128
Figure 4-50: Strain gauges prepared in the footing and cage connection for Specimen #2 and S3-S-AASH9-45..... 128
Figure 4-51: Location of strain gauges for Specimen S2-R-AASH9-45 and S3-S-AASH9-45. 129
Figure 4-52: Footing preparation for Specimens S2-R-AASH9-45 and S3-S-AASH9-45 130
Figure 4-53: Footing preparation to place the precast columns on Specimens S2-R-AASH9-45 and S3-S-AASH9-45. 131
Figure 4-54: Placing of precast column on Specimen S2-R-AASH9-45. 132
Figure 4-55: Placing of precast column on Specimen S3-S-AASH9-45. 133
Figure 4-56: Precast column preparation before casting. 134
Figure 4-57: Steel connectors on the top of the precast column. 134
Figure 4-58: Concrete casting for precast columns 135

Figure 4-59: Precast column preparation before placing the bent cap..... 136
Figure 4-60: Placing of the bent cap for Specimen S2-R-AASH9-45..... 137
Figure 4-61: Placing of the bent cap for Specimen S3-S-AASH9-45. 137
Figure 4-62: Precast columns prepared for bent cap's void concrete casting. 138
Figure 4-63: Concrete casting for Specimens S2-R-AASH9-45 and S3-S-AASH9-45. 139
Figure 4-64: Specimens ready for testing. 139
Figure 4-65: Location of strain gauges for Specimen S4-R-Tx-34 (Left) and S5-R-ZABORAC-28 (Right). 140
Figure 4-66: Strain gauges were prepared in the footing and cage connection for Specimen S4-R-Tx-34 and S5-R-ZABORAC-28. 141
Figure 4-67: HDEP shims ready to place the precast columns..... 142
Figure 4-68: Lifting and placing of Precast Column for Specimen S4-R-Tx-34. 143
Figure 4-69: Lifting and placing of Precast Column for Specimen S5-R-ZABORAC-28. 143
Figure 4-70: Preparation for concrete casting in the precast column's void. 144
Figure 4-71: Placing of steel connectors on top of precast columns. 145
Figure 4-72: Precast columns' void concrete casting. 146
Figure 4-73: Precast Column for Specimen S4-R-Tx-34 after removing steel forms on the bottom..... 147
Figure 4-74: Precast Column for Specimen S5-R-ZABORAC-28 after removing steel forms on the bottom. 148
Figure 4-75: Precast columns prepared to place the bent cap..... 149
Figure 4-76: Placing of the bent cap on top of Specimen S4-R-Tx-34 150
Figure 4-77: Placing of the bent cap on top of Specimen S5-R-ZABORAC-28 150
Figure 4-78: Precast columns prepared for bent cap void's concrete casting. 151
Figure 4-79: Concrete casting for bent cap's void for Specimens S4-R-Tx-34 and S5-R-ZABORAC-28..... 152
Figure 4-80: Surface roughened to a CSP 4 or higher for Specimen S4-R-Tx-34 and S5-R-ZABORAC-28. 152
Figure 4-81: Surface cleaned and saturated for Specimen S4-R-Tx-34 and S5-R-ZABORAC-28..... 153
Figure 4-82: Steel forms placed and spray foam sealing for Specimen S4-R-Tx-34 and S5-R-ZABORAC-28. 153
Figure 4-83: Grout pouring for Specimen S4-R-Tx-34 and S5-R-ZABORAC-28. 154

Figure 4-84: Steel formwork removed from Specimen S4-R-Tx-34 and S5-R-ZABORAC-28 154
Figure 4-85: Precast columns ready for test. 155
Figure 4-86: Sensor location on the column 156
Figure 4-87: Location of LVDT sensors. 157
Figure 4-88: Location of L-Pots during the test. 157
Figure 4-89: Location of S-Pots during the test. 158
Figure 4-90: Location of load cells (silver) and rams (yellow) on the top of the specimens. 158
Figure 4-91: Load pattern for eccentricity of 6-in and 12-in. 160
Figure 4-92: Load pattern for eccentricity of 20-in. 160
Figure 4-93: Load pattern for eccentricity of 40.25-in. 161
Figure 4-94: Comparison in the lateral displacement for Specimen S1-CIP using the L-Pot 5 located at the top of the column. 163
Figure 4-95: Cracks after 6-in Test for Specimen S1-CIP. 164
Figure 4-96: Cracks after 12-in Test for Specimen S1-CIP. 164
Figure 4-97: Cracks after 40.25-in Test for Specimen S1-CIP. 165
Figure 4-98: Opening in connection during the 40.25 in Test for Specimen S1-CIP. 165
Figure 4-99: Comparison in the lateral displacement for Specimen S2-R-AASH9-45 using the L-Pot 5 located at the top of the column. 167
Figure 4-100: Specimen S2-R-AASH9-45 after the 6-in eccentricity test, and the 12-in eccentricity test. 168
Figure 4-101: Specimen S2-R-AASH9-45 after the 20-in. eccentricity test. 168
Figure 4-102: Specimen S2-R-AASH9-45 during the 40.25in eccentricity test. 169
Figure 4-103: Specimen S2-R-AASH9-45 after the 40.25in eccentricity test. 170
Figure 4-104: Comparison in the lateral displacement for Specimen S3-S-AASH9-45 using the L-Pot 5 located at the top of the column. 171
Figure 4-105: Specimen S3-S-AASH9-45 after the 6-in eccentricity test, and the 12-in eccentricity test. 172
Figure 4-106: Specimen S3-S-AASH9-45 after the 20-in. eccentricity test. 173
Figure 4-107: Specimen S3-S-AASH9-45 during the 40.25in eccentricity test. 174
Figure 4-108: Specimen S3-S-AASH9-45 after the 40.25-in eccentricity test. 175
Figure 4-109: Comparison in the lateral displacement for Specimen S4-R-Tx-34 using the L-Pot 5 located at the top of the column. 177
Figure 4-110: Specimen S4-R-Tx-34 after the 6-in eccentricity test, and the 12-in eccentricity test. 178

Figure 4-111: Specimen S4-R-Tx-34 after the 20-in. eccentricity test..... 178
Figure 4-112: Specimen S4-R-Tx-34 during the 40.25in eccentricity test..... 179
Figure 4-113: Specimen S4-R-Tx-34 after the 40.25in eccentricity test..... 180
Figure 4-114: Comparison in the lateral displacement for Specimen S5-R-ZABORAC-28 using the L-Pot 5 located at the top of the column..... 182
Figure 4-115: Specimen S5-R-ZABORAC-28 after the 6-in. eccentricity test, and the 12-in. eccentricity test..... 183
Figure 4-116: Specimen S5-R-ZABORAC-28 under an eccentricity of 20 in. 184
Figure 4-117: Specimen S5-R-ZABORAC-28 under an eccentricity of 42.25 in. 185
Figure 4-118: Specimen S5-R-ZABORAC-28 after the 42.25in eccentricity test 185
Figure 5-1: Strain profile for each specimen the footing-to-column connection after the 40.25-in. eccentricity test 187
Figure 5-2: Strain reported for each specimen after the 40.25-in. eccentricity test according to the label for each sensor on the bars in the Column-Bent Cap Connection. 188
Figure 5-3: Comparison of development lengths in the footing-to-column Connection. 189
Figure 5-4: Comparison of development length in the column at the bent cap-to-column connection..... 190
Figure 5-5: Comparison of development lengths in the bent cap at the bent cap-to-column connection..... 191
Figure 5-6: Load – Normalized Displacement against Specimen S1-CIP for 6-in. eccentricity test 192
Figure 5-7: Load – Normalized Displacement against Specimen S1-CIP for 12-in. eccentricity test 193
Figure 5-8: Load – Normalized Displacement against S2-R-AASH9-45 for 20-in. eccentricity test..... 194
Figure 5-9: Rotation calculation from vertical deflections measured with the S-Pots 197
Figure 5-10: Ratio of Effective stiffness “EI” vs “EI” from the material properties as the moment increased during the test 197
Figure 5-11: Lateral displacement estimated for the column’s top 198
Figure 5-12: Lateral displacement estimated for L-Pot 3 and Lpot-4 for the specimen S1-CIP..... 199
Figure 5-13: Lateral displacement estimated for L-Pot 5 the specimen S1-CIP 200
Figure 5-14: Moment – Displacement Normalized against Specimen S1-CIP 201

Figure 5-15: Moment – Crack width for precast columns during the 40.25-in. eccentricity test 202
Figure 5-16: General view of the opening in the connections during the 40.25-in. test..... 203
Figure 5-17: Opening in the bottom connection during the 40.25-in. test..... 204
Figure 5-18: Opening in the top connection during the 40.25-in. test..... 205
Figure 5-19: Idealized relationship between steel stress and distance from the free end of the strand, taken from AASHTO 9th edition C5.9.4.3.2-1..... 206
Figure 5-20: P-M Interaction Diagrams developed for all the specimens subjected to an eccentricity of 40.25 in considering the f_{px} in the prestressing strands. 207
Figure 5-21: Comparison of the load obtained from the test and the calculated with AASHTO and ACI. 208
Figure 5-22: Strain compatibility for a case when c = 18-in.: a) Layered section and stress profile and b) Strain in the prestressing strands due to flexure, compression, and prestressing. 209
Figure 5-23: P-M curves obtained for the precast column design using different models to represent the concrete behavior. 210
Figure 6-1: Top and Bottom view of Shear Interface Model Built in ATENA 3 (Kotha, 2024)..... 214
Figure 6-2: Experimental Setup of Interface Models (Small, 2022) 214
Figure 6-3: Mohr-Coulomb Criterion for Contact Elements in ATENA 3D..... 217
Figure 6-4: Contact Stiffness 217
Figure 6-5: Comparison of Load-Slip Behavior of Smooth Interface Specimens (Kotha, 2024)..... 219
Figure 6-6: Shell-Core Interface at the End of Test, Smooth Interface Model (Kotha, 2024)..... 220
Figure 6-7: FEA Results of all Interfaces in terms of Load-Slip Behavior (Kotha, 2024) 220
Figure 6-8: Bilinear Stress-Strain Law for Reinforcement in ATENA 3D (ATENA Theory, 2021)..... 223
Figure 6-9: Input Bond Stress-Slip Relationship for Prestressing Strands..... 225
Figure 6-10: Meshed Finite Element Model for CIP column (Kotha, 2024)..... 226
Figure 6-11: CIP Model with Components and Supports (Kotha, 2024) 226
Figure 6-12: Bent Cap being Prestressed to 75% of f_{pu} (Kotha, 2024)..... 227
Figure 6-13: Principal Stress in Strands After Release (Kotha, 2024) 227
Figure 6-14: Monitors Location for FEM of CIP column (Kotha, 2024)..... 228
Figure 6-15: Comparison of 6-in. Eccentricity Analytical and Experimental Results (Kotha, 2024)..... 229

Figure 6-16: Comparison of 12-in. Eccentricity Analytical and Experimental Results (Kotha, 2024) 229
Figure 6-17: Comparison of 40.25-in. Eccentricity Analytical and Experimental Results (Kotha, 2024) 230
Figure 6-18: Loading Setup for 6-in. Eccentricity Analysis (Kotha, 2024) 231
Figure 6-19 Stress Levels in ksi and Cracking at the end of 6-in. Eccentricity Loading (Kotha, 2024) 232
Figure 6-20: Total Axial Load-Displacement Behavior for 6-in. Eccentricity Loading (Kotha, 2024) 233
Figure 6-21: Moment-Curvature Plot for 6-in. Eccentricity Loading (Kotha, 2024) 233
Figure 6-22: Comparison of Crack Pattern at the end of 6-in. Eccentricity Loading (stress levels in ksi) (Kotha, 2024) 234
Figure 6-23: Loading Setup for 12-in. Eccentricity Analysis (Kotha, 2024) 235
Figure 6-24: Stress Levels in ksi and Cracking at the end of 12-in. Eccentricity Loading (Kotha, 2024) 236
Figure 6-25: Total Axial Load-Displacement Behavior for 12-in. Eccentricity Loading (Kotha, 2024) 237
Figure 6-26: Moment-Curvature Plot for 12-in. Eccentricity Loading (Kotha, 2024) 237
Figure 6-27: Comparison of Crack Pattern at the end of 12-in. Eccentricity Loading (Stress Levels in ksi) (Kotha, 2024) 238
Figure 6-28: Loading Setup for 40.25-in. Eccentricity Analysis (Kotha, 2024) 239
Figure 6-29: Stress Levels in ksi and Cracking at the end of 40.25-in. Eccentricity Loading (Kotha, 2024) 240
Figure 6-30: P-M Interaction Diagram of the CIP Column Specimen (Kotha, 2024) 241
Figure 6-31: Total Axial Load-Displacement Behavior for 40.25-in. Eccentricity Loading (Kotha, 2024) 241
Figure 6-32: Principal Stress (in ksi) in Reinforcement at 2 Different Axial Loads (Kotha, 2024) 242
Figure 6-33: Moment-Curvature Plot for 40.25-in. Eccentricity Loading (Kotha, 2024) 242
Figure 6-34: Comparison of Crack Pattern at the end of 40.25-in. Eccentricity Loading (Stress Levels in ksi) (Kotha, 2024) 243
Figure 6-35: Axial Load-Displacement (Mid Height) Curves for Experimental Specimen and FEA Models (Kotha, 2024) 245
Figure 6-36: Crack Pattern in Tensile Region of Experimental Specimen, Model 1, Model 3, Respectively. (Kotha, 2024) 246
Figure 6-37: Crack Pattern in Compressive Region of Model 1, Model 3 Respectively (Kotha, 2024) 247

Figure 6-38: Macroelements used in the Precast Column Model (Kotha, 2024) 252
Figure 6-39: Mesh Details of Precast Column Model in ATENA 3D Software (Kotha, 2024) 253
Figure 6-40: Precast Column Model and Boundary Conditions (Kotha, 2024) 254
Figure 6-41: Bond Stress-Slip Relationship for Prestressing Strands in Bent Cap (Kotha, 2024) 254
Figure 6-42: Strands in Bent Cap being Prestressed to 75% of f_{pu} (Kotha, 2024) 255
Figure 6-43: Principal Stress in Strands After Release (Kotha, 2024) 255
Figure 6-44: Bond Stress-Slip Relationship for Strands in the Precast Shell (Kotha, 2024) 256
Figure 6-45: Prestressing Forces and Stress Levels after Prestressing Strands in Precast Shell (Kotha, 2024) 257
Figure 6-46: Monitors Location for FEA of Precast column (Kotha, 2024) 258
Figure 6-47: Comparison of 6-in. Eccentricity Analytical and Experimental Results (Kotha, 2024) 259
Figure 6-48: Comparison of 12-in. Eccentricity Analytical and Experimental Results (Kotha, 2024) 259
Figure 6-49: Comparison of 20-in. Eccentricity Analytical and Experimental Results (Kotha, 2024) 260
Figure 6-50: Comparison of 40.25-in. Eccentricity Analytical and Experimental Results (Kotha, 2024) 261
Figure 6-51: Loading Setup for 6-in. Eccentricity Analysis (Kotha, 2024) 262
Figure 6-52: Stress Levels (in ksi) and Cracking at the end of 6-in. Eccentricity Loading (Kotha, 2024) 263
Figure 6-53: Total Axial Load-Displacement Behavior for 6-in. Eccentricity Loading (Kotha, 2024) 264
Figure 6-54: Moment-Curvature Plot for 6-in. Eccentricity Loading (Kotha, 2024) 264
Figure 6-55: Comparison of Crack Pattern at the end of 6-in. Eccentricity Loading (stress levels in ksi) (Kotha, 2024) 265
Figure 6-56: Loading Setup for 12-in. Eccentricity Analysis (Kotha, 2024) 266
Figure 6-57: Stress Levels in ksi and Cracking at the end of 12-in. Eccentricity Loading (Kotha, 2024) 267
Figure 6-58: Total Axial Load-Displacement Behavior for 12-in. Eccentricity Loading (Kotha, 2024) 268
Figure 6-59: Moment-Curvature Plot for 12-in. Eccentricity Loading (Kotha, 2024) 268
Figure 6-60: Comparison of Crack Pattern at the end of 12-in. Eccentricity Loading (stress levels in ksi) (Kotha, 2024) 269

Figure 6-61: Loading Setup for 20-in. Eccentricity Analysis (Kotha, 2024) 270
Figure 6-62: Stress Levels in ksi and Cracking at the end of 20-in. Eccentricity Loading (Kotha, 2024) 271
Figure 6-63: Total Axial Load-Displacement Behavior for 20-in. Eccentricity Loading (Kotha, 2024) 272
Figure 6-64: Moment-Curvature Plot for 20-in. Eccentricity Loading (Kotha, 2024) 272
Figure 6-65: Comparison of Crack Pattern at the end of 20-in. Eccentricity Loading (stress levels in ksi) (Kotha, 2024) 273
Figure 6-66: P-M Curve and Loading Setup for 40.25-in. Eccentricity Analysis (Kotha, 2024) 274
Figure 6-67: Stress Levels in ksi and Cracking at the end of 40.25-in. Eccentricity Loading (Kotha, 2024) 275
Figure 6-68: Total Axial Load-Displacement Behavior for 40.25-in. Eccentricity Test (Kotha, 2024) 276
Figure 6-69: Reinforcement Stresses at 300 kips of Axial Load (Kotha, 2024) 277
Figure 6-70: Moment-Curvature Plot for 40.25-in. Eccentricity Loading (Kotha, 2024) 278
Figure 6-71: Tensile Side Comparison at the end of 40.25-in. Eccentricity Loading (stress levels in ksi) (Kotha, 2024) 279
Figure 6-72: Neutral Stress Side Comparison at the end of 40.25-in. Eccentricity Loading (stress in ksi) (Kotha, 2024) 280
Figure 6-73: Compressive Side Comparison at the end of 40.25-in. Eccentricity Loading (stress levels in ksi) (Kotha, 2024) 281
Figure 6-74: Comparison of 40.25 in. analysis for Experimental Specimen and Analytical model with imperfect connection (Kotha, 2024) 283
Figure 6-75: Comparison of 40.25 in. analysis for Analytical Model with Perfect and Imperfect Connections (Kotha, 2024) 283
Figure 6-76: Experimental and Analytical results of Models with different Prestressing Levels (Kotha, 2024) 284
Figure 6-77: Experimental Results of CIP and Precast Columns under 40.25 in. Eccentricity Analysis 287
Figure 6-78: Comparison of 40.25-in. Eccentricity Analysis and Experimental Results (Kotha, 2024) 288
Figure 6-79: Tensile Side Comparison at the end of 40.25-in. Eccentricity Loading (stress levels in ksi) (Kotha, 2024) 288
Figure 6-80: Compressive Side Comparison at the end of 40.25-in. Eccentricity Loading (stress in ksi) (Kotha, 2024) 289
Figure 6-81: 40.25 in. Eccentricity Analysis Results of Precast Columns with Reinforcement Length of 2’-4” and 3’-10” (Kotha, 2024) 290

Figure 6-82: Reinforcement Stresses at Failure Load, 300 Kips of Axial Load (Kotha, 2024) 291
Figure 6-83: Tensile Region Crack Pattern Comparison for 40.25 in. Eccentricity Analysis at 300 Kips of Axial Load (Kotha, 2024) 292
Figure 7-1: P-M interaction diagram design flow chart 296

Chapter 1. Introduction

1.1. Overview

In today's fast-paced world, the prefabrication of reinforced concrete (RC) bridge components stands as a beacon of hope for accelerating the construction of vital infrastructure projects. This innovative approach not only expedites construction timelines but also minimizes traffic disruptions and, most importantly, enhances the safety of workers during the construction process.

While the utilization of prefabricated RC components has become a global norm, the potential of precast bridge substructures, specifically precast columns, remains underexplored in Texas. Recognizing the need to bridge this gap and develop suitable solutions, the Texas Department of Transportation (TxDOT) initiated Project #0-6978-1 in 2019. The project's primary objective was to gather information on successful precast column implementations from across the United States and around the world. It aimed to collect invaluable design guidelines and construction insights to facilitate the effective and confident use of precast column systems in the Lone Star State.

During the course of Project #0-6978-1, three major types of connections for precast columns were identified: individually grouted connectors, post-tensioning, and socket/pocket connections. Following a comprehensive analysis of these connection methods, it was suggested that details involving pocket connections and connections with reinforcing bars extending into corrugated grouted ducts are among the most suitable choices for Texas bridge constructions. These approaches have already proven their effectiveness in several construction projects in the state. Additionally, the system involving precast shells with a cast-in-place (CIP) core was recommended for cases where the self-weight of the column is a constraint. However, it was noted that this system required further improvement and investigation for better implementation.

Building upon the conclusions of Project #0-6978, TxDOT launched Project #0-7089, the ongoing research project aimed at further refining precast column solutions that align with TxDOT standards. The chosen approach for this project centers on precast shells with a CIP core and pocket connections to anchor column reinforcement. This system was selected for its practicality and efficiency in providing a lightweight precast solution when column self-weight is a consideration.

A similar system had previously been used in Waco, Texas; however, it embedded the reinforcing cage within the CIP core, which reduced the effective depth of reinforcement and did not yield significant construction time savings. To address this, the design of the precast column shell system must be improved by rearranging the steel reinforcement within the concrete shell. Furthermore, the project investigates and optimizes the composite action between the shell and the core. It also focuses on developing and validating connection details for footings and precast bent caps, with a primary consideration being rebar extensions into pocket connections in the bent cap and rebar extensions from the footing anchored in the concrete core.

This comprehensive research project combines both experimental and analytical techniques to design and validate standard practices and connection details for the proposed precast column system. To achieve its objectives, the research team has outlined six key tasks: literature review, conceptual design of precast column systems, experimental investigation of interface shear behavior between concrete elements, large-scale structural testing on precast column systems, finite element modeling of precast column systems, and the formulation of design recommendations. The findings and procedures of each work task are presented in this report, collectively paving the way for Texas to revolutionize bridge construction with faster, safer, and more efficient precast column solutions.

1.2. Project Objectives

Texas Department of Transportation (TxDOT) Research Project 0-7089 is funded by the TxDOT. This project develops precast column solutions and provides appropriate design guidelines for Texas. The primary goals of the project include (a) developing cost-effective bridge column solutions employing precast hollow sections with a cast-in-place (CIP) core, (b) characterizing the composite behavior between precast elements and CIP concrete in precast shell columns and connections, (c) conducting large-scale laboratory tests and finite element analysis to validate the constructability and structural performance of the proposed precast column systems and connections, and (d) developing design guidelines and draft specifications for implementation of precast columns in Texas bridges.

1.3. Project Scope

The current research project aims to address the following technical tasks:

- Developing design concepts and construction details for precast concrete columns including precast shell sections with a CIP core. The proposed system targets the use of pocket connections with bent caps and CIP connections with footings for simplicity.
- Experimentally investigating interface shear strength between precast elements and CIP concrete. Different surface preparation and types of concrete are investigated to ensure composite action while optimizing designs by eliminating interface reinforcement.
- Evaluating the constructability and structural performance of precast column systems and the connections using large-scale laboratory tests and finite element analysis.
- Developing design guidelines, standard details, and draft specifications for the proposed precast column systems based on the results of the research.

1.4. Organization

Chapter 1: Introduction

- Provides an overview of the research objectives, significance, and the need for innovation in precast column solutions in Texas.
- Outlines the structure and organization of the report.

Chapter 2: Literature Review

- Offers a review of existing literature, including the bridge constructions utilizing precast columns across the states.
- Reviews studies related to precast column systems and interface shear behavior worldwide. Relevant code provisions are included.
- Highlights key findings and identifies knowledge gaps to be addressed in this research.

Chapter 3: Precast-CIP Interface Shear Behavior

- Introduces the experimental program designed to evaluate the behavior of interface shear capacity between a concrete shell and a concrete core using smaller specimens.
- Describes the methodology, instrumentation, and data collection procedures used in the experiments.
- Presents test results, data analysis, and evaluation of the strength of precast-CIP interface.

Chapter 4: Full-Scale Experimental Program

- Presents the full-scale experimental program conducted to assess the behavior of the developed precast column solution.
- Provides insights into the testing procedures, results, and their implications.
- Introduces a procedure step by step of the precast column solution assembly.

Chapter 5: Data Analysis from Large-Scale Testing

- Analyzes the results of experiments and compares them to the conventional column system in terms of serviceability and ultimate strength.
- Studies the embedment length used in the specimens, the differences in the internal roughness, and its effect on the capacity.
- Presents the effect of the development length of the prestressing strands in the precast column solution's capacity.
- Provides several models to determine the precast column solution capacity.

Chapter 6: Finite Element Analysis

- Presents a finite element analysis of the test specimens in the previous chapters.
- Discusses modeling techniques for precast column systems with interface shear behavior and complicated connection performance.
- Provides parametric analysis and numerical data to assist in developing design recommendations.

Chapter 7: Design Guidelines and Recommendations

- Offers practical design guidelines and recommendations for engineers and practitioners to implement the developed precast column system effectively.

Chapter 8: Conclusions

- Summarizes the key findings and contributions of the study.
- Highlights the significance of the research in advancing bridge construction technology.

Chapter 2. Literature Review

The chapter presents a review of studies and construction projects related to precast column systems with an emphasis on full-height precast reinforced concrete (RC) columns and precast concrete column shells. Connection design and detailing are also focused. Studies and code provisions about interface shear properties are also included.

2.1. Precast Column Systems

In 2019, TxDOT launched a project that reviewed and recommended potential precast column solutions to be used in Texas. The results were summarized in the synthesis report in TxDOT Project 0-6978 (Fawaz et al. 2019).

In the synthesis report, it was identified that three major types of precast column systems (full-height precast RC column, precast segmental columns, and precast concrete column shells with CIP core) have been used in bridge projects, as shown in Figure 2-1.

(a) Full-height precast column

(b) Precast segmental column

(c) Precast column shell

Figure 2-1: Main types of precast column systems

- Full-height precast RC columns:

  This system uses a single precast column element that is designed and detailed like conventional cast-in-place (CIP) reinforced concrete columns, shown as Figure 2-1(a). It is generally considered as the most practical system in terms of fabrication due to the small

number of connections. However, its application may be limited by the column self-weight and erection equipment capacity. The system comprises two connections, one at the footing level and a second one between the column and the bent cap. These connections can be executed by embedding the column longitudinal reinforcement into the adjacent member using grouted ducts or pockets. Alternatively, the column longitudinal bars can be coupled with reinforcement dowels from the adjacent member using grouted splice couplers or mechanical splice connectors. Another method used to connect a precast column to a footing is through a socket connection where the entire column section is embedded in the footing before the casting of the footing. A variety of cross-sections can be used for this system, but in general rectilinear shapes are preferred over curvilinear geometries for fabrication and transport (Atkan and Attanayake 2013). While this system is prevalent in states using precast columns, it has not been used in Texas (Fawaz et al. 2019).

- Precast segmental columns:

  This system comprises several precast column segments that are joined together on site (Figure 2-2f). This system is efficient for tall bridges and is generally required when the height or size of the columns is such that the use of a full-height system is not practical or not possible due to limitations in weight and/or dimensions for transportation and on-site erection. Column segment connections can be executed by splicing the vertical reinforcement with grouted splice couplers or by post-tensioning the joints.

- Precast concrete column shells with CIP core:

  This system comprises precast hollow elements with thin walls that serve as permanent formwork of a CIP concrete core (Figure 2-1c). The system could be regarded as an alternative to segmental systems when full-height column systems cannot be used due to weight limitations. The system has been used only once in the United States in Texas. During the construction, a shell was first precast to serve as permanent formwork. The shell was then erected on site at the spot where a reinforcement cage was installed. CIP concrete core was cast after the installation.

  However, this design reduces the effective depth of the reinforcement and the composite action between the shell and the core remains unclear. Fabricating massive reinforcement cages on site does not provide major savings. The system needs could be improved by embedding the reinforcing cage in the precast shell, and more investigation into the composite action is needed to ensure good structural performance.

  A similar system developed in Japan uses precast panels as permanent formwork for short solid piers; for taller piers, the panels are used as structural elements to build hollow sections (Ralls et al. 2005). The structural performance of the Japanese system is similar to that of the CIP piers according to experimental testing.

In addition to precast columns, different types of connections and technologies have been used to connect a precast column to a footing or cap beam and to connect precast column segments

together. Generally, six types of connections used in previous bridge projects were identified in the project 0-6953 (Fawaz et al. 2019).

- Rebar extension into corrugated ducts (see Figure 2-2(a)):

  These connections use corrugated ducts (such as standard post-tensioned ducts) that are installed in the precast element during fabrication. During erection, vertical bars are inserted into those ducts before grouting is applied. It accommodates large tolerances and is not expensive. When using this connection, special attention should be given to durability problems due to relatively large, exposed areas. This connection is widely used in Texas.

- Rebar extensions into grouted pockets (see Figure 2-2(b)):

  This type of connection requires voided pockets in the adjacent elements. During erection, rebars extending from the columns are inserted into the pockets before grout or concrete is injected. The system can be used to connect precast column elements to a footing and a cap beam. As expected, this connection provides larger tolerances than grouted vertical duct connection, but it also has a higher risk of moisture penetration and durability problems. Another possible disadvantage is the more significant interference of column longitudinal bars and reinforcement in adjacent elements. Similar to the grouted duct connection, the pocket connection is also frequently used in Texas.

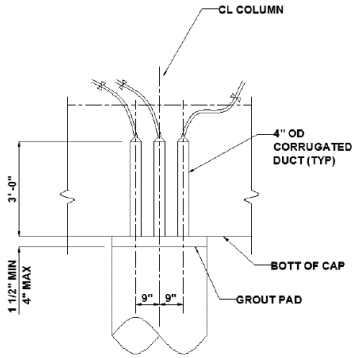

(a) Rebar extended in to corrugated ducts
Aktan and Attanayake (2013)

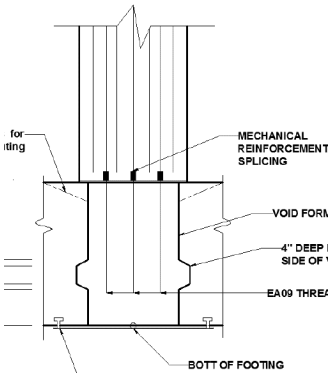

(b) Rebar extensions into grouted pockets
Aktan and Attanayake (2013)

(c) Socket-type connections
Haraldson (2013)

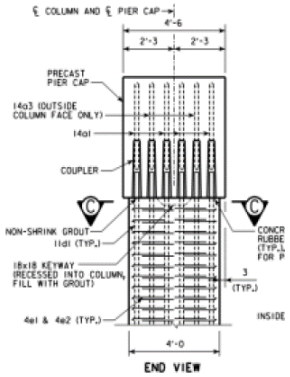

(d) Grouted splice/sleeve couplers
Khalegi et al. (2012)

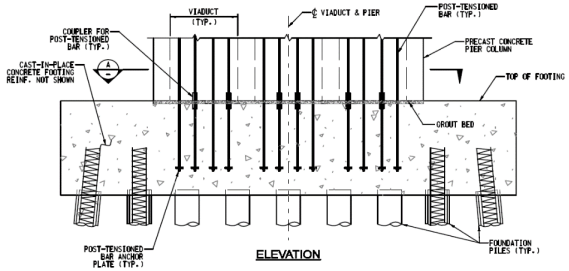

(e) Post-tensioned joints
FHWA (2009)

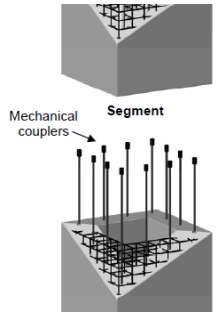

(f) Mechanical splice connectors
Ou (2007)

Figure 2-2: Summary of precast column connection details

- Socket-type connections (see Figure 2-2(c)):

  This connection is executed by extending the precast column into the footing and casting the reinforced concrete footing around it. This approach provides excellent structural performance according to the experimental program by Haraldsson et al. (2013). Socket connections require no bars extended cross the footing interface, and no grouting is required, which can lead to better constructability. The connection has been used only once in a bridge project, and that was in a demonstration project in Washington State.

- Grouted splice/sleeve couplers (see Figure 2-2(d)):

  The connection is executed by splicing the vertical reinforcing bars in grouted coupling devices, which are typically proprietary. Sleeves are first cast in the precast element and are grouted. After that, the connecting reinforcement is inserted into the sleeves during erection. This type of connection can be used to connect a column to a cap beam, a column to a footing, and a column-to-column joints. Grouted couplers provide reliable performance and ensure the full development of longitudinal reinforcement. In addition, due to the minimal exposed surface, no durability problems are expected. These couplers are, however, proprietary and require higher construction accuracy, which can lead to excessive costs. Pressure grouting may also be considered as another limitation of this technique.

- Post-tensioned joints (see Figure 2-2(e)):

  Post-tensioning steel bars are installed in the column elements and adjacent members. The bars are coupled at the joint levels and post-tensioned. This connection is generally applied with segmental precast columns. The execution of this connection is time-consuming and can lead to longer construction times. Nevertheless, column segments reduce weight and required size for delivery.

- Mechanical splice connectors (see Figure 2-2(f)):

  Mechanical couplers are used to connect vertical reinforcing bars extending from the column or adjacent member. This connection has been rarely used in the U.S.

2.2. Projects with Precast Column Systems

This section summarizes the construction projects involved precast column systems in the U.S. Selected cases according to Project 0-6978 (Fawaz et al. 2019) are reviewed in this section. Two categories are generally identified: full-height precast RC columns and precast concrete column shells with CIP core.

2.2.1. Projects with Full-height Precast RC Columns

According to a survey conducted in Project 0-6978 (Fawaz et al. 2019), the full-height precast column was found to be the most popular precast column system used by State DOTs. The survey

showed that out of 18 DOTs that reported using precast columns in bridge projects, 15 DOTs had used the full-height precast column.

As part of an interchange on 85 Interstate, the Georgia DOT constructed its first bridge with substructure elements in 2006. With the use of precast columns, construction time was reduced, impact to traffic was minimized, and worker and work zone safety was increased. The project used the design-build contracting method, which, in combination with the precast construction methods, saved 45% over traditional methods, according to Mallela et al. (2013). Full-height square precast columns and precast pier caps were used in this bridge. Figure 2-3 shows the column and pier cap installation procedure. The connection between the column and the footing consists of reinforcing bars extending from the footing and grouted into splice couplers embedded at the base of the column. The connections between the columns and bent caps also comprise grouted splice couplers, which are shown in Figure 2-4. The splice couplers had a built-in tolerance in order to account for construction errors, facilitating the assembly of the substructure elements.

Figure 2-3: Precast columns and pier caps in I-85 interchange project (Mallela et al. 2013)

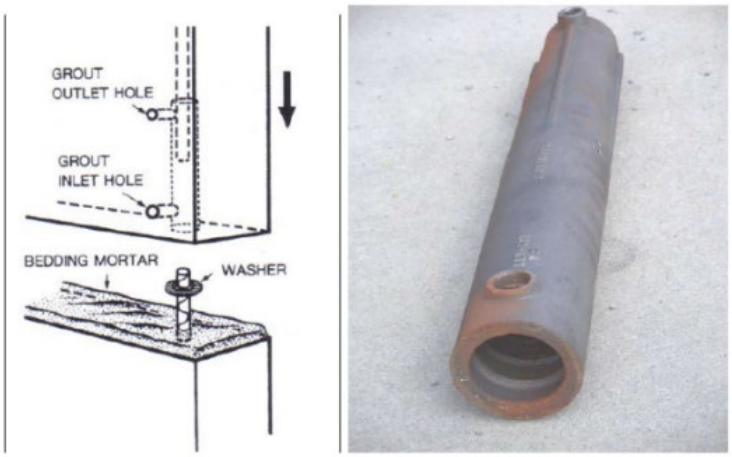

Figure 2-4: Coupler used to splice rebar used in I-85 interchange project (Mallela et al. 2013)

The Parkview Avenue over U.S. 131 is another pioneer project that used full-height precast columns. The project was built by Michigan DOT in 2008 and is the first ABC project in the state. The Parkview Bridge in Kalamazoo has four spans and three lanes. Piers, abutments, I-beam girders, and full-depth deck panels were all prefabricated off-site. Four 10-ton round precast columns were used for each interior support (see Figure 2-5). CIP footings contained square pockets at the column locations, and column longitudinal reinforcing bars extended into the pockets and were grouted in place. The columns were connected to the precast cap by means of column longitudinal rebar extensions grouted into 4-in. vertical metal corrugated ducts embedded in the cap beam as shown in Figure 2-6. Difficulties in aligning the column bars and the corrugated ducts in the cap beam have been reported by Attanyake et al. (2012).

Figure 2-5: Precast columns in casting yard in Parkview Avenue Bridge (Attanyake et al. 2012)

Figure 2-6: Precast bent cap being erected in Parkview Avenue Bridge (Attanyake et al. 2012)

Due to high traffic volumes, Wisconsin DOT used the full-height precast column system in the Rawson Avenue Bridge and the Siggelkow Road bridge in 2013 and 2014, respectively. The former project was a replacement of the two-span bridge crossing I-94 on Rawson Avenue. Project goals included limiting the impact to I-94 to just one 12-hour closure and reducing the Rawson Avenue closure from six months (as required using conventional construction methods) to three weeks. Precast caps and full-height precast columns with varying cross-sections along their heights were used in this project. Figure 2-7 shows a photo during the construction of the bridge. Grouted couplers were used in the column connections at both the footing and cap beam levels (see Figure 2-8). The second project, Siggelkow Road Bridge on I-39, is part of the I-39/90 Expansion Project in Madison, Wisconsin. It was the first bridge project on I-39 to use ABC techniques. The project used five 16-ft-5-in.-tall square precast columns, which were erected over CIP footings (see Figure 2-9). Grouted sleeves were used to connect the precast columns to the footings and pier caps. During construction, the contractor found that the size and location of the couplers left no room to place stirrups in the column. This required DOT involvement to approve a change in design, but no major delays were reported.

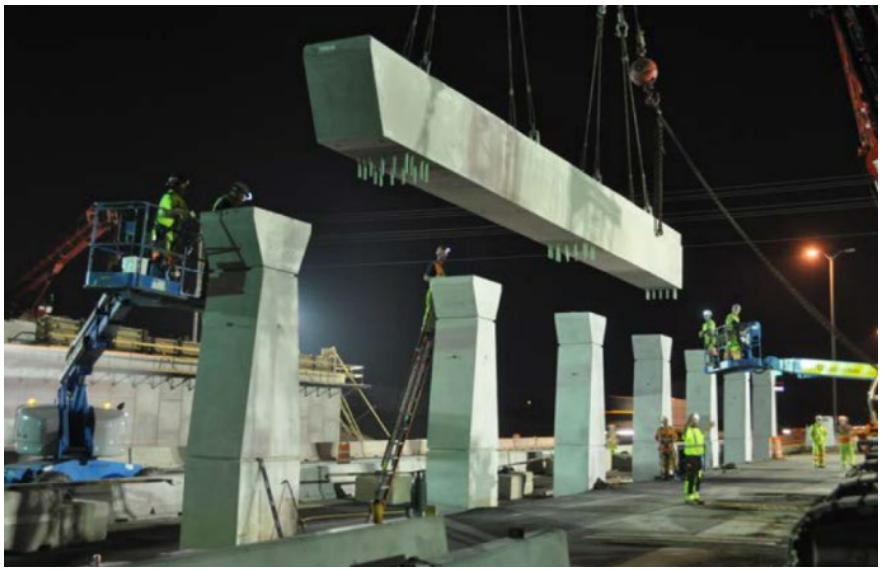

Figure 2-7: Pier cap erection in Rawson Avenue Bridge (Olivia 2014)

Figure 2-8: Precast column in Rawson Avenue Bridge (Olivia 2014)

Figure 2-9: Precast column during placement, Siggelkow Road Bridge (source: www.countymaterials.com)

Full-height precast columns were also used with drilled shaft foundations, as in the case of the replacement of the existing U.S. 6 Bridge over the Keg Creek in Iowa in 2014. The structure was completely prefabricated except for the CIP drilled shafts. The use of prefabricated elements reduced the time the bridge was out of service to 16 days, which significantly benefited the mobility of the area. Figure 2-10 shows the installation of the square full-height precast columns in the new Keg Creek Bridge. The project was the first bridge to use grouted splice couplers in Iowa. Individual grouting was used instead of mass grouting. Figure 2-11 and Figure 2-12 show the column connection to the column cap and drilled shaft, respectively. Based on the project experience, it was recommended to have templates for the grouted splice connections, given their reduced tolerances.

Figure 2-10: Precast column installation using grouted splice couplers in Keg Creek Bridge (Littleton 2013)

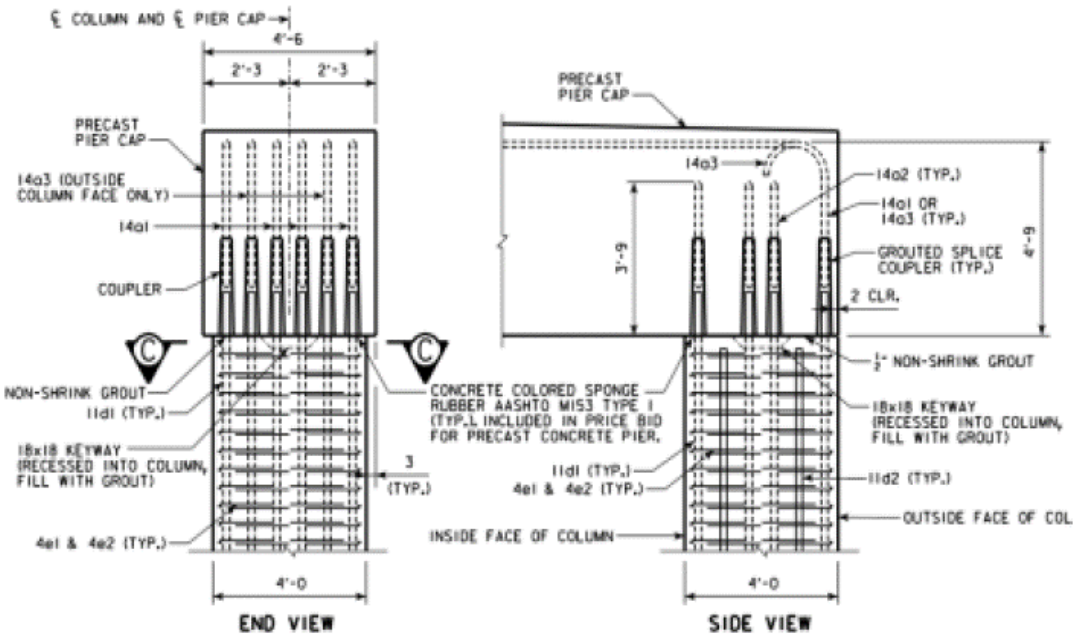

Figure 2-11: Precast column-to-cap beam connection in Keg Creek Bridge (Littleton 2013)

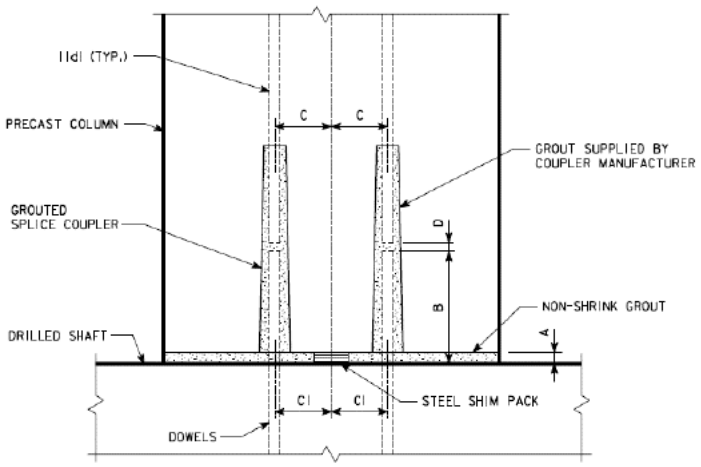

Figure 2-12: Precast column-to-footing connection in Keg Creek Bridge (Littleton 2013)

The full-height precast column system completed in the Moore's Mill Road Bridge in Alabama in 2019 shows a way of improving the column surface aesthetics (see Figure 2-13). This surface modification was achieved by using metal forms, which included a faux brick form liner. The bridge is a five-lane prestressed concrete bridge that was built to replace an old two-lane reinforced concrete deck bridge. Six full-height precast columns were used in this project. The use of precast columns resulted in a time saving of eight days and improved safety at the construction site. The columns were 19 ft 9 in. tall and had a 3-ft square section. The columns were connected to the footing using grouted splice couplers. To provide reasonable tolerance during the erection, No.14 sleeves were used for the No.11 longitudinal dowel bars. Some complications were reported for

injecting the grout in the bottom port of the couplers. The contractor solved the problem by partially grouting the couplers from the top port and then continued the grouting in the bottom port.

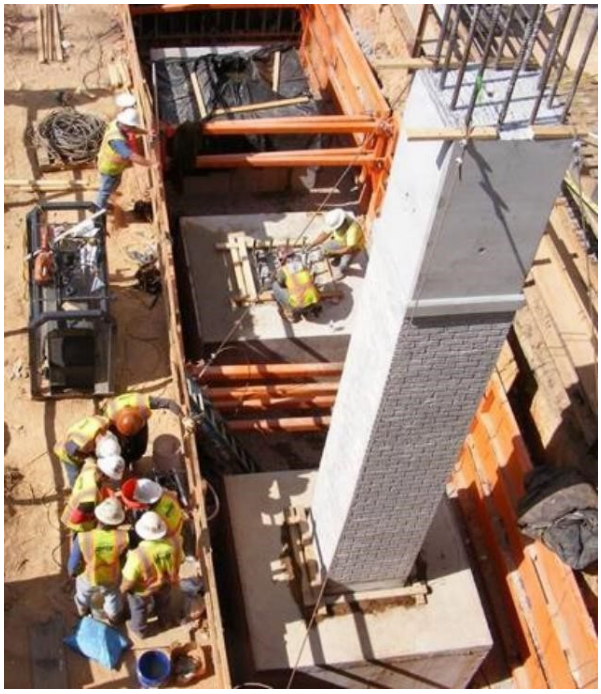

Figure 2-13: Erection of the precast column in Moore's Mill Road Bridge (City of Auburn 2019)

The Laurel Street Overcrossing in California is an example of using the full-height precast column system in a seismic region. The bridge in Vallejo is the first multi-span full ABC project in the state. This pilot project, conducted in 2017, implemented research on seismic connections of precast elements and involved round precast columns (19-ft-long and 5-ft-diameter), precast bent caps, and precast wide flange girders. The columns were cast with an oversized formed hole (20 in.) to be connected to the footings using a 12-in.-diameter shear key, as shown in Figure 2-14. The column-to-cap connection was finished using ducts filled with ultra-high-performance concrete (UHPC). Twenty No.14 column reinforcing bars extended in 4-in.-diameter galvanized metal ducts embedded in the bent cap. After installing the bent cap, the shear keys at the base of the columns supporting the bent cap were grouted with non-shrink grout (see Figure 2-14), and the ducts of the column-to-cap connection were filled with UHPC. The full erection of the two columns and the bent cap took only one morning. After this project, a second ABC pilot project was conducted by Caltrans on Route 46/99. The main difference with the Laurel Street Overcrossing was the use of slightly smaller diameter columns (4.5 ft instead of 5 ft) that caused congestion issues in the cap. Accordingly, Caltrans recommended the use of a larger column size to alleviate congestion in the cap.

Figure 2-14: Erection of precast column in Laurel Street Overcrossing (Mellon 2018)

2.2.2. Projects with Precast Concrete Column Shells and CIP Core

There has been only one bridge that used the precast shell system in the United States, according to a study by Fawaz et al. (2019). The bridge was constructed on LP-340 over IH-35 in Waco in the late 2000s. It consisted of four multi-span bridges and used full-height precast column shells infilled with CIP concrete. The column shells, which had 7-in thick walls, were lowered down over the column cages, secured in place, and filled with CIP concrete. The use of column shells eliminated the need for column forms and accelerated the construction process. The use of a CIP core reduced the weight of the precast elements, which allowed the use of larger elements and eased the handling on site. However, this concept presented some limitations related to the grade control and reduced effective depth of the column longitudinal reinforcement, as reported by Hewes (2013). Since the column cage was not included in the precast shell, the system did not offer significant time savings. Figure 2-15(a) through (c) show various stages of construction of the LP340/SH 6 bridges.

(a) Lifting

(b) Before core filling

(c) Core filling

Figure 2-15: Precast column shells, LP-340 over IH-35 (Wolf 2005)

2.2.3. Precast Column Systems Proposed in Studies

This section presents past studies on precast column systems, including both analytical and experimental research. Several DOTs in the U.S. have sponsored projects to collect information and provide recommendations related to precast column systems. These include recommendations regarding the geometry of the precast column element, limits on the weights, and the type of connections to be used.

2.2.4. Analytical Studies and Design Recommendations

The first study is an analytical investigation by Hieber et al. (2005) and sponsored by Washington State DOT. Two different precast column solutions were proposed and studied analytically in order to accelerate bridge construction in seismic regions. One had longitudinal reinforcement only, and the other one was a hybrid system with longitudinal reinforcement and unbonded post-tensioning

tendons to provide self-centering capabilities. The configurations of the reinforced concrete system and the hybrid system are shown in Figure 2-16(a) and (b), respectively. Both systems were composed of circular full-height precast columns, precast bent caps, and cast-in-place footings. A socket-type of connection was proposed to connect the precast column to the footing as shown in Figure 2-17. Three types of connections were proposed to connect the column with the cap beam, including a slotted opening connection, a complete opening connection, and an individual splice sleeve connection. While the first two types can be used in both column systems, the individual splice sleeve connection was proposed for the hybrid system, which has less mild reinforcing steel. The results of the analytical study conducted by Hieber et al. (2005) showed that both proposed systems are adequate for seismic applications.

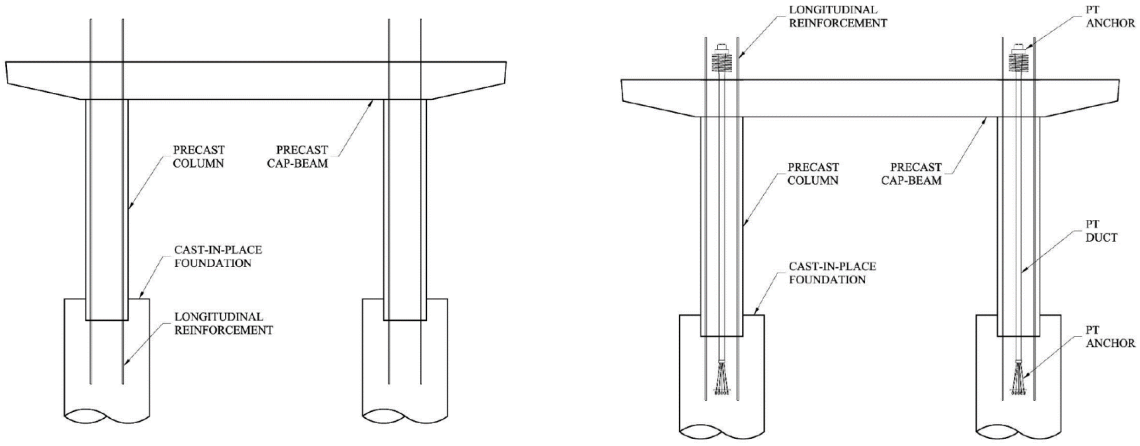

(a) Precast reinforced concrete system *(b) Precast hybrid system*

Figure 2-16: Precast column system proposed by Hieber et al. (2005)

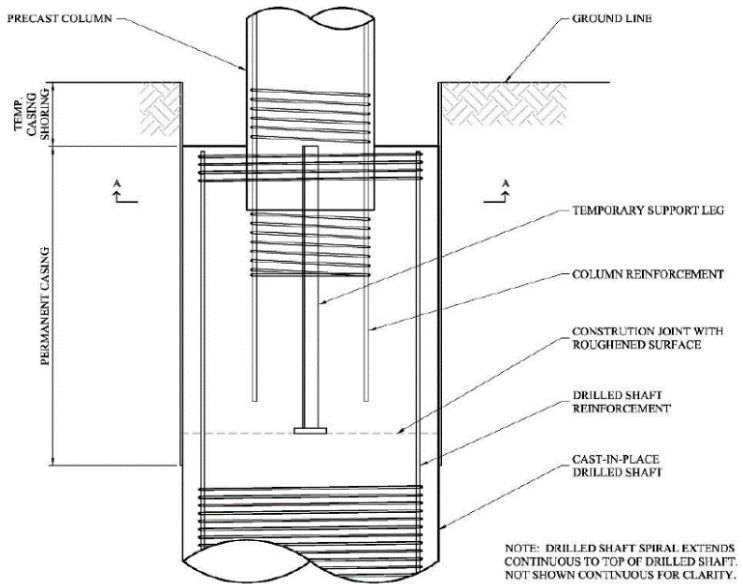

Figure 2-17: Footing-to-column connection proposed by Hieber et al. (2005)

Fouad et al. (2006) conducted a research study for the Alabama DOT and proposed a prefabricated precast concrete bridge system for short-to-medium-span bridges. This system includes bulb-tee girders, rectangular voided bent caps, rectangular hollow columns (see Figure 2-18), and precast abutment caps. A one-piece rectangular hollow precast column was selected for its simplicity and functionality. The use of a hollow section limits the weight of the column and facilitates construction processes. Four different column dimensions are considered in this system, as shown in Figure 2-19. For each column dimension, the required prestressing force, number and size of couplers, and size of longitudinal dowels were provided. All columns satisfy the maximum weight criteria of 100,000 pounds, and a maximum column slenderness ratio, defined by Eq. (2-1), of 100.

$$\frac{(KL)}{r} \leq 100 \tag{2-1}$$

where L is the length of the column, r is the radius of gyration determined as $r = 0.3W$, where W is the width of the column, and K is the effective length factor, assumed to be 2.0 considering fixed end-free end condition.

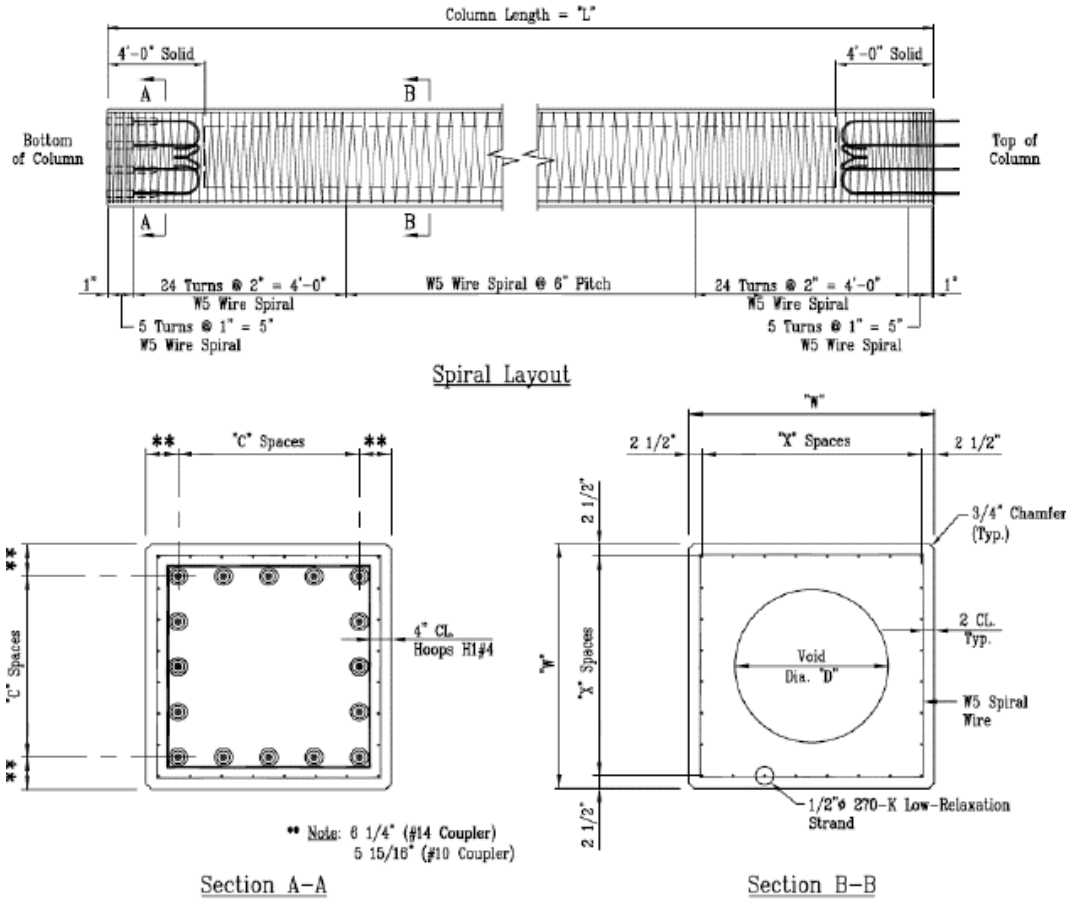

Figure 2-18: Precast column design proposed by Fouad et al. (2006)

Column Properties

Column Size "W"	Void Diameter "D"	Voided Weight per Lin. ft. (kips./ft.)	Area of Voided Cross Section ($in.^2$)	Voided Moment of Inertia ($in.^4$)	Strand Layout ("X" Spaces)	Total Number of Strands	Initial Prestress (psi)	Maximum Casting Length "L"	Mechanical Coupler Layout "C" Spaces (Maximum)	Maximum # of Couplers	Mechanical Coupler Size *	Dowel Size
36"	18"	1.085	1,041.53	134,815	5	20	536	45'-0"	3	12	#10	#9
42"	24"	1.366	1,311.61	243,022	6	24	511	52'-0"	3	12	#14	#11
48"	30"	1.664	1,597.14	402,607	7	28	489	56'-0"	4	16	#14	#11
54"	36"	1.977	1,898.12	626,140	8	32	470	46'-0"	5	20	#14	#11

* Mechanical coupler is oversized to provide additional erection tolerance.

36" – 54" Column Details

Figure 2-19 Characteristics of column systems proposed by Fouad et al. (2006)

The proposed precast column system uses concrete with a specified compressive strength of 6,000 psi at 28 days. A proprietary mechanical coupling system, supplied by Nisso Master Builders (NMB) splice sleeve system, is recommended to connect the column bars with the dowels extending from the footing. After the columns are erected, sleeves are grouted with a non-shrink grout meeting AASHTO requirements. The column is connected to the bent cap in a similar manner. Figure 2-20 shows the connection details at the bottom and the top of the precast column.

In order to reduce cracking in the column, the entire length of the column is pretensioned. Also, chamfering of column corners is recommended to avoid breaking and chipping of those corners during transportation and erection. The report by Fouad et al. (2006) includes a design example for the proposed precast column system.

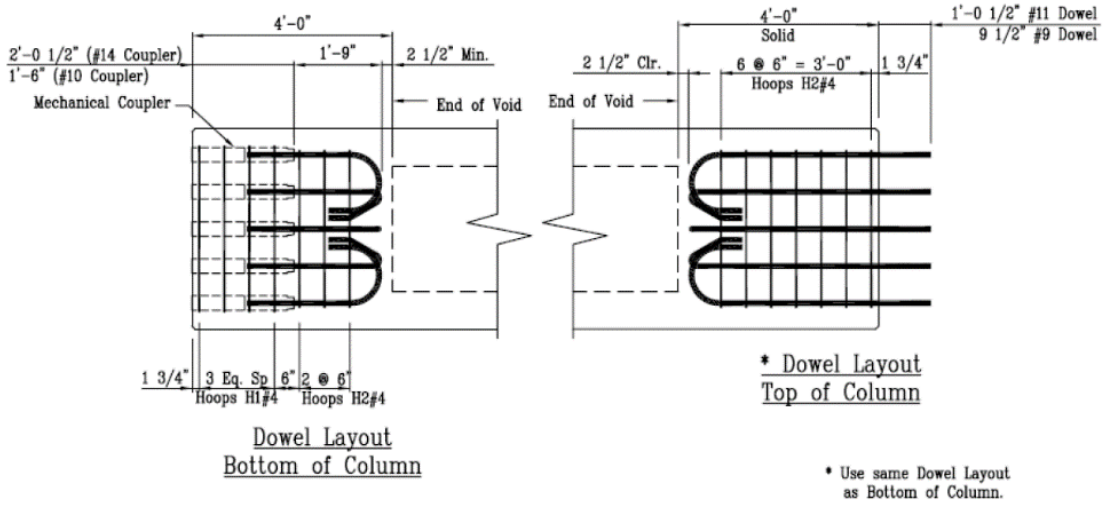

Figure 2-20: Column connections proposed by Fouad et al. (2006)

Another study entitled "Improving Bridges with Prefabricated Concrete Systems" was conducted by Atkan and Attanayake (2013) to investigate prefabricated bridge elements and systems (PBES) and accelerated bridge construction (ABC) technologies to be implemented by the state of Michigan. The study reviewed ABC implementations and provided recommendations for project planning and design, precast fabrication procedures, and construction and operation methods. Recommendations addressed different superstructure and substructure elements, including precast columns and their connections to adjacent elements. The study recommended using rectangular, square, or octagonal column sections over circular sections. The reason is that circular cross-section columns can only be cast vertically, and this makes the fabrication process harder. Also, the octagonal columns and square/rectangular columns are more stable during the shipping and handling process. Some fabrication procedures were recommended in order to overcome the weight limitations of precast segments.

Two types of column-footing connections were recommended in this study. The first one was a grouted splice sleeve and a socket at the footing level (see Figure 2-21), and the second was a pocket connection with a shear key (see Figure 2-22). Three types of pier cap-to-column connections were recommended: a grouted pocket with two layers of reinforcement (see Figure 2-23), a grouted corrugated duct connection (see Figure 2-24), and a vertical splice duct connection (see Figure 2-25). For the different types of connections, the use of a template was recommended, which will allow stringent tolerances for enhanced constructability. This study also provided recommendations for grout material and construction techniques.

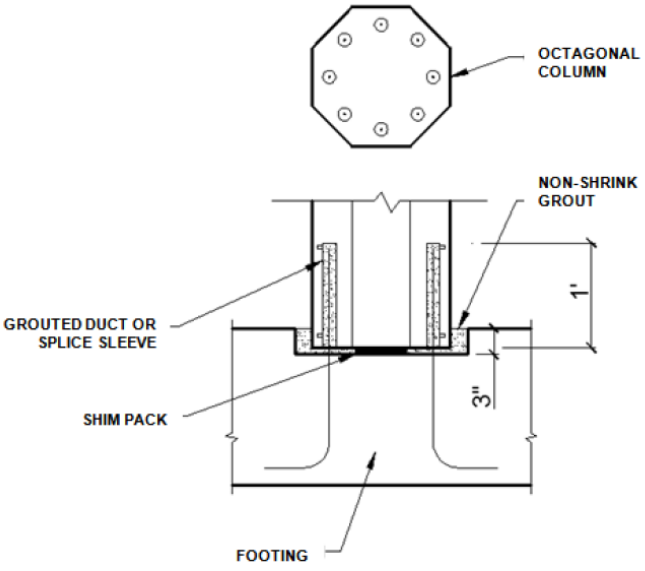

Figure 2-21: Precast column-footing connection with grouted duct/splice sleeve and socket connection proposed by Aktan and Attanayake (2013)

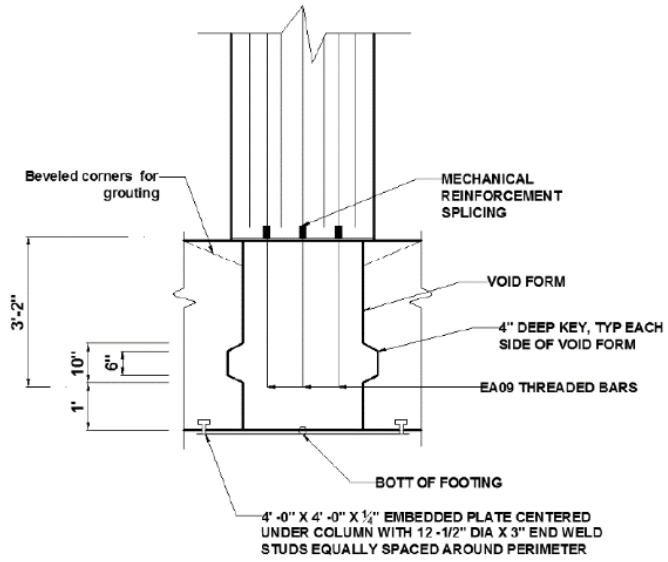

Figure 2-22: Precast column-footing connection with grouted void/pocket and shear key proposed by Atkan and Attanayake (2013)

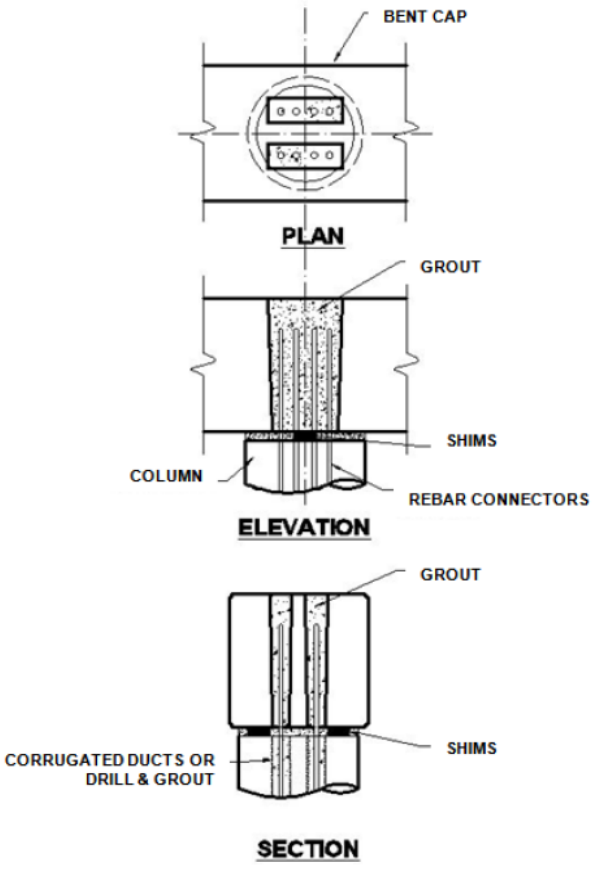

Figure 2-23: Precast column to bent cap connection with grouted pocket (Restrepo et al. 2011)

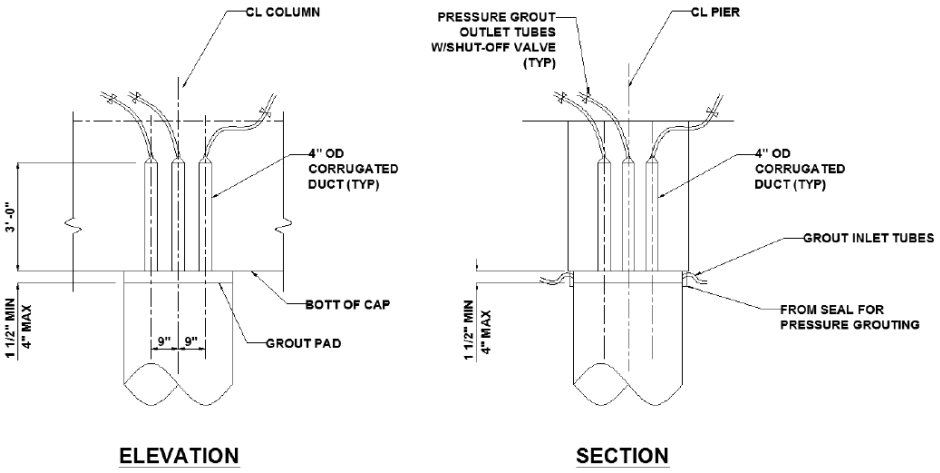

Figure 2-24: Precast column to bent cap with grouted corrugated duct connection (Atkan and Attanayake 2013)

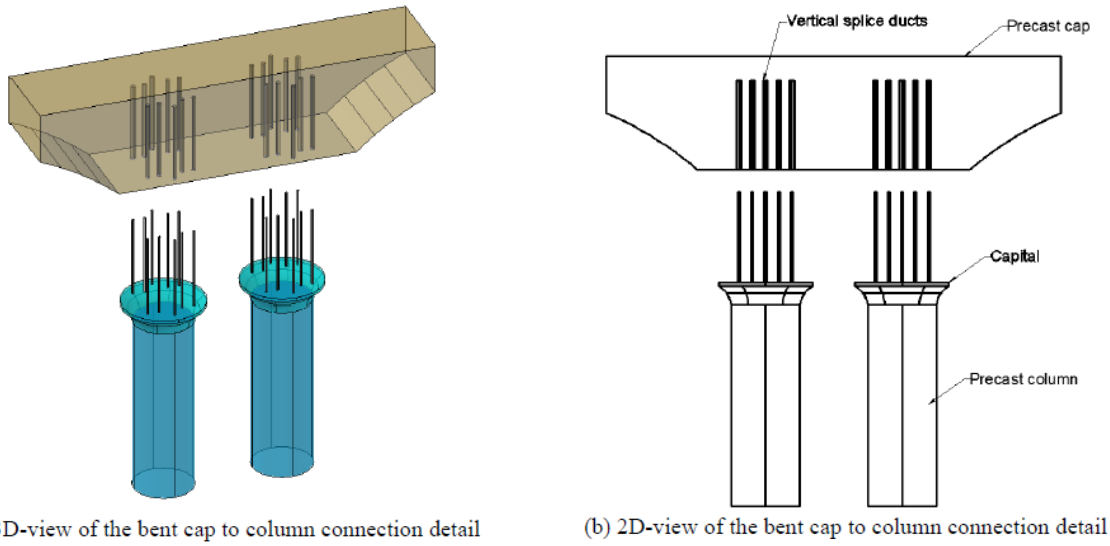

Figure 2-25: Vertical splice duct connection between precast column and precast bent cap (FHWA 2009)

In 2004, the FHWA, the American Association of State Highway and Transportation Officials (AASHTO), and the National Cooperative Highway Research Program (NCHRP) sponsored a scanning study to collect information about the use of prefabricated bridge elements and systems in Japan and Europe (Ralls et al. 2005). The outcome of the study was a report entitled "Prefabricated Bridge Elements and Systems in Japan and Europe." Regarding the use of precast substructure systems, the report only recommended the Japanese SPER (Sumitomo Precast form for resisting Earthquakes and for Rapid construction) system, which is similar to the precast shell system. The system is comprised of bridge piers that employ stay-in-place precast concrete panels to work as both structural elements and formwork for a CIP concrete core. In this system, short piers are solid and have precast panels in the exterior, as shown in Figure 2-26. Tall, hollow piers have panels for both the inner and outer faces, as shown in Figure 2-27. For both short and tall panels, segments are stacked on top of each other using joints epoxied together and then are filled with CIP concrete. The system was proven to have an outstanding seismic performance while reducing construction time and providing a high quality, durable external finish.

Figure 2-26: SPER system using short pier panels (Ralls et al. 2005)

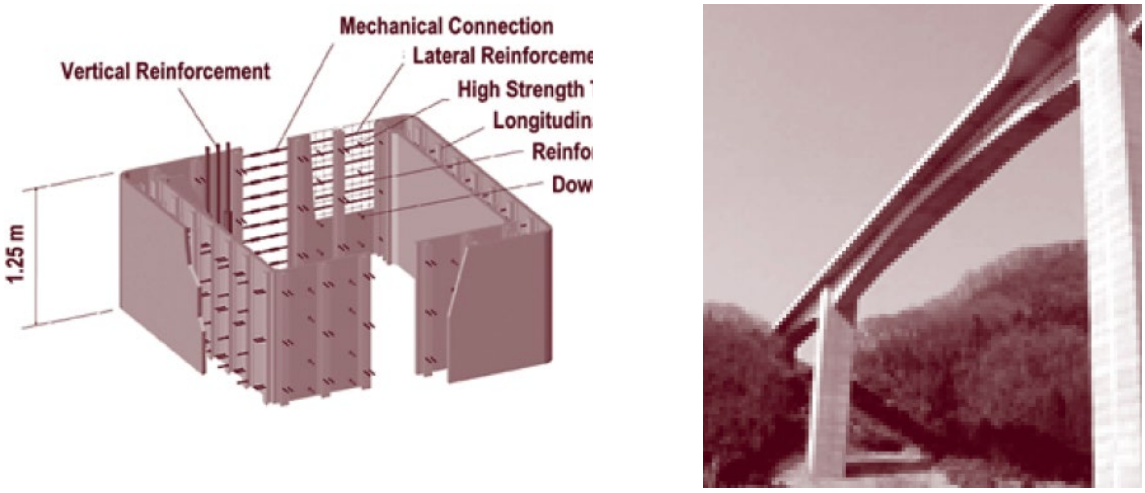

Figure 2-27: SPER system using tall pier panels (Ralls et al. 2005)

2.2.5. Experimental Research

This section includes four studies related to columns and their connections, some within seismic regions. There were a few experimental investigations about precast column systems and precast column connections. Cases related to the segmental precast column system are excluded from the discussion.

The first investigation was conducted by Pang et al. (2008) and sponsored by Washington State DOT. It studied the connection between precast columns and bent caps using large-diameter vertical column bars extended into corrugated grouted ducts embedded in the cap beam. It was considered that using a smaller number of large bars speeds up the connection process and results in more generous construction tolerances. Large-scale tests were conducted on column-cap beam subassemblies. The cap beam joint reinforcement and grouted ducts are shown in Figure 2-28(a); Figure 2-28(b) shows one of the test specimens, which were subjected to cyclic lateral loading. The test specimens included a reference cast-in-place specimen and three precast specimens with a large bar connection. The bars of one of the precast specimens were fully grouted into corrugated ducts, while in the other two specimens, bars were debonded over a length of eight bar diameters using two different debonding methods.

Test results showed that the cyclic behavior of the proposed connection is comparable to a cast-in-place connection in terms of both strength and ductility. Short length debonding had little effect on the seismic performance of the connection. The study provided recommendations for the design and field implementation of the system. The development lengths of the vertical column bars in the grouted ducts were selected based on the recommendations of Steuck et al. (2007). These recommendations established minimum development lengths of six times the bar diameter to yield the bar, and 14 times the bar diameter to fracture the bar, given an 8,000-psi grout and monotonic loading. For cyclic loading, the minimum lengths should be increased by 50%.

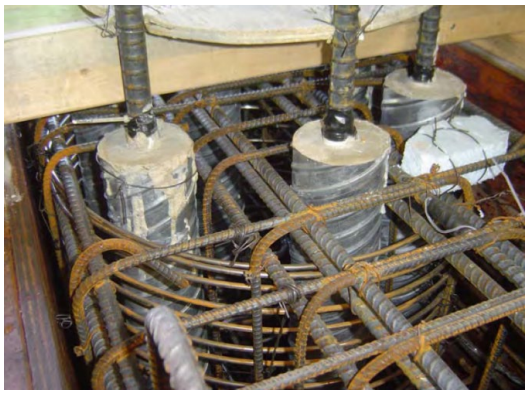

(a) Cap beam joint region with grouted ducts

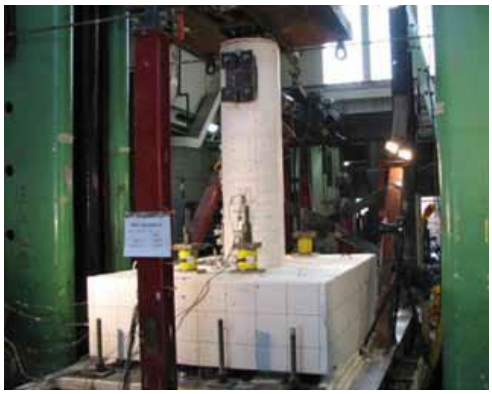

(b) Testing of the column-bent cap connection

Figure 2-28: Precast column system developed by Pang et al. (2008)

The second investigation conducted by Haraldsson et al. (2013) was also sponsored by Washington State DOT. The study developed and tested a socket connection between a precast column and a footing as shown in Figure 2-29. This system can result in major construction time reductions and can provide better constructability with no bars crossing the column-footing interface. The approach grouting required no grouting. The socket connection results in transfer of forces in the connection region as illustrated in a strut-and-tie model presented in Figure 2-29(a). Column-footing subassemblies using this type of connection were tested under axial and cyclic lateral loading. The columns had a circular cross-section with a diameter of 20 in. The embedment length of the column inside the footing was 1.1 times the column diameter. The portion of the column embedded in the footing had an octagonal cross-section and was roughened using the saw-tooth pattern prior to casting the footing [see Figure 2-29(b)]. The roughness, which was in accordance with the WSDOT design manual, satisfied the AASHTO LRFD requirement for surface transfer shear friction terms of minimum amplitude. Some additional diagonal reinforcement was provided in the horizontal plane to induce shear friction resistance to the column pushing through the footing.

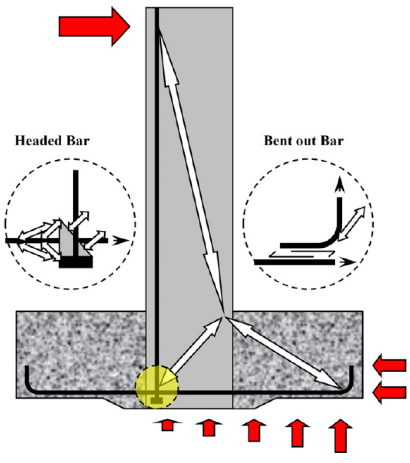

(a) Force transmission for socket connections

(b) Construction in the field

Figure 2-29: Socket connections proposed by Haraldsson et al. (2013)

Test results showed that columns with this type of connection behave similarly to cast-in-place systems under cyclic loading, and no column slip was observed in the tested specimens under axial loading. Diagonal reinforcement was found unnecessary and could be eliminated. In addition, the study recommended the use of headed bars in the column to provide partial anchorage.

In 2011, the proposed socket connection was used in the replacement of the U.S. 12 bridge over Interstate 5 in Washington State. Figure 2-30 shows the precast column erection before casting the footing. It is worth mentioning that precast column segments were used in the project; however, using the full height column would have been better, according to the contractor.

Figure 2-30: Socket connection between precast column and footing in U.S. 12 bridge (Khalegi et al. 2012)

A more recent study was performed by Cheng et al. (2020) for the Iowa Department of Transportation. The study aimed to create a fully prefabricated bridge pier system, including precast columns and pile caps. Relevant to this project, Cheng et al. (2020) tested a variety of different socket connections, shown in Figure 2-31(a) and (b). The remaining space between the socket and the columns were filled using high-strength, rapid strength-gaining grout. This prevented grout curing from causing construction delays. The fluted fins were found to not be as stiff a connection as the exposed aggregate, and the larger the distance between the socket and column, the less stiff the connection was. The tests were conducted outdoors using a half-scale system. The system was first subjected to vertical loading; then the lateral loadings gradually increased. The test setup is shown in Figure 2-31(c). The study found that under factored design loads, there was no visible damage to the socket connections. It was also found that the embedment depth to develop full flexural capacity sufficiently and safely was roughly the same as one diameter of the column into the footing. An important result from the study was that when there was

predominantly an axial load, most of the force transfer effectively took place in the top half of the connection. The study concluded that socket connections were effective and efficient and were easy to construct and transport. The study also stressed the importance of roughening the interface, as this was necessary to develop satisfactory side shear strength to sustain axial loads used in routine design practice.

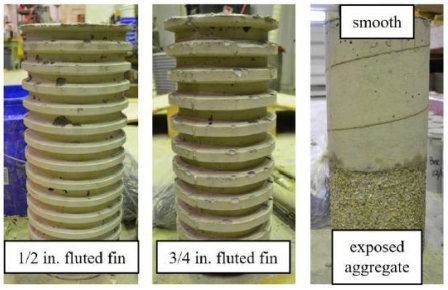

(a) Column socket connections

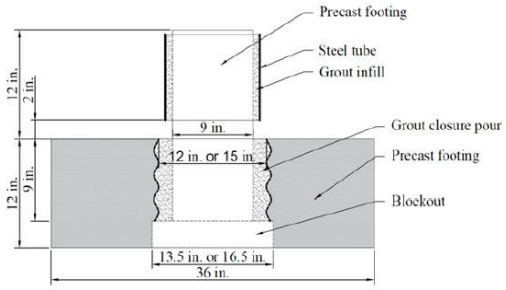

(b) Details of socket connection specimens

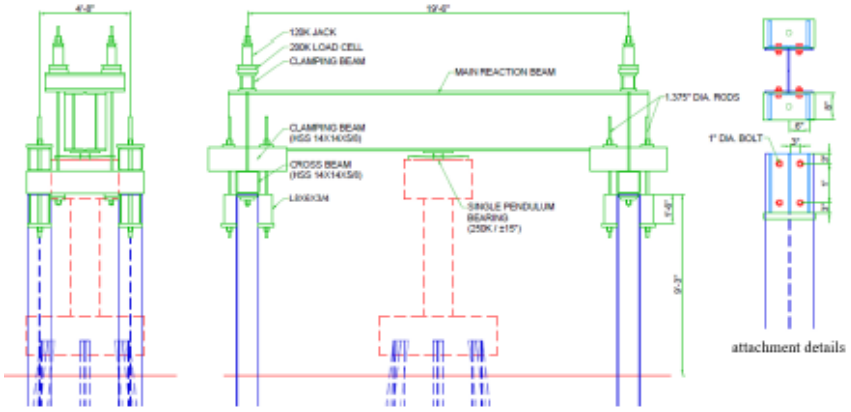

(c)Test setup

Figure 2-31: Study on socket connections by Cheng et al. 2020.

Experimental research has also been performed internationally. Kim et al. (2016) conducted cyclic loading tests on an experimental column design consisting of a CIP concrete-filled precast column. Two experimental columns were developed as shown in Figure 2-32. The first specimen was cast one side at a time, allowing for reinforcement to cross the hollow part of the section. This also allowed easier access to roughening of the interior of the precast portion. The second specimen was cast using an internal mold. This prevented reinforcement from crossing the hollow section. Instead, an additional inner hoop was used to supplement the traditional outer hoop. This led to a slightly thicker outer shell and heavier lifting weight, but easier construction.

This study also investigated the lateral pressure exerted in the column by CIP concrete as it was being poured. The sides of the column were modeled as simply supported beams, and a uniform load was calculated using a modified form of ACI 347-04, reproduced as

$$\rho_{max} = 7.2 + \frac{785R}{T + 17.8} \leq \rho g h \tag{2-2}$$

where R is the rate of concrete placement, T is the temperature of concrete in degrees Celsius, ρ is the concrete density, g is the gravitational constant, and h is the height of the fluid. A maximum flow rate was obtained to prevent cracking. This proved to be an effective method, as measured pressures were generally lower than predicted, but the study notes that more research into this topic is required.

Specimen 1, specimen 2, and a monolithic control column were all tested under combined axial compression and lateral cyclic loading using the testing setup shown in Figure 2-33. The study concluded that by using hollow sections with a CIP core, the lifting weights were reduced by 62% and 51% for specimens 1 and 2, respectively. The study also found that both specimens showed similar hysteresis behavior compared to an RC column. However, both specimens were shown to have a much lower ductility compared to the control column, but the initial stiffness of all three was roughly equivalent.

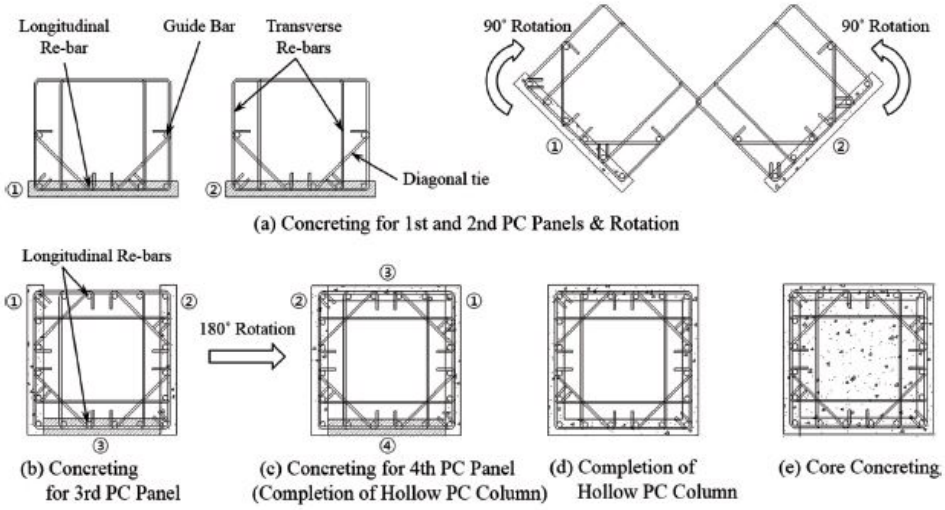

(a) Specimen 1

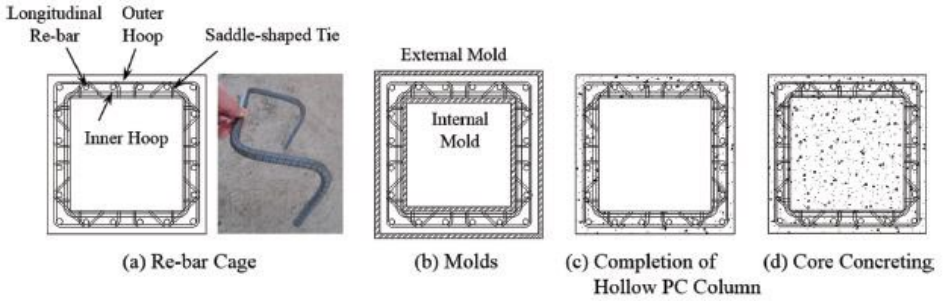

(a) Specimen 2

Figure 2-32: Production method for specimens by Kim et al. (2016)

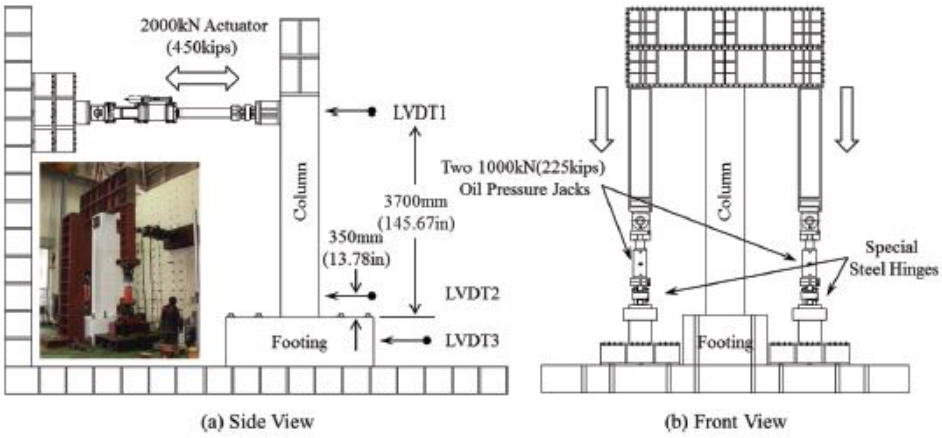

Figure 2-33: Test setup used by Kim et al. (2016)

2.3. Characterization of Interface Shear Properties

As stated earlier, many constraints have been identified when using a full-height precast RC column. An alternative system of a precast shell with a cast-in-place (CIP) core is considered more viable. Such a system is thought to be an appropriate solution because of the potential for a significantly reduced lifting weight compared to monolithic precast columns. A similar system was previously used in Texas but encountered many issues due to the rebar cage not being included in the precast shell (Hewes 2013). It is desired to remedy those issues by developing a system that reduces reinforcing bars over the entire CIP core. The design and implementation of a competitive precast column shell system with a CIP core requires ensuring composite action between the shell and the core. This composite action is provided by the shear resistance of the vertical interface between the precast and CIP concretes. Further, understanding interface behavior will also be beneficial in characterizing socket connections, which interact with the members they connect to through interface shear.

This section reviews current specifications and previous research regarding concrete interface shear to better understand vertical interface shear strength to assist in the design of a precast concrete column shell with a CIP core.

2.3.1. Existing Code Expressions

Design codes provide slightly differing expressions for interface shear strength. It is important to review design specifications to better characterize the current use of interface shear strength in design practice. This review includes three design specifications: ACI 318-19 (2019), AASHTO LRFD Bridge Design Specifications (2020), and fib Model Code 2010 (2010).

2.3.1.1. ACI 318-19

Concrete interface shear strength in accordance with Section 22.9.4 of ACI 318-19 considers the shear friction induced from reinforcement across the interface.

- When reinforcement is perpendicular to the interface:

$$V_n = \mu A_{vf} f_y \tag{2-3}$$

- When reinforcement is not perpendicular to the interface:

$$V_n = A_{vf} f_y (\mu \sin\alpha + \cos\alpha) \tag{2-4}$$

where V_n = nominal shear strength of interface
μ = coefficient of friction
A_{vf} =area of reinforcement crossing the shear plane
f_y = minimum yield strength of reinforcement

In Eqs. (2-3) and (2-4), the coefficient of friction plays an important role in determining the interface shear strength. The factor reflects the roughness of the interface. Three different interface conditions are identified for selecting coefficients of friction in accordance with Table 22.9.4.2 of ACI 318-19, as summarized below.

- For concrete placed against a clean and intentionally roughened concrete:

$$\mu = 1.0\lambda \tag{2-5}$$

- For concrete placed against clean and non-roughened concrete:

$$\mu = 0.6\lambda \tag{2-6}$$

- For concrete placed against clean, as-rolled structural steel:

$$\mu = 0.7\lambda \tag{2-7}$$

In Eqs. (2-5) through (2-7), λ is a factor for lightweight concrete as prescribed by Section 19.2.4 of ACI 318-19.

For example, an intentionally roughened surface between two normal-weight concretes receives a μ-factor of 1.0, while smoother surfaces and different concrete types obtain reduced coefficients. Also, a μ-factor of 1.4λ is specified for monolithically placed concrete. Based on the equations, the minimum required reinforcement across the interface can be determined to resist the shear demand on the interface. It should also be noted that the value of V_n has upper limits under different conditions as prescribed in Table 22.9.4.4 in ACI 318-19.

2.3.1.2. AASHTO LRFD Bridge Specifications 2020

Unlike ACI 318-19, which only accounts for the shear friction mechanism, AASHTO LRFD 2020 allows shear forces across an interface to be resisted by not only shear friction but also cohesion

and aggregate interlock. The nominal interface shear resistance V_{ni} can therefore be formulated given by:

$$V_{ni} = cA_{cv} + \mu(A_{vf}f_y + P_c) \quad (2\text{-}8)$$

where V_{ni} = nominal interface shear resistance (kip)
c = cohesion factor (ksi)
A_{cv} = area of concrete considered to be engaged in shear transfer (in^2)
A_{vf} = area of interface shear reinforcement crossing the interface (in^2)
f_y = minimum yield strength of reinforcement (ksi)
P_c = permanent net compressive force normal to the shear plane (kip)

The equation includes terms for crossing reinforcement, contact area, cohesion, and friction coefficients of the interface. AASHTO LRFD 2020 prescribes cohesion and friction factors for different surface conditions in its Section 5.7.4.4. For instance, for normal-weight concrete placed against a clean concrete surface with roughened amplitudes of 0.25 inches, the code sets cohesion to 0.24 ksi and coefficient of friction to 1.0. For smoother interfaces, the coefficient of friction becomes a reduction factor.

The code requires a minimum amount of reinforcement across the interface, as provided by Eq. 5.7.4.2-1 in AASHTO LRFD 2020. Furthermore, AASHTO LRFD 2020 also specifies maximum allowable shear forces, expressed as equations 5.7.4.3-4 through 5.7.4.3-6 to prevent crushing and/or the shearing of aggregate. These equations consider concrete strength, interface surface area, and factors also specified in its Section 5.7.4.4. Compared to ACI 318-19, the factors provided by AASHTO LRFD 2020 are more in-depth and cover a wider variety of situations. However, the determination of the interface condition is still qualitative before the new layer of concrete is poured.

2.3.1.3. *fib* Model Code 2010

The *fib* 2010 code has a more detailed expression and includes adhesion/interlocking and dowel action in addition to shear friction. According to the *fib* design equations, the strength of the interface (τ_u) is influenced by adhesive or interlocking, shear friction, and dowel action. There is a larger variety of properties incorporated in the *fib* code, and the equation is shown below and in Table 1 (Eq. 6.3-8 fib 2010):

$$\tau_u = \tau_a + \mu\left(\rho k_1 f_y + \sigma_n\right) + k_2\rho\sqrt{f_y f_{cc}} \leq \beta_c v f_{cc} \quad (2\text{-}9)$$

where τ_a = shear resistance due to adhesive bond/interlocking (MPa)
k_1 = interaction effectiveness factor
k_2 = interaction coefficient for slipping

σ_n = lowest compressive stress resulting from a normal force across the interface (MPa)
f_y = minimum yield strength of reinforcement (MPa)
f_{cc} = strength of confined concrete (MPa)
ρ = ratio of reinforcement crossing the interface
β_c = coefficient for strength of compression strut
v = effectiveness factor for the concrete

For shear friction, like the other two design codes, friction coefficients and forces across the interface are considered, primarily from the normal compressive stresses across the interface induced from the reinforcing bars. Ranges for coefficients of friction are provided for defined interface roughness types. For smooth interfaces, 0.5-0.7, rough interfaces 0.7-1.0, very rough interfaces 1.0-1.4.

For adhesive and interlocking, the *fib* Model Code 2010 (2010) provides two possible values for the strength, which are determined based on the roughness of the interface: ~1.5-2.5 N/mm^2 for rough interfaces and ~2.5-3.5 N/mm^2 for very rough interfaces. For smooth interfaces, it is noted that the effects from interlocking become very small or even disappear completely.

In addition to terms of friction and adhesive, *fib* Model Code 2010 (2010) takes dowel action of reinforcement across the interface into consideration, as described in the third term of the equation. *fib* Model Code 2010 (2010) also provides commentary about the presence of reinforcement in the interface and includes provisions for required minimum reinforcement across the interface, given in its Section 6.3.5 – Detailing.

Commentary regarding unreinforced interfaces is also present in *fib* Model Code 2010 (2010). The specification describes these types of interfaces as very brittle with failures occurring with loss of adhesion and mechanical interlocking. This can occur with slips of 0.05 mm and sometimes less. In addition, without reinforcement across the interface, all shear strength across the interface would be provided from adhesive/interlocking forces and shear friction, both of which heavily depend on the roughness of the interface. The code suggests that strong adhesive bonding and mechanical interlocking is imperative in the case of unreinforced interfaces.

2.3.1.4. Comparison of Specifications

All three selected design codes' interface shear strength models include shear friction and reinforcement crossing the interface. All three codes also provide values based on the roughness of the interface, usually a qualitative choice (e.g., visually rough, or smooth interfaces). Moreover, all three codes require minimum reinforcement area across the interface and impose upper limits on the calculated interface shear strength.

ACI 318-19 (2019) has the simplest expression of interface shear strength. That is, the code considers clamping effect from internal bar stresses, and no adhesive nor cohesive effects are incorporated. The other two codes, on the other hand, allow external clamping forces to provide normal stress for friction, and adhesion/ cohesion are quantified.

A major difference between the *fib* Model Code 2010 (2010) and the other two codes is the quantification of the interface roughness. Compared to the other two, *fib* Model Code 2010 (2010) provides a much more rigorous method for measuring roughness. However, the provided method is likely impractical due to the complexity and need for special equipment. In addition, *fib* Model Code 2010 (2010) quantifies dowel action of interface reinforcement, while the other two codes do not explicitly use contribution from dowel action.

2.3.2. Properties Affecting Interface Shear Strength

While design expressions for interface shear strength provided in current design codes consider shear friction and/or interface adhesive and cohesive, there are more factors influencing interface strength but excluded from code design expressions. For instance, a study by Santos et al. (2014) maintains that differential stiffness and differential shrinkage are also essential. In addition, past studies suggested that the code expressions can be too conservative. It is necessary to review more studies on interface shear properties for the development of composite action in both the proposed precast column system and socket connections.

The most important factors, as deemed from previous research, are roughness and cleanliness of contact surface, age of concretes, curing conditions, compressive stress across the interface, concrete quality, and type of loading. All these factors can be organized into three main categories: interface preparation, differential stiffness, and differential shrinkage. This section discusses the factors mentioned above, their relation to the broader categories, and their effect on interface shear strength. It should be noted that reinforcement has also been included briefly in this section to provide details on how the reinforcement can increase shear strength.

2.3.2.1. Interface Preparation

Nearly every study researching interface shear has brought up the importance of the roughness of the interface in developing strength in terms of contributing to shear friction. Birkeland and Birkeland (1966) proposed a shear friction hypothesis that characterized the interface shear at joints as a sawtooth crack, as illustrated in Figure 2-34. As a result of the imperfect contact surface, shear forces acting over the interface could also cause normal forces across the interface, allowing friction between the concretes to develop. Mattock (1976) confirmed the mechanism of shear friction experimentally.

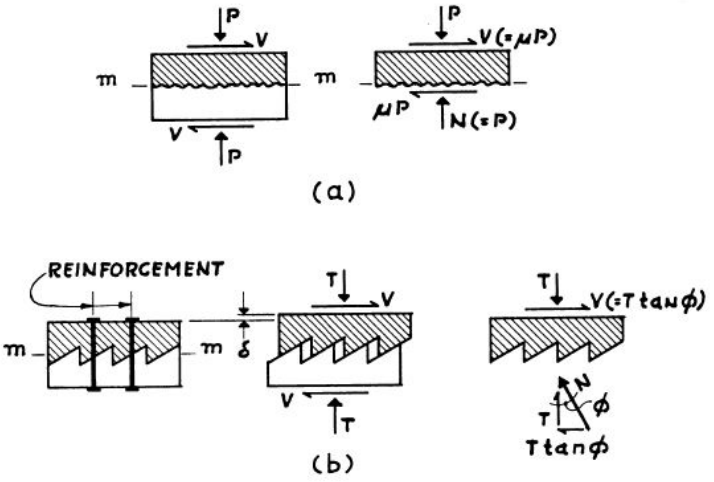

Figure 2-34: Illustration of Shear Friction Hypothesis proposed by Birkeland and Birkeland (1966)

Santos et al. (2014) conducted a large experimental study to characterize the influence of interface surface preparation, differential shrinkage, and differential stiffness between concrete layers cast at different times. The study tested five different surface preparations of left as-cast, wire-brushing, sandblasting, shot-blasting, and hand scrubbed. A variety of curing conditions (exterior and laboratory) and durations between casting were set to determine differential stiffness and shrinkage effects. The tests consisted of slant shear and splitting tests with five specimens from every considered situation prepared for each test, resulting in 300 specimens. Test results showed that the pure shear strength of an interface increased with an increase in interface roughness, echoing other studies and the shear friction model proposed by Birkeland and Birkeland (1966). The study also calculated average coefficients of friction and cohesion for each roughness created by the surface preparation. The coefficients of friction all exhibit excellent coefficients of variation, with the highest being 10.5% for the left as-cast case and the rest being under 8.7%. The cohesion values obtained also exhibited good coefficients of variations, all less than 19% except for the hand-scrubbed case, which recorded a COV of 25.4%. Compared to the code equations evaluated previously, these values of cohesion and friction all fall within the ranges specified by *fib* Model Code 2010. Figure 2-35 details the relationship of roughness compared to shear strength. In the figure, LAC, WB, SAB, SHB, and HS represent left as-cast, wire-brushing, sandblasting, shot-blasting, and hand-scrubbing, respectively. These results are in good agreement with other studies, including Mattock (1976), Seible et al. (1988), Barnoff et al. (1974), and Aziz (2010).

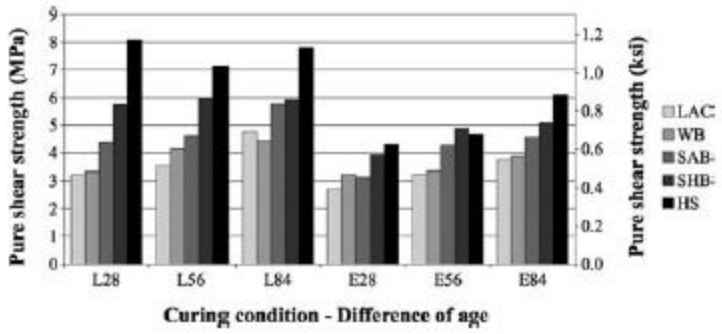

Figure 2-35: Shear strength for various conditions from Santos et al. (2014).

Aziz (2010) conducted 16 push-off tests with specimens including monolithic specimens, smooth interface, rough interface, shear keys, and with varying levels of reinforcement, as illustrated in Figure 2-36. In the specimens without reinforcement nor shear keys, the study found an increase in shear strength with an increase in roughness. This study also highlighted the variable nature of the unreinforced interfaces. One specimen with a smooth interface did not resist any force, while the test strength of other specimens with a rough interface differed by about twenty percent from each other. Given the limited number of tests performed, the need for a larger scale testing project is made clear by the results published by Aziz (2010).

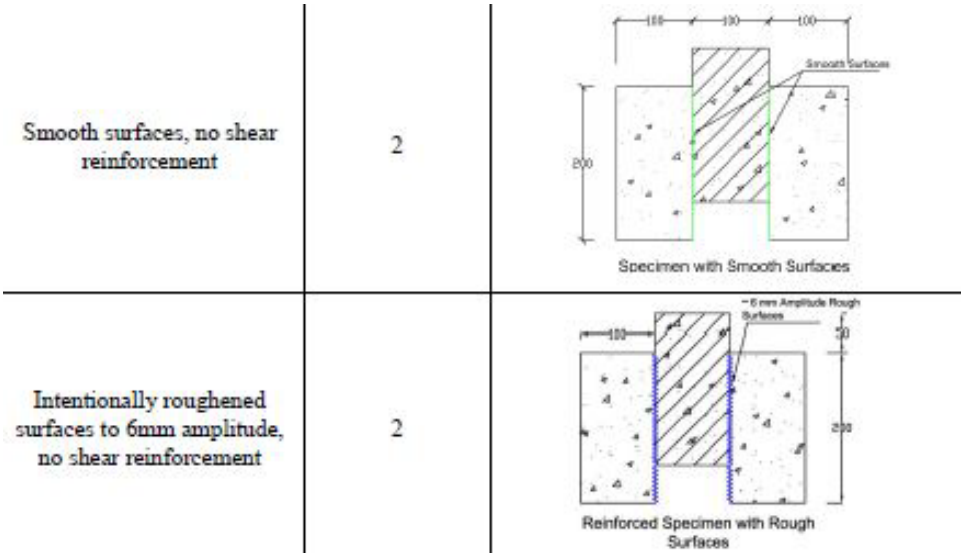

Figure 2-36: Test specimens prepared and tested by Aziz 2010. The number listed in the middle denotes the number of specimens made for each case.

Seible et al. (1988) conducted a study on bridge deck rehabilitation. As part of the research, push-off tests were conducted with specimens having a vertical interface between two layers of concrete. In the unreinforced sections, it was found that interface shear strength was controlled by surface preparation, which allowed the specimen to develop shear friction without the presence of compression across the interface in the form of dowels. As roughness increased, the interface shear

strength also increased. The study also noted a significant reduction in the strength of vertical unreinforced interface compared to horizontal ones.

Hanson (1960) characterized the strength and slip comparisons for a rough and bonded interface. The research showed an early peak with very low slip, followed by a slightly higher maximum strength at higher slips, attained much more gradually, as shown in Figure 2-37.

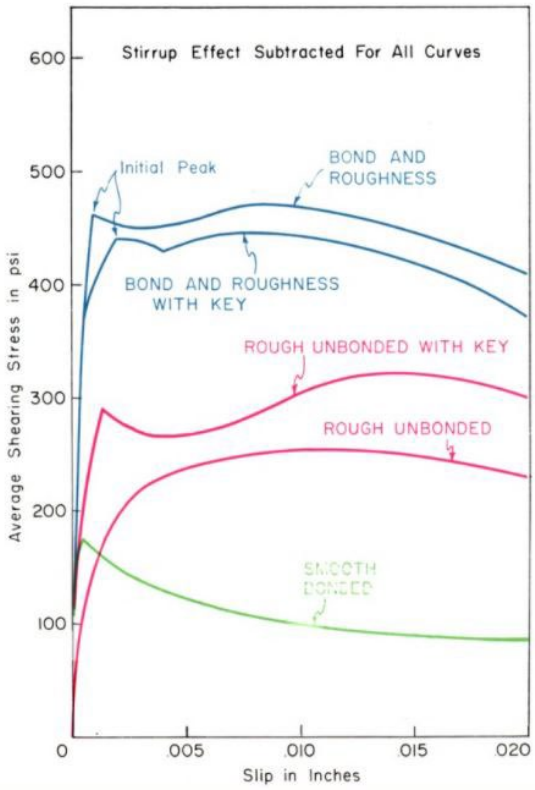

Figure 2-37: Strength and Slip for various push-off tests as performed by Hanson (1960)

Although some studies confirmed that increase of roughness results in increase of interface shear strength, other studies have found that this trend only continues until a certain level of roughness is achieved. Barnoff and Orndorff (1974) found in a study on horizontal interfaces that after a certain level of roughness, the interface shear strength remains roughly the same, and then starts to decrease.

Seible et al. (1988) stressed the importance of a clean interface free of laitance prior to casting. When reinforcement is not present across the interface, the bond between old and new concrete becomes the main method of resistance. Because the bond is thought to be related to cleanliness, a clean contact surface between layers is essential in interface shear strength.

In addition, previous research has suggested that some lubricants present on highways can lead to delamination due to differential stiffness prior to loading. The perspective is supported by push-off tests performed by Hanson (1960), who concluded that debonding of the interface prior to loading leads to significant strength reductions.

2.3.2.2. Differential Stiffness

Differential stiffness can exist in composite concrete structures due to a difference in compressive strength in the layers of concrete (Santos 2011). Currently, ACI 318-19, AASHTO LRFD (2020), and *fib* Model Code (2010) all do not account for differential stiffness in their models for interface shear strength. Instead, the code provisions only account for the lesser compressive strength of the two concretes.

Few studies have investigated the effects of differential stiffness on interface shear strength. Santos et al. (2011) found that there is a correlation between increasing differential stiffness (i.e., difference between the Young's moduli of the concretes) and the number of cohesive failures, as shown in Figure 2-38. It was concluded that the failure mode of the interface could possibly be controlled using intentional differential stiffness. The study also included an analytical model that revealed an increase in differential stiffness resulting in an increase in normal stress across the interface in slant shear testing. Such an increase might improve interface shear strength by increasing shear friction for interfaces with a roughened surface.

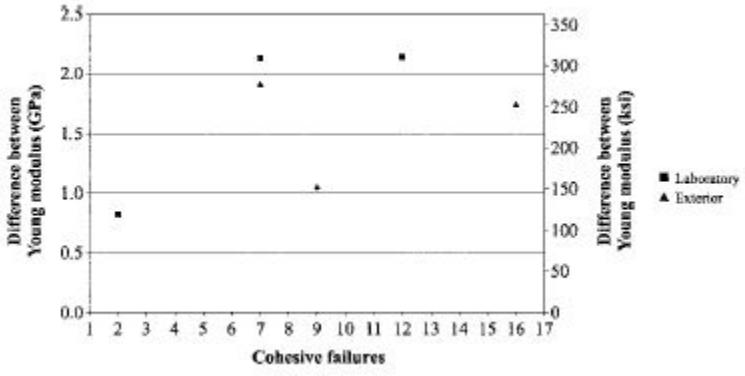

Figure 2-38: Differences in Young's Modulus vs Number of Cohesive Failures (Santos et al. 2011)

2.3.2.3. Differential Shrinkage

Studies have also suggested differential shrinkage of different layers of concrete affects the interface shear strength. Factors affecting differential shrinkage include difference in age of concretes and curing conditions. Santos et al. (2011) studied the effects of differences in ages of the concretes that make up the interface. It was found that with an increase in a difference in ages, there was an increase in interface shear strength. The study characterizes the stress state induced by shrinkage as being opposite as the stress state induced by loading, leading to an overall increase in strength.

Sieble et al. (1988) discussed shrinkage in the context of a large difference of ages between concretes. Their study raised questions regarding excessive shrinkage caused by largely different ages of concrete, leading to delamination of the interface. Birkeland (1960) also discussed shrinkage effects. The report detailed that near the ends of composite beams, shrinkage will cause

tensile stresses across the interface. At positions close to the middle of composite beams, shrinkage causes compressive stresses across the interface, as illustrated in Figure 2-39.

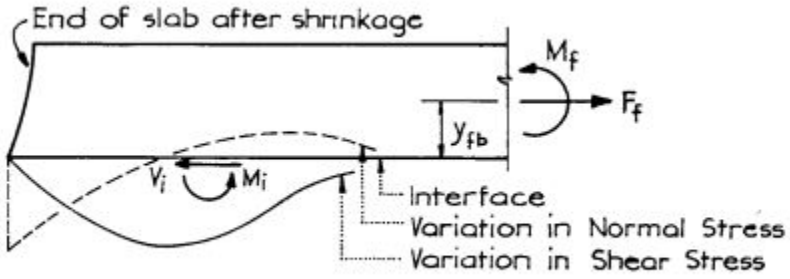

Figure 2-39: Depiction of variation of normal and shear stresses across an interface due to shrinkage of added concrete (Birkeland 1960)

In conclusion, while shrinkage can increase the interface shear strength, excessive shrinkage can lead to debonding of the layers causing the interface to lose nearly all shear strength without the presence of reinforcement. Differential shrinkage should also gain more attention.

2.3.2.4. Reinforcement

Reinforcement contributes to interface shear strength primarily through providing compressive stresses over the interface that develop shear friction and dowel action. To be specific, reinforcement is taking tension when the interface subjected to shear forces begins to open, which in turn creates compressive stress across the interface. The compressive stress then increases shear friction and strengthens the interface, given a sufficiently roughened surface. The mechanism was introduced by Birkeland and Birkeland (1966)

On the other hand, dowel action is the resistance of the reinforcing bars from bending caused by longitudinal slipping along the interface. Once the crack opens enough and the resistance from shear friction begins to decrease, dowel action becomes the only mechanism preventing failure. The contribution of dowel action to interface shear strength is incorporated in fib Model Code (2010).

2.3.2.5. Other Properties Affecting Shear Strength

Santos et al. (2011 and 2014) found that it is detrimental to the interface shear strength if composite members are cured outside and exposed to fluctuation of temperature and humidity, compared to specimens cured within a laboratory. While the overall averages in humidity and temperature were relatively similar, the large fluctuations of both led to a decrease in the vertical interface shear strength.

Compressive stress across the interface can increase the interface shear strength. Such stress is usually achieved using reinforcement across the interface. Seible et al. (1988) characterizes the effects of compressive stress as providing an increase in normal force, in turn providing an increase

in resisting force provided by shear friction. This conclusion was reached in a study on horizontal interface shear for bridge decks but could be applicable for certain situations for vertical interfaces.

It has been believed that surface adhesive is another factor to be experimented with for interface shear. However, previous research has shown that special adhesive applied to the interface generally does not increase the strength of the interface, according to Seible et al. (1988).

2.3.2.6. Summary of Factors Affecting Interface Shear Strength

A review of previous research has found that various factors affect interface shear strength. A summary of all the factors discussed above in this section are listed below:

- Interface preparation – As roughness increases, the shear strength of the interface increases until a certain amount of roughness is achieved. Ensuring a clean interface is also important, as some lubricants common to highways can cause severely weaken the adhesive bonding, allowing stress caused by differential shrinkage to crack the interface prior to loading. For an unreinforced interface, roughness is the largest factor contributing to interface shear strength.

- Differential stiffness – It was revealed that the difference in Young's modulus between concretes that form the interface affects the occurrence of adhesive failure. Differential stiffness can be potentially used to control the failure mode of concrete from adhesive to cohesive. Differential stiffness can also induce normal stress across the interface, increasing the strength produced via shear friction.

- Differential shrinkage – Differential shrinkage is caused by a difference in concrete ages or from curing conditions and increases the shear strength of the interface by inducing stress across the interface opposite to the stress induced by the loading of the interface in shear.

- Reinforcement – Steel reinforcement provides compressive stress across the interface and dowel action. The compressive stress across the interface is caused when a crack at the interface begins to open. Dowel action is also provided when the slip of the interface begins to grow. Steel reinforcement can greatly increase the strength of the interface.

2.4. Development Length for Steel Reinforcement and Prestressing Strands Embedded in Concrete

In a reinforced concrete member, there is a point when the concrete cannot support more tension, and a crack appears on it. For this reason, the compression forces are supported by the concrete, and the steel reinforcement carries the tensile forces. In order to make these two materials work together, the bond between the reinforcement and the concrete becomes very important. However,

these bonding forces could vary along the length of the reinforcement due to the variability of the concrete materials, the size of the reinforcement, and the threads used in the bars or prestressing strands. Consequently, it should be a way of calculating the length needed for a bar or prestressing strand to support the concrete against tensile forces. The development length is the distance needed for a bar or a strand to reach the yielding stress f_y when subjected to a tension force (Wight, 2016).

This section reviews current specifications and new research regarding development length for rebar and prestressing strands in the concrete, which is a fundamental variable in the project.

2.4.1. Existing Code Expressions

Design codes provide formulae to estimate the development length for the reinforcement steel. The development length varies if the force is in compression or tension. Therefore, the main focus of this research will be bars and prestressing strands subjected to tension forces. This review includes two design specifications: ACI 318-19 (2019) and AASHTO LRFD Bridge Design Specifications (2020).

2.4.1.1. ACI 318-19

2.4.1.1.1. Development length for deformed bars

The following equations are presented by ACI 318-19 in its section 25.4.2 to determine the development length for straight bars in tension:

- The development length should be the greater of Eq. (2-10) and (2-11):

$$l_d = \left(\frac{f_y \Psi_t \Psi_e \Psi_g}{20\lambda\sqrt{f'_c}}\right) d_b \tag{2-10}$$

$$l_d = \left(\frac{3}{40} * \frac{f_y}{\lambda\sqrt{f'_c}} \ \frac{\Psi_t \Psi_e \Psi_s \Psi_g}{\left(\frac{c_b + K_{tr}}{d_b}\right)}\right) d_b \tag{2-11}$$

$$\left(\frac{c_b + K_{tr}}{d_b}\right) \leq 2.5 \tag{2-12}$$

$$K_{tr} = \frac{40 A_{tr}}{sn} \tag{2-13}$$

where f_y = minimum yield strength of reinforcement (psi)
f'_c = specified compressive strength of concrete (psi)
d_b = nominal diameter of bar, wire, or prestressing strand (in.)

λ = modification factor to reflect the reduced mechanical properties of lightweight concrete relative to normal-weight concrete of the same compressive strength. (0.75 for lightweight – 1.0 for normal concrete)
c_b = lesser of (a) the distance from the center of a bar or wire to the nearest concrete surface, and (b) one-half the center-to-center spacing of bars or wires being developed (in.)
K_{tr} = transverse reinforcement index (in.)
Ψ_t = casting position (1.0 if there is 12 in. less of fresh concrete below the horizontal rebar or other)
Ψ_e = epoxy (1.0 if uncoated)
Ψ_s = bar size (1.0 for #7 or larger)
Ψ_g = reinforcement grade (1.0 for grade 60)
n = number of bars being developed, or lap spliced along the plane of spitting
s = spacing of the transverse reinforcement (in.)

2.4.1.1.2. Development of pretensioned seven-wire in tension

The following equation is presented by ACI 318-19 in its section 25.4.8 to determine the development length for pretensioned seven-wire strands in tension:

$$l_d = \left(\frac{f_{se}}{3000}\right) d_b + \left(\frac{f_{ps} - f_{se}}{1000}\right) d_b \quad (2\text{-}14)$$

where f_{ps} = stress in prestressed reinforcement at nominal flexural strength (psi)
f_{se} = effective stress in prestressed reinforcement, after allowance for all prestress losses, psi
d_b = nominal diameter of bar, wire, or prestressing strand (in.)

2.4.1.2. AASHTO LRFD Bridge Specifications 2020

2.4.1.2.1. Development length for deformed bars

The following equations are presented by AASHO LRFD in its section 5.10.8.2.1a to determine the development length for straight bars #11 or smaller in tension:

- The development length should be calculated using Eq. (2-15) and modified according to equations (2-16) through (2-18).

$$l_{db} = 24 d_b \frac{f_y}{\sqrt{f'_c}} \quad (2\text{-}15)$$

$$l_d = l_{db}\left(\frac{\lambda_{rl}\lambda_{cf}\lambda_{rc}\lambda_{er}}{\lambda}\right)l_{db} \quad (2\text{-}16)$$

$$0.4 \le \lambda_{rc} = \left(\frac{d_b}{c_b + K_{tr}}\right) \le 1.0 \quad (2\text{-}17)$$

$$k_{tr} = \frac{40A_{tr}}{sn} \quad (2\text{-}18)$$

where
l_{db} = basic development length (in.)
f_y = minimum yield strength of reinforcement (ksi)
f'_c = specified compressive strength of concrete (ksi)
d_b = nominal diameter of bar (in.)
c_b = the smaller of the distance from center of the bar or wire being developed to the nearest concrete surface and one-half the center-to-center spacing of the bars or wires being developed (in.)
k_{tr} = transverse reinforcement index (in.)
λ = concrete density modification factor as specified in Article 5.4.2.8. (1.0 for normal concrete)
λ_{rl} = reinforcement location factor (1.0 if there is 12 in. less of fresh concrete below the horizontal rebar or other)
λ_{cf} = coating factor (1.0 if uncoated)
λ_{rc} = reinforcement confinement factor
λ_{er} = excess reinforcement factor (Required A_s / Provided A_s)
A_{tr} = total cross-sectional area of all transverse reinforcement which is within the spacing s and which crosses the potential plane of splitting through the reinforcement being developed (in.^{2})
n = number of bars being developed, or lap spliced along the plane of spitting
s = maximum center-to-center spacing of transverse reinforcement within l_d (in.)

2.4.1.2.2. Development of pretensioning strands

AASHTO LRFD in section 5.9.4.3 introduces a procedure to calculate the development length for pretensioning strands assuming that the stress in the strand is zero at the end increasing linearly until reaching the effective stress after losses, f_{pe}, being this the transfer length. Between the end of the transfer length, it can be assumed to increase linearly until reaching the stress at nominal resistance, f_{ps}, at the development length.

The following equations are presented by AASHTO to determine the development length for bonded strands:

$$l_d \geq \kappa \left(f_{ps} - \frac{2}{3} f_{pe} \right) d_b \tag{2-19}$$

where
f_{ps} = average stress in prestressing steel at the time for which the nominal resistance of the member is required (ksi)
f_{pe} =effective stress in prestressed reinforcement, after allowance for all prestress losses, psi
d_b = nominal strand diameter (in.)
κ = 1.0 for pretensioned panels, piling, and other pretensioned members with a depth of less than or equal to 24.0 in. Should be taken as 1.6 for pretensioned members with a depth greater than 24.0 in.

From the point where bonding commences to the end of transfer length:

$$f_{px} \geq \frac{f_{pe} l_{px}}{60 d_b} \tag{2-20}$$

From the end of the transfer length and to the end of the development of the strand:

$$f_{px} \geq f_{pe} + \frac{l_{px} - 60 d_b}{l_d - 60 d_b} \left(f_{ps} - f_{pe} \right) \tag{2-21}$$

where
f_{px} = design stress in pretensioned strand at nominal flexural strength at the section of the member under consideration (ksi)
l_{px} = distance from the free end of pretensioned strand to section of member under consideration (in.)

2.4.2. Recent research

Zaborac and Bayrak (2022) presented a study with the intention of unifying the method for calculating the development lengths for straight bars, hooks, and headed bars subjected to tension forces based on the approach followed by the *fib* Model Code 2010. Nowadays, ACI 318-19 (2019) and AASHTO LRFD Bridge Design Specifications (2020) have their procedure to calculate these values, however, these considerations are completely separate. As a result, there has been always discrepancies between both codes, and which characterizes more accurately the development length needed to yield the bars. Finally, AASHTO LRFD has announced the intention of adopting this unified approach in the following code (Bayrak, 2023).

The following equations are proposed by Zaborac and Bayrak (2022) to determine the development length for deformed bars and lap splices in tension:

- The development length should be the calculated using of Eq. (2-22) and modified according to equations (2-23) through (2-25).

$$l_d = 0.17 d_b \left(\frac{\lambda_{er} f_y - \frac{F_h}{A_b}}{350\lambda * \sqrt[4]{f'_c}} \right)^2 \lambda_{rl} \lambda_{cf} \lambda_{rc} \geq 0.25 \left(\frac{f_y - \frac{F_h}{A_b}}{18\sqrt{f'_c}} \right) d_b \quad (2\text{-}22)$$

$$F_h = 0 \quad (2\text{-}23)$$

$$\lambda_{rc} = \left(\frac{d_b c_b}{c_b(1 - \beta_t) + (1.67 n_s K_{tr})^2} \right) \quad (2\text{-}24)$$

$$k_{tr} = \frac{n_{tr} A_{btr}}{s n_b} \quad (2\text{-}25)$$

where

l_d = development or splice length fora straight bar (in.)
f_y = reinforcement yield strength (psi)
f'_c = specified compressive strength of concrete (psi)
d_b = reinforcement bar diameter (in.)
A_b = reinforcement bar area (in.^{2})
β_t = ratio of unfactored compressive stress due to permanent loads (taken as a negative value) transverse to the plane of splitting to the modulus of rupture as determined by Article 5.4.2.6 of the AASHTO LRFD specifications $(-1 \leq \beta_t \leq 0)$
F_h = force developed through other measures (lbs.)
c_b = concrete cover parameter (one-half the rein-forcing bar diameter plus the minimum of the side clear cover, bottom/top clear cover, and one-half the clear spacing of the rein-forcing bars) (in.)
k_{tr} = transverse reinforcement index (in.)
λ = concrete density modification factor as specified in Article 5.4.2.8. (1.0 for normal concrete)
λ_{rl} = 1.3 for horizontal reinforcement with 12 in. of fresh concrete below it
λ_{cf} = coating factor (1.0 if uncoated)
λ_{er} = (Required A_s / Provided A_s)
A_{btr}= area of a single leg of the confinement reinforcement (in.^{2})
n_s = steel-to-concrete modular ratio (E_s / E_c)
n_b = number of bars crossed by the spitting plane
n_{tr} = number of confinement-reinforcing bars crossing the assumed splitting plane
s = spacing of the confinement reinforcement (in.)

2.5. Finite Element Analysis (FEA) Parameters

Finite element analysis in the structural engineering field is widely used, as it can be very helpful in assessing the structural performance of members, including ultimate capacity, stiffness, displacements, stress flow, and failure mechanisms. Many studies were conducted to check different structural components in bridges. For instance, Mondal and Prakash (2016) have conducted nonlinear FEA on bridge columns with different shapes, and slenderness ratios subjected to torsional loading. It was concluded from the study that the analytical models could accurately predict torque-twist response, failure pattern, and cracks including details such as strain fields (Mondal and Prakash, 2016). Another study was conducted by Huria et al. (1993) on RC slabs in bridges, subjected to flexure. Parameters such as boundary conditions, stiffness at abutments, material models were studied to check the influence on analysis results (Huria et al. 1993). With advancements in technology, faster computational analysis enabled to explore minor details in analytical results. In this section, previous studies related to parameters in FEA are presented.

2.5.1. Element Shapes

In the typical FEA software, users can choose to divide the structural members into many elements called mesh, and the most widely used mesh shapes are tetrahedral and hexahedral. These elements are present in the ATENA 3D software as well, shown below in Figure 2-40, the computational tool used to model in this study.

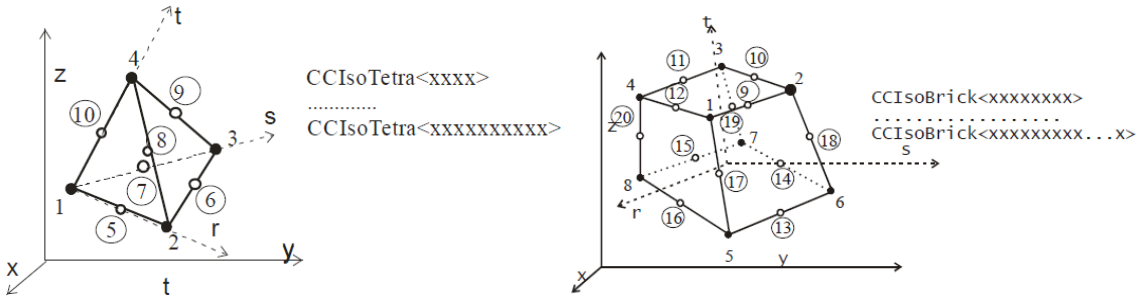

(a) Tetrahedral (b) Hexahedral (Brick)

Figure 2-40 Element types used in ATENA 3D software (Atena Theory)

Many studies have been conducted in past to check the accuracy and applicability of these elements to structural elements. For example, Cifuentes and Kalbag (1992) have conducted parametric analysis on structural members subjected to varied type of loading like axial, bending, shear, and torsional with different elements: tetrahedral, and brick (Hexahedral). They have concluded that both elements have attained decently accurate results in the same computational time (Cifuentes and Kalbag, 1992). However, this study has focused on cuboid-shaped members. For structural members with complex outer surfaces like curvilinear, meshing with hexahedral elements can be complicated (Nguyen-Hoang et al. 2017).

2.5.2. Mesh size

Mesh size is an essential parameter, which may sometimes be challenging to select. The ATENA software manual recommends using at least 4 elements per dimension for satisfactory results (ATENA 3D manual). Taghia and Bakar (2013) have conducted parametric FE studies on short columns, and mesh size is one of the factors. The researchers have tried mesh size to column dimension ratio as high as 75000:1 and concluded that finer mesh indeed provided accurate results, especially in post-yield behavior during flexural analysis (Taghia and Bakar, 2013). In addition, an FEA study was conducted by Gribniak et al. (2010) on a three-span RC bridge girder using ATENA software. The authors made a conclusion that finest mesh produced most realistic solution in predicting crack pattern, crack width under flexural analysis (Gribniak et al. 2010). It should be noted that adopting finer mesh can be computationally costly, and a parametric study focusing on mesh size was conducted for the specimen S1-CIP (cast in place) in section 6.2.4.

2.5.3. Reinforcement Bond Models

There is no guarantee that all the reinforcement in concrete yields under substantial load, as it depends on development length, and bond strength of concrete-steel interface which depends on bar type, concrete strength, and confinement. As shown in Figure 2-41, category pull-out failure is applicable for regular reinforcement when suitable confinement and cover are present. The shear values on Y-axis are calculated from compressive strength, distance between bars, and clear cover values. On the other hand, splitting failure occurs when the standards mentioned above are not met. These bond models can be adopted in FEA software for capturing accurate stress flow under RC members loading.

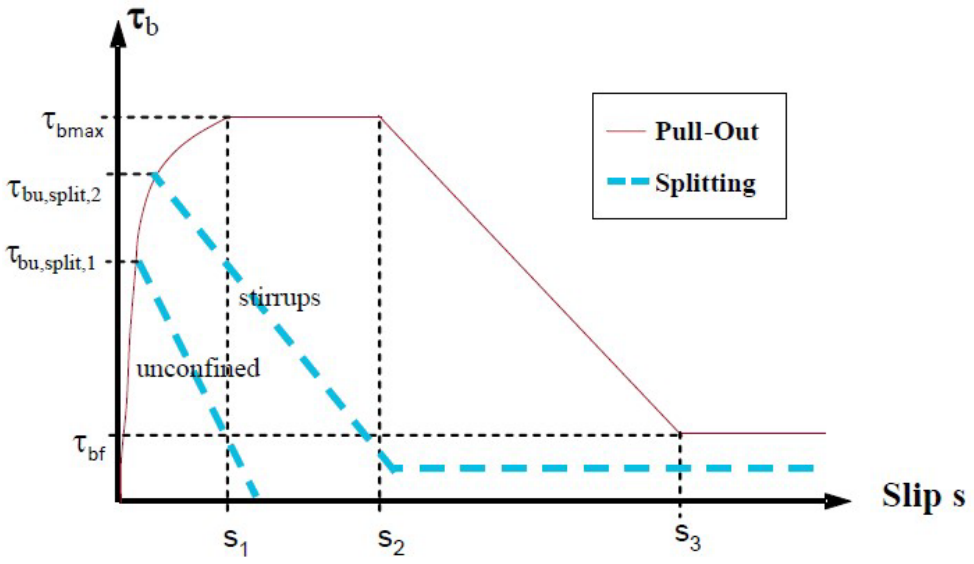

Figure 2-41 Analytical Bond Stress-Slip Relationship (CEB-FIP, 2010).

Apart from regular reinforcement, prestressed reinforcement is another important area. Complete prestressing in the strands of precast members is not guaranteed, as prestressing is developed after

'transfer length' from the face of the member. This length depends on factors like strand diameter, level of prestressing, and compressive strength (Oh et al. 2014). The concrete in this transition region cannot have the benefits of prestressing, so accurate modeling of transfer length and prestressing in the analytical model is important. One of the pre-defined models in the ATENA software is the Bigaj 1999 model, as shown in Figure 2-42 below (Bigaj 1999). The coordinates depend on the bar diameter, bond condition, and compressive strength of the surrounding concrete. This model was used by past researchers who concluded that it can accurately detect the transfer length of the strands (Alirezaei Abyaneh 2016).

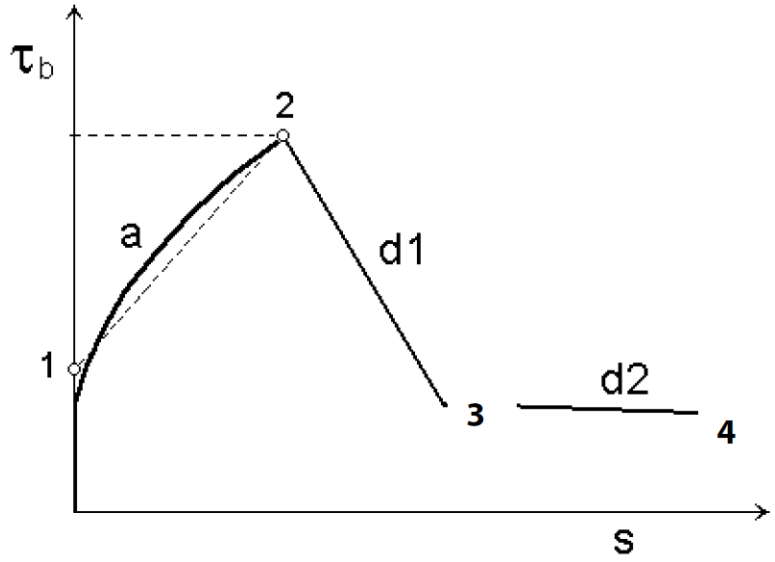

Figure 2-42 Bond Model for Reinforcement (Bigaj, 1999)

2.6. Summary

This literature review was conducted on a wide range of research, projects, and publications related to precast columns, column connections, and interface shear. From this literature review, the following conclusions can be drawn:

- Using precast column systems can greatly increase the speed of construction. However, current systems still face a variety of constraints such as lifting weight and transportation, causing full-height precast column systems to be unpractical.
- Experimental research has shown promising results by using a precast concrete shell with a CIP concrete core. Such a system provides a greatly reduced lifting weight allowing for easier installation and transportation. However, the number of relevant studies is limited.
- Connections are critical when using precast column systems. Experimental studies have shown that socket connections can be used as an effective method to connect precast columns to footings. They have been found to provide sufficient resisting capacity through

interface shear and be easy to construct. The interface within the connection can be critical and proper surface preparation is necessary.

- Interface shear in unreinforced interfaces comes predominantly from shear friction. Factors such as differential shrinkage and differential stiffness were found to be influential on interface shear strength. However, limited experimental research has been conducted to characterize the behavior.
- The development length for the reinforcement bars and prestressing strands in the concrete presents a high importance in the behavior of the reinforced concrete. ACI 318-19 and AASHTO LRFD present procedures to estimate this variable and new research has been proposed to unify the procedure of calculating the development length.
- Regarding finite element method, some variables like the shape and mesh size of the elements could bring some difficulties, and the accuracy of results and computational time depend directly on these variables. In addition, the bond for the reinforcement could be integrated to the analysis, which has not appropriately integrated column connectors by using models which represent this parameter and assist in estimating the performance of the structure.

Chapter 3. Precast-CIP Interface Shear Behavior

This chapter presents an experimental investigation into the shear strength of interfaces between precast concrete and cast-in-place (CIP) concrete. The purpose of the investigation was to understand factors that affect interface shear strength between concretes cast at different times.

3.1. Introduction

The goal of Project 0-7089 was to develop and validate practical standard designs and connection details for precast concrete columns for Texas bridges. Primary proposed precast column systems comprise connections that require concrete interfaces to transfer shear stress or to form appropriate composite actions. For instance, socket/pocket connections transfer shear stress through the interface between the column/bent cap connection and column/foundation connection without the contribution of crossing steel reinforcement. Also, For the precast column system that consists of a hollow concrete shell in which core concrete is cast after erected, it includes a vertical a vertical interface between precast and cast-in-place concrete. As summarized in the previous chapter, there was little previous research characterizing such vertical interface shear, especially interfaces without crossing reinforcement. To bridge this knowledge gap and to allow a thorough and complete design of the proposed precast column system, the research team conducted a small-scale testing regimen to investigate interface shear between precast concrete and cast-in-place concrete.

The main goal of this study was to investigate factors affecting interface shear strength between precast and cast-in-place concrete identified in the literature review. The target factors included interface roughness, interface shape, shrinkage compensating concrete, and cast sequence. To achieve the objectives, 27 specimens with a concrete shell and a core were tested under push-off loading. Evaluations of existing code design expressions were conducted. An analytical method based on observations in the experimental program was introduced.

3.2. Experimental Program

This chapter serves to provide details into how the research team planned to implement the testing regimen and the development of the experimental program, including the testing matrix, specimen design, fabrication of specimens, test setup, and instrumentation.

3.2.1. Specimen Design and Test Matrix

The design specimen configuration in the current study, as schematically shown in Figure 3-1, included a square hollow shell and a core of which the shape could be circular or square. In the shell, a minimum amount of reinforcement was provided. Concrete material for the core and the shell could be conventional concrete, precast self-consolidating concrete, or shrinkage compensating concrete. The interface could be smooth or textured to create roughness. When testing, the shell of a specimen was meant to be supported on the strong floor while a vertical load

was applied through a bearing plate on the top of the core, creating shear stress between the interfaces.

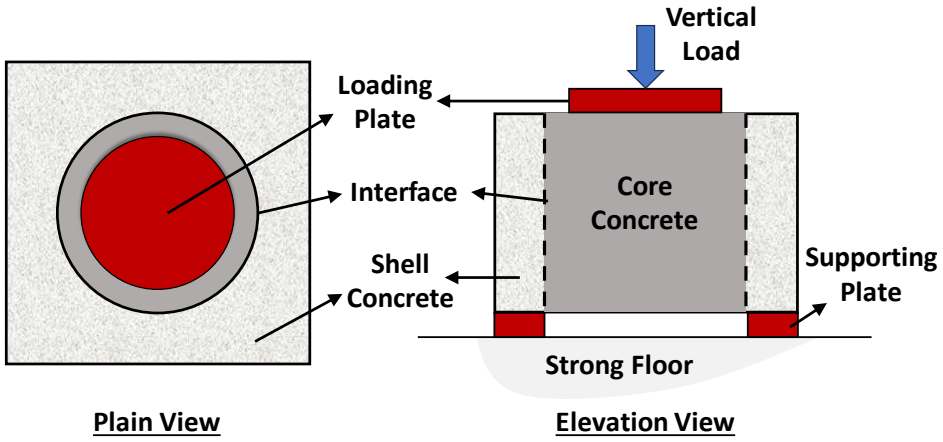

Figure 3-1: Schematic Specimen and test method

With the concept, Table 3-1 presents the planned test matrix for achieving the objectives of the study, and nine specimen groups categorized into two series were developed. The first series, including six specimen groups, was meant to have a precast concrete shell and a cast-in-place core. In other words, the concrete shell was cast first, and the core was cast after the shell was fully hardened. Each specimen group had three specimens with the same configuration shown in the table.

Table 3-1. Test Matrix

Series	Specimen Group ID	Interface Shape	Interface Condition	Concrete Mixture*	
				Shell	Core
I Precast Shell/CIP Core Interface	I-C-S	Circle	Smooth	CON	CON
	I-C-S-SR	Circle	Smooth	SCC	SRC
	I-C-T	Circle	Textured	SCC	CON
	I-C-T-SR	Circle	Textured	SCC	SRC
	I-Sq-S	Square	Smooth	SCC	CON
	I-Sq-T	Square	Textured	SCC	CON
II CIP Shell/Precast Core Interface	II-C-S	Circle	Smooth	CON	SCC
	II-Sq-S	Square	Smooth	CON	SCC
	II-C-T	Circle	Textured	CON	SCC

* The convention used for concrete mixtures is as follows:
CON – Conventional Concrete (TxDOT Class C concrete)
SCC – Self Consolidating Concrete (Precast Concrete)
SRC – Shrinkage Reducing Concrete (TxDOT Class C concrete with Masterlife SRA 035)

Different from Series I, Series II, comprising three specimen groups and each also had three identical specimens, was intended to have the core cast first as a precast element and then to have a cast-in-place shell. The series was to investigate the potential effects of construction sequence on the interface behavior.

A nomenclature was developed to identify the specimens as shown in Figure 3-2. A specimen ID includes four parts: the series No., the interface shape, the interface condition, and whether shrinkage reducing concrete was added. More information is provided in the figure.

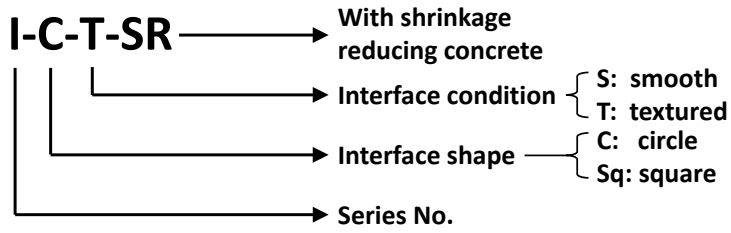

Figure 3-2 Nomenclature of push-off specimens

3.2.2. Specimen Details

3.2.2.1. Geometry and reinforcement

As mentioned above, each of the specimens consisted of a core and a shell. Overall, the shell had a width of 28 in. a length of 28 in., and a height of 20 in, as shown in Figure 3-3. For specimens with a circular interface, the core was designed to have a diameter of 20 in. positioned right at the center, leaving the smallest thickness of the shell to be 4 in. In addition, for specimens with a square interface, the core had dimensions of 20 in. by 20 in., also causing the shell to have a thickness of 4 in.

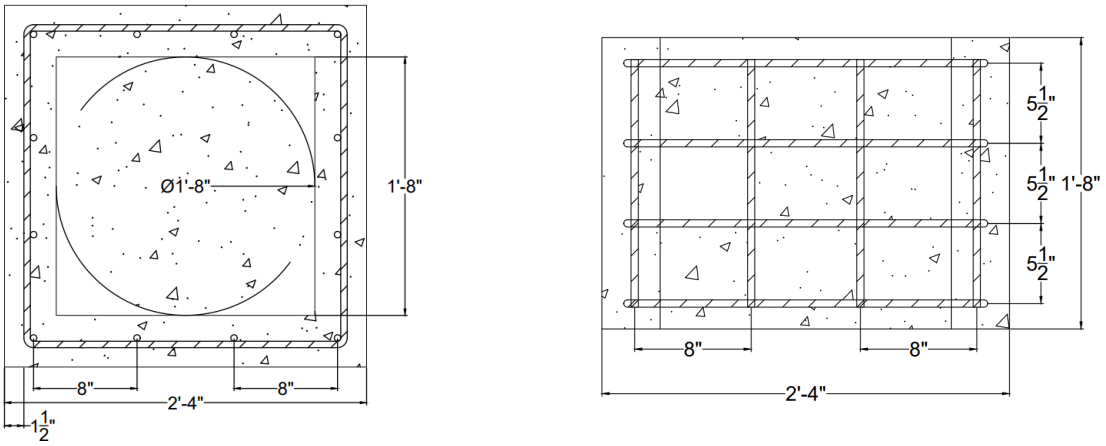

(a)Plan view (b)Elevation view

Figure 3-3: Typical specimen

Each specimen was reinforced with a rebar cage inside its shell. This cage was designed to serve as temperature reinforcement to control shrinkage and creep cracks during the curing process. Per ACI 318-19 and AASHTO LRFD, the minimum required reinforcement ratio, 0.0018, was satisfied, while the No. 4 rebar was chosen to provide stability for construction and transportation. Consequently, the cage consisted of four No. 4 closed-ties spaced at 5.5 in. throughout the height and twelve No. 4 vertical dowels distributed evenly along the inside perimeter of the closed-ties, as seen in Figure 3-3. The cage was designed to have a 1.5 in. cover from any concrete surface.

3.2.2.2. Materials

Three types of concrete mixtures were utilized in this experimental program: conventional concrete (CON), self-consolidating precast concrete (SCC), and shrinkage reducing concrete (SRC). A summary of target concrete strengths for the classes used is presented in Table 3-2. The concrete type CON followed TxDOT Specification Item 421 for class C concrete. The SCC concrete followed TxDOT Specification Item 421 for class H concrete. The SRC concrete mix was produced by creating a TxDOT Class C concrete and adding a dosage of 0.5 gallons/yd^3 of shrinkage reducing admixture, Masterlife SRA 035. For each cast, concrete cylinders were created per ASTM C31 for the compressive strength of concrete. In addition, concrete prisms for shrinkage tests were produced for each cast according to ASTM C192. Further, cylinders and prisms were cured similarly to the specimens they represent. This included keeping the samples in the same environment and providing cylinders with a bath while specimens were curing underneath tarps in the first seven days. These samples were used for testing throughout the experimental program to quantify concrete compressive and tensile strength on each test day. The concrete cylinders were tested per ASTM C39, and prisms were monitored per ASTM C878 for length change. All rebar used in reinforcement cages conformed to the requirements of Grade 60 in ASTM A615. Material test data is presented in later sections.

Table 3-2. Summary of Concrete Mixtures

Concrete Type	Target 28-day Strength (psi)	Max w/cm Ratio	Aggregate Size
TxDOT Class C (CON)	3,600	0.45	2” – 1/2”
Precast Concrete (SCC)	11,000	0.45	1.5” – 1/2”
TxDOT Class C w/ SRA (SRC)	3,600	0.45	2” – 1/2"

3.2.3. Fabrication of Specimens

3.2.3.1. Rebar cage

The rebar cage was assembled according to the design shown in Figure 3-3. The completed rebar cage is shown in Figure 3-4. Upon completion, a few plastic chairs and wheel spacers were installed to maintain sufficient room for a clear concrete cover. In addition, vibrating wire gauges were mounted on the rebar cage for monitoring strains during testing.

Figure 3-4: Completed rebar cage

3.2.3.2. Exterior Formwork

Exterior formwork was constructed using four pieces of plywood braced with 2x4s to prevent buckling under fluid pressure caused by concrete. The form walls were designed with two sides being the exact width of the specimen and two sides being the length of the specimen plus the wall width. This allowed for easy removal of the walls and fastening the walls to each other. This completed exterior formwork is shown in Figure 3-5.

Figure 3-5: Exterior formwork used for all specimens

3.2.3.3. Void Formwork

Void formwork was made of steel or a Sonotube® with dimensions that fulfilled the design for circular interfaces. A void form was placed in the exterior form as shown in Figure 3-6 before casting the concrete shell. Wooden stiffeners were placed in the void form to maintain the shape of the void.

Figure 3-6: 1/8" steel void, 1/4" steel void, sonotube void

Similarly, for the square voids, square void forms were made of steel or wood with a seam cut into one corner to allow the form to buckle away were constructed and installed, as seen in Figure 3-7. The square wood form design consisted of four sides with two panels per side. Between the two panels, a rabbeted groove was added to allow the panels to interlock yet make for easy buckling. Wooden gussets were then nailed across the groove and along the corners to prevent buckling during casting. Form tape was also put across the exterior of the groove to provide a smooth finish across the crack. Finally, 2x4s were used to brace the grooves in each direction to provide stiffness during casting (see Figure 3-8).

Figure 3-7: Initial square steel void form

Wooden void form

breakaway panel used

Figure 3-8: Wooden form and fabrication

3.2.3.4. Precast

The research team recruited the help of a local precast concrete facility to better replicate the actual concrete that will be used in a precast column system. The facility was provided with prebuilt molds and rebar cages, into which the facility's self-consolidating concrete (SCC) product was cast. The SCC conformed to the requirements set forth in TxDOT Specification Item 421 as introduced in Section 3.2.2.2. There were two rounds of precasting for the specimens. The first round consisted of six specimen shells, as shown in Figure 3-9. The second precasting consisted of ten shells for Series I and nine cores for Series II, and photos of core casting are shown in Figure 3-10.

It is of note that one of the molds failed, causing the specimen to be unusable, so the first trip netted five precast shell specimens. The reason for this failure was due to a lack of screws connecting one of the side forms to the plywood base, causing it to swing open once enough fluid pressure was exerted on it during casting, as seen in Figure 3-11. This problem was remedied for future casts by ensuring a proper number of screws were present on all formwork before casting, as well as installing ratchet straps around the bottom third of all formworks as a redundancy to prevent blowouts.

(a) Specimens' molds before casting

(b) Shell with a circular void after casting

(c) Shell with a square void after casting

Figure 3-9: First round of precasting

(a) Circular core cast for Series II tests

(b) Square core cast for phase two test

Figure 3-10: Second round of precasting

Figure 3-11: Formwork blow out due to missing screws connecting sidewall to base

3.2.3.5. Core Formwork Removal

After the specimens were transported back to Ferguson Structural Engineering Laboratory, the formwork was promptly removed. Due to the high early strength of SCC concrete, reaching 8,900 psi at seven days, the forms could be removed quickly without causing damage to the specimens. The circular steel forms were relatively easy to remove by buckling the form at the seam and reducing its diameter. Mallets were then utilized to break the bond between the steel form and the concrete. Finally, a crane was employed to vertically extract the formwork from the specimen. The resulting interface was consistently smooth, except for the area where form tape was used to secure the seam. Along the tape, the finish was ultra-smooth with a few bubble spots that formed as the fluid pressure of the concrete pushed out air from beneath the tape. An example of the finished surface can be observed in Figure 3-12.

Figure 3-12: Example of finished shell and interface

Removing the initial square void forms posed a challenge since the free corners were prone to slight buckling, causing the edges to become embedded in the concrete and preventing easy

removal. Even in cases where seam buckling was not an issue, extracting the square steel forms proved significantly more difficult than their circular counterparts. Furthermore, the removal process resulted in the steel forms becoming mangled and, in some instances, requiring cutting, as depicted in Figure 3-13(a). Consequently, these forms became unusable for future casts. To address this issue, the research team transitioned to wooden breakaway forms. Removing the wooden breakaway forms proved exceptionally easy and consistently produced a suitable interface for testing. Figure 3-13(b) displays the finishes obtained from the square steel forms.

(a) cut steel formwork (b) Interface finish

Figure 3-13: Finished shell for square cores

3.2.3.6. Sandblasting

Sandblasting was selected as the preferred method to achieve roughened interfaces. The sandblasting service was outsourced and completed within a couple of hours. This process effectively created a roughened surface, as depicted in Figure 3-14. The textured surface resulting from sandblasting can also be observed in Figure 28, showing a precast core awaiting the casting of a cast-in-place shell.

(a) Shell interface (b) Core interface

Figure 3-14: Roughened interface after sandblasting

3.2.3.7. Lab Cast (Cast-in-Place Concrete)

Cast-in-place (CIP) concrete was cast at Ferguson Structural Engineering Laboratory. For specimens with a precast shell (Series I), the shell was placed on either plywood or a smooth concrete floor with plastic sheeting, and the interface was pretreated with water prior to casting. Concrete was then placed directly into the shell until the void was completely filled and consolidated, as shown in Figure 3-15.

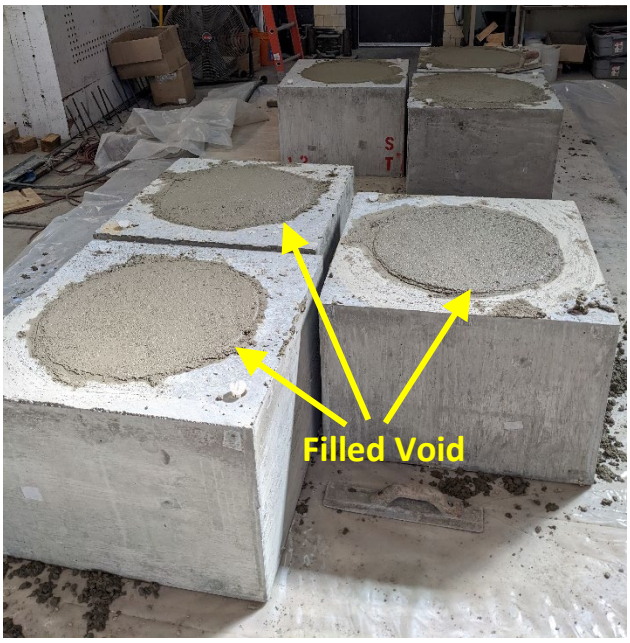

Figure 3-15: Specimens with filled void

For specimens with a precast core (phase two), exterior formworks were reused from phase one. The precast core was then centered inside the formwork, and a rebar cage was placed in the remaining space, as seen in Figure 3-16 (a). Concrete was then cast around the cage to form the CIP shell for Series II, as shown in Figure 3-16.

(a) Placing recast core and rebar cage

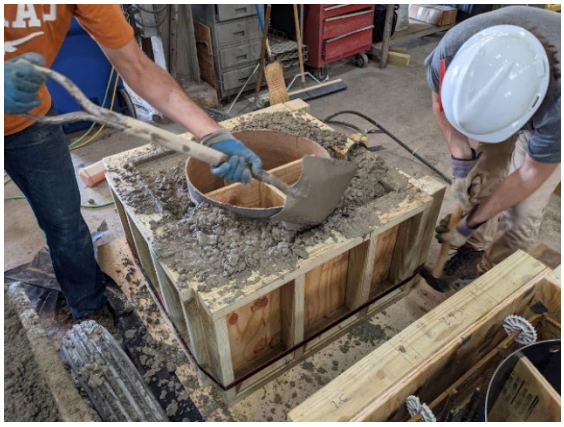

(b) Placing concrete and consolidation

Figure 3-16: Cast of phase-two specimens

3.2.4. Test Setup

3.2.4.1. Loading Frame

The loading frame, as depicted in Figure 3-17, comprised of four columns connected by two edge beams, which supported a reaction beam. An 800-kip capacity ram was then attached to the reaction beam. This ram was utilized to exert pressure on a 750 kip rated load cell, positioned on steel plates that were bonded to the surface of the specimen. Hydrostone was used to bond and level these plates with the specimen's surfaces. The attachment is shown in Figure 3-17(b). Figure 3-17(c) shows the specimens resting on steel plates covered with a thin layer of rubber, placed on the strong floor in Ferguson Structural Engineering Laboratory. In cases where circular voids were present, triangular steel and rubber inserts (see Figure 3-17(d)) were added to provide a bearing face as close to the interface as possible. To prevent tensile forces from exceeding the capacity of the strong floor, each column was prestressed to a load of at least 90 kips, as shown in Figure 3-17(e). Consequently, the overall capacity of the testing frame was 360 kips.

(a) Main components

(b)Placement of load cell and load plates

(c)Support and bearing

(d)Triangular inserts

(e)Post-tensioning

Figure 3-17: Load frame

3.2.4.2. Instrumentation

3.2.4.2.1. Vibration wire gauges

In Group I-C-S, the specimens were equipped with embedded strain gauges in the concrete. Each specimen in this series had four Geokon vibrating wire gauges, positioned parallel to each face. Two gauges were placed closer to the top of the specimens, while the other two were placed closer to the bottom when the rebar cage was assembled as mentioned previously. Figure 3-18 provides a visual representation of the gauge locations. The purpose of these gauges was to measure and quantify the opening force and subsequent confinement resulting from the interaction between the shell and the core.

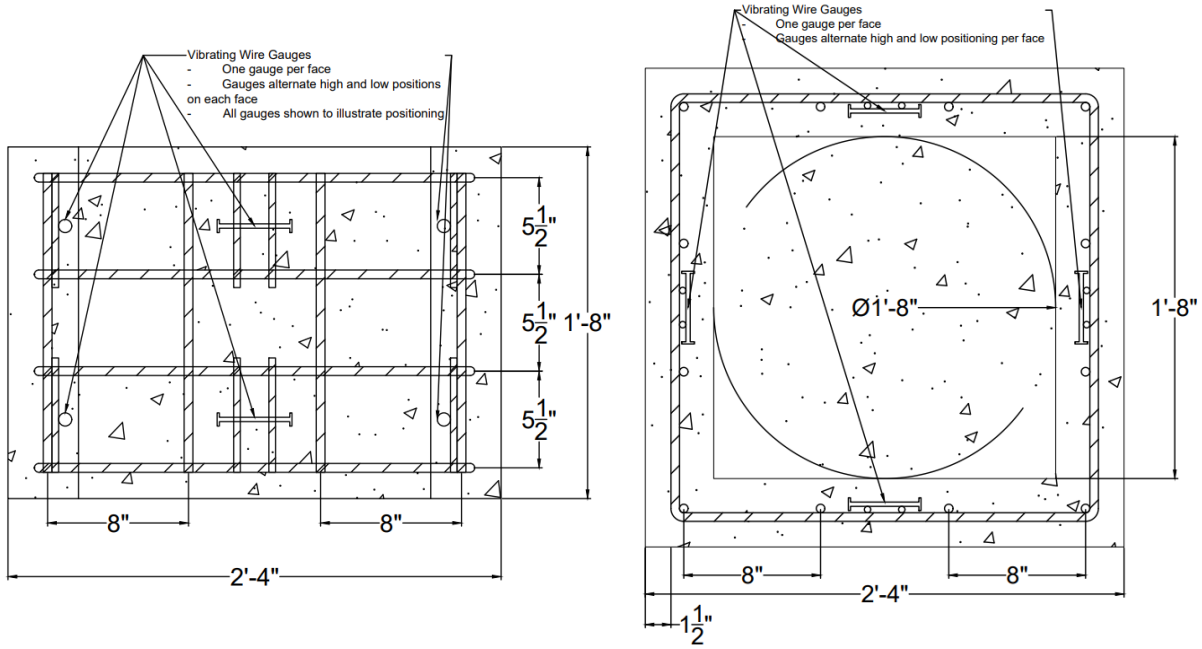

(a) Elevation view (b) Plan view

Figure 3-18: Vibrating wire strain gauge locations

3.2.4.2.2. Load Measurement

During testing, the load was measured using a 750 kip rated StrainSense load cell. This load cell allowed for accurate measurements to be collected every second throughout the testing process. Prior to the start of testing, the load cell was calibrated across a range of 0-600 kips. Regular calibration checks were conducted during the experimental program, considering its extended duration. In addition to the load cell, the research team employed an analog pressure gauge as a backup. This gauge served to measure the pressure in the ram and verify the accurate readings of the load cell during the tests.

3.2.4.2.3. Slip Measurement

Slip measurements were obtained using eight Novotechnik 100mm linear potentiometers (LPots). Two LPots were installed on each side of the specimen, adjacent to the interface, as shown in Figure 3-19. The difference between these two measurements represented the interface slip. To obtain a comprehensive measurement, the four slip measurements (two from each side) were averaged, providing an average slip measurement at each recorded data point.

Figure 3-19: Arrangement of potentiometers for slip measurement

3.2.4.2.4. Data Collection & Monitoring

Data collection was conducted using a Campbell Scientific CR6 Datalogger. This equipment was compatible with all load cells and L-Pots used during the testing process, enabling data collection at a frequency of once per second. The CR6 also facilitated real-time monitoring of load and deflections throughout the test. Following each test, the collected data was saved in a raw format on a computer and subsequently processed using MATLAB and Excel.

3.2.5. Test Procedure

The testing procedure for the specimens began by placing them onto the steel and rubber bearing plates. Care was taken to align the specimens as accurately as possible with the outer dimensions, ensuring that each face was flush with the previously aligned steel bearing plates beneath the testing frame. A steel loading plate was then securely fixed to the top of the specimen using hydrostone. This bonding process not only ensured a strong attachment between the plate and the specimen but also allowed for leveling of the plate to provide a flat loading surface. To create a pedestal for the load cell, larger steel blocks were placed on top of the loading plate. The load cell made contact with a tilt saddle on the ram.

Next, the specimens were preloaded to approximately 10 kips to verify the proper functioning of sensors and equipment. Once the satisfactory equipment performance was ensured, all sensors were zeroed or tared.

The test would then commence with a target loading rate of 500 lbs. per second. At approximately every 50 kips, the tests were temporarily halted to inspect the specimens and equipment for any unexpected behaviors. Load rates were adjusted as needed during these intervals. This process was repeated until failure was observed. Failures during the tests were characterized by a sudden, sometimes violent, slip of the interface, resulting in an approximate displacement of $1/8^{th}$ of an inch. These failures were clearly identifiable in the load graphs as a peak followed by a sharp drop-off in load. The research team would carefully document the failed specimen and record the corresponding peak load. After documentation, the research team would continue advancing the ram to determine if the specimen could withstand any additional load.

3.3. Experimental Results and Discussion

This section presents the experimental results of the current task. First, test results of interface strength are summarized, and observations of each specimen group are presented. A discussion about the effects of different variables on the interface strength is presented.

3.3.1. Summary of Test Results

Table 3-3 presents an overview of material test results and push-off test results. In the Table 3-3, the compressive strength of concrete is the average of the test strengths from three concrete cylinder samples for each specimen group. The peak load is measured by the load cell and the interface shear strength is calculated by dividing the peak load by the product of the perimeter and height of the interface (otherwise known as interface shear area).

Table 3-3. Summary of Test Results

Series	Specimen Group ID	Compressive Strength of Concrete (psi)		Peak Load (kip)	Interface Shear Strength (psi)
		Shell	Core		
I Precast Shell/CIP Core Interface	I-C-S	3863	7660	173	138
		3863	7660	255	203
		3640	7548	211	168
	I-C-S-SR	10540	5020	106	84
		12000	5600	90	71
		10850	5430	52	41
	I-C-T	11240	6020	271	216
		12500	5880	202	161
		11760	5140	293	233
	I-C-T-SR	11210	5430	221	176
		10280	5160	192	153
		10250	5160	208	166
	I-Sq-S	12173	5188	147	92
		12425	5770	130	81
		12085	5895	85	53
	I-Sq-T	11220	5950	309	193
		10720	5600	248	155
		10720	5600	166	104
II CIP Shell/Precast Core Interface	II-C-S	5690	5690	153	122
		5760	5760	194	154
		5710	5710	274	218
	II-Sq-S	4900	4900	72	45
		4610	4610	207	129
		5190	5190	290	181
	II-C-T	5480	5480	275	219
		5950	5950	261	208
		5880	5880	308	245

3.3.2. Damage Pattern and Shear Stress-Slip Behavior

This section presents the damage pattern and interface shear stress-slop behavior of each specimen group. The interface shear stress presented in the charts of this section is determined by the load-carrying capacity divided by the interface area. For circular voids, the interface shear area was 1257 in.^{2}; for square voids, the interface shear area was 1600 in.^{2}

3.3.2.1. Series I

3.3.2.1.1. Specimen Group I-C-S

For Group I-C-S (in which specimens had a precast shell, cast-in-place core, and smooth circular interface), the recorded peak load-carrying capacities were 173 kips, 255 kips, and 211 kips, corresponding to interface shear strengths of 138 psi, 203 psi, and 168 psi for the three specimens respectively. The interface shear-slip relationships of the three specimens exhibited ductile matter, as seen in Figure 3-20. Test 2 and Test 3 showed a slow load drop after reaching the load peak and had ultimate slip larger than 0.15 in. and 0.2 in. respectively; Test 1 had a different behavior in that the peak load occurred after having a large slip.

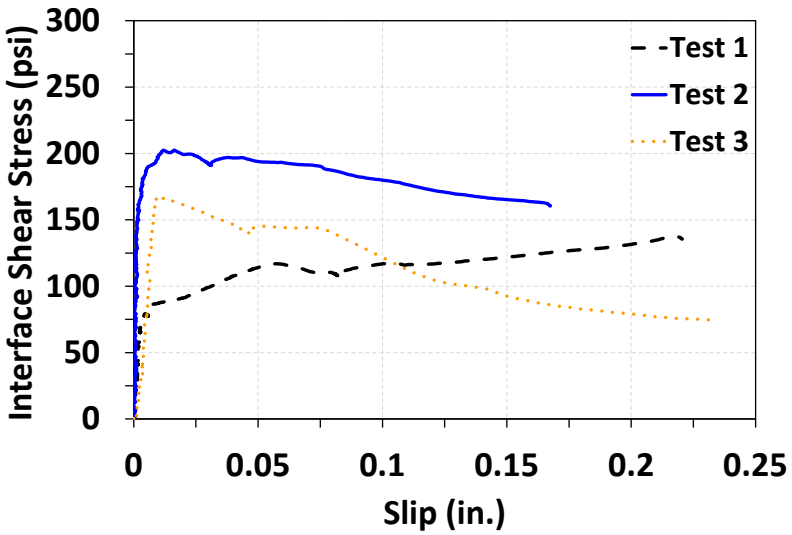

Figure 3-20: Load vs average slip for Group I-C-S

At the ultimate failure, all three specimens in this group exhibited a significant slip of the core accompanied by concrete spalling and crushing around the perimeter of the core, as shown in Figure 3-21. In the meantime, the shell cracked through the height. The through-height shell cracks distributed more in the middle where the thickness was smaller. Other than those cracks, a few cracks occurred near the corners but did not propagate through the entire height.

Figure 3-21: Pure slip failure as seen on the top and bottom of Group I-C-S

3.3.2.1.2. Specimen Group I-C-S-SR

For Group I-C-S-SR (in which the specimens had a precast shell, cast-in-place shrinkage reducing core, and smooth circular interface), the peak load-carrying capacities were 106 kips, 90 kips, and 52 kips, corresponding to interface shear stress of 84 psi, 71 psi, and 41 psi, respectively. Notably, these specimens were significantly weaker compared to their non-shrinkage reducing counterparts, but they still exhibited ductile post-peak behavior. The load drops after the peak load seemed to be less significant. In other words, the post-peak behavior tended to be a load plateau, as shown in Figure 3-22.

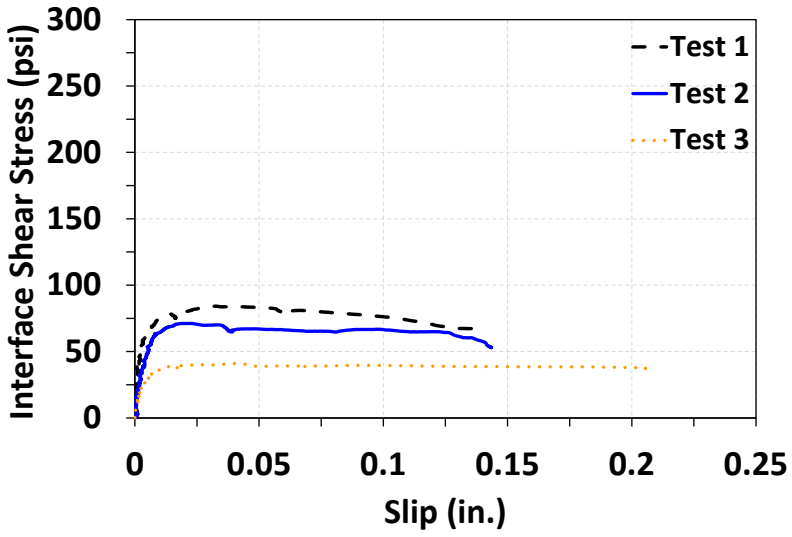

Figure 3-22: Load vs average slip for Group I-C-S-SR

The specimens in the group exhibited a similar failure mode to their non-shrinkage reducing counterparts. That is, the failure mode was characterized as a significant slip of the core accompanied by concrete spalling and crushing around the perimeter of the core, as shown in

Figure 3-23. Through-height cracks were also observed on the shell, but the quantity of through-height cracks was fewer than their non-shrinkage reducing counterparts.

The length change of concrete used in Series I-2 was measured, as introduced in Section 3.2.2.2, and the results are presented in Figure 3-24. It can be seen in the figure that Class C significantly shrunk in length after the 7th day and the shrinkage became slower after the 14th day. The SRC, on the other hand, expanded in length initially, which compensated following shrinkage, resulting in a length change of only -0.003%. Therefore, SRC was effective in controlling shrinkage.

Figure 3-23: Interface slip failure as observed in top and bottom of Group I-C-S-SR

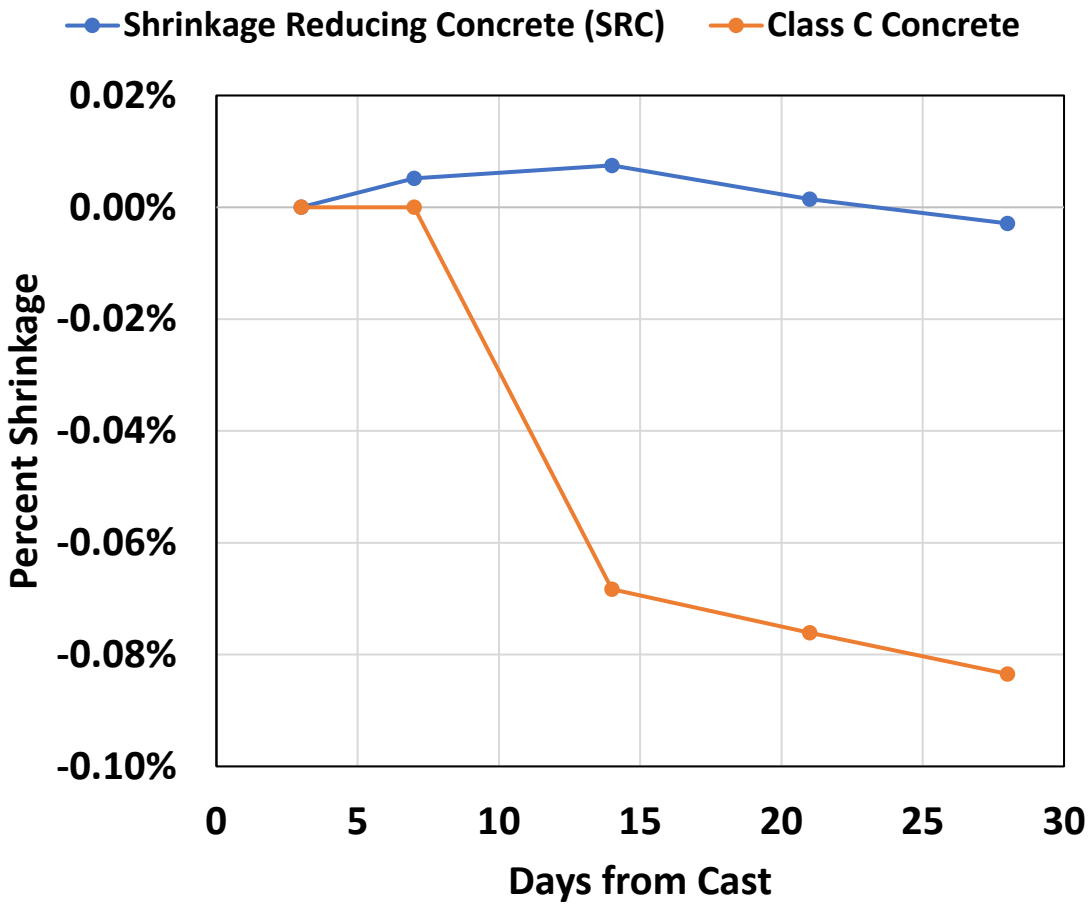

Figure 3-24: Length change of monitored companion prisms

3.3.2.1.3. Specimen Group I-C-T

For Group I-C-T (in which specimens had a cast-in-place core, a precast shell, and a textured circular interface), the recorded peak load carrying capacities were 271 kips, 216 kips, and 293 kips, corresponding to peak interface shear strength of 216 psi, 161 psi, and 233 psi, respectively. Compared to their non-textured counterparts (Groups I-C-S and I-C-S-SR), this group demonstrated higher interface shear strength but the slip right before failure was smaller. No specimens in this group sustained a slip larger than 0.8 in, as shown in Figure 3-25.

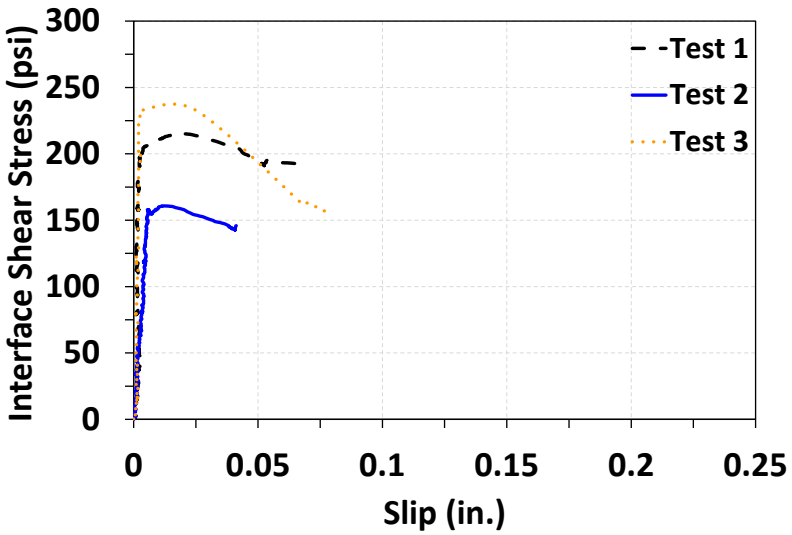

Figure 3-25: Load vs average slip for Group I-C-T

All three specimens in this group also exhibited noticeable slip and concrete spalling around the perimeter of the core, accompanied by cracking in the shell. In this case, a large amount of cracking was observed in the shell with cracks running from the interface on the top surface to the edge of the shell and then down to the bearing plates, as shown in Figure 3-26 and Figure 3-27 for example.

Figure 3-26: Slip failure as observed on the top of specimens in Group I-C-T

Figure 3-27: Representative examples of shell cracking observed in Group I-C-T

3.3.2.1.4. Specimen Group I-C-T-SR

For Group I-C-T-SR (in which specimens had a precast shell, a cast-in-place core made of shrinkage reducing concrete, and a textured circular interface), the recorded peak load carrying capacities were 176, 152, and 167 kips, corresponding to interface shear strengths of XXX psi, respectively. The interface shear stress-slip relationships of the specimens in the group are shown in Figure 3-28. The interface shear stress-slip relationships were found to be relatively consistent between the three specimens. This group demonstrated a lower interface shear strength but a better post-peak behavior than its non-shrinkage reducing counterpart (Group I-C-T). In addition, this group performed higher interface shear strength and comparable ductility compared to its non-textured counterpart (Group I-C-S-SR).

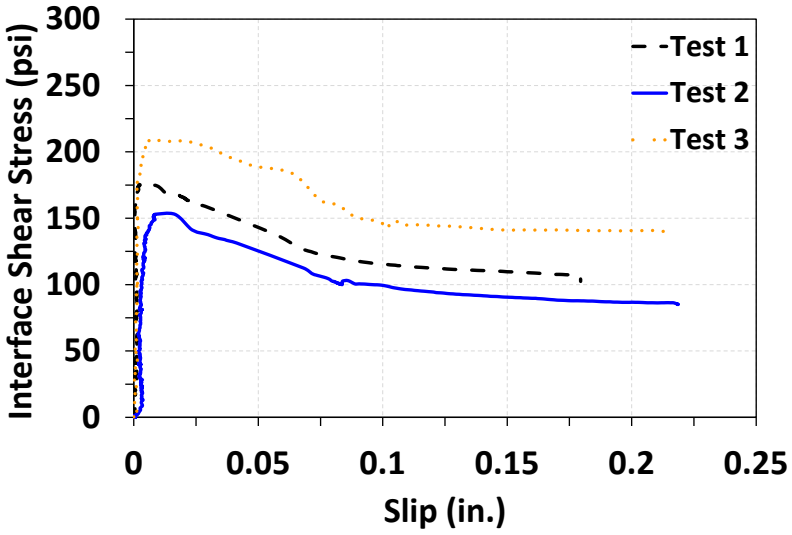

Figure 3-28: Load vs average slip for Group I-C-T-SR

All specimens in this group also exhibited a similar damage pattern after failure to other groups mentioned above as shown in Figure 3-29 and Figure 3-30. However, compared to its non-shrinkage-reducing counterpart (Group I-C-T), an average amount of cracking was observed running from the interface down the face of the shell.

Figure 3-29: Slip failure as observed on the top of Group I-C-T-SR

Figure 3-30: Shell cracking representative of Group I-C-T-SR

3.3.2.1.5. Specimen Group I-Sq-S

For Group I-Sq-S (in which specimens had a cast-in-place core, a precast shell, and a smooth square interface), the peak measured load-carrying capacity were 147 kips, 130 kips, and 85 kips, corresponding to 92 psi, 81 psi, and 53 psi, respectively. Figure 3-31 presents the measured

interface shear stress with regard to the slip. It should be noted that Test 3 is not included due to a testing anomaly with the operation of the linear potentiometers causing poor slip measurement data. It can be seen from the figure that the presented two tests, although having similar interface shear strengths and a close magnitude of load drop, had significant differences in terms of post-peak behavior. The specimen of Test 1 suffered a slow load drop after reaching the first peak load until a slip of approximately 0.08 in., followed by re-gaining load carrying capacity and sustaining almost the same level of the first peak load. The specimen ended up with a final slip of approximately 0.425 in. The second test, however, had a behavior far from the first test. Test 2 did not re-gain the load-carrying capacity after the load drop and failed at a slip smaller than 0.12 in. The considerable difference made it difficult to compare to its circular interface counterparts in terms of ductility. Nevertheless, it can still be observed that this group at least had comparable ductility but lower interface strength in general.

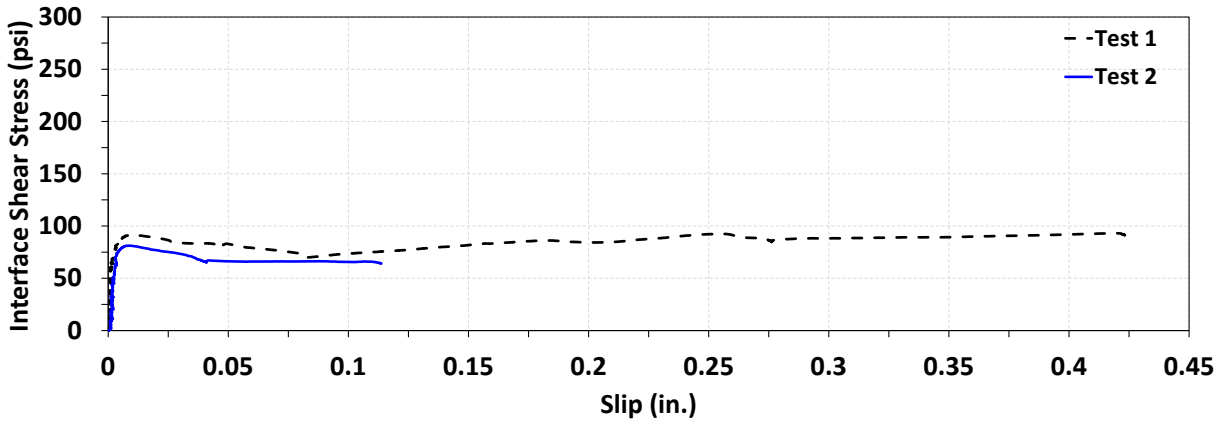

Figure 3-31: Load vs average slip for Group I-Sq-S

The specimens in this group all exhibited noticeable slip and local crushing of concrete along the perimeter of the square core, as shown in Figure 3-32. Similarly, cracks were observed running from the interface on the top of the shell down to the side wall. However, only a few cracks in general were identified; only one crack fully propagated through the height on one of the shell walls. Other side walls did not have such cracking patterns.

Figure 3-32: Group I-Sq-S after failure

3.3.2.1.6. Specimen Group I-Sq-T

For Group I-Sq-T (in which specimens had a precast shell, a cast-in-place core, and a textured square interface), the peak load-carrying capacities were 309 kips, 248 kips, and 166 kips, corresponding to 191 psi, 153 psi, and 104 psi, respectively. From the interface shear stress-slip relationships shown in Figure 3-33, all three specimens in this group experienced brittle failure when reaching the peak load; no post-peak behavior was observed.

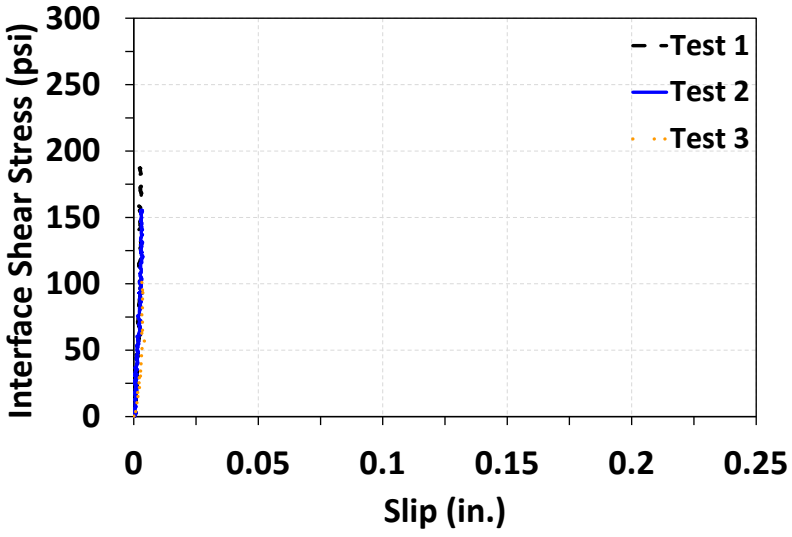

Figure 3-33: Load vs average slip for Group I-Sq-T

Failures in this group occurred when significant slips and some crushing of concrete along the perimeter of the core, as shown in Figure 3-34 and Figure 3-35. However, the crushing at the corners was not necessarily along the perimeter; instead, some bearing cracks penetrated from the perimeter into the core near the bearing surface. In addition, cracks were observed on the side walls of the shell; more amount of cracking appeared, compared to its smooth-interface counterpart (Group I-Sq-S).

Figure 3-34: Interface failure modes at the top of Group I-Sq-T

Figure 3-35: Shell cracking seen in Group I-Sq-T

3.3.2.2. Series II

3.3.2.2.1. Specimen Group II-C-S

Group II-C-S consisted of specimens with a precast circular core, a cast-in-place shell, and a smooth interface. The test load carrying capacities were 153 kips, 194 kips, and 274 kips, corresponding to 122 psi, 154 psi, and 218 psi, respectively. The interface shear stress-slip

relationships shown in Figure 3-36, reveal that the specimens all had brittle failure and no post-peak behavior was observed.

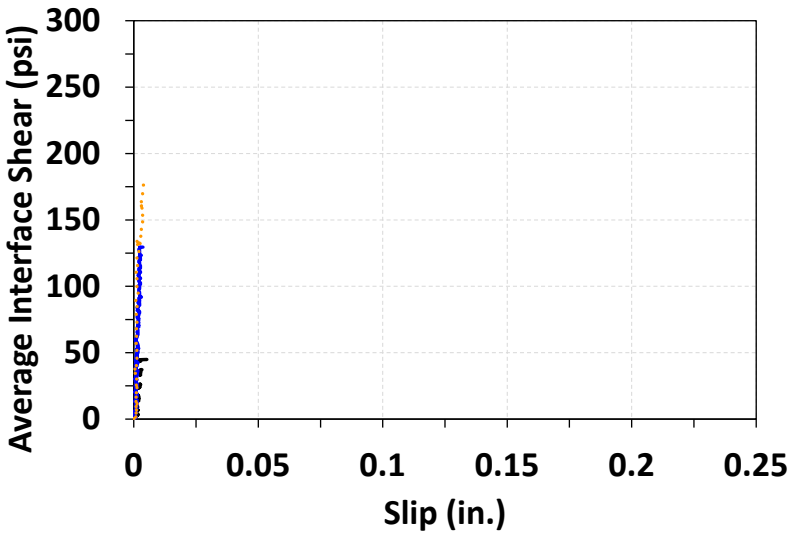

Figure 3-36: Load vs Average Slip for Group II-C-S

This series also had extensive shell cracking upon failure on all four sides, and the quantity of the shell cracks on each side was more, compared to their Series I companion, as shown in Figure 3-37. In addition, significant slip and crushing of concrete along the perimeter of the core were observed along with some bearing failures. Upon inspection of the bottom of the specimens, a slip along the perimeter of the core was observed, as seen in Figure 3-38.

Figure 3-37: Group II-C-S after failure.

Figure 3-38: Group II-C-S exhibiting a partial bearing failure on the surface

3.3.2.2.2. Specimen Group II-Sq-S

Specimen Group II-Sq-S contained specimens with a precast core, a cast-in-place core smooth, and a square interface. The measured load-carrying capacities were 72 kips, 207 kips, and 290 kips, corresponding to interface shear strengths of 45 psi, 129 psi, and 181 psi. The first specimen in this group had a much lower strength than the other two specimens; the specimen was observed to have a significant bearing failure around the load plate aside from slipping and cracking on the shell as shown in Figure 3-39, which might have been the cause of the low strength. The phenomenon suggests the possibility of construction or material defects in the specimen. The other two specimens, on the other hand, did not have a serious bearing failure on the top surface but had similar failure damage patterns to their companion specimens in Group I-Sq-S, also as shown in Figure 3-40. The interface shear stress-slip relationships of the specimens, as shown in Figure 3-41, reveal that none of the specimens in the group exhibited post-peak behavior.

Figure 3-39: Group II-Sq-S after failure showing side face cracking

Figure 3-40: Group II-Sq-S after failure

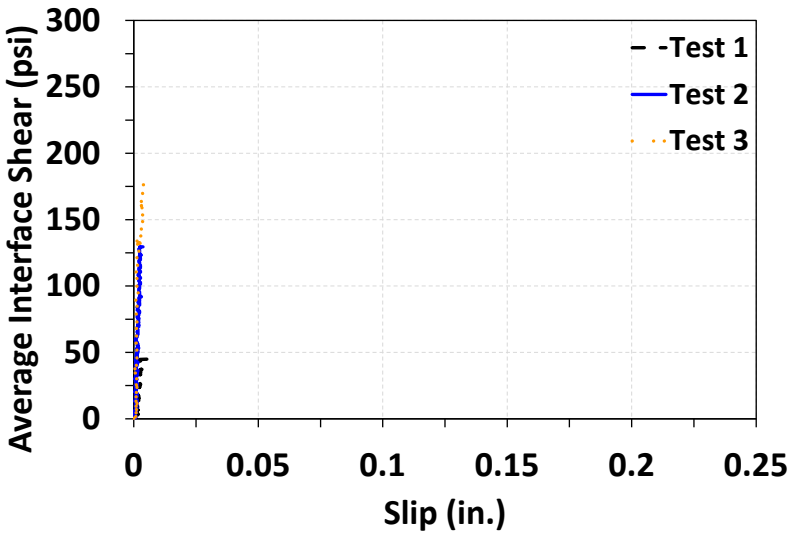

Figure 3-41: Load vs average slip for Group II-Sq-S

3.3.2.2.3. Specimen Group II-C-T

For Group II-C-T (precast core, cast-in-place shell, circular roughened interface), the peak strengths recorded were 210, 199, and 236 psi. Full slips were observed as the final failure mode of all three specimens, as shown in Figure 3-42. Additionally, larger pieces of the core were sheared off after the final failure (Figure 3-42). Specimens in this series also had a fair amount of shell cracking, as shown in Figure 3-43. Finally, in terms of load versus slip behavior, all three specimens in this series demonstrated no obvious post-peak behavior, which is different from their counterpart in Series I (Group I-C-T), as shown in Figure 3-44.

Figure 3-42: Pure slip failures as seen on the top of Group II-C-T

Figure 3-43: Representative examples of cracking in Group II-C-T

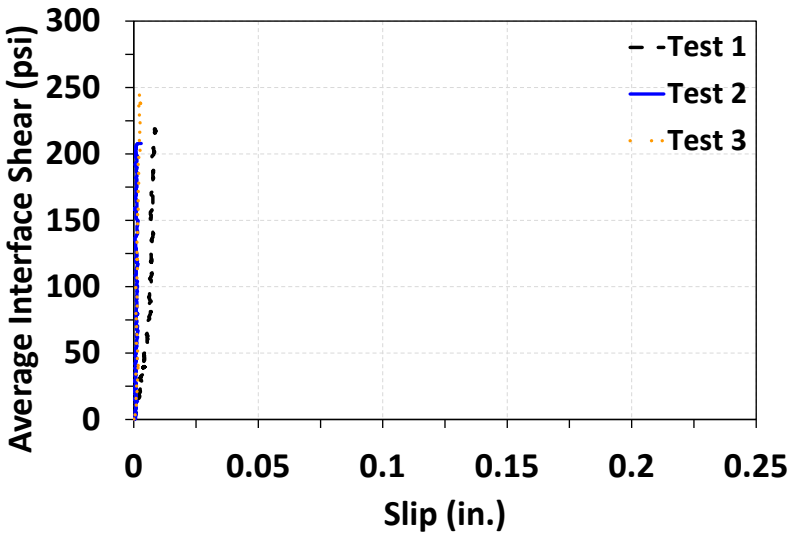

Figure 3-44: Load vs average slip for Group II-C-T

3.3.2.3. General Discussion

Several insights can be derived from the observations in the interface shear stress-slip relationships and damage patterns, as follows:

1. Smooth interfaces demonstrate a tendency to avoid sudden drops in the push-off load-carrying capacity, exhibiting a more gradual post-peak behavior. On the other hand, textured interfaces, while showcasing higher interface shear strength, are more likely to experience a sudden load drop once they reach the peak load. In addition, textured interfaces cause more amount of cracking on the shell than smooth interfaces.

2. The addition of shrinkage-reducing admixture to the core concrete proves beneficial in preventing abrupt reductions in the load-carrying capacity. However, this improvement comes at the cost of lower interface shear strength.

3. Interfaces between a precast core joined by a CIP shell show a propensity for causing sudden drops in the load-carrying capacity. Notably, none of the specimens in Series II exhibited stable post-peak behavior.

4. Square interfaces exhibit varying outcomes concerning the interface shear strength and often lack ductility after reaching the peak load.

3.3.3. Evaluation of Test Variables

This section presents discussion about the effect of each of the test variables on the interface shear strength in the experimental program investigated. The test variables include interface shape, differential shrinkage, interface roughness, and cast sequence. In the following discussion, test results of relevant specimen groups are plotted as bar charts together to make an informative

comparison. In the bar charts, the average of the three test interface shear strengths of each specimen group (denoted as τ_{avg}) is calculated and compared to others. Error bars are marked to inform the data variation.

3.3.3.1. Interface Shape

To evaluate the effect of the interface shape on the interface shear strength, four specimen groups from Series I were employed. In Series One, Groups I-C-S and I-Sq-S had a smooth interface but different shapes. Similarly, Groups I-C-T and I-Sq-T had a textured interface but different shapes. It is therefore possible to evaluate the effect of the interface shape on either smooth interfaces or roughened interfaces using the four specimen groups, as shown in Figure 3-45.

It can be seen from Figure 3-45(a) that the smooth circular interface performed significantly better than the smooth square interface. In average, the smooth circular interface reached an interface shear strength of 170 psi, which was 127% stronger than the smooth square interface (75 psi).

A similar phenomenon can be observed for textured interfaces as shown in Figure 3-45(b). The roughened circular interface had a higher average interface shear strength (203 psi) than that of the roughened square interface (151 psi). However, the difference was 34.4%, not as significant as the smooth cases. In addition, Group I-Sq-T had the largest data variety and the high of the test data appeared to be higher than the low of its circular counterpart.

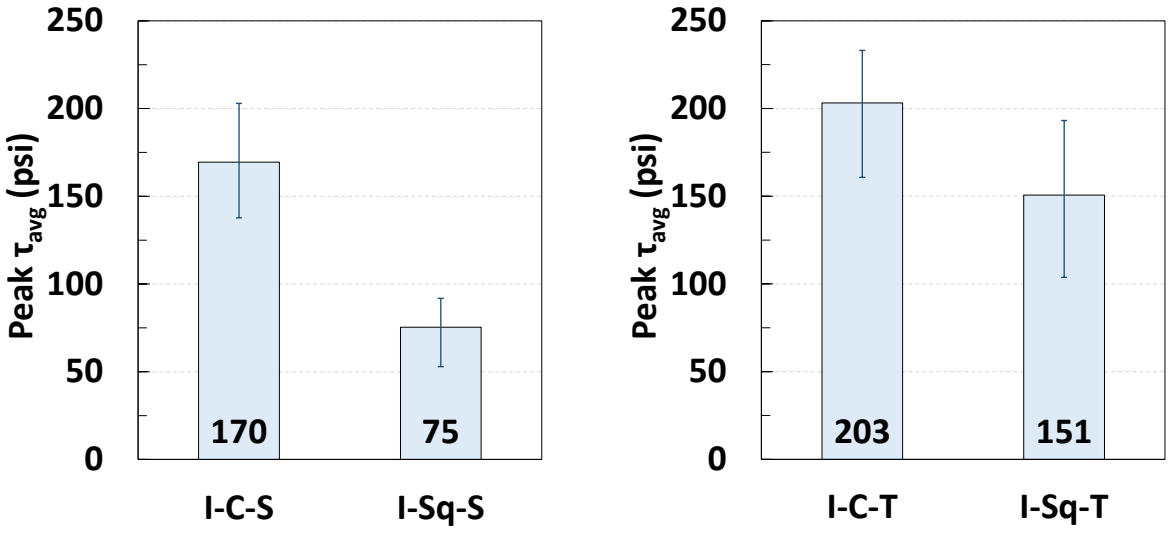

(a) Smooth interface (b) Textured interface

Figure 3-45: Effect of shape on peak interface shear stress in Series I

In addition to Series II, tests on specimen groups with different interface shapes in Series II delivered a similar result; the average interface shear strength of circular interfaces was higher than that of square interfaces, as suggested in Figure 3-46. In particular, the circular interface was 39.8% stronger than its square counterpart. It should be noted that Group II-Sq-S had a

considerable variation in test results. If the lowest data point was ruled out, the average of the remaining data points was 155 psi, which was comparable to that of Group II-C-S.

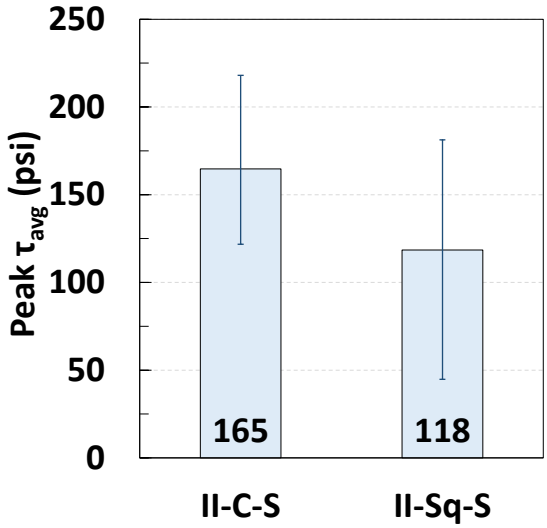

Figure 3-46: Effect of shape on peak interface shear stress in Series II

Based on the overall trend of interface shape, it can be concluded that circular interfaces can be anticipated to have higher interface shear strength than square interfaces. Roughening the interface or casting the shell after the core may be able to lower the difference. In relation to design of precast columns, using a circular void in the hybrid column design will yield more interface strength compared to a square void.

3.3.3.2. Differential Shrinkage

The effects of differential shrinkage on the interface shear strength were evaluated by comparing Groups I-C-S and I-C-S-SR; the two specimen groups had the same configuration and a smooth circular interface, but the last one had the core concrete added with shrinkage-reducing admixture. As shown in Figure 3-47, it was found that the addition of shrinkage-reducing admixture significantly reduces interface shear strength. Group I-C-S reached an average interface shear strength of 170 psi, while Group I-C-S-SR only reached 66 psi, suggesting a 61.2% reduction in strength.

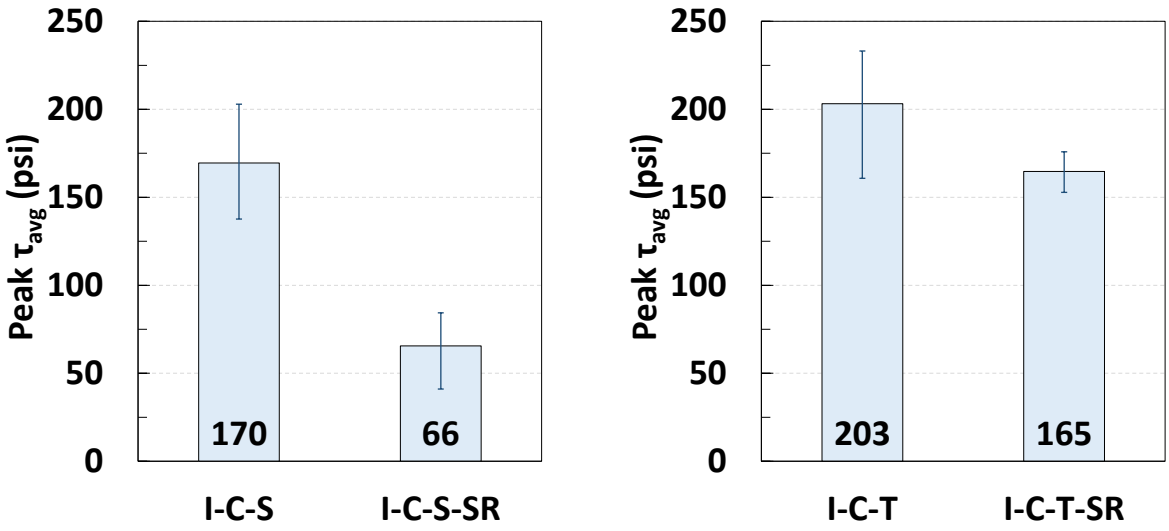

(a) Smooth interface (b) Textured interface

Figure 3-47: Effect of SRC on peak interface shear stress

A reduction in strength due to adding shrinkage-reducing admixture also occurred for specimen groups with a textured circular interface (Groups I-C-T and I-C-T-SR). However, the magnitude of the strength reduction was not as considerable as specimen groups with a smooth circular interface. In particular, as shown in Figure 3-47, Group I-C-T reached an interface shear strength of 203 psi and Group I-C-T-SR, 165 psi. The addition of shrinkage-reducing admixture caused a reduction in strength of 18.7%

This is somewhat of an unexpected result, as the theory was that the addition of shrinkage-reducing admixture to the core would assist in avoiding the detachment between the core and the shell increase normal force across the interface, and therefore induce better shear friction behavior. However, despite conflicting evidence from the literature reviews, there were studies linking shrinkage and interface shear strength with a positive correlation. It was possible that a shrinkage-reducing mixture might cause a lower cohesion on the interface. More research should be conducted in this regard.

Nevertheless, the presence of shrinkage reducing admixture was found to provide a more consistent interface strength compared to specimens without the admixture. Additionally, those specimens were also found to have improved post-peak behavior compared to their counterparts without the shrinkage-reducing admixture.

3.3.3.3. Interface Roughness

Interface roughness was found to profoundly increase the interface shear strength for both circular and square interfaces, as can be seen in Figure 3-48. For circular interfaces with a precast shell (Specimen Groups I-C-S and I-C-T), the roughened interface was found to increase the strength by 33 psi or 19.4% on average. For square interfaces with a precast shell (Specimen Groups I-Sq-S and I-Sq-T), the roughened interface increased the interface shear strength by 76 psi or 101% on

average. The strength enhancement was more significant on square interfaces than on circular interfaces, but the variation in test results became considerable. Also, the roughened square interface still had a lower peak shear stress than the smooth circular interface on average.

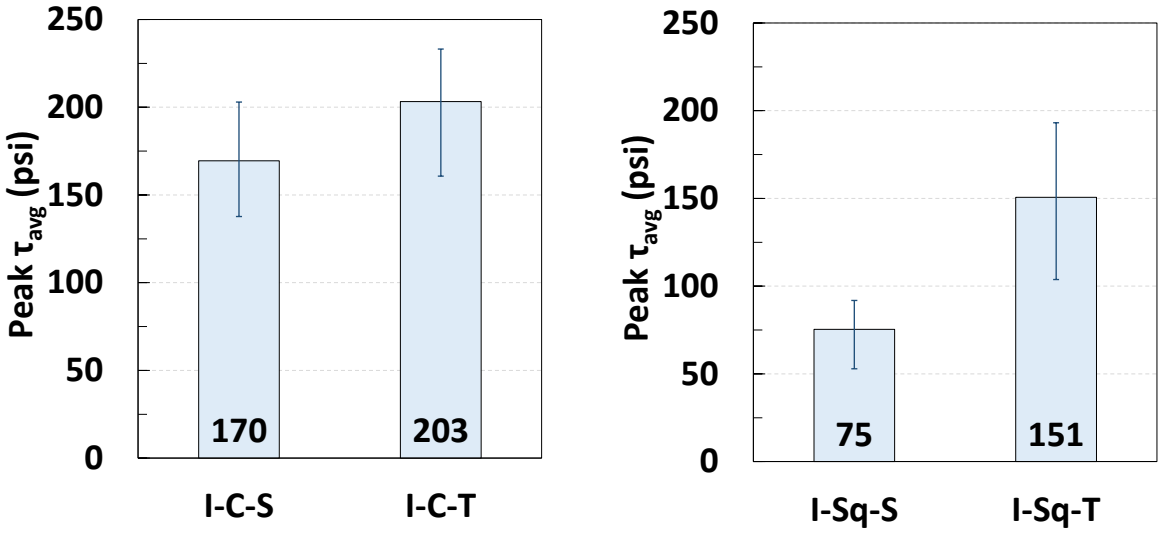

(a) Round interface (b) Square interface

Figure 3-48: Effect of roughness on peak interface shear stress in Series I

In Series II, the roughened interface increased strength by 59 psi or 35.8% for the circular interface, as seen in Figure 3-48 in which the comparison between Specimen Groups II-C-T and II-C-S was presented. The observation indicates that the enhancement was similar whether the shell or the core was cast first.

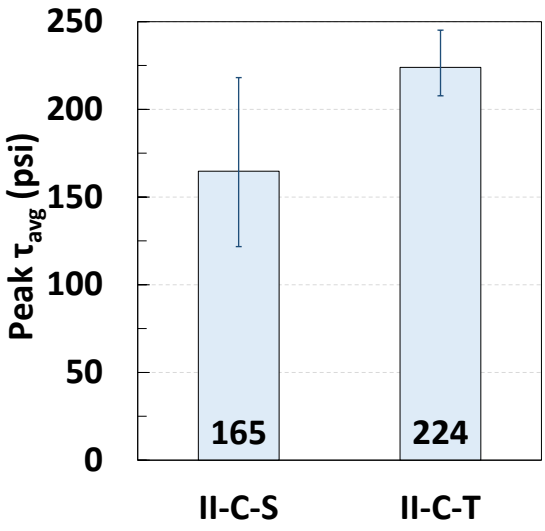

Figure 3-49: Effect of roughness on peak interface shear stress in Series II

3.3.3.4. Sequence of Cast

The effects of the sequence of cast, otherwise differential strength, on the interface shear strength were evaluated by comparing specimens in Series II to their counterparts in Series I, as shown in Figure 3-50. The results reveal that no significant difference in the interface shear strength for circular interfaces whether the core or the shell was cast first. In particular, for smooth circular interfaces, the difference in the interface shear strength was only -2.9%; for textured circular interfaces, the difference was 10.3%. Considering the data scattering, it is difficult to conclude that casting the shell first or casting the core first would affect the interface shear strength for circular interfaces.

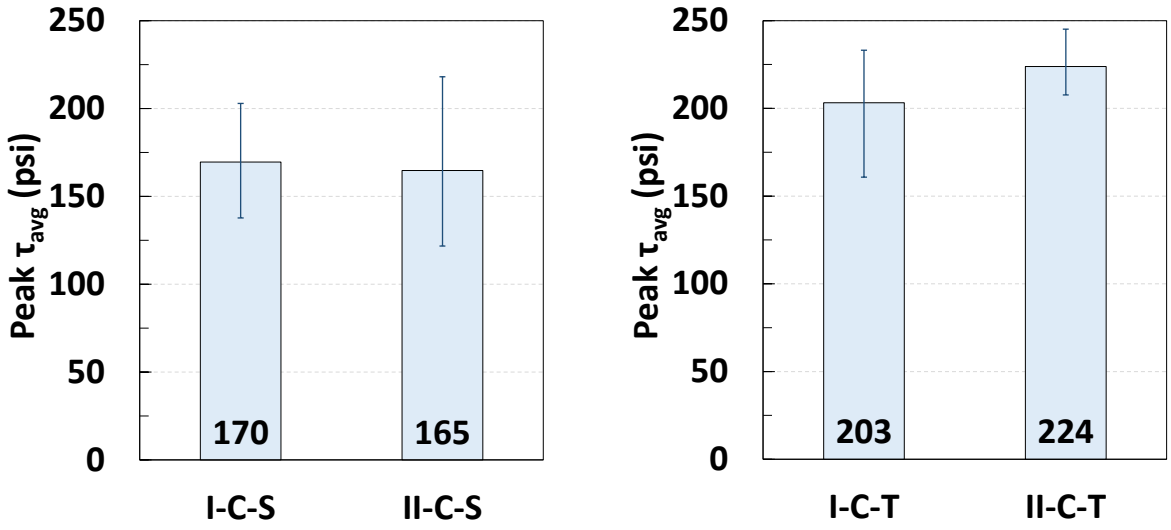

(a) Smooth interface (b) Textured interface

Figure 3-50: Effect of the sequence of cast on peak interface shear stress for round interface

For square interfaces, on the other hand, having a precast core and the cast-in-place shell seemed to increase the interface shear strength by 43 psi, as indicated in Figure 3-51. However, it is not decisive because there existed considerable variation in the interface shear strength of Specimen Group II-Sq-S. More studies are needed to investigate the effect of the sequence of cast or differential strength on the interface shear strength.

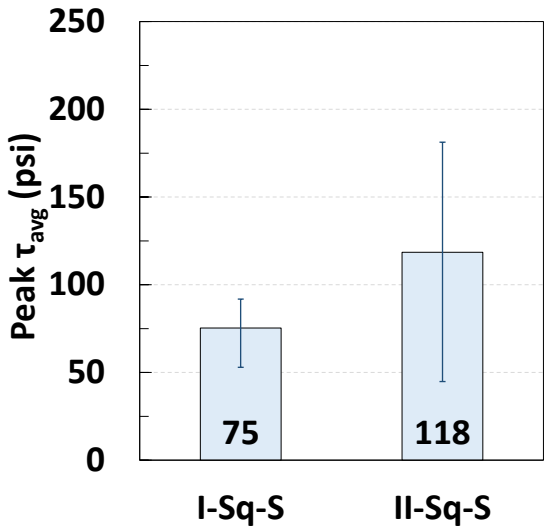

Figure 3-51 Effect of the sequence of cast on peak interface shear stress for square interface

3.4. Evaluation of Strength using Code Design Expressions

In this section, test results were used to evaluate major code design expressions including AASHTO LRFD and ACI 318-19. The interface shear resistances of the test specimens were calculated using the design expressions and compared to the test results.

3.4.1. ACI 318-19

The equations for interface shear resistance in ACI 318-19 include only the contribution of reinforcement across the interface, given by

- When reinforcement is perpendicular to the interface:

$$V_n = \mu A_{vf} f_y \tag{3-1}$$

- When reinforcement is not perpendicular to the interface:

$$V_n = A_{vf} f_y (\mu \sin\alpha + \cos\alpha) \tag{3-2}$$

where V_n = nominal shear strength of the interface
μ = coefficient of friction
A_{vf}=area of reinforcement crossing the shear plane
f_y = minimum yield strength of reinforcement

As no reinforcement across the interface was provided with the test specimens, the ACI equations [Eqs. (3-1) and (3-2)] were not applicable, otherwise zero resistance would be derived from the equations. It is implied that the method for interface shear resistance of ACI 318-19 has limited applicability.

3.4.2. AASHTO LRFD 2020

Interface shear strengths of the test specimens were calculated using the current AASHTO LRFD code provisions. The nominal interface shear resistance in AASHTO LRFD is presented in Chapter 2 and repeated here for the reader's convenience as follows:

$$V_{ni} = cA_{cv} + \mu(A_{vf}f_y + P_c) \quad (3\text{-}3)$$

where V_{ni} = nominal interface shear resistance (kip)
c = cohesion factor (ksi)
A_{cv} = area of concrete considered to be engaged in shear transfer (in^2)
A_{vf} = area of interface shear reinforcement crossing the interface (in^2)
f_y = minimum yield strength of reinforcement (ksi)
P_c = permanent net compressive force normal to the shear plane (kip)

When using Eq. (3-3) to calculate the interface shear strengths of the test specimens, a few assumptions were made. Firstly, the cohesion factor was 0.075 ksi and the coefficient of friction was 0.6 for smooth interfaces; the cohesion factor was 0.24 ksi and the coefficient of friction was 1.0 for textured interfaces based on Section 5.7.4.4 of AASHTO LRFD. The A_{cv} value was assumed to be the area of the interface, which is the length of the perimeter of the interface multiplied by the height as introduced previously. For the test specimens in the experimental program, no reinforcement crossing the interface nor permanent net compressive force normal to the shear plane existed; therefore, the second term of the equation did not contribute to the interface shear resistance.

Consequently, the analytical results are summarized in Figure 3-52. In the figure, each datapoint is represented as a shape with a vertical coordinate of test load-carrying capacity and with a horizontal coordinate of calculated load-carrying capacity per AASHTO LRFD. Each series is assigned a particular shape for identification. A diagonal dashed line is drawn in the figure and separates the chart into two regions. The upper half contains datapoints that had a test load-carrying capacity higher than the calculated load-carrying capacity, meaning that AASHTO LRFD delivered conservative predictions. On the other hand, the lower half contains datapoints with a test load-carrying capacity lower than the load-carrying capacity, meaning that AASHTO LRFD delivered unconservative predictions. Datapoints close to the diagonal represent accurate results.

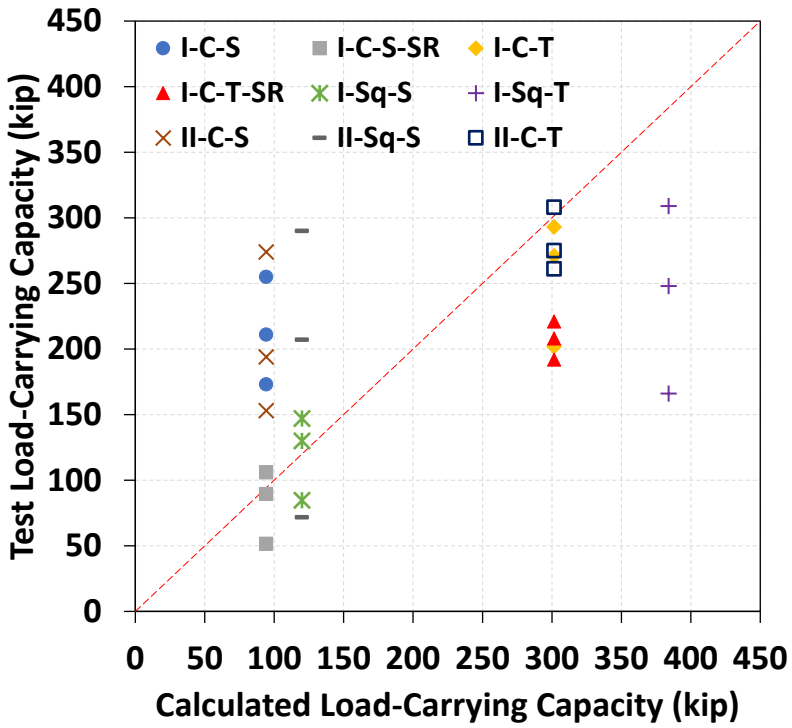

Figure 3-52: Test interface shear capacity versus calculated interface shear capacity per AASHTO LRFD

It can be seen from Figure 3-52 that in most cases, the results found that this AASHTO LRFD equation does not provide accurately predicted strengths. Although the average ratio of the test load-carrying capacity to the calculated one is 1.22, most cases fall away from the diagonal and the coefficient of variation is 56.5%. The unconservative counts are 15 out of 27 tests. There is no evident trend that indicates what types of specimens were better predicted. The observation reveals that the AASHTO LRFD equation has shortcomings when applied to such unreinforced core-shell interfaces or interfaces with shrinkage reducing concrete. Also, the AASHTO LRFD equation cannot reflect potential confinement from the shell with different shapes.

3.4.3. Modifications to AASHTO LRFD for Core-Shell Interfaces

As stated previously, AASHTO LRFD does not allow unreinforced interfaces and does not reflect shell confinement. The effect of shrinkage-reducing admixture on the cohesion of concrete is not considered. It is needed to introduce modifications to the AASHTO LRFD equation that would account for the investigated factors in the experimental study.

The primary way in which AASHTO LRFD accounts for different interface conditions is by using the cohesion strength. However, the code specified cohesion values could not derive accurate predictions and were needed to be calibrate against the test results. Consequently, new cohesion factors and modification factors that account for the confined interface shell and the effect of shrinkage-reducing admixture were integrated into Eq. (3-3), forming Eq. (3-4):

$$V_{ni} = cA_{cv}\lambda_{shape}\lambda_{shrinkage} \quad (3\text{-}4)$$

where V_{ni} = nominal interface shear resistance (kips), c = cohesion factor (ksi) as defined in Table 3-4, A_{cv} = area of concrete considered to be engaged in shear transfer (in^2), and λ_{shape} is the shape factor, as defined in Table 3-5, and $\lambda_{shrinkage}$ is the shrinkage-reducing concrete factor, as defined in Table 3-6.

Table 3-4. Proposed cohesion values

Interface Conditions	Proposed Factors
Smooth, confined interface between two concretes placed at different times	c = 0.110 ksi
Rough, confined interface between two concretes placed at different times	c = 0.175 ksi

Table 3-5. Proposed shape factors

Interface Shape	Shape Factor, λ_{shape}
Circular	1.00
Square	0.50

Table 3-6. Proposed Shrinkage Factors

Concrete Type	Shrinkage Factor, $\lambda_{shrinkage}$
Normal Concrete	1.00
Shrinkage Reducing Concrete	0.40

The proposed factors were calibrated and adjusted using the average load from each series, ensuring that the proposed recommended strength, Eq. (3-4), with the addition of a factor of safety that considered the low test result in each series. As a result, Eq. (3-4) improved the calculated strengths of such core-shell interfaces, as shown in Figure 3-53. Similarly, each series is assigned a particular shape for identification. A diagonal dashed line is drawn in the figure and separates the chart into two regions. Datapoints close to the diagonal represent accurate results.

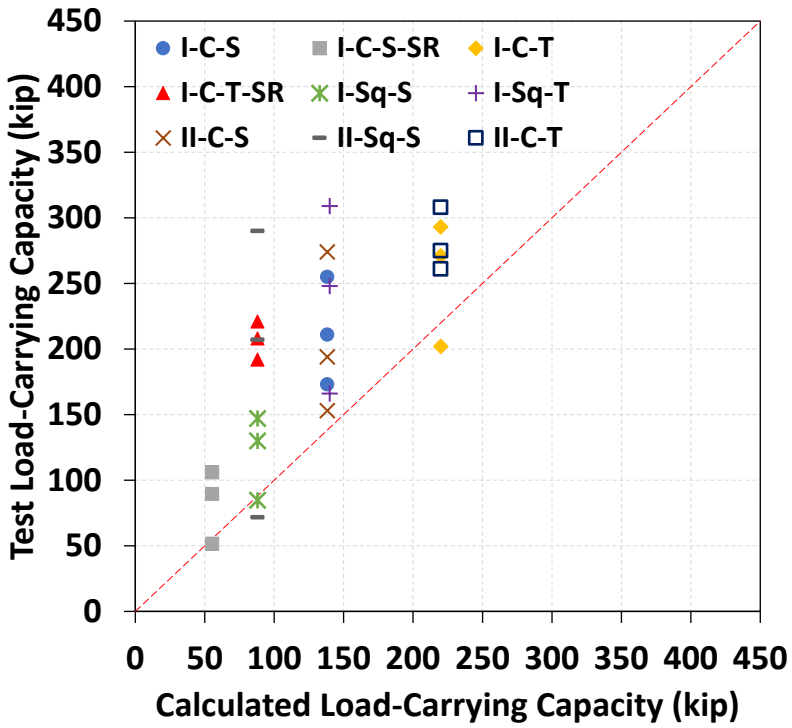

Figure 3-53: Test interface shear capacity versus calculated interface shear capacity per the proposed method

It can be seen from Figure 3-53 that Eq. (3-4) delivered more conservative results with an average ratio of 1.62. The number of unconservative counts is four out of 27 specimens. Furthermore, the coefficient of variation is 35.6%. The proposed factors significantly benefit the modeling of core-shell interfaces, and the proposed equation provides insights into the design of core-shell interfaces.

3.5. Summary

Following the completion of the testing program and the comprehensive analysis of various factors influencing interface shear strength, the subsequent recommendations for the interface shear properties are outlined as follows:

- **Interface Geometry:** Circular interfaces exhibited a higher strength over square interface. Notably, circular interfaces demonstrated a 127% increase in strength for smooth interfaces and a 34.4% increase for roughened interfaces compared to square interfaces.

- **Differential Strength:** Different strengths between the precast shell and the core was found to have no detrimental impact on interface strength. Lower differential strength seemingly led to ductile failure modes, albeit the number of specimens was limited.

- **Shrinkage Reducing Admixture (SRA):** While the use of SRA in the core concrete reduced interface strengths (smooth interfaces by 61.2% and rough interfaces by 18.7%), it enhanced consistency and post-peak behavior.

- **Interface Roughness:** Interface roughness emerged as the most significant factor influencing shear strength. Modest roughening through sandblasting increased interface strengths by 19.4% and 101% on average for circular and square interfaces, respectively.

- **AASHTO Interface Shear Equation:** The current AASHTO LRFD interface shear equation is deemed inadequate for accurately capturing the behavior of unreinforced core-shell interfaces. It tends to be generally unconservative when utilizing the code-provided cohesion strengths with interface areas.

- **Modified Equation (Eq. (3-4)):** A modified equation incorporating a shape factor, reduction factor, and updated cohesion values for various scenarios provides a more accurate representation of the behavior of unreinforced confined core-shell interfaces.

Chapter 4. Full-Scale Experimental Program

This chapter presents the experimental program that was developed to investigate and validate the precast column solution. In this experimental program, five specimens, including one cast-in-place (CIP) column as the control group based on the current TxDOT standard, and four specimens using the precast column system developed in this project were tested. The following sections document the design concept, test variables, test setup, specimen fabrication sequence, instrumentation, and test method.

4.1. Specimen Design and Test Variables

4.1.1. Overview of Design Concept

Five test specimens were planned in this test program; one CIP column specimen serving as the control group and four specimens based on the developed precast columns system, as schematically shown in Figure 4-1. The CIP control specimen consisted of a footing, a bent cap, and the column of interest. The column was 8 ft in height with a cross-sectional diameter of 3 ft, corresponding to one of the most commonly used dimensions for multi-column bents in Texas. The bent cap and the footing were designed to facilitate the application of loading and to have sufficient capacity during the test. Loads were planned to be applied on the bent cap and anchored on the footing, forming a self-reacting frame to create both axial load and bending moment in the column.

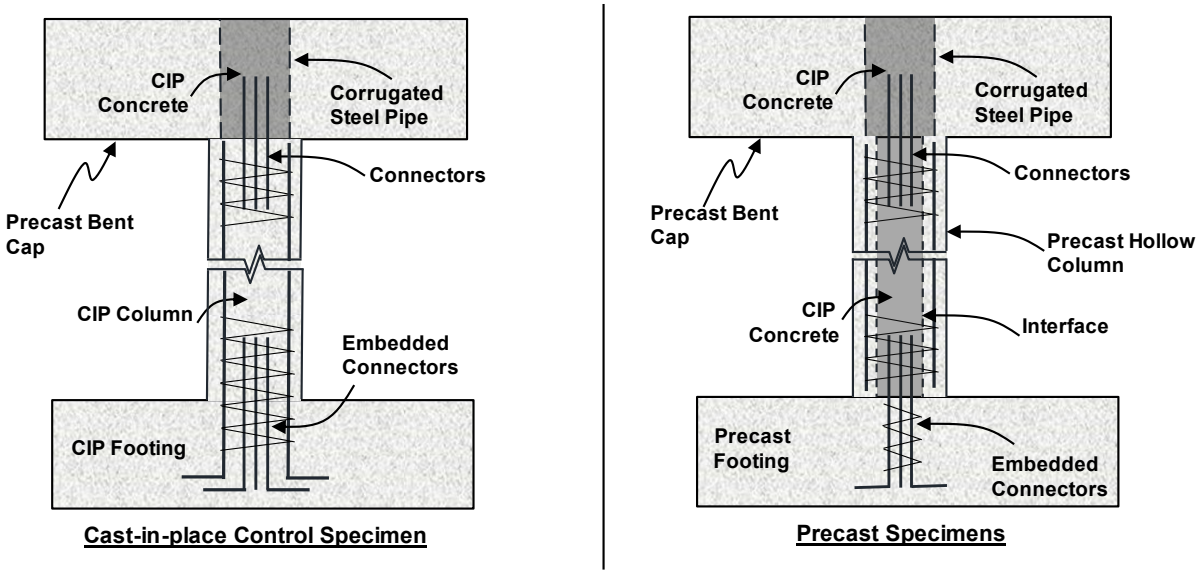

Figure 4-1: Schematic design of the specimens used in the study.

Similarly, the four test specimens consisted of a bent cap and a footing for the application of the load. The column consisted of a precast shell and a CIP concrete core with the same overall height and cross-sectional diameter as that of the control specimen. The shell was designed to be

prestressed. Longitudinal reinforcement extruding from the footing entered the core of the hollow shell as connectors. Similar connectors were used between the top of the column and the bent cap, which had a hollow pocket lined with a corrugated steel pipe to receive the connectors. This system relies on stress transfer across the interface between the shell and the core, as well as between the connectors and prestressing strands in the shell through non-contact splice. Although the use of non-contact splice for regular reinforcement has been codified, their application with prestressing strands remains unclear. Also, the complexity of stress transfer of non-contact splices across the concrete interface requires further investigation. Therefore, the primary factors to be investigated were the roughness of the interface and the embedment length of the connectors.

These specimens were to be tested under different combinations of the magnitudes of the axial loads and bending moments, namely under different eccentricities, to evaluate their behavior. The four test specimens were compared to the CIP control specimen to validate the design concept.

4.1.2. Test Matrix

The planned five specimens and the test variables are summarized in Table 4-1. The nomenclature for the specimens is presented in Section 4.1.3. The test variables included the void interface and the embedment length of the connectors. The interface roughness was shown to significantly affect the interface shear capacity between the void and the shell in Chapter 3, and the interface shear capacity was considered a key factor in forming a composite action. Therefore, the full-scale test program included a roughened interface and a smooth interface to investigate the impact of the interface roughness.

Table 4-1. Test Matrix

Specimen ID	Void Interface	Bar extension inside the column	Bar extension inside the bent cap	Concrete Mix Cast in place	Concrete Mix Precast Columns
S1-CIP	N.A.	3'-9" Min. Lap Length	2'-10" Min. Lap Length	TxDOT Class C*	N.A.
S2-R-AASH9-45	Roughened	3'-9" Min. Lap Length	2'-10" Min. Lap Length	TxDOT Class C	Spun Cast Concrete
S3-S-AASH9-45	Smooth	3'-9" Min. Lap Length	2'-10" Min. Lap Length	TxDOT Class C	Spun Cast Concrete
S4-R-Tx-34	Roughened	2'-10" Min. Lap Length	2'-10" Min. Lap Length	TxDOT Class C	Spun Cast Concrete
S5-R-ZABORAC-28**	Roughened	2'-4" Min. Lap Length	2'-4" Min. Lap Length	TxDOT Class C	Spun Cast Concrete

Notes:
* The cast-in-place concrete was TxDOT Class C for the entire column.
** Based on the study by Zaborac and Bayrak (2022), which has been approved in AASHTO

Furthermore, the embedment length of the connectors was investigated to verify the required development length for the connection design. Three different embedment lengths were selected, including 1) 3'-9", based on the AASHTO 9th Edition formula 5.10.8.2.1.a-1 for development

length and the TxDOT Bridge Division Standards, “Common Foundation Details FS”, 2) 2'-10", based on the TxDOT Standard, “Interior Bents IG-BIG2400-17”, and 3) 2'-4", based on Zaborac and Bayrak (2022), which has been approved to be included in AASHTO LRFD.

Concrete used for the specimens included cast-in-place concrete and precast concrete. For the control specimen and the cast-in-place concrete cores, TxDOT Class C concrete was used while the concrete used for the precast shells was spun cast concrete with a target compressive strength of 7 ksi. In addition, the concrete for the bent cap was TxDOT Class H.

4.1.3. Nomenclature

The nomenclature for the specimens' names is explained in Figure 4-2.

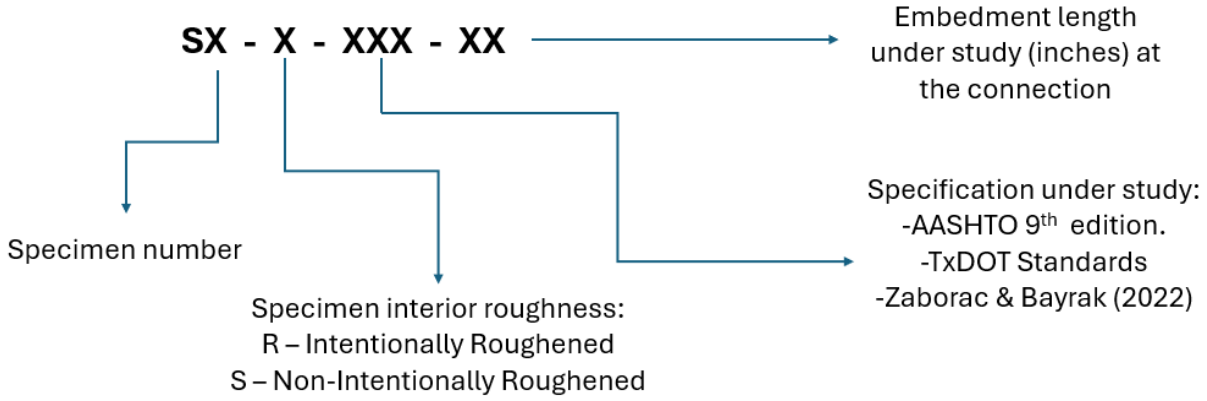

Figure 4-2: Specimen’s nomenclature.

4.2. Specimens Fabrication and Test Setup

4.2.1. Components and Dimensions

The specimens were to be tested by applying loads from the top bent cap while the footing provided reaction, as a self-reacting system. In particular, loading was applied on top of the bent cap through tensioning rods which were anchored at the bottom of the footing as shown in Figure 4-3. The bent cap featured four 4-in. PVC sleeves, and the footing included four 3-in. PVC sleeves through which tensioning rods of 1-3/4 in. diameter were installed; couplers were also used to facilitate the installation of the rod segments. These rods were used to apply loads and had a yield strength of 150 ksi. Four 200-kip rams and four 500-kip load cells were assembled and mounted on the rods with dished steel plates and spherical nuts on both ends. The assembly allowed for flexibility in loading from each side with different magnitudes, creating the required eccentricities.

The specimens were elevated approximately 12 in. above ground level to facilitate anchoring the loading rods on the bottom of the footing. The CIP control specimen was supported on concrete masonry units (CMUs), as shown in Figure 4-3 and Figure 4-4. The CMUs were arranged around the anchorage and occupied nearly the entire area under the footing, as shown in Figure 4-5.

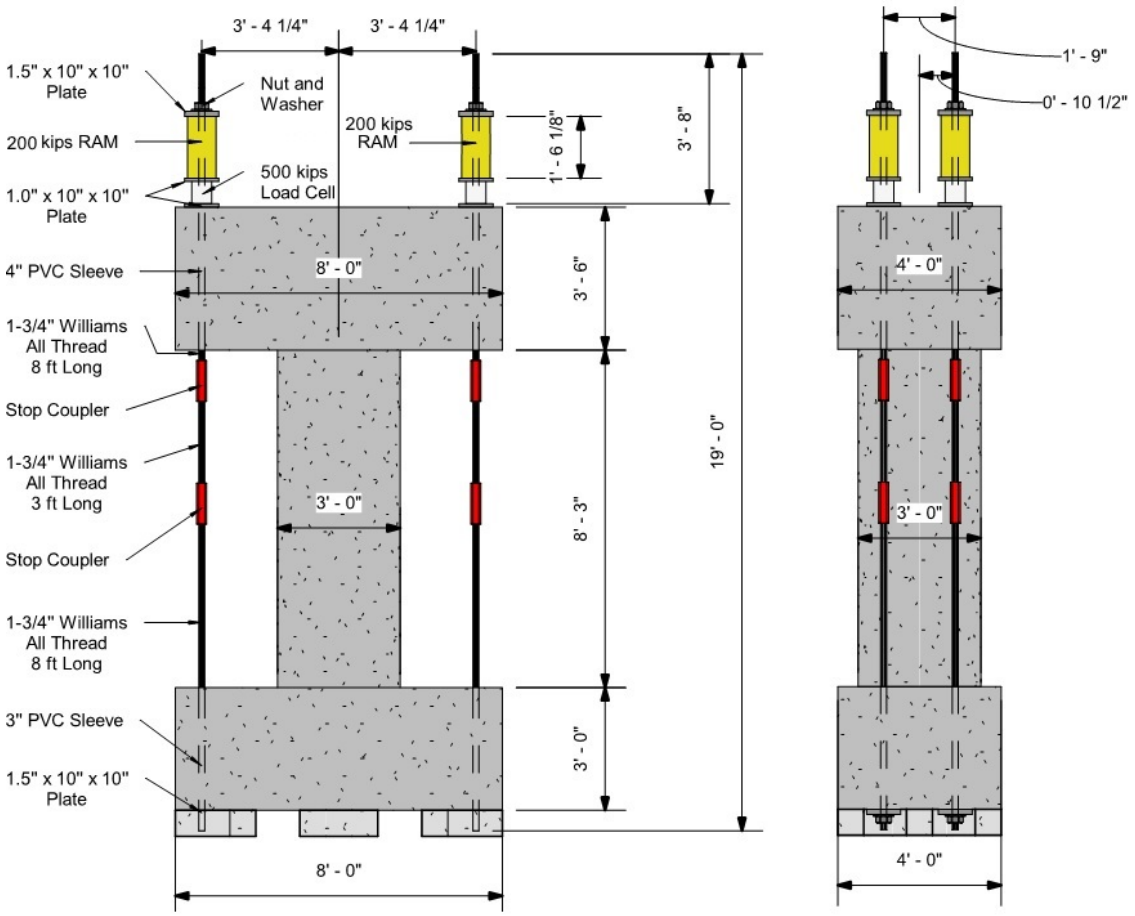

Figure 4-3: Testing Setup for Specimen S1-CIP

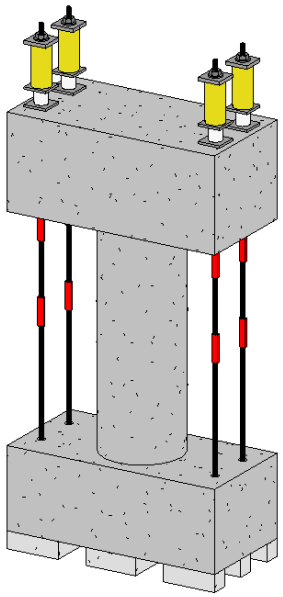

Figure 4-4: 3D representation of the Test Setup for the Specimen S1-CIP

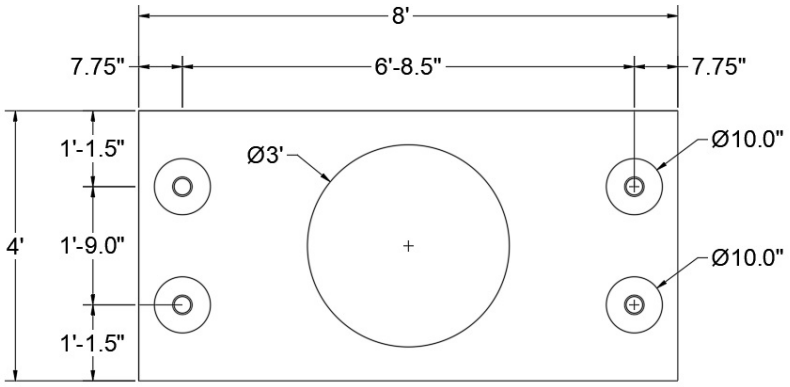

(a) Location of the steel plates and holes on the footing

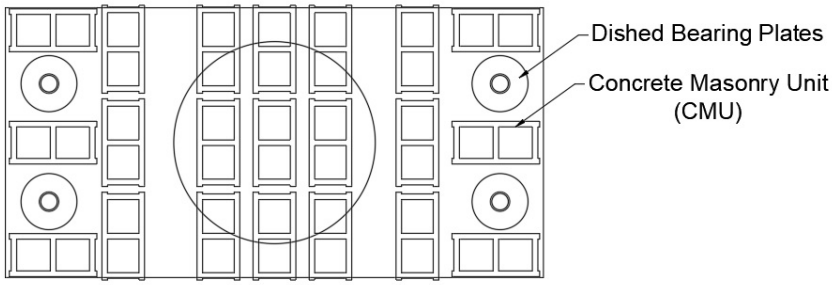

(b) Location of the CMU units under the footing

Figure 4-5: Test Setup Footing Top View for Specimen S1-CIP

In the test setup for precast specimens, all elements remained the same except for two top rams and the bottom supports, as shown in Figure 4-6, Figure 4-7, and Figure 4-8. To ensure adequate loading capacity, two 200-kip rams on one side of the bent cap were replaced with 300-kip rams to ensure sufficient loading capacity, as the Specimen S1-CIP was not loaded to ultimate failure due to insufficient loading capacity. In addition, the CMU support was replaced with three W12x96 steel sections for sturdier supports. The steel shapes were modified by cutting the internal flanges of the W12x96 sections to generate space to pass the steel plates and rods. A 0.5-in. thick rubber sheet was used to ensure full contact between the specimen and the steel support.

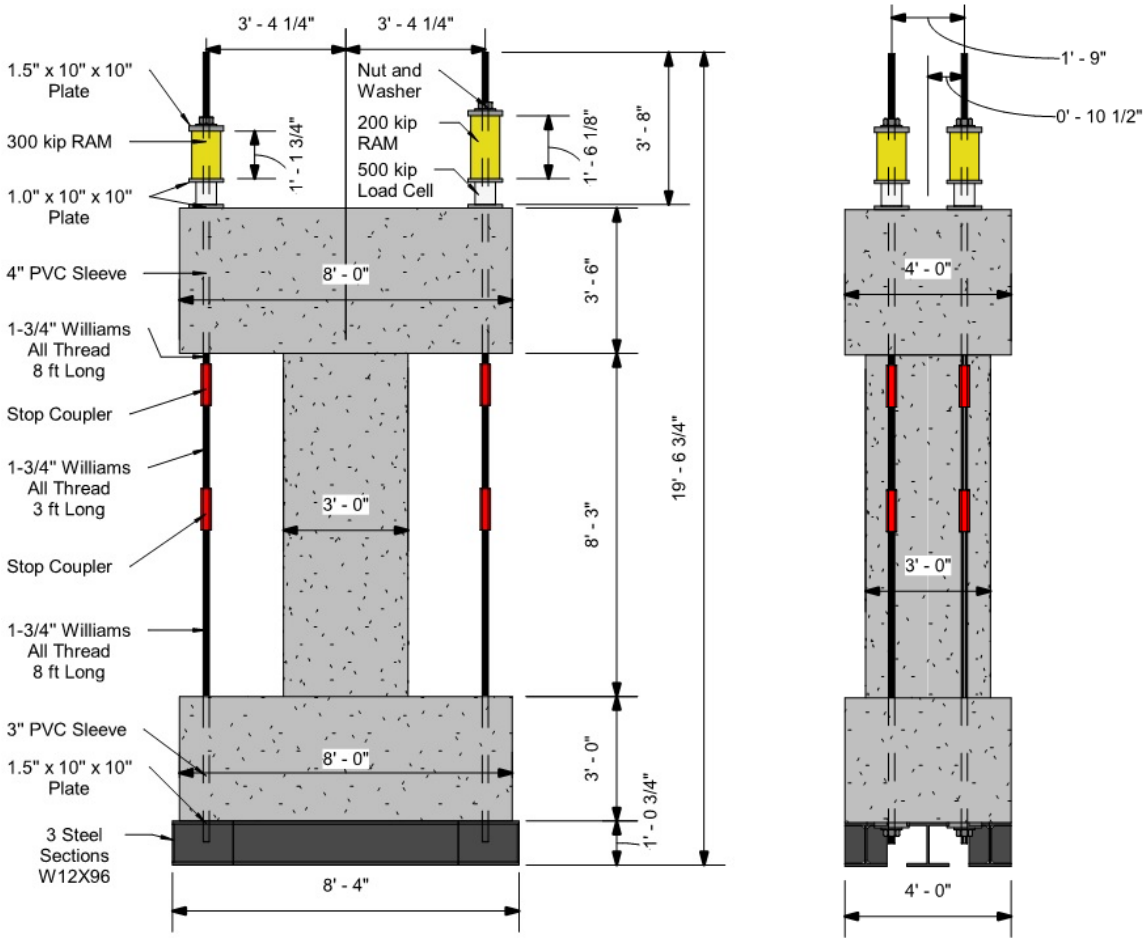

Figure 4-6: Testing Setup for Precast Specimens

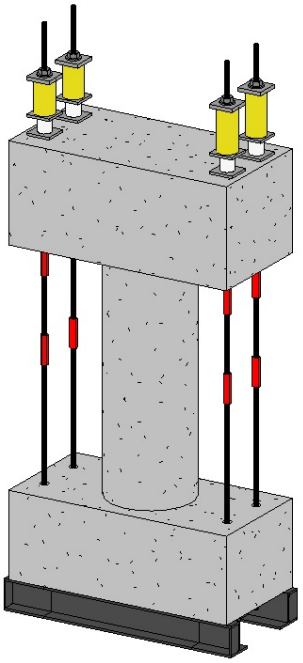

Figure 4-7: 3D representation of the Test Setup for Precast Specimens

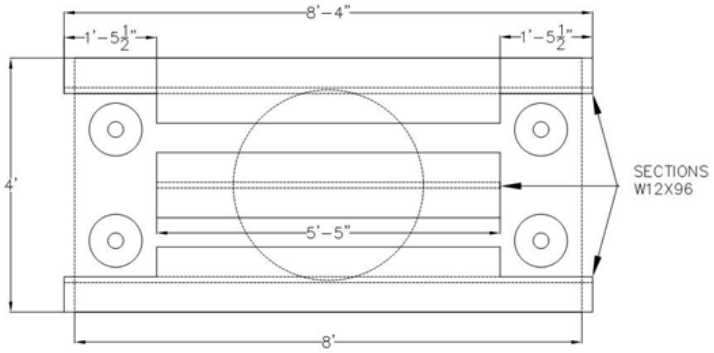

(a) Location of the steel beams under the footing

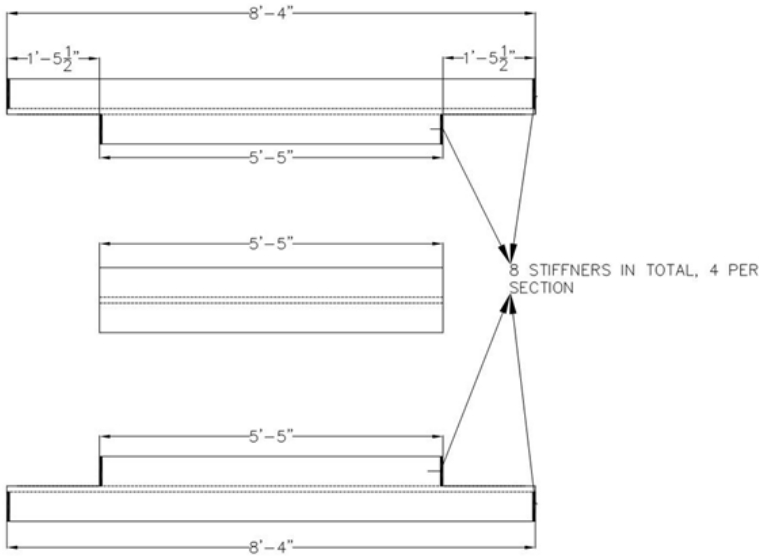

(b) Detailed dimensioning of the steel beams

Figure 4-8: Test Setup Footing Top View for Precast Specimens

4.2.2. Footing and Bent Cap Detailing

The footing design considered a bending moment of 1400 kip-ft and a shear force of 400 kips. Two footing variations were implemented, one for the specimen S1-CIP and the second one for the precast specimens. This variation was due to the column diameter for S1-CIP (36 in.) and the internal diameter of the precast columns (24 in.). The outside diameter of the connecting bars for specimen S1-CIP was 29 in. and for the precast column was 21 in. For S1-CIP, the footing had 10-#9 bars as connectors and for the precast columns, the number of bars had to be increased to 12-#9 to maintain the flexural capacity. The layout for the footing used in specimen S1-CIP is presented in Figure 4-9 and Figure 4-10. For the precast columns, it is shown in Figure 4-11 and Figure 4-12.

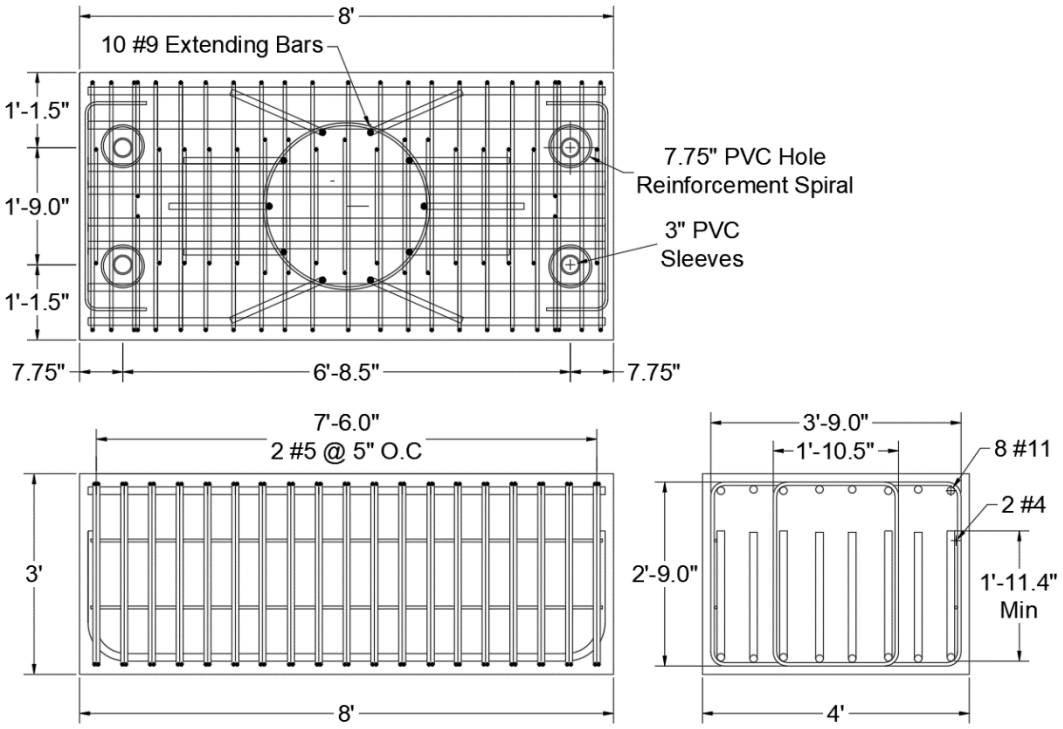

Figure 4-9: Final Rebar Layout for Specimen S1-CIP.

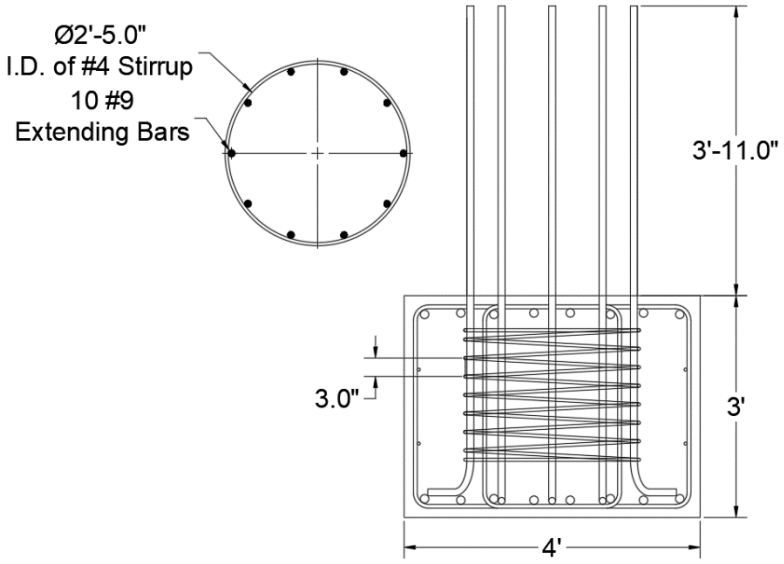

Figure 4-10: Final Footing Extending Bars for Specimen S1-CIP.

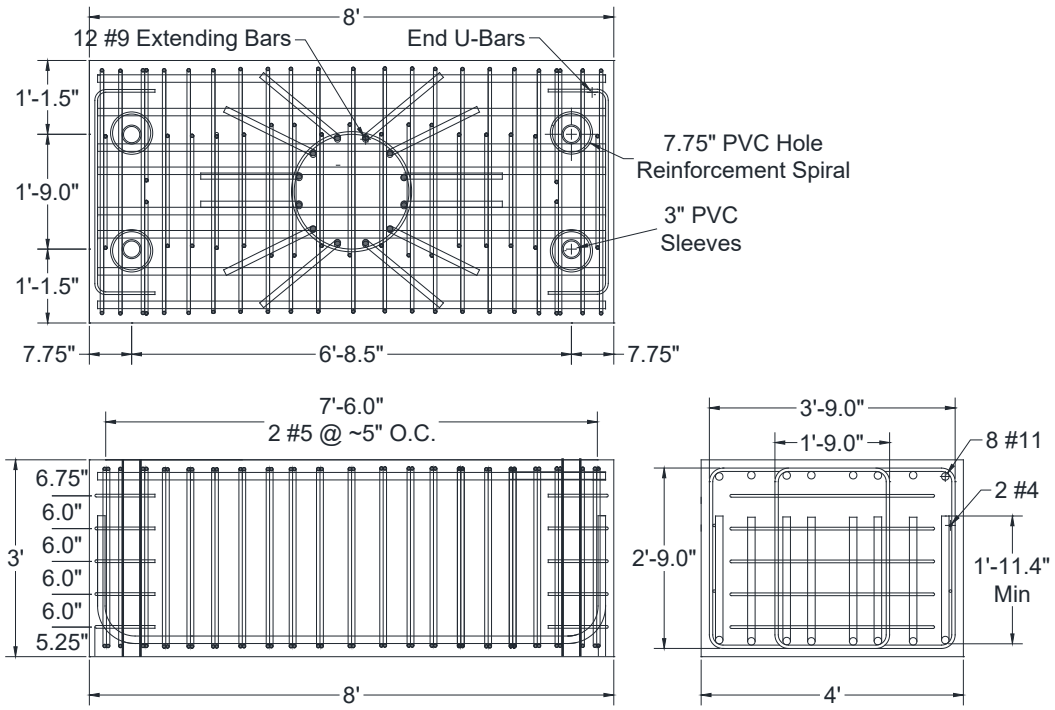

Figure 4-11: Final Precast Footing Rebar Layout

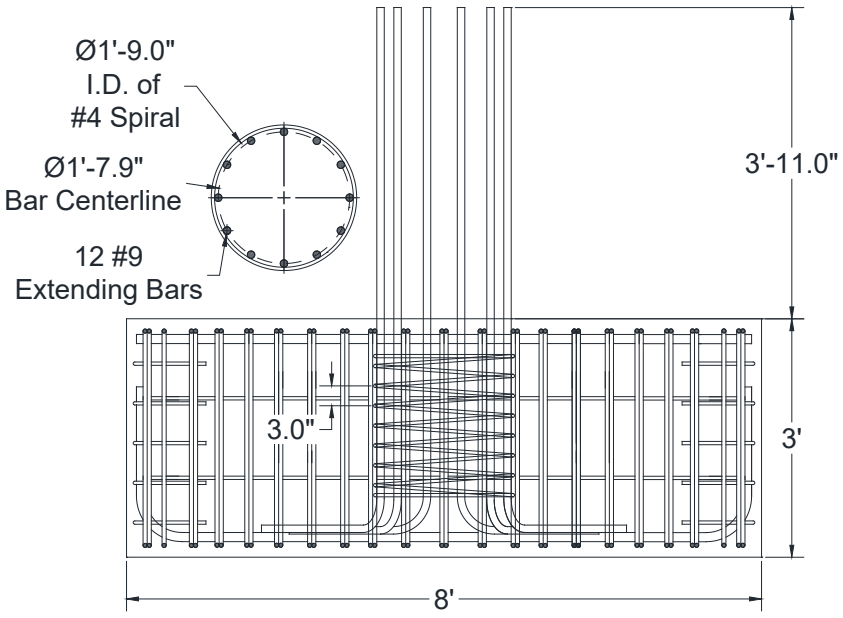

Figure 4-12: Final Precast Footing Extending Bars (length of extending bars is variable)

Similarly to the footing, the bent cap was expected to support a flexural moment of 1400 kip-ft and a shear force of 400 kips. The bent cap layout was based on the established TxDOT Standard "Prestressed, precast bent cap option for round columns" (2019), as shown in Figure 4-13. This type of bent cap is designed for a superstructure type "I-Girders (Tx28- Tx54)" with a flexural strength of 2484 kip-ft. Here, the PVC pipe with a diameter of 4 in. was added to the detailing to avoid problems during the construction of the test setup. Additional dimensions, geometries, and requirements for the construction of the bent caps are summarized in Figure 4-14.

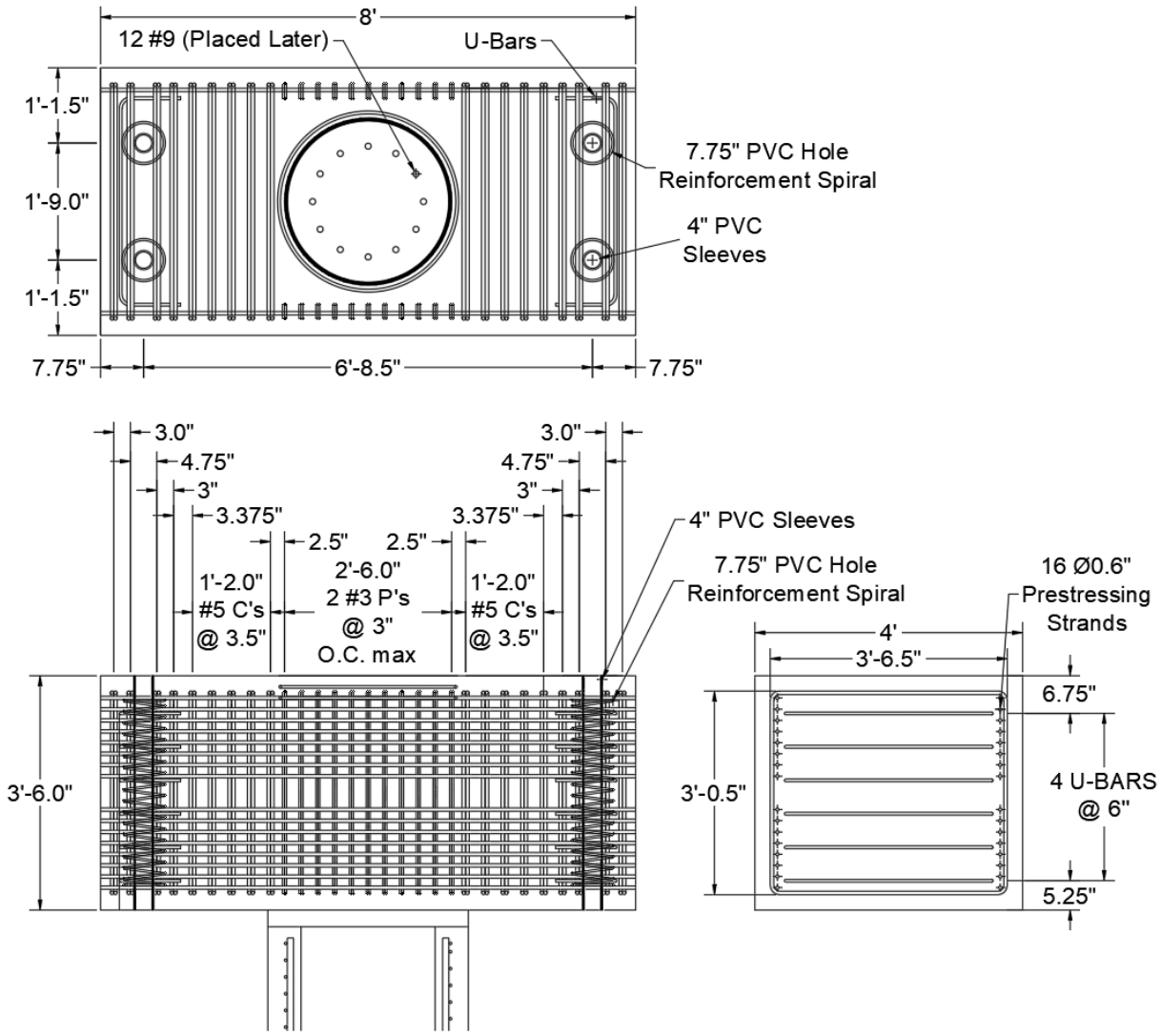

Figure 4-13: Final Precast Bent Cap Rebar Layout

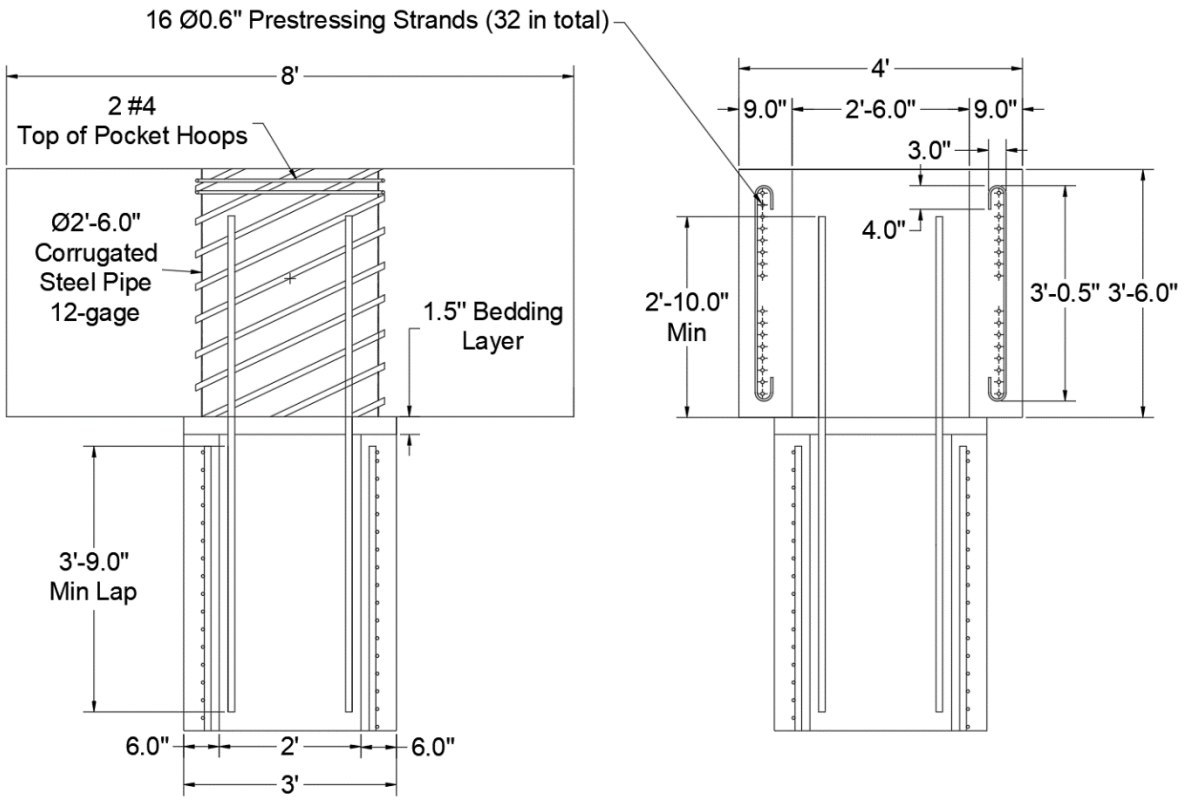

Figure 4-14: Bent Cap connecting bars detail

4.2.3. Construction of CIP Control Specimen

4.2.3.1. CIP Footing

For the CIP footing construction, the first step was the design and building of the formwork. Since only one CIP footing needed to be built, the formwork was made using wood, with ample kickers and other braces to withstand the concrete pressure, as shown in Figure 4-15. The formwork consisted of a bottom mat made of three laterally placed 4'x8' pieces of ¾-in. plywood, supported on 2x4s spaced at 12 in. on center in the longitudinal direction, and intermediate 2x4 struts between these placed at 16 in. on center. For the longitudinal lateral form, one and a half sheets of 4'x8' plywood of ¾-in. thickness were oriented to create 12'x3' sheets on either side. These were reinforced placing one 2x4 longitudinally on the top and bottom, with vertical 2x4 struts placed at 10 in. on center. Lastly, the end forms were made using the same kind of plywood cut to 4'x3'. These were reinforced with longitudinal 2x4s placed along the top and bottom, with vertical 2x4 struts placed 10 in. from the center. In order to prevent toppling, additional braces were installed around the lateral forms. These came in two sizes, some 2x4 kickers at 45 degrees around the third points all along the perimeter, as well as additional triangular buttresses at the bottom at key locations along the long side. Furthermore, to ensure the end piece stability and tie the lateral formwork to the ends, 4x4s were placed in all corners, which were screwed into the sides, ends, and bottom mat. Additionally, since the PVC pipes needed to be placed in a precise location, small

pieces of plywood were screwed into the correct location to act as guides and seals for the bottom of the pipes. Once all pieces were screwed into place, the edges and seams were caulked.

Figure 4-15: CIP Footing Formwork

In conjunction with the formwork construction, the CIP footing rebar cage was assembled. Since the footing was not the point of interest for this investigation, the cage was substantially over-reinforced. This ensures that the failure does not arise from the footings but from either the connections or the column in the subsequent tests.

For the footing, the key parts were the flexural reinforcement, the shear reinforcement, the extending rebars which act as connectors to the column, the spiral for these extending rebars, the PVC pipes for the eventual loading, the spirals around the PVC to control radial cracking, skin reinforcement along the long dimension, and the end U-Bars which further controlled potential cracks propagating from the load location, as shown in Figure 4-16. With these numerous elements, substantial clash detection and mitigation were first conducted in AutoCAD, resulting in tight construction tolerances. This resulted in a small margin of error in the placement of the bars for them all to fit in the space. Once the rebar cage was completed, it was lowered into the formwork, and the PVC pipes were held in place using 2x4s which were pushed down on the PVC, to ensure minimal movement during the pour. Subsequently, during the TxDOT Class C concrete pour, extra attention was given to the concrete placed in the more congested regions. The finished footing is shown in Figure 4-17.

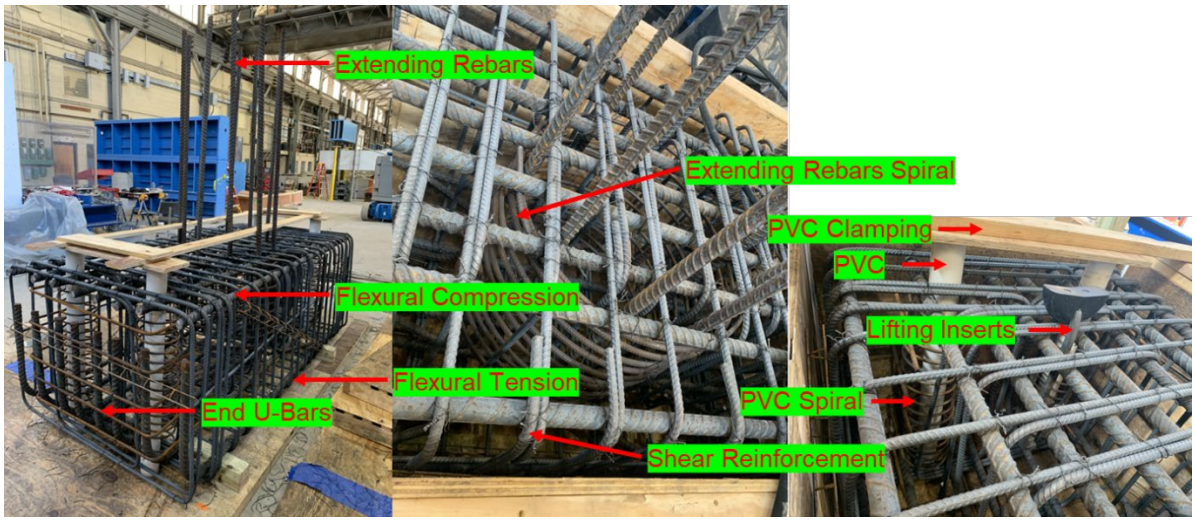

Figure 4-16: CIP Footing Rebar Cage

Figure 4-17: Finished CIP Footing

Measurements were taken on the foundation to position the location of the sleeve holes, as shown in Figure 4-18. It can be seen that there was a slight difference between the specifications and the actual location; however, all of them were under tolerance and would not affect the installation of all-thread tensioning rods. Considering the difficulties of exactly installing the all-thread tensioning rods and running through the PVC sleeves in the bent caps, the research team decided to increase the diameter of the PVC sleeve to 4 inches to allow for more tolerance.

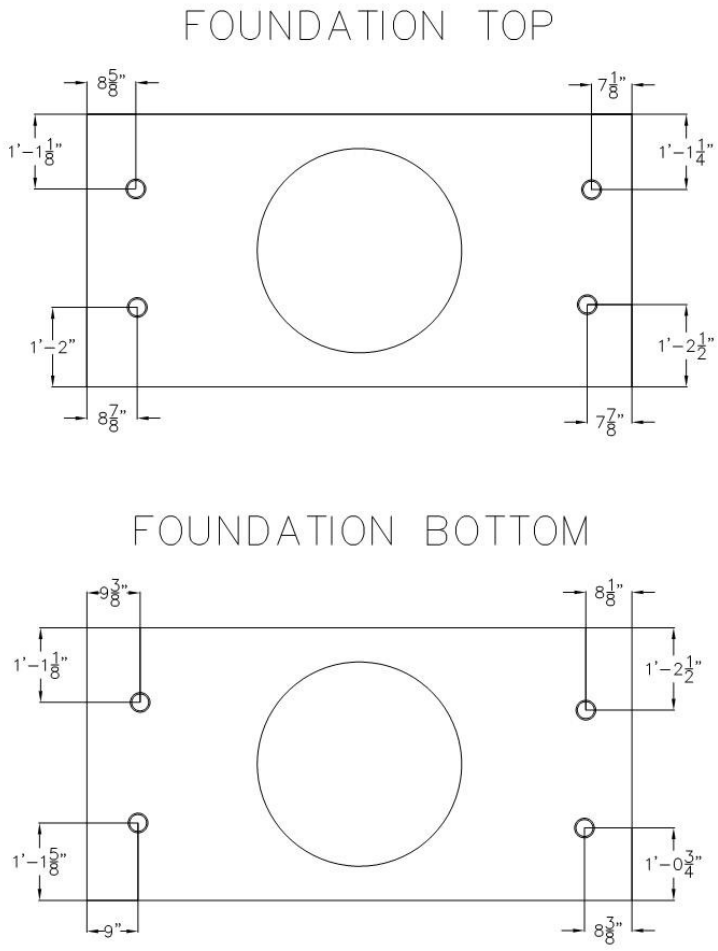

Figure 4-18: As-built hole location in the CIP Foundation

4.2.3.2. CIP Column

After the CIP footing had cured, construction of the CIP column began. For the Specimen S1-CIP, both the column reinforcing and the subsequent extending bars which connect with the bent cap needed to be assembled and cast in one pour. These bars were offset towards the inside of the column by around three inches and only extended into the uppermost half of the column. In short, these bars needed to be "floating" in the center of the large column reinforcement cage.

The solution to this problem was first the fabrication of the internal splice bars around inner hoops. This process allowed the bars to be placed in the correct location and spacing, and the hoops were internal since the outside of these bars is critical to the behavior of the non-contact splice with the longitudinal bars of the column. Three hoops were placed in the segment, which was lowered into the column, and three hoops were above the column, as can be seen during the assembly of the two cages in Figure 4-19.

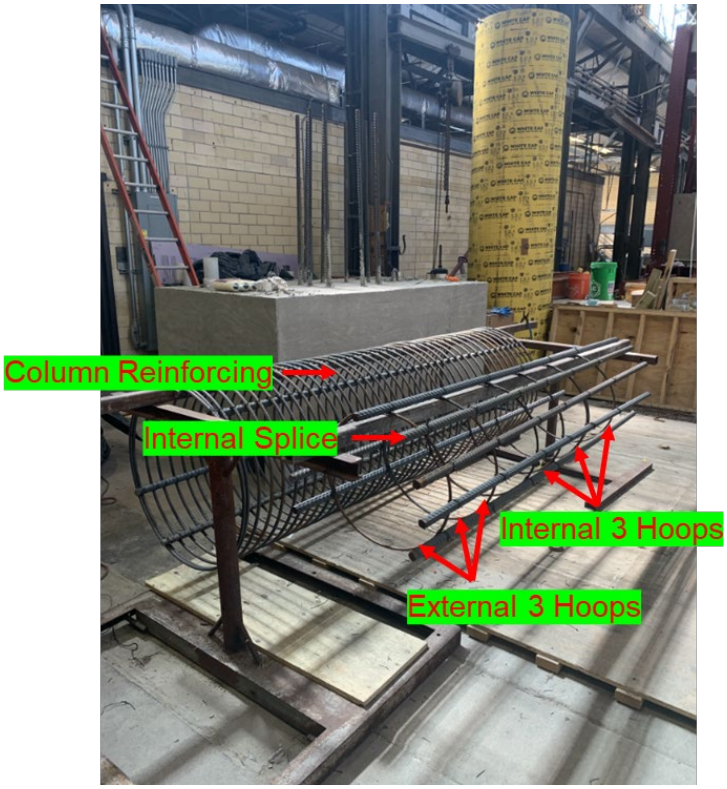

Figure 4-19: CIP Column Cage Construction

The second issue of floating the interior cage was resolved with the same interior hoops and "X" bars placed across the main column's spiral reinforcement, as shown in Figure 4-20. These "X" bars created bays on which the hoops could rest. Additionally, since the "X" bars were made out of two separate bars, they could be placed while the interior cage was still held aloft by the crane.

After all the steps were completed, the bars were erected, and the formwork was placed around the column, as shown in Figure 4-21. During the erection process, the column rebar cage was slightly leaning, which was resolved by placing shims of steel under the longitudinal bars until the lean was within the construction tolerances.

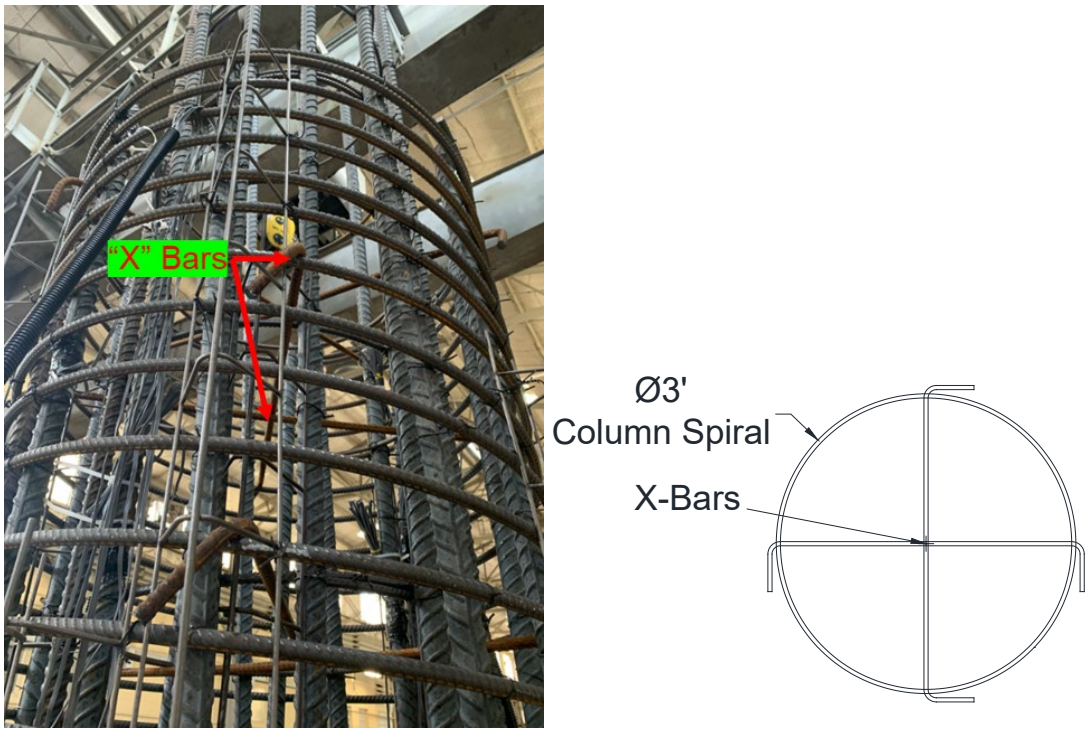

Figure 4-20: CIP Column "X" Bars

Figure 4-21: CIP Column Final Cage and Pre-Bracing

The next step in the construction procedure was bracing design and construction. In the laboratory setting, the research team built self-reacting wooden bracing around the footing and column. This formwork included a piece of centering plywood at the base of the column to ensure minimal formwork tube movement and to seal the base fully. On top of that, vertical wood pieces anchored lateral braces and increased the pressure resistance of the formwork tube in conjunction with steel banding. Next, self-reacting square bracing supports were built around the footing, reacting onto the sides of the footing on one axis and the PVC pipes and loading rebars on the other. From this frame, angled lateral braces buttressed the column in eight primary directions to ensure stability. The resulting bracing formwork is shown in Figure 4-22.

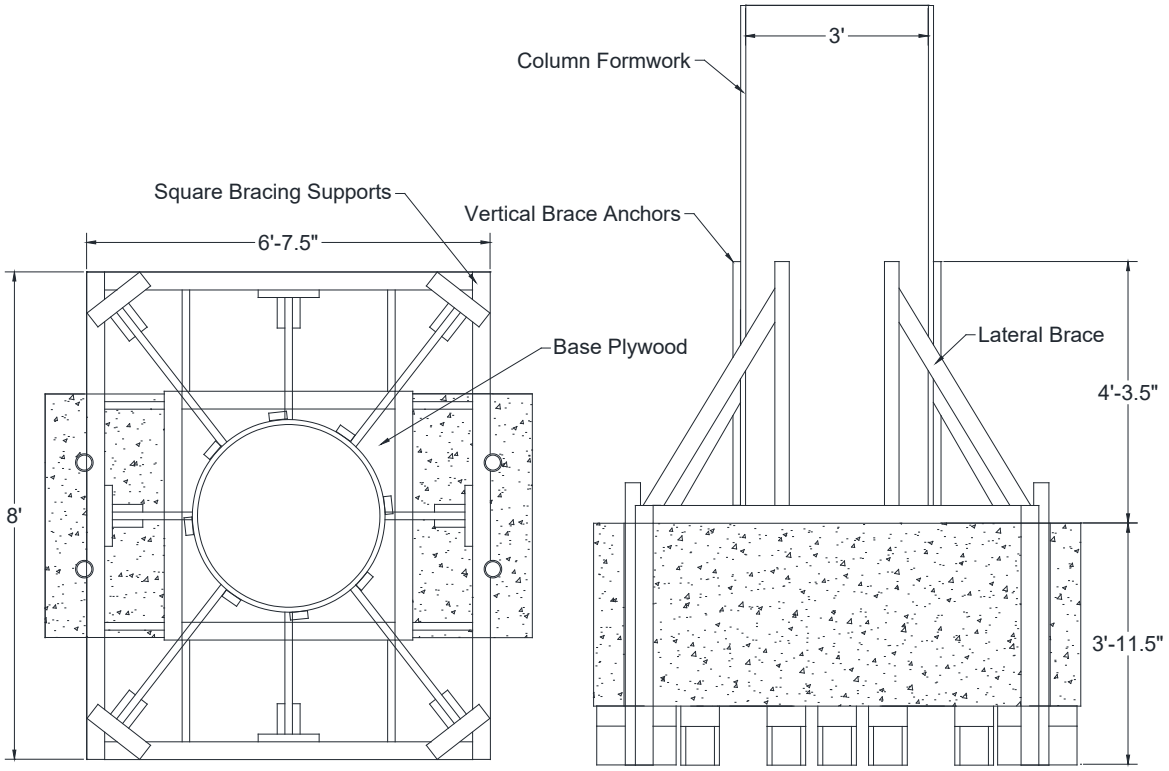

Figure 4-22: CIP Column Bracing Design

Finally, the column was cast as shown in Figure 4-23. The slump measured for the concrete mix was 6 inches, and the cylinder samples were made as seen in Figure 4-24. After removing the framework, the column specimen can be seen in Figure 4-25.

Figure 4-23: Casting of CIP Column

Figure 4-24: Slump measurement and cylinder samples for CIP Column

Figure 4-25: CIP Column after removing formwork.

4.2.4. Spun Cast Precast Column Shells

The last four test specimens utilized spun-cast precast prestressed piles as precast column shell components. The dimension of the precast columns with the reinforcing in the cage was 36-in. outer diameter with a 6-in. shell thickness, and 24 low-relaxation strands, as shown in Figure 4-26.

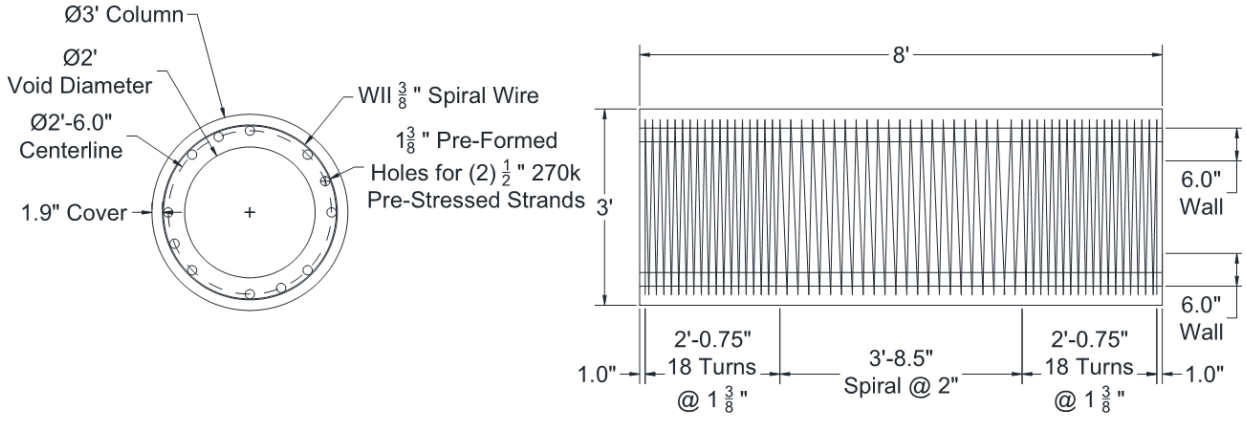

Figure 4-26: Precast hollow column details.

These elements were fabricated using a machine that spins and tacks the spiral onto guide wires, as can be seen in Figure 4-27. These guide wires were subsequently used as locations onto which the strain gauges were installed, as seen in Figure 4-28 since all reinforcing in the columns comes in the form of post-tensioned reinforcing.

Figure 4-27: Precast Columns Reinforcing Spiral

Figure 4-28: Precast Column Strain Gauge Installation

Once the strain gauges were installed onto the wires, the cage was brought outside where it was lowered into steel tube formwork. Then, the post-tensioning ducts were lowered into the same formwork, as shown in Figure 4-29. Special additions were made to the standard formwork to ensure that the strain gauge cables would be safe during the pour and that the steel tube remained balanced for the subsequent spinning.

Figure 4-29: Precast Column Placing into Formwork

The next steps in the pour preparation and subsequently spun cast are presented in Figure 4-30. The steel formwork with the cage inside was moved to the tightening and quality control area. Here, the post-tensioning rods were verified, and the formwork was tightened. Then, the steel tube was brought to the spinning location where a conveyor belt runs through the length of the spinning tube and drops the predetermined concrete mix into the formwork. Spun cast concrete had zero slump, and the centrifugal force of the spinning metal drum ensures a well-compacted pour. The formwork ended up spinning at speeds of over 50 miles per hour. Towards the end of the spinning process, for the elements that were desired to have an intentionally roughened interface, it was introduced coarse aggregate while spinning at a slower speed, so these ended up forming the roughened protrusions. For a non-intentionally roughened interface, this step was skipped.

After steam curing for one day, the precast elements were demolded, and shortly thereafter they were delivered to the FSEL. Two precast shells are shown in Figure 4-31, with one having an intentionally roughened interface and the other having a non-intentionally roughened interface.

Figure 4-30: Precast Column Pour Preparation and Pour

Figure 4-31: Final Precast Column Elements

4.2.5. Precast Foundations

A local precaster helped construct the remaining four foundations to fulfill the rest of the precast column specimens. The research team visited the precaster to inspect the location of the steel, rebar, PVC sleeves, and the dimensions of the foundations. The location of the PVC sleeves was important because it allowed passing through the all-tread tensioning rods to apply loads.

As shown in Figure 4-32 and Figure 4-33, the steel and stirrups were well located, and the connecting bars at the connection were located as in the drawings. The foundations were cast with SCC, which reached a strength between 9.5 ksi and 11 ksi after 28 days. These foundations were delivered to the FSEL after curing, as shown in Figure 4-34.

Figure 4-32: Inspection of the foundations at Valley Prestress

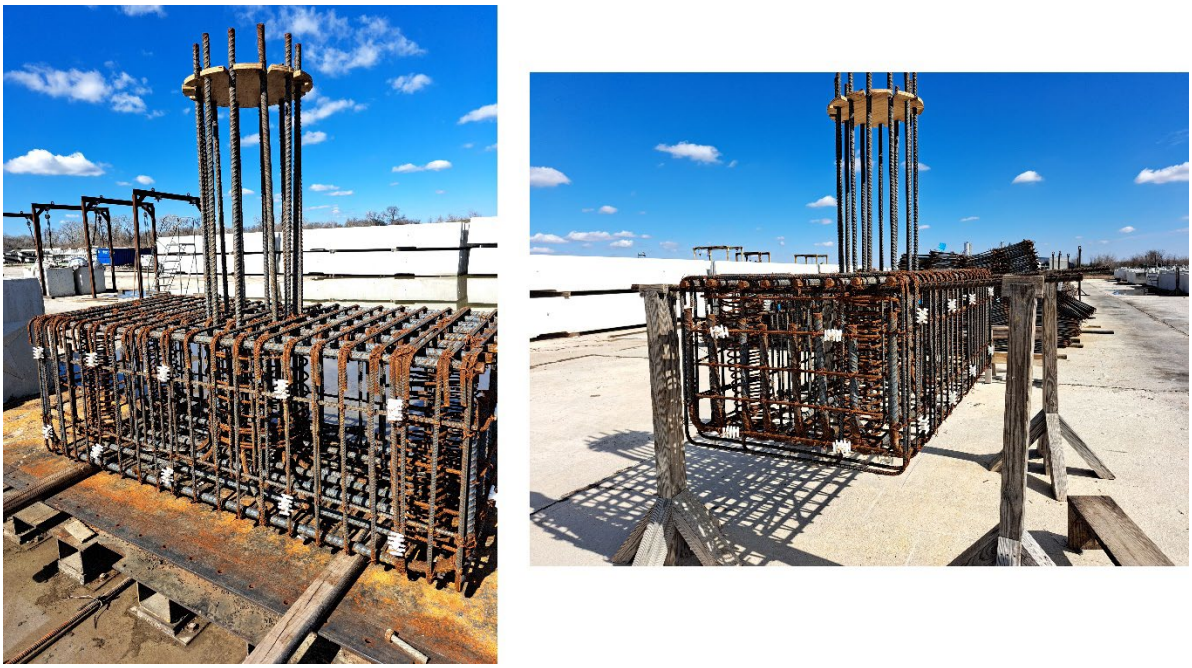

Figure 4-33: Steel cage of the foundations at Valley Prestress

Figure 4-34: Precast foundations in the FSEL yard

4.2.6. Precast Bent Caps

The local precaster also helped construct precast bend caps for the control specimen and the other four test precast column specimens. The research team visited its installations to inspect the tension on the strands, the location of stirrups, and the PVC sleeves. For these members, the PVC pipe diameter was 4 in. to avoid future issues with the tolerance between the PVC pipes in the foundation and the bent caps. All the details specified in the section 4.2.1 were followed, and the cover between the steel pipe and the #4 spirals was 1-5/8-in., satisfying cover requirement practice.

All the bent caps were prepared the day before the research team arrived at the plant, and the force in the 0.6-in. strands corresponded to 40.3 kips each, as was confirmed by the local precaster. The reinforcement cage can be seen in Figure 4-35.

Figure 4-35: Precast bent caps prepared in Valley Prestress

The corrugated steel pipe was a 12-gage pipe as specified in TxDOT Standard "Prestressed, precast bent cap option for round columns" (2019) and had a diameter of 30 in., as shown in Figure 4-36. The corrugated steel pipe height was equal to the bent cap height; no longitudinal rebar at the top or the bottom of the bent cap was needed in the design, as seen in Figure 4-37.

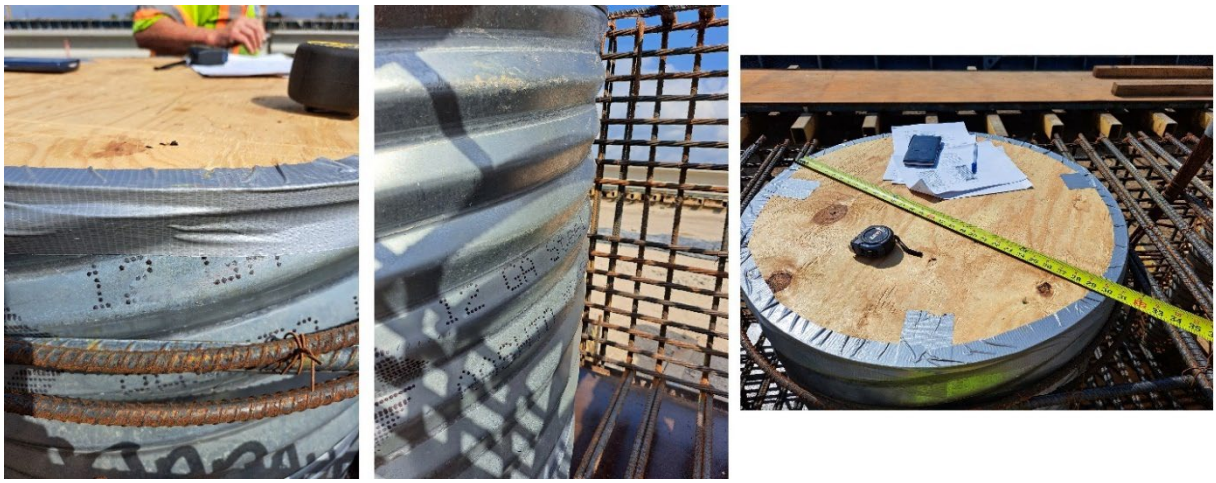

Figure 4-36: Corrugated steel pipes used in the bent caps.

Figure 4-37: Steel cage and corrugated steel pipe in the bent caps.

The inspection of the location of the PVC pipes is shown in Figure 4-38. Some difficulties were discovered with the location of the spirals at the top of the corrugated steel pipe; therefore, spacers were provided during the inspection in order to warrant the spacing of the spirals, as seen in Figure 4-39.

Figure 4-38: Inspection of the PVC sleeves in the bent caps.

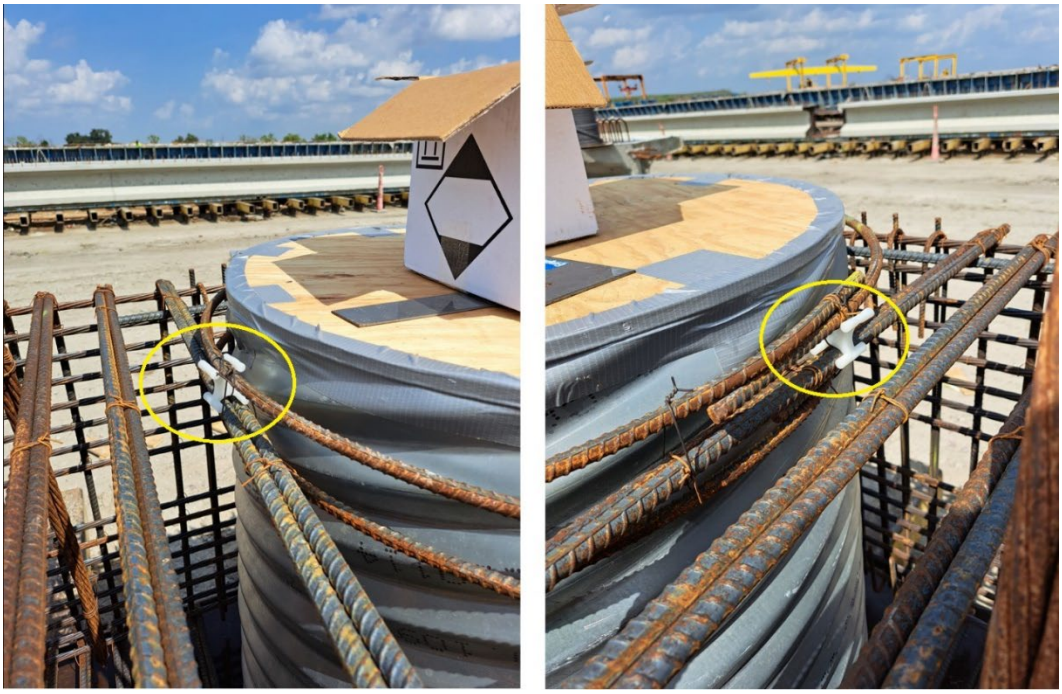

Figure 4-39: Spacers used to warranty spacing in the top spirals.

4.2.7. Construction Sequence of Precast Specimens

The research team devised a systematic approach for assembling the precast elements into test specimens, as shown in Figure 4-40, Figure 4-41, and Figure 4-42. The steps are presented below:

1. **Foundation Preparation:** Construct a foundation with connector bars arranged in a circular pattern inside the hollow concrete column, positioned 1.5 in. from the internal void.

2. **Gap Creation:** Use steel plates or high-density polyethylene (HDPE) sections to establish a 1-2 in. gap between the foundation and the hollow column for leveling purposes.

3. **Column Placement:** Use a crane to position the hollow column onto shimming made of steel or HDPE (1.5" x 4" x 4"), ensuring vertical alignment using a level.

4. **Formwork Installation:** Utilize a steel formwork to contain the poured concrete and prevent spillage around the precast column shell during casting. Vibrating the bottom of the column during concrete casting minimizes honeycombing.

5. **Connector Steel Installation:** Install 12 #9 bars and a #3 spiral or hoops with 10-in. spacing to connect the bent cap. Maintain a 1.5-in. free cover between the vertical rebars and the internal surface of the column shell.

6. **Concrete Filling:** Fill the precast column void with Class C concrete of 3.6 ksi compressive strength at 28 days, ensuring proper vibration near the connections to prevent honeycombing.

7. **Gap Maintenance:** Place steel or HDPE shims on the top of the column to maintain a 1-2 in. gap between the column and the bent cap for leveling.

8. **Bent Cap Placement:** Use a crane to position the bent cap onto the steel or HDPE shims after the column concrete achieves 70% of its specified strength. Adjust the cap's final position and place the steel formwork between the precast column and the cap to prevent leakage.

9. **Void Filling:** Fill the connection void with TxDOT Class C or Class S concrete. The all-threaded tensioning rods were utilized to stabilize the bent cap until the concrete gained strength (not shown in Figure 4-42).

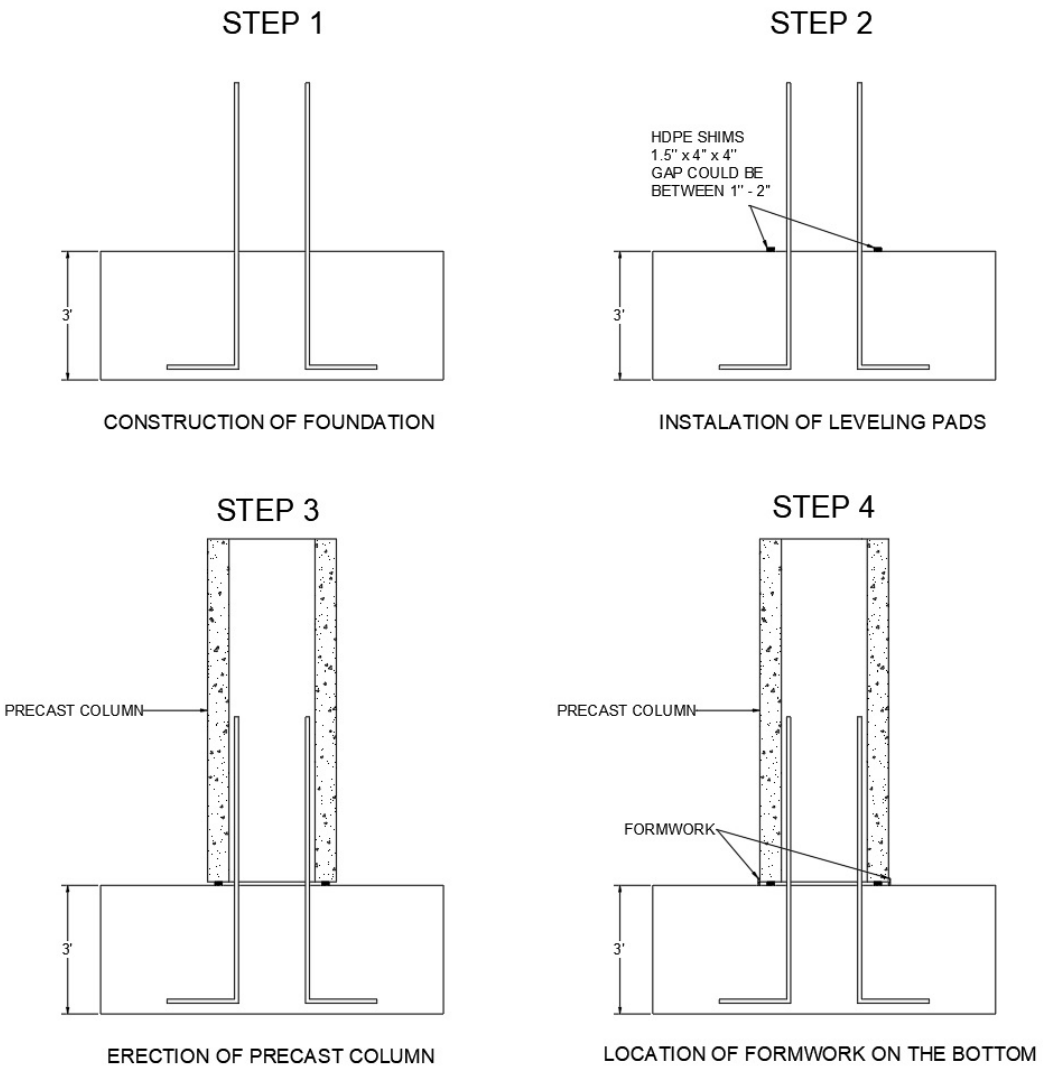

Figure 4-40: Construction sequence: Step 1 to Step 4

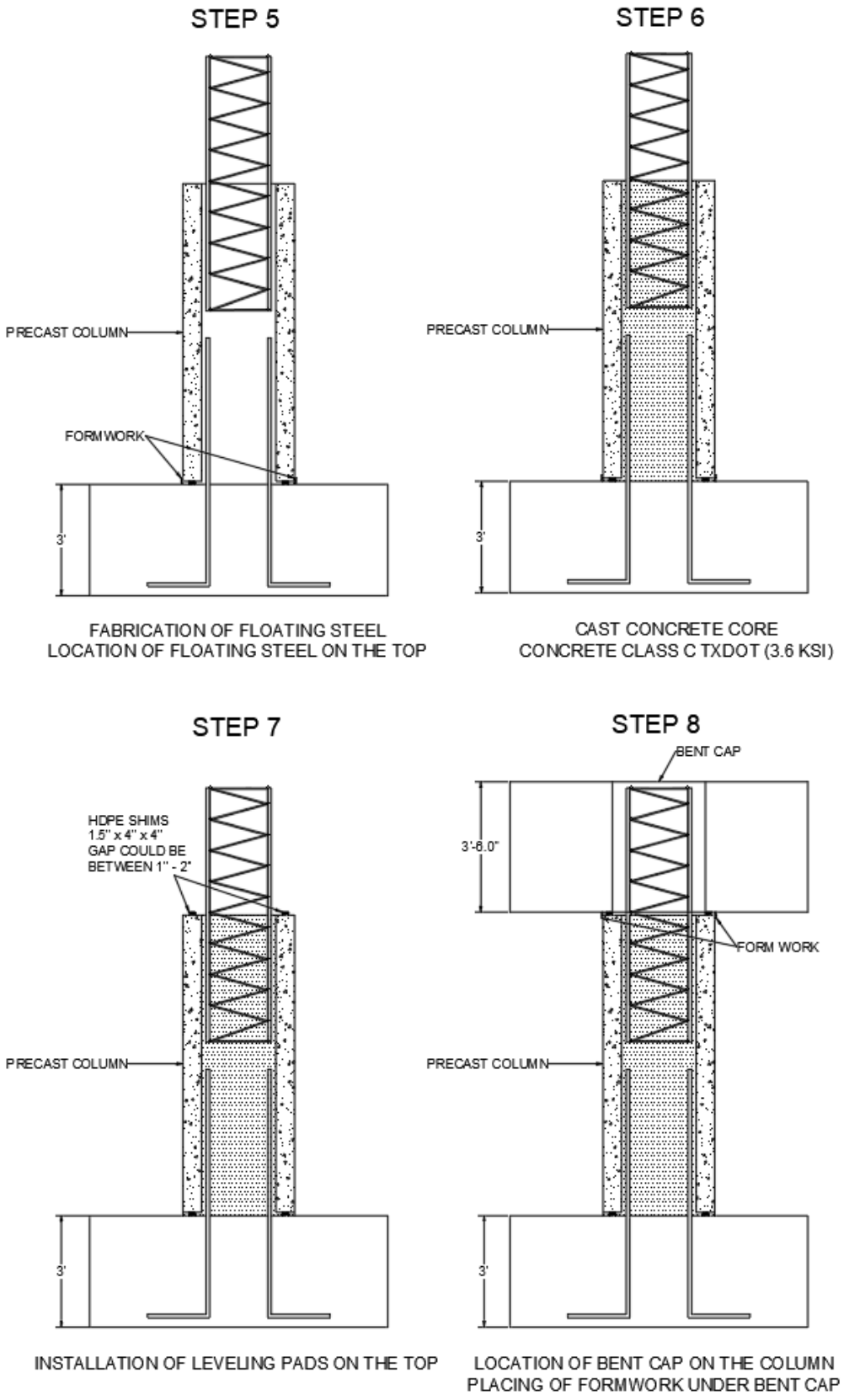

Figure 4-41: Construction sequence: Step 5 to Step 8

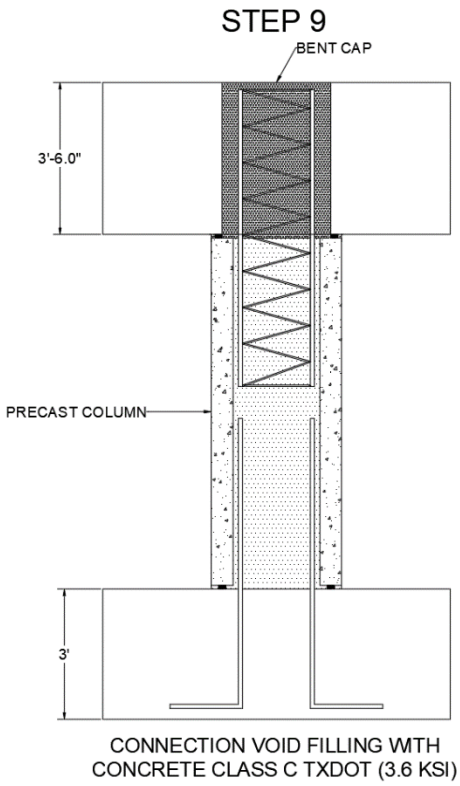

Figure 4-42: Construction sequence: Step 9

4.2.8. Assembly of Specimens in the Laboratory

4.2.8.1. Assembly of Specimen S1-CIP

The assembly process for the bent cap and the CIP column involved initially positioning high-density polyethylene (HDPE) shims measuring 3 in. by 4 in. by 1.5 in. to maintain a 1.5-in. gap and level the bent cap, as shown in Figure 4-43. These shims were located 2.5 inches away from the edge of the column. Before positioning the shims between the bent cap and the column, some grinding was carried out to create a flat surface and prevent hard protrusions.

Figure 4-43: HDPE shims located on the top of the column

Once the shims were carefully positioned and leveled, a precast bent cap was lifted onto the column using a crane, as illustrated in Figure 4-44. Following the placement, the research team verified the alignment of the bent cap by utilizing a laser level with the foundation's middle marks and those on the cap, as shown in Figure 4-45.

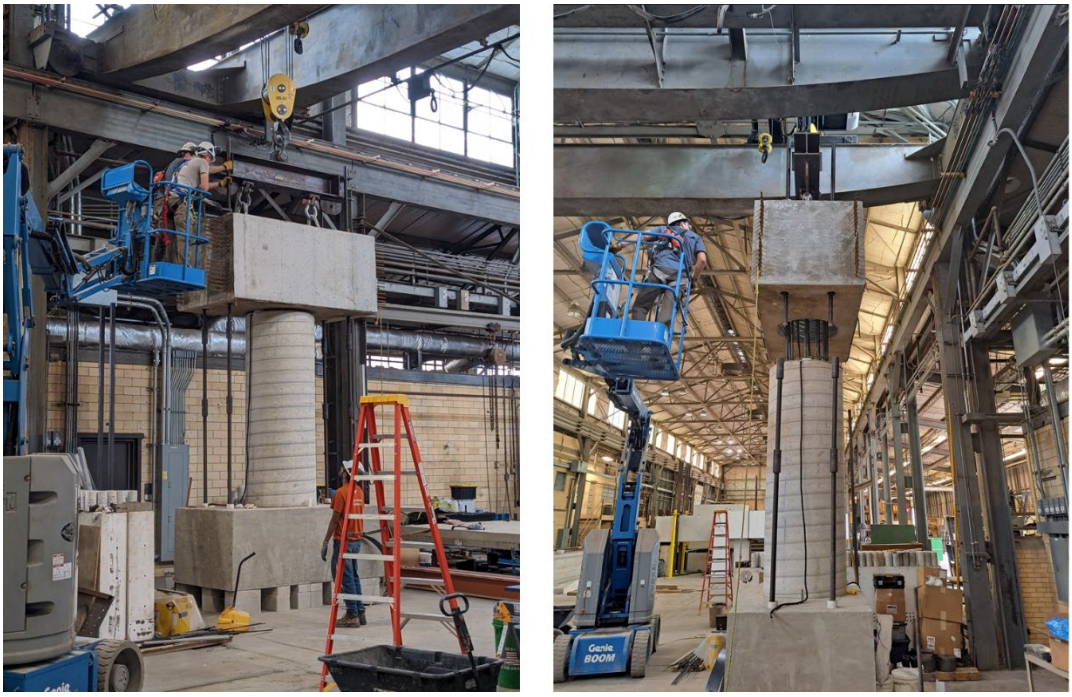

Figure 4-44: Installation of the bent cap.

Figure 4-45 Alignment of the bent cap with the marks using a laser level

After verifying the levels and positioning of the bent cap, the next step involved placing a steel form on top of the column to prepare for pouring concrete into the void in the bent cap. The steel form was used to prevent any leakage from the space between the bent cap and the column. To ensure full contact between the steel form and the column, an expansion foam was applied. Subsequently, the research team secured the steel form in place using a ratchet strap, as shown in Figure 4-46.

Figure 4-46: Placement of steel form between the bent cap and the column

After placing the bent cap and steel form, the research team filled the void and the 1.5-in. gap with TxDOT Type S concrete following the specifications in the PPBC-RC standard drawings. The concrete was poured using a bucket, and careful vibration was applied near the void edges to prevent honeycombing, as shown in Figure 4-47. Once the steel form was removed, the finishing between the column and bent cap was revealed, as presented in Figure 4-48. The Specimen S1-CIP completed is shown in Figure 4-49.

Figure 4-47: Casting of concrete in the void and vibration close to the edges

Figure 4-48: State of the void after removing the formwork.

Figure 4-49: Cast-in-Place Specimen after casting the void.

4.2.8.2. Assembly of Specimen S2-R-AASH9-45 and S3-S-AASH9-45

Specimen S2-R-AASH9-45 and S3-S-AASH9-45 were assembled at the same time. The difference between the two specimens was the interior roughness of the hollow section. The concrete mix poured inside the precast column and in the bent cap void connection was Class C for both specimens.

Before the assembly of the two specimens, the research team had attached strain gauges on the rebar in the footings and on the rebar cage for the connection for the column with the bent cap as is presented in Figure 4-50. The location of the sensors followed the pattern shown in Figure 4-51.

Figure 4-50: Strain gauges prepared in the footing and cage connection for Specimen #2 and S3-S-AASH9-45.

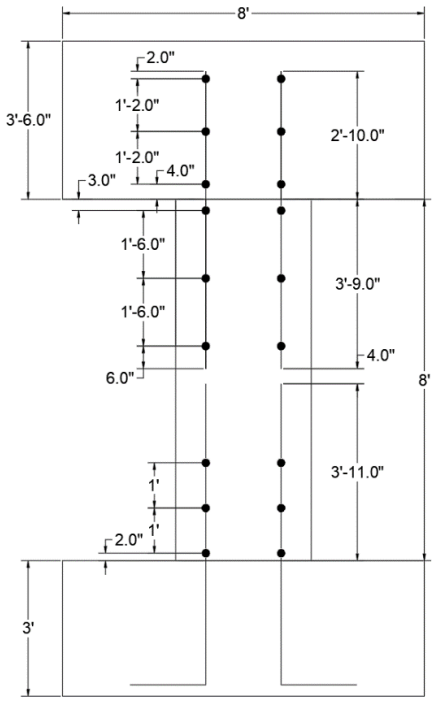

Figure 4-51: Location of strain gauges for Specimen S2-R-AASH9-45 and S3-S-AASH9-45.

After installing the strain gauges, the footings were repositioned on top of the steel sections, and the research team proceeded to mark the positions of the HDPE shims on the footings. A circular wood frame was then prepared to ensure the column's center position and to place the shims 1.5 in. away from the edge. This allowed for a gap to accommodate the concrete between the shims and the formwork, as shown in Figure 4-52.

(a) Location of footings on the steel sections

(b) Wood formwork used to place the precast columns and HDEP shims on position

(c) HDEP shims placed at 1.5-in. from the external edge of the precast column.

Figure 4-52: Footing preparation for Specimens S2-R-AASH9-45 and S3-S-AASH9-45

After marking the position of the column and shims, the research team continued grinding the concrete to create a flat and level surface for the HDEP shims. Epoxy was used to secure the shims in place and prevent any movement during the installation of the precast hollow shell, as shown in Figure 4-53. Since the precast shell was supported only on the 4 shims, the research team built a wooden frame anchored to the footing to enhance safety for the researchers and the precast shell section for later casting. The wood frame was constructed using 4”x4” sections for the vertical and lateral members, with a height of 8 ft. and maintaining a 1-in. gap for placing the precast columns. Despite the challenge of placing the precast columns, the research team ensured that the column was positioned correctly to avoid any future issues related to the load pattern and accidental eccentricities.

(a) HDEP leveled after grinding

(b) Wood frame anchored to the footing to keep in place the precast column during mounting and concrete cast.

Figure 4-53: Footing preparation to place the precast columns on Specimens S2-R-AASH9-45 and S3-S-AASH9-45.

After securing the wood frames to the footings with bolts, the Intentionally Roughened precast shell was moved using two 10 ft. straps as shown in Figure 4-54. The friction between the straps and the concrete allowed the lifting and positioning of the precast column. Due to crane height limitations, one side of the wood frame remained open, enabling the crane operator to lift until the height of the rebar in the footing and move in the column. The crane operator carefully descended, avoiding clashes with the rebar and the interior threads of the precast shell. Once the precast shell was positioned correctly, the team completed the wood frame by adding the missing horizontal members. The crane was then released, leaving the precast column resting on four HDEP shims with a 1.5-in. gap between the column and the footing.

(a) Internal view of the "Intentionally Roughened" Precast Column

(b) Placing of the precast column

(c) Close view of the 1.5-in. gap between the precast column and footing

Figure 4-54: Placing of precast column on Specimen S2-R-AASH9-45.

After ensuring that the precast column for Specimen S2-R-AASH9-45 was correctly positioned and plumbed, the research team proceeded with the precast column featuring the Non-Intentionally Roughened precast shell that corresponded to Specimen S3-S-AASH9-45. The procedure used for this column was identical to the previous one, as depicted in Figure 4-55.

(a) Precast Column with "Non-Intentionally Roughened" Internal Section

(b) Placing of the precast column

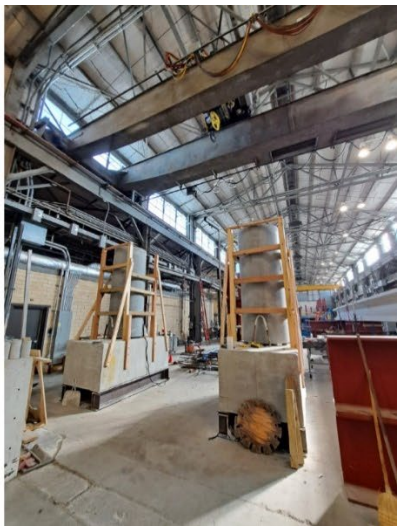

(c) View of Specimen S2-R-AASH9-45 and S3-S-AASH9-45 positioned on their respective footing.

Figure 4-55: Placing of precast column on Specimen S3-S-AASH9-45.

As strain gauges were placed on the steel in the footing, to accommodate this, a small hole was created using a chisel and a hammer to run the cables from the sensors, leaving a space of 3.5 in. long and 1 in. wide. A ¾-in. by ½-in. foam was then attached around each precast column to prevent leaking from the top of the steel formwork (see Figure 4-56(a) and (b)). Subsequently, the steel formwork was positioned at the base of each column and secured with ratchet straps. Since each of the precast shells had strain gauges located on the internal cage, the cables were placed on the tension side of each column, requiring a hole to be created to allow the cables to pass through during the spun cast process. To facilitate this, a small formwork had to be constructed to accommodate the cables, which were then secured with ratchet straps similar to the ones used for the steel formwork (see Figure 4-56(c)).

Before pouring the concrete into the precast columns, the last step was to place the steel cage that would provide the connection from the column to the bent cap. As previously explained, these cages were equipped with strain gauges, and some steel hoops were used to maintain the necessary circular shape for the connection. Additionally, they were fitted with lateral bars to provide vertical support and to position the cages on the precast column (these bars are removed after casting), as seen in Figure 4-57. The cages were lifted into place on top of each precast shell using a crane and positioned in accordance with the drawings, ensuring a distance of 3’-9" inside the columns and 2’-10" extending out to allow for the necessary embedment length for connection to the bent cap.

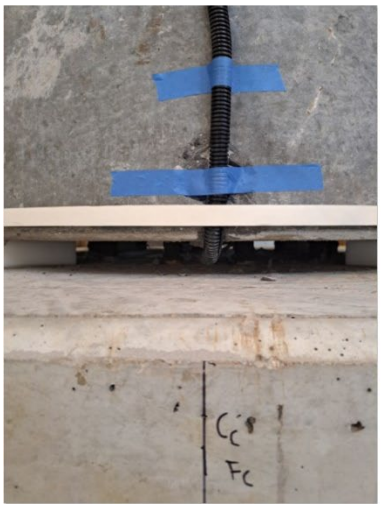

(a) Cables for strain gauges going out of the columns

(b) Foam attached around the column to avoid concrete leaking

c) Steel formwork located at the bottom of each column using ratchet straps and wood formwork using the close the hole for the internal strain cages in the precast column

Figure 4-56: Precast column preparation before casting.

(a) Steel cages prepared with lateral bars that will bring vertical support on the top of each precast column

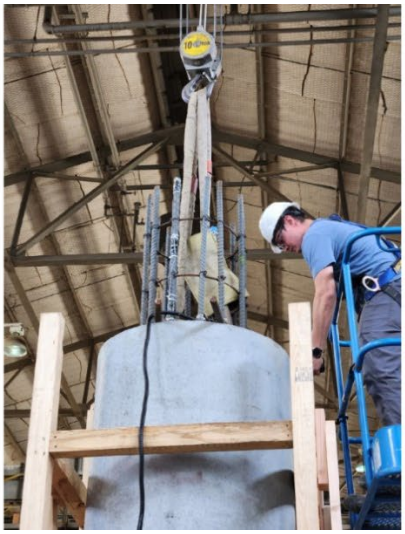

(b) Placing of each steel cage on the top of the precast columns

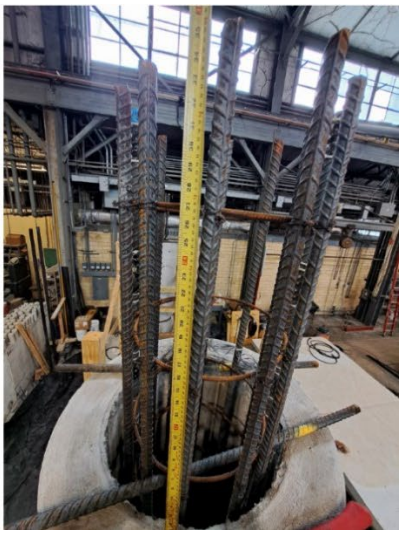

(c) Development length needed according to TxDOT for the connection with the bent cap

Figure 4-57: Steel connectors on the top of the precast column.

After preparing the rebar cages, steel forms, and wood frame, the next step was to cast the column voids with concrete. The concrete was TxDOT Class C with a target f'_c of 3.6 ksi and a 6 in. slump, with a coarse aggregate of 1 in. maximum. This allowed the concrete to pass under the precast columns and fill the 1.5-in. gap created with the HDPE shims. As shown in Figure 4-58, the concrete was poured with a 6.25 in. slump, by pouring 4 to 5 layers of concrete inside each column, vibrating near the edges to prevent honeycombing at the column bottom. After completing Specimen S2-R-AASH9-45, the research team refilled the bucket and continued with Specimen S3-S-AASH9-45 using the same procedure.

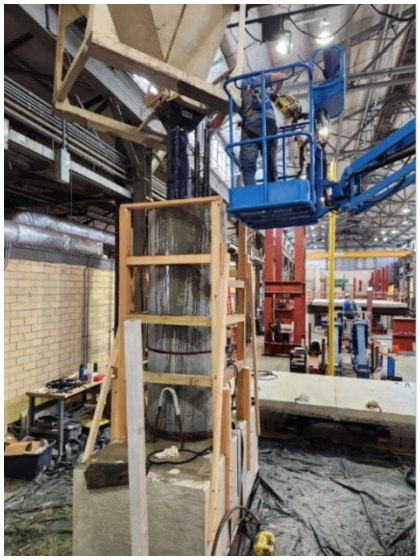

(a) Specimen S2-R-AASH9-45

(b) Specimen S3-S-AASH9-45

(c) Slump test prepared before the cast.

Figure 4-58: Concrete casting for precast columns

The research team covered the columns with plastic sheets to prevent water from seeping out of the core concrete. After allowing the concrete to cure for 7 days, the research team removed the steel forms from the bottom of the columns and the rebar that held the cages on top, as shown in Figure 4-59. Following this, the method employed for the HDPE shims at the base of the precast columns was followed to position more shims on the top, maintaining a 1.5-in. gap between the columns and the bent caps. Four shims were placed at each column after grinding and leveling the surface, maintaining a 1.5-in. distance from the edge.

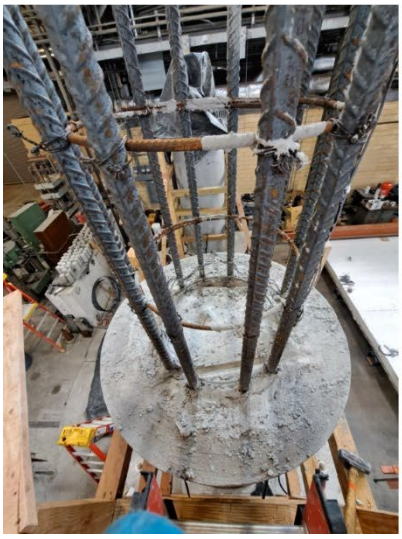

(a) Horizontal bars that were holding the rebar cages were removed

(b) HDEP shims leveled and glued to the columns

(c) Four HDEP shims on the top of each column keeping a gap of 1.5-in. between the column and the bent cap.

Figure 4-59: Precast column preparation before placing the bent cap.

The shims were positioned, and then four all-threaded rods, along with their respective steel plates and nuts, were placed on top of each bent cap. Center lines were marked on all external faces of the bent caps. The bent caps were then lifted and brought towards the columns, with the research team ensuring that the height was sufficient for placement. Once it was confirmed that the lifting setup was adequate, the bent caps were positioned using the marks on the footing and bent cap, which had to match the laser used during assembly, as shown in Figure 4-60 and Figure 4-61. Before releasing the crane, the all-threaded rods were assembled with couplers to complete the setup. Then, the nuts on the top and bottom of each column were tightened to secure the bent caps in position and allow the self-reacting system to bring stability during casting and curing.

(a) Placing of the bent cap

(b) Alignment of the bent cap with marks and laser

(c) Bent cap sitting on the four HDEP shims.

Figure 4-60: Placing of the bent cap for Specimen S2-R-AASH9-45.

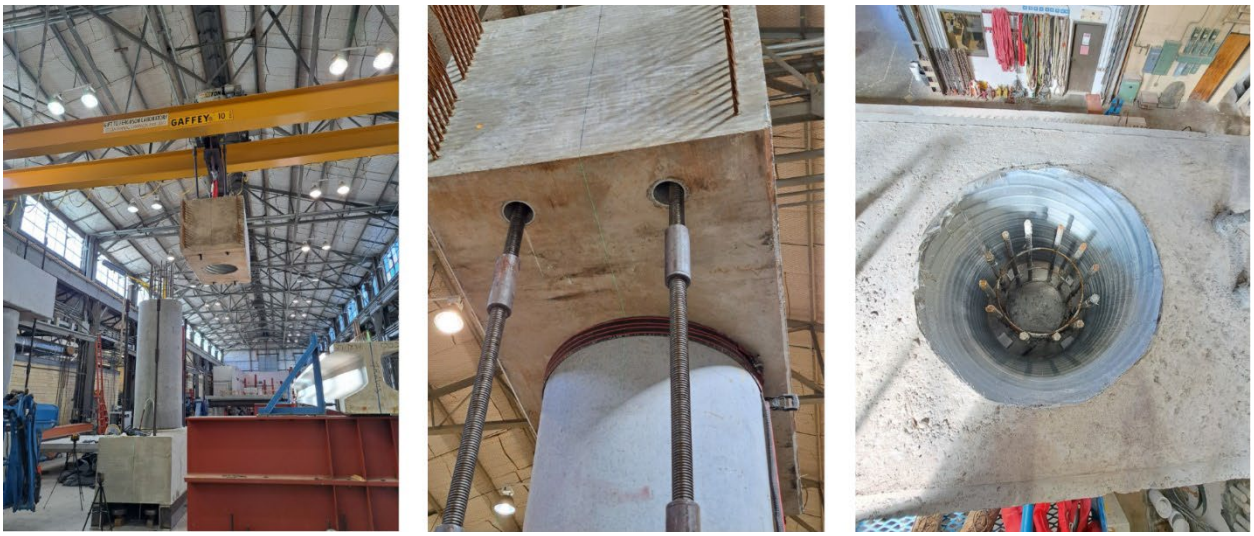

(a) Placing of the bent cap

(b) Alignment of the bent cap with marks and laser

(c) Bent cap sitting on the four HDEP shims

Figure 4-61: Placing of the bent cap for Specimen S3-S-AASH9-45.

When placing steel formwork on the top of each column, a process similar to the one used at the bottom of the columns was followed. Initially, a chisel was used to create a small hole measuring 1-in. by 3.5-in. on the top of the column, allowing the cables of the strain gauges to exit the column without being affected by the pressure on the forms. Subsequently, a foam strip measuring ¾-in. in width by ½-in. in thickness was attached around the columns to seal the forms and prevent

leaking from the cast. Finally, the steel form was positioned on the top of the column and secured using ratchet straps to complete the ring and keep the form in place, as shown in Figure 4-62.

(a) Foam attached to the columns before placing the steel formwork

(b) Steel forms placed on Specimen S2-R-AASH9-45

(c) Steel forms placed on Specimen S3-S-AASH9-45.

Figure 4-62: Precast columns prepared for bent cap's void concrete casting.

After preparing both bent caps with the forms, the research team proceeded with the concrete cast in the bent caps void. The specified concrete was TxDOT Class C with a 6-in. slump and 1-in. coarse aggregate, the same specification as the one used for the precast columns void. On the day of the cast, the research team received the concrete with a slump of almost 8 in. and concrete was poured in 4 layers, with special attention given to vibrating the zones close to the forms to avoid honeycombing. Due to the height of the assembled specimens, certain considerations were taken during the cast to ensure the bucket was positioned correctly over the bent caps, as indicated in Figure 4-63.

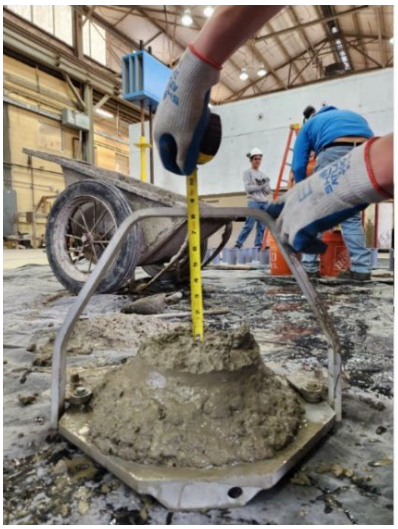

(a) Slump measured before pouring the concrete

(b) Pouring concrete for Specimen S2-R-AASH9-45

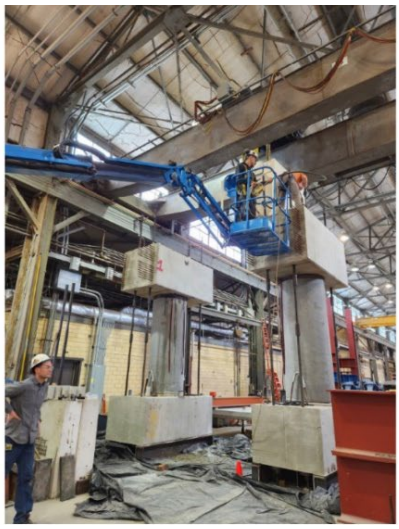

(c) Pouring concrete for Specimen S3-S-AASH9-45

Figure 4-63: Concrete casting for Specimens S2-R-AASH9-45 and S3-S-AASH9-45.

The completed specimens after assembling can be seen in Figure 4-64. While the concrete was being cured, the research team prepared the sensors, load cells, rams, and hydraulics on Specimen S2-R-AASH9-45, and the test was completed. After moving the sensors from this specimen to S3-S-AASH9-45, the third test was finished. On the day of the test, the average f'_c obtained for the precast columns was 4.369 ksi and the average f'_c for the bet cap voids was 5.022 ksi.

(a) Specimen S2-R-AASH9-45

(b) Specimen S3-S-AASH9-45

Figure 4-64: Specimens ready for testing.

4.2.8.3. Assembly of Specimen S4-R-Tx-34 and S5-R-ZABORAC-28

Following the process established for the previous two precast specimens, specimens S4-R-Tx-34 and S5-R-ZABORAC-28 were both constructed using the same batch of concrete for the void in the precast columns and the void in the connections with the bent caps. The main difference between the two specimens was the embedment length of connectors. Specimen S4-R-Tx-34 followed TxDOT Standards and had an embedment length of 2'-10" for the connections for the bent cap with the column, and between the footing and the column. Specimen S5-R-ZABORAC-28 was meant to test the formula for the development length established by Zaborac and Bayrak (2022), delivering an embedment length of 2'-4" for #9 bars; this approach was approved by AASHTO LRFD.

The research team commenced the construction by preparing the strain gauges on the rebar in the footings and the rebar cage for the connection from the column to the bent cap, following the pattern outlined in Figure 4-65. Initially, the footings were positioned next to Specimens S2-R-AASH9-45 and S3-S-AASH9-45, and the rebar cages were subsequently completed adjacent to the footing, as illustrated in Figure 4-66.

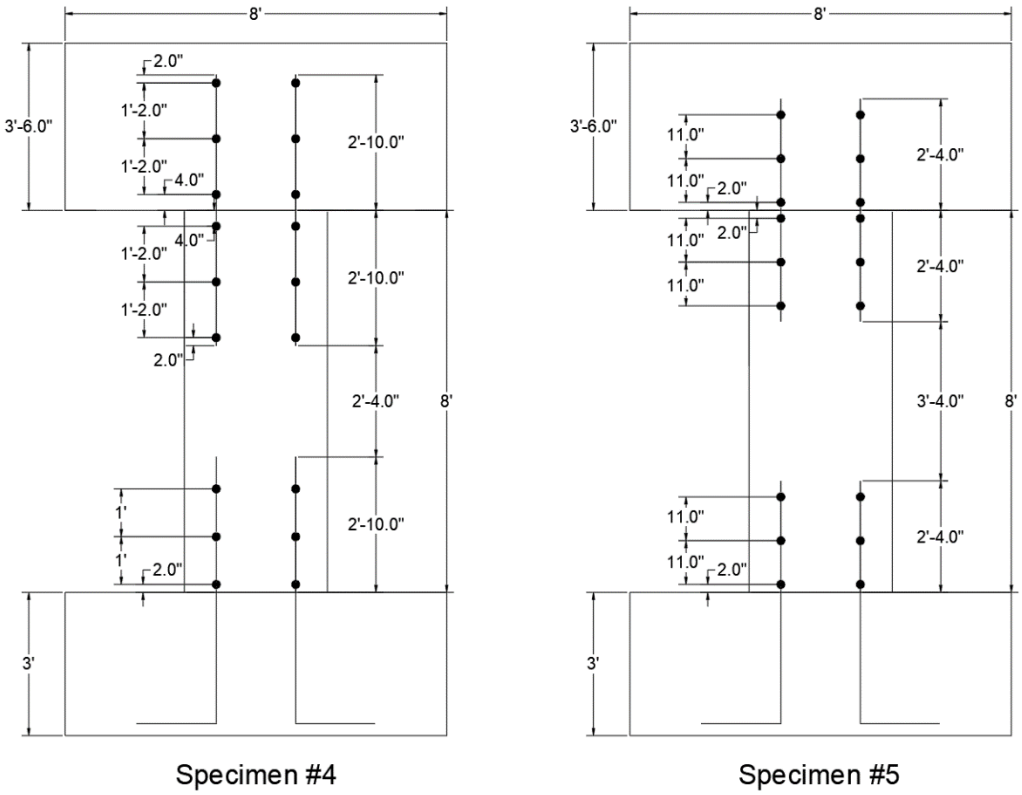

Figure 4-65: Location of strain gauges for Specimen S4-R-Tx-34 (Left) and S5-R-ZABORAC-28 (Right).

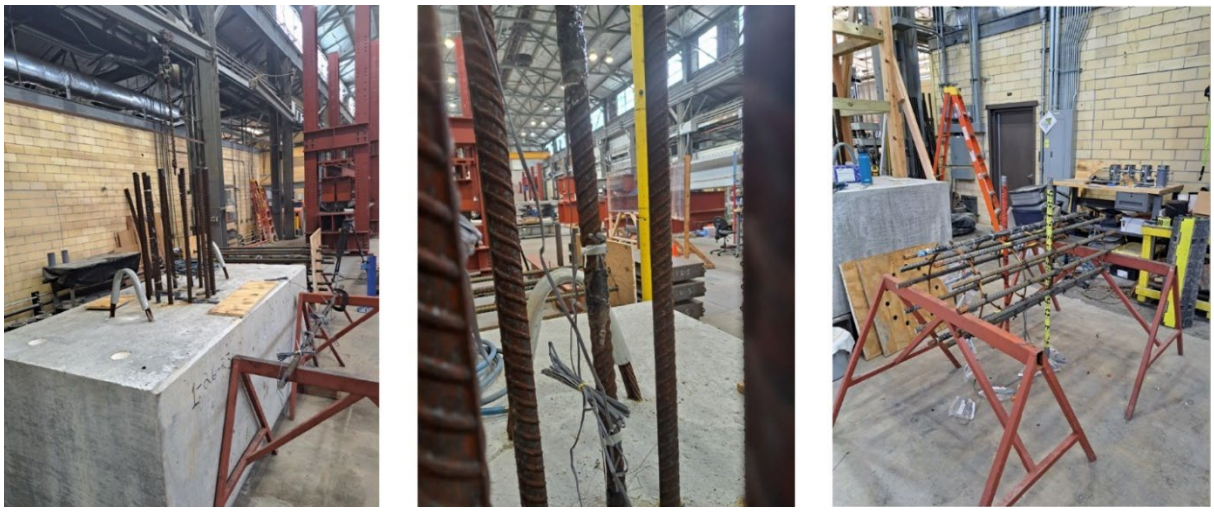

Figure 4-66: Strain gauges were prepared in the footing and cage connection for Specimen S4-R-Tx-34 and S5-R-ZABORAC-28.

After preparing the strain gauges, the footings were positioned on top of the steel sections, and the research team proceeded to mark the locations for the HDPE shims and the precast column. A circular wooden frame was constructed to ensure the column was centered and to place the shims 1.5-in. from the edge, creating space for the concrete to flow between the shims and the formwork, as shown in Figure 4-67(a). In the case of Specimen S4-R-Tx-34, no issues were encountered, as the footing and column centers aligned perfectly. However, Specimen S5-R-ZABORAC-28 presented a challenge as the column center had shifted 2 in. off-centered due to a fabrication error, resulting in additional eccentricity and impacting the load distribution, as shown in Figure 4-67(b). This was addressed by adjusting the load values, however, the eccentricity for the final test measured 42.25 in. instead of the intended 40.25 in., which was considered not affecting the final conclusions. Once the column and shims were marked, the team proceeded to grind the concrete at the shim locations to create a flat and level surface. Epoxy was then applied to secure the shims in place and prevent movement during the installation of the hollow sections.

(a) Specimen S4-R-Tx-34 with the HDEP shims glued to the footing

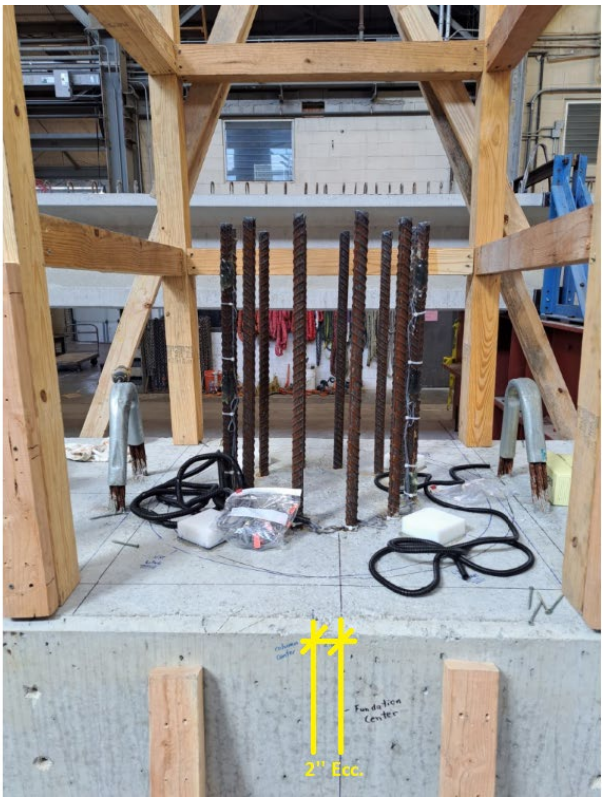

(b) Specimen S5-R-ZABORAC-28 with the marks of the center of the footing and the column

Figure 4-67: HDEP shims ready to place the precast columns.

After securing the wood frames to the footings with tightened bolts, the team used two 10-ft. straps to carefully move the precast column for Specimen S4-R-Tx-34. The straps created enough friction with the concrete to lift and position the column, as shown in Figure 4-68. Due to crane height limitations, one side of the wood frame remained open, allowing the crane operator to maneuver the column without interfering with the rebar and interior threads of the hollow section. Once the column was in place, the research team completed the wood frame with the missing horizontal members and safely released the crane. The precast column was then set on four HDEP shims, maintaining a 1.5-in. gap between the column and the footing.

Figure 4-68: Lifting and placing of Precast Column for Specimen S4-R-Tx-34.

After confirming that the precast column for Specimen S4-R-Tx-34 was properly positioned and plumbed, the research team proceeded with the precast column for Specimen S5-R-ZABORAC-28. The procedure used for this column was identical to the one used for Specimen S4-R-Tx-34, as shown in Figure 4-69.

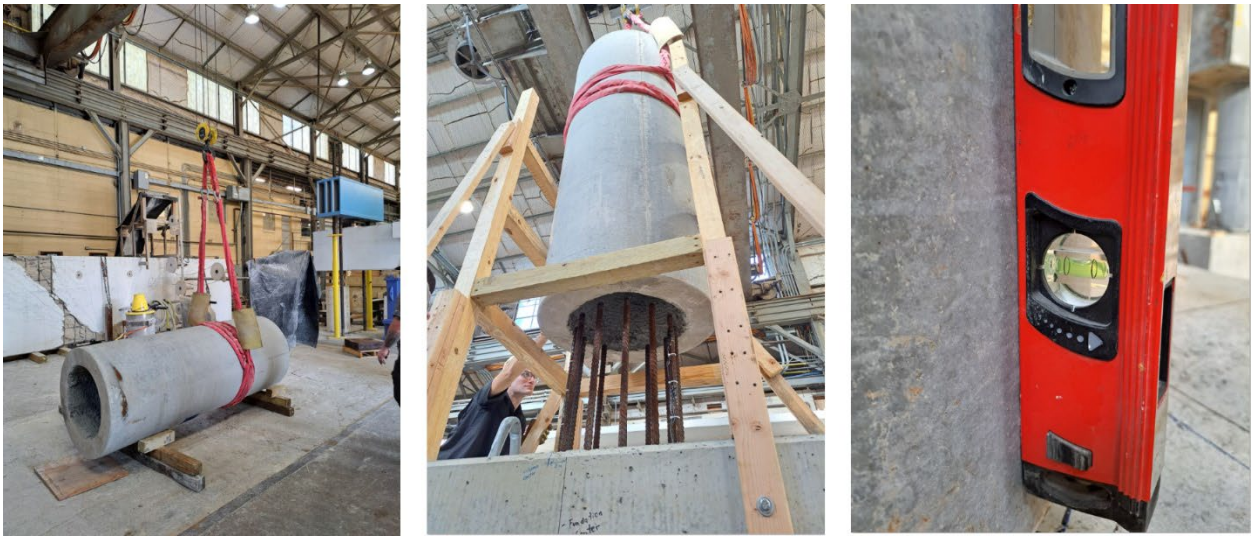

Figure 4-69: Lifting and placing of Precast Column for Specimen S5-R-ZABORAC-28.

To allow the cables from the strain gauges on the steel footing to extend outside the column, a small hole was created using a chisel and a hammer, measuring 3.5 in. long and 1 in width. The team then wrapped each precast column with a ¾-in. by ½-in. foam to prevent any leakage from the top of the steel formwork. Subsequently, the steel formwork was positioned at the base of each column and tightened by using ratchet straps. As the strain gauges were situated on the internal cage of each precast column, a hole in the precast column was created to allow the cables to pass

through during the spun cast process. This required the design and attachment of a small formwork using ratchet straps similar to those used for the steel formwork, see Figure 4-70.

(a) Steel formwork located at the bottom of Specimen S4-R-Tx-34 using ratchet straps

(b) Cables for strain gauges going out of the column for Specimen S4-R-Tx-34

(c) Steel formwork located at the bottom of Specimen S5-R-ZABORAC-28 using ratchet straps

(d) Cables for strain gauges going out of the column for Specimen S5-R-ZABORAC-28.

Figure 4-70: Preparation for concrete casting in the precast column's void.

The last step before pouring the concrete into the precast columns involved placing the steel cage that served as a connection between the column and the bent cap. As previously noted, these cages were equipped with strain cages and steel hoops to maintain the necessary circular shape for the connection. Additionally, they were reinforced with lateral bars to provide vertical support and to

position the cages on the precast columns. These bars were removed after the casting process, as shown in Figure 4-71. Using a crane, the cages were carefully positioned on top of each precast column according to the provided drawings. For Specimen S4-R-Tx-34, the cages were positioned with 2'-10" inside the column and 2'-10" outside, while for Specimen S5-R-ZABORAC-28, the position was 2'-4" inside and 2'-4" outside, ensuring the embedment length for the connection with the bent cap.

(a) General procedure for lifting the steel cages

(b) Steel cage for Specimen S4-R-Tx-34

(c) Steel cage for Specimen S5-R-ZABORAC-28

Figure 4-71: Placing of steel connectors on top of precast columns.

Once the rebar cages, steel forms, and wood frames were prepared, the next step involved casting the concrete into the column voids. Due to the small volume required for each void, the team opted to cast both specimens simultaneously to streamline construction and ensure uniformity by using the same batch of concrete for each. The concrete specified was TxDOT Class C with a target f'_c of 3.6 ksi, a 6-in. slump, and a coarse aggregate of 1-in. maximum to fill the 1.5-in. gap under the precast columns with HDPE shims. As shown in Figure 4-72, the actual cast had a 7.5-in. slump and started with Specimen S4-R-Tx-34. The concrete was poured in 4 to 5 layers into the interior of each column and vibrated near the edges to prevent honeycombing on the bottom. After completing the first specimen, Specimen S4-R-Tx-34, the team refilled the bucket and continued with Specimen S5-R-ZABORAC-28 using the same process.

(a) Precast Column for Specimen S4-R-Tx-34 being poured

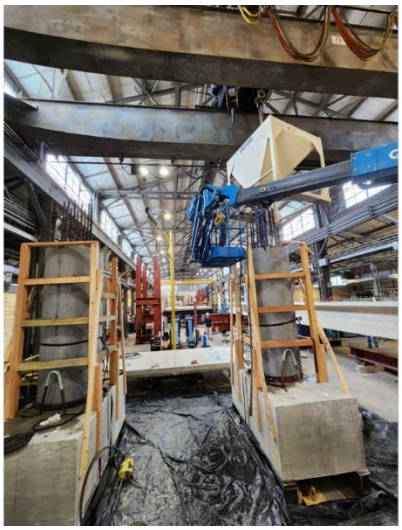

(b) Precast Column for Specimen S5-R-ZABORAC-28 being poured

(c) Slump test prepared before the cast

Figure 4-72: Precast columns' void concrete casting.

The team placed some plastic sheets on the top of each column to avoid losing water from the concrete and to avoid exposure to air. After 7 days of curing, the steel forms on the bottom of the columns were removed. However, the team noticed that concrete did not perfectly consolidate under the precast shells, resulting in 1.5-in. gap not filled completely in the two specimens. It was found that a gap of 0.5-in. to 2-in. was not filled with concrete. Specifically, Specimen S4-R-Tx-34 filled close to 90%, and Specimen S5-R-ZABORAC-28 had issues at 75% of the section, as shown in Figure 4-73 and Figure 4-74.

The specimen S4-R-Tx-34 displayed some minor issues on the northern side of the column. Nevertheless, these concerns are not significant and do not present any major problems. Specimen S5-R-ZABORAC-28 encountered issues on the western side that extended to certain portions of the southern and northern sides, resulting in significant issues for the test. This incomplete area on the compression side could potentially affect the specimen's resistance.

The next task involved fitting the bent cap on top. After careful consideration of the logistics, the team determined that repairing the honeycomb after casting the void in the bent caps was the best approach. Considering that the same steel forms would be used for both the casting of the bent caps and the grout pouring for the repair.

(a) South-West View

(b) North-West View

(c) North-East View

(d) South-East View

Figure 4-73: Precast Column for Specimen S4-R-Tx-34 after removing steel forms on the bottom.

(a) South-East View

(b) South-East View (closer view)

(c) South-West View

(d) North-West View

(e) North-East View

Figure 4-74: Precast Column for Specimen S5-R-ZABORAC-28 after removing steel forms on the bottom.

With the rebar that was holding the cages on the top of each column being removed, the same procedure established for the HDPE shims on the bottom of the precast columns was followed to place them on the top of each column and create a gap of 1.5-in. between the columns and the bent caps. Four shims were located at each column keeping 1.5-in. from the edge and the surface was ground until achieving a leveled surface, as shown in Figure 4-75.

(a) HDEP shims on the top of each column (1.5-in. from the edge) keeping a gap of 1.5-in. between the column and the bent cap

(b) HDEP shims leveled and glued to the Specimen S4-R-Tx-34

(c) HDEP shims leveled and glued to the Specimen S5-R-ZABORAC-28

Figure 4-75: Precast columns prepared to place the bent cap.

With the shims positioned, four all-threaded rods and their anchoring steel plates and nuts were placed on the top of each bent cap to be tightened after placing the beams on the top of the columns. After marking the center lines in all the external faces of the bent caps, the bent cap was craned and approached the column to be placed. The bent caps were then positioned using the marks on the footing. Similarly, a laser positioner was used to assist in the assembling, as shown in Figure 4-76. The all-threaded rods were coupled with the couplers, and nuts on the top and the bottom of each column were tightened to keep the bent caps in position and to stabilize the specimens during the cast and curing.

Although the column for Specimen S5-R-ZABORAC-28 was moved 2-in. off-centered, it was still needed to keep the bent cap for this specimen aligned with the footing's center in order to allow for the all-threaded rods through the PVC sleeves located on the footing and the bent cap, as shown in Figure 4-77.

(a) Placing of the bent cap

(b) Alignment of the bent cap with marks and laser

(c) Bent cap sitting on the four HDEP shims

Figure 4-76: Placing of the bent cap on top of Specimen S4-R-Tx-34

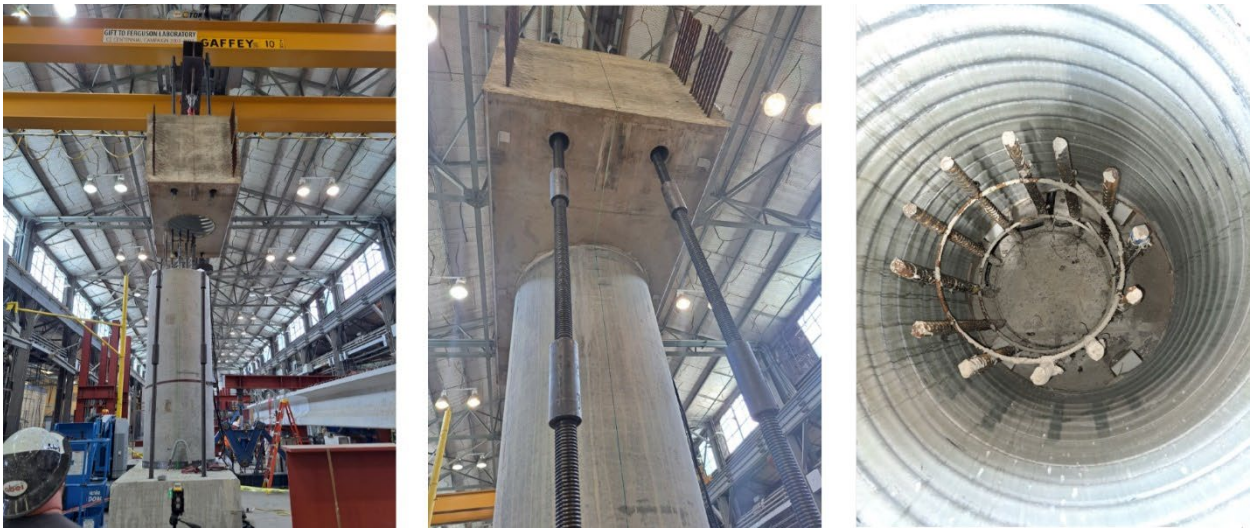

(a) Placing of the bent cap

(b) Alignment of the bent cap with marks and laser

(c) Bent cap sitting on the four HDEP shims

Figure 4-77: Placing of the bent cap on top of Specimen S5-R-ZABORAC-28

With the bent caps on the top of each column, the procedure followed to place the steel formwork on the bottom of the column was similar to the one needed on the top of the columns. First, a chisel was used to create a small hole of 1-in. by 3.5-in. on the top of the column to allow the cables of the strain cages to go out of the column without being affected by the pressure on the forms, and a foam of ¾-in. width by ½-in. thick was attached around the columns to seal the forms and avoid

leaking from the cast. Then, the steel form was held on the top of the column and tightened using ratchet straps to complete the ring and keep the form in place, as shown in Figure 4-78.

(a) Foam attached to the columns before placing the steel formwork

(b) Steel forms placed on Specimen S4-R-Tx-34

(c) Steel forms placed on Specimen S5-R-ZABORAC-28

Figure 4-78: Precast columns prepared for bent cap void's concrete casting.

When both bent caps were prepared with the forms, the research team continued with the concrete cast in the bent caps void. The concrete specified was TxDOT Class C with a 6-in. slump and a 1-in. coarse aggregate, the same specification as the one used for the precast columns void. On the day of the cast, the research team received concrete with a slump of 8.5-in., and it was poured in 4 layers, being vibrated in the zones close to the forms with extra attention to avoid honeycombing, as shown in Figure 4-79. On the day of the test, the average f'_c obtained for the precast columns was 3.15 ksi and the average f'_c for the bet cap voids was 4.6 ksi.

(a) Slump measured before pouring the concrete

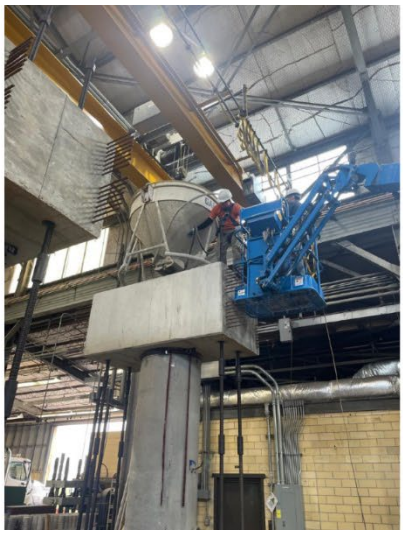

(b) Pouring concrete for Specimen S4-R-Tx-34

(c) Pouring concrete for Specimen S5-R-ZABORAC-28.

Figure 4-79: Concrete casting for bent cap's void for Specimens S4-R-Tx-34 and S5-R-ZABORAC-28

It waited for 7 days before removing the steel formwork from the top of the columns; meanwhile, grouting was prepared to fix the honeycombing present on the connection on the bottom of the columns. At the bottom of the specimens, loose aggregates were removed and some degree of roughness that matched CSP-4 or higher was targeted using a hammer, leaving out portions of concrete of approximately ¼-in. This preparation was conducted around the entire column perimeter, as shown in Figure 4-80.

Figure 4-80: Surface roughened to a CSP 4 or higher for Specimen S4-R-Tx-34 and S5-R-ZABORAC-28.

The next step was to clean the prepared surface using air pressure and to keep the zone saturated for 3 days by spraying water. It was to warrant that the concrete from the column specimen was absorbing water from the grout mixture, as shown in Figure 4-81. In order to keep the grout in the forms without leaking, the team used spray foam to seal the forms from the outside one day before the cast of core concrete, as shown in Figure 4-82.

Figure 4-81: Surface cleaned and saturated for Specimen S4-R-Tx-34 and S5-R-ZABORAC-28.

Figure 4-82: Steel forms placed and spray foam sealing for Specimen S4-R-Tx-34 and S5-R-ZABORAC-28.

With all these steps completed, a small grout mixer was used inside the lab and then poured into buckets and placed on each form. The grout used for this mixture was SikaGrout-212 which had a compressive strength at 28 days of 5.8 ksi, similar to the f'_c specified for the precast column specimen cores from the previous specimens. As the surface was a little irregular, the mixture was maintained to have an appropriate thickness to fill the spaces where concrete did not well-

consolidate. The product was mixed with 8 pints of water per 50 lb. bag (1 gallon per bag). The grout was poured using a funnel on one side, then it was moved to another location of the form until completing the circle and a steel rod was used to vibrate the grout mixture for consolidation and removal of air, as shown in Figure 4-83. The forms were removed one day after the cast, and some water was sprayed on the grout four times per day for the next three consecutive days, as shown in Figure 4-84. The compressive strength obtained from four cube samples two weeks after pouring was 7.8 ksi in average.

Figure 4-83: Grout pouring for Specimen S4-R-Tx-34 and S5-R-ZABORAC-28.

Figure 4-84: Steel formwork removed from Specimen S4-R-Tx-34 and S5-R-ZABORAC-28.

The research team completed the construction of the specimens in the laboratory as shown in Figure 4-85. While the concrete was being cured, the research team prepared the sensors, load cells, rams, and hydraulics on Specimen S4-R-Tx-34. After completing the test on this specimen, the sensors were moved from Specimen S4-R-Tx-34 to S5-R-ZABORAC-28 and the test was

completed afterward. Detailed information about the instrumentation and test are documented in later sections.

(a) Specimen S4-R-Tx-34 (b) Specimen S5-R-ZABORAC-28

Figure 4-85: Precast columns ready for test.

4.2.9. Instrumentation

The specimens were instrumented with sensors including strain gauges, linear variable displacement transducers (LVDTs), linear potentiometers (L-Pots), and string potentiometers (S-Pots). The quantity of each sensor used is listed in Table 4-2. Figure 4-86 illustrates the layout of the sensors. Strain gauges were distributed along the height of the column rebars. These strain gauges were used to monitor strains and determine how stress transferred between the connectors and the column reinforcement through the non-contact splice. Besides, the strain gauges were used to monitor if the connectors were able to develop the yield stress, assisting in determining the required development length that could be used for the design guidelines.

Table 4-2. Setup sensors

Sensor	Quantity
LVDT	12
L-Pot (Lateral Displacement)	5
S-Pot (Vertical Displacement)	6
Load Cells	4
Strain Gauges	30

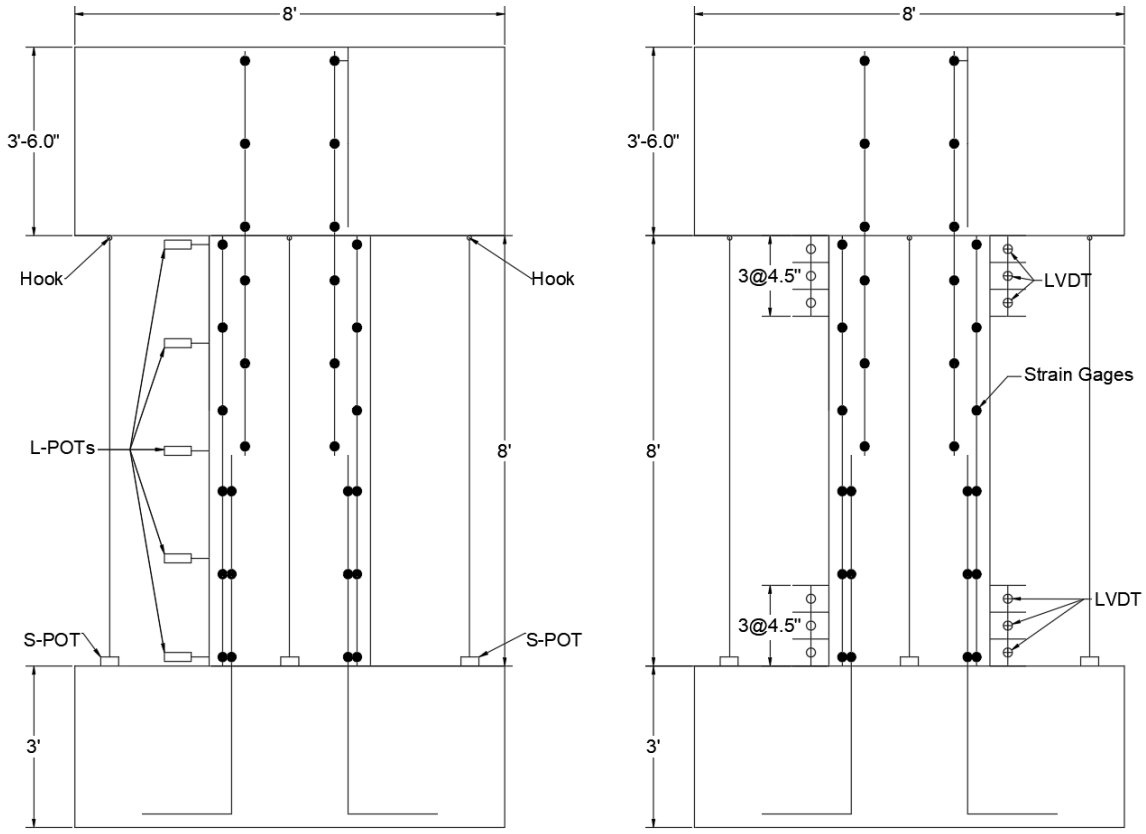

(a) Locations of Lpots and String Pots (b) Locations of strain gauges and LVDTs

Figure 4-86: Sensor location on the column

LVDTs were mounted on the edges of the column near the two connections to measure the vertical deformations on both sides of the column. The gauge length of the LVDTs was 1-in. The data could be used to determine the curvature. The setup and installation of the LVDTs are shown in Figure 4-87.

Linear potentiometers (L-Pots) were also mounted laterally along the height of the column at a spacing of 24-in., as shown in Figure 4-86. These L-Pots measured the lateral displacement as the load increased and helped reconstruct deflection shapes at different load stages, as seen in Figure

4-88. The L-Pots were supported using two steel poles, which were connected to a brace to avoid disruption from external disturbances.

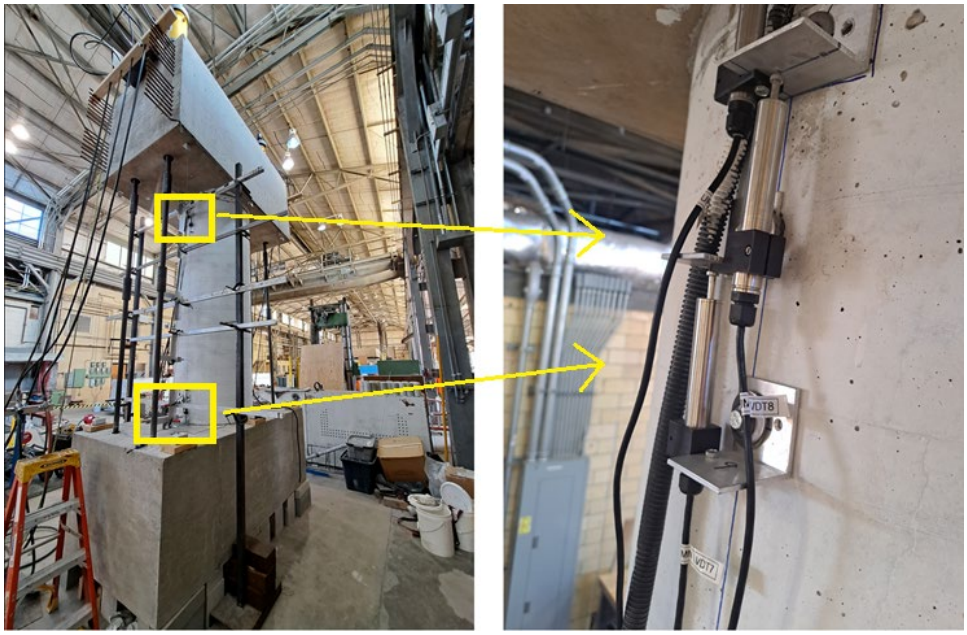

Figure 4-87: Location of LVDT sensors.

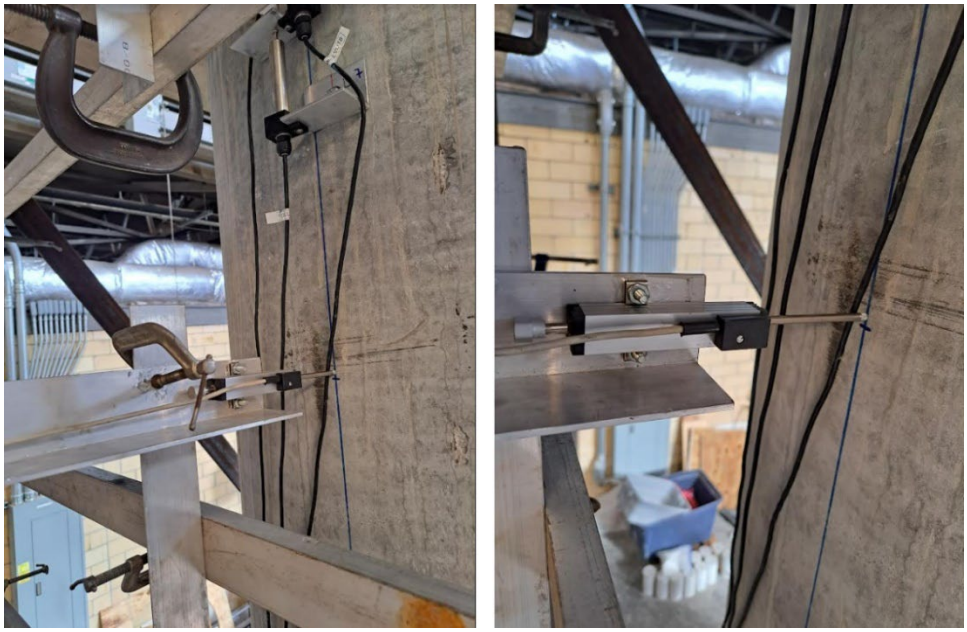

Figure 4-88: Location of L-Pots during the test.

Six string potentiometers (S-Pots) were installed close to the all-threaded tensioning rods and close to the column center in the middle of the foundation, as shown in Figure 4-89. This configuration allowed the research team to measure the vertical displacements near the loading points and the axial shortening of the column, thereby facilitating the determination of rotation due to the moment generated by the load.

Figure 4-89: Location of S-Pots during the test.

Four load cells were placed on top of the specimen, and each of them was mounted on a ram, as shown in Figure 4-90. The load cells were used to measure the load applied through the rams. Hydraulic pumps were used on both sides of the specimen, and the load cells played a key role during the test to control the load ratio between the north and south sides to achieve the desired eccentricity.

Figure 4-90: Location of load cells (silver) and rams (yellow) on the top of the specimens.

4.3. Test Method

To achieve the required eccentricity, the load applied on one side of the specimen must be proportionately larger than that on the other side. Three eccentricities were employed in each test: 6-in., 12-in., and 40.25-in. For eccentricities of 6-in., 12-in., and 20-in. the target axial load is approximately 15% of the maximum axial compressive capacity of the column considering a nominal f'_c of 3.6 ksi. The 40.25-in. eccentricity was meant to fail the column in flexure. To achieve a certain eccentricity, the ratio of the load on one side to the other side (α) can be determined using the following equation:

$$\alpha = \frac{x + e}{x - e} \tag{4-1}$$

where e is the target eccentricity, and x is the distance of a load point to the center of the column, which is 40.25 in. or 42.25in. for the test setup. For the 40.25-in. eccentricity test the load was applied on one side only. The ratio of the load on one side to the other side (α) is presented in Table 4-3 for all the eccentricities.

Table 4-3. Test load ratio according to the eccentricities

	Eccentricity (in.)	Distance from the center of the column "x" (in.)	Ratio α
S1-CIP to S4-R-Tx-34	6.00	40.25	1.35
	12.00	40.25	1.85
	20.00	40.25	2.98
S5-R-ZABORAC-28	6.00	42.25	1.33
	12.00	42.25	1.79
	20.00	42.25	2.80

Note: For the 40.25-in. eccentricity test, only one side was loaded

The load path of each of the first two cases is graphically presented in Figure 4-91, where the orange curve indicates the P-M interaction diagram of the Specimen S1-CIP. The blue line, which has a slope of 1/e, represents the load path for testing. In other words, the applied load and moment would be increased along the path during the test. The horizontal line represents the target total axial level, 15% of the anticipated axial ultimate load-carrying capacity (approximately $f'_c A_g$), otherwise 0.15 $f'_c A_g$ or 549.65 kips.

According to calculations made for the precast column specimens, it was anticipated that these specimens would not suffer any damage during the 6-in. and 12-in. eccentricities tests and remain in the elastic range. Considering this possibility, it was decided to perform an additional 20-in. eccentricity test for the precast columns, as shown in Figure 4-92.

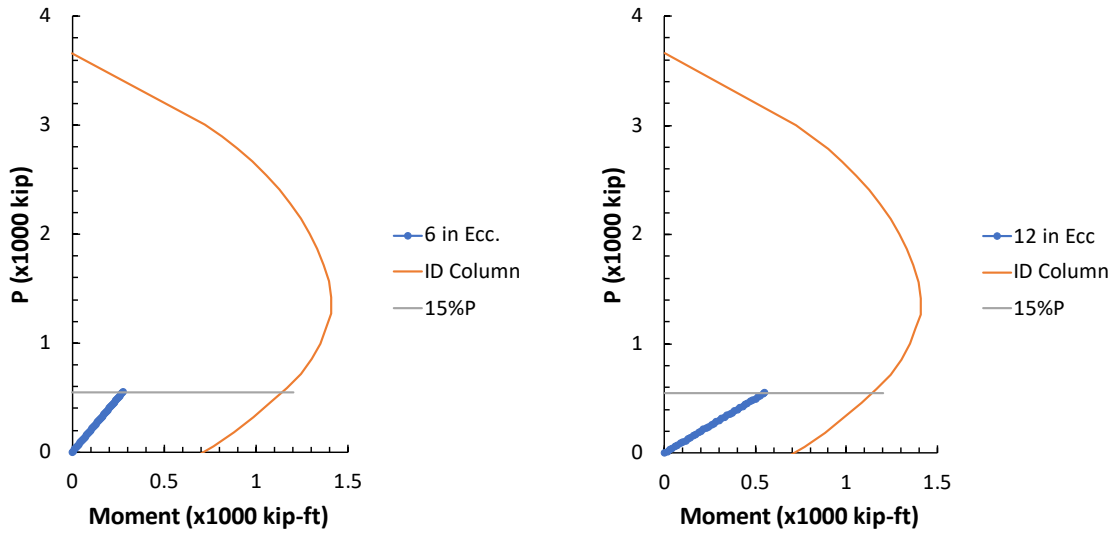

(a) e = 6 in. (b) e = 12 in.

Figure 4-91: Load pattern for eccentricity of 6-in and 12-in.

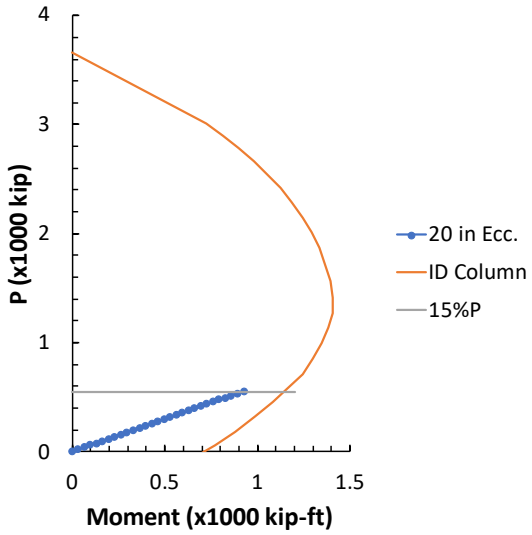

Figure 4-92: Load pattern for eccentricity of 20-in.

For the final case, which had a target eccentricity of 40.25 in., only the North-side rams were loaded. The interaction diagram and the load path are shown in Figure 4-93. In this case, loading was applied with ten to twelve increments until the anticipated failure load, represented by the intersection of the blue line and the P-M curve. In each load increment, crack patterns were inspected and recorded. It was not anticipated to reach the load level of $0.15 f'_c A_g$ because the load would touch the capacity envelope first, with an axial load of 285.35 kip-ft and a moment of 957.11 kip-ft.

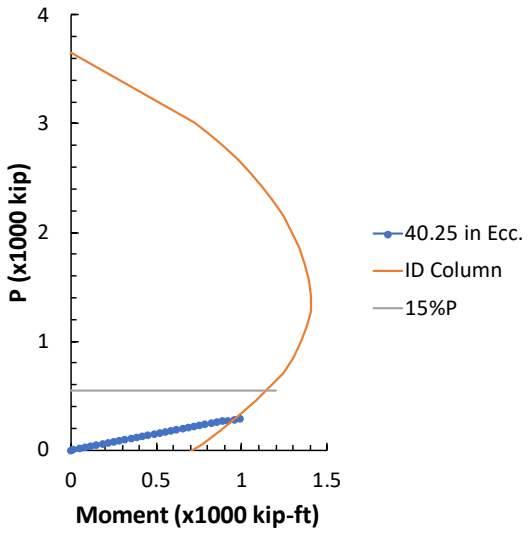

Figure 4-93: Load pattern for eccentricity of 40.25-in.

The load increments were 15 kips in terms of the total axial load on the South side, and on the North side, the load was adjusted according to the ratio α to accomplish the target eccentricity. After reaching the total increment, the test was paused for crack inspection and documentation. The procedure was repeated until the specified total axial load was attained for the first three eccentricities. For the last case, crack marking was stopped at 80% of the anticipated peak load for safety considerations.

4.4. Laboratory Results

This section considers the behavior of the specimens during the tests following the load pattern described in Section 4.3. Each of the specimens was tested after achieving 28 days of curing the core and void concrete. Following subsections present the test results of Specimen S1-CIP, Specimen S2-R-AASH9-45, evaluating a roughened interior section. Also, they present the test results of Specimen S3-S-AASH9-45, testing a non-roughened internal section, Specimen S4-R-Tx-34 using an embedment length of 2'10'' according to TxDOT Standards and Specimen S5-R-ZABORAC-28 analyzing an embedment length of 2'4'' according to a new development length approach based on Zaborac and Bayrak (2022), which is approved to be included in AASHTO LRFD.

4.4.1. Specimen S1-CIP (Cast-In-Place, Specimen as Baseline)

4.4.1.1. Overview

The footing and column for Specimen S1-CIP were completely cast in the laboratory, and the prestressed bent cap was produced externally. The details followed in its construction engage the standards from TxDOT for footings, columns, and prestressed bent caps and are illustrated in the section 4.2.1. This specimen allowed for investigating the behavior of columns based on the

current standards, which served as the baseline to evaluate the performance of the developed precast column solution.

4.4.1.2. Mechanical Properties of Concrete and Rebar

The mechanical properties tests for the concrete were prepared for this specimen as shown in Table 4-4 and Table 4-5. Is noticeable that the compressive strength of concrete (f'_c) and the yield strength of the reinforcement (f_y) was higher than the specified. Nevertheless, the planned load pattern that was established previously remained unchanged.

Table 4-4. Summary of concrete properties for Specimen S1-CIP

	f'_c (ksi)	MOE (ksi)
Foundation	6.95	6597.84
Column	4.90	4353.09
Bent Cap	9.73	6262.13

Table 4-5. Summary of rebar properties for Specimen S1-CIP

Steel	f_y (ksi)	f_u (ksi)
A615	65.45	101.67

4.4.1.3. Structural Testing Results

The total axial load versus the lateral displacement at the top of the column of each eccentricity is plotted as shown in Figure 4-94. In this plot, the vertical axis represents the total axial load applied to the column, while the horizontal axis is the measured lateral displacement at the column's top. The eccentricities of 6-in and 12-in are based on the load moments that aim to represent common eccentricities that columns are subjected to in Texas; in these cases, it shows that the performance of the specimen was nearly linear below the target axial load (representing the typical design axial load for columns).

For the 40.25-in eccentricity test, the plot includes a measured portion (indicated by the yellow line) and an extrapolated part (indicated by the black line), because the top L-Pot malfunctioned at a load level of 300 kips. The extrapolation considered the decrease of the column's rigidity as the applied moment increased. The decrease rate was based on the reading from the L-Pots at 6 ft. of the column's height and the one in the middle. It should also be noted that the test was stopped at a load of 360 kips without attaining the ultimate failure for safety concerns. A more detailed procedure for the extrapolation is presented in the section 5.2.4.1.

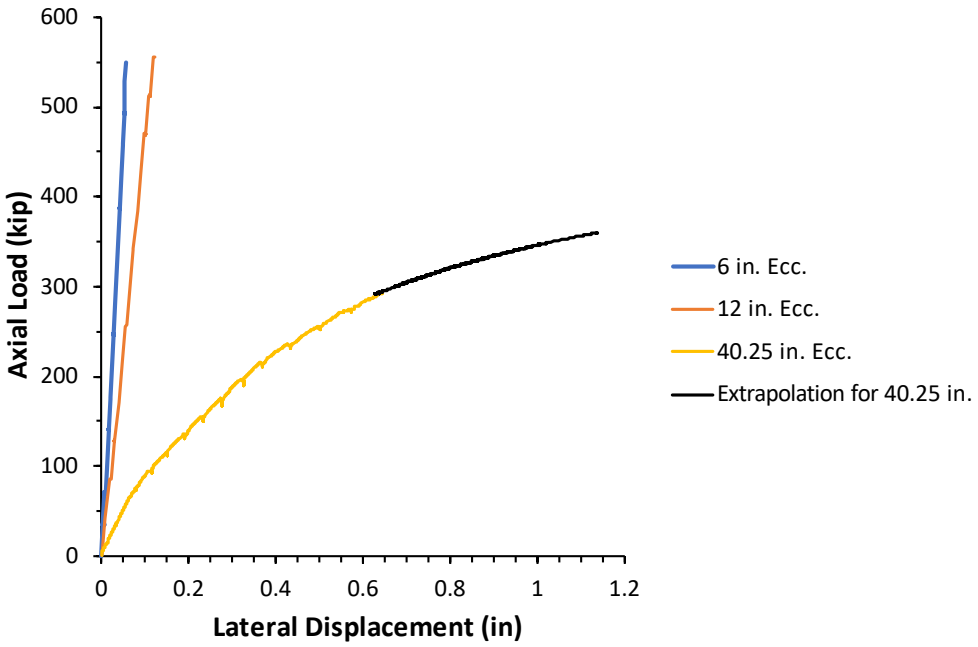

Figure 4-94: Comparison in the lateral displacement for Specimen S1-CIP using the L-Pot 5 located at the top of the column.

The 6-in eccentricity test started by making load increments of 15 kips on the South side while adjusting the loads on the North side until the eccentricity was attained. At certain checkpoints, loading was paused for crack marking. Loading was finished at total load of 550 kips. For this test, the Specimen S1-CIP presented some cracks in the middle of the height of the column, as shown in Figure 4-95. The first crack was reported at 212 kips, then at 246 kips, and 387 kips.

The research team unloaded the specimen and continued with the 12-in eccentricity test. Similarly, the load increments remained 15 kips on the South side, and the North-side load was adjusted to obtain the eccentricity. The test was finished when reaching a total axial force of 555 kips. The cracks propagated through the height of the specimen as shown in Figure 4-96, and the crack width reached 0.005 in.

The test for 40.25 in eccentricity was performed after the completion of the previous test. For this test, the cracks propagated more along the height of the specimen, seemingly equally spaced, as shown in Figure 4-97. The crack width was larger, and an opening was observed in both connections, as shown in Figure 4-98. In the end, a lateral displacement of approximately 1.5 in was achieved.

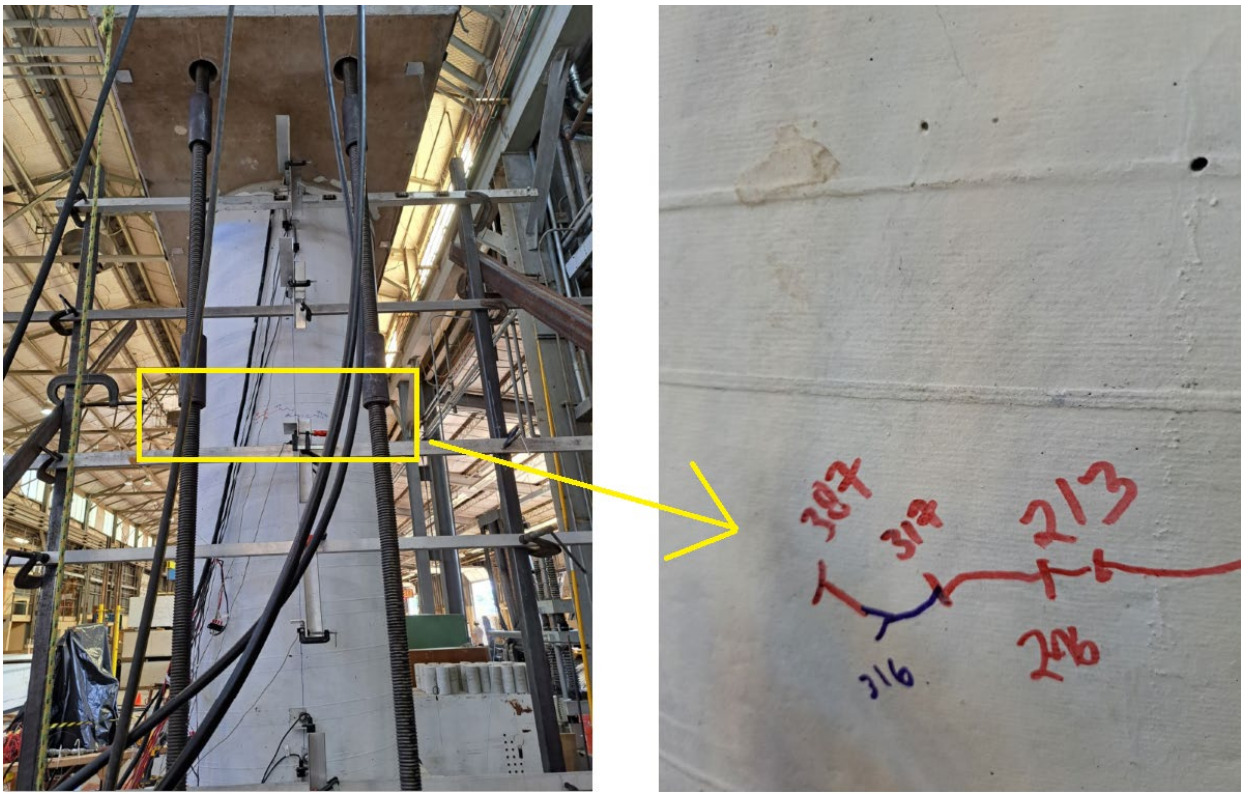

Figure 4-95: Cracks after 6-in Test for Specimen S1-CIP.

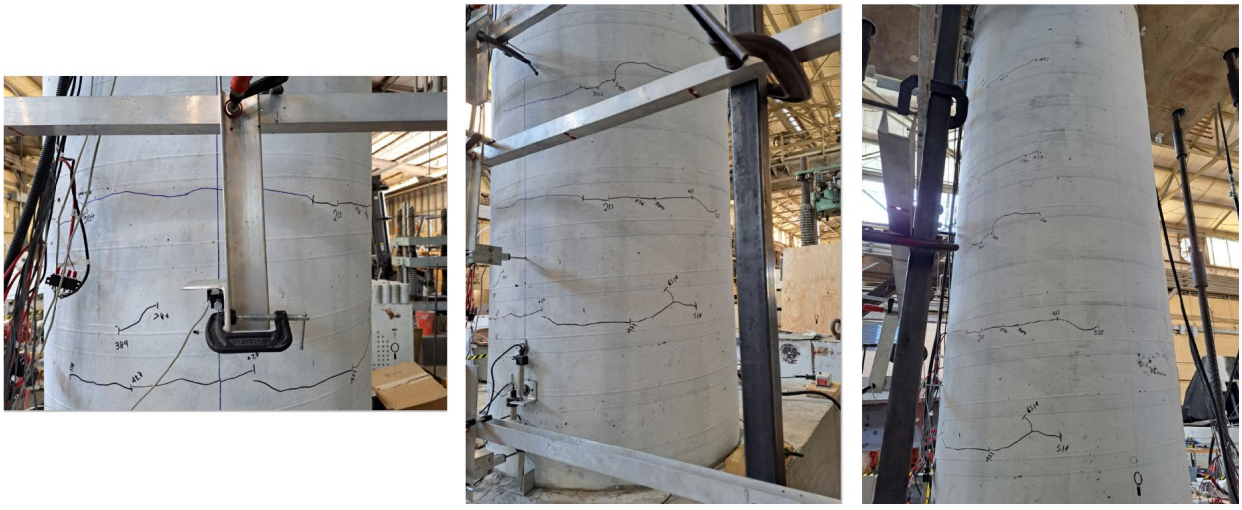

Figure 4-96: Cracks after 12-in Test for Specimen S1-CIP.

Figure 4-97: Cracks after 40.25-in Test for Specimen S1-CIP.

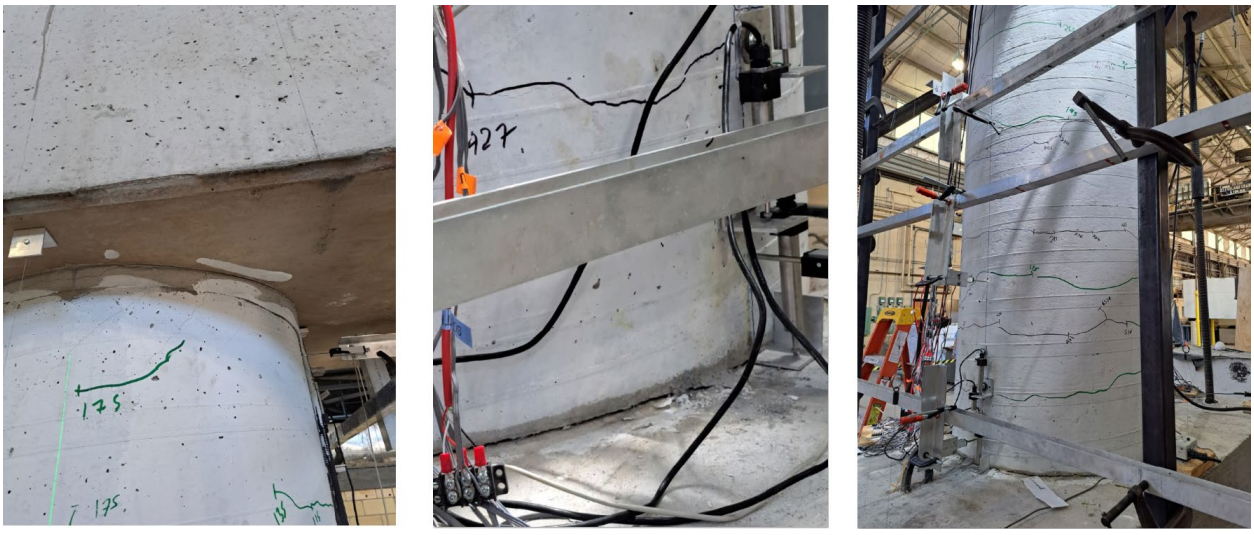

Figure 4-98: Opening in connection during the 40.25 in Test for Specimen S1-CIP.

4.4.2. Specimen S2-R-AASH9-45 – Intentionally Roughened

4.4.2.1. Overview

The specimen was purposefully constructed with an "intentionally roughed" precast shell to study the effect of interface shear on the composite behavior. The specimen also was tested to investigate the effect of rebar embedment length. A comparative analysis was to be conducted with its counterparts featuring less roughness or shorter rebar embedment lengths to discern the impact of these variables on the outcome.

4.4.2.2. Mechanical Properties of Concrete and Rebar

The concrete mechanical properties were tested for this specimen, as shown in Table 4-6. Similar to Specimen S1-CIP, the test properties of the concrete were higher than specified. Nevertheless, the planned load pattern that was established previously remained unchanged. The rebar used for the four precast column specimens was also tested from the same batch, as presented in Table 4-7.

Table 4-6. Summary of mechanical properties for Specimen S2-R-AASH9-45

	f'_c (ksi)	MOE (ksi)
Foundation	11.42	6381.80
Precast Column (Shell)	10.31	---
Column core	4.25	5034.61
Bent cap	10.65	5210.40
Bent cap void	4.93	4391.92

Table 4-7. Summary of rebar properties for Precast Column Specimens

Steel	f_y (ksi)	f_u (ksi)
A615	64.54	103.38

4.4.2.3. Structural Testing Results

The test for Specimen S2-R-AASH9-45 allowed the study of the specimens' behavior under the test eccentricities in terms of the lateral displacements. The axial load-displacement chart for the tests was plotted, as shown in Figure 4-99. The vertical axis represents the total axial load applied to the specimen and the horizontal axis shows the lateral displacements measured during each test. For the test of 6 in. and 12 in. eccentricity, the behavior was elastic until the end of the tests. On the other hand, for the 20 in. eccentricity test, the specimen's performance showed an elastic behavior until reaching 350 kips, followed by a softening when cracking was reported, reaching a larger displacement. For the test with the largest eccentricity, 40.25 in., a lateral displacement of 1.17 in. was achieved at the ultimate failure corresponding to a load of 596 kips.

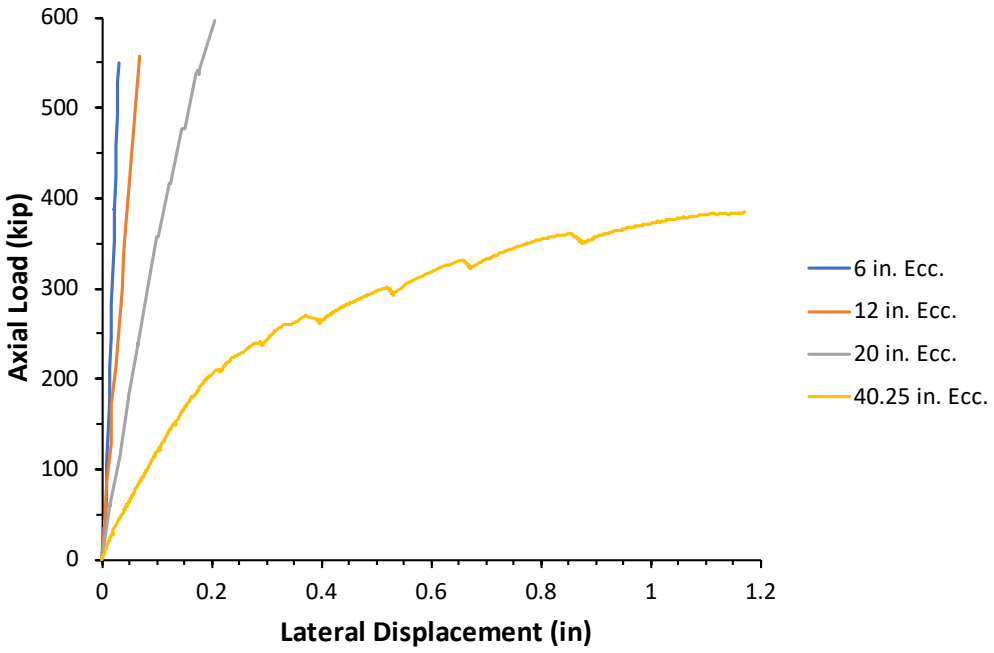

Figure 4-99: Comparison in the lateral displacement for Specimen S2-R-AASH9-45 using the L-Pot 5 located at the top of the column.

The test for 6-in eccentricity started with the same test protocol used for the Specimen S1-CIP, increasing the load by 15 kips on the South side and adjusting the North side to attain the eccentricity. The loading was paused at predetermined checkpoints for crack inspection. For this case, no crack was observed in the precast column, as shown in Figure 4-100(a), echoing its elastic behavior.

The team continued with the 12-in eccentricity test following the same load pattern established for the Specimen S1-CIP, finishing with a total axial load of 555 kips. Loading was also paused for crack inspection. The specimen did not show any noticeable cracks before the end of the test, as shown in Figure 4-100(b). This observation contradicted a previous analysis for cracking load that expected cracks to appear at the 11th increment of load with a total axial load of 470 kips (11th increment of 13), meaning that the specimen had a better behavior.

A third test considering an eccentricity of 20 in. was conducted afterwards. The North-Side load was adjusted to a ratio of 2.975 times the South-Side Load to get this eccentricity and the increments of load remained 15 kips on the South side. The first crack was expected to occur at the fourth increment of load with an axial load of 238 kips; however, the specimen showed a higher cracking load than expected. In particular, the first crack appeared at the connection with the bent cap with an axial load of 417 kips, as shown in Figure 4-101(a). After this, the first crack on the shell was observed at an axial load of 477 kips at the location where the connectors were terminated, as shown in Figure 4-101(b). Finally, the test concluded with an axial load of 596 kips and a moment of 994 kip-ft and the last crack occurred where the rebar from the footing was cut, as shown in Figure 4-101(c).

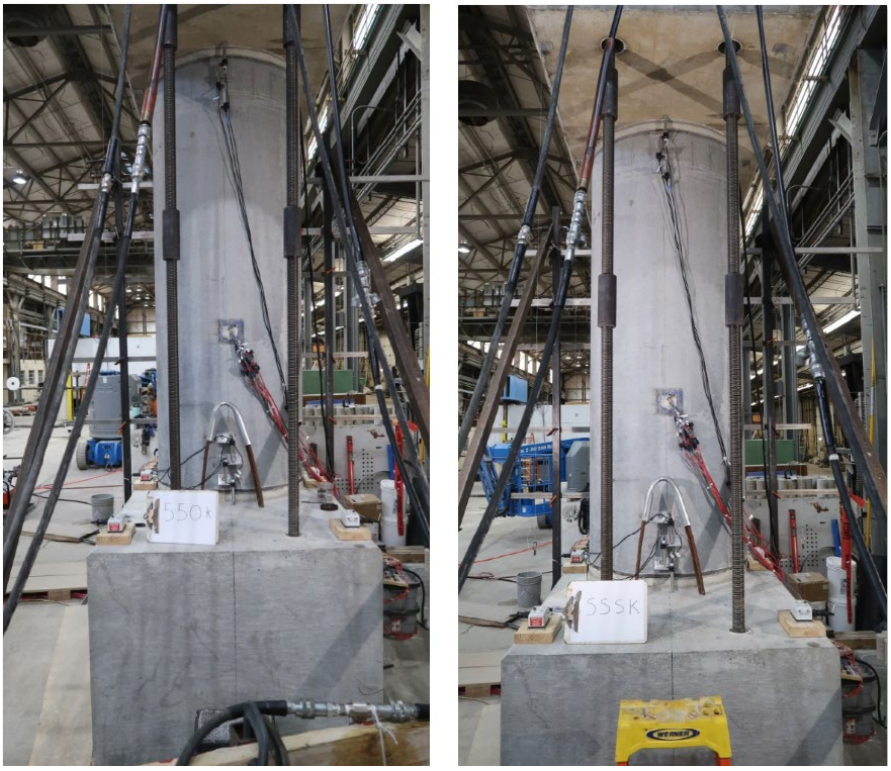

(a) without cracks after the 6-in test (b) without cracks after the 12-in test

Figure 4-100: Specimen S2-R-AASH9-45 after the 6-in eccentricity test, and the 12-in eccentricity test.

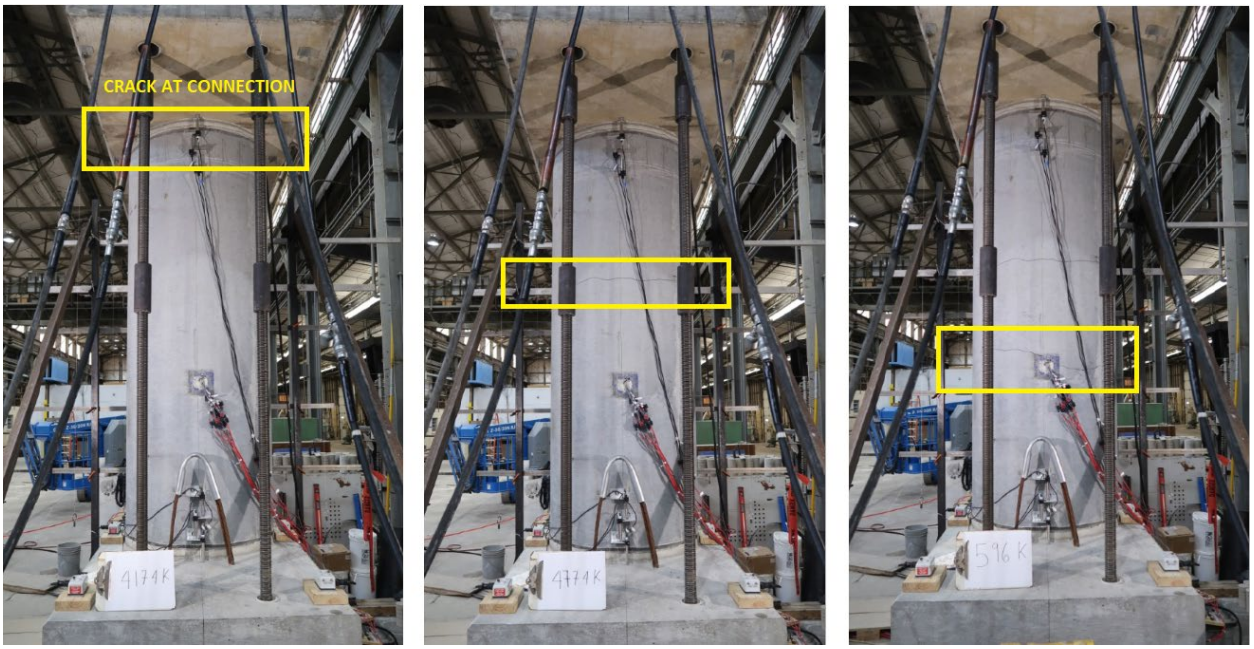

(a) Crack at the connection with the bent cap at 417 kips

(b) Crack at the middle-top of the specimen at 477 kips

(c) Crack at the middle-bottom of the specimen at 596 kips

Figure 4-101: Specimen S2-R-AASH9-45 after the 20-in. eccentricity test.

The research team started the 40.25-in eccentricity test by applying load only on the North Side of the specimen. Some cracks that were present from the previous test started opening from 0.004 in. to 0.1 in., and the cracks on the connections started to increase considerably, while new cracks showed up in the specimen at 240 kips close to the bottom connection, as shown in Figure 4-102(a). The test continued and a new crack just at the middle of the height of the column at 270 kips, a crack located in the zone where the strands were present, but connectors were not, as shown in Figure 4-102(b). This crack started to widen until reaching 0.1 in. at 330 kips. The test continued until reaching a maximum axial load of 384 kips and the failure of the specimen occurred due to crushing in the compression side of the precast column in the middle to the upper part of the column, leaving a residual crack of 1/8'' thick as shown in Figure 4-103.

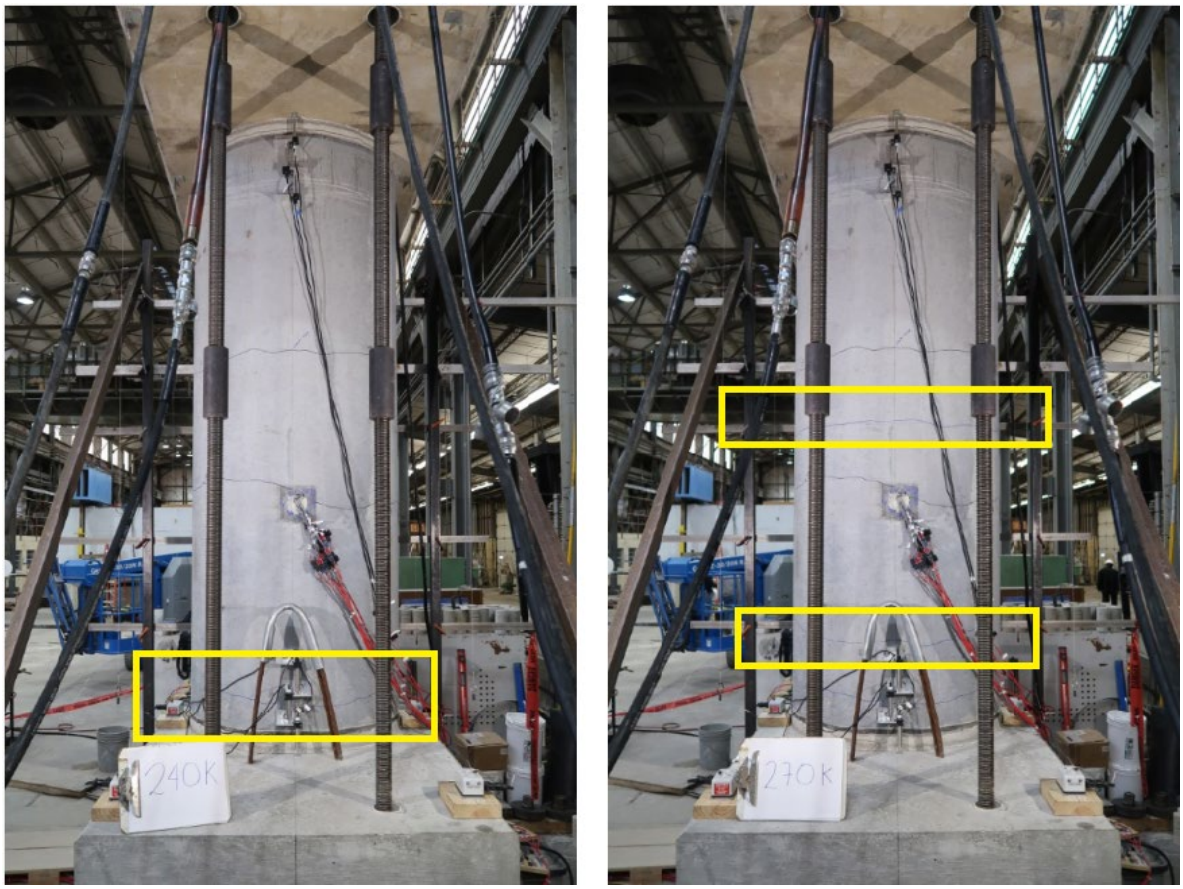

(a) cracks at the bottom at 240 kips (b) crack at the middle of the precast column

Figure 4-102: Specimen S2-R-AASH9-45 during the 40.25in eccentricity test.

(a) Crushing at the compression side after the failure of the specimen

(b) Crack pattern in the tension side of the specimen

Figure 4-103: Specimen S2-R-AASH9-45 after the 40.25in eccentricity test.

4.4.3. Specimen S3-S-AASH9-45 – Not Intentionally Roughened

4.4.3.1. Overview

This specimen was constructed to investigate the performance of a composite section between a precast column and concrete cast in place without any shear connectors or physical connection, relying only on the bond between the old and new concrete in the void. The goal was to assess the minimum capacity of the composite section and compare it to the intentionally roughened specimen (S2-R-AASH9-45), maintaining consistent development length for connections and concrete composition.

4.4.3.2. Mechanical Properties of Concrete and Rebar

The concrete mechanical properties were determined for this specimen, as shown in Table 4-8. As Specimen S2-R-AASH9-45 and S3-S-AASH9-45 were built simultaneously, the test properties of the concrete were higher than specified. Nevertheless, the planned load pattern that was established previously remained unchanged. The rebar used for the four precast column specimens was also tested from the same batch, as presented in Table 4-7.

Table 4-8. Summary of mechanical properties for Specimen S3-S-AASH9-45

	f'_c (ksi)	MOE (ksi)
Foundation	11.06	5192.43
Precast Column/ Shell	10.31	---
Column core	4.48	4728.86
Bent cap	10.37	6191.55
Bent cap void	5.11	3837.37

4.4.3.3. Structural Testing Results

The axial load-displacement chart was plotted using the data gathered from the test for Specimen S3-S-AASH9-45, as shown in Figure 4-104. Its vertical axis shows the total load applied to the column, and the horizontal axis represents the displacement measured at the top of the column. During the 6 in. and 12 in. eccentricity tests, the behavior was mostly linear and elastic. For the 20 in. test, some softening appeared at 400 kips, corresponding to the formation of cracks. Regarding the largest eccentricity, the specimen achieved an axial load of 382 kips, similar to Specimen S2-R-AASH9-45 with an axial load of 383 kips, accompanied by a load drop. At the failure of the specimen, a lateral displacement of 1.20 in. was achieved, comparable to 1.13 in. for specimen S2-R-AASH9-45 and 1.19 in. extrapolated for Specimen S1-CIP.

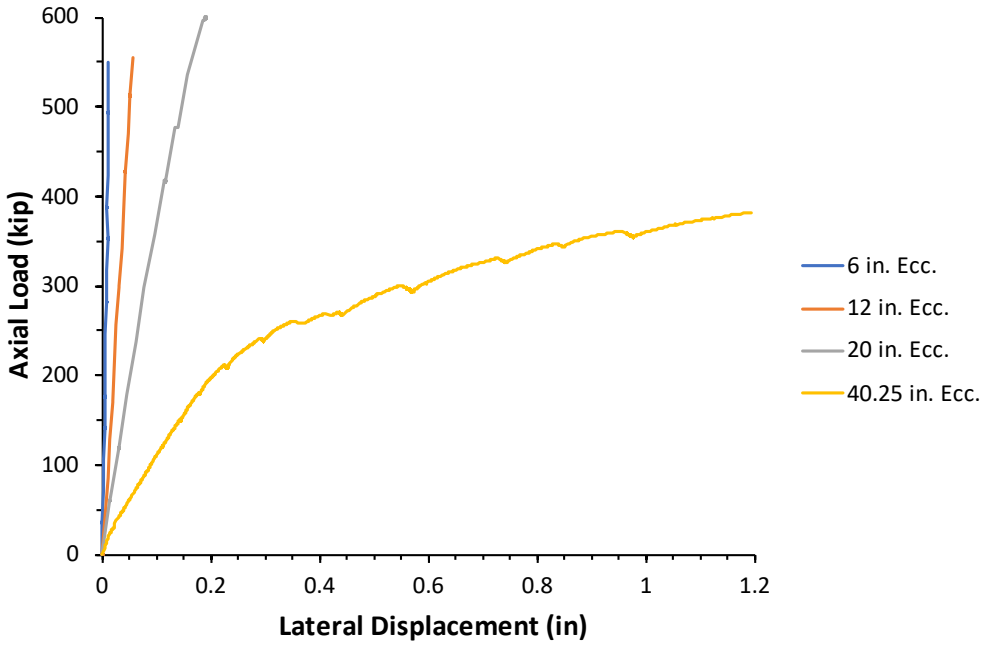

Figure 4-104: Comparison in the lateral displacement for Specimen S3-S-AASH9-45 using the L-Pot 5 located at the top of the column.

The test for 6-in eccentricity started with the same test protocol used for the Specimen S1-CIP, increasing the load by 15 kips on the South side and adjusting the North side to attain the

eccentricity. The loading was paused at predetermined checkpoints for crack inspection. For this case, no crack was observed in the precast column in Figure 4-105(a), echoing its elastic behavior.

The team continued with the 12-in eccentricity test following the same load pattern established for the Specimen S1-CIP, finishing with a total axial load of 555 kips. Loading was also paused for crack inspection. The specimen did not show any noticeable cracks before the end of the test, as shown in Figure 4-105(b). This observation contradicted a previous analysis for cracking load that expected cracks to appear at the 11th increment of load with a total axial load of 470 kips (11th increment of 13), meaning that the specimen also had a better behavior, similar to the results obtained from Specimen S2-R-AASH9-45.

(a) without cracks after the 6-in test (b) without cracks after the 12-in test

Figure 4-105: Specimen S3-S-AASH9-45 after the 6-in eccentricity test, and the 12-in eccentricity test.

A third test considering an eccentricity of 20 in. was conducted afterwards. The North-Side load was adjusted to a ratio of 2.975 times the South-Side load to get this eccentricity and the increments of load remained 15 kips on the South side. The first crack was expected to occur at the fourth increment of load with an axial load of 238 kips; however, the specimen showed a higher cracking load than expected. In particular, the first crack appeared in the middle of the precast column with an axial load of 537 kips, as shown in Figure 4-106(a), this crack had a width of 0.005 in. After this, at the final increment of load, with a total axial load of 600 kips, a new crack appeared at the middle of the precast column, and another one formed just on the top of the specimen. At this load level, the largest crack width was 0.008 in, as shown in Figure 4-106(b). These cracks occurred in the section where there was no rebar and only the strands were resent.

(a) crack at an axial load of 537 kips with a width of 0.005 in.

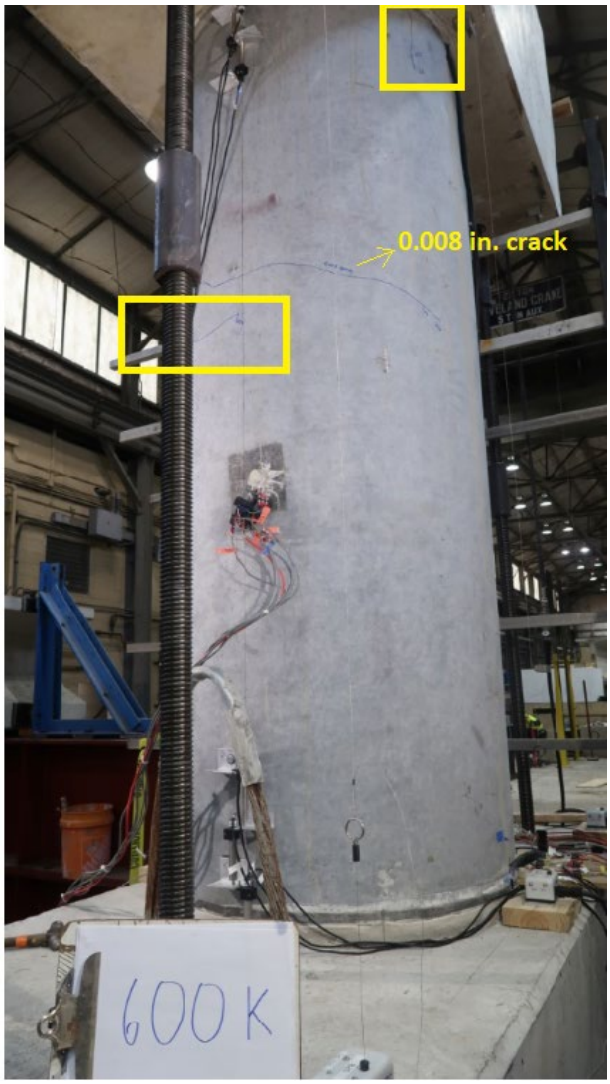

(b) New crack at an axial load of 600 kips below previous crack and new crack at the connection. Crack width at the middle of 0.008 in.

Figure 4-106: Specimen S3-S-AASH9-45 after the 20-in. eccentricity test.

The research team started the 40.25-in eccentricity test by applying load only on the North side of the specimen. Some cracks that were present from the previous test started opening from 0.01 in. to 0.04 in., and the cracks on the connections started to increase considerably while new cracks showed up in the specimen at 210 kips close to the middle of the precast column, as shown in Figure 4-107(a). The test continued and some cracks extended just at the middle of the height of the column at 270 kips, and new cracks appeared on the bottom side of the column, as shown in Figure 4-107(b). The test continued until reaching a maximum axial load of 382 kips, and the failure of the specimen occurred due to crushing on the compression side of the precast column, as shown in Figure 4-108.

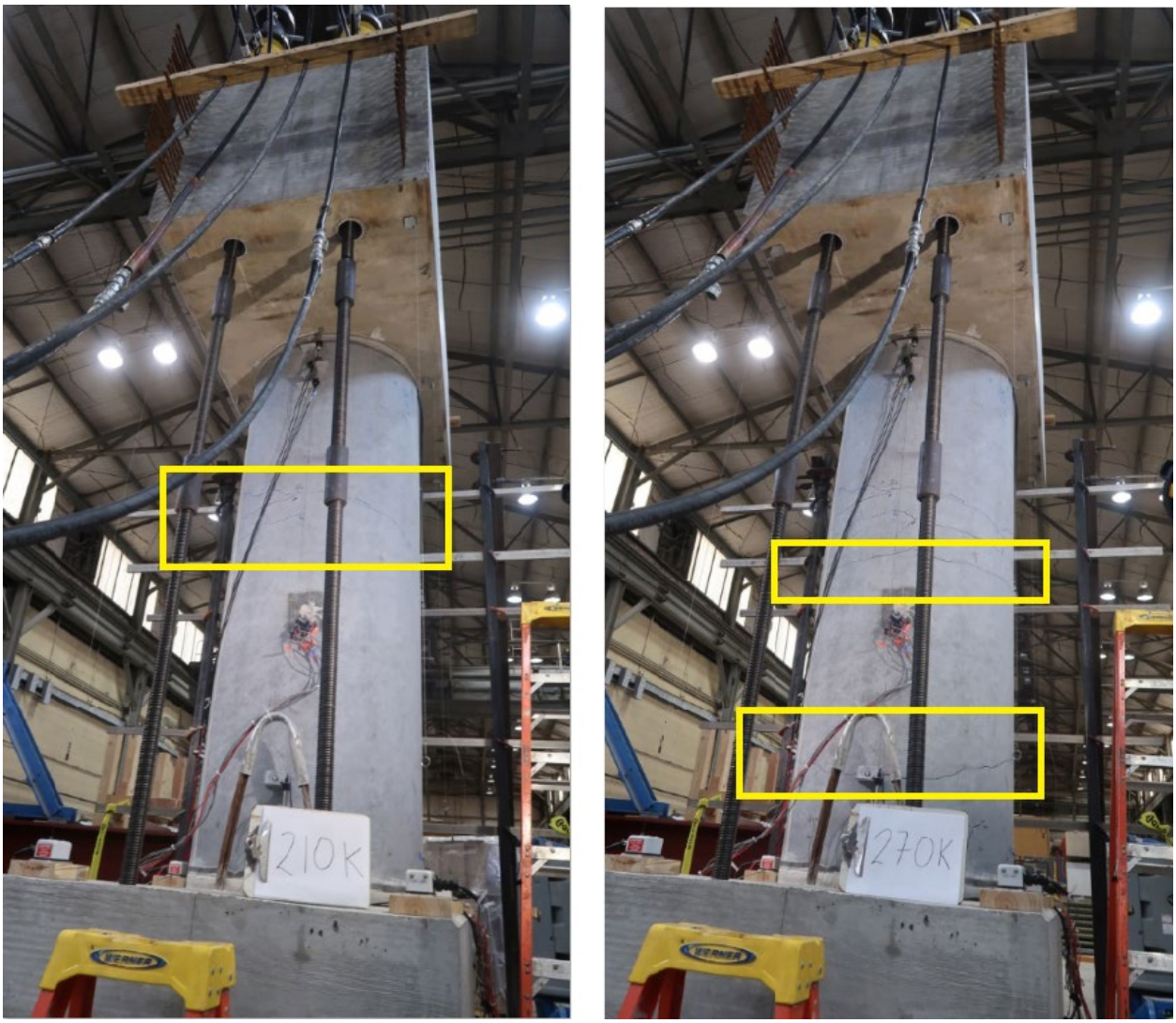

(a) cracks at the middle of the precast column at 210 kips

(b) new crack at the middle of the precast column and at the bottom of the column with an axial load of 270 kips

Figure 4-107: Specimen S3-S-AASH9-45 during the 40.25in eccentricity test.

(a) Crack pattern in the tension side of the specimen after the 40.25in eccentricity test

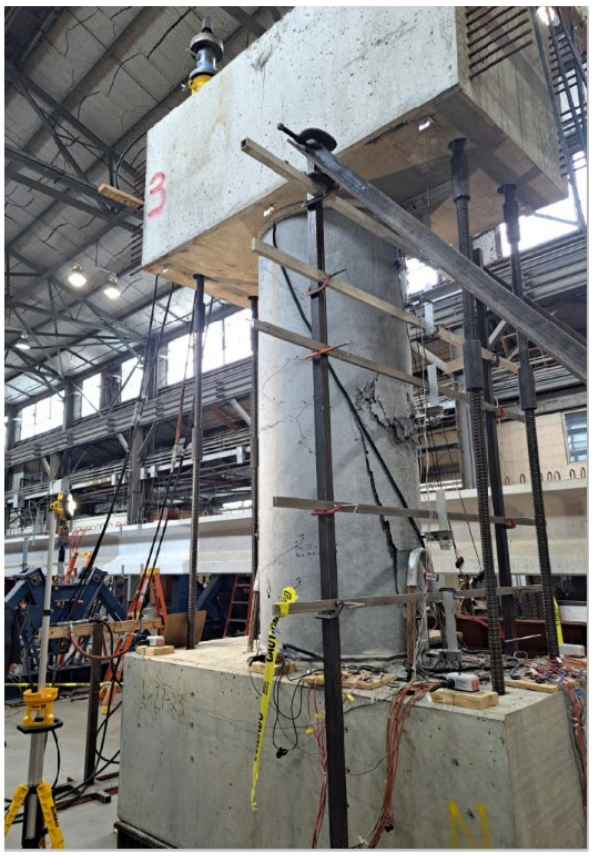

(b) Crushing at the compression side after the failure of the specimen

Figure 4-108: Specimen S3-S-AASH9-45 after the 40.25-in eccentricity test.

4.4.4. Specimen S4-R-Tx-34 – Embedment length of 2’10’’

4.4.4.1. Overview

This specimen featured “Intentionally roughed” precast shell and a decreased embedment length of the connector bars from 3’10’’ (AASHTO LRFD) to 2’10’’ (TxDOT Standard Drawings). This length was used both for the footing-to-column and bent cap-to-column connections. The main idea of this specimen was to investigate the effects of embedment lengths on the behavior capacity using TxDOT Standards in the case of non-contact splices. Besides, this specimen had a precast shell, potentially providing more fresh concrete around the connectors to be developed. This specimen also used a corrugated steel pipe 12-gage thick, delivering more factors that affect the required embedment length.

4.4.4.2. Mechanical Properties of Concrete and Rebar

The concrete mechanical properties were tested for this specimen, as shown in Table 4-9. Similar to Specimen S1-CIP, the test properties of the concrete were higher than specified except for the core concrete. Therefore, a core extraction was conducted to confirm the concrete strength after demolition, and the extracted sample had a compressive strength of 4.00 ksi, which were used for later analysis. The planned load pattern that was established previously remained unchanged. The rebar properties are shown in Table 4-7, considering that the rebar used for the precast columns is from the same batch.

Table 4-9. Summary of mechanical properties for Specimen S4-R-Tx-34

	f'_c (ksi)	MOE (ksi)
Foundation	8.27	5301.93
Precast Column/ Shell	10.31	---
Column core	3.15 / 4.06*	3979.51
Bent cap	7.82	4799.25
Bent cap void	4.61	4140.78
Grout**	7.89 (14 days)	---

Note:
*Core samples obtained from the specimen
**Repair material at the bottom of the column

4.4.4.3. Structural Testing Results

The test for Specimen S4-R-Tx-34 allowed for determining the importance of the embedment length for the bars in non-contact Splice and the development of the strands. For the cases of 6 in. and 12 in., the response of the specimen was mostly elastic, as presented in the axial load-displacement relationship in Figure 4-109. In this plot, the vertical axis represents the total axial load of the column, and the horizontal axis the displacement reported at the top of the column. For the 20 in. test, it is seen that slight softening appeared, indicating the column's effective moment of inertia was gradually reduced along with the loading. Regarding the largest eccentricity (40.25 in.), significant softening and bilinear behavior was observed, ending up with failure at 333 kips. At the failure of the specimen, a lateral displacement of 1.02 in. was achieved.

The test for 6-in eccentricity started with the same test protocol used for the other previously tested specimens, increasing the load by 15 kips on the South side and adjusting the North side to attain the eccentricity. The loading was paused at predetermined checkpoints for crack inspection until 550 kips. For this case, no crack was observed in the precast column in Figure 4-110(a), confirming its elastic behavior.

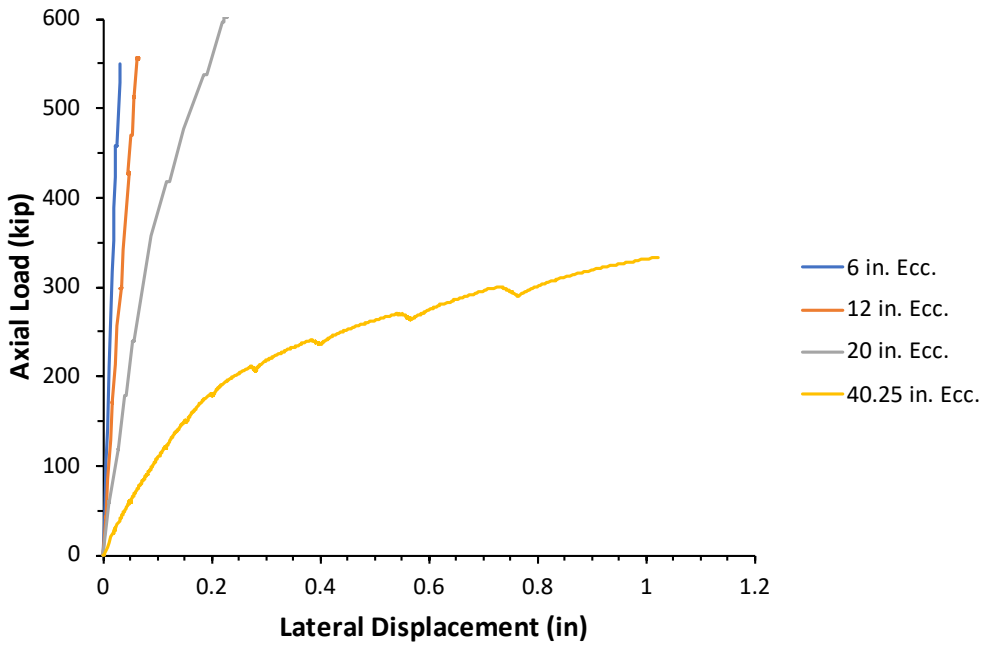

Figure 4-109: Comparison in the lateral displacement for Specimen S4-R-Tx-34 using the L-Pot 5 located at the top of the column.

The team continued with the 12-in eccentricity test following the load pattern established for the previous three specimens, finishing with a total axial load of 555 kips. Loading was also paused for crack inspection. The specimen did not show any noticeable cracks before the end of the test, as shown in Figure 4-110 (b).

A third test considering an eccentricity of 20 in. was conducted afterward. The North-Side load was adjusted to a ratio of 2.975 times the South-Side load to get this eccentricity and the increments of load remained 15 kips on the South side. The first crack was expected to occur at the fourth increment of load with an axial load of 178 kips; however, the specimen showed a higher cracking load than expected. In particular, the first crack appeared 34 in. below the top of the precast column, with an axial load of 417 kips, as shown in Figure 4-111(a). After this, a second crack occurred at 36 in. above the precast column at 537 kips at the section where the rebar was cut, and the strands were present alone. At the final increment of load, with a total axial load of 596 kips, the previous cracks extended and widened to a width of 0.010 in, as shown in Figure 4-111(b).

(a) without cracks after the 6-in test

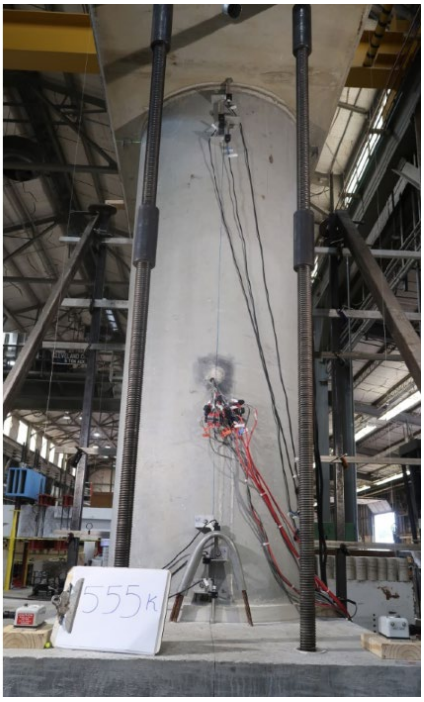

(b) without cracks after the 12-in test

Figure 4-110: Specimen S4-R-Tx-34 after the 6-in eccentricity test, and the 12-in eccentricity test.

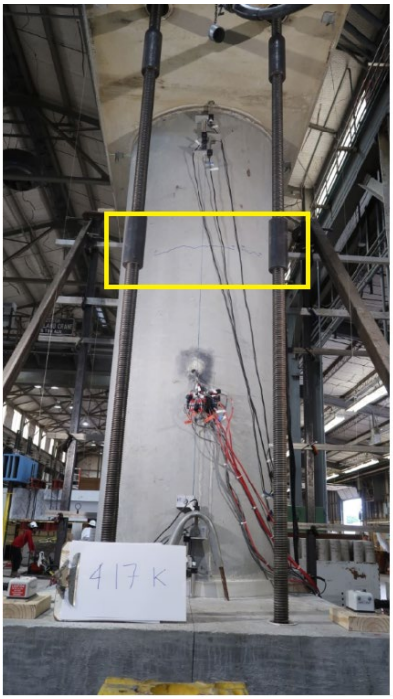

(a) crack at an axial load of 417 kips at 34 in. from the top of the precast column

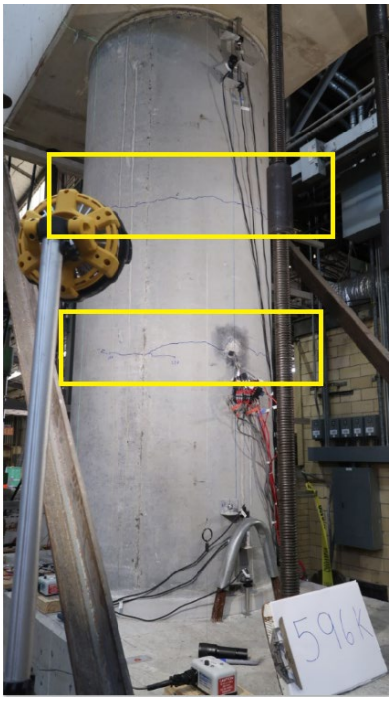

(b) New crack at an axial load of 537 kips at 36 in. from the bottom of the precast column. Crack width at the middle of 0.010 in. at 596 kips

Figure 4-111: Specimen S4-R-Tx-34 after the 20-in. eccentricity test.

The research team started the 40.25-in eccentricity test by applying load only on the North side of the specimen. Some cracks that were present from the previous test started opening from 0.0025 in. to 0.125 in., and the cracks on the connections started to increase considerably, while new cracks showed up in the specimen at 210 kips close to the middle-bottom of the precast column, as shown in Figure 4-112(a). The test continued and some cracks extended just at the middle-top of the height of the column at 270 kips, as shown in Figure 4-112(b). The test continued until reaching a maximum axial load of 333 kips, as shown in Figure 4-113, and the failure of the specimen occurred due to crushing on the compression side at the middle-top (34 in. from the top) of the precast column. This specimen's peak load-carrying capacity was less than Specimen S1-CIP (360 kips), Specimen S2-R-AASH9-45 and S3-S-AASH9-45 (383 kips).

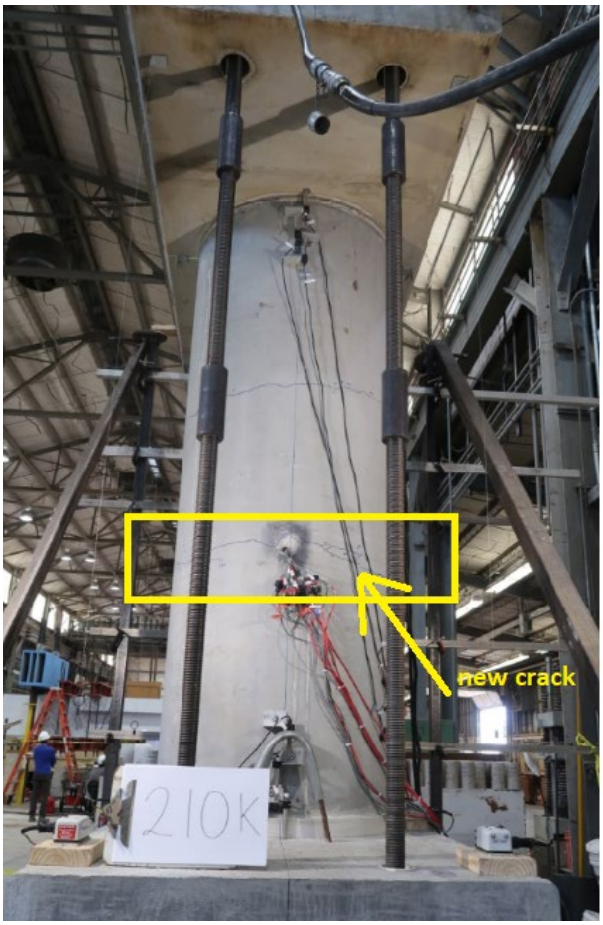

(a) new crack at the middle-bottom of the precast column at 210 kips

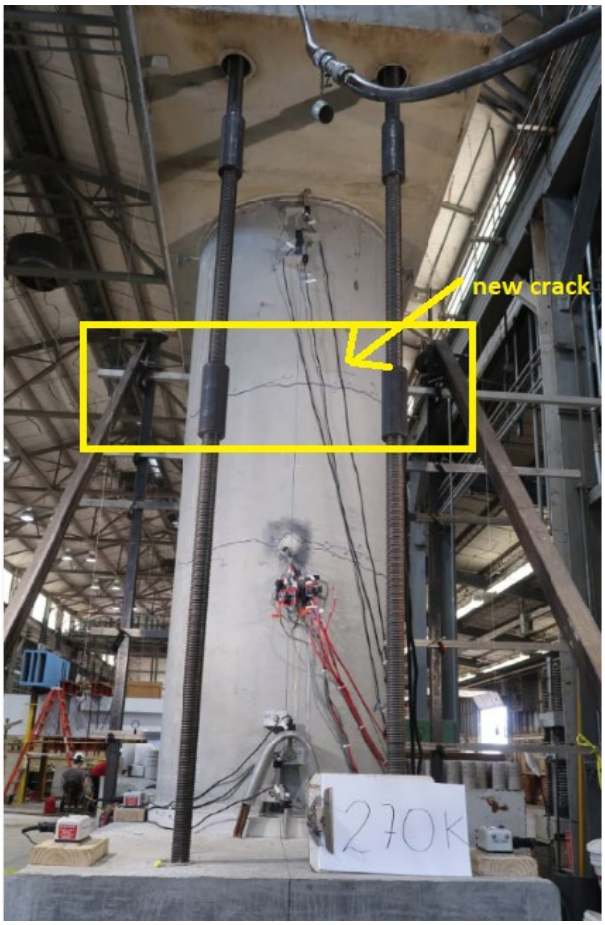

(b) new crack at the middle-top of the precast column with an axial load of 270 kips

Figure 4-112: Specimen S4-R-Tx-34 during the 40.25in eccentricity test.

(a) Crushing at the compression side after failure (b) Crack pattern in the tension side

Figure 4-113: Specimen S4-R-Tx-34 after the 40.25in eccentricity test.

4.4.5. Specimen S5-R-ZABORAC-28 – Embedment length of 2’4’’

4.4.5.1. Overview

This specimen featured an “Intentionally Roughed” interface and a reduced embedment length of the rebars from 3'-9" (ASSHTO 9th edition.) to 2'-4" (using the formula from Zaborac and Bayrak (2022), which has been approved to be included in the newest AASHTO version). This length was used both for the footing-to-column and bent cap-to-column connections. The main objective of this specimen was to determine the capacity using the newest standards but in this case with non-contact splice and determine if the length is enough to transmit the forces and reach yielding. The foundation had a fabrication error in the connectors, causing the footprint of the column to shift 2-in. off center. The ratio of load on one side to the other was adjusted accordingly for eccentricities of 6-in. through 20-in. as presented in Table 4-3. In the last case, the eccentricity was corrected to 42.25-in. instead of 40.25-in.

4.4.5.2. Mechanical Properties of Concrete and Grout

Mechanical properties tests were conducted for this specimen using concrete cylinders sampled along with the cast of each component, and the results are shown in Table 4-10. Concrete strength in all parts of the specimen achieved higher than the specified strength except the concrete of the column core. Therefore, three core samples were extracted from the column core after the demolition of the specimen to verify the concrete strength. In addition, grout was used to repair voids at the bottom of the column, and the strength of the grout on the 14th day is also included. The rebar properties are shown in Table 4-7, considering that the rebar used for the precast columns is from the same batch.

Table 4-10. Summary of mechanical properties for S5-R-ZABORAC-28

	f'_c (ksi)	MOE (ksi)
Foundation	8.42	5301.93
Precast Column (Shell)	10.31	---
Column core	3.12 / 3.33*	3979.51
Bent cap	8.21	4799.25
Bent cap void	4.47	4140.78
Grout	7.89 (14 days)	---

Note:
*Core samples obtained from the specimen
**Repair material at the bottom of the column

4.4.5.3. Structural Testing Results

The load-displacement relationships extracted from the test under eccentricities of 6-in., 12-in., 20-in., and 42.25-in. are plotted in Figure 4-114. The vertical axis represents the total axial load, which is the summation of the readings of all four load cells, and the horizontal axis is the reading of the L-Pot at the top of the column. The test for 6-in. eccentricity started with a test protocol stated previously, increasing the load by 15 kips in each step and finishing with a total axial load of 566 kips. Similarly, the test for 12-in. eccentricity was conducted and reached a total axial load of 559 kips. For both test eccentricities, the load-displacement behavior remained linear and elastic until the end of the tests.

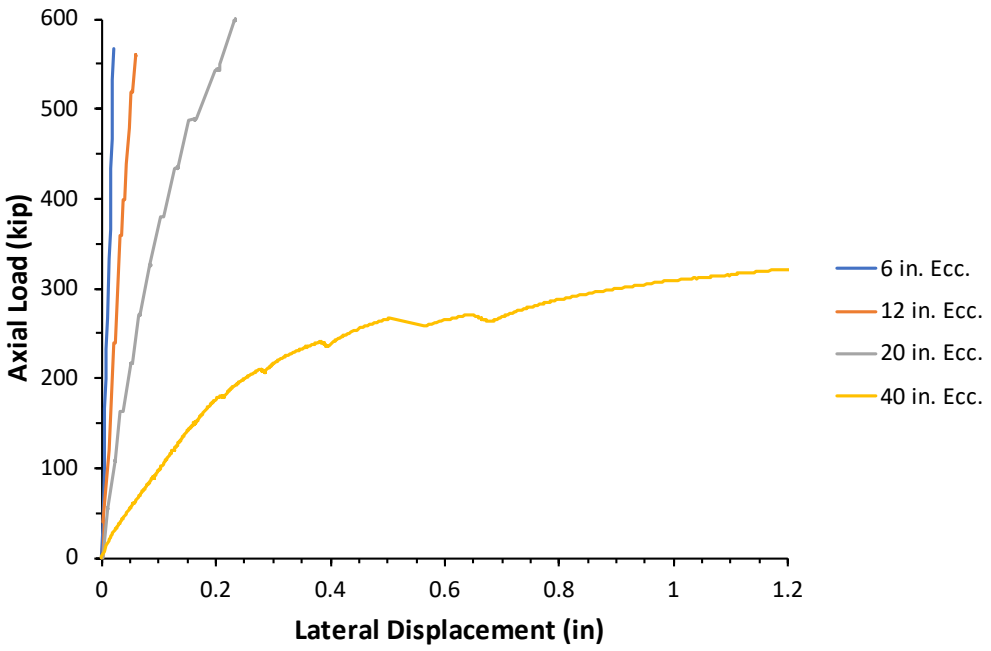

Figure 4-114: Comparison in the lateral displacement for Specimen S5-R-ZABORAC-28 using the L-Pot 5 located at the top of the column.

For the case of 6-in. eccentricity, no cracks formed on the column until the end of the test, as shown in Figure 4-115(a). In addition, for the 12-in eccentricity test, no noticeable cracks formed until the load reached 559 kips, which was the specified load at the end of the test, as shown in Figure 4-115(b). Although the expected theoretical cracking moment was surpassed, these results confirmed the load-displacement behavior in which no post-cracking stiffness was observed.

(a) without cracks after the 6-in test (b) without cracks after the 12-in test

Figure 4-115: Specimen S5-R-ZABORAC-28 after the 6-in. eccentricity test, and the 12-in. eccentricity test.

Unlike the first two tests, in the 20-in. eccentricity test, the first crack was encountered in the specimen at 271 kips in the bottom connection, specifically at the cold joint and where the grout was placed for the repair. At this load level, stiffness was slightly reduced, and continuous softening was observed in the load-displacement curve as shown in Figure 4-114. Subsequently, a crack formed in the precast column at an axial load of 488 kips, 33 in. down from the top of the precast column, as shown in Figure 4-116(a). Another crack occurred at 37 in. from the bottom of the precast column at 597 kips, where the rebar connectors were terminated. At the end of the test, the initial cracks had extended and widened, ending up with a width of 0.013 in, as shown in Figure 4-116(b).

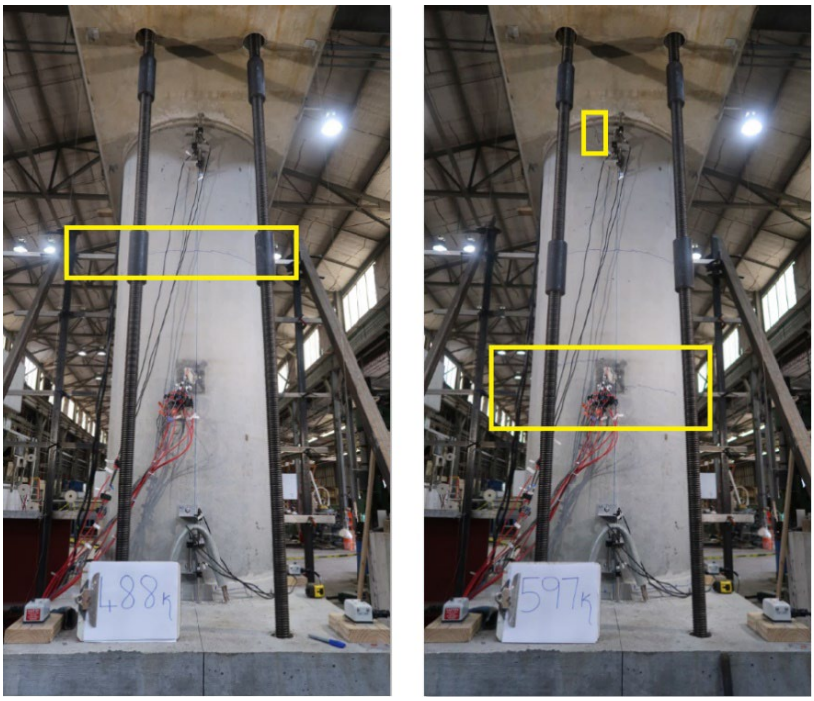

(a) crack at an axial load of 488 kips (b) crack at an axial load of 597 kips

Figure 4-116: Specimen S5-R-ZABORAC-28 under an eccentricity of 20 in.

The 40.25-in eccentricity test was conducted by applying load only on one side of the bent cap (the North side). It should be noted again that this specimen had a fabrication error, leading to a total eccentricity of 42.25 in. In this test, a significant plateauing was observed in the load-displacement curve after a load of approximately 240 kips, as shown Figure 4-114. The load level also corresponded to cracks extending and widening, as shown in Figure 4-117(a). When the loading continued, a new crack formed at approximately one-third of the height from the bottom while a significant opening at the bottom and the top connections appeared at a load of 270 kips, as shown in Figure 4-117(b). This new crack appeared at the height where the footing connectors were terminated. The test continued until reaching a maximum axial load of 321 kips, as shown in Figure 4-118. Failure of the specimen was reached due to crushing in the compression side at the middle-top (30 in. from the top). At the ultimate failure of the specimen, a lateral displacement of 1.19 in. was achieved, as shown in Figure 4-114.

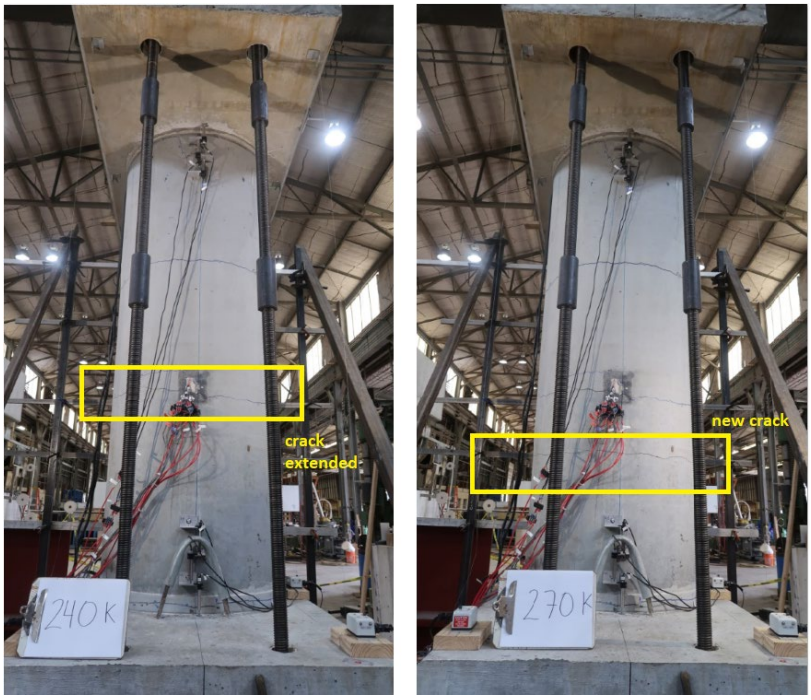

(a) cracking at 240 kips (b) cracking at 270 kips

Figure 4-117: Specimen S5-R-ZABORAC-28 under an eccentricity of 42.25 in.

(a) Crushing at the compression side (b) Crack pattern in the tension side of the specimen

Figure 4-118: Specimen S5-R-ZABORAC-28 after the 42.25in eccentricity test

Chapter 5. Data Analysis from Large-Scale Testing

This chapter presents data analysis including the development length of the rebar used for the connections. The purpose was to evaluate the applicability of the test embedment length of the rebar for the connections. In addition, a comparison of each test specimen to the control specimen in terms of moment-displacement behaviors is included. Lastly, an analytical method for calculating the strength and the P-M interaction diagram of the developed precast column solution is proposed.

5.1. Development Length of the Rebars in the Connections

From the tests, one of the principal concerns was to determine if the vertical bars in the connections would reach the yielding point. As discussed in the Section 4.2.9, three strain gauges were placed on one bar in both the tension and compression zones to determine if the embedment length used in each specimen would be sufficient to yield the bars under extreme eccentricities. The development lengths were evaluated by comparing strain profiles along the instrumented connector on the tension side of each specimen under the largest test eccentricity near the peak load.

5.1.1. Strain Profiles

Firstly, the strain profile of each specimen on the footing-to-column connectors was constructed and plotted along the height, as shown in Figure 5-1. The strain readings were extracted as data points from strain gauges SG1, SG2, and SG3 corresponding to positions as shown in the diagram in Figure 5-1. The vertical dashed line indicates the yield strain. For Specimen S1-CIP, it is noticed from Figure 5-1 that the connector rebar reached the yield strain at the bottom of the column (SG1). It should be noted that SG2 and SG3 on Specimen S1-CIP did not respond when reaching the peak load preventing the construction of a complete strain profile. Unfortunately, similar issues occurred in the test of Specimen S2-R-AASH9-45; strain gauges SG1 and SG2 did not respond, and no data was extracted; the strain gage close to the edge of the bar (SG3) reported a value of 1,562 microstrains.

The other three specimens had strain gauges functioning correctly. Specimens S3-S-AASH9-45 and S5-R-ZABORAC-28 developed similar strain levels near the bottom (SG1), reaching 9,393 microstrains and 10,000 microstrains, respectively. The two specimens also had similar strain readings from SG2, and the largest difference occurred at SG3. Nevertheless, they appeared to have similar strain variation trends through the height. On the other hand, Specimen S4-R-Tx-34 had the lowest reading in SG1 compared to the previous two specimens, reaching 2557 microstrains, but it also had a similar strain reading at SG2. The strain profile indicates that all column specimens based on the precast solution were able to fully develop bar stress at the footing-to-column connection regardless of the embedment length. Although Specimen S2-R-AASH9-45 lost the strain reading at SG1, it can be inferred that the bar stress was fully developed from its

load-displacement behavior and from its companion specimen (Specimens S3-S-AASH9-45), which had the same structural configuration but a non-intentionally roughened interface.

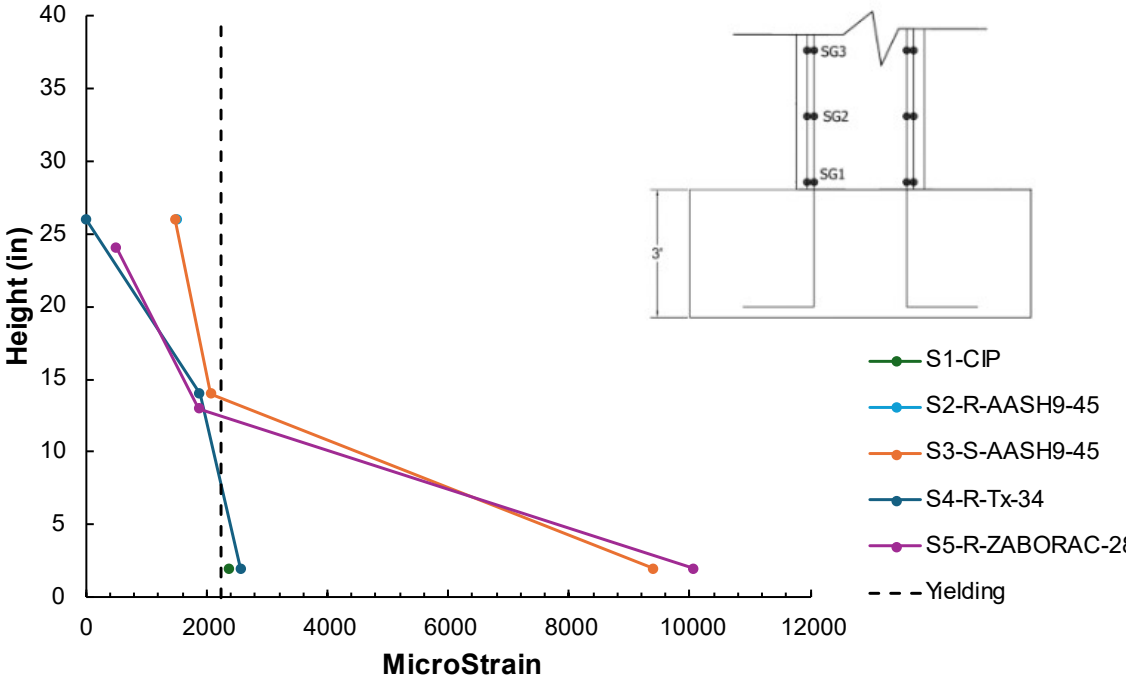

Figure 5-1: Strain profile for each specimen the footing-to-column connection after the 40.25-in. eccentricity test

Similarly, strain gauges were strategically placed at various locations near the column-to-bent cap connection to study the embedment length. Figure 5-2 illustrates the strain profiles based on the sensor labels, facilitating comprehension. All specimens demonstrated the ability to yield bars close to the connection, as indicated by strain gauges SG6 and SG7 in Figure 5-2. Notably, strain gauges SG4 and SG9 exhibited low strain for their proximity to the edge of the bars in all cases. As the position approaches the joint, as observed with strain gauges SG5 and SG8, the strain also increases. Finally, strain gauges SG6 and SG7 were positioned at the connection where yielding was expected. This result indicates that the embedment length is sufficient to transfer forces to the bar and reach the plastic zone. A major discrepancy was observed in Specimen S3-S-AASH9-45; the strain reading from SG6 was the lowest, while other precast specimens demonstrated a similar trend.

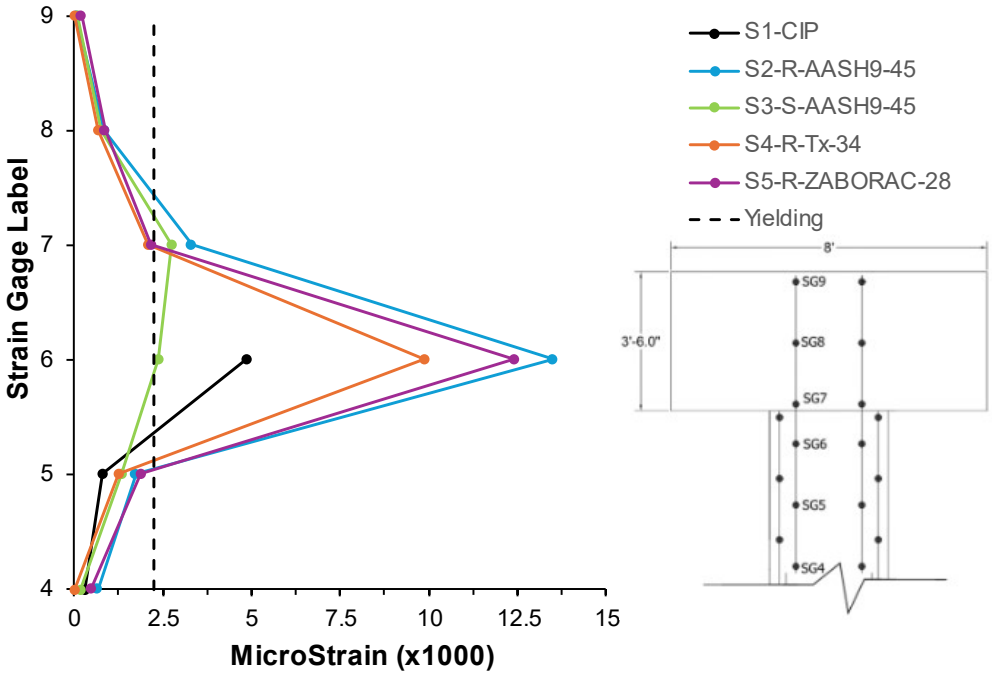

Figure 5-2: Strain reported for each specimen after the 40.25-in. eccentricity test according to the label for each sensor on the bars in the Column-Bent Cap Connection.

5.1.2. Evaluation of Development Length

The length required to develop the yield stress of the connectors during the tests for each specimen was extracted from the strain profile discussed in the previous section. In particular, the distance between the position where the strain profile intersects the yield strain, and the nearest end of the connector was determined for each specimen from Figure 5-1 and Figure 5-2. This distance was defined as the measured development length. The measured development length was compared to the provided embedment length and the current AASHTO LRFD's required development length, as summarized in Table 5-1.

Table 5-1. Summary of development lengths

Specimen ID	Footing				Column				BentCap			
	Exp. (in)	Total (in)	Ratio Exp/Total	Ratio AASHTO	Exp. (in)	Total (in)	Ratio Exp/Total	Ratio AASHTO	Exp. (in)	Total (in)	Ratio Exp/Total	Ratio TxDOT
S1 CIP	43.23	48	90.07%	96.07%	26.12	48	54.41%	58.03%	---	---	---	---
S2 R-AASH9-45	28.35	45	63.00%	63.00%	24.76	45	55.01%	55.01%	23.95	34	70.45%	70.45%
S3 S-AASH9-45	31.27	45	69.49%	69.49%	39.98	45	88.85%	88.85%	26.44	34	77.77%	77.77%
S4 R-Tx-34	28.04	34	82.47%	62.31%	17.58	34	51.70%	39.06%	32.45	34	95.45%	95.45%
S5 R-ZABORAC-28	15.49	28	55.34%	34.43%	15.36	28	54.87%	34.14%	26.78	28	95.64%	78.76%

Figure 5-3 illustrates the comparison of the footing-to-column joint for each specimen. Light blue represents the development length stated by AASHTO 9th edition, dark blue is the embedment length used in each test for the connecting bars and orange is the development length needed to reach yielding according to the sensor data. In Specimen S1-CIP, nearly the entire embedment length was required to reach yielding. For Specimen S2-R-AASH9-45, the sensor malfunctioned

but the result was extrapolated from Figure 5-1, considering a linear trend from zero stress at the end of the bar and the value from the strain gauge SG1. With the linear equation, the value of f_y is used to extrapolate the development length, which indicates that 63% of the embedment length was needed to reach yielding. In contrast, Specimen S3-S-AASH9-45 required approximately 70% of the embedment length. It can be inferred that a smoother interface might need a longer embedment length, though this is not definitive. The results also demonstrate that using an embedment length in line with the AASHTO LRFD for the non-contact lap-splice for the precast column solution should be satisfactory.

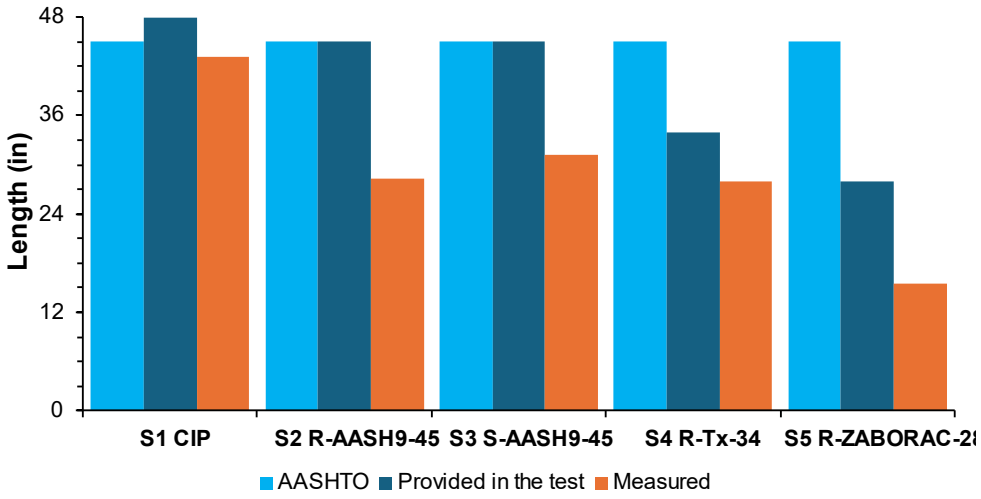

Figure 5-3: Comparison of development lengths in the footing-to-column Connection.

Specimen S4-R-Tx-34 needed 82% of the embedment length to reach yielding, while Specimen S5-R-ZABORAC-28 achieved yielding with 55% of the embedment length. These results suggest that for a roughened precast column, an embedment length of approximately 28.5 in. is sufficient, whereas for a smoother precast column shell interface, an embedment length of 32 in. is recommended.

When comparing the experimental development length to the AASHTO LRFD 9th Edition specified length, all specimens required a shorter length to reach yielding, as shown in Figure 5-3. Additionally, the measured lengths were consistently shorter than the embedment lengths provided in the test for the footing-to-column connection, indicating that the AASHTO and TxDOT Standards may be conservative for this type of connection.

In the case of the bent cap-to-column connection, all sensors indicated that the bars yielded within the column at a shorter distance compared to the provided embedment length, as shown in Figure 5-4. For most specimens, the embedment length required to yield the bars was approximately 55% of the provided one. However, for Specimen S3-S-AASH9-45, which featured a smoother interface inside the precast shell, the percentage increased to nearly 90%. This observation suggests that while the bars reached yielding, the smoothness of the interface of the precast column

for non-contact splice assembly can significantly affect the required development length of the bars.

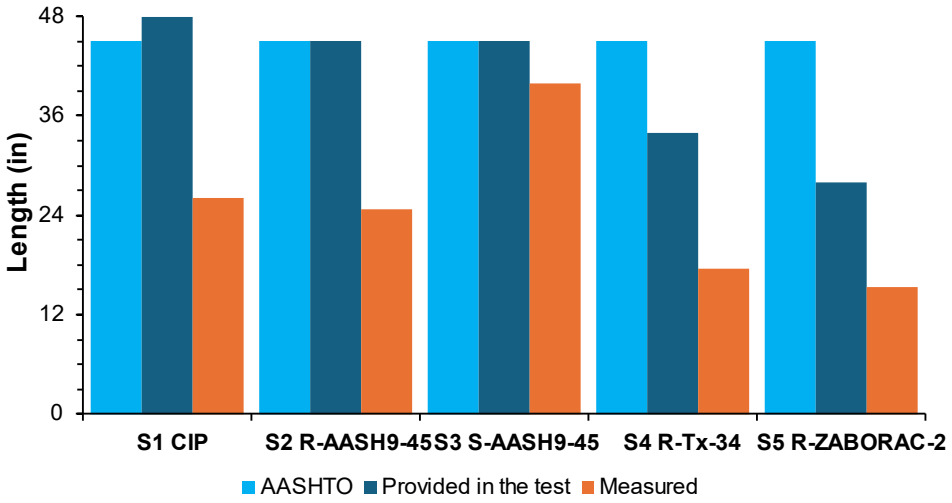

Figure 5-4: Comparison of development length in the column at the bent cap-to-column connection.

When comparing the experimental development length to the development length specified by AASHTO LRFD, all specimens required a shorter length to reach yielding, similar to the footing connection, as shown in Figure 5-4. Light blue represents the development length stated by AASHTO 9th edition, dark blue is the embedment length used in each test for the connecting bars and orange is the development length needed to reach yielding according to the sensor data. Additionally, the measured development lengths were consistently shorter than the actual embedment lengths used in the footing-to-column connection.

Similarly, upon analyzing the bars in the bent cap at the bent cap-column connection, it was observed that when the experimental development length was compared to the length specified by TxDOT Standards, all specimens required a shorter length to reach yielding, as shown in Figure 5-5. Light blue represents the development length stated by TxDOT Standards, dark blue is the embedment length used in each test for the connecting bars and orange is the development length needed to reach yielding according to the sensor data. Additionally, the development length measured was found to be shorter than the embedment length provided in the test in this connection. However, it is notable that Specimen S4-R-Tx-34 almost exhausted the provided embedment length, proving the compatibility of the precast column solution with the standard precast bent cap.

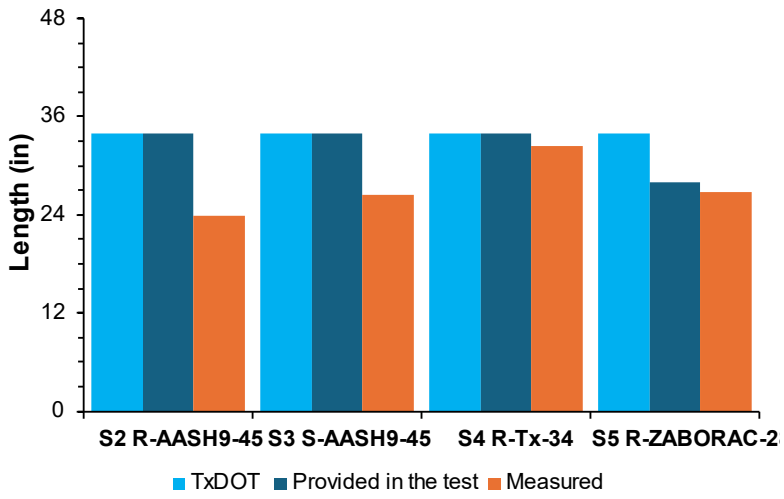

Figure 5-5: Comparison of development lengths in the bent cap at the bent cap-to-column connection

5.2. Comparison of Load-Displacement Behavior

One of the primary purposes of the current experimental program was to validate the use of precast hollow columns filled with CIP concrete. The design aimed to ensure a comparable or higher capacity than the TxDOT standard circular column design, represented by Specimen S1-CIP. Four eccentricities were programmed during the tests to analyze the precast specimens' behavior by comparing their lateral displacement against the control specimen.

5.2.1. Load-Displacement at 6-in. eccentricity Test

The first test was performed with an eccentricity of 6-in. representing a load pattern with a high axial load and a small flexural moment. The axial load was applied with incremental steps of 35 kips until reached a total axial load of 550 kips and a bending moment of 275 kip-ft.

The test for Specimen S1-CIP was performed, measuring a maximum lateral displacement of 0.056 in., and some cracks were present in the column without affecting its structural capacity. In the case of the precast specimens, no cracks were reported for any specimen, and they showed a stiffer behavior compared to the control specimen. Specimen S2-R-AASH9-45 had an initial behavior similar to S1-CIP until reaching 50 kips, from that point, it showed a stiffener behavior reporting a maximum lateral displacement of 0.031 in., representing a 55.6% displacement for the control specimen, as presented in Figure 5-6. Specimen S3-S-AASH9-45 reported a lateral displacement of 0.01 in., being the minimum lateral displacement for the precast specimens, representing 20% of the control specimen's displacement. Specimens S4-R-Tx-34 and S5-R-ZABORAC-28 behaved similarly to S3-S-AASH9-45 until reaching 100 kips, after this load, they reported a lateral displacement of 0.031 in. and 0.02 in. respectively.

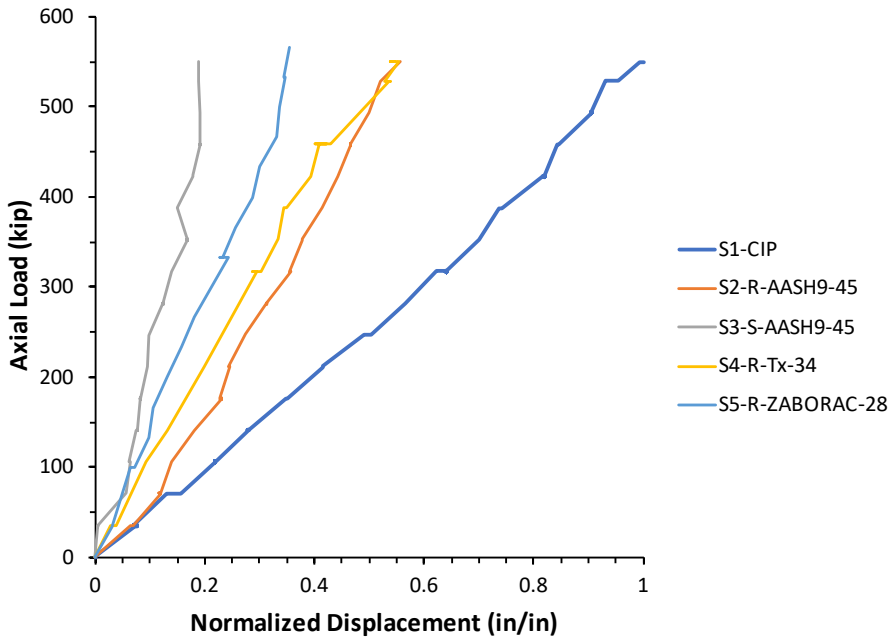

Figure 5-6: Load – Normalized Displacement against Specimen S1-CIP for 6-in. eccentricity test

5.2.2. Load-Displacement at 12-in. eccentricity Test

In this test, the axial load was applied in incremental steps of 43 kips until a total axial load of 555 kips and a bending moment of 555 kip-ft were reached. The flexural moments in this test were twice the values used in the 6-inch eccentricity test.

After the test for Specimen S1-CIP, it showed a maximum lateral displacement of 0.12 in. and cracking increased in the column without affecting its structural capacity. In the case of the precast specimens, as happened during the 6-in. eccentricity test, no cracks were reported during this test for any specimen and their structural behavior showed to be superior, reporting a maximum lateral displacement of 0.068 in. for S2-R-AASH9-45 representing a 56% of the displacement for the control specimen, as presented in Figure 5-7. Specimen S3-S-AASH9-45 reported a lateral displacement of 0.056 in., once again being the minimum lateral displacement for the precast specimens representing 46.2% of the total displacement from S1-CIP. Specimens S4-R-Tx-34 and S5-R-ZABORAC-28 reported a lateral displacement of 0.064 in. and 0.059 in. respectively, equivalent to 53.1% and 48.7% of S1-CIP.

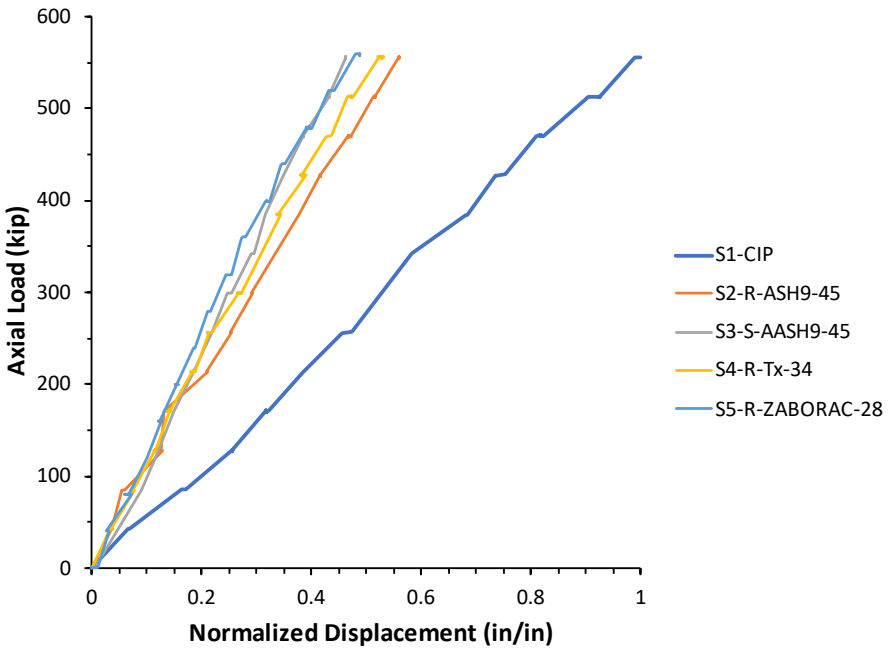

Figure 5-7: Load – Normalized Displacement against Specimen S1-CIP for 12-in. eccentricity test

5.2.3. Load-Displacement at 20-in. eccentricity Test

After completing the 6-in. and 12-in. eccentricity tests on the first precast column, no damage was observed, confirming the predicted outcome. As a result, a 20-in. eccentricity test was planned for the precast columns. The goal was to gain a better understanding of how this new solution behaves under axial loads and flexural moments and to identify a cracking point before subjecting it to extreme eccentricity.

In this test, an axial load was applied in increments of 60 kips until reaching a total load of 596 kips and a bending moment of 994 kip-ft. Given the good performance of the precast specimens in previous tests, the flexural moments for this test were more than three times higher than those used in the 6-inch eccentricity test.

For this test, Specimen S2-R-AASH9-45 was used to normalize the plot in Figure 5-8 due to the intentional roughness present in its interior and the embedment length of the steel connectors (45 in.). After completing the test for the Specimen S2-R-AASH9-45, it showed a maximum lateral displacement of 0.206 in. At the last load increments, some cracks appeared at the end of the steel connectors, being the regular behavior of all the precast specimens. Specimen S3-S-AASH9-45 reported a lateral displacement of 0.192 in., once again being the minimum lateral displacement for the precast specimens representing 93.1% of the total displacement from S2-R-AASH9-45, as presented in Figure 5-8. Specimens S4-R-Tx-34 and S5-R-ZABORAC-28 reported a lateral displacement of 0.227 in. and 0.235 in. respectively, equivalent to 110.3% and 114% of S2-R-AASH9-45.

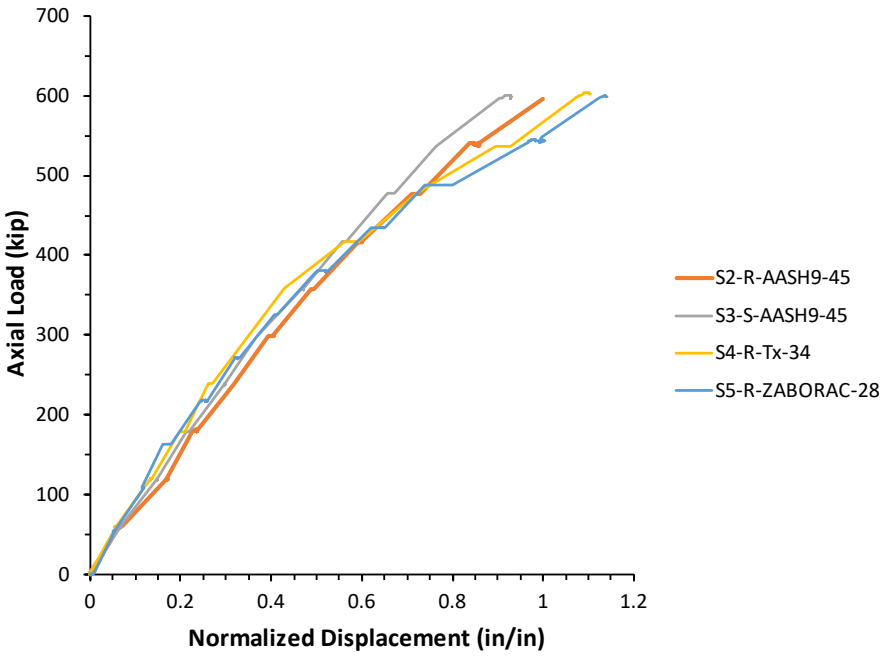

Figure 5-8: Load – Normalized Displacement against S2-R-AASH9-45 for 20-in. eccentricity test

5.2.4. Load-Displacement at 40.25-in. eccentricity Test

The test of Specimen S1-CIP under an eccentricity of 40.25-in. stopped at a load-carrying capacity of 360 kips for the axial load and 1207 kip-ft for the bending moment. This load level surpassed the prediction using the P-M interaction diagram introduced in Section 2.3, without showing signs of failure. This indicated an overstrength of at least 13% compared to the pre-test strength calculations. The specimen S1-CIP was considered as the baseline to compare against the precast column specimens and to evaluate the performance of the test specimens. It was essential to study the load-displacement behavior of Specimen S1-CIP and compare the result to those of the test specimens, as presented in the following sections.

5.2.4.1. Lateral displacement Extrapolation for S1-CIP

The lateral displacement results for the specimen S1-CIP are presented in section 4.4.1, however, the L-Pot located at the column's top malfunctioned during the test, generating that the lateral displacement at this location was not tracked after 300 kips. An extrapolation for the unrecorded data was completed in order to extend the lateral displacement at the top by using the L-Pots located at 6 ft from the base and at the middle of the column's height. The goal of the procedure was using the experimental rotation at the top of the column to determine the apparent effective rigidity *EI* along with the applied moment. The *EI* value was then used to extrapolate for displacement after 300 kips for the specimen.

Considering the column as a cantilever beam-column element with a fixed support at the bottom, using solid mechanics to solve this condition for the effective rigidity EI, and starting with the moment that is a known variable from the tests:

$$EI\frac{d^2v}{dx^2} = M \tag{5-1}$$

Integrating to get the rotation:

$$EI\frac{dv}{dx} = Mx + C_1 \tag{5-2}$$

As there is zero rotation at x = 0 (at the support), C_1 = 0:

$$EI\frac{dv}{dx} = Mx \tag{5-3}$$

$$EI\theta = Mx \tag{5-4}$$

Evaluating x = L (column's height), $\theta(L)$:

$$\theta(L) = \frac{ML}{EI} \tag{5-5}$$

Solving for the column's effective stiffness, EI:

$$EI = \frac{ML}{\theta(L)} \tag{5-6}$$

Integrating the rotation from Eq. (5-3) to get the lateral displacement:

$$EIv = \frac{1}{2}Mx^2 + C_2 \tag{5-7}$$

As there is no lateral displacement at x = 0 (at the support), C_2 = 0:

$$EIv = \frac{1}{2}Mx^2 \tag{5-8}$$

Evaluating x = L (column's height), $v(L)$:

$$v(L) = \frac{1}{2}\frac{ML^2}{EI} \tag{5-9}$$

From the test, the moment and the column's height are known variables; the rotation at the column's top could be calculated by using the S-Pots located at the position of the all-threaded rods as described in Figure 5-9. As the rotation at the column's bottom is considered zero, the rotation between the top and the bottom could be calculated by taking the vertical displacement measured with the S-Pots and dividing this by the distance from the sensors to the column, as follows:

$$\alpha\ (rad) = \frac{|SPOT1| + |SPOT3|}{40.25 * 2} \tag{5-10}$$

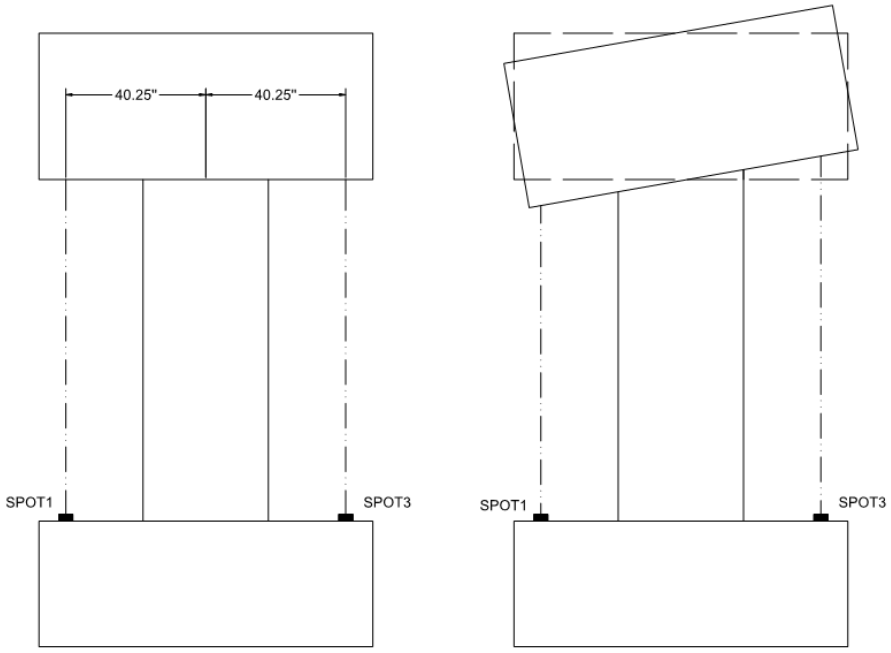

(a) Column without deformation before the test

(b) Idealized deformation from the test

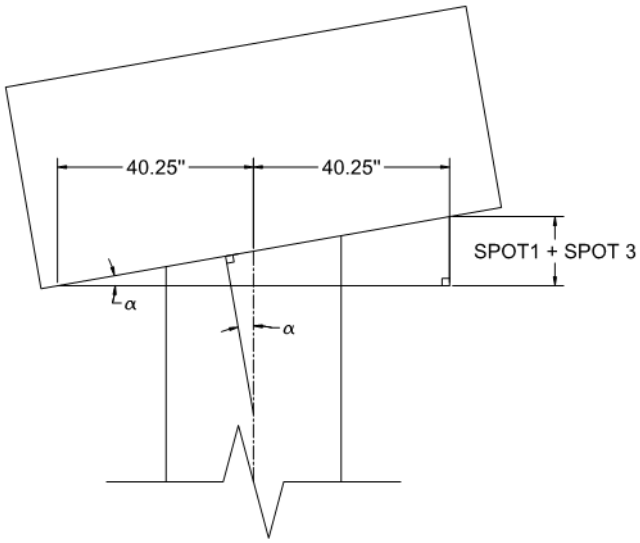

(c) Rotation from the column's center line

Figure 5-9: Rotation calculation from vertical deflections measured with the S-Pots

After calculating the rotation at the column's top and having the moment applied during the test, Eq. (5-6) can be used to determine the effective rigidity when the moment increases as the load is applied to the specimen, as shown in Figure 5-10. In this figure, the vertical axis shows the EI factor that is defined as the ratio of the EI calculated from Eq. (5-6) and the EI using the values from the test MOE presented in Table 4-4 and the second moment of inertia of the gross section. It is noticeable that $EI\ factor$ is not constant and changes as the moment increases through the test, showing that the specimen was losing rigidity as the cracking is propagating along the column's height.

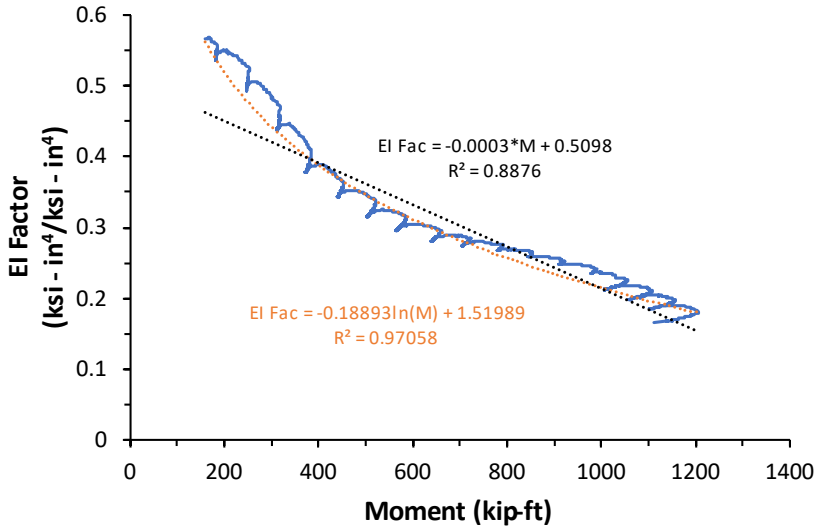

Figure 5-10: Ratio of Effective stiffness "EI" vs "EI" from the material properties as the moment increased during the test

In Figure 5-10, two approaches are used to represent the reduction in the apparent *EI*, one trend line with a logarithmic shape (Eq. (5-11)) and the other with a linear shape (Eq. (5-12)). These two equations were used to calibrate the final formula to extrapolate the lateral deformation for the column's top. First, the lateral displacement was calculated for the L-Pot5 (top) using the data gathered from the test using Eq. (5-9) modified by the *EI Factor* as presented in Eq. (5-13). However, either approach did not perfectly match the *EI Factor* curve shown in Figure 5-10; therefore, a calibration factor was applied to match the maximum displacement calculated by each trend equation with the lateral deflections until reaching a load of 295 kips, as presented in Eq. (5-14). Figure 5-11 presents the results from the two equations used to estimate the lateral displacement at the column's top with a load of 295 kips.

$$EI_{factor.Log} = -0.18893 * \ln(M) + 1.51989 \quad (5\text{-}11)$$

$$EI_{factor.Linear} = -0.0003 * M + 0.5098 \quad (5\text{-}12)$$

$$v(L) = \frac{1}{2}\frac{ML^2}{EI * EI_{factor}} \quad (5\text{-}13)$$

$$v(L) = \frac{1}{2}\frac{ML^2}{EI * EI_{factor} * Cal} \quad (5\text{-}14)$$

$Cal = 1.202$ for the lineal trend
$Cal = 1.183$ for the logaritmical trend

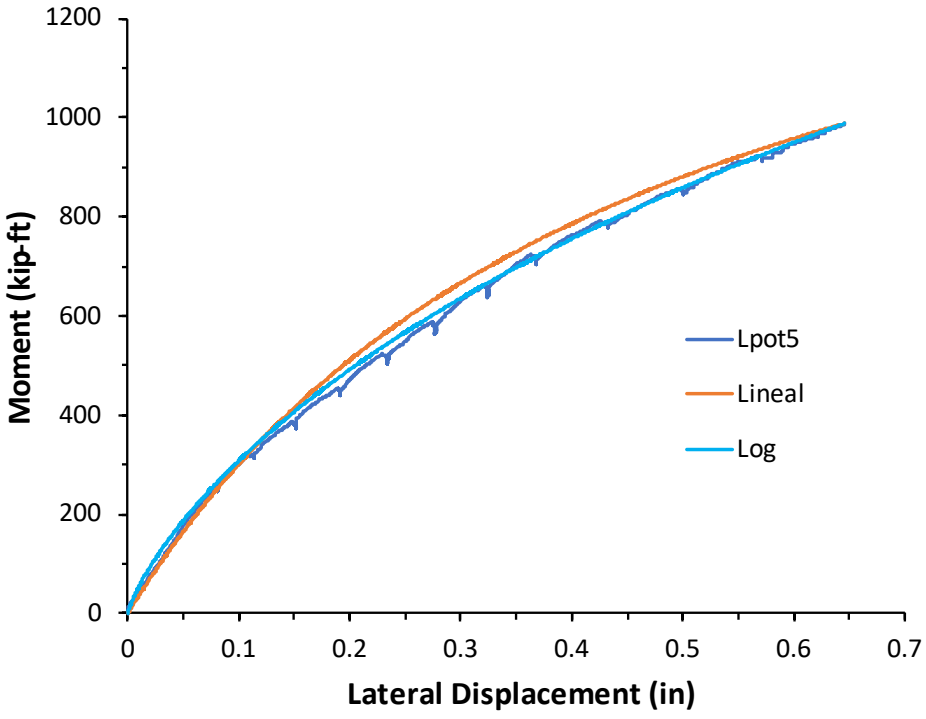

Figure 5-11: Lateral displacement estimated for the column's top

From Figure 5-11, it is noticeable that the equations for the logarithmic and linear trend matched the data gathered for the column's top. The logarithmic trend seems to be close to the experimental data and the linear trend matches for low displacements and matches again with the maximum moment. Besides, it seems to be conservative for the middle displacements bringing higher moments.

The equations for the *EI Factor* from Figure 5-10 (Eq. (5-11) and (5-12)) was verified by being applied to L-Pot 4 and L-Pot 3 located at 6 ft and 4 ft from the column's bottom respectively to determine the lateral displacement using Eq. (5-14), as presented in Figure 5-12.

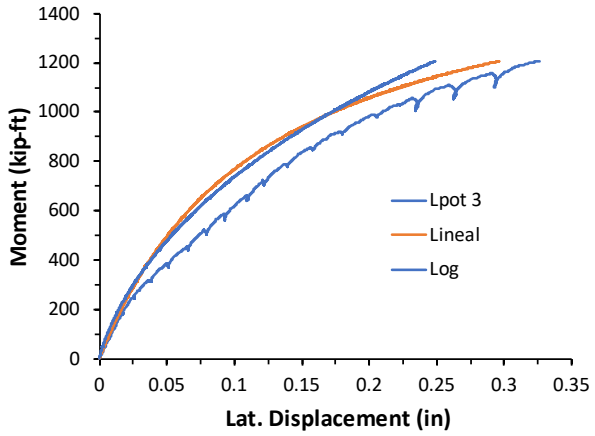

(a) Lateral displacement for L-Pot 3 located at the middle of the column

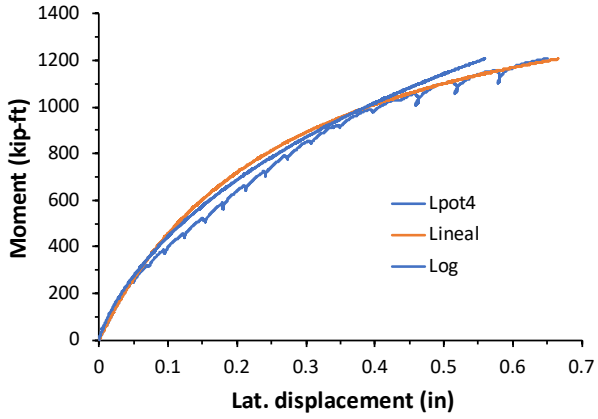

(b) Lateral displacement for L-Pot 4 located at 6 ft. from the column's bottom

Figure 5-12: Lateral displacement estimated for L-Pot 3 and Lpot-4 for the specimen S1-CIP

From Figure 5-12, it is noticeable that the linear trend (orange) is closer to the final displacement than the logarithmic trend for L-Pot 3, and the linear trend appears to be more accurate for the middle-high displacements for L-Pot 4. As the goal of using these trend lines for the effective stiffness is to extrapolate the lateral displacements for L-Pot 5 at the column's top, the linear trend line presents a better fit for this calculation. For this reason, the extrapolation for Lpot-5 for loads higher than 295 kips was calculated using Eqs. (5-12) and (5-14), as illustrated in Figure 5-13. From this extrapolation, the maximum lateral displacement estimated for specimen S1-CIP is 1.138 in with an axial load of 360 kips and a moment of 1207.5 kip-ft.

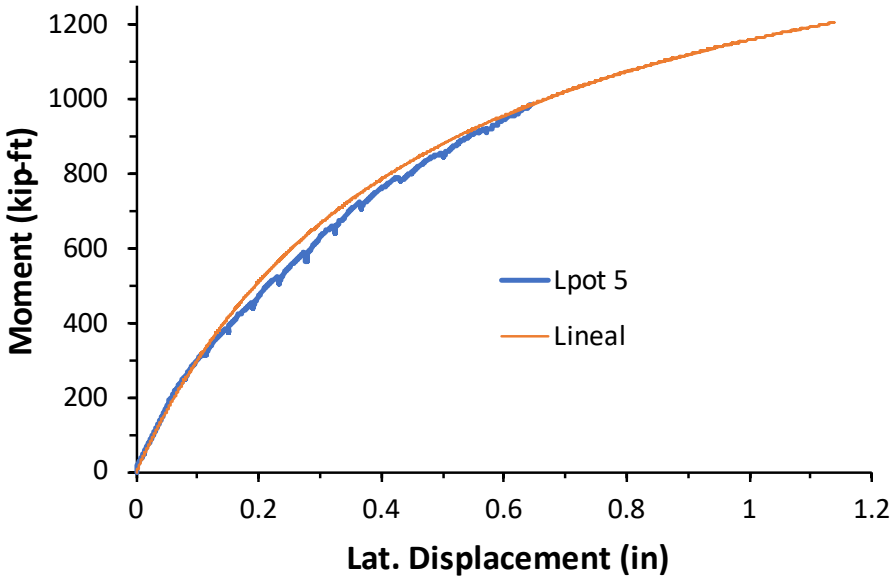

Figure 5-13: Lateral displacement estimated for L-Pot 5 the specimen S1-CIP

5.2.4.2. Lateral Displacement Analysis

Validation was achieved by normalizing the moment-displacement behaviors under the largest test eccentricity of the specimens against Specimen S1-CIP, as shown in Figure 5-14. This normalization was built with the ratio of the moment that each specimen supported during the test against the maximum moment that S1-CIP achieved at the end of the 40.25 in. eccentricity test. The same procedure was realized with the lateral displacement and the maximum lateral displacement from S1-CIP. It is noticeable that Specimens S2-R-AASH9-45 (orange) and S3-S-AASH9-45 (gray) exhibited stiffness softening at 55% of the maximum load presented for CIP, where the first crack was observed. This caused a reduction in the effective second moment of inertia. The maximum capacities of these specimens were 384 kips for Specimen S2-R-AASH9-45 and 383 kips for Specimen S3-S-AASH9-45, resulting in an overstrength of approximately 6.6% compared to CIP. These results indicate that the precast columns can achieve a similar capacity to the Specimen S1-CIP, which complies with standard TxDOT requirements.

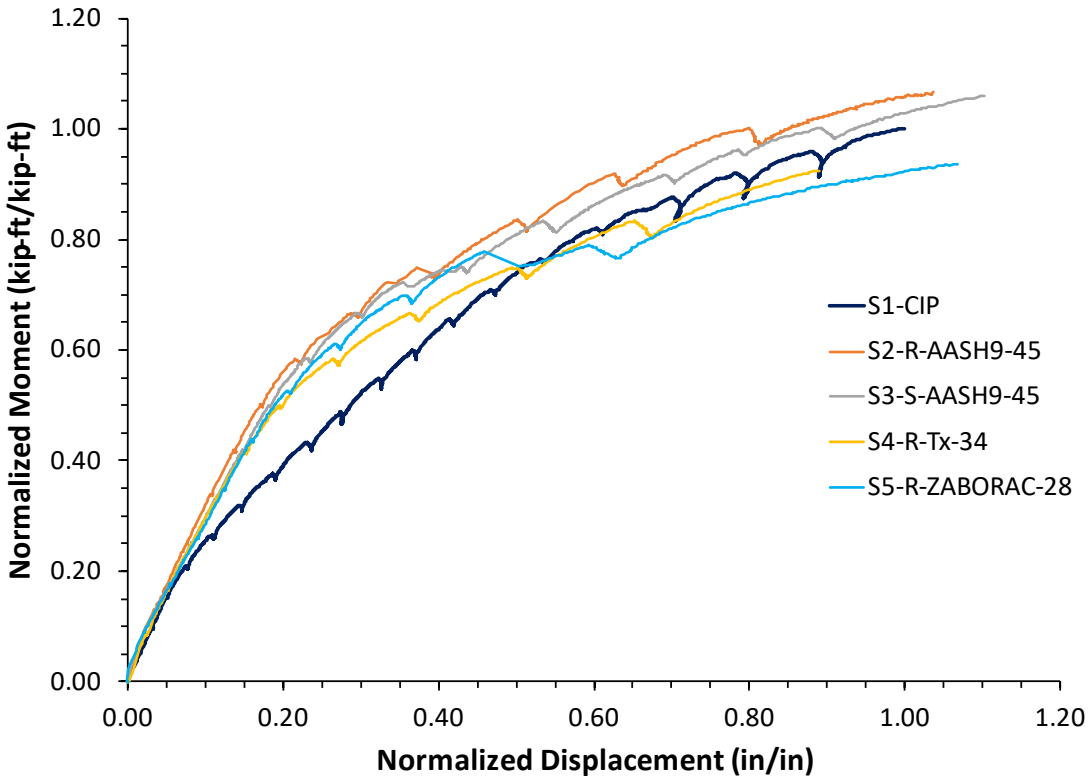

Figure 5-14: Moment – Displacement Normalized against Specimen S1-CIP

Specimens S4-R-Tx-34 and S5-R-ZABORAC-28, featuring shorter connectors, showed similar initial stiffness but seemingly lower cracking moments, as shown in Figure 5-14 .In addition, the specimens exhibited capacities lower than that of S1-CIP, reaching load-carrying capacity ratios of 92.4% and 93.6%, respectively. The likely reason for this is that the embedment length used in these specimens shifted the critical section higher, not allowing the prestressing strands to be fully developed.

5.3. Damage Pattern and Opening at the Connections

5.3.1. Crack width associated with the applied load

During the 40.25-inch test, the crack width at the middle of the column was measured and plotted along with the applied moment to evaluate the degree of damage of the precast columns prior to reaching failure. Trend line equations are offered as a tool for inspection engineers, as outlined in Figure 5-15. This enables field engineers to approximate the bending moment that the column is supporting.

From Figure 5-15, Specimen S2-R-AASH9-45 (purple line) had a maximum crack width of 3/16 in. and S3-S-AASH9-45 (orange line) reported 0.25 in., showing that an internal roughness could help with less crack width in a column. This situation was reflected at the end of the test with a

higher residual deformation for Specimen S3-R-AASH9-45. Specimens S4-R-Tx-34 (dark green) and S5-R-ZABORAC-28 (light blue) showed the maximum crack width values, 3/8 in., and 5/16 in., respectively. Although S4-R-Tx-34 supported a lower moment, it presented more local damage at the end of the connectors, otherwise a wider crack width. On the other hand, S5-R-ZABORAC-28 presented more damage distributed in a higher quantity of cracks at the top and bottom of the column, making the crack width smaller than S4-R-Tx-34.

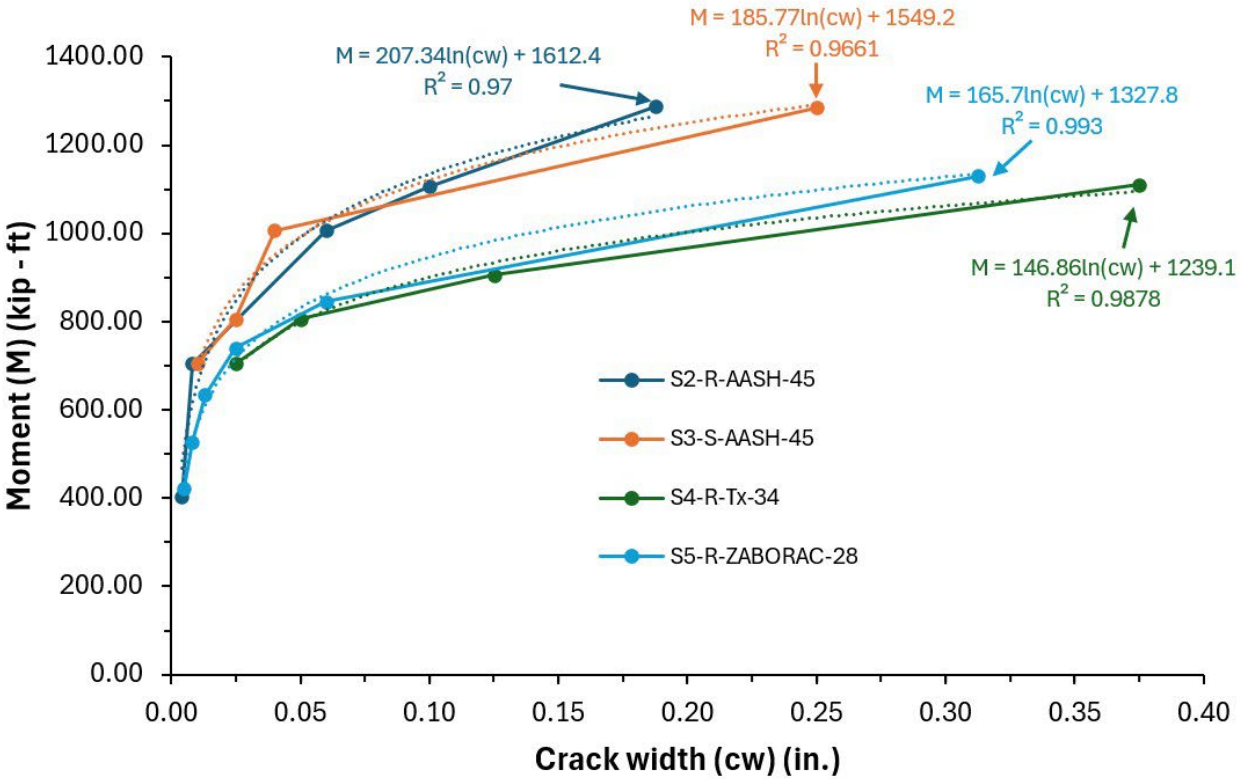

Figure 5-15: Moment – Crack width for precast columns during the 40.25-in. eccentricity test

5.3.2. Opening in the connections for precast columns

The precast column solution described in this research uses precast members and concrete cast-in-place (CIP) to fill the internal void. This method can lead to cold joints in the connections that may cause visible openings when the column undergoes combined axial loads and bending moments. The force is transferred through the connectors from the bent cap to the column and then from the column to the footing. When the tension side of the connection experiences a bending moment, resulting in noticeable openings as presented in Figure 5-16. The opening was measured during each of the tests and plotted along with the applied moment, as shown in Figure 5-17 and Figure 5-18.

(a) *Crack width ruler next to the connection* (b) *Crack width ruler inside the connection*

Figure 5-16: General view of the opening in the connections during the 40.25-in. test

For the case of the bottom connection, the opening registered by the LVDTs is presented in Figure 5-17. Specimen S2-R-AASH9-45 (light blue) happened to be the stiffer specimen showing a higher moment when the opening occurred. It reported a maximum opening of 0.123 in. with a moment of 1285 kip-ft. On the other hand, Specimen S3-S-AASH9-45 (dark blue) reported a maximum opening of 0.143 in. and had a similar behavior compared to the other two precast columns. Specimens S4-R-Tx-34 (orange) and S5-R-ZABORAC-28 (purple) reported a maximum opening of 0.118 in. and 0.115 in., respectively. A trend line equation is presented for an opening less than 0.07 in. and a second one when the opening is higher than 0.07 in. With these equations, considering that the approach of this study was four precast column specimens, an inspection engineer could approximate the stress state of the precast columns.

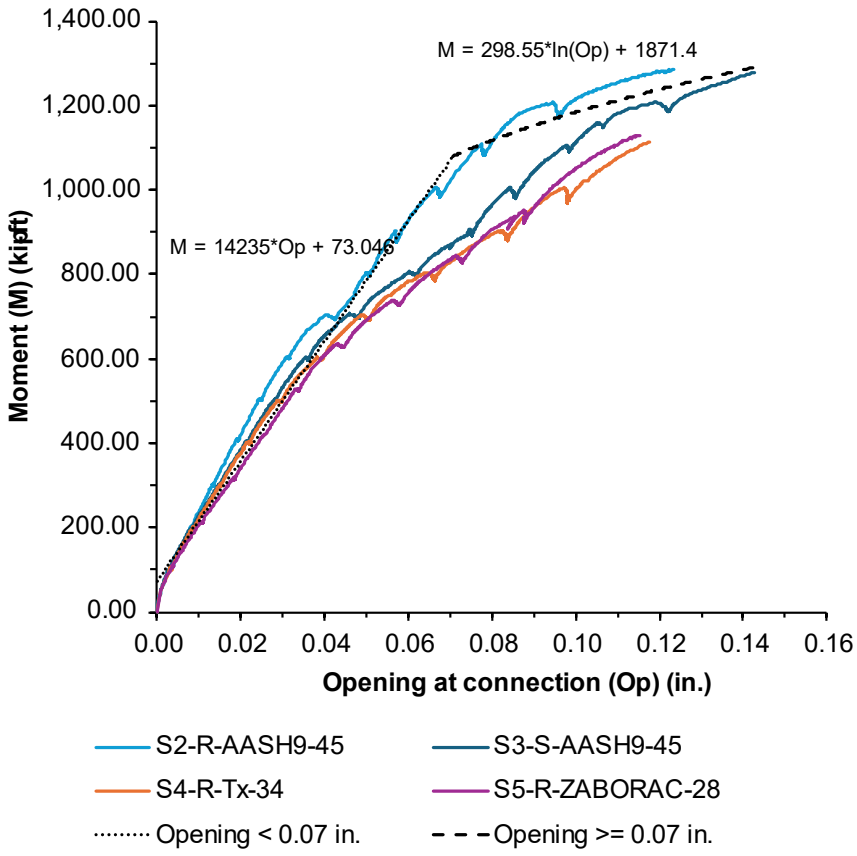

Figure 5-17: Opening in the bottom connection during the 40.25-in. test

For the case of the top connection, the opening reported by the LVDTs was wider than the bottom connection. This behavior was followed by all the precast specimens, as illustrated in Figure 5-18. This connection presented a linear behavior until reaching a bending moment of 600 kip-ft, as the moment increased the specimens showed some differences. Specimen S2-R-AASH9-45 (light blue) presented the largest opening with a reported value of 0.302 in. Although specimen S3-S-AASH9-45 (dark blue) reached a similar bending moment compared to S2-R-AASH9-45, the maximum opening reported for this specimen was 0.213 in. Specimen S4-R-Tx-34 (orange) performed as well as S3-S-AASH9-45, however, it measured an opening of 0.14 in. associated with a bending moment of 1114 kip-ft. Specimen S5-R-ZABORAC-28 (purple) reported an opening of 0.174 in. A trend line equation is presented for an opening less than 0.07 in. and a second one when the opening is higher than 0.07 in. As it was stated for the bottom connection, considering that the approach of this study was four precast column specimens, an inspection engineer could approximate the stress state of the precast columns using the equations presented.

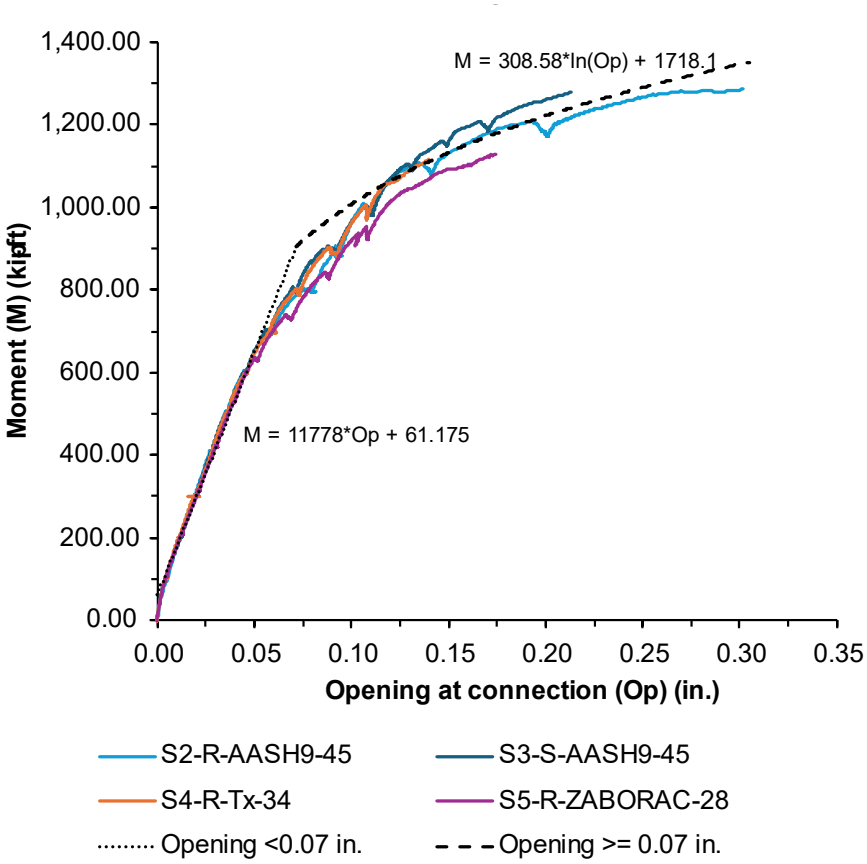

Figure 5-18: Opening in the top connection during the 40.25-in. test

5.4. Capacity of the Precast Column Solution

In this section, the estimated capacity of the precast column is determined using a layered section analysis with a parabolic shape for the concrete stresses based on the Collins and Mitchell model. The stress in the prestressing strands is computed in accordance with AASHTO and ACI specifications and is then compared to the load supported by the specimen in the tests. Subsequently, an analysis is conducted to compare various concrete stress shapes in order to establish an engineering method for approximating the capacity of the precast column.

5.4.1. Column Capacity Considering Stress in Prestressing Strands

From the large-scale experimental tests on the precast column specimens, it was observed that the biggest crack at failure and crushing of concrete occurred at the height where the connectors were terminated in the column. This observation indicates that the critical section of flexural failure is located at the section where prestressing strands in the shell solely resisted flexural tension. To calculate the flexural capacity at the critical section, the design stress at nominal flexural strength (f_{px}) in the prestressing strands is needed.

In a typical sectional analysis, the value of f_{px} should be taken according to a bilinear relationship associated with the distance to the free end per Section 5.9.4.3.2 of AASHTO LRFD 9th edition, as illustrated in Figure 5-19. Applying the method to the test specimens based on the actual distance between the critical section to the free end, denoted as L_d, the values obtained for f_{px} are summarized in Table 5-2.

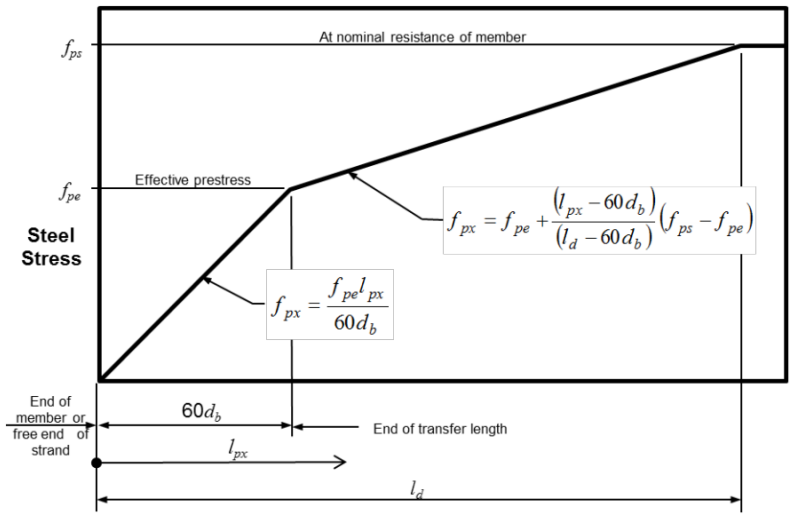

Figure 5-19: Idealized relationship between steel stress and distance from the free end of the strand, taken from AASHTO 9th edition C5.9.4.3.2-1.

Table 5-2. Precast Column Capacity using the formula for development length from AASHTO.

	Ld Strands(ft)	*fpx* AASHTO (ksi)	Ratio *fpx/fpu* AASHTO	P with Ld AASHTO [1] (kip)	P from test [2] (kip)	% Error AASHTO	Capacity Ratio
S100% [3]	10.44	270.00	100.00%	459.39	---	---	100.00%
S2-R-AASH9-45	3.75	185.83	68.82%	382.32	384.29	0.51%	83.65%
S3-S-AASH9-45	3.75	185.83	68.82%	382.32	382.18	-0.03%	83.19%
S4-R-TX-34 [4]	2.83	174.29	64.55%	363.78	333.39	-9.11%	72.57%
S5-R-ZABORAC-28	2.33	158.76	58.80%	316.42	321.49	1.58%	69.98%

[1] Axial Load calculated with AASHTO is presented after removing the Self-Weight at the failure zone

[2] Axial Load reported from Load Cells during the test

[3] Expected capacity with a development length of 100% for the prestressing strands

[4] S4 meets the load with a stress of 57.5% of *fpu*

Considering strain compatibility and a layered section analysis, the P-M interaction diagrams for each specimen were generated to estimate the axial load needed to reach flexural failure, as presented in Figure 5-20. S100% corresponds to the required development length (10.44 ft, based on Equation 5.9.4.3.2-1 in AASHTO LRFD) to reach its full f_{ps} = 270 ksi and therefore full flexural capacity. Using the P-M interaction diagram for S100% and the 40.25 in. load pattern, the total axial load needed to reach failure is calculated and the self-weight from the specimen at the failure zone is removed, showing an axial load of 459.39 kips under an eccentricity of 40.25 in. as shown in Table 5-2. This load represents the theoretical axial load that should be applied to the specimen to reach failure if the strands are fully developed.

Another important parameter to be used for this model is the effective prestress f_{pe}, which can be determined using various methods. In the current analysis, the first method adopted was using a design prestress loss of 30 ksi, corresponding to a $\Delta\varepsilon_p$ of 0.006 in/in (Collins and Mitchel (1991) and Gulf Coast Prestress, Inc). Substituting these parameters allowed for the determination of f_{px} for each specimen and the calculations of flexural capacity under the largest test eccentricity, as summarized in Table 5-2. Appendix A provides an example of the procedure used to develop the P-M Interaction Diagram considering the development length of the prestressing strands and layer section analysis.

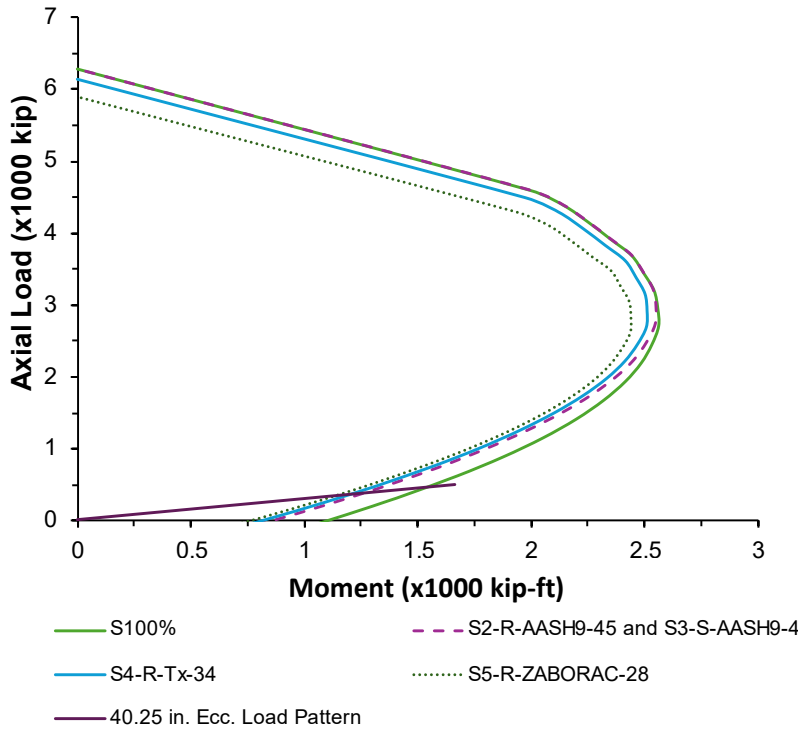

Figure 5-20: P-M Interaction Diagrams developed for all the specimens subjected to an eccentricity of 40.25 in considering the f_{px} in the prestressing strands.

For Specimen S2-R-AASH9-45 and S3-S-AASH9-45, using a value of l_{px} of 45-in. with f_{pe} = 171 ksi, the stress calculated at that distance is f_{px} = 185.83 ksi. In this case, the strands were not able to develop a stress close to 270 ksi, resulting in a calculated capacity of 382.32 kips. When this capacity is compared with the axial load obtained from the tests, the error is 0.51% and 0.03%.

For Specimen S4-R-Tx-34 and S5-R-ZABORAC-28, the same procedure was followed using l_{px} of 34-in. and l_{px} of 28-in., and the stress developed in the strands was f_{px} = 174.29 ksi and f_{px} = 158.76 ksi, respectively, resulting in a capacity of 363.78 kips for S4-R-Tx-34 and 316.42 kips for S5-R-ZABORAC-28, with an error of 9.11% and 1.58%, respectively.

As the method introduced previously was proven accurate, the same procedure was followed using Section 25.4.8.1 of ACI 318-19, which resulted in the required development length of the strands

being shorter than the one calculated using AASHTO LRFD. In this case, the development length calculated to reach $f_{ps} = f_{pu}$ = 270 ksi is approximately 6.52 ft. For this reason, the theoretical capacity that was obtained from this method was higher than the capacity reported from the test for all the specimens, as summarized in Table 5-3. It is revealed that ACI's development length for strands appeared to be less conservative affecting the final precast column capacity as presented in Figure 5-21.

Table 5-3. Precast Column Capacity using the formula for development length from ACI.

	Ld Strands(ft)	*fpx* ACI (ksi)	Ratio *fpx/fpu* ACI	P with Ld ACI [1] (kip)	P from test (kip) [2]	% Error ACI	Capacity Ratio
S100% [3]	6.53	270.00	100.00%	459.39	---	---	100.00%
S2-R-AASH9-45	3.75	203.40	75.33%	408.40	384.29	-5.90%	88.90%
S3-S-AASH9-45	3.75	203.40	75.33%	408.40	382.18	-6.42%	88.90%
S4-R-TX-34**	2.83	181.40	67.19%	374.98	333.39	-11.09%	81.63%
S5-R-ZABORAC-28	2.33	168.00	62.22%	330.26	321.49	-2.66%	71.89%

[1] Axial Load calculated with ACI is presented after removing the Self-Weight at the failure zone

[2] Axial Load reported from Load Cells during the test

[3] Expected capacity with a development length of 100% for the prestressing strands

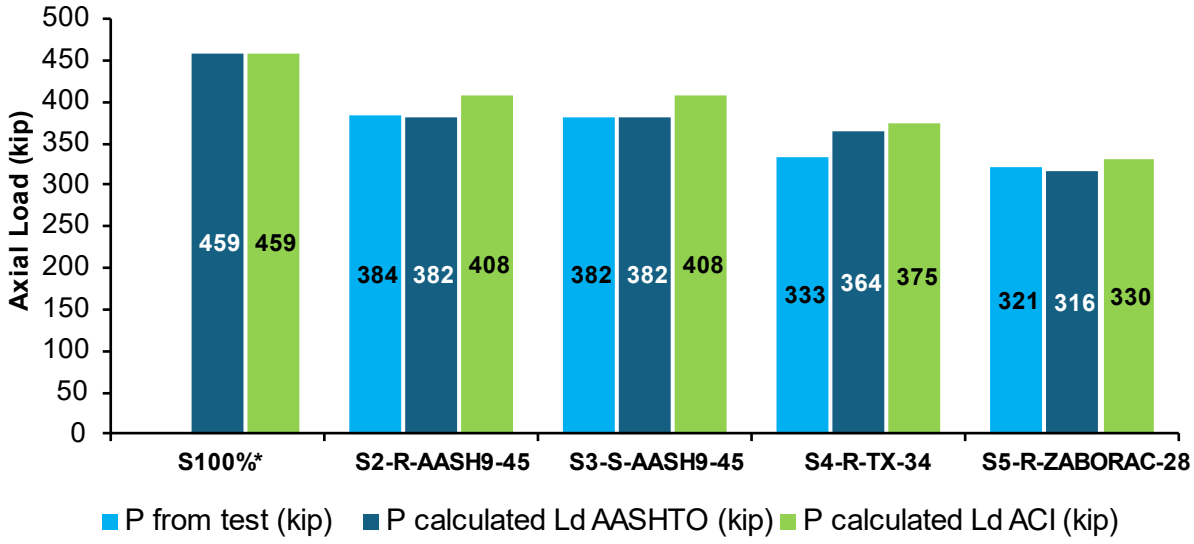

Figure 5-21: Comparison of the load obtained from the test and the calculated with AASHTO and ACI.

5.4.2. P-M Curves by Various Sectional Stress Distribution Models

From the tests, one important finding is that the specimens demonstrated composite behavior, with the prestressed hollow sections effectively compatible with the concrete cast in the void. This behavior provides insight into calculating the capacity of the precast columns working as one structural member. The complexity of determining the ultimate strength of the precast column solution arises because of the composite action, complicated geometry, and different concrete strengths of the shell and the core. There should be a method for constructing the P-M interaction

diagram of this system that considers the interaction of the shell and the core. This section introduces the method of constructing the P-M interaction diagram based on various concrete stress distribution models.

Considering that the f'_c from the prestress section is 10.3 ksi and the f'_c obtained for the core is 4.37 ksi, the solution to this problem should be addressed using a method of equilibrium and strain compatibility. Another aspect to take into account is that the section is composed of a ring that represents the prestressed section and a circle that represents the core with the concrete cast in place, making a layered analysis the best option. For instance, sectional strain compatibility when the neutral axis has a depth of 18-in. is shown in Figure 5-22. Taking advantage of the strain compatibility and the layered section, the cross-section could be divided into small rectangles to calculate the centroid and the stress, based on each of the aforementioned models, present in each layer, and finally to integrate all the stresses until the axial force and moment in equilibrium converged. The procedure was repeated for the value of "c" varying from 1.5-in. to 36-in. It should be noted that the strands' stress was based on the Ramberg-Osgood relationship and assumed to be fully developed to focus on the variation of concrete models.

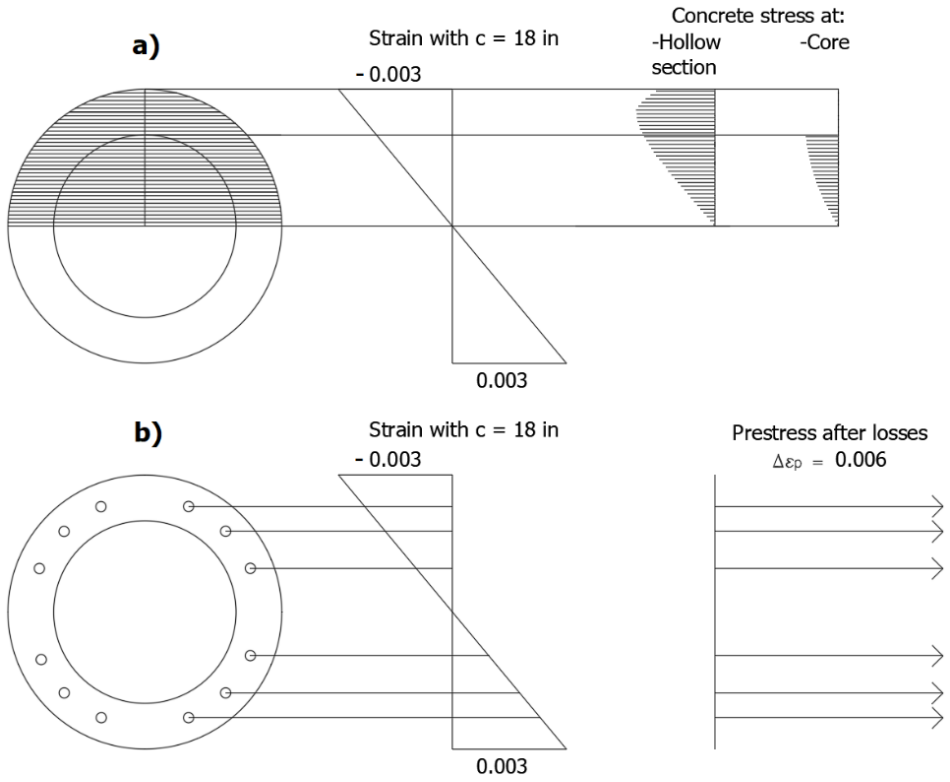

Figure 5-22: Strain compatibility for a case when c = 18-in.: a) Layered section and stress profile and b) Strain in the prestressing strands due to flexure, compression, and prestressing.

The used concrete stress distribution models were named 1) Collins 10-4.3 ksi, 2) Rectangular Block 10.3 ksi, 3) Rectangular Block 4.3 ksi, 4) Rectangular Block f'_c average, and 5) Collins Hollow 10 ksi. The first model, Collins 10-4.3 ksi, is the most detailed method of describing the

stress in the shell and the core based on the sectional strain and the concrete constitutive relationship. The fifth model, Collins Hollow 10 ksi, neglects the contribution of the core.

In addition to incorporating the concrete constitutive relationship, the equivalent rectangular stress block method was also used for simplicity. The equivalent rectangular stress block method, acknowledged by AASTHO LRFD and ACI 318, replaces the parabolic function of the concrete constitutive relationship with a rectangular stress block, providing a faster and easier way to establish sectional force equilibrium. In this analysis, three ways of calculating the capacity from the rectangular stress model are considered, one is using the maximum f'_c that corresponds to 10.3 ksi, the second one is using the minimum f'_c that is 4.3 ksi, and the third one is using the average f'_c, that corresponds to a value of 7.34 ksi. Applying all five models, the P-M interaction diagrams related to each model are presented in Figure 5-23.

With the P-M interaction diagrams generated, the load pattern corresponding to the 40.25-in. eccentricity could be used to determine the load that each model predicts for failure. The predicted load for all the models is summarized in Table 5-4. In the table, Collins 10-4.3 ksi is used as the baseline for comparison as it was considered the closest to the actual behavior and most accurate among all models, based on the load prediction presented in section 5.4.1.

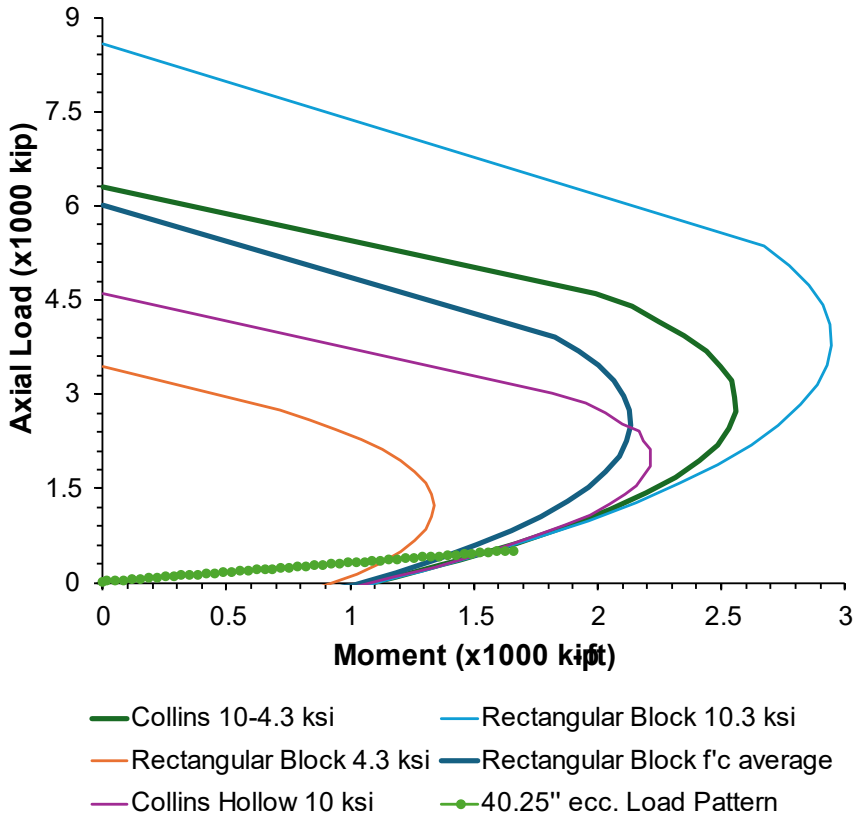

Figure 5-23: P-M curves obtained for the precast column design using different models to represent the concrete behavior.

Table 5-4. Precast column capacity prediction using different concrete models.

Model	Axial Load P (kip)	Moment M (kip-ft)	P % Diff.	M % Diff.
Collins 10-4.3 ksi	480.43	1540.86	---	---
Rectangular Block 10.3 ksi	485.97	1559.46	-1.15%	-1.21%
Rectangular Block 4.3 ksi	361.27	1141.17	24.80%	25.94%
Rectangular Block f'$_c$ average	437.80	1397.86	8.87%	9.28%
Collins Hollow 10 ksi	481.17	1543.33	-0.15%	-0.16%

As presented in Table 5-4, using a concrete rectangular model with the maximum f'_c could be unconservative, predicting a higher capacity. Conversely, using a minimum f'_c of 4.3 ksi results in a conservative estimate with a difference close to 26% compared to the Collins and Mitchel model. However, using an f'_c calculated as the average of the maximum and minimum values predicts a load conservatively, with a difference of 9.28%. Given the simplifications involved in using a rectangular stress block and not employing a layered section, using the average f'_c appears to be a reliable method for calculating the capacity of this type of precast column. Finally, using the Collins and Mitchell model, considering only the concrete from the precast column, provides a satisfactory solution; however, the effort required to calculate this solution is the same as when considering the concrete from the core.

5.5. Summary

Five specimens were built and tested in this research, evaluating the performance of developed precast column solution by comparing the structural responses to the CIP control specimen. For this precast solution, two main variables were studied: a) interior roughness inside the precast column, and b) embedment length of the rebar at the connections. From the tests and data analysis, the main findings are summarized below:

- **Control Specimen Performance:** The cast-in-place control specimen demonstrated robust performance under the tested eccentricities, creating the baseline to evaluate other specimens based on the precast column solution.
- **Precast Column Performance at Low Eccentricities:** The precast columns exhibited elastic behavior at low eccentricities (6 in. and 12 in.), indicating satisfactory performance under typical design load condition in Texas.
- **Post-Cracking Behavior:** At an eccentricity of 20 in., the precast columns displayed slight post-cracking behavior with softening in the stiffness.
- **High Eccentricity Capacity:** The largest eccentricity test (40.25 in.) revealed that the precast columns could achieve capacities comparable to the control specimen. Specifically, the specimen with a 45 in. embedment length supported 383 kips, exceeding the control specimen by 23 kips, whereas the shorter embedment length specimen supported the lowest

load (321 kips). The observation signifies proper design for the embedment length of the connectors.

- **Effect of Internal Roughness:** The internal roughness of the precast columns had minimal impact on final resistance, with a negligible difference of 1 kip between the roughened and non-roughened specimens.

- **Damage Comparison:** The control specimen exhibited significantly more damage compared to the precast columns, suggesting that prestressed members provide better crack control and reliability.

- **Rebar Yielding:** Rebar at the connections reached yielding in all specimens regardless of internal roughness and embedment length, which varied from 28 in. to 45 in.

- **Embedment Length Impact:** The embedment length of connecting bars significantly influenced the capacity of the precast columns, affecting the development of prestressing strands and consequently reducing flexural capacity.

- **Analytical Modeling:** A layered section analysis with a parabolic stress shape and considering the effective prestress of the strands effectively estimated the capacity of the precast columns with minimal error. A rectangular stress block model also yielded accurate results when using the average f'_c values from both the precast column and the cast-in-place concrete.

Chapter 6. Finite Element Analysis

This chapter is a summary of the Master's Thesis presented by Chakravarthi Kotha, for further details this document should be consulted. It presents a finite element analysis on test specimens of interface shear push-through testing and full-scale specimens of precast column solution. It includes model preparation and validation. The modeling method and parameters used are also presented.

6.1. Shear Interface Model

Complete load transfer cannot be guaranteed in unreinforced interfaces between two different concrete members, as it depends on numerous factors like friction and surface roughness, the shape of the interface, and shrinkage properties. The circular precast columns used in this project contained two components: a prestressed precast outer shell, and the void of shell filled with CIP concrete. The interface between CIP concrete and the precast shell is not reinforced, and a detailed study of the surface's physical properties is necessary.

As part of the project, twenty-seven experimental specimens with varying interface surface shapes (curvilinear, flat), surface roughness (roughened with sandblasting, naturally smooth), and concrete type (precast, conventional, shrinkage reducing) were tested by push-through testing to evaluate key parameters like shear strength and stiffness, and the results are presented in Chapter 3.The push-through specimens were used as benchmark tests; therefore, finite element models were constructed and calibrated. In this section, modeling and difficulties faced during the preparation of analytical concrete shear interface models using ATENA 3D are presented. Three models with a circular interface, and having different surface roughness like naturally smooth, shrinkage-reducing concrete, and intentionally roughened were prepared. Necessary experimental properties like material strength, interface shear strength, and stiffness were taken to model the analytical interface specimens. The analytical results were considered necessary for the development of FE models of precast columns.

6.1.1. Interface Models Design

As shown in Figure 6-1, a model for push-through tests was built in ATENA 3D. The model consisted of a shell macroelement shaped like a cuboid with a cylindrical void, a core macroelement that fit perfectly in the shell, and a load plate on top and a support plate on the bottom of the shell macroelement. The bottom surface of the support plate was restricted in all three directions. The diameter of the load plate (top) and the one of the support plate (bottom) were smaller than the core's diameter. This was modeled to resemble the experimental program, shown in Figure 6-2. The assembly allowed the load to be applied only to the core, and the only resistance to the applied load was the shear strength of the interface between the shell and the core.

With all the macroelements created and assigning the interface element to the shell-core connection, load increments of 5 kips were applied on the center of the load plate. A monitoring

point was kept at the top of the load plate and the bottom of the core macroelement to study the vertical interface displacements.

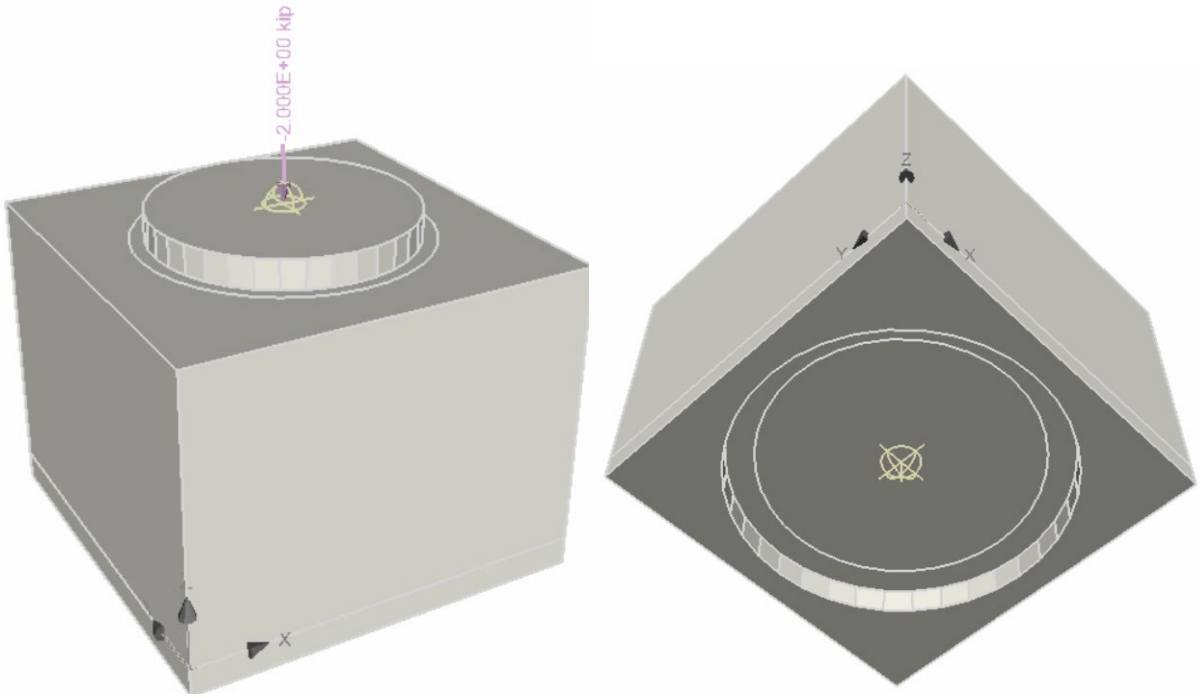

Figure 6-1: Top and Bottom view of Shear Interface Model Built in ATENA 3 (Kotha, 2024)

Figure 6-2: Experimental Setup of Interface Models (Small, 2022)

6.1.2. Material Models and Properties

Concrete material in the FE analysis was modeled as CC3DNonLinCementitious2 in the software. The concrete material model had a uniaxial stress-strain relationship, the plastic behavior of concrete was defined by assigning specific fracture energy, which is defined by the area under the tensile stress-strain curve, on the tension side, and the reduction factor on the compressive side. Besides, the biaxial failure profile is based on a study by Kupfer et al (1969) in which the failure envelope should be defined by a parameter of failure surface eccentricity, all as suggested by ATENA Theory (2021).

This concrete material model was assigned to macroelements in the FE model for the shell and core macroelements. The material properties were allotted differently for each macroelement to represent the test specimen based on the actual concrete used in each member. In particular, the test compressive strength of concrete was taken and assigned as f'_c in the concrete material model, and other parameters were determined accordingly. For instance, the elastic modulus and tensile strength were calculated based on ACI 318-19, given by Eq. (6-1) and Eq. (6-2) respectively.

$$E_c \text{ (in psi)} = 57000\sqrt{f'_c} \tag{6-1}$$

$$f'_t \text{ (in psi)} = 4\sqrt{f'_c} \tag{6-2}$$

In addition, the specific fracture energy G_f was calculated based on the recommendation given by Eq. (6-3) (Rejane et al. 2014).

$$G_f \text{ (in kip/in)} = 0.0009843 f'_t \tag{6-3}$$

All the other material properties were left as the default values. Table 6-1 summarizes the material properties used for the shell macroelement and of the core macroelement (ATENA 2021) and Table 6-2 lists the properties of reinforcement steel used in the specimen, following a bilinear elastoplastic relationship.

Table 6-1. Material Properties of Concrete for Shell Macroelement and Core Macroelement

Subset	Parameters	Shell		Core	
		Applied Value	Unit	Applied Value	Unit
Basic	Elastic modulus, E_c	3.439E+03	ksi	4.952E+03	ksi
	Poisson's ratio, ν	0.200	-	0.200	-
	Tensile strength, f'_t	3.840E-01	ksi	3.475E-01	ksi
	Compressive strength, f'_c	-3.640E+00	ksi	-7.548E+00	ksi
Tensile	Specific Fracture energy, G_F	2.915E-04	kip/in.	4.098E-04	kip/in
	Crack spacing, s_{max}	Inactivated		Inactivated	
	Tension stiffening, c_{ts}	Inactivated		Inactivated	
	Unloading	Inactivated		Inactivated	

Compressive	Critical compression displacement, w_d	-1.969E-02	in.	-1.969E-02	in.
	Plastic strain at compressive strength, ε_{cp}	- 8.285E-04	-	-8.285E-04	-
	Reduction of comp. strength due to cracks, $r_{c,lim}$	0.800	-	0.800	-
Shear	Crack Shear Stiff. Factor, S_F	20.000	-	20.000	-
	Aggregate interlock, MCFT	Activated		Activated	
	Aggregate Size	0.787	in.	0.787	in.
Miscellaneous	Fail. Surface eccentricity	0.520	-	0.520	-
	Multiplier for the plastic flow dir. β	0.000	-	0.000	-
	Specific material weight, ρ	8.473E-05	ka	8.473E-05	ka
	Coefficient of thermal expansion, α	6.667E-06	1/°F	6.667E-06	1/°F
	Fixed crack model coefficient	1.000	-	1.000	-

Table 6-2. Assigned Material Parameters of Reinforcement and Load Plates

Subset	Parameters	Applied Value	Unit
Basic	Elastic modulus, E_c	2.901E+04	ksi
	Yield strength, σ_y	60.000	ksi
Miscellaneous	Specific material weight, ρ	2.892E-04	ka
	Coefficient of thermal expansion, α	6.667E-06	1/°F

6.1.3. Shell-Core Interface Behavior and Properties

Contact elements were used to simulate the interface between two different concrete materials, the precast concrete shell, and the cast-in-place core. ATENA 3D has a default interface element, CC3Dinterface, where the properties should be defined. The contact elements had material properties based on the Mohr-Coulomb criterion with a tension cut-off, as shown in Figure 6-3: Mohr-Coulomb Criterion for Contact Elements in ATENA 3D. It can be seen from the figure that concrete tensile strength, cohesion, and friction dictate the shear strength of the interface according to this model.

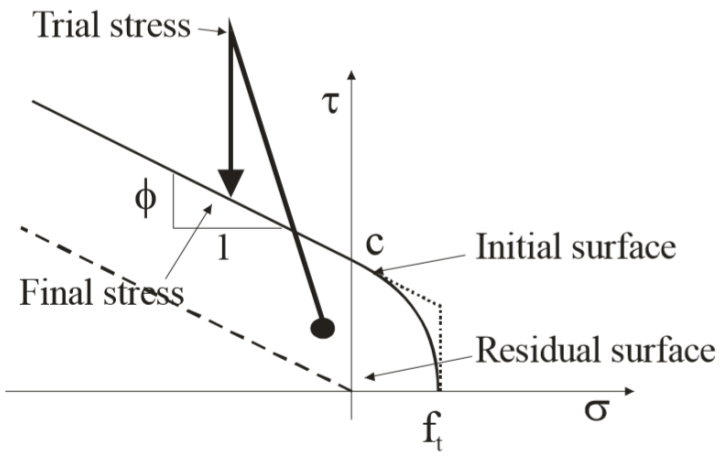

Figure 6-3: Mohr-Coulomb Criterion for Contact Elements in ATENA 3D

In addition to the shear strength, contact material required normal stiffness K_{nn} and tangential stiffness K_{tt} to describe its complete behavior, as shown in Figure 6-4: Contact Stiffness. For numerical purposes, minimal normal and tangential stiffnesses were specified to avoid convergence issues caused by zero stiffness in the region of residual dry friction in shear.

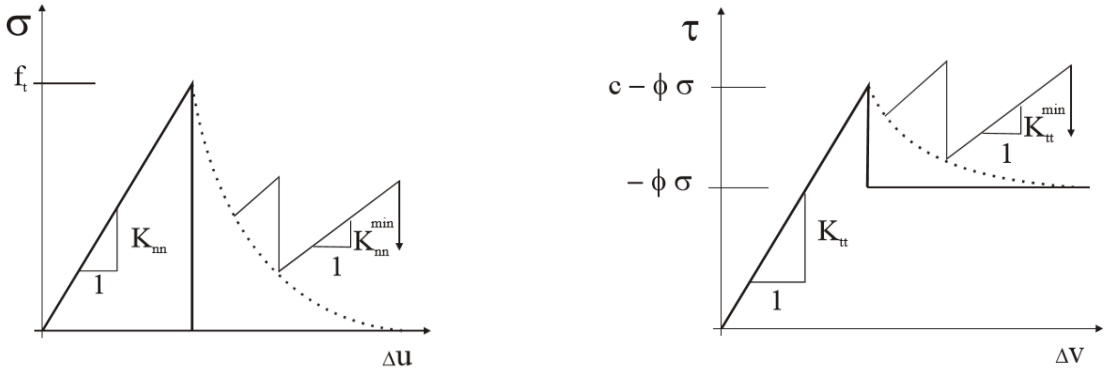

(a) Normal stiffness (b) Tangential stiffness

Figure 6-4: Contact Stiffness

It is recommended in the user manual of ATENA 3D that the values of K_{nn} and K_{tt} be estimated using the following Eq. (6-4) and Eq. (6-5) respectively:

$$K_{nn} = \frac{E}{t} \tag{6-4}$$

$$K_{tt} = \frac{G}{t} \tag{6-5}$$

where E is the minimal elastic modulus of the interface material, G is the shear modulus of the interface material, and t is the width of the interface zone. The width of the interface was unknown in this case; therefore, it was recommended to take it as 10-20 mm (0.4 to 0.8 in.), by the ATENA theory manual. However, the results of the analysis with these parameters were found to be unreliable, and an alternative method was followed, which is discussed below.

It can be seen from Figure 6-3 and Figure 6-4 that the introduced parameters were essential to capture the structural behavior of the full-scale precast column system. That is why data from experimental small-scale interface tests were taken to calibrate for the required parameters. After extensive research and analysis, a step-by-step procedure for calculating the interface properties was proposed as follows:

Step 1: Select the shell/core concrete with lower compressive strength; assume a 12-in. concrete test cylinder with compressive strength f'_c; calculate elastic modulus E_c from the Eq. (6-1) and tensile strength f'_t from Eq. (6-2).

Step 2: Calculate the tensile fracture strain from the Eq. (6-6); calculate the change in length Δu from Eq. (6-7), which is the deformation at tensile fracture. It is the multiplication of ε_t and the size of the test sample. Since the size of the precast shell is 6 in., it is assumed that 6 in. of core undergoes tensile stresses as well. Therefore, 6 in. on either side of the interface adds up to 12 in. and this value is taken for the calculations.

$$\varepsilon_t = f_t'/E_c \tag{6-6}$$

$$\Delta u \text{ (in in.)} = 12\varepsilon_t \tag{6-7}$$

Step 3: As seen in Figure 6-4(a), the normal stiffness K_{nn} (in kci) can be calculated using Eq. (6-8). It is the slope of f'_t and Δu.

$$K_{nn}(\text{in kci}) = f'_t/\Delta u \tag{6-8}$$

Step 4: From test data obtained from experimental results of the push-through interface tests, select an interface (smooth, roughened, or from shrinkage-reducing concrete). Peak load, Shear strength or cohesion, and the interface slip (Δv) at peak load can be interpreted. From Figure 6-4(b), in the case of zero principal stress, K_{tt} can be calculated from Eq. (6-9).

$$K_{tt}(\text{in kci}) = \text{cohesion}/\Delta v \tag{6-9}$$

Step 5: $K_{tt,min}$ and $K_{nn,min}$ are taken as 0.1% of K_{tt} and K_{nn} respectively, as suggested from the ATENA theory manual.

Step 6: Coefficient of friction values can be selected from AASHTO LRFD 9th Edition.

Following the step-by-step procedure mentioned above, parameters of smooth, roughened, and shrinkage-reducing concrete (SRC) interfaces were calculated and provided in Table 6-3.

Table 6-3. Interface Properties for Different Types of Surfaces

Interface Type	K_{nn} (kci)	K_{tt} (kci)	Cohesion (ksi)	Tensile Strength, f'_t (ksi)	Friction Coefficient
Smooth	295.220	31.315	0.149	0.384	0.600
Rough	340.552	57.722	0.197	0.351	1.000
Smooth, Shrinkage reducing concrete (SRC)	336.551	103.251	0.163	0.364	0.600

6.1.4. Analysis and Results

Figure 6-5 shows the comparison between the experimental results and FEA results for the smooth interface model with a circular core presented in the section 3.3.2.1.1. In the figure, blue, orange, and grey lines represent the experimental results of three specimens. The test results were scattered and with noise; however, the load-slip behavior could be generalized as a linear portion followed by a sharp slip when reaching the failing load. Therefore, it was convenient to use an average bilinear behavior before evaluating numerical results, as a target for the parametric analysis prepared with the FE model. A yellow line was plotted to represent the average load-slip for these specimens. Lastly, a green line denotes FEA results in the figure, showing a close behavior compared to the idealized bilinear average. As most of the load is taken by the core and interface during loading, no cracks were observed on the shell concrete at failure.

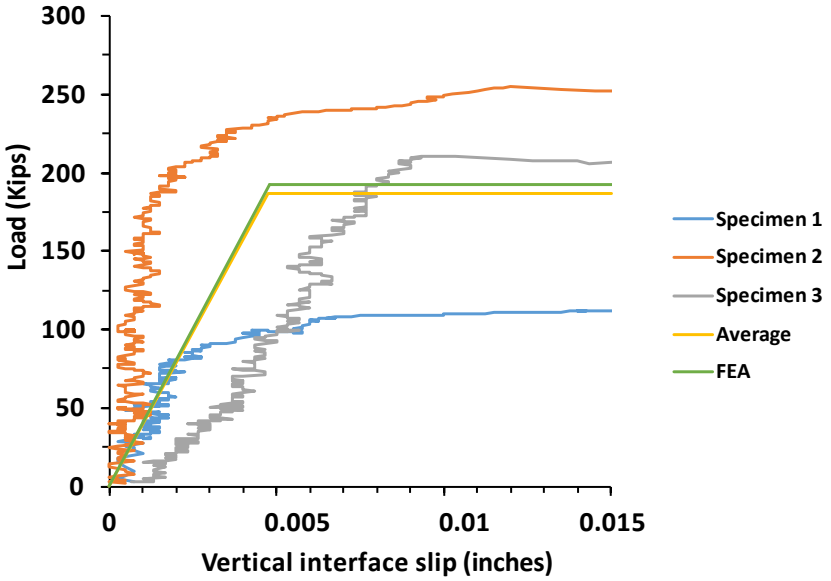

Figure 6-5: Comparison of Load-Slip Behavior of Smooth Interface Specimens (Kotha, 2024)

Checking the ATENA model, the interface stress reached the shear strength value (0.15 ksi for smooth interface) just before failure as seen in Figure 6-6. The scale is in ksi, blue region represents failure.

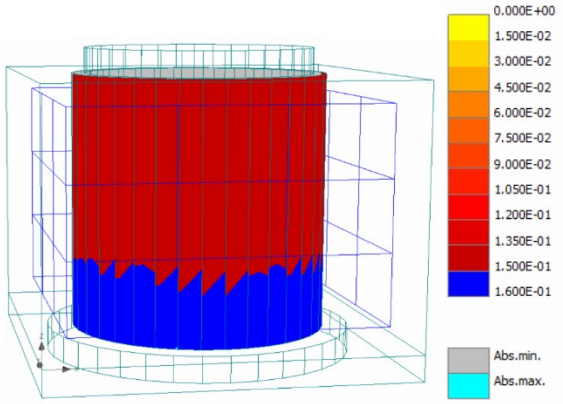

Figure 6-6: Shell-Core Interface at the End of Test, Smooth Interface Model (Kotha, 2024)

A similar procedure was endured with two interfaces presented for the circular core, texturized (C-T) and smooth shrinkage-reducing concrete (C-SRC), and the values for the average are presented in Table 6-4. In Figure 6-7, the FEA results of smooth, texturized, and SRC interface models are shown in the same graph. Looking at the trend, the roughened interface has higher shear strength than the smooth interface, which is almost equal to the SRC interface. However, the texturized interface model and SRC interface model failed at relatively lesser interface shear slip, this could be attributed to higher tangential stiffness K_{tt} value.

Table 6-4. Summary of shear strength obtained from FE models

	Smooth	Texturized	SRC
Maximum Load (kip)	192	248	206
Elastic Slip (in)	0.00479	0.00332	0.00164
Maximum Plastic Slip (in)	0.02	0.02	0.02

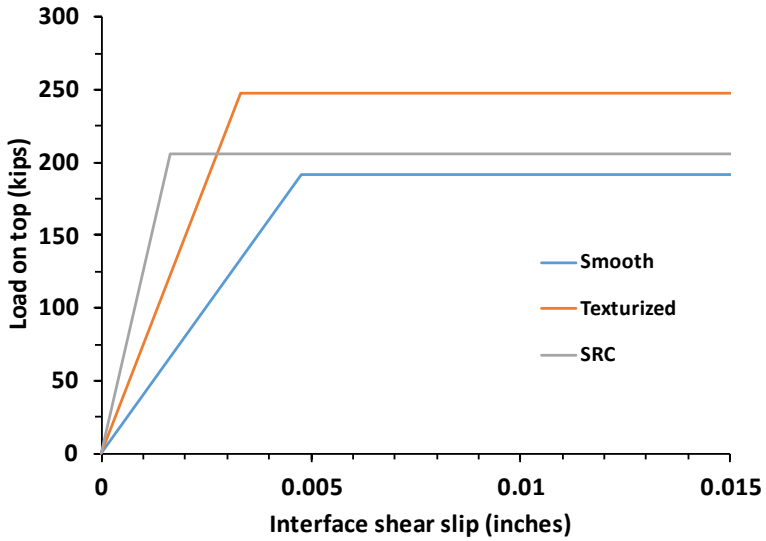

Figure 6-7: FEA Results of all Interfaces in terms of Load-Slip Behavior (Kotha, 2024)

6.1.5. Summary

- An interface model simulating the experimental push-through specimens was prepared using ATENA 3D. A step-by-step procedure that can be used to determine appropriate interface parameters was introduced. The procedure is applicable for smooth, texturized (by sandblasting), and SRC interfaces, which are beneficial to modeling the precast column specimens in the upcoming test program.

- The determined interface parameters were calculated and validated against the test results. Besides, the analysis results are in good agreement with the experimental results.

6.2. Cast in place (CIP) column 3D Modeling and Analysis

In this section, finite element analysis of Specimen S1-CIP, which was cast in the laboratory and tested by axial loading with eccentricities of 6 in., 12 in., and 40.25 in. Analysis results, comparison with experimental results, and other parameters of FEA are discussed in a detailed manner. Reasonable agreement with experimental results of the CIP column model is essential for accurate simulation of relatively involved precast column models. Before discussing the analytical model details, components of the experimental specimen are discussed in section 4.2.1 and 4.2.2.

6.2.1. Model Preparation

This section addresses the modeling methodology which includes material properties, model configurations/boundary conditions, meshing, and numerical monitoring points.

6.2.1.1. Material Model and Properties for Concrete

Concrete material in the FE analysis was modeled as CC3DNonLinCementitious2 in the software. Important parameter compressive strength was evaluated in the laboratory, and other parameters like elastic modulus and tensile strength were calculated based on ACI 318-19 given by Eq. (6-1) and Eq. (6-2) respectively. In addition, the specific fracture energy G_F was calculated based on the recommendation given by Eq. (6-3) (Rejane et al. 2014).

All the other material properties were kept default. Table 6-5 summarizes the material properties used for the column and the footing and the concrete material properties of the SCC (Class H) used for the bent cap. (ATENA 2021).

Table 6-5. Material Parameters of Concrete for Column-Footing and Bent Cap

Subset	Parameters	Column-Footing		Bent Cap	
		Applied Value	Unit	Applied Value	Unit
Basic	Elastic modulus, E_c	3.420E+03	ksi	5.534E+03	ksi
	Poisson's ratio, v	0.200	-	0.200	-
	Tensile strength, f'_t	2.770E-01	ksi	3.884E-01	ksi
	Compressive strength, f'_c	-5.234E+00	ksi	-9.426E+00	ksi
Tensile	Specific Fracture energy, G_F	2.840E-04	kip/in.	3.823E-04	kip/in.
	Crack spacing, s_{max}	Inactivated		Inactivated	
	Tension stiffening, c_{ts}	Inactivated		Inactivated	
	Unloading	Inactivated		Inactivated	
Compressive	Critical compression displacement, w_d	-1.969E-02	in.	-1.969E-02	in.
	Plastic strain at compressive strength, ε_{cp}	-8.285E-04	-	-1.046E-03	-
	Reduction of comp. strength due to cracks, $r_{c,lim}$	0.8	-	0.8	-
Shear	Crack Shear Stiff. Factor, S_F	20.0	-	20.0	-
	Aggregate interlock, MCFT	Activated		Activated	
	Aggregate Size	0.787	in.	0.787	in.
Miscellaneous	Fail. Surface eccentricity	0.520	-	0.520	-
	Multiplier for the plastic flow dir. β	0.000	-	0.000	-
	Specific material weight, ρ	8.473E-05	ka	8.473E-05	ka
	Coefficient of thermal expansion, α	6.667E-06	1/°F	6.667E-06	1/°F
	Fixed crack model coefficient	1.000	-	1.000	-

6.2.1.2. Reinforcement Material Model

Two reinforcement types were used in this model: regular reinforcing bars with a yield strength of 65 ksi, and high-strength strands with an ultimate strength of 270 ksi. For that reason, two separate stress-strain profiles were taken into consideration. However, the same bilinear with strain hardening relationship, the CCReinforcement model was implemented. As shown in Figure 6-8, the model required the elastic modulus of steel (E_s) and yield stress of steel (R_s). In addition, steel load plates were also modeled for loading in the FE analysis. In summary, regular reinforcement and load plates were assigned with the material properties shown in Table 6-6; prestressing strands were assigned with properties in Table 6-7.

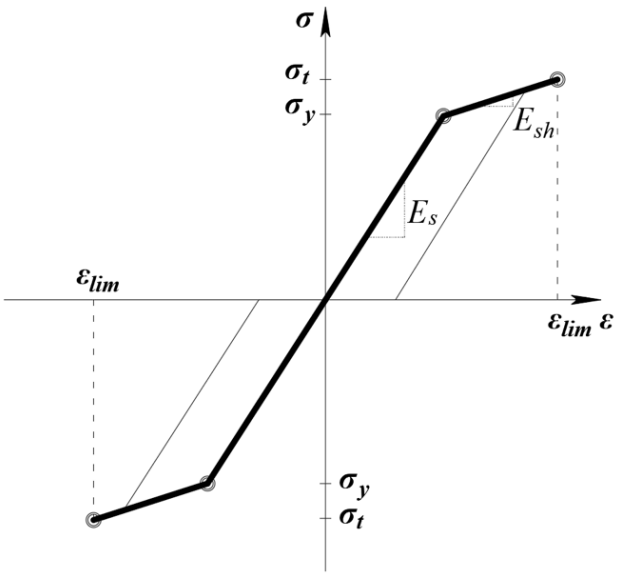

Figure 6-8: Bilinear Stress-Strain Law for Reinforcement in ATENA 3D (ATENA Theory, 2021)

Table 6-6. Assigned Material Parameters of Reinforcement and Load Plates

Subset	Parameters	Applied Value	Unit
Basic	Elastic modulus, E	2.901E+04	ksi
	Yield strength, σ_y	65.450	ksi
	Ultimate strength, σ_t	82.080	ksi
	Strain at fracture, ε_{lim}	0.027	-
Miscellaneous	Specific material weight, ρ	2.892E-04	ka
	Coefficient of thermal expansion, α	6.667E-06	1/°F

Table 6-7. Assigned Material Parameters of Prestressing Strand

Subset	Parameters	Applied Value	Unit
Basic	Elastic modulus, E	2.901E+04	ksi
	Yield strength, σ_y	230.000	ksi
	Ultimate strength, σ_t	270.000	ksi
	Strain at fracture, ε_{lim}	0.109	-
Miscellaneous	Specific material weight, ρ	2.892E-04	ka
	Coefficient of thermal expansion, α	6.667E-06	1/°F

Most of the reinforcement was assumed to be perfectly bonded with the concrete, except for several areas where imperfect bond behavior was considered. In particular, the bond behavior of reinforcement extending in footing-to-column connection and bent cap-to-column was incorporated as it is crucial to the connections. The bond behavior depends on the reinforcement

type, concrete mechanical properties, confinement, and cover thickness. Moreover, the bond degrades after experiencing a certain stress level.

Based on the confining reinforcement, clear cover, and space between bars, the code categorizes two failure modes: pull-out failure and splitting failure (CEB-FIP 2010). The bond stress-slip relationships of the two categories are schematically in Figure 2-41. It can be seen in the figure that pull-out behavior is more efficient than splitting behavior with a more ductile-like post-peak behavior. In the case of the FE model for the CIP specimen, suitable confinement and sufficient clear cover were provided; therefore, the pull-out failure category was applied, described by the solid red line in Figure 2-41.

In order to define the bond stress-slip relationship of pull-out failure, slip parameters s_1, s_2, and s_3 are determined depending on the clear cover of the reinforcement, and bond stress parameters τ_{bmax} and τ_{bf} depending on the compressive strength of the concrete. The initial curve portion has the relation provided in Eq. (6-10, and alpha in the equation was 0.4 for this FE analysis, as suggested by the code. In summary, software-generated parameters were used, as presented in Table 6-8, for the FE analysis.

$$\tau_b = \tau_{bmax}\left(\frac{s}{s_1}\right)^{\alpha} \tag{6-10}$$

Table 6-8. Parameters Defining the Bond Stress Slip Relationship of Reinforcement

Parameter	Value
τ_{bmax}	1.807 ksi
S_1	0.0394 in.
S_2	0.079 in.
S_3	0.625 in.
α	0.400
τ_{bf}	0.400 τ_{bmax}

A different bond model was assigned to all the prestressing reinforcement to represent the FE model to the CIP specimen. When released, the prestressing force was not constant on the entire length of the bent cap. Instead, the prestressing force developed at the ends was minimal, and the full prestressing was gradually achieved after the transfer length. To model the mechanism, a predefined reinforcement bond model named Bigaj 1999 was used in ATENA 3D software. Similarly, an automated bond model was generated with the inputs of bar diameter, concrete properties, and bond quality, as shown in Figure 6-9. Studies have shown that this bond model is in good agreement with the test results of prestressed end zones (Hossein et al. 2018).

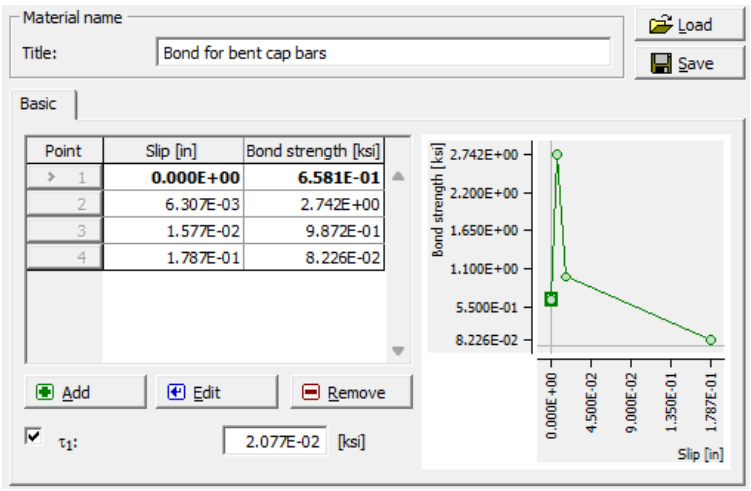

Figure 6-9: Input Bond Stress-Slip Relationship for Prestressing Strands

6.2.1.3. Macroelements, Meshing, and Boundary Conditions

All the solid concrete and auxiliary members (the column, the footing, the bent cap, and steel plates) in ATENA 3D were modeled as macroelements. After generating geometries of the members, suitable material properties were assigned accordingly. Reinforcement was modeled as 1-D elements, with the diameter and the type (i.e., smooth/ribbed) as input. Similarly, material properties for the reinforcement and prestress were assigned again accordingly.

The macroelements were then meshed into elements with desired sizes and mesh types: hexahedral or tetrahedral. According to ATENA, hexahedral elements are advised for typical cuboidal macroelements and tetrahedral for other shapes like cylindrical and shell elements. For that reason, macroelement mesh shapes and sizes were chosen in this manner: the footing presented a mesh using 8-node hexahedral elements of 12 in., the bent cap used 8-node hexahedral elements of 6 in., and the column, which was considered the area of interest, to 4-node tetrahedral elements of 4 in. for more refined analytical results, as shown in Figure 6-10. The bent cap and the column are meshed relatively finer because those were the elements that undergo prestressing and loading, respectively. Even though the experimental specimen was cast and placed on the ground without constraining in horizontal directions, the FE model's bottom surface of the footing was fixed in all three X, Y, and Z directions, as shown in Figure 6-11. This is followed to ensure that the column does not undergo any displacement during both prestressing and loading phases.

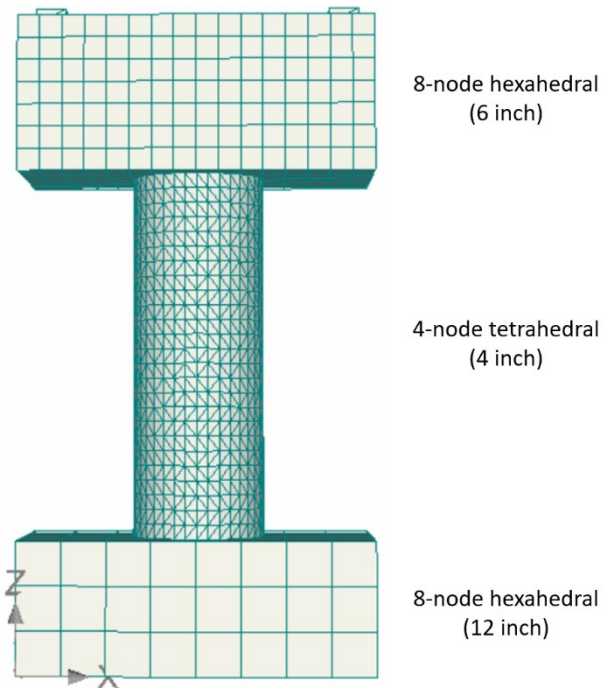

Figure 6-10: Meshed Finite Element Model for CIP column (Kotha, 2024)

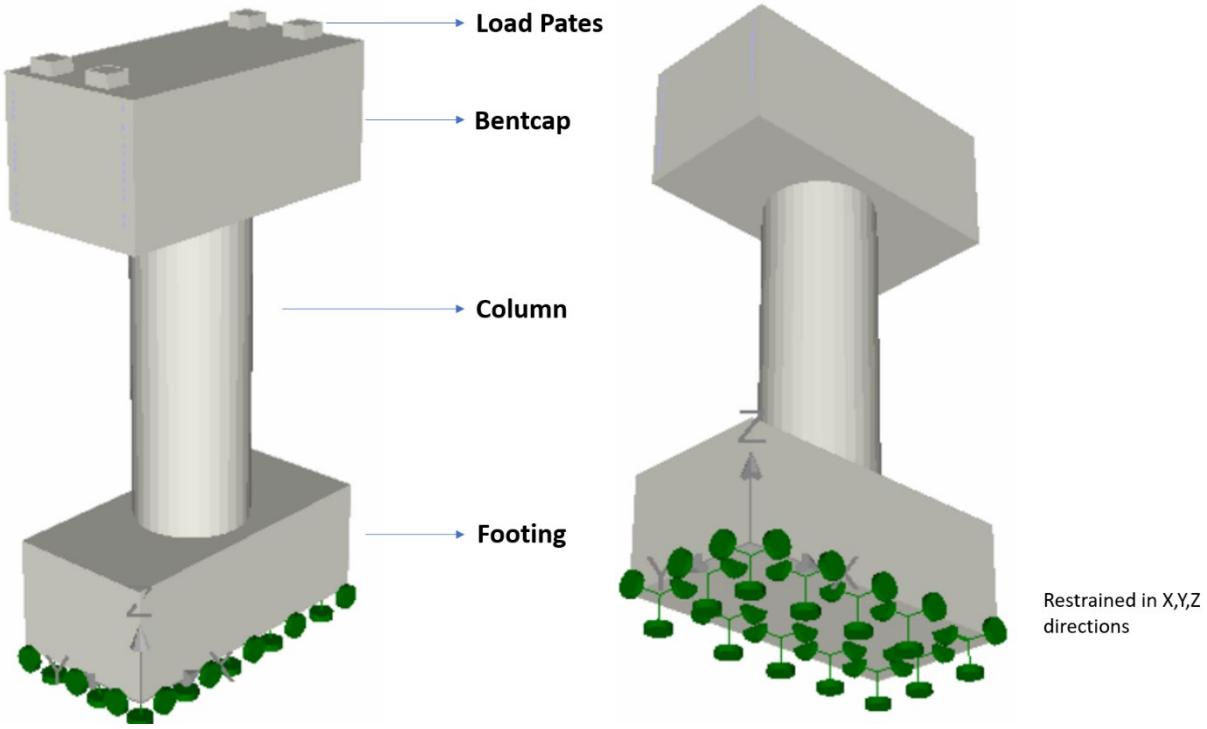

Figure 6-11: CIP Model with Components and Supports (Kotha, 2024)

6.2.1.4. Prestressing the Bent Cap

The bent cap was reinforced with prestressing strands that were prestressed to 75% of f_{pu}, which was 202.5 ksi. Sixteen prestressing strands with 0.6-in. diameter were used to prestress the bent cap on either side. Each prestressing strand was seven-wired with an ultimate tensile strength of 270 ksi and had a total effective area of 0.217 in^2. To achieve 75% of f_{pu}, each strand was tensioned with a force of 43.94 kips (0.75 times tensile strength time effective area), as shown in Figure 6-12.

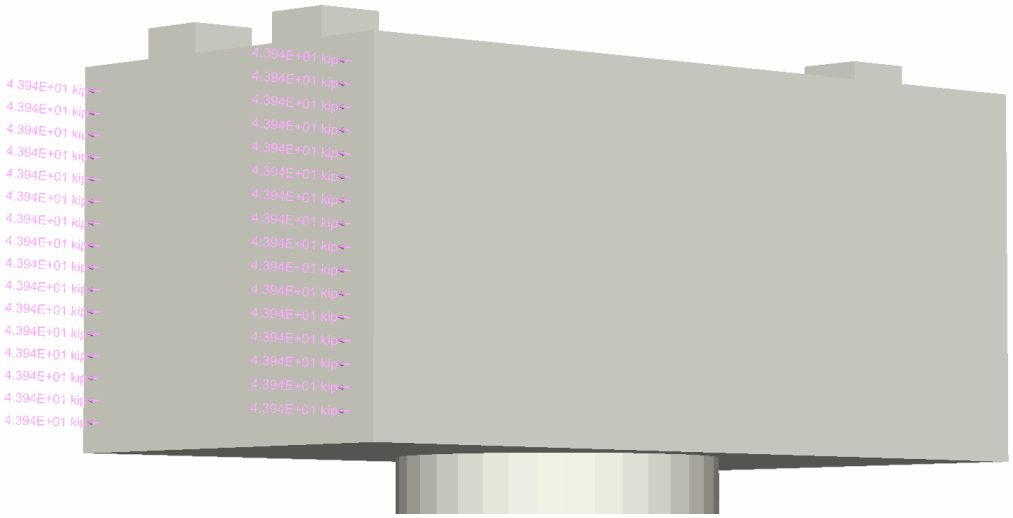

Figure 6-12: Bent Cap being Prestressed to 75% of f_{pu} (Kotha, 2024)

After assigning the bond model to all the reinforcement, the bent cap was numerically prestressed. As anticipated, some portions near both ends of the strands were not in prestressing (yellow and orange regions), as shown in Figure 6-13, and the complete prestressing (bright red regions) was developed at approximately 17 in. away from the face of the bent cap.

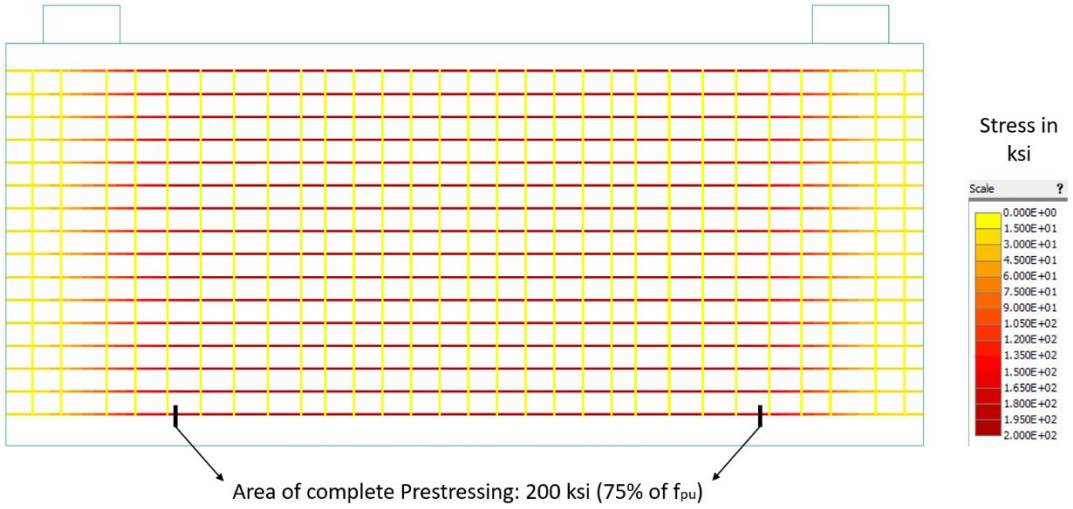

Figure 6-13: Principal Stress in Strands After Release (Kotha, 2024)

6.2.1.5. Monitoring Points

In ATENA 3D, the analytical values of deformation and deflection of structure, responding to the applied load, can be captured by applying monitoring points. In this case, monitoring points were distributed to the numerical structure, as shown in Table 6-9 and Figure 6-14.

Table 6-9. Assigned Monitors for Full-Scaled Cast-in-Place Specimen

Monitor	Purpose
A	A monitor for measuring the vertical deflection was assigned under the bent cap.
B-1 (Mid Height) **B-2 (Top)**	A monitor for capturing the horizontal displacement of the column was applied at the mid-height and top of the tension side of the column.
C-1 **C-2**	Vertical displacement monitors were applied to capture the strain at the bottom of the column joint, for calculating the curvature

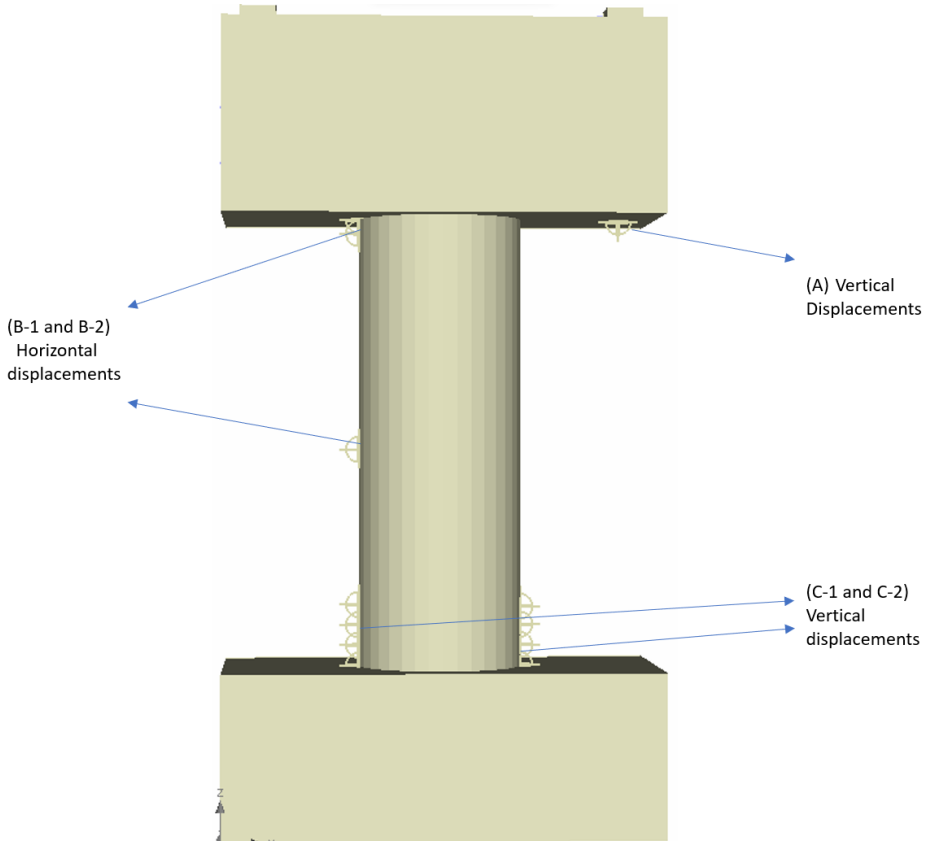

Figure 6-14: Monitors Location for FEM of CIP column (Kotha, 2024)

6.2.2. FE Model Validation

This section compares the analytical and experimental results derived from testing the large-scale CIP specimen. The comparison specifically focuses on the displacement data.

6.2.2.1. Axial Load versus Displacement Curves

The test axial load-displacement curves were selected to validate the developed FE model. The analytical axial load-displacement curves derived from ATENA 3D presented in previous sections were plotted and super-positioned with corresponding experimental ones, as shown in Figure 6-15 through Figure 6-17 for the analysis cases of 6-in., 12-in., and 40.25-in. in the eccentricity, respectively. In the figures, the blue curve represents results at mid-height, and the orange represents the top. The dotted line shows the FEA results, which are the same as discussed in previous sections. The solid line represents the experimental results, which are not smooth because of the loading scenario used to achieve the desired eccentricity for each load increment in the experimental program. The solid line connects all the checkpoints, resembling the load steps used in the FE analysis.

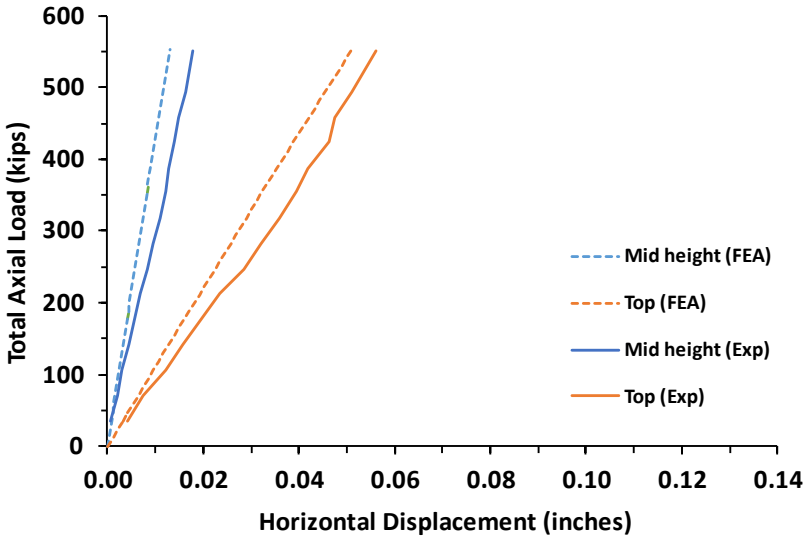

Figure 6-15: Comparison of 6-in. Eccentricity Analytical and Experimental Results (Kotha, 2024)

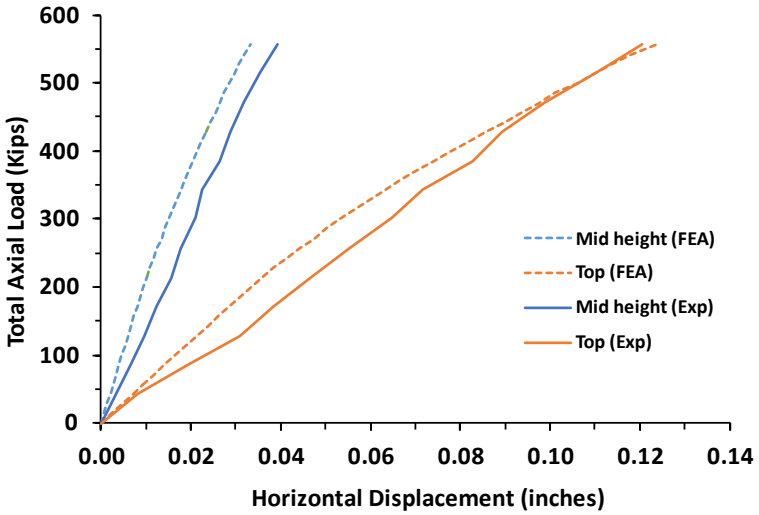

Figure 6-16: Comparison of 12-in. Eccentricity Analytical and Experimental Results (Kotha, 2024)

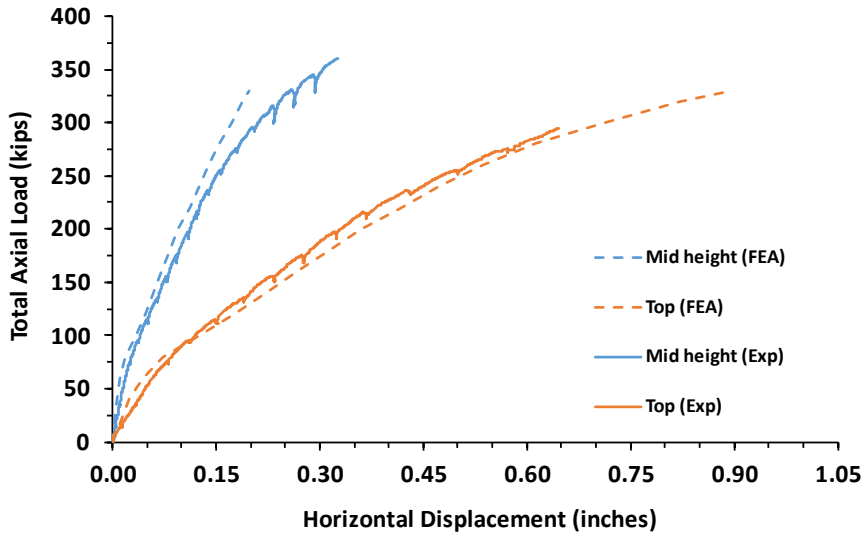

Figure 6-17: Comparison of 40.25-in. Eccentricity Analytical and Experimental Results (Kotha, 2024)

It should be noted that the experimental CIP specimen was able to sustain a load as high as 360 kips under a load with a 40.25-in. eccentricity, but experimental deflection data at the top of the column was lost after 290 kips due to the stroke limit of the linear potentiometer. On the other hand, the FEA indicated that the column failed at a load of 340 kips.

As observed from all the graphs, firstly, the analytical column displacements under all eccentricity loadings were similar to the respective experimental ones. The software was able to properly capture the increase of the displacement in terms of linear or nonlinear behaviors for different eccentricities. Secondly, the analytical displacement values at the end of tests were also accurate compared to experiment values, especially for 12-in. and 40.25-in. eccentricity loading. The model built in ATENA 3D behaved stiffer than the experimental specimen built in the lab; the numerical displacements at the mid-height of the column were smaller. However, the values were almost the same at the top of the column, as seen in Table 6-10. In particular, the mid-height had an average percentage difference of -21.97%. Nevertheless, the top of the column had a significantly lower average error percentage of only -1.15%. Overall, it can be concluded that the FE model is slightly stiffer, but the analytical displacement values were in reasonable agreement.

Table 6-10. Horizontal Displacement Values for all the Loading Cases at the End of Test

Eccentricity	Monitoring point	FEA value (in)	Experimental value (in)	% Difference
6 in.	Mid height	0.013	0.0179	-27.4%
	Top	0.0512	0.0562	-8.9%
12 in.	Mid height	0.0332	0.039	-14.9%
	Top	0.124	0.121	2.5%
40.25 in.	Mid height	0.199	0.260	-23.62%
	Top (@ 280 kips)	0.613	0.596	2.95%

6.2.3. FE Analysis and Discussion

6.2.3.1. CIP Specimen under 6-in. Eccentricity Load Pattern

After preparing the FE model mentioned in previous sections, the load was applied on either side of the bent cap maintaining a ratio of 1.35 to create a 6-in eccentric axial load in the column, resembling the experimental setup. In the experiment, the column was loaded until 552 kips of total axial load on the column was achieved (15% of the theoretical axial compressive capacity of the column). To simulate the experimental loading procedure, the numerical column was loaded by 5 kips on one side, divided by two load plates, and similarly, 6.75 kips on the other side in each load step, as shown in Figure 6-18, and 47 load steps were applied to reach the final load level.

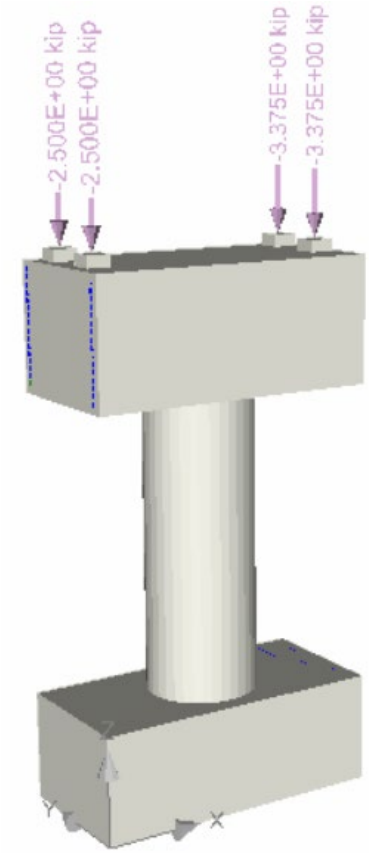

Figure 6-18: Loading Setup for 6-in. Eccentricity Analysis (Kotha, 2024)

The loading resulted in a few fine cracks at the top of the column on the tensile side at a load level of 550 kips in total, as shown in Figure 6-19(a). In the middle of the numerical test at a load level of 530 kips, it was observed that principal tensile stress on the upper tension side of the column reached 280 psi, resulting in horizontal cracks. At the end of the test, some other regions of the central column reached almost 240 psi. On the compression side of the column, no cracks or crushing was observed, and the maximum principal compressive stress was 0.7 ksi at the bent cap-column connection on the top, as shown in Figure 6-19(b). The principal compressive stress was only almost 15% of f'_c, hardly causing vertical cracks or signs of crushing. Cracks and stress levels

on the bent cap are due to prestressing before testing, which did not affect the column during loading.

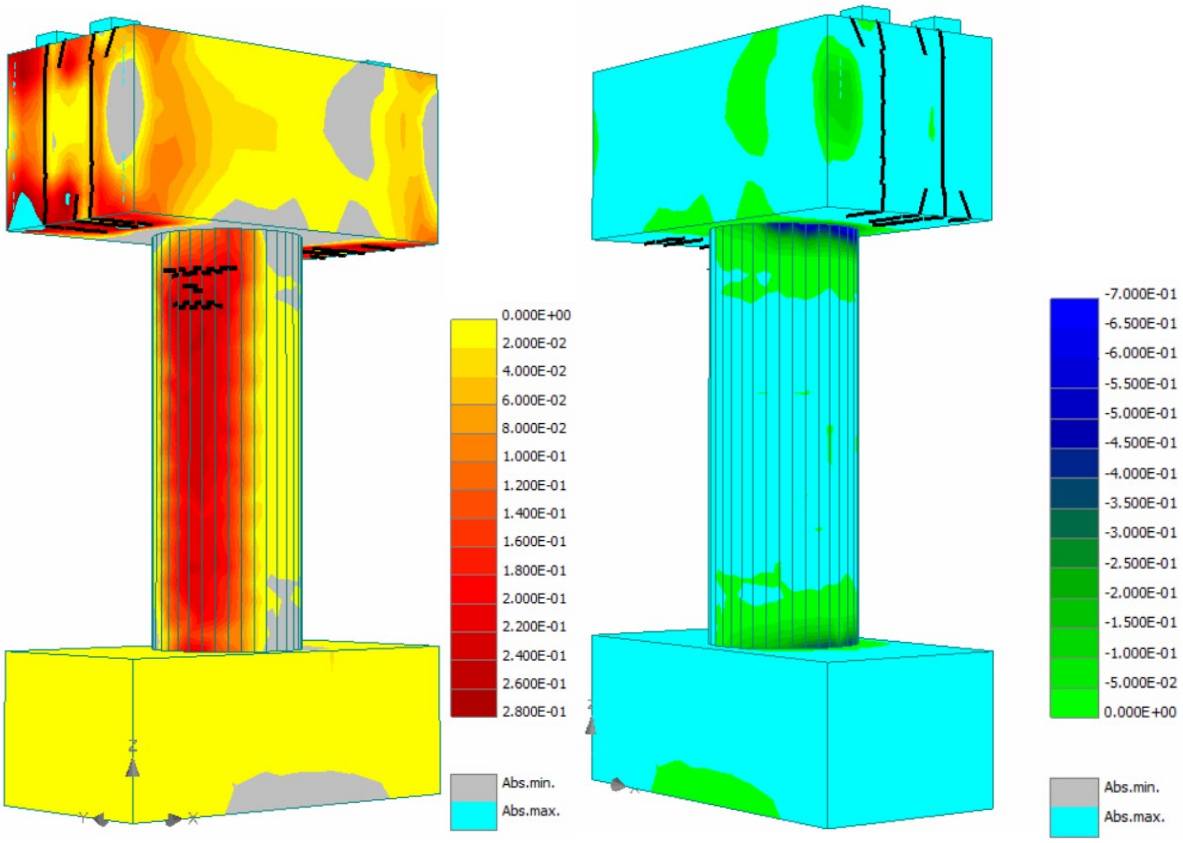

(a) Tensile side (b) Compressive side

Figure 6-19 Stress Levels in ksi and Cracking at the end of 6-in. Eccentricity Loading (Kotha, 2024)

The column was meshed into 4-in. tetrahedral elements, making it 24 elements through the height, which was considered sufficiently fine to predict the displacements and concrete strain accurately per the ATENA manual (Vladimír et al., 2021). This particular mesh size was selected to calculate the strain at the bottom of the column. The strain in the experimental specimen was calculated by using LVDTs at 4.5 in. intervals at either side of the column, so each element was given a dimension of 4 in. to calculate the deformations. At each load step, displacements at monitoring points B-1 and B-2 were extracted to represent the horizontal displacements at the top and the mid-height, respectively, for the establishment of the load-displacement curve, as presented in Figure 6-20. It should be noted that the y-axis represents the total axial load taken by the column, which was the summation of loads on both compressive and tensile sides.

Similarly, strain values are calculated by tracking the vertical displacement at the bottom of the column at 4.5-in. intervals, from C-1 and C-2 monitoring points. From this data, the moment-curvature (M-ϕ) curve is provided in Figure 6-21. Each point represents the M-ϕ value for a load

step of total axial load 11.75 kips. The moment at a particular load step can be calculated using Eq. (6-11). As the load plates are 40.25 in. away from the center of the column, the applied force multiplied by this distance gives the moment on the column. And curvature can be calculated by Eq. (6-12), the resultant strain divided by the dimension of the column's diameter which is 36 in.

$$\text{Moment (kip-in)} = P_c(40.25\text{ in.}) - P_t(40.25\text{ in.}) \tag{6-11}$$

$$\text{Curvature}\left(\frac{1}{\text{in.}}\right) = (\varepsilon_c - \varepsilon_t)/36\text{ in.} \tag{6-12}$$

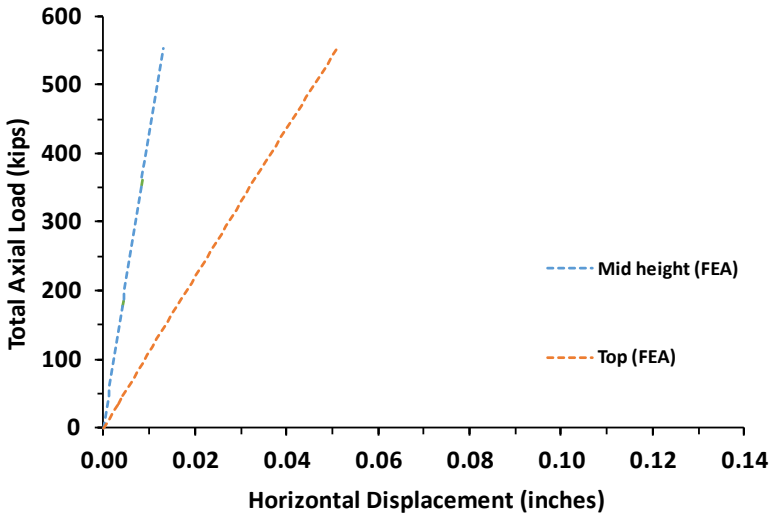

Figure 6-20: Total Axial Load-Displacement Behavior for 6-in. Eccentricity Loading (Kotha, 2024)

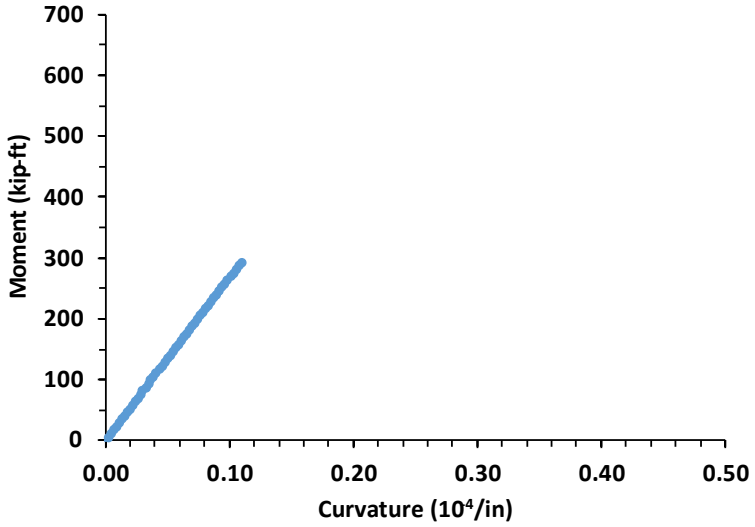

Figure 6-21: Moment-Curvature Plot for 6-in. Eccentricity Loading (Kotha, 2024)

As seen from the graphs, the displacements and curvature values increased proportionally with load increment, which suggests that the column remained in the elastic region. Along with that, reinforcement in the tensile region reached a maximum strain of approximately 3.5×10^{-4}, which was much lower than the yield strain of 2.07×10^{-3}. Also, the cracks in the top region were not significant enough to cause a softening in the load-displacement relationship. In conclusion, the column was in the elastic region with a maximum horizontal displacement of 0.0512 in. at the top, and a few cracks appeared at the top of the column.

6.2.3.1.1. 6-in. Eccentricity Analysis Crack Comparison

In the FE analysis, after the application of 550 kips of total axial load, the tension side reached a tensile stress close to 240 psi. Some upper parts of the column past 280 psi (the tensile strength of concrete), resulting in horizontal tensile cracks 6-7 feet from the bottom. As seen in Figure 6-22, cracks formed in the upper column at approximately 5 ft from the bottom in the large-scale specimen, where the ATENA FE model indicated that the concrete reached 90% of the tensile strength. The analytical cracking pattern agreed with the experimental one in general. The cracking patterns were unexpected according to sectional analysis, but it was captured by ATENA 3D.

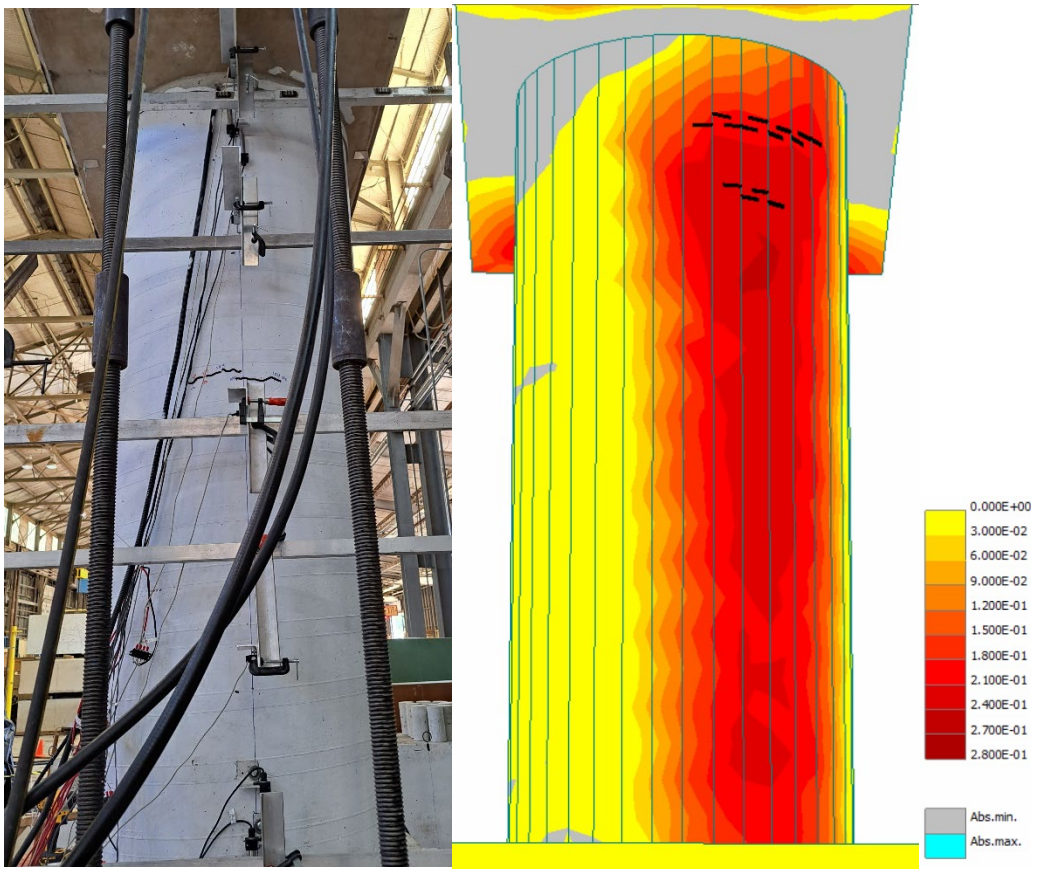

Figure 6-22: Comparison of Crack Pattern at the end of 6-in. Eccentricity Loading (stress levels in ksi) (Kotha, 2024)

6.2.3.2. CIP Specimen under 12-in. Eccentricity Load Pattern

For the 12-in. eccentricity loading, the Specimen S1-CIP was similarly loaded on both sides of the bent cap, maintaining a ratio of 1.85. The analysis was carried out until the total axial load reached 552 kips (approximately 15% of the theoretical axial compressive capacity of the column). To simulate the load pattern, the numerical column was loaded by 5 kips on one side, divided by two load plates, and similarly, 9.25 kips on the other side of the bent cap element in each load step, as shown in Figure 6-23.

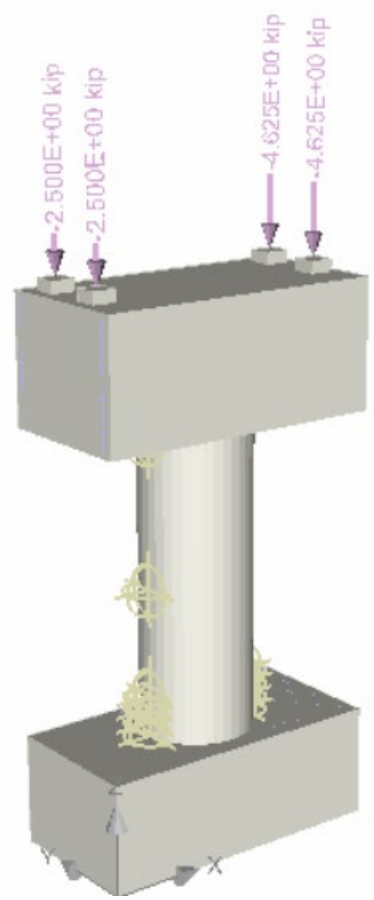

Figure 6-23: Loading Setup for 12-in. Eccentricity Analysis (Kotha, 2024)

This eccentricity axial loading resulted in many horizontal cracks on the tensile side, as seen in Figure 6-24(a). In the figure, cracks wider than 0.0025 in. are displayed for readability. These cracks started at the 10^{th} load step, corresponding to a total axial load of 142.5 kips. The cracks propagated and widened until the total load reached 552 kips. These cracks appeared through the entire column height, as the concrete experienced tensile stresses greater than the tensile strength (280 psi). When cracks formed, concrete near the cracks no longer took tensile stress, as indicated by the yellow regions in the figure. Coming to the compression side shown in Figure 6-24(b), the mid-height of the column did not take compressive stress, but the column-bent cap and column-footing connections did experience compressive stress with a magnitude of approximately 1.1 ksi,

or 22% of the compressive strength of the concrete; therefore no crushing nor vertical cracks were observed.

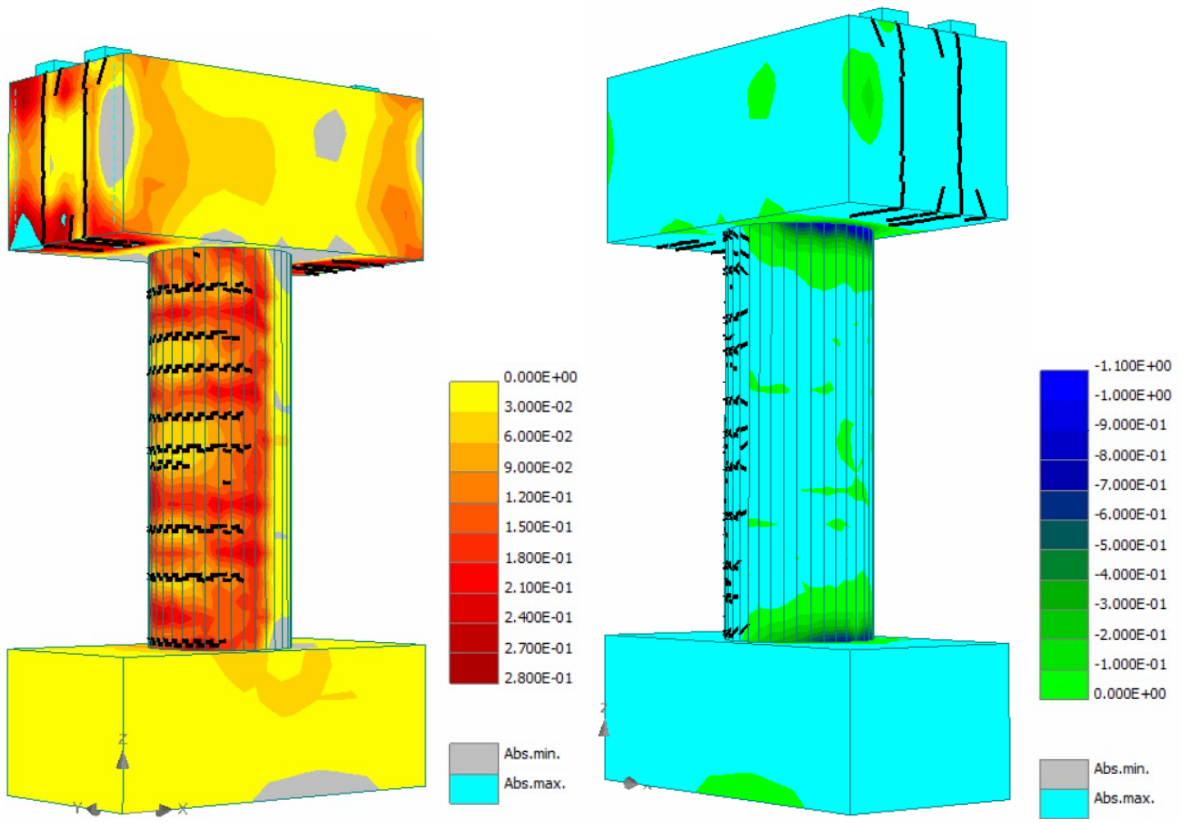

(a) Tensile side (b) Compressive side

Figure 6-24: Stress Levels in ksi and Cracking at the end of 12-in. Eccentricity Loading (Kotha, 2024)

Similar to the previous case, the column had a 4-in. mesh, making 24 elements through the entire height. From the monitoring points data at each load step, load-displacement relationships extracted from monitoring points B-1 and B-2 were plotted as shown in Figure 6-25. The Y axis of this chart is the total axial load acting on the column. In addition, the moment-curvature relationship was plotted as shown in Figure 6-26.

Unlike the column under the 6-in. eccentricity axial loading, the displacement and curvature were not linear with the increase in load. A change of stiffness was observed gradually, and extensive cracking of concrete as well as higher tensile stress in the reinforcement at the mid-height of the column was observed.

As seen in load-displacement curves, the top has reached almost 0.124 in., more than double that of the case under 6-in. eccentricity at the same total axial load of 550 kips. The displacement at the top is 3.73 times that of the one at the mid-height of the column, indicating the column behaved like a cantilever beam with a moment acting at the end (curvilinear shape).

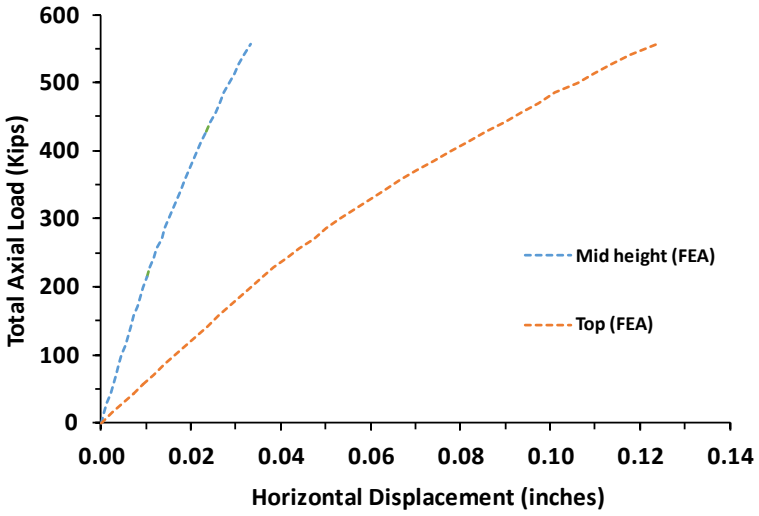

Figure 6-25: Total Axial Load-Displacement Behavior for 12-in. Eccentricity Loading (Kotha, 2024)

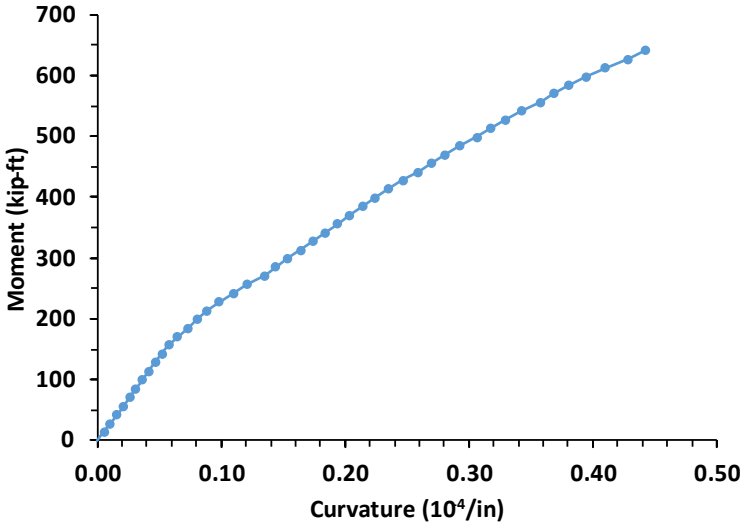

Figure 6-26: Moment-Curvature Plot for 12-in. Eccentricity Loading (Kotha, 2024)

In the case of the moment-curvature relationship shown in Figure 6-26, linearity was observed until 200 kip-ft, corresponding to the total axial load of approximately 200 kips. At the load step, a change of slope was observed and attributed to the crack initiation of concrete in the tensile region. It should be noted that the phenomenon was not observed in the case of 6-in. eccentricity, as the cracking of concrete was barely initiated.

6.2.3.2.1. 12-in. Eccentricity Analysis Crack Comparison

In the case of 12-in. eccentricity, concrete in most regions of the column reached 280 psi in tensile stress under 550 kips of the total axial loading in the ATENA 3D model, causing the entire column to experience horizontal cracks on the tension side, as shown in Figure 2-27. It should be noted

that a crack filter of 0.005 in. was applied for better visualization of essential cracks. At the end of the test, as seen from the experimental case, five horizontal cracks were distributed evenly from top to bottom in general, which was captured by the FE analysis.

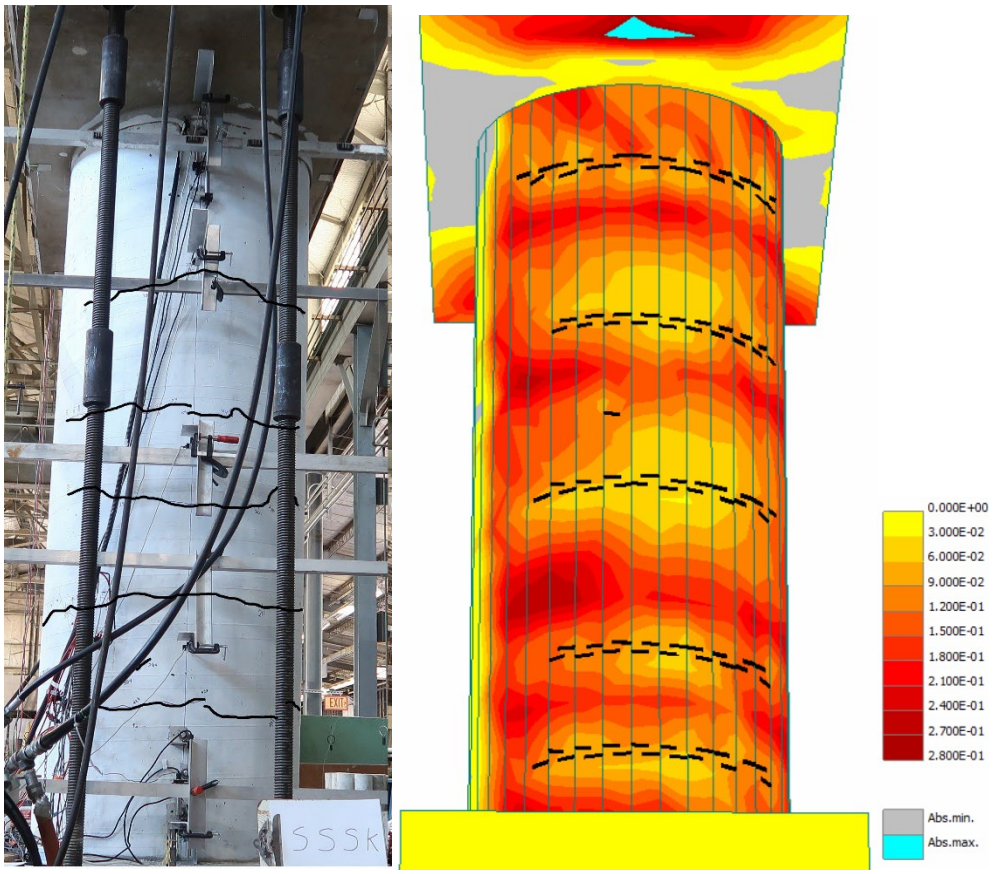

Figure 6-27: Comparison of Crack Pattern at the end of 12-in. Eccentricity Loading (Stress Levels in ksi) (Kotha, 2024)

6.2.3.3. CIP specimen under 40.25 in. Eccentricity Load Pattern

The last case was 40.25-in. eccentricity loading in which each load step consisted of 20 kips only acting on a single side, as shown in Figure 6-28. From the Axial Load- Moment curve in Figure 6-30, the column was expected to fail around 305 kips. of total axial load, but 20 load steps were added, which includes 1 load step of prestressing the bent cap. A mesh size of 4 in. was applied, making it 24 elements along the height of the column.

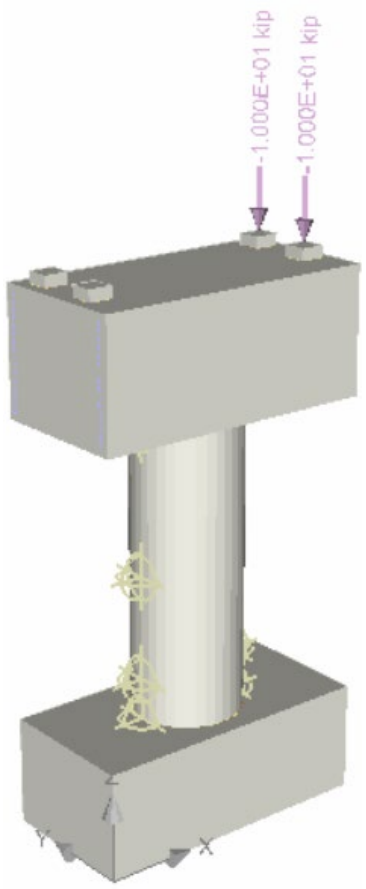

Figure 6-28: Loading Setup for 40.25-in. Eccentricity Analysis (Kotha, 2024)

After the end of the analysis, the column experienced severe cracking and failure at a total load of 340 kips due to the high eccentricity used during loading. The largest crack width was found at the tensile region of the column around the mid-height; vertical cracking and crushing of concrete cannot be seen on the compression side, indicating that the column failed by flexure, as shown in Figure 6-29. A crack filter of 0.001 in. was applied for better visualization. The cracking of concrete started at a total axial load of 50 kips, and it continued to increase up to the failing load of 340 kips. Along with that, a few cracks on the footing were also observed. Cracks and stresses on the bent cap were due to prestressing before the analysis and were considered irrelevant.

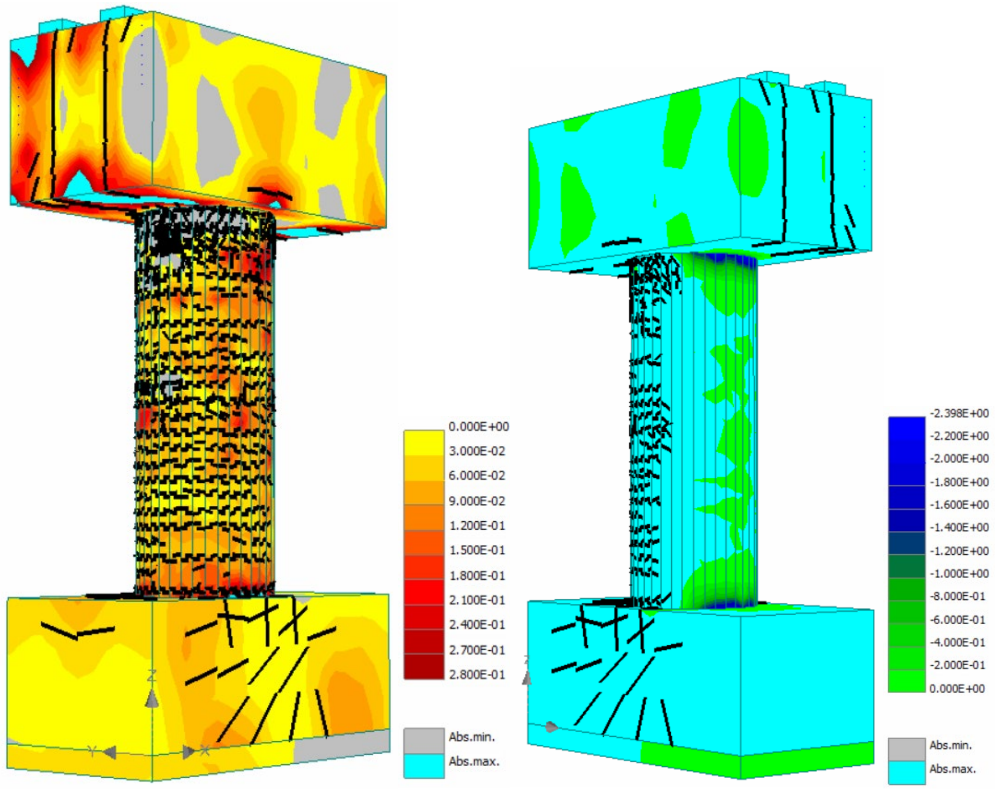

(a) Tensile side (b) Compressive side

Figure 6-29: Stress Levels in ksi and Cracking at the end of 40.25-in. Eccentricity Loading (Kotha, 2024)

The column failed at an axial load of 340 kips applied with a 40.25 in. eccentricity from the center, resulting in a bending moment of 1140.42 kip-ft. As seen from the developed P-M interaction diagram shown in Figure 6-30, the column was expected to fail at a load of 306 kips and a moment of 1026.38 kip-ft. Although this estimation from the P-M curve cannot be perfectly accurate, it can be initially checked before comparing it with experimental results.

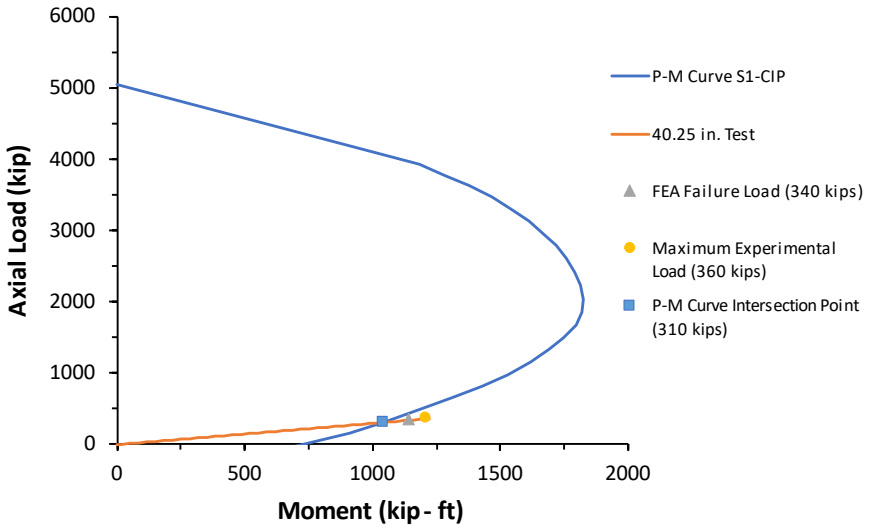

Figure 6-30: P-M Interaction Diagram of the CIP Column Specimen (Kotha, 2024)

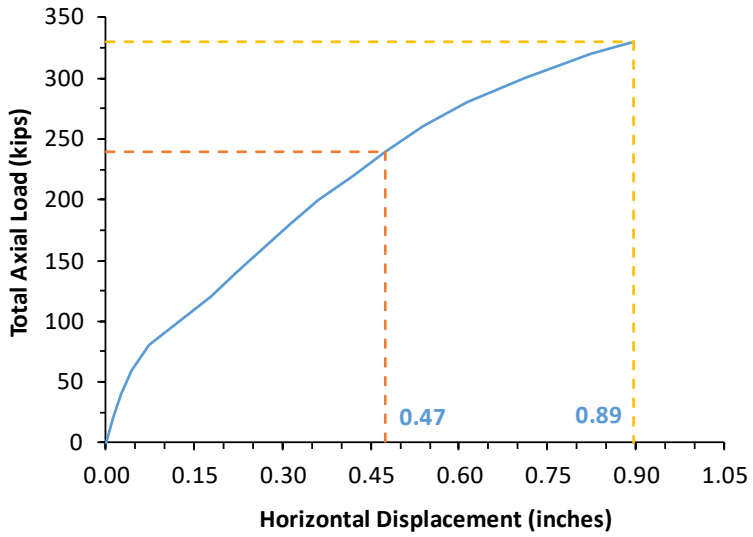

Figure 6-31: Total Axial Load-Displacement Behavior for 40.25-in. Eccentricity Loading (Kotha, 2024)

The load-displacement curve shown in Figure 6-31 indicates that the column behaved differently from the previous two cases that were relatively lower eccentricity loading. The high resulting moment led the column to experience serious cracking and yielding. In addition, the displacement at failure was 0.89 in. at the top after a higher displacement increase from 0.50 in. when the load increased from 240 kips to the failure load of 340 kips. Upon reaching a load of 250 kips, it was seen that yielding in the longitudinal reinforcing bars appeared and continued to intensify until the failure, as shown in Figure 6-32. In the figure, blue and cyan regions represent that the reinforcement bars achieved 65 ksi (yield strength). Most of the yielding was observed at the mid-height of the column and near the column-to-bent cap connection.

Figure 6-33 shows the moment-curvature plot and the behavior is similar to the load-displacement curve shown in Figure 6-31, except there was no sudden increment due to yielding. This phenomenon was attributed to the fact that the yielding was not observed at the bottom of the column, where strain values are taken for curvature calculations. Also, sharp yielding in moment-curvature curves was generally not observed in circular sections, as reinforcement in circular sections was distributed surrounding the cross-section, and yielding occurs gradually from the outermost bars into the inner bars, unlike rectangular sections where reinforcement is lumped at one particular strip. Apart from that, the sudden shift in curvature values in the middle of the analysis can be attributed to cracks at the bottom of the column and foundation.

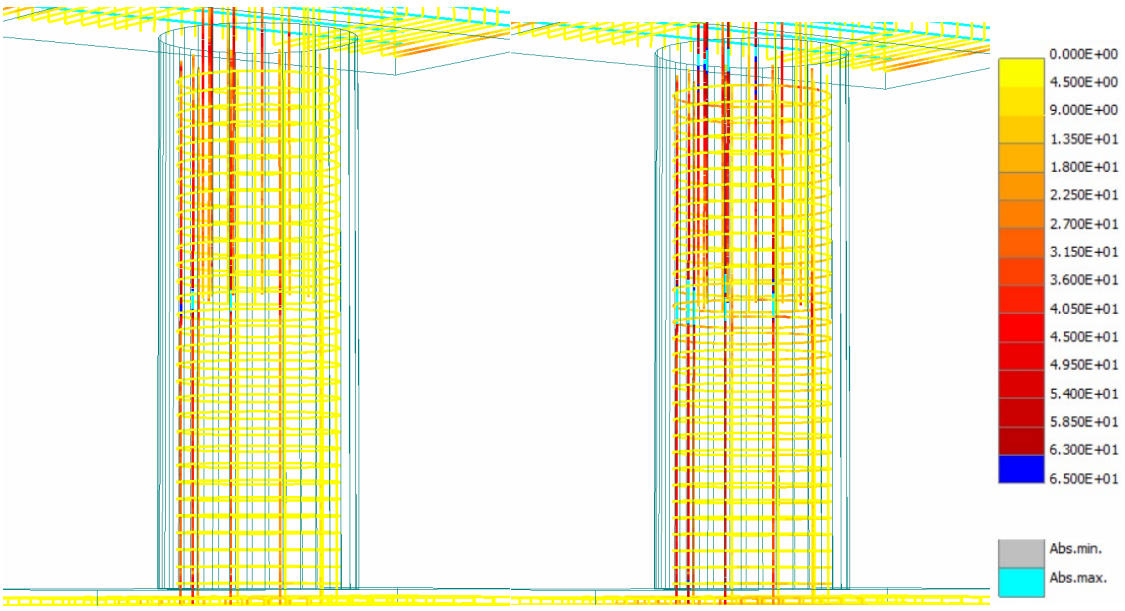

(a) 240 kips (b) 330 kips

Figure 6-32: Principal Stress (in ksi) in Reinforcement at 2 Different Axial Loads (Kotha, 2024)

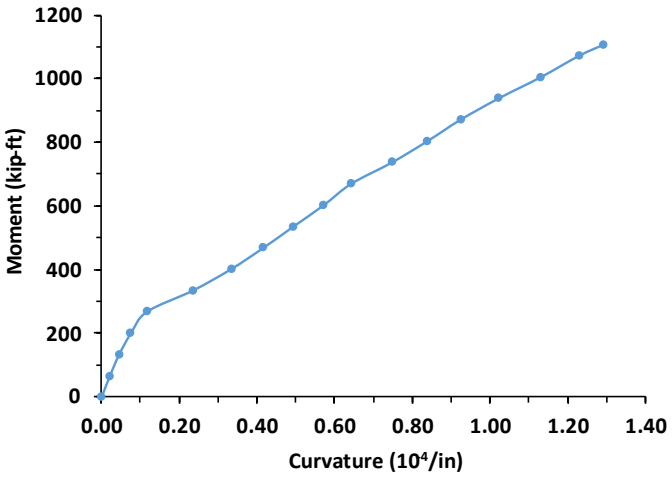

Figure 6-33: Moment-Curvature Plot for 40.25-in. Eccentricity Loading (Kotha, 2024)

6.2.3.3.1. 40.25-in. Eccentricity Analysis Crack Comparison

From Figure 6-34, the imposition of an exceedingly high eccentricity load led to many horizontal cracks along the tension side of the column. Furthermore, no vertical cracks were manifested in this same region. Conversely, a combination of vertical cracks and cracks at angles to the ground were identified around the neutral axis of the column. Notably, when progressing from the tension side to the compression side of the column, an array of tensile cracks transitioned to cracks oriented at varying angles from the horizontal.

For enhanced clarity of crucial cracks, a crack filter of 0.001 in. was applied. A parallel pattern was discerned within the experimental results. This pattern encompasses numerous evenly spaced tensile cracks traversing the column's height, complemented by intermittent vertical cracks within the tensile region. Similarly, a combination of angle-oriented and vertical cracks was detected on the neutral axis at various heights from the bottom of the column. Remarkably, both the ATENA 3D model and the physical specimen exhibited the most substantial cracks at the midpoint of the column.

The ATENA 3D model was proven to be an exemplary representation of the large-scale specimen in the lab. This consistency extends to the crack patterns observed under diverse loadings, including the 6 in., 12 in., and notably eccentricity 40.25-in. loading rates.

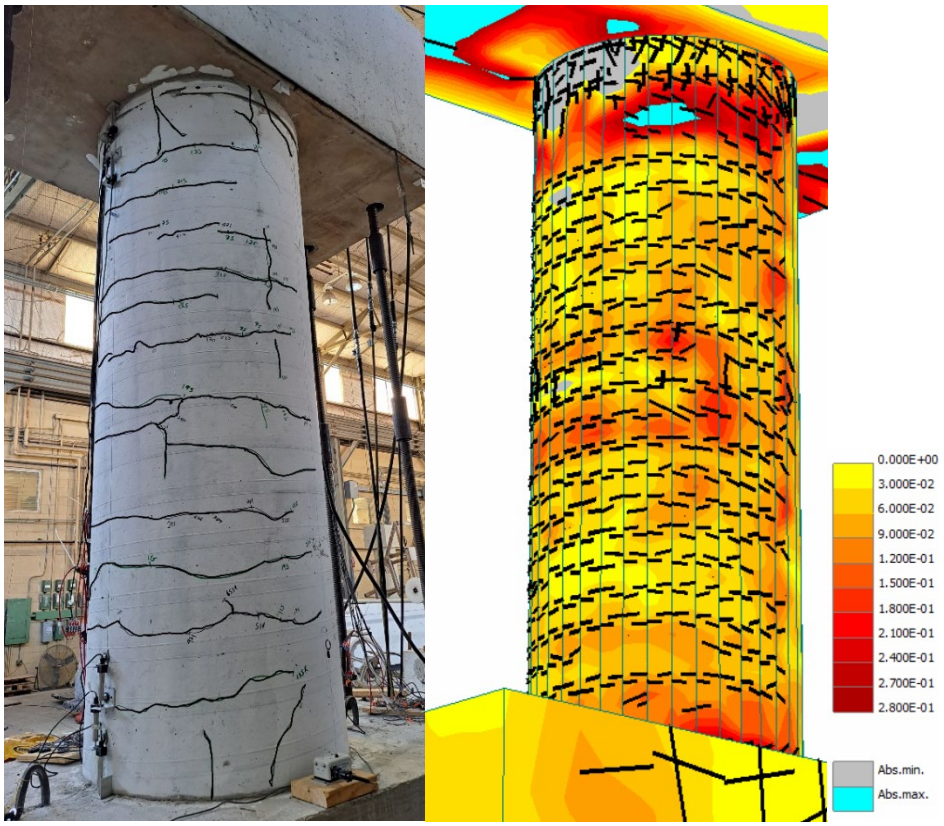

Figure 6-34: Comparison of Crack Pattern at the end of 40.25-in. Eccentricity Loading (Stress Levels in ksi) (Kotha, 2024)

6.2.4. Influence of Mesh Size and Loading Rate on the Accuracy

In this section, two parameters: mesh size and loading rate were studied and these are the only changes to the model. In the case of 40.25 in. eccentricity loading, the 8' column was divided into 24 elements with a 4 in. element size. This is relatively extremely fine because the software recommends using 4 to 12 elements per dimension for reasonably accurate results. Along with that, the model was loaded with 20 kips on the compressive side per load step, and it took 17 load steps to fail the specimen. A total of 4 models were studied in this particular section with varying mesh sizes and loading rates as shown in Table 6-11. By choosing a coarse mesh size and higher load per step, computational cost can be greatly reduced. It can be interpreted that Model 2 and Model 3 took the highest and lowest computational time, respectively.

A comparison between Model 1 and Model 2 gives an idea about the loading rate. Comparing Model 2 and Model 4 shows the effect of the mesh size. Lastly, Model 5 is the one that was adopted for the study for all eccentricity analyses presented in previous sections.

Table 6-11. FEA Models with Different Parameters for 40.25-in. Eccentricity Loading-Analysis

Model number	Mesh size	Number of Elements	Load per step	Load steps to fail
Model 1	4 in	17592	5	63
Model 2	4in	17592	2	141
Model 3	12 in	1348	5	70
Model 4	12 in	1348	2	161
Model 5	4 in	17592	20	17

6.2.4.1. Accuracy on Capacity and Displacement Estimation

From Table 6-11, it can be seen that the number of load steps taken to fail is different for each model which implies that the capacity of the column was affected by mesh size and loading rate. As seen in Figure 6-35, each model has a different endpoint, and numerical details have been presented in Table 6-12.

Firstly, a slight capacity increase can be seen from Model 1 to Model 2 where the difference was the loading rate, and it implies that slower loading leads to premature failure without affecting the accuracy in displacement. And displacements are almost the same throughout the test except for the end regions (>250 kips). In the experimental case, the specimen was loaded 20 kips per step, which is Model 5. This model has given reasonably satisfactory results without premature failure.

On the other hand, increasing the mesh size has resulted in increased capacity but at the cost of accuracy, as seen from the difference of Model 3 to Model 4. FEA models are stiffer than experimental specimens throughout the testing, but with sufficiently finer mesh, accurate results can be achieved at the cost of computational time. Although capacity estimation is good in this case, it is not recommended as displacements recorded almost a 25% difference.

From this section, it can be said that it is best to apply the load steps followed in the experimental specimen and mesh size of 4 in. instead of 12 in., for accurate representation. Making the load per step smaller resulted in premature failure and a coarser mesh of 12 in. has given a higher error percentage when compared with experimental results.

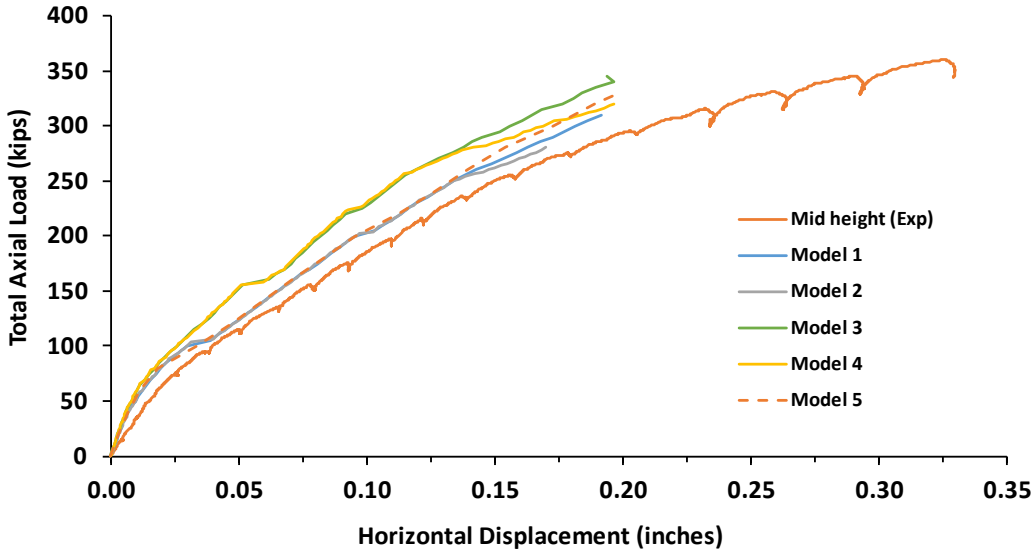

Figure 6-35: Axial Load-Displacement (Mid Height) Curves for Experimental Specimen and FEA Models (Kotha, 2024)

Table 6-12. FEA results of Different Models at the Mid-Height of the Column

Model	Capacity (kip)	Displacement @ 280 kip	Displacement @ Failure load	%Difference @ 280 kip
1	315	0.163	0.192	-11.892
2	282	0.170	0.170	-8.108
3	350	0.138	0.194	-25.405
4	322	0.142	0.197	-23.243
5	340	0.154	0.199	-16.757

6.2.4.2. Accuracy on Crack Pattern Estimation

In this subsection, crack patterns are compared between Model 1, Model 3, and experimental specimen. Model 1 and Model 3 differed in the mesh size with Model 1 being finer. It can be seen from Figure 6-36 that both Model 1 and Model 3 could accurately predict the crack pattern at failure load in the tensile region. Evenly distributed horizontal cracks throughout the column in the tensile region and they start to diverge making an angle in the central regions (neutral stress regions).

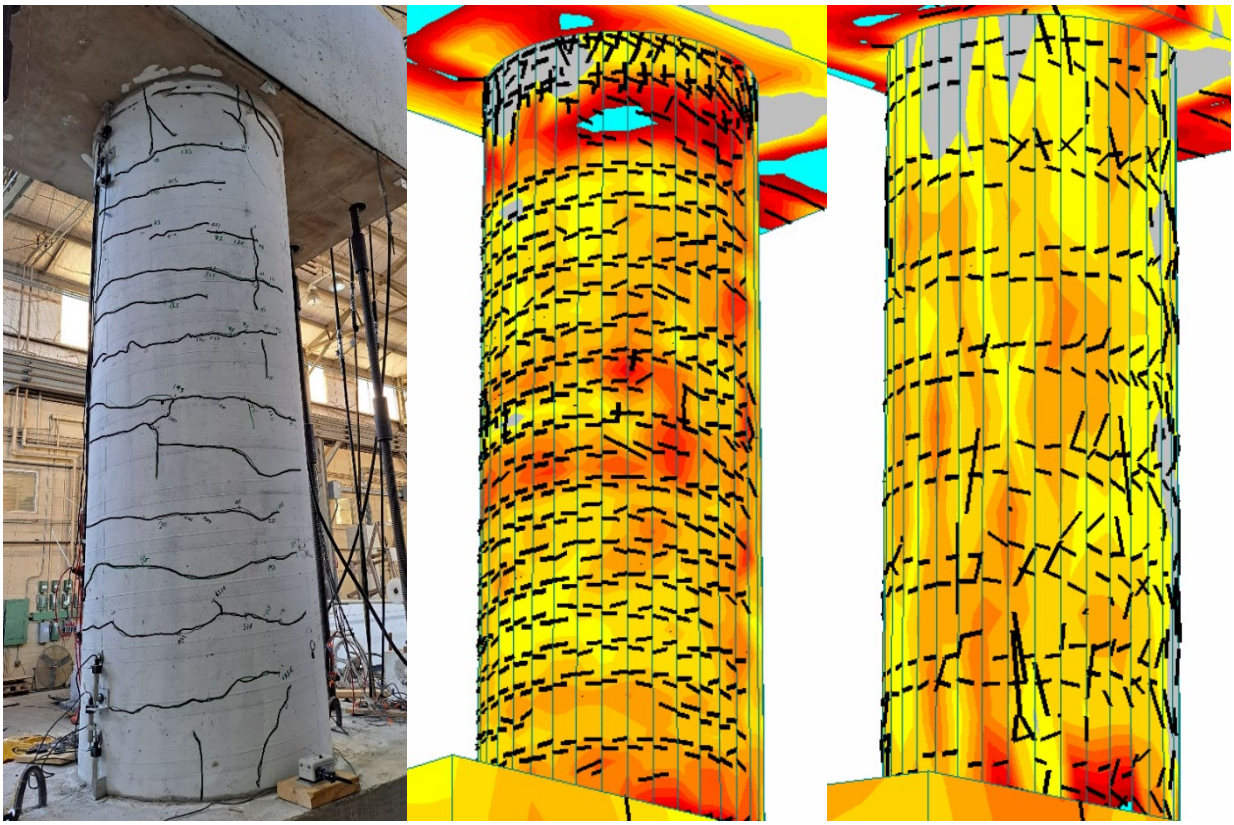

Figure 6-36: Crack Pattern in Tensile Region of Experimental Specimen, Model 1, Model 3, Respectively. (Kotha, 2024)

However, as seen from Figure 6-37, it can be observed that Model 3 has experienced vertical cracks in the compressive region which is not observed in finer mesh Model 1 and the experimental specimen as well. Although both Model 1 and Model 3 are good in capturing tensile cracks in the tensile region, it is unexpected to see crushing due to compression in Model 3.

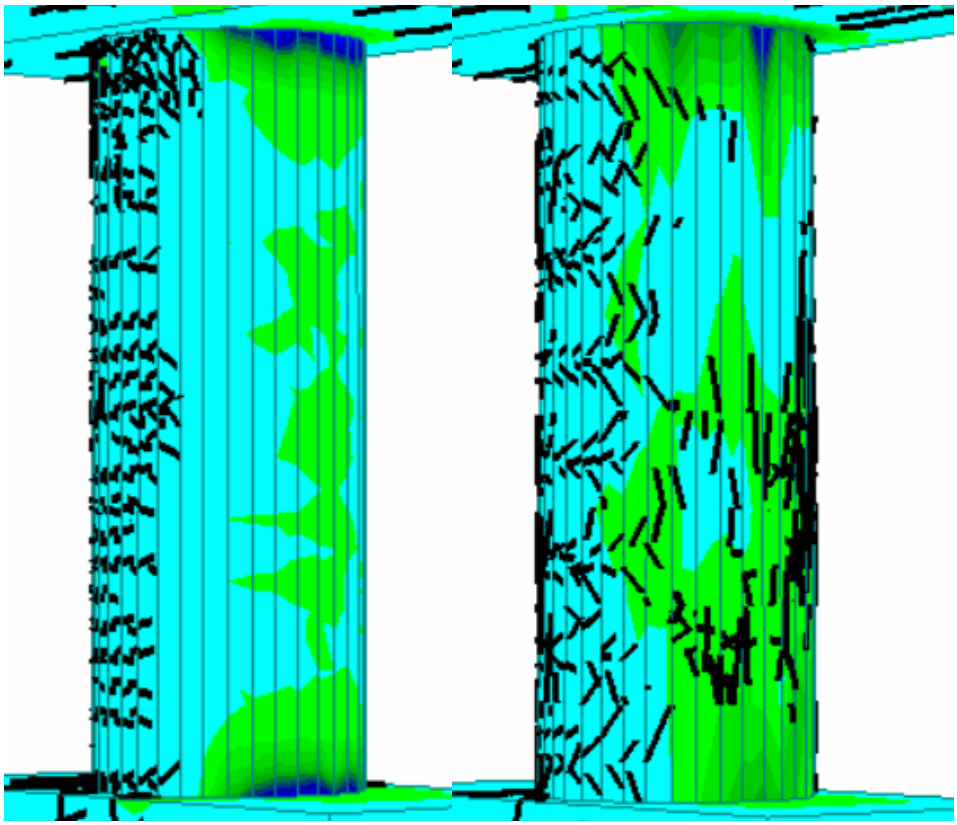

Figure 6-37: Crack Pattern in Compressive Region of Model 1, Model 3 Respectively (Kotha, 2024)

Hence, it can be concluded from this parametric study that a sufficiently finer mesh, which is 4 in. for this model is necessary for precisely estimating the displacements, capacity, and crack pattern. On the other hand, the loading rate/load per step in this FEA study has given rise to a similar displacement profile, but a slower loading rate gave rise to premature failure.

6.2.5. Summary of CIP model

- Utilizing ATENA 3D software, a comprehensive 3D model of a cast-in-place column (CIP column) was meticulously developed to replicate the loading process of a large-scale CIP column in the FSEL.

- The model was subjected to rigorous testing under three distinct eccentricity loadings: 6 in., 12 in., and 40.25 in. The investigation was carried out until the total axial load reached 15% of the theoretical compressive strength of the column, 550 kips for the 6-in. and 12-in. loading scenarios, which were the same as used in the large-scale experimental program.

- In the case of the 40.25-in. eccentricity load pattern, the FE model was subjected to loading until reaching failure at a load of 340 kips. The failing load exhibited a remarkable correspondence with the experimental results, differing by a mere 5.6%.

- Concurrently, the analytical outcomes from the FEA showcased a commendable alignment with the experimental findings. The response of the column specimen to eccentricity loads, overall displacement values, and strain magnitudes displayed similarity. The lower section of the numerical column exhibited slightly higher stiffness than the experiment.

- The model exhibited the occurrence of tensile cracks during the application of eccentricity loading, with the software adeptly capturing these occurrences in a manner closely mirroring the experimental column specimen.

- Finer mesh is necessary for providing accurate results in terms of capacity, displacements, and crack pattern. Loading rate/load per step has little to no influence in predicting the displacements and crack pattern but it is affecting the capacity estimation.

- Given the substantial agreement observed across various parameters, this model can be suitably adapted for scenarios involving precast columns, necessitating modifications in terms of macroelements, material properties, and reinforcement configurations.

6.3. Precast Column 3D Modeling and Analysis

In this project, a total of five columns were tested under four eccentricity loading patterns as presented in Section 4.3. The Specimens S1-CIP was prepared and analyzed to observe the differences between a column cast-in-place and a precast column. Specimen S2-R-AASH9-45 and Specimen S3-S-AASH9-45 are precast columns that differ in the column's inner interface. Specimen S4-R-Tx-34 and S5-R-ZABORAC-28 had intentionally roughened interfaces and different embedment lengths at the footing-column and column-bent cap connections.

This section presents modeling and analysis results of precast column Specimen S2-R-AASH9-45 with an intentionally roughened interface. Along with that, comparison with experimental results, parametric analysis, some problems, and possible improvements are also presented. Given the reliability of the FE model of specimen S1-CIP, similar modeling techniques and parameters were directly translated to constructing FE models of precast column specimens.

6.3.1. Components and Reinforcement of Experimental Specimen

The primary components of the precast specimen are a precast concrete column and a CIP core. The inner surface was kept undisturbed for Specimen S3-S-AASH9-45. But for specimen S2-R-AASH9-45, which is the subject of study in this section, the inner surface was specially roughened for better shear resistance. The details used for modeling this specimen are the ones used for the construction of the specimen in the laboratory as presented in the section 4.2.5 and 4.2.6.

6.3.2. Model Preparation

In this section, all the steps required to model the specimen in the software are discussed, such as material stress-strain models and properties, meshing of macroelements, prestressing and loading steps.

6.3.2.1. Material Model and Properties of Concrete

Concrete material in the FE analysis was modeled as CC3DNonLinCementitious2 in the software. The compressive strength was evaluated in the laboratory, and other parameters like elastic modulus and tensile strength were calculated based on ACI 318-19 given by Eq. (6-1) and Eq. (6-2) respectively. In addition, the specific fracture energy G_F was calculated based on the recommendation given by Eq. (6-3) (Rejane et al., 2014). All the other material properties were kept default. Table 6-13 summarizes the material properties used for the column core and the footing and the concrete material properties of the SCC used for the bent cap.

Table 6-13. Material Parameters of Concrete for Column Core-Footing and Bent Cap

Subset	Parameters	Column Core-Footing		Bent Cap	
		Applied Value	Unit	Applied Value	Unit
Basic	Elastic modulus, E_c	3.717E+03	ksi	5.534E+03	ksi
	Poisson's ratio, ν	0.200	-	0.200	-
	Tensile strength, f'_t	2.683E-01	ksi	3.884E-01	ksi
	Compressive strength, f'_c	-4.252E+00	ksi	-9.426E+00	ksi
Tensile	Specific Fracture energy, G_F	2.756E-04	kip/in	3.823E-04	kip/in
	Crack spacing, s_{max}	Inactivated		Inactivated	
	Tension stiffening, c_{ts}	Inactivated		Inactivated	
	Unloading	Inactivated		Inactivated	
Compressive	Critical compression displacement, w_d	-1.200E-02	in.	-1.969E-02	in.
	Plastic strain at compressive strength, ε_{cp}	-1.230E-03	-	-1.046E-03	-
	Reduction of comp. strength due to cracks, $r_{c,lim}$	0.800	-	0.800	-
Shear	Crack Shear Stiff. Factor, S_F	20.000	-	20.000	-
	Aggregate interlock, MCFT	Activated		Activated	
	Aggregate Size	0.787	in.	0.787	in.
Miscellaneous	Fail. Surface eccentricity	0.520	-	0.520	-
	Multiplier for the plastic flow dir. B	0.000	-	0.000	-
	Specific material weight, ρ	8.473E-05	ka	8.473E-05	ka
	Coefficient of thermal expansion, α	6.667E-06	1/°F	6.667E-06	1/°F

	Fixed crack model coefficient	1.000	-	1.000	-

Along with that, the material properties of the precast column shell had to be defined as well. The shell had a compressive strength of 10.31 ksi. Since the compressive strength of the concrete used for the shell was almost 10 ksi, the typical ACI formulae used were producing highly conservative values for E_c and f'_t. For that reason, E_c was calculated using the AASHTO formula (6-13) (AASHTO LRFD 2020). This formula can be used for concrete with compressive strength less than 10 ksi. As the shell had a compressive strength only slightly higher than 10 ksi, typical E_c from the formula below was used, where f'_c is used in ksi units.

$$\mathrm{Ec} = 1820\sqrt{\mathrm{f}'_\mathrm{c}} \tag{6-13}$$

The tensile properties of high-strength concrete are also conservative when calculated by the ACI 318-19 formula. It is typically 7% of concrete strength for high-strength concrete. Due to some prestressing-related complications in the software which are discussed in the next sections, this particular value was adopted even though its value is higher than the ACI formula. All the other properties were kept default. Either way, regions with lesser than 0.7 ksi can anyways be seen in the software, so cracks can be predicted. Table 6-14 given below summarizes the properties of concrete shell.

Table 6-14. Material Parameters of Concrete for Precast Concrete Shell

Subset	Parameters	Applied Value	Unit
Basic	Elastic modulus, E_c	5.844E+03	ksi
	Poisson's ratio, v	0.200	-
	Tensile strength, f'_t	7.217E-01	ksi
	Compressive strength, f'_c	-1.031E+01	ksi
Tensile	Specific Fracture energy, G_F	9.843E-04	kip/in
	Crack spacing, s_{max}	Inactivated	
	Tension stiffening, c_{ts}	Inactivated	
	Unloading	Inactivated	
Compressive	Critical compression displacement, w_d	-1.200E-02	in.
	Plastic strain at compressive strength, ε_{cp}	-1.750E-03	-
	Reduction of comp. strength due to cracks, $r_{c,lim}$	0.800	-
Shear	Crack Shear Stiff. Factor, S_F	20.000	-
	Aggregate interlock, MCFT	Activated	
	Aggregate Size	0.787	in.
Miscellaneous	Fail. Surface eccentricity	0.520	-
	Multiplier for the plastic flow dir. B	0.000	-
	Specific material weight, ρ	8.473E-05	ka
	Coefficient of thermal expansion, α	6.667E-06	1/°F
	Fixed crack model coefficient	1.000	-

6.3.2.2. Reinforcement Material Model

Similar to the CIP column, the same reinforcement details were used for precast concrete specimens as well as presented in Figure 6-8. Two reinforcement types were used in this model: regular reinforcement bars with a test yield strength of 65 ksi bars, and high-strength strands with an ultimate strength of 270 ksi. For that reason, two separate stress-strain profiles were taken into consideration. In addition, steel load plates were also modeled for loading in the FE analysis. In summary, regular reinforcement and load plates were assigned with the material properties shown in Table 6-15; prestressing strands were assigned with properties in

Table 6-16.

Table 6-15. Assigned Material Parameters of Reinforcement and Load Plates

Subset	Parameters	Applied Value	Unit
Basic	Elastic modulus, E	2.901E+04	ksi
	Yield strength, σ_y	65.450	ksi
	Ultimate strength, σ_t	82.080	ksi
	Strain at fracture, ε_{lim}	0.027	
Miscellaneous	Specific material weight, ρ	2.892E-04	ka
	Coefficient of thermal expansion, α	6.667E-06	1/°F

Table 6-16. Assigned Material Parameters of Prestressing Strands

Subset	Parameters	Applied Value	Unit
Basic	Elastic modulus, E	2.901E+04	ksi
	Yield strength, σ_y	230.000	ksi
	Ultimate strength, σ_t	270.000	ksi
	Strain at fracture, ε_{lim}	0.109	
Miscellaneous	Specific material weight, ρ	2.892E-04	ka
	Coefficient of thermal expansion, α	6.667E-06	1/°F

6.3.2.3. Interface between Precast Shell and CIP Core

As discussed before, the surface between two different macroelements was defined by contact elements. This special surface's properties can be defined as a material property CC3Dinterface in the interface section. As Specimen S2-R-AASH9-45 surface is intentionally roughened, properties listed in Table 6-17 are used. These parameters are calibrated from the experimental results of shear interface models, as indicated in Section 6.1.4.

Table 6-17. Assigned Material Properties for Shell-Core Interface

Interface Type	Rough
K_{nn} (kci)	340.550
K_{tt} (kci)	57.720
Cohesion (ksi)	0.197
Tensile strength, f_t (ksi)	0.351
Friction coefficient	1.000

6.3.2.4. Macroelements, Meshing and Boundary Conditions

As discussed in the previous sections, many of the macroelements, material stress-strain profiles, and properties were similar to that of the CIP column model. Instead of one macroelement for each column, in this case, two separate components were modeled. In Figure 6-38 all the macroelements in the precast column model are shown individually. The 24-in. diameter core macroelement perfectly fits in the shell macroelement with an inner diameter of 24-in. and outer diameter of 36-in. In the ATENA 3D software, macroelements of non-cuboidal shapes cannot be modeled. For that reason, a cuboidal model with 36 outer surfaces was prepared to bring the model closer to a cylinder. Similarly, the shell macroelement was also prepared with 36 outer surfaces. All these 36 surfaces were assigned with intentionally roughened contact elements.

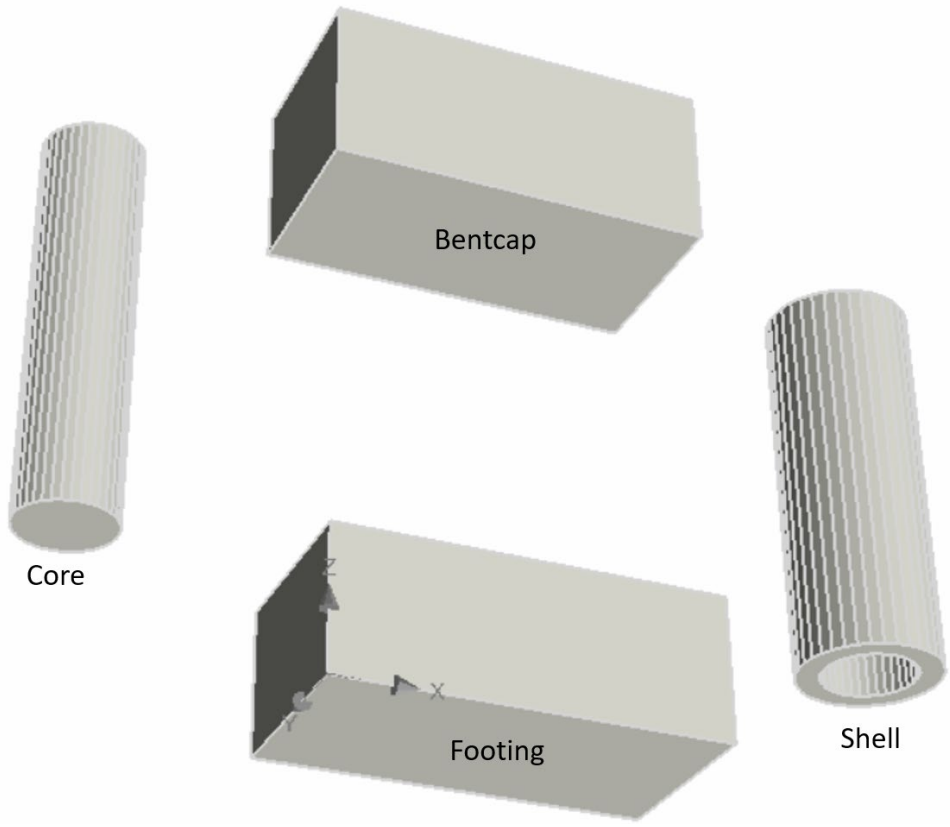

Figure 6-38: Macroelements used in the Precast Column Model (Kotha, 2024)

As tetrahedral elements are recommended for macroelements that are not cuboidal, both the precast shell and CIP core were meshed into 4 in. tetrahedral elements. Since the shell had a thickness of 6-in., there are two elements per thickness as it can be meshed in whole numbers only. However, in the longitudinal direction, it was divided into 4 in. elements. On the other hand, the bent cap and the foundation were meshed into a relatively coarser mesh of 6 in. and 12 in. respectively as these macroelements were not of primary importance. All the details are presented in Figure 6-39.

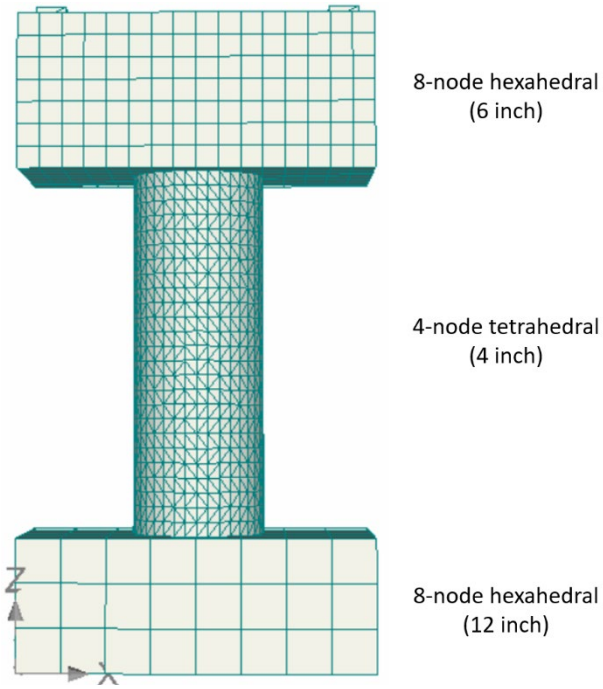

Figure 6-39: Mesh Details of Precast Column Model in ATENA 3D Software (Kotha, 2024)

The prepared FE model foundation's bottom surface was restrained in X-, Y-, and Z-directions to facilitate the loading process, and to avoid convergence issues during the prestressing of bent cap and precast shell. Figure 6-40 describes the boundary conditions of the precast column model.

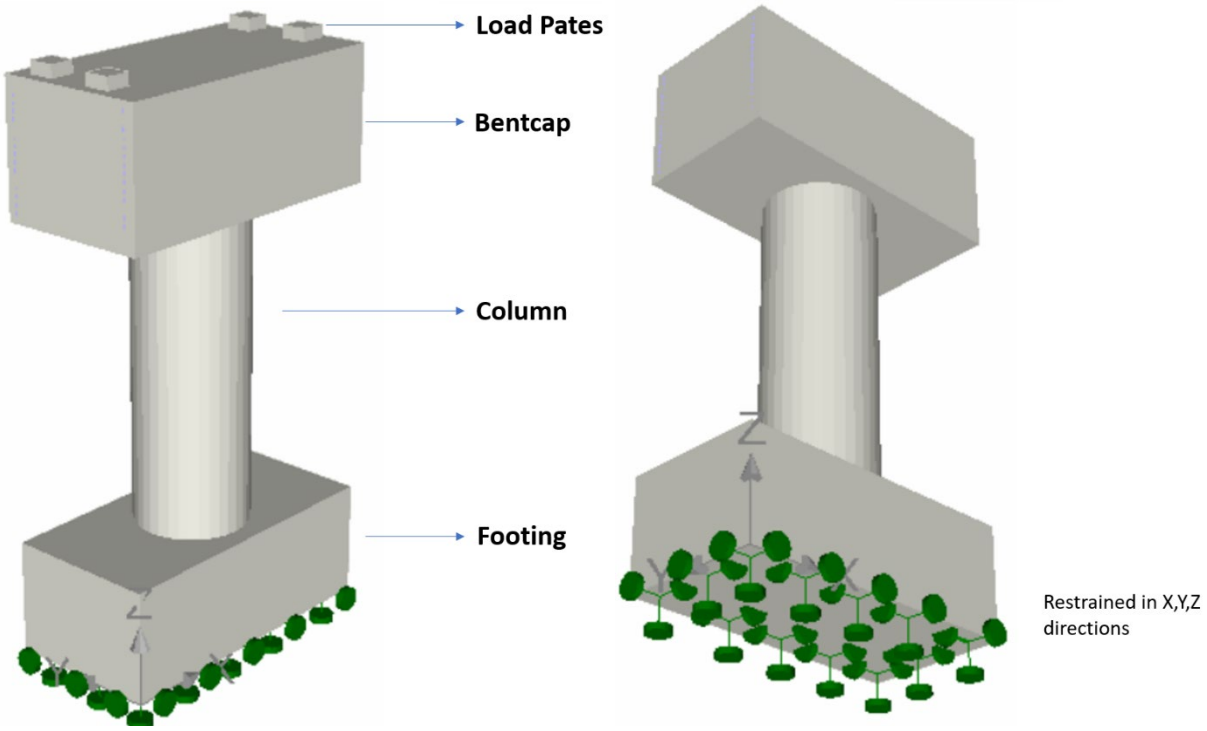

Figure 6-40: Precast Column Model and Boundary Conditions (Kotha, 2024)

6.3.2.5. Prestressing the Bent Cap and Precast Concrete Shell

One of the last steps of precast column modeling before loading was the prestressing step of the bent cap and the precast concrete shell. For an accurate representation of transfer length, a bond model was necessary. Following Bigaj's (1999) bond-slip model, the assigned bond stress-slip relationship is shown for strands in the bent cap in the Figure 6-41.

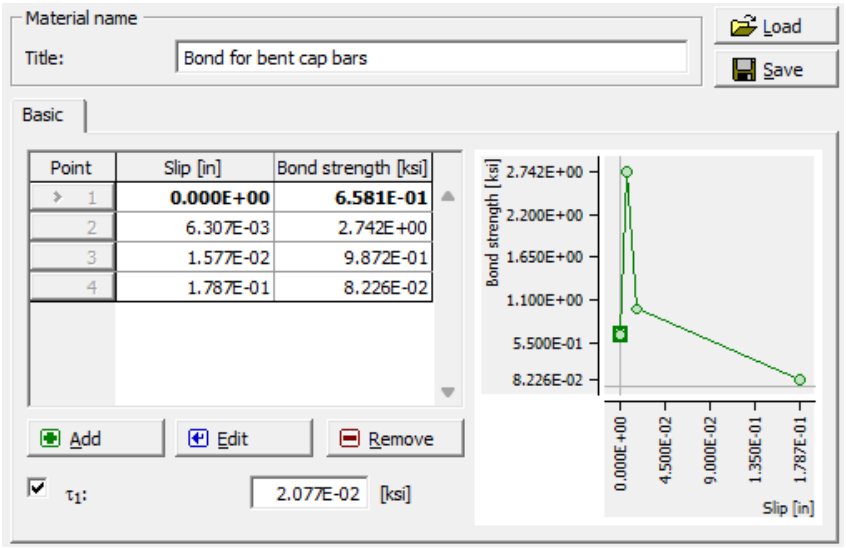

Figure 6-41: Bond Stress-Slip Relationship for Prestressing Strands in Bent Cap (Kotha, 2024)

As the effective strand area was 0.217 in^2 for 7-wire 0.6-in. strands, all the strands were assigned a prestressing force of 43.94 kips It resulted in a stress of 202.5 ksi, which is 75% of f_{pu}. Application of prestressing force and prestressing stresses after release are presented in Figure 6-42 and Figure 6-43 respectively. As anticipated, prestressing was not achieved at both ends, but 17 in. away from the end of the bent cap, the total prestressing stress is transferred to the strands.

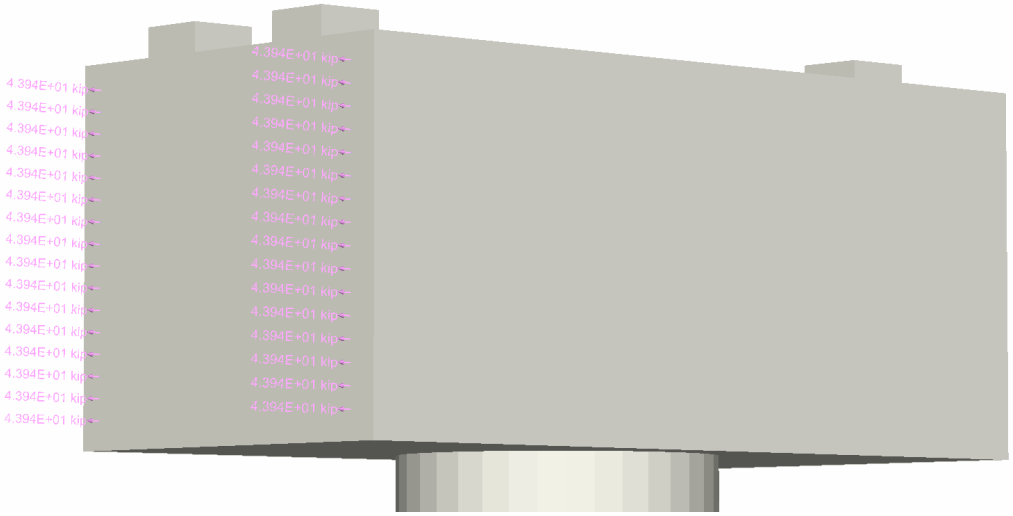

Figure 6-42: Strands in Bent Cap being Prestressed to 75% of f_{pu} (Kotha, 2024)

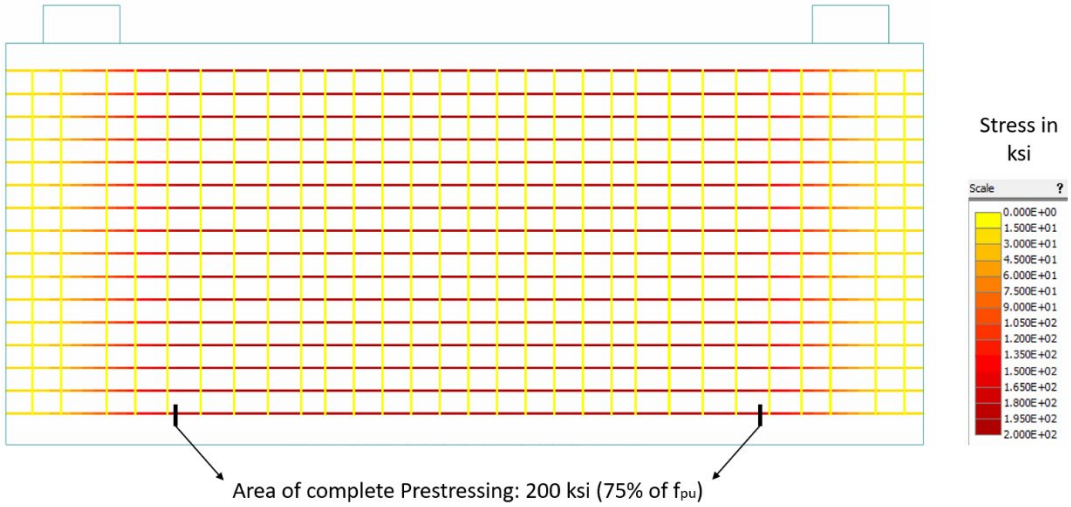

Figure 6-43: Principal Stress in Strands After Release (Kotha, 2024)

The next step of the model preparation was prestressing the shell. There were two problems associated with this step. The shell could only be prestressed to 200 ksi maintaining contact with the core. The interface between the core and shell was not a perfect connection, and this prestressing step might damage the interface even before the actual moment loading process. Additionally, in the case of the experimental specimen, the shell was prestressed before arriving at the laboratory, later, the core was CIP on the footing top, and the bent cap was placed and cast on top of the column. However, in the software, the prestressing on the precast column can only

be done after the assembly of all the macroelements, and this prestressing step influences the bent cap, and the foundation stress levels even before the actual analysis.

This problem could be partially solved by using the construction case feature in the ATENA software. Two separate construction cases were created, the prestressing was completed in the 1st case, and loading was implemented in the 2nd stage. In the 1st stage, the core macroelements were disabled so that the interface between the core and shell was not damaged during prestressing. This method solved the first problem. However, the foundation and bent cap could not be disabled during the prestressing stage even after creating a separate construction case, making this a limitation of the software used in the analysis.

With the first construction stage, the core macroelements were disabled, and both the bent cap and the precast shell were prestressed preventing the interface between the core and shell from being stressed before the loading process. In the second stage, where loading steps had to be added, no macroelements were disabled. The bond stress-slip relationship for reinforcement in the shell is shown in Figure 6-44.

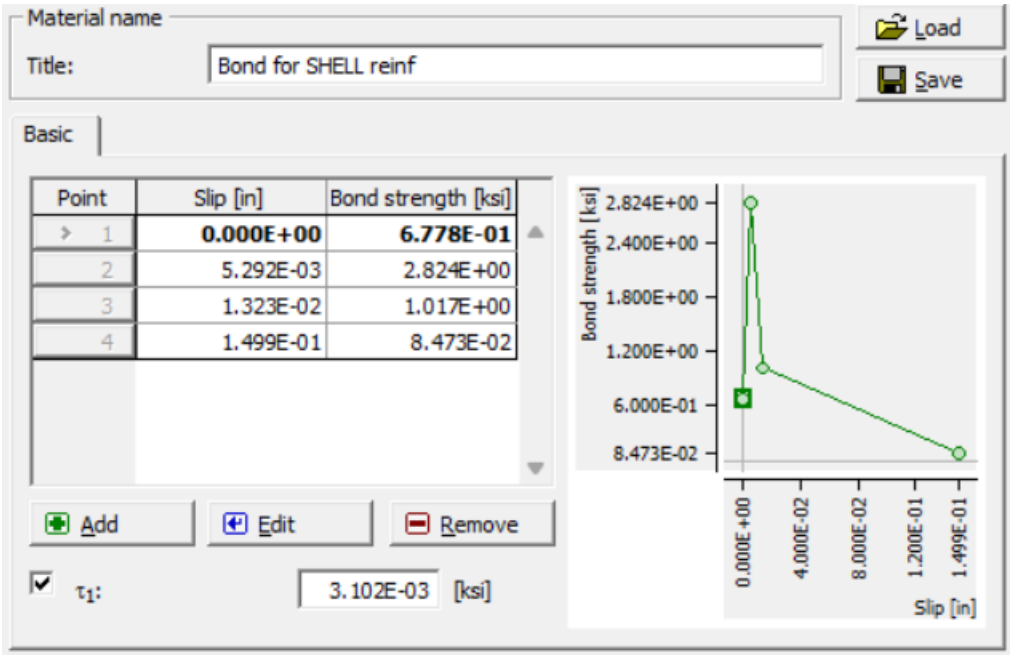

Figure 6-44: Bond Stress-Slip Relationship for Strands in the Precast Shell (Kotha, 2024)

The shell is equipped with twenty-four ½-in. strands at 12 locations. Thus, at each location, two ½-in. 7 wire strands are present making the effective area 0.306 in^2. Each strand was assigned a prestressing force of 61.97 kips as shown in Figure 6-45, which took the stress levels in strands to 202.52 ksi, 75% of f_{pu}. In the same figure, the stress distribution of strands after prestressing is shown. As anticipated, complete prestressing is observed after approximately 20 in. from the end of the precast column.

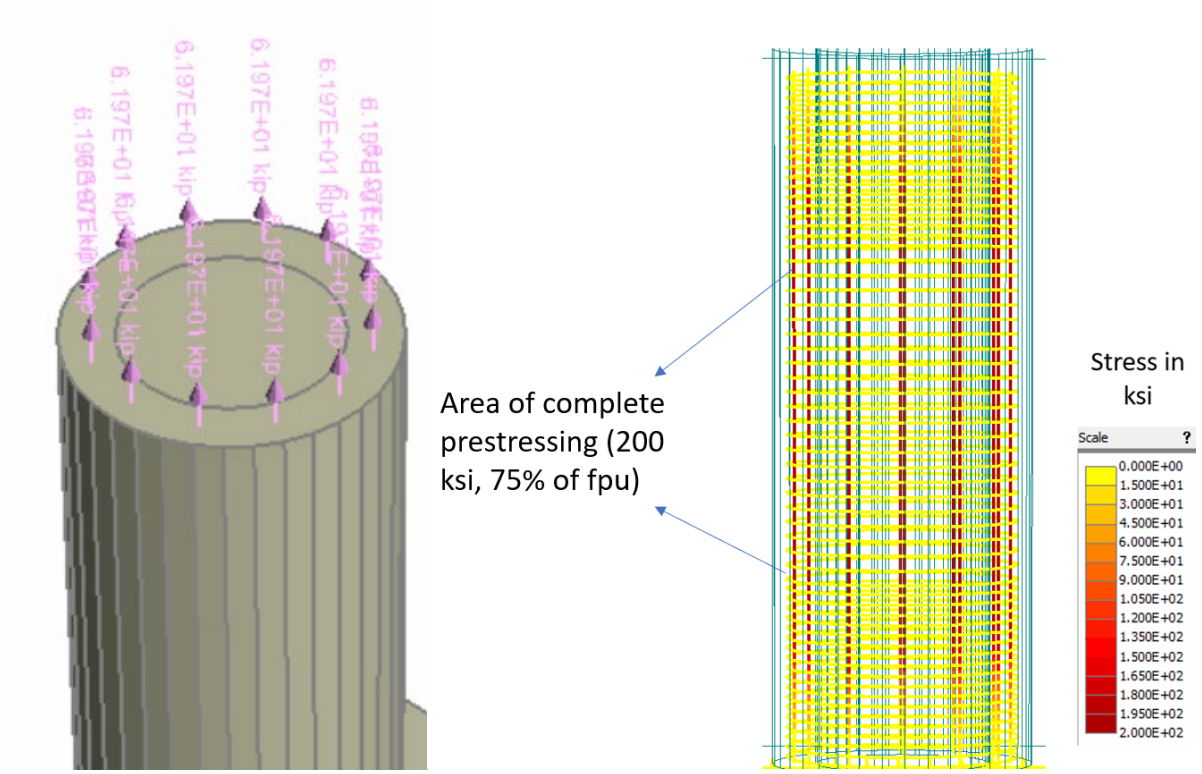

Figure 6-45: Prestressing Forces and Stress Levels after Prestressing Strands in Precast Shell (Kotha, 2024)

6.3.2.6. Monitoring Points

In ATENA 3D, the analytical values of deformation and deflection of structure, responding to the applied load, can be captured by applying monitoring points. In this case, monitoring points were distributed to the numerical structure, as shown in Table 6-18 and Figure 6-46.

Table 6-18. Assigned Monitors for Full-Scaled Cast-in-Place Specimen

Monitor	Purpose
A	A monitor for measuring the vertical deflection was assigned under the bent cap.
B-1 (At 6') **B-2 (Top)**	A monitor for capturing the horizontal displacement of the column was applied at the 6' and top (8') of the compressive side of the column.
C-1 **C-2**	Vertical displacement monitors were applied to capture the strain at the bottom of the column joint, for calculating the curvature

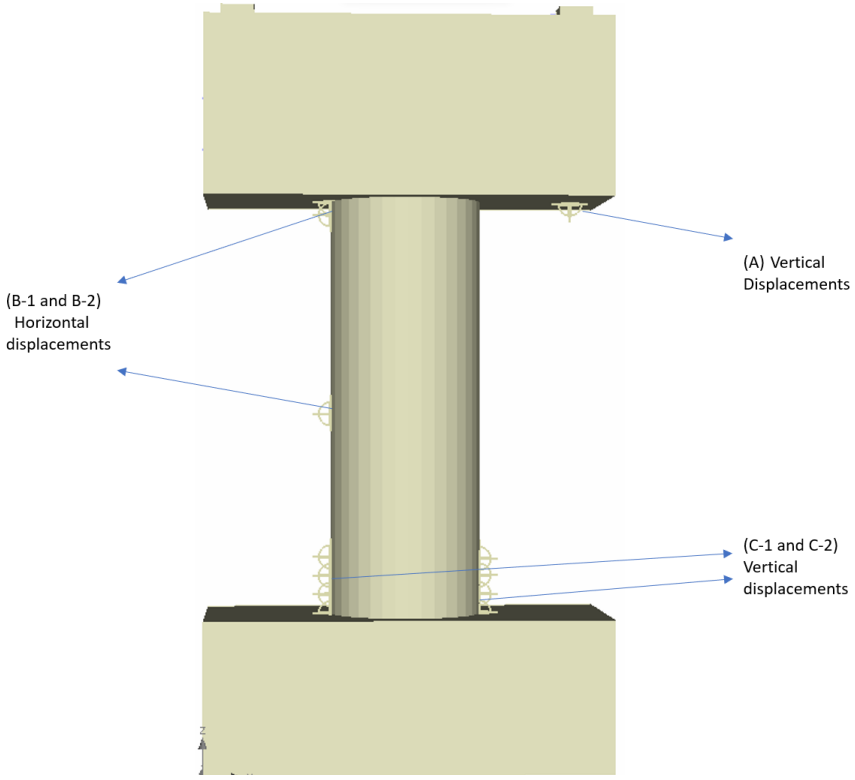

Figure 6-46: Monitors Location for FEA of Precast column (Kotha, 2024)

6.3.3. FE Model Validation

After preparing and checking the parameters used in the model, the analysis results are considered in good agreement with the initial estimations of the P-M Interaction diagram and results from Specimen S1-CIP. Similar to section 6.2.2, analytical results in terms of load-displacement data are validated with experimental results. The prepared FE model's results are in reasonable agreement with both linear-range load patterns used to test the experimental specimen.

6.3.3.1. Axial Load versus Displacement Curves

One of the best ways to check if the analytical model is a good representation of the experimental model is the comparison of the deflections, as it would convey the details of specimen behavior like crack formation, openings, and yielding of bars. This section is divided into two parts, the first part deals with linear-range eccentricity analyses which are 6-in., 12-in., and 20-in. The second part deals with a comparison of the 40.25-in. eccentricity analysis.

The comparison of 6-in., 12-in., and 20-in. analysis results are presented in Figure 6-47 through Figure 6-49 respectively. The dashed lines in the graphs are FEA results, and the solid ones are experimental results. Blue colored are the monitoring points 6' from the bottom of the column and orange is at the top, 8' from the bottom. Firstly, ignoring minor disturbances in the experimental results, it can be observed that graphs are mostly linear, especially for 6-in., 12-in., first half of 20-in. analysis implying crack formation or yielding is not observed. The behavior of the FEA model

is also similar, and it is slightly soft (experiencing more displacement for the same load) for 6-in. and 12-in. analyses. In addition, the non-linearity of the experimental specimen in the second half of the 20-in. analysis is also captured well by the software, as displacements matched perfectly.

Coming to the end-displacement values, the values were in reasonable agreement with an average error of 0.28% with the highest individual error of 12.95% at the top of the column. Whereas for the 6' monitoring points an average error of 7.71%, and at most 15.02%. A summary of the results is presented in Table 6-19 at the end of the section. It can be said that the model is working well for linear-range eccentricity flexural analysis.

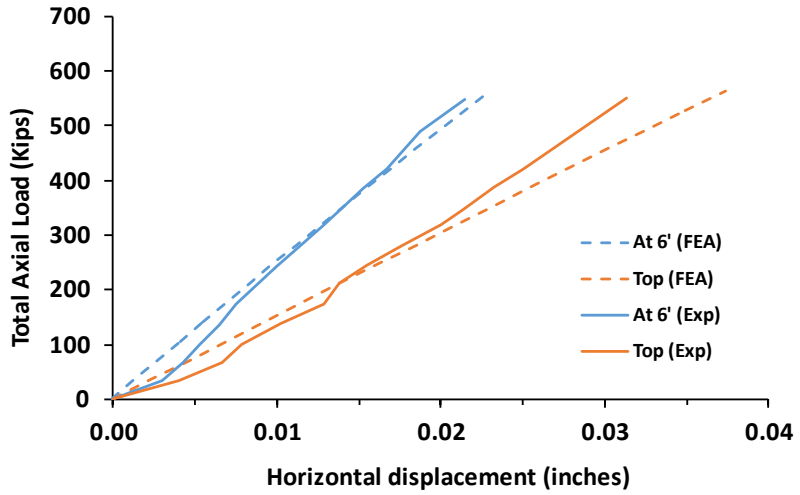

Figure 6-47: Comparison of 6-in. Eccentricity Analytical and Experimental Results (Kotha, 2024)

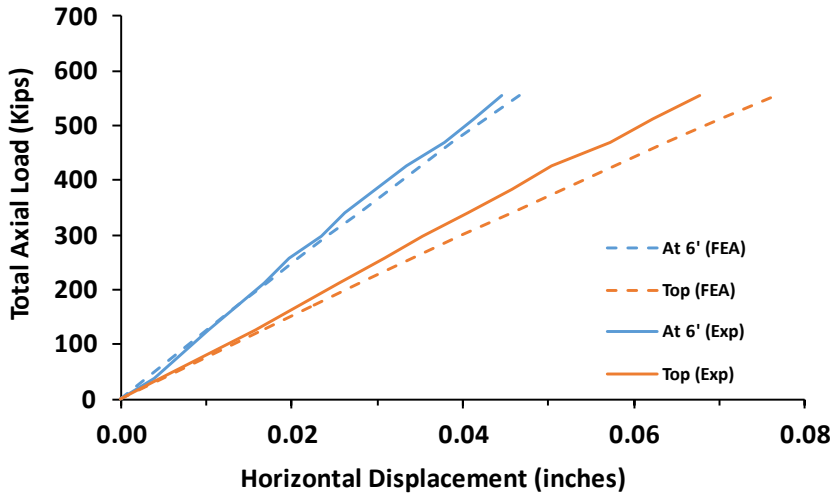

Figure 6-48: Comparison of 12-in. Eccentricity Analytical and Experimental Results (Kotha, 2024)

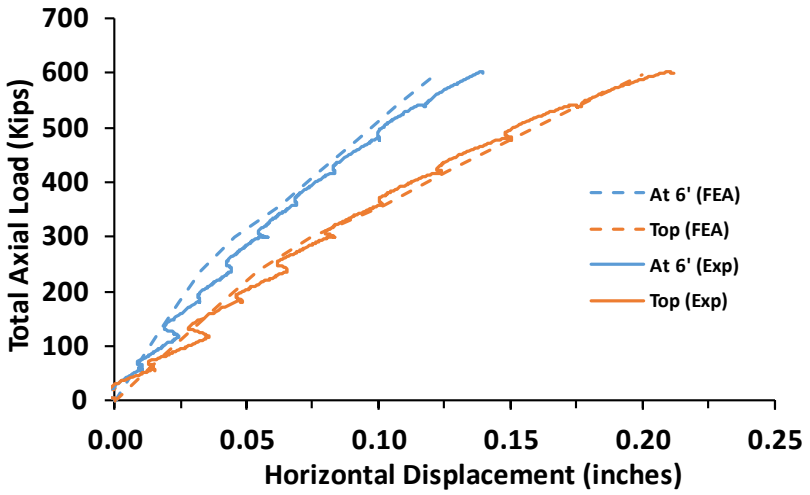

Figure 6-49: Comparison of 20-in. Eccentricity Analytical and Experimental Results (Kotha, 2024)

Similar to the graphs for linear-range eccentricity analyses, a comparison for 40.25 in. analysis is shown in Figure 6-50. For simplicity, the analysis results are compared only to 400 kips as the experimental specimen failed at 383 kips, but the analytical model showed post-peak yielding behavior. In this analysis, the experimental specimen was subjected to flexural loading until failure and the specimen encountered multiple cracks and yielding of bars. As seen from the solid lines, the experimental specimen has reacted linearly with the load up to 200 kips, encountered crack openings, and then huge deformation attributed to the yielding of the bars.

A similar trend is observed in the FEA model, by showing a linear relationship up to 100 kips, again linear with a shift, up to 200 kips, and it is no longer observed after that until failure. The model can be seen stiffer, and softer at various instances compared to the experimental specimen throughout the analysis, but the results are always close. However, the displacement values are in very good agreement in the second half of the analysis, highlighting the software's ability to capture the cracks and the column yielding. An error of just 2.4% was observed at the end of the analysis for both the monitoring points. After the test, the experimental specimen failed after enduring 383 kips of 40.25-in. eccentricity axial load, which is 1284.65 kip-ft of bending moment, while the FEA model failed at 440 kips showing an accuracy of a reasonable 85%.

The FEA model's premature non-linearity after 100 kips can be attributed to the connection cracks, which are caused due to the assignment of the bond model, and loss of prestress in end regions. For that reason, concrete in end regions became relatively weak in central parts.

In addition, the prestressing strands are present only in the shell and are not continuous to the footing or bent cap, implying the bent cap-column connection, and footing-column is not perfect and are only bonded by unreinforced concrete. Since the properties of surfaces between the bent cap-column and foundation-column are not known accurately, a perfect connection was maintained in the software, which could be the probable reason for the overstrength of the FEA

model compared to the experimental specimen. A detailed parametric study on the bond model and connections is presented in section 6.3.5.

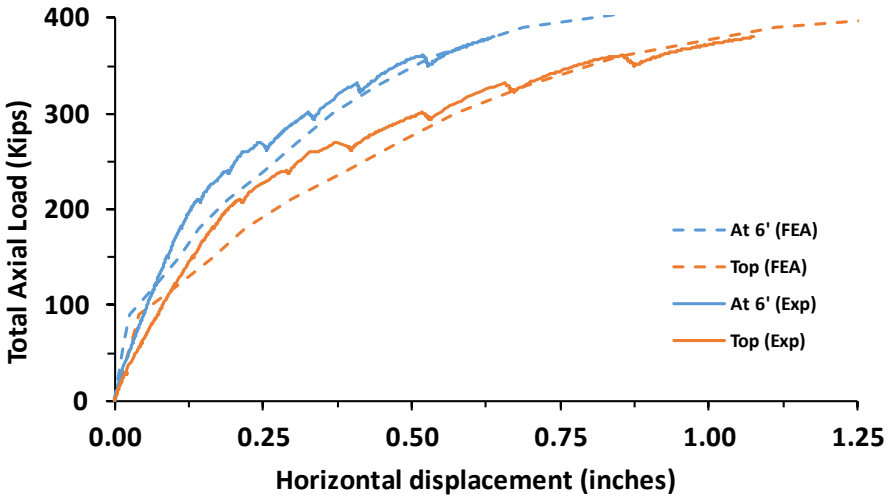

Figure 6-50: Comparison of 40.25-in. Eccentricity Analytical and Experimental Results (Kotha, 2024)

Table 6-19. Analytical and Experimental Results of Precast Column (Specimen S2-R-AASH9-45)

Eccentricity	Monitoring point	FEA value (in.)	Experimental value (in.)	% Difference
6 in.	Top	0.036	0.031	7.48
	At 6’	0.023	0.021	15.02
12 in.	Top	0.077	0.068	4.63
	At 6’	0.047	0.045	13.31
20 in.	Top	0.200	0.211	-12.95
	At 6’	0.121	0.139	-5.21
40.25 in.	Top (@383 Kips)	1.150	1.180	-2.40
	At 6’	0.652	0.668	-2.54

In total, the results from the FEA model showed a good resemblance to the experimental specimen tested in the laboratory, in terms of displacements for both linear range analyses, and the 40.25 in. eccentricity test.

6.3.4. FE Analysis and Discussion

In this section, the results from the precast column FE model are analyzed. After modeling the specimen in software, two load steps were allotted for prestressing, before applying the load pattern established in the section 4.3. The first step was prestressing the bent cap strands and, later,

the strands in the precast concrete shell. It should be noted that prestressing the strands in the model has not damaged the imperfect interface between the precast shell and the CIP core.

6.3.4.1. Precast Column Model under 6-in. Eccentricity Load Pattern

The first load pattern was the 6 in. eccentricity test. By adjusting the load both on the left and right side of the column, an axial load with specific eccentricity can be applied, creating a bending moment in the column. As seen from Figure 6-51, each load step consists of 15 kips on the tensile side and 20.25 kips on the compressive side, divided by 2 load plates on each side which are 40.25 in. from the center of the column. This analysis was continued until the total axial load on the column reached 550 kips (15% of the theoretical axial load capacity of the CIP column). To achieve this load, along with prestressing steps, 16 load steps were added.

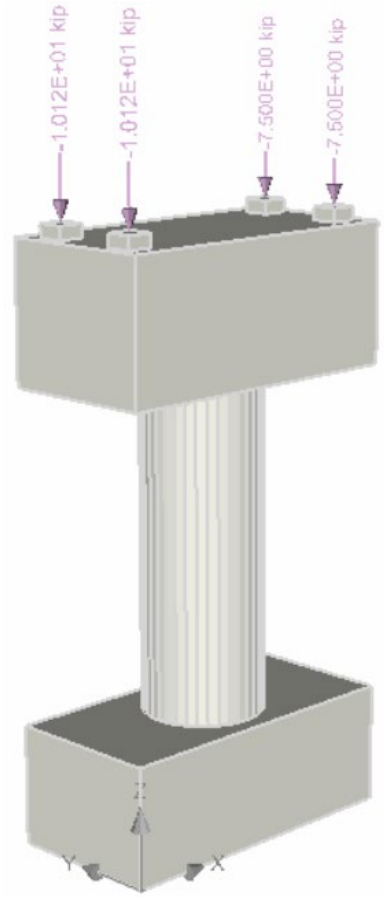

Figure 6-51: Loading Setup for 6-in. Eccentricity Analysis (Kotha, 2024)

After completing the test simulation, the column was examined for stresses and cracks. As seen in Figure 6-52 (a), it is interesting to note that the column experienced little to no tensile stress on tensile region. This could be attributed to the effect of prestressing before loading. The prestressing led to compressive effects on the concrete, since the applied flexural loading was less (eccentricity of 6 in.), tensile stresses were not sufficient to overcome the compressive effects of prestressing. For that reason, most portion of the column on the tensile side is yellow or gray, implying zero

tensile stress. On the other hand, the compressive side of the column has experienced stresses as high as 0.75 ksi near the bent cap and foundation connections. The central regions of the column experienced little to no compressive stresses. The analysis resulted in no cracks as both the tensile and compressive stresses were not enough to reach f'_t and f'_c, respectively.

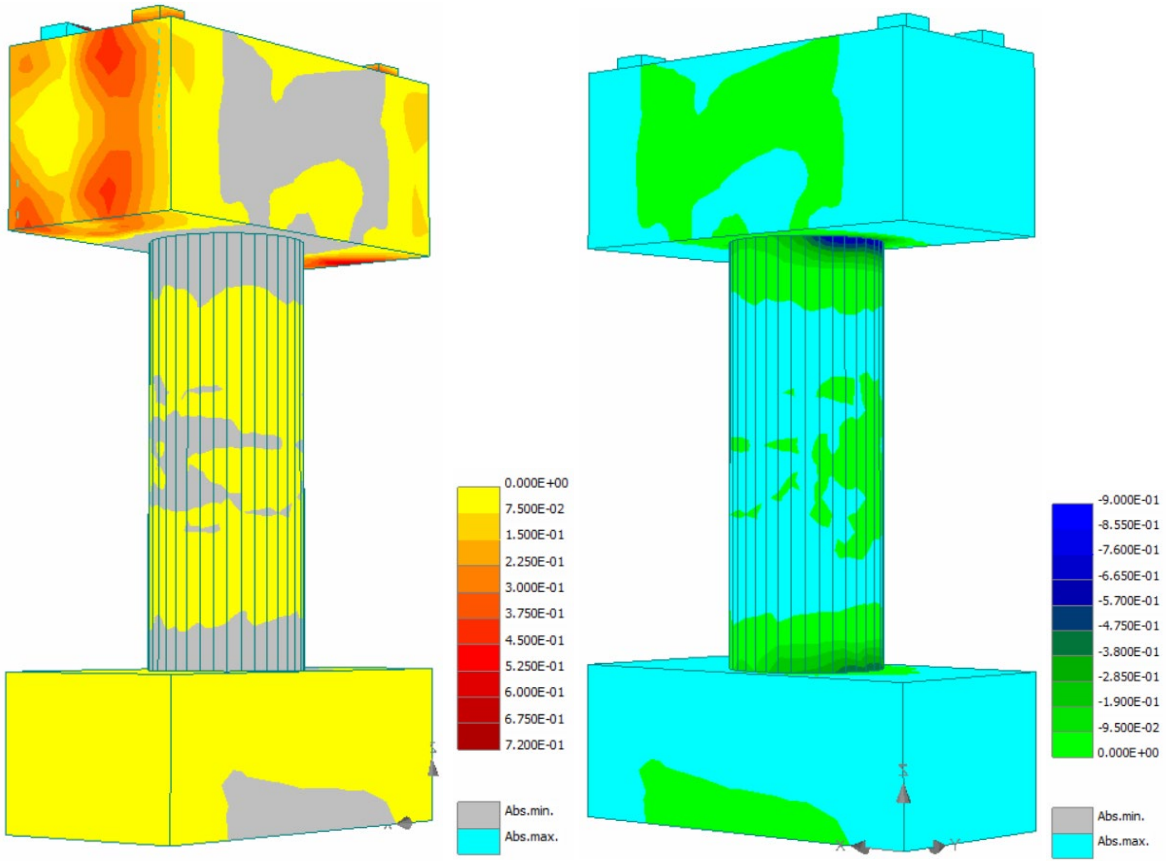

(a) Tensile side (b) Compressive side

Figure 6-52: Stress Levels (in ksi) and Cracking at the end of 6-in. Eccentricity Loading (Kotha, 2024)

The software could capture displacements at various locations as well. From the previous section, monitoring points B-1 and B-2 captured the horizontal movement of the column at 6 ft. and top of the column. The results are presented in Figure 6-53, and it is observed that the displacements were linear throughout the analysis until it reached the end axial load of 550 kips maintaining an eccentricity of 6 in., implying that the structure presented an elastic behavior without any yielding or cracks. The axes of the graph were adjusted to maintain uniformity with analysis results of 12 in. and 20 in. eccentricities, to be discussed in subsequent sections. A displacement of 0.0369 in. was recorded at the top of the column.

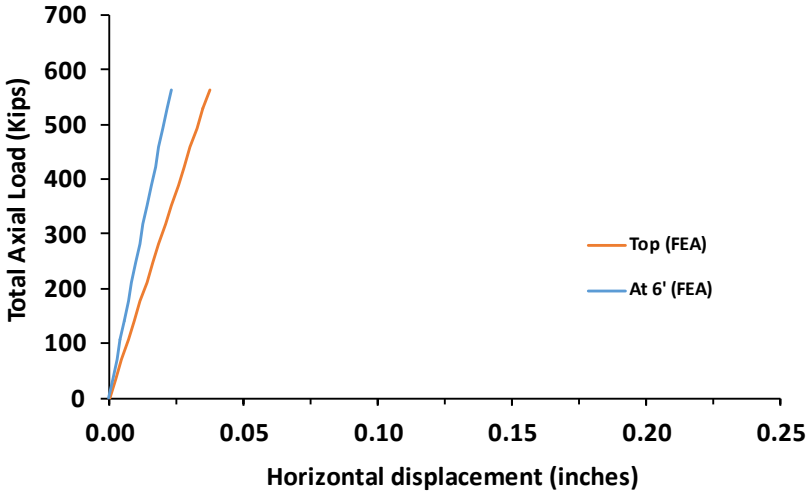

Figure 6-53: Total Axial Load-Displacement Behavior for 6-in. Eccentricity Loading (Kotha, 2024)

From the monitoring points C-1 and C-2, vertical displacements and strain values experienced by the column were calculated. Curvature and bending moment are evaluated and the results are presented in Figure 6-54. For an end moment of 282 kip-ft, the column has seen a curvature of 7.45×10^{-6} in/in. As discussed, the graph is linear implying the materials behave elastically.

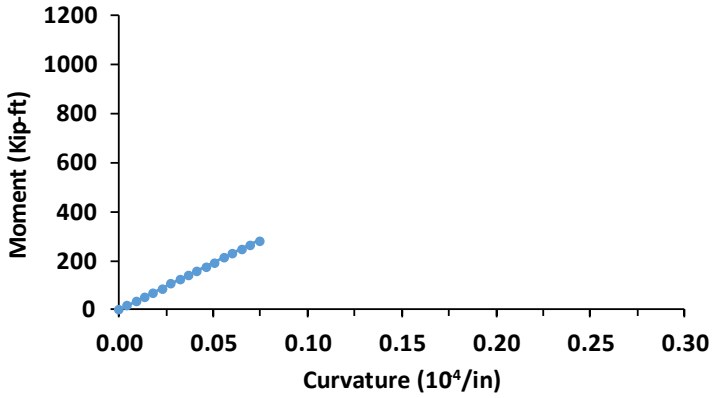

Figure 6-54: Moment-Curvature Plot for 6-in. Eccentricity Loading (Kotha, 2024)

6.3.4.1.1. Crack Pattern Comparison for the 6-in. Eccentricity Test

In the FEA for linear range loading rates which are 6-in., 12-in., and 20-in., although the tensile part of the column has gone through stresses, cracks are not observed until the end of the 20-in. analysis. For the 6-in. analysis, the tensile stress was not even enough to overcome the compressive effects due to prestressing, that is the reason no red regions (positive stresses or tensile stresses) are observed in Figure 6-55. Since the stress levels were minimal no cracks were observed in both the experimental specimen and the FEA model.

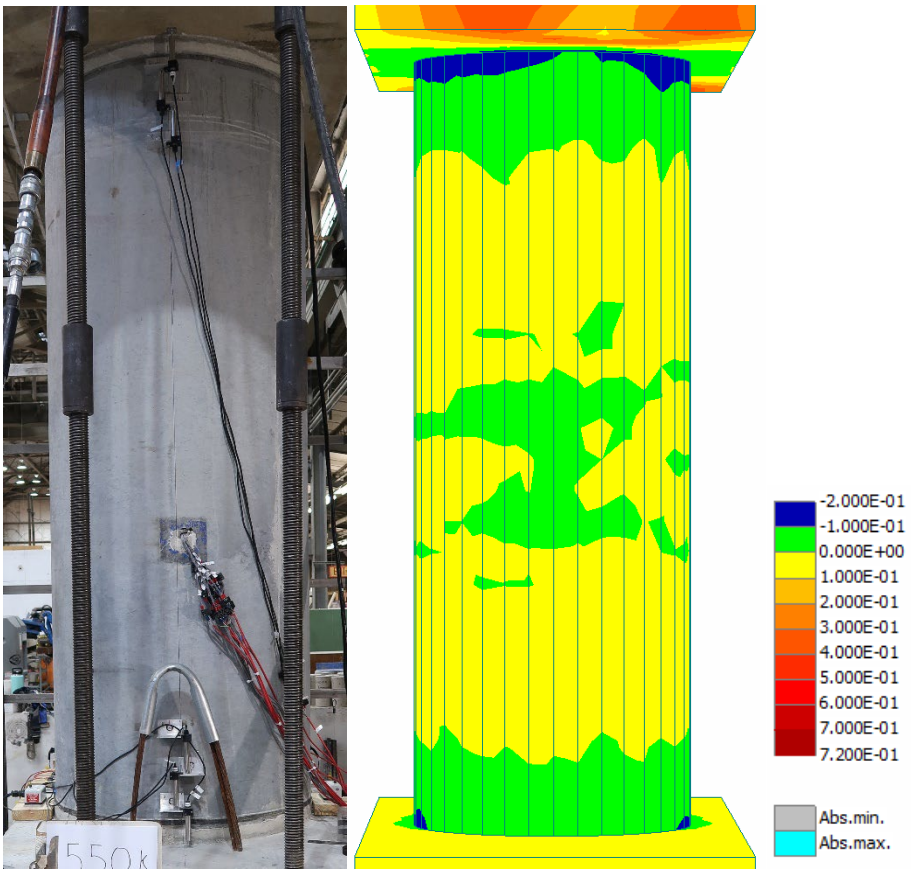

Figure 6-55: Comparison of Crack Pattern at the end of 6-in. Eccentricity Loading (stress levels in ksi) (Kotha, 2024)

6.3.4.2. Precast Column Model under 12-in. Eccentricity Load Pattern

The second load pattern is the 12 in. eccentricity test. In this analysis, a load of 27.76 kips was applied on the compressive side and 15 kips was applied on the tensile side per load step. The same details are presented in the below Figure 6-56, each step creates a flexural load with an eccentricity of 12 in., and these load steps were added until the total axial load reached 550 kips. Along with prestressing, 13 load steps were added.

Figure 6-56: Loading Setup for 12-in. Eccentricity Analysis (Kotha, 2024)

After all the load steps were assigned and analyzed, the column faced higher flexural stresses compared to the previous test. Figure 6-57(a) showcases the tensile side of the precast column at the end of the analysis. It can be observed that the zones close to the connections experienced tensile stresses as high as 0.5 ksi but the central regions of the column did not, and this could be because of two reasons. Firstly, since the end regions were not prestressed because of the bond model used and the transfer length, those regions are relatively weaker. Otherwise, since the prestressing of the precast shell was done maintaining the perfect connection between the bent cap and footing, end regions are affected even before loading. More details are presented in the section 6.4.1, where stress regions and crack patterns of the experimental specimen are discussed.

Additionally, the compressive side of the column experienced only 1 ksi of stress near the connections. Since the stresses were not high enough to reach the capacities, no sign of crushing was observed from the model, consistent with the observations from the experimental specimen during this test.

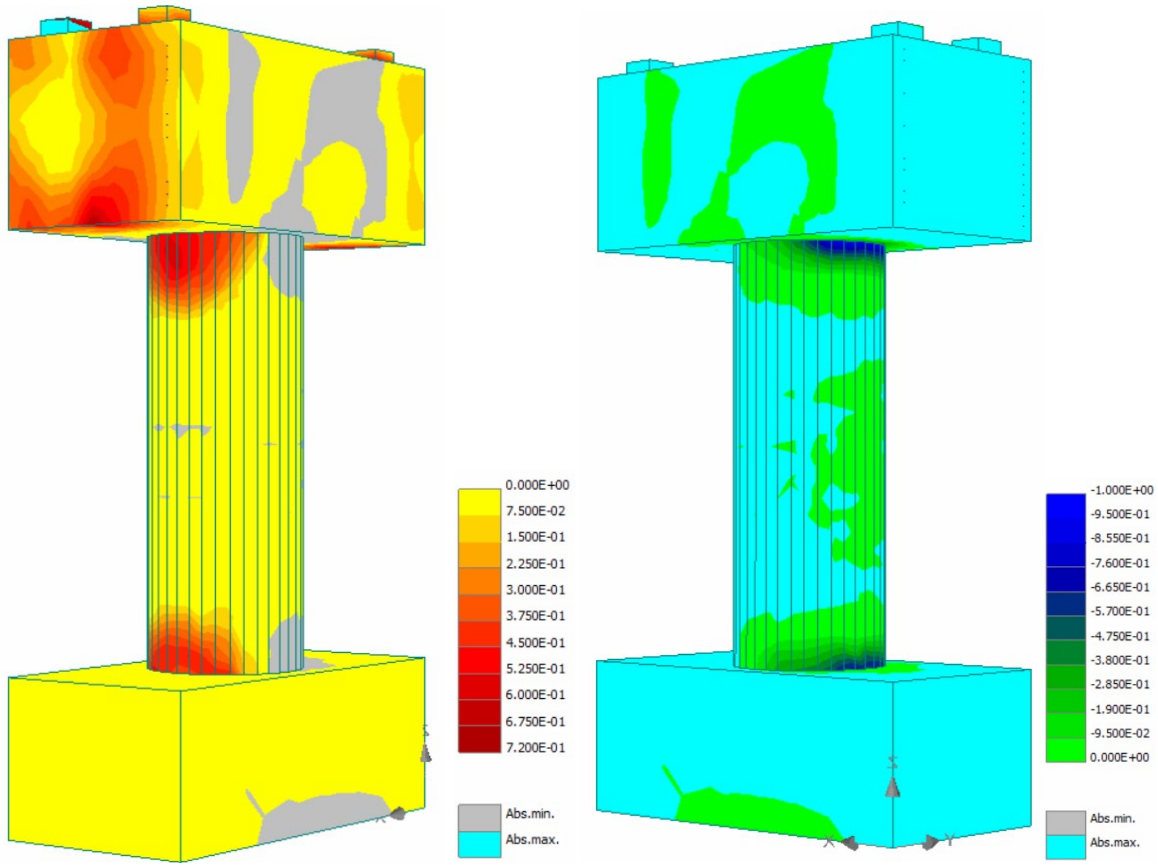

(a) Tensile side (b) Compressive side

Figure 6-57: Stress Levels in ksi and Cracking at the end of 12-in. Eccentricity Loading (Kotha, 2024)

The displacements were also captured, and data is presented in Figure 6-58 below. Similar to the 6-in. eccentricity analysis, the displacements are in a linear relationship with the total axial load. Cracks and yielding were not observed in any part of the column, and the column reached an end displacement of 0.0766 in., which is 2.1 times the end displacement of 6-in. eccentricity analysis.

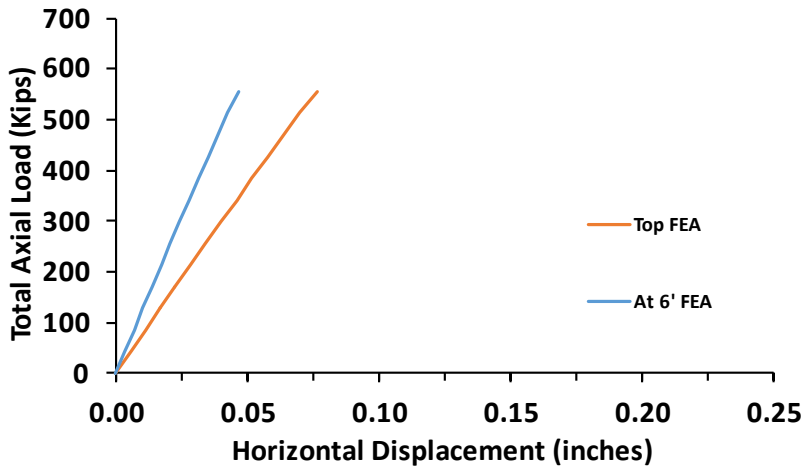

Figure 6-58: Total Axial Load-Displacement Behavior for 12-in. Eccentricity Loading (Kotha, 2024)

Looking at the bending moment-curvature plot for 12-in. eccentricity loading analysis in the Figure 6-59, a mostly linear behavior was observed, which is expected for the mildly flexural load of 12-in. eccentricity. For the end moment of 556.39 kip-ft, a curvature of 1.73×10^{-5} in/in was observed. Both the 6-in. and 12-in. eccentricity tests resulted in no yielding, no cracks, and linear load-displacement relationships, as observed in the laboratory.

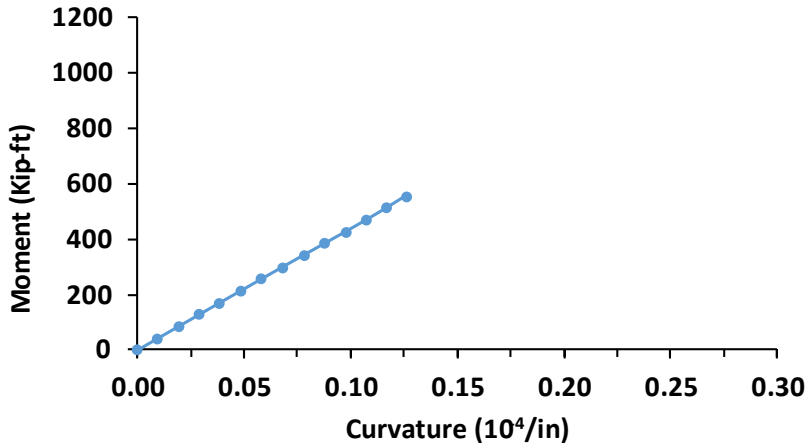

Figure 6-59: Moment-Curvature Plot for 12-in. Eccentricity Loading (Kotha, 2024)

6.3.4.2.1. Crack Pattern Comparison for the 12-in. Eccentricity Test

For the 12-in. eccentricity analysis shown in Figure 6-60, the end regions were first to pick up the stress as they are not prestressed. However, a maximum of 0.5 ksi is observed which is not enough to reach f_t' of 0.72 ksi. For this reason, no cracks are observed for both experimental and analytical models.

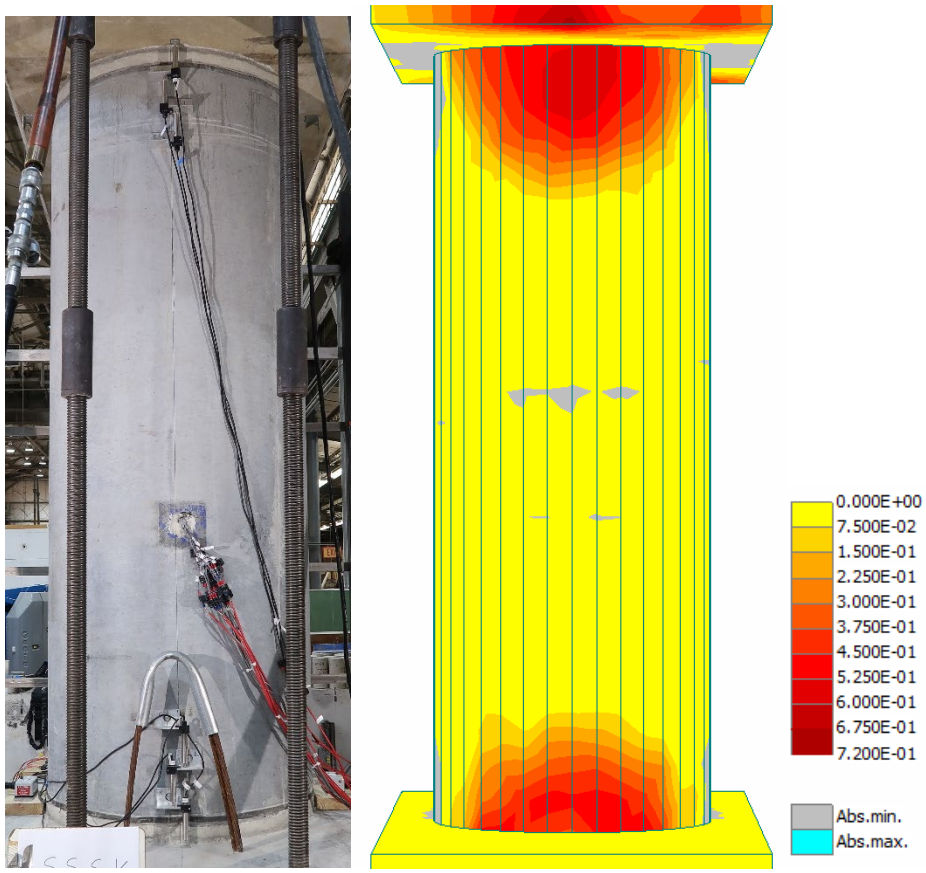

Figure 6-60: Comparison of Crack Pattern at the end of 12-in. Eccentricity Loading (stress levels in ksi) (Kotha, 2024)

6.3.4.3. Precast Column Model under 20-in. Eccentricity Load Pattern

The next load pattern to be discussed is the 20 in. eccentricity test. Similar to the previous analyses, 15 kips were applied on the tensile side of the column at each load step. On the compressive side, it was increased to 44.64 kips instead of 27.76 kips. As shown in Figure 6-61, ten load steps were added to achieve the total axial load of 596.3 kips.

After checking the analysis with the bond model, it was observed that the column experienced a lot more cracks near the connection regions than those regions that are not prestressed. Although the removal of the bond model may not be the accurate representation of the experimental specimen, it was required to control the unwanted cracks and achieve reasonably accurate results. A detailed parametric study was conducted on this bond model and is presented in section 6.3.5.2. Therefore, one important change in the model for 20-in. analysis was the removal of the bond model for strands in the precast shell. When there was no bond model assigned, the strands in the precast shell could get 75% of f_{pu} from start to end.

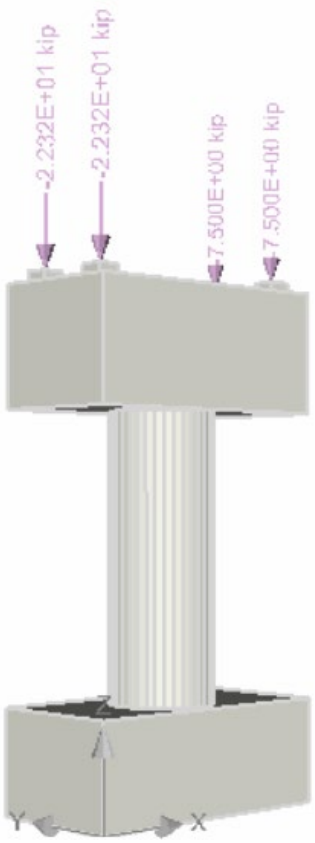

Figure 6-61: Loading Setup for 20-in. Eccentricity Analysis (Kotha, 2024)

After the analysis, it was seen that the column encountered a relatively high amount of flexural demand. From the Figure 6-62, it can be seen on the tensile side that the column experienced multiple cracks. The first cracks were observed at the connections since they are the critical regions and the cracks in the central region are initiated during the final stages of loading (in the last load step). Just before the cracking, the regions experienced tensile stress greater than 0.72 ksi. In contrast, no vertical cracks are seen on the compressive side of the column, as the maximum stress observed is only 1.96 ksi near the connections, which is only 19% of the compressive strength of the shell.

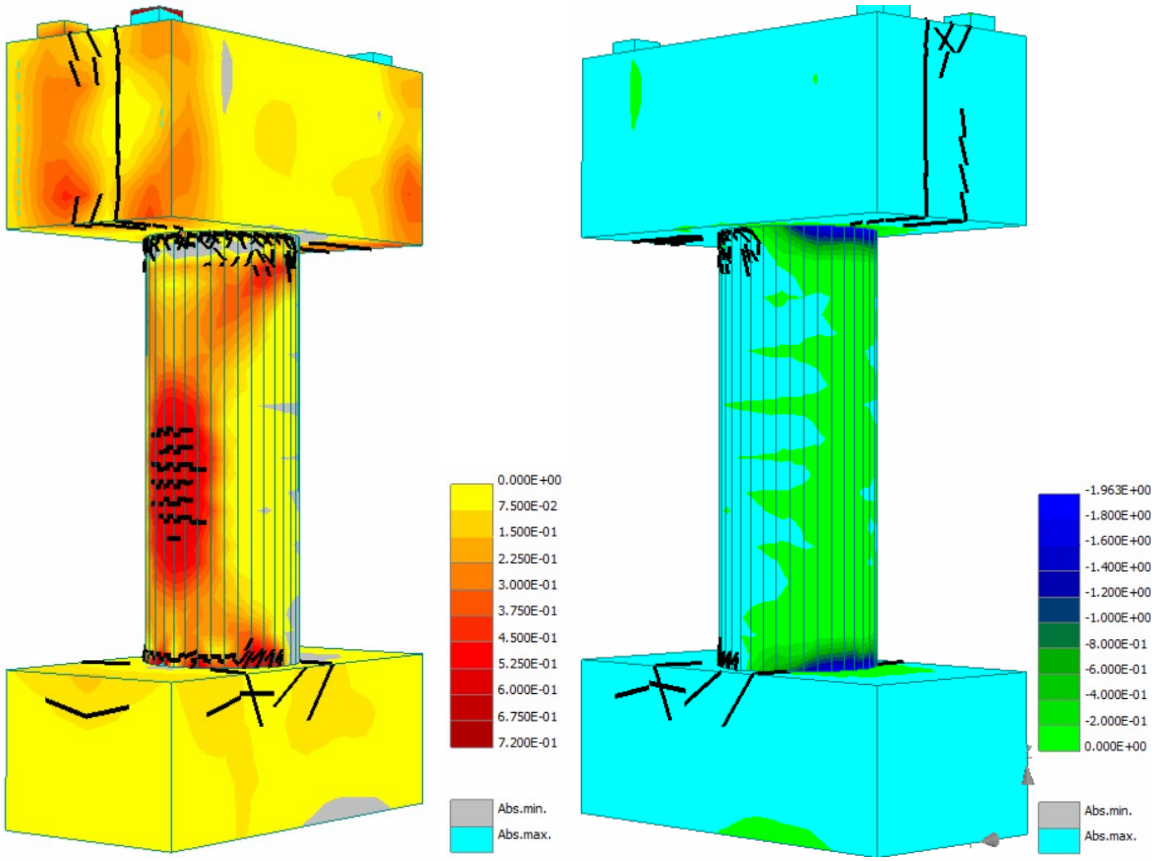

(a) Tensile side (b) Compressive side

Figure 6-62: Stress Levels in ksi and Cracking at the end of 20-in. Eccentricity Loading (Kotha, 2024)

Detailed load-displacement curves are presented in Figure 6-63, and the linear relationship between load and displacement is no longer observed. From the software, at nearly 300 kips of axial load, the cracks at the bent cap-column connection and column-foundation connection started to form. After increasing the load to 597 kips (final load increment), the cracks at the connection widened. Besides, cracks in the central region also started to form and further application of load from 597 kips would have resulted in even more displacements.

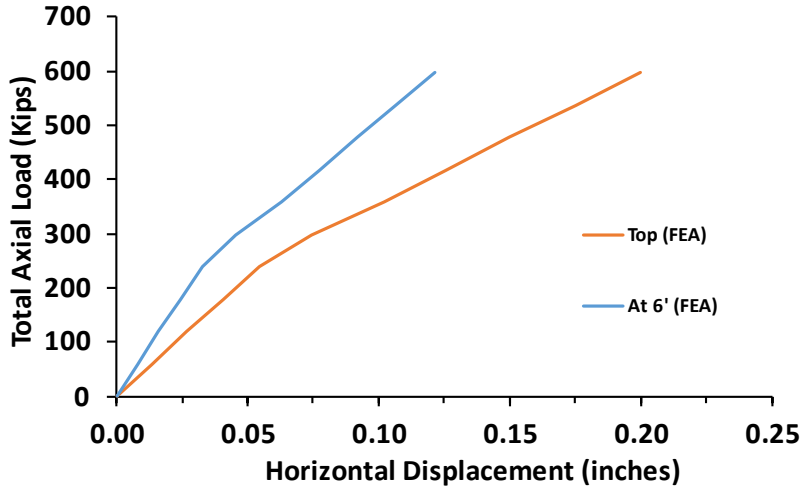

Figure 6-63: Total Axial Load-Displacement Behavior for 20-in. Eccentricity Loading (Kotha, 2024)

Looking at the moment-curvature plot for 20-in. eccentricity test analysis in the Figure 6-64, a mostly linear curve is observed, even though cracks are observed. Although a significant number of cracks appeared, the bars experienced no yield, and a slight shift was seen at 600 kip-ft point. For the end moment of 994.175 kip-ft, a curvature of 2.73×10^{-5} in/in was observed.

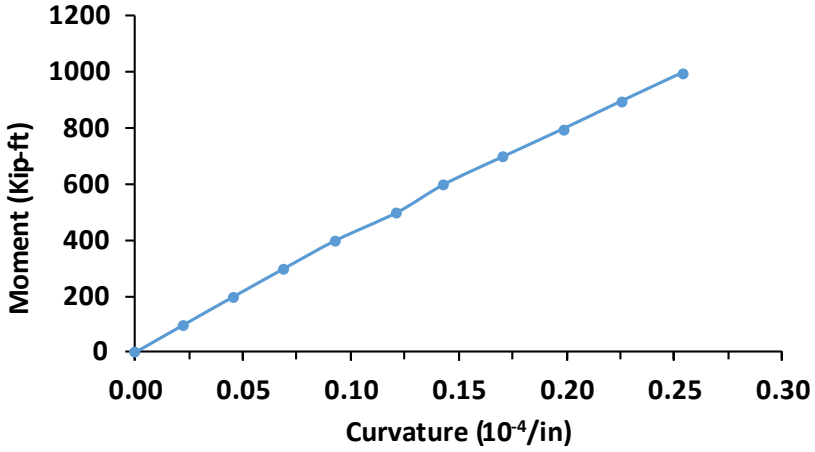

Figure 6-64: Moment-Curvature Plot for 20-in. Eccentricity Loading (Kotha, 2024)

6.3.4.3.1. Crack Pattern Comparison for the 20-in. Eccentricity Test

For the 20 in. eccentricity studied in this section, as observed from Figure 6-65, a crack at the top connection and 2 cracks at central regions are seen. For the FEA model, cracks are observed after the stress buildup near both the connections. After that, at the load step of 597 kips, central regions started to take the stress and reached f_t' causing all the elements to crack. Relatively more cracks are seen in the FEA model which can be attributed to a very fine mesh of 4 in. As each element participates on its own, cracks are shown in all the elements that reached f_t'. In total, the model

can accurately capture the stress flow and crack pattern for all the linear-range eccentricity load rates.

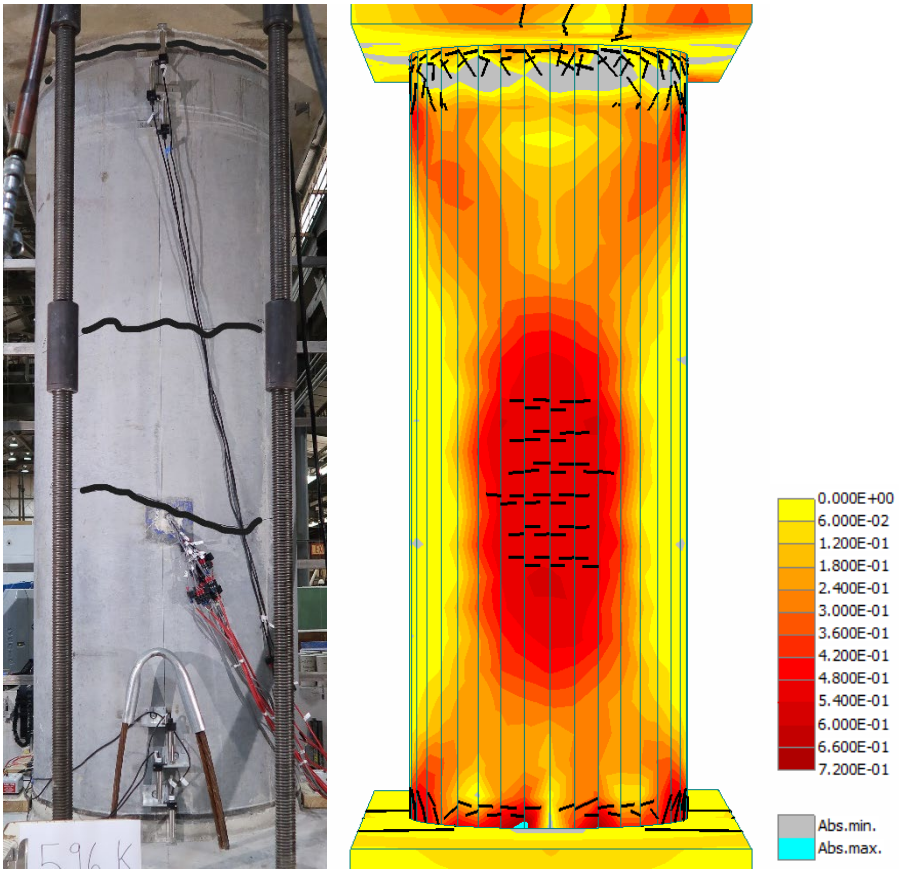

Figure 6-65: Comparison of Crack Pattern at the end of 20-in. Eccentricity Loading (stress levels in ksi) (Kotha, 2024)

6.3.4.4. Precast Column Model under 40.25-in. Eccentricity Load Pattern

Lastly, the most important load analysis was the 40.25-in. eccentricity analysis, which resulted in extremely high flexural demand, and the analysis was conducted until the numerical ultimate failure. According to the precast column P-M Interaction Diagram shown in Figure 6-66, the column was expected to fail around 384 kips at 40.25 in eccentricity. For that reason, each load step consisted of 30 kips on the compressive side and no load on the tensile side, the same was followed for the experimental specimen as well. Fifteen incremental load steps were applied after the prestressing stage established in the model.

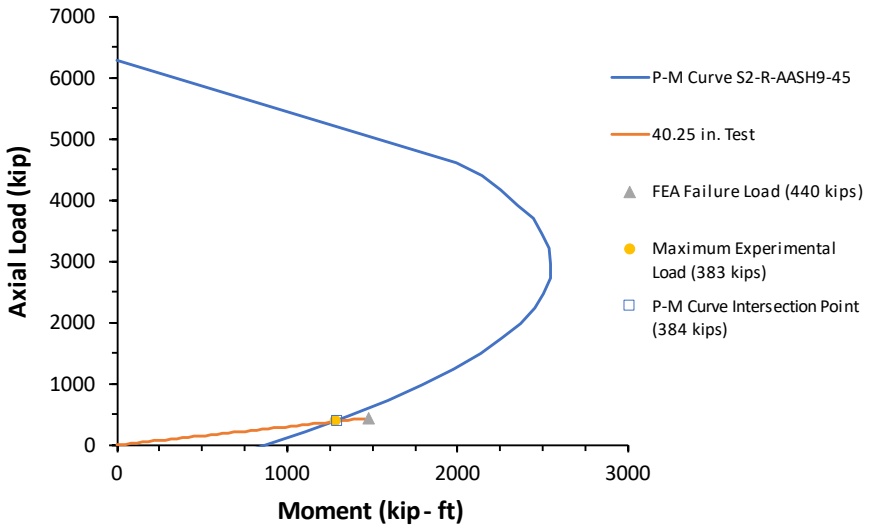

Figure 6-66: P-M Curve and Loading Setup for 40.25-in. Eccentricity Analysis (Kotha, 2024)

The tensile side of the column exhibited a lot of cracks and openings. Similar to the 20-in. analysis, initial cracks opened at the top and bottom connections of the column, as illustrated in Figure 6-67(a); then after the connection cracked, the stress began to build up in the central regions of the column, which led to more cracks. A crack filter of 0.005 in. was applied for better visualization of cracks. Along with the typical horizontal cracks that occur due to excessive tensile stress, diagonal cracks were observed at the zero stress areas, the transition zone from the tensile side to the compressive side. These were the regions that experienced a combination of tensile and compressive stresses which led to diagonal cracks, a similar pattern was observed in specimen S1-CIP as well.

Simultaneously, the compressive side of the column has experienced higher stress than previous cases as well, and only small cracks were observed which could be due to stress levels higher than compressive strength. But, as observed from in Figure 6-67(b), the connection of the column received only 4.81 ksi, which was 47% of compressive strength and these areas were no longer in a linear relationship with the load. For Figure 6-67(b), a crack filter was not applied since the number of cracks was very low.

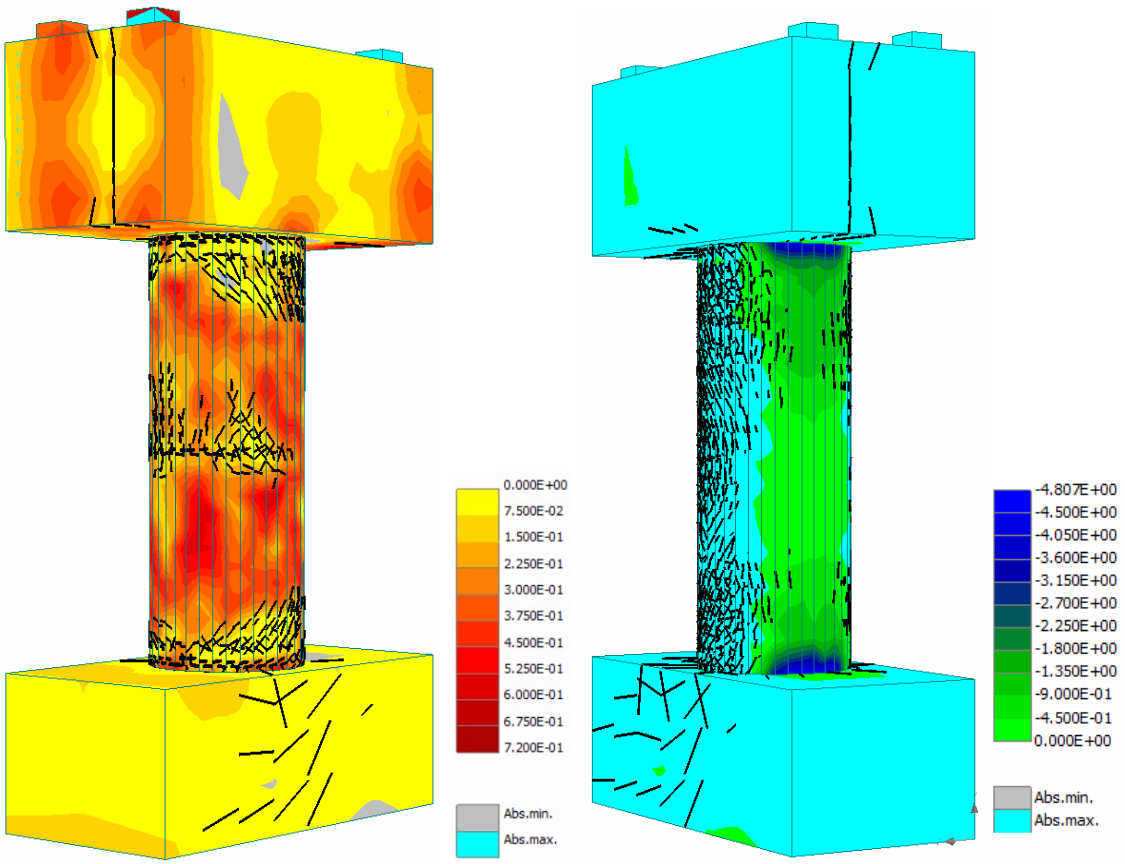

(a) Tensile side (0.005-in. crack filter) (b) Compressive side (No crack filter)

Figure 6-67: Stress Levels in ksi and Cracking at the end of 40.25-in. Eccentricity Loading (Kotha, 2024)

Considering the load-displacement curve shown in Figure 6-68, it can be interpreted from the initial impressions that the column behaved elastically at the start of the analysis when the load was below 100 kips but started to slip into a non-linear behavior after that. Given that monitoring points at the column's top (8' from the bottom) and at 6' from the bottom show a similar trend until failure, it can be interpreted that most of the column was behaving similarly and slipped into a non-linear behavior. The failure load for this analysis is 440 kips with a displacement of 3.27 in., to detect the failure load precisely load steps of 10 kips are applied instead of the typical 30 kips. The curves are shown only until 2 in. for readability.

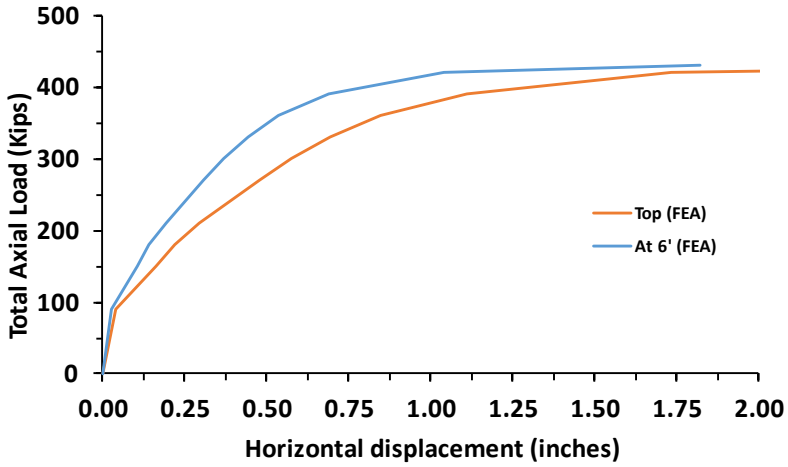

Figure 6-68: Total Axial Load-Displacement Behavior for 40.25-in. Eccentricity Test (Kotha, 2024)

From the previous graph, it can be observed that both concrete and reinforcement experienced non-linear stresses until failure. The graph can be divided into three zones: 1) load up to 90 kips where the column demonstrated crack-free, 2) load from 90 kips to 300 kips where reinforcement was in the elastic region, and 3) load from 300 kips to 440 kips (Failure load) where both regular bars and prestressed strands experienced post-yield stresses and the column underwent huge displacements.

The axial load-displacement plot at the top can be divided into 3 regions. The first point 90 kips was the load where the column experienced connection cracks. The second point 300 kips is the load when both the tensile reinforcement at connection and in the shell crossed respective yield points. Figure 6-69(a) and (b) show the stress levels in connection and shell reinforcement, respectively. Scales have been provided in the respective figures; the blue color represents stresses equal to yield stress where 65 ksi is blue for Figure 6-69(a) and 230 ksi for Figure 6-69(b). At failure load, which is 440 kips, the reinforcement at connection reached stress levels as high as 77 ksi, and the prestressing strands inside the precast shell reached 245 ksi. For that reason, the displacements at 300 kips to failure load increased from 0.57 to 3.27 in.

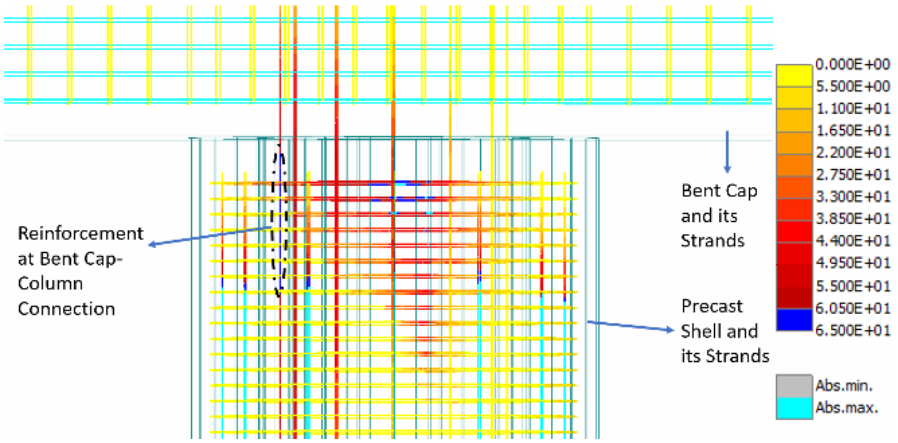

(a) Connection Reinforcement Yielding

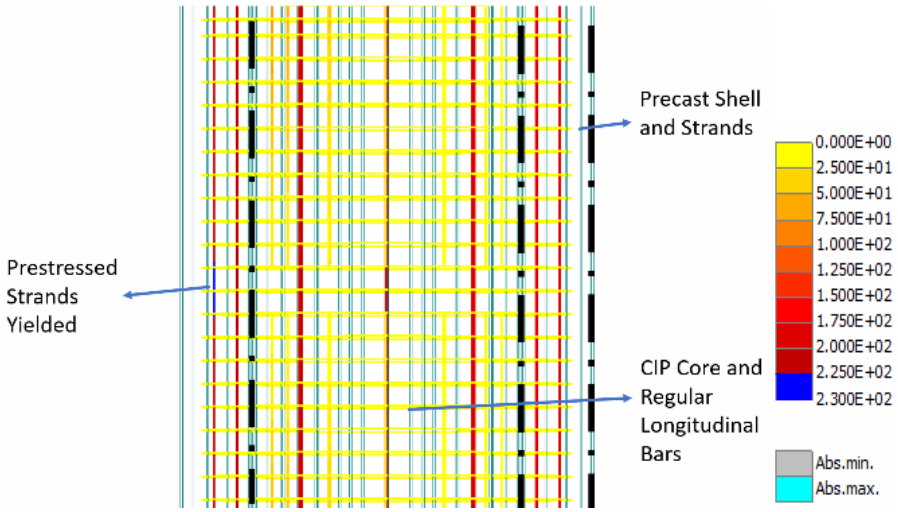

(b) Prestressed Strands Yielding

Figure 6-69: Reinforcement Stresses at 300 kips of Axial Load (Kotha, 2024)

Looking at the moment-curvature plot for 40.25-in. eccentricity loading analysis in the Figure 6-70, a similar trend as the load-displacement curve was observed. The curvature at the first three load steps barely changed as no cracks or yielding was observed. A semi-linearity can be observed until the 1000 kip-ft point as reinforcement started to increase stress, but they were still in the elastic region. Many cracks started to form before the 1000 kip-ft point. Later from that point, both regular bars and prestressed strands started to yield and deformed exceedingly until failure.

Overall, the software could capture displacements, strains in concrete and reinforcement, and crack patterns efficiently. The analytical model for specimen S2-R-AASH9-45, a precast column with an intentionally roughened interface failed at 440 kips, which is a moment of 1475.83 kip-ft with reasonable accuracy according to the P-M Interaction Diagram built for the experimental specimen.

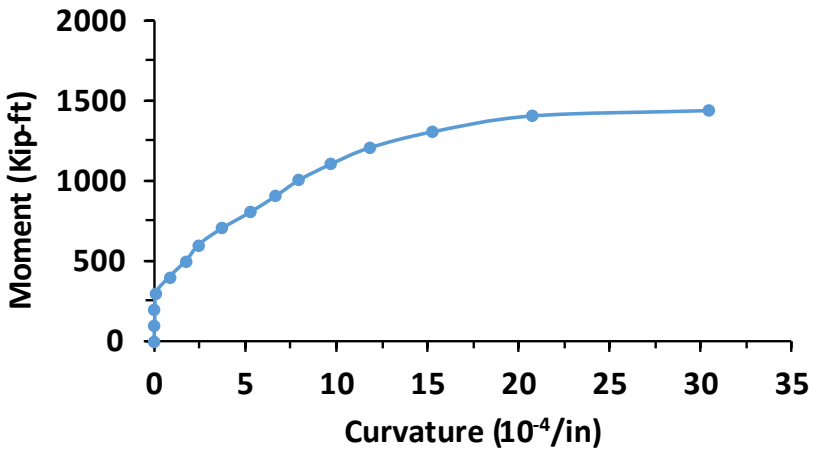

Figure 6-70: Moment-Curvature Plot for 40.25-in. Eccentricity Loading (Kotha, 2024)

6.3.4.4.1. Crack Pattern Comparison for 40.25 in. analysis

Given the reliability of the model accurately capturing both displacements and crack patterns for linear range eccentricity loadings, displacement-related data for 40.25 in. eccentricity loading is discussed in the section 6.3.3.1, and crack pattern comparison is done in this sub-section. As discussed in the FE model analysis in the section 6.3.4.4, the model has gone through tensile cracks at connection, tensile cracks in central regions, diagonal cracks in neutral-stress regions, and a few vertical cracks in the compressive region. These patterns are observed in the experimental specimen as well, and a detailed discussion is presented below.

It should be noted that the experimental specimen has failed at 383 kips of axial load, but the FE model has shown a failure at 440 kips. For the comparison, the analytical model's cracks are not completely developed at 383 kips. So, the crack comparison is done at respective failure loads, and the model has gone through more cracks than expected because of the very fine mesh size so a crack filter of 0.04 in. is applied.

The images presented in Figure 6-71 are the tensile sides of the experimental specimen and the FE model at respective failure points. At the initial glance, the experimental model is seen with horizontal cracks distributed from top to bottom implying the column has surpassed f_t'. Along with that, a crack at the top of the connection and, a gap at the foundation-column connection.

The same pattern was observed in the analytical model as well. Most of the column is yellow implying the regions are cracked and are no longer able to take stress. A crack is found at both connections, as perfect connection was maintained at connections which is not the case with the experimental specimen, the cracks at connection have relatively larger widths. The next crack with a bigger width was found at the center, where the experimental specimen faced failure.

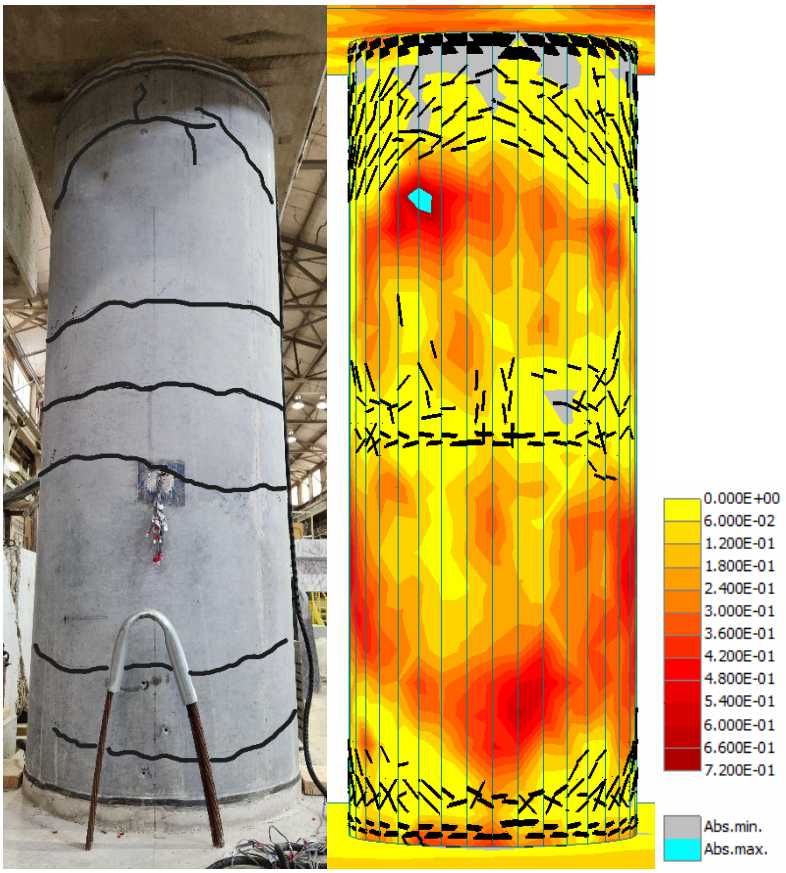

Figure 6-71: Tensile Side Comparison at the end of 40.25-in. Eccentricity Loading (stress levels in ksi) (Kotha, 2024)

Some other cracks near the connection are horizontal on the tensile side but they are making an angle going from the tensile side to the compressive side. This can be seen in below Figure 6-72, and the cracks near the connection in the software model follow the same pattern as experimental ones as well, horizontal at the tensile side and going diagonal in neutral stress regions. Because of finer mesh and perfect connection, more cracks are observed at the connection regions.

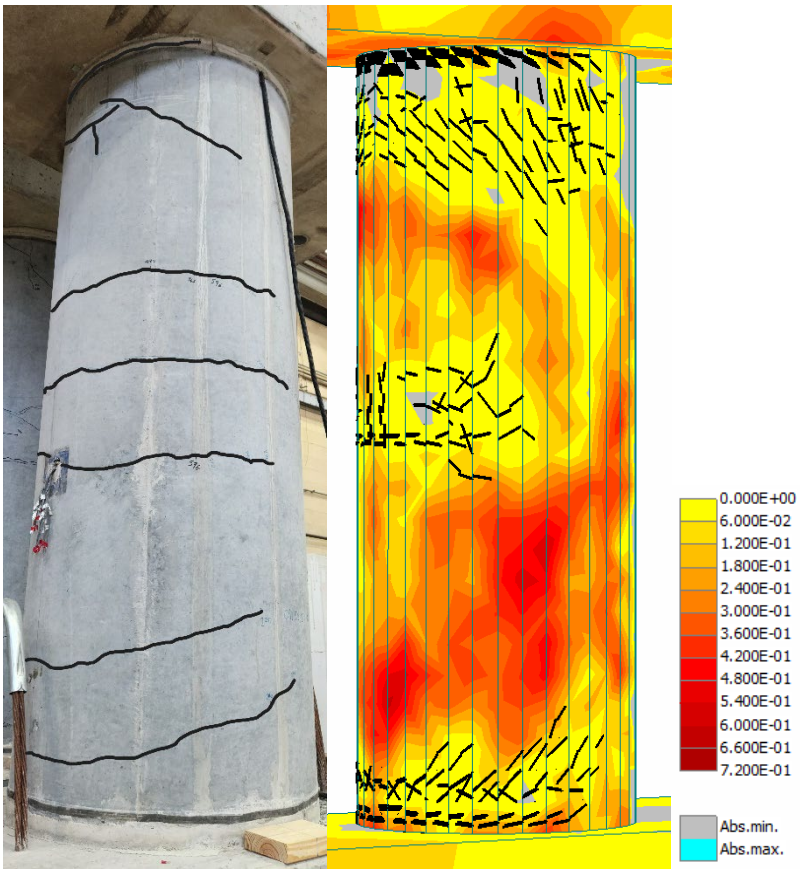

Figure 6-72: Neutral Stress Side Comparison at the end of 40.25-in. Eccentricity Loading (stress in ksi) (Kotha, 2024)

The next cracks to be discussed after tensile and diagonal cracks are the cracks in compressive regions, presented in Figure 6-73. A huge chunk of concrete can be seen spalling out near the center which is caused by compressive stresses higher than f'_c. No cracks are seen at connection regions. On the analytical side, vertical cracks are seen at the top half and bottom half of the column which indicates the model's ability to capture the stresses going beyond compressive strength, although exact location was not predicted.

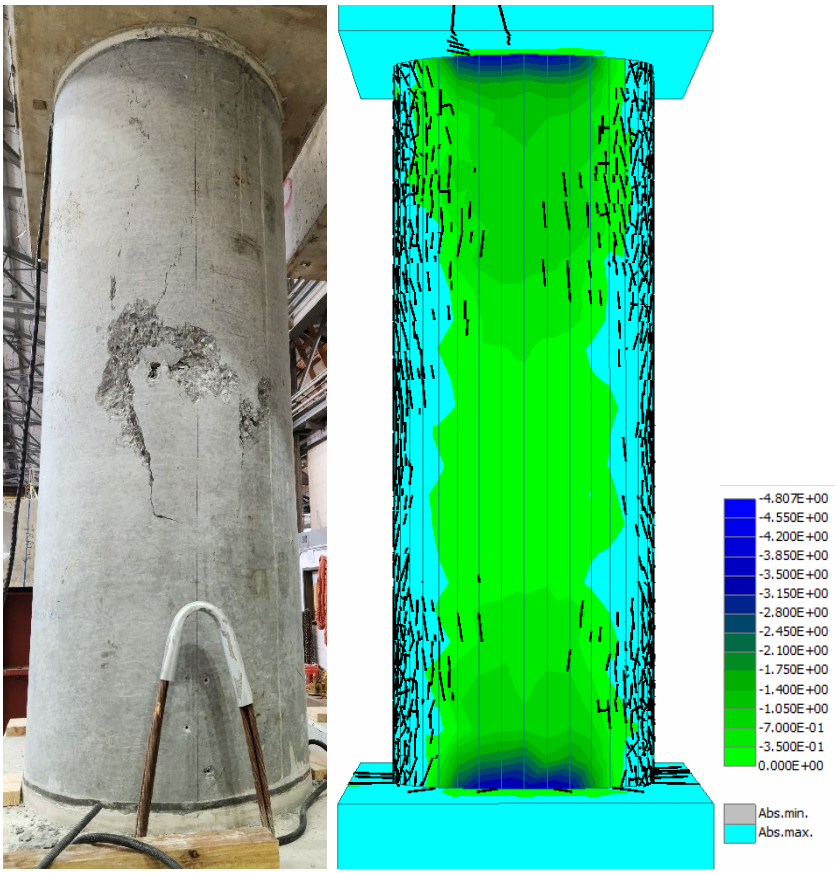

Figure 6-73: Compressive Side Comparison at the end of 40.25-in. Eccentricity Loading (stress levels in ksi) (Kotha, 2024)

In sum, the prepared precast column model in FEA software could capture horizontal, diagonal tensile, and vertical compressive cracks in all the regions accurately, for extreme flexural loading of 40.25 in. eccentricity.

6.3.5. Parametric analysis on connections and bond model

From the previous sections where discussions on computational analysis, and the comparison between experimental results are presented, it is clear that the prepared model could capture the displacements, flow of stress, and crack patterns accurately for all the eccentricity loading rates. However, there are a few areas where refinement can be necessary. For example, the bond model was removed (which enabled complete prestressing from top to bottom) for the 20-in. eccentricity analytical model because significantly higher cracks are observed at joints. The same was observed for the 40.25-in. analysis as well, especially during the first half of the analysis. In addition, the analytical column model failed at a higher load (440 kips) than the experimental specimen (383 kips). This suggests that the connection is not behaving accurately, but only during the final stages of 20-in. and initial stages of 40.25-in. eccentricity analyses where connection cracks are initiated.

In this section, the precast shell connections, and strands' bond model are studied. In real life, as discussed before, the connections are not perfect as reinforcement in the precast shell does not

extend into the foundation and the bent cap. A gap was observed in these connections as well, at the end of testing implying that complete load transfer is not guaranteed. In addition, prestressing and transfer length plays a key role in concrete's strength and modulus but these parameters are not known accurately as well since the process of prestressing is not monitored. For this reason, the best and worst cases of connections and bond models are studied and presented in the next sections.

6.3.5.1. Analysis of Precast Shell Connections

During the construction process of the experimental specimen, after placing the footing, four 1.5-in. HDPE shims were placed on it at the location of the precast shell. Then, the 8 ft. tall precast column was placed on the shims, and the core of the shell was filled with regular concrete with the plastic shims warranting a gap of 1.5-in. Although the inner core of the column is bonded with the footing through the extending reinforcement, the precast shell was bonded with the footing by the unreinforced core concrete, and this part undergoes tensile and compressive stresses on either side of the column during testing. For that reason, instead of a perfect connection, imperfect contact elements with the properties mentioned in Table 6-20 are assigned for the respective connections. These are calculated in the procedure mentioned in the section 6.1.3 with a test sample size of 3 in., as the height of the plastic shim is 1.5 in.

Table 6-20. Estimated Precast Shell Connection Properties

Parameter	Values
K_{nn} (kci)	295.22
K_{tt} (kci)	1333.79
Cohesion (ksi)	0.15
Tensile Strength, f_t (ksi)	0.28
Friction Coefficient	0.60

The entire model and loading steps are the same except the connections are replaced from perfect bonding to these parameters. As perfect connection is tested before, this case is relatively very conservative because the bond between connections is completely lost once the tensile stress reaches 0.28 ksi. But that is not the case, as the shell in the experiment experienced huge tensile stresses until the end of analysis which led to tensile cracks throughout the specimen. For simplicity, this model is tested only the 40.25 in. analysis, and the results are discussed below.

After applying the prestressing with the bond model and load steps on the model, the displacement data is provided in Figure 6-74. This particular model failed at the load of 400 kips, closer to the experimental failure value. However, the displacements had significant differences of 64.4% and 95.1% at the B-2 and B-1. monitoring points respectively, at experimental failure load. Just after the first load step (30 kips of load), it is seen in the software that the connection has lost its bond, and it continued to widen until failure.

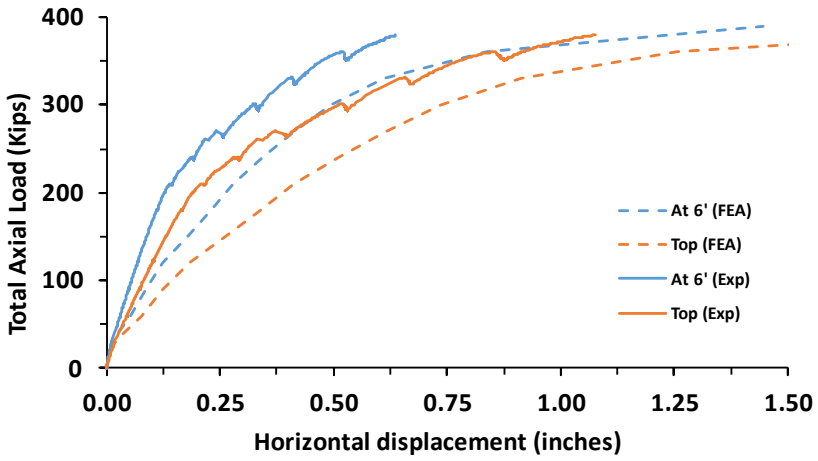

Figure 6-74: Comparison of 40.25 in. analysis for Experimental Specimen and Analytical model with imperfect connection (Kotha, 2024)

As anticipated, the results were very conservative and a comparison between perfect connection and imperfect connection is presented in Figure 6-75. Similar to the model with perfect connection, yielding was observed in the prestressing strands and bars at connection but cracks at connection, and compressive side are not observed. With reasonable failure load estimation but inaccurate displacements and cracks, this model with imperfect connection is not dependable and can be concluded that the experimental specimen has indeed completely or mostly perfect connections, as results were matching more accurately.

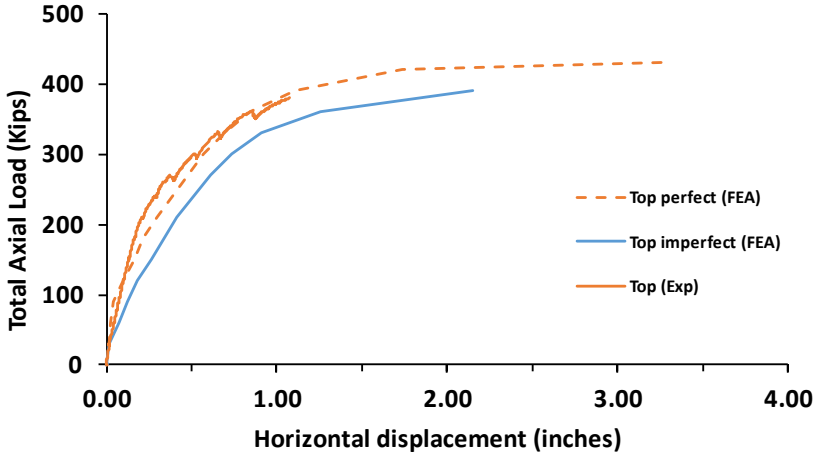

Figure 6-75: Comparison of 40.25 in. analysis for Analytical Model with Perfect and Imperfect Connections (Kotha, 2024)

6.3.5.2. Analysis of the Bond Model for Prestressing Strands

For the strands in the precast shell, the bond model assigned is the Bigaj 1999 model, and for a user input diameter, transfer length is automatically calculated, and the stress is distributed accordingly throughout the bars. In this case, the transfer length is about 20.5 in. which is close to

$50d_b$, the typical transfer length for prestressing strands with pre-tension process. In the case of the experimental specimen, the action is post-tensioned which means the prestressing is achieved throughout the column, but there are some actions during prestressing to say that complete prestressing is not guaranteed. Strands are not anchored during the action, losses of prestressing due to shrinkage, and two strands are prestressed per duct, bond between grout and precast shell is not known. For that reason, in this section three analytical models are studied for the 40.25 in. eccentricity analysis: a very conservative model with no prestressing, a model following Bigaj's 1999 model, and a model with no bond model meaning the prestressing is achieved throughout the column without any transfer length. It should be noted that a perfect connection between the bent cap, foundation, and precast shell was maintained since that gave an accurate representation of the experimental specimen as discussed in the previous section.

Figure 6-76 presents the displacement data for all the 3 models. It can be observed that choosing a good bond model is very important for accurately predicting the behavior. The dashed orange line is the model with Bigaj 1999 bond, which gave a transfer length of approximately 20.5 in., and this was followed for all the eccentricity analyses. The blue line represents the model with complete prestressing from the start to the end of the shell, and the yellow line represents the model with no prestressing at all. The model with no prestressing has failed at a load of 340 kips since it has evidentially lesser modulus which led to serious cracks at earlier load rates.

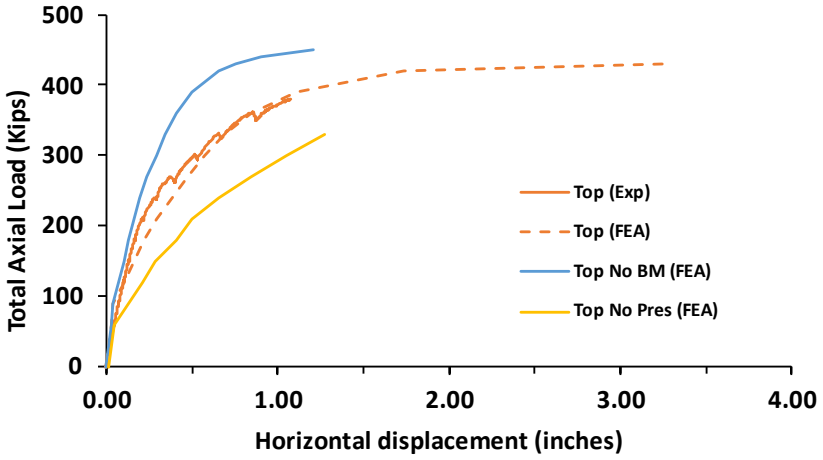

Figure 6-76: Experimental and Analytical results of Models with different Prestressing Levels (Kotha, 2024)

The next model to be discussed is the one with complete prestressing. Due to the absence of a bond model, fewer cracks were found near the connection which led the column to stay in the elastic region for a longer time. The model has failed at 460 kips, 20 kips higher than the Bigaj 1999 model, and almost 80 kips higher than the experimental specimen. It has a difference of 60% in displacement at 383 kips, the experimental failure load point. Although this model can be said inaccurate for heavy eccentricity like 40.25 in. analysis, for linear range eccentricity load rates, the model is well coinciding with Bigaj (1999) model and the experimental specimen as cracks are not formed in these levels. At the end of the analysis, a similar crack pattern was found in tensile

regions, and compressive regions but displacement values were not in good agreement with experimental values.

In conclusion, Bigaj (1999) bond model is a good selection for this test as it was reasonable in predicting the displacements for both linear range and highest 40.25 in. eccentricity analyses but exhibited post-peak behavior. Other bond models and element types can be explored.

6.3.6. Summary of Precast Model

- From the parameters of interface shear models, and modeling techniques from the CIP column model, a refined precast column model with an intentionally roughened interface was prepared in the ATENA 3D software and subjected to various loading rates.

- The 6-in., 12-in., and 20-in. eccentricity analyses were within elastic-linear loading range, and yielding was not achieved. These eccentricity values were achieved by maintaining a specific axial load ratio on either side of the column but not exceeding the total axial load of 550 kips.

- The model followed a load pattern corresponding to a 40.25 eccentricity until reaching failure, allowing to check the flow of stresses, and displacements. The model has failed at an axial load of 440 kips, showing a reasonable resemblance with the P-M Interaction Diagram, and 14.9% higher strength than the experimental failure load of 383 kips. It could be attributed to the higher bond strength of reinforcement, compressive parameters of concrete in the analytical model, or lack of surety in the prestressing level.

- At the end of analyses, the model could predict the tilt and displacements accurately with a mere 7.7% difference for linear range eccentricities, and only 2.4% for 40.25-in. eccentricity analysis at experimental failure load. Additionally, the software could accurately predict all the cracks in tensile and compressive regions for all eccentricity loading rates.

- Parametric analyses were conducted on special areas of the model like member connections and prestressing levels of the precast shell. After extensive analyses, it is concluded that the perfect connection between members and the Bigaj 1999 bond model for prestressing strands has given accurate results when compared with experimental results.

- Shell elements and bond model for bars could be further explored for more accurate results, as substantial yielding was not observed in the experimental specimen.

6.4. Precast Columns with Different Interfaces and Reinforcement Length

In the previous section, modeling, and analysis of the precast column with an intentionally roughened interface were studied. After selecting the details like connection strength, a bond model for bars, and prestressing strands, construction case features, the analysis results are observed to be in good agreement with experimental outcomes. The same precast column analytical model was taken to study the behavior of other precast columns in the project, the one with a naturally smooth interface between shell and core (S3-S-AASH-45) instead of roughened, and other columns with different reinforcement embedment lengths connecting the bent cap and the foundation to the column core (specimens S4-R-Tx-34 and S5-R-ZABORAC-28).

In this section, changes in the model of these particular precast columns are discussed and analytical results of only 40.25 in. eccentricity analysis are presented since the column has not encountered cracks or yielding in linear range eccentricity analyses.

6.4.1. Precast Column with Smooth Interface Analysis and Results

The only change between the precast column discussed in the previous chapter (specimen S2-R-AASH9-45) and the column with a smooth interface was the inner surface of the shell (specimen S3-S-AASH9-45). The same concrete was used to cast the core of the column and other elements of the test specimen are precast, so their properties are also kept unchanged.

6.4.1.1. Changes in Modeling Precast Column with Smooth Interface

The properties of both interfaces are presented in Table 6-21 and the graphs explaining the terms are shown in Figure 6-4. As observed, tensile strength was mostly the same but shear-related properties like cohesion and friction coefficient are higher for the intentionally roughened interface. Along with that, normal stiffness and tangential stiffness parameters are also higher in value, implying that normal/tangential interface slip is lesser for the same application of tensile/shear stress. Other parameters like the minimum value of stiffness are kept at 0.1% of the original stiffness value to avoid convergence issues, as suggested by the software manual.

Table 6-21. Interface Properties for Different Types of Surfaces

Interface Type	K_{nn} (kci)	K_{tt} (kci)	Cohesion (ksi)	Tensile Strength, f_t (ksi)	Friction Coefficient
Smooth	295.22	31.31	0.1487	0.384	0.6
Rough	340.55	57.72	0.1972	0.351	1.0

6.4.1.2. 40.25-in. Eccentricity Analysis and Results

Similar to the previous analytical model, the column was loaded 30 kips per load step and added until failure. The Figure 6-77 shows the 40.25 in. eccentricity experimental results of a completely

cast-in-place (CIP) column, a precast column with an intentionally roughened interface, and a precast column with a natural smooth interface, at the top of the column. Firstly, it can be observed that the CIP column has a similar stiffness to that of the precast column as the displacements are mostly the same in linear range-loading below 100 kips. However, due to the lesser tensile strength of the CIP column, more crack openings led to higher displacements, which triggered yielding in earlier stages.

On the other hand, it can be observed that precast columns have experienced similar displacements from the start of the analysis and failed at the same load of 382 kips, but the column with a smooth interface has slightly higher displacements. For instance, at the load of 380 kips (close to failure loads), the column with a roughened interface has a top displacement of 1.075 in., and the one with a smooth interface has 1.170 in., only 8.8% higher displacement. Overall, the column has behaved similarly with the same failure load, only with slightly lower displacements.

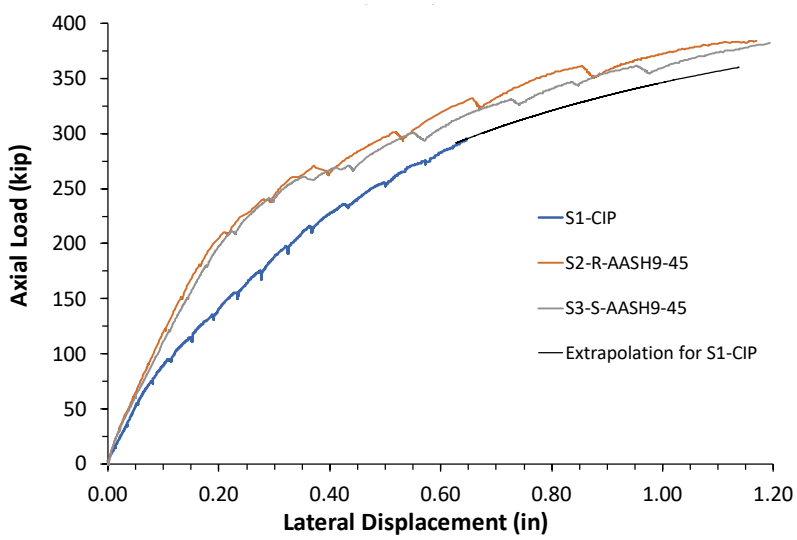

Figure 6-77: Experimental Results of CIP and Precast Columns under 40.25 in. Eccentricity Analysis

The analytical results were in good agreement as well. As shown in Figure 6-78, similar pattern can be seen in both experimental and FE model. Firstly, the column started in the linear region and then experienced cracks and yielding, which led to failure ultimately at a load of 430 kips, 10 kips less than the previous analytical model with an intentionally roughened interface. Although, the column experienced displacements up to a load of 430 kips, displacement data until 400 kips is presented for comparison. At the load of 360 kips (just before the experimental failure load), 12.0% and 16.5% displacement differences were seen at the top and 6' monitoring points on the column.

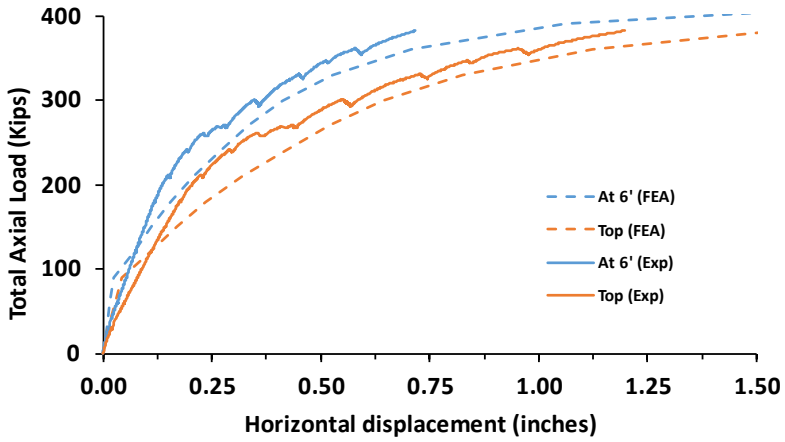

Figure 6-78: Comparison of 40.25-in. Eccentricity Analysis and Experimental Results (Kotha, 2024)

Along with that, a crack comparison is presented in Figure 6-79. The main horizontal cracks at the center and the connections occurred at the failure load. The cracks just near the center were horizontal on the tensile side but they started to make an angle going to neutral stress areas. This was observed in the analytical model as well, and a few vertical cracks in the compressive region were found, which was the place where the experimental specimen failed.

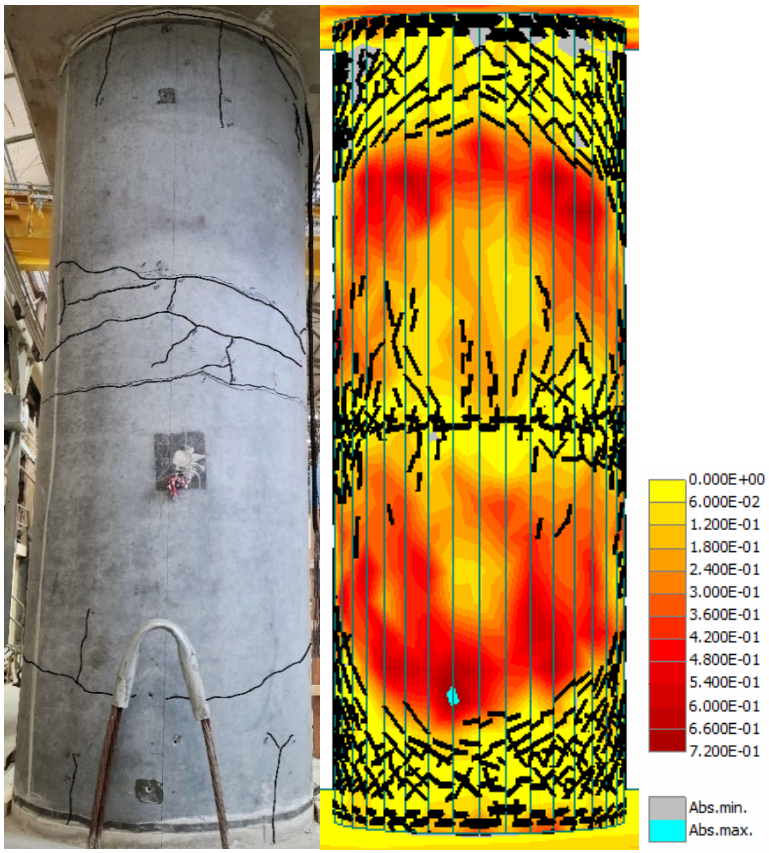

Figure 6-79: Tensile Side Comparison at the end of 40.25-in. Eccentricity Loading (stress levels in ksi) (Kotha, 2024)

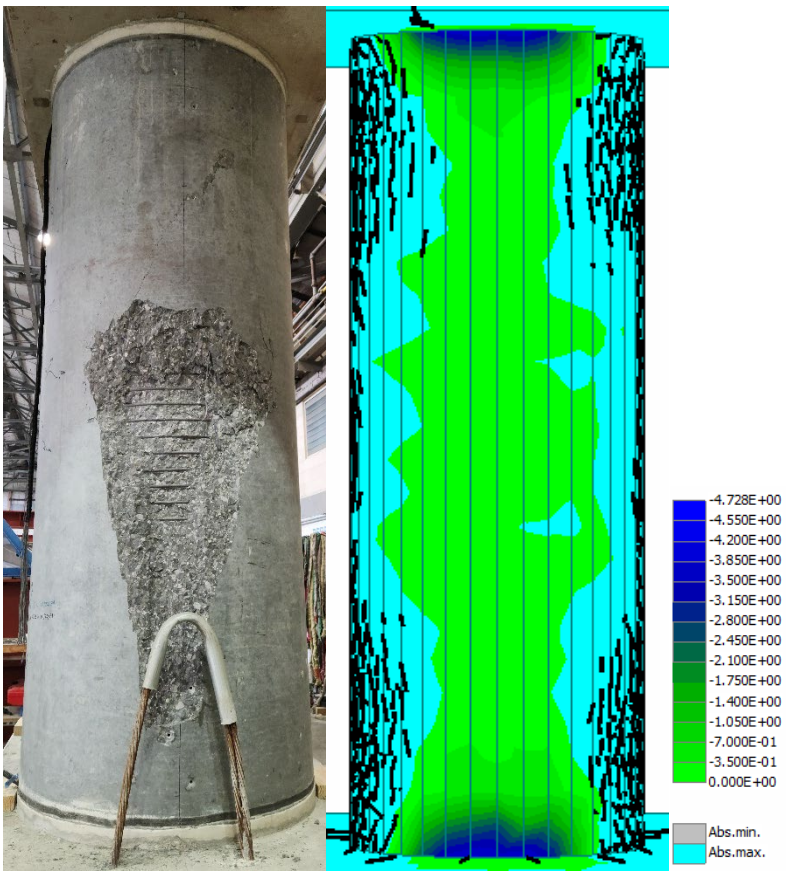

Figure 6-80: Compressive Side Comparison at the end of 40.25-in. Eccentricity Loading (stress in ksi) (Kotha, 2024)

In sum, both displacement and crack patterns were predicted with reasonable accuracy. implying that the analytical model could capture the stress flow, crack openings, and yielding of the experimental specimen.

6.4.2. Precast Column with Different Lap Splice Length (2'-4")

The next model to be discussed is the precast column with a different reinforcement length inside the column's core. As shown in the previous section, the 8' column consists of mainly 3 sections of longitudinal reinforcement. Firstly, prestressing strands extended from top to bottom of the precast shell. Next, ten #9 bars went through the bent cap and the column's core, and twelve #9 bars entered the column's core from the footing. In the previous section, a precast column with an intentionally roughened interface had bars length of 3'-10" that penetrated the core of the column from the bent cap and foundation, leaving almost 7 in. without any lap-splice at the center of the column. Regarding the model in this section, the rebar embedment length was reduced from 3'-10" to 2'-4", to examine the changes in analysis results, if any. Apart from that, the interface was assigned the same parameters.

6.4.2.1. Analysis and Results for 40.25 in. Eccentricity Test

The first two load steps of the analysis are prestressing the bent cap and prestressing the precast shell. After that, load steps of 30 kips each are added until the model fails. The load-displacement data has been shown in Figure 6-81. For comparison, the FEA results of the precast column with 3'-10" reinforcement length are also shown in the figure. Until 150 kips, the model showed similar displacements at both 6' and top monitoring points, implying that the column's linear region was not affected by development length. However, a shift of the graphs was seen after that load step which can be attributed to bigger crack openings, as yielding cannot be observed in early loading stages. After many crack openings until an axial load of 310 kips, the model failed with a displacement of 0.98 in. at the top, and 0.59 in. at 6' monitoring points, which is almost 70.7% and 60.2% higher than that of the column with 3'-10" bar length.

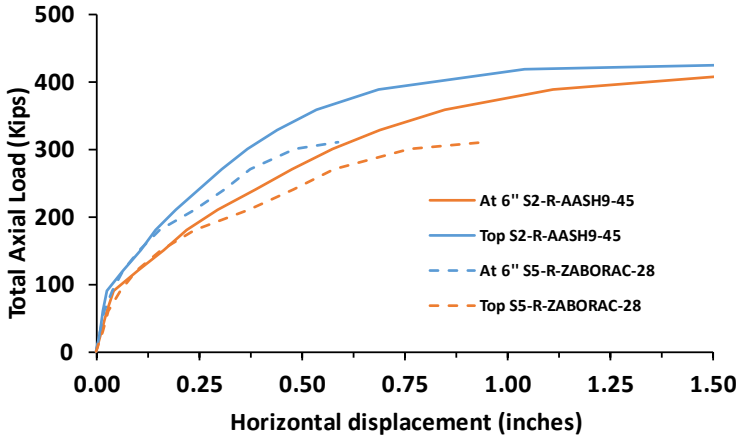

Figure 6-81: 40.25 in. Eccentricity Analysis Results of Precast Columns with Reinforcement Length of 2'-4" and 3'-10" (Kotha, 2024)

At the end of the analysis, no yielding was observed at the bent cap-core connection, and strands in the precast shell. As observed from Figure 6-82, the bars on the left are the ones that experienced the highest tensile stress but they did not reach blue regions, which means yield stress of 65 ksi and 230 ksi for normal reinforcement bars and prestressing strands, respectively. They reached close to 55 ksi, and 200 ksi respectively before failure, implying that bars were not developed at failure load. It is interesting to note that prestressing strands did not take any load since the 200 ksi stress was achieved even before the start of load, in the prestressing stages.

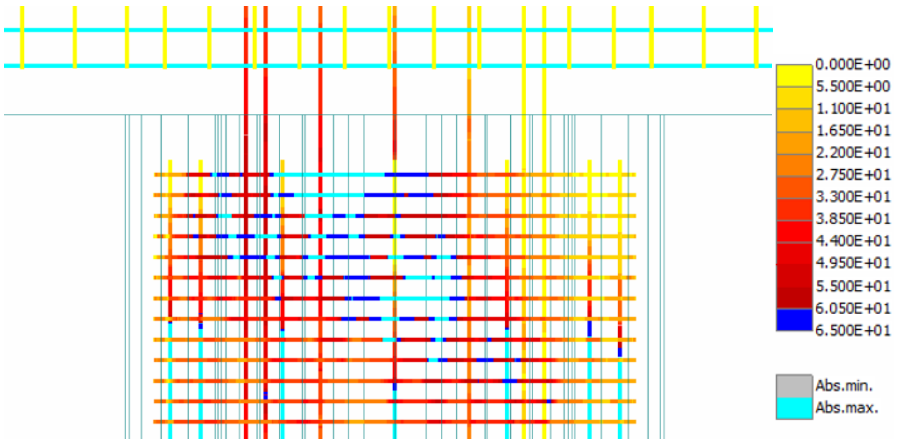

(a) Bent Cap- Column Connection Reinforcement

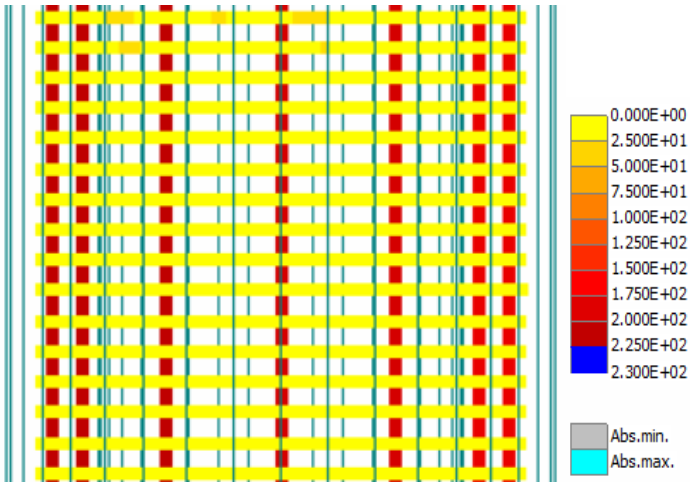

(b) Central Regions of Prestressed Strands

Figure 6-82: Reinforcement Stresses at Failure Load, 300 Kips of Axial Load (Kotha, 2024)

From the crack pattern at failure presented in Figure 6-83(a), it can be seen that the central regions of the column did not take any stress at all. Instead, the cracks started at a certain distance above the center. In the previous case of specimen S2-R-AASH9-45, there is no lap splice in the central region for only 7 in. as the bars are extending 3'-10" from the top and bottom of the column. But the specimen S5-R-ZABORAC-28 column had only 2'-4" extending reinforcement length, the central region of 3'-1" did not have any lap splice. This shell and core in this region barely took any stresses. Crack pattern in tensile region for analytical model and experimental specimen of precast column with 3'-10" lap splice was presented in Figure 6-83(b), and Figure 6-83(c) respectively, loaded until 300 kips. Since the bars were developed, the stress distribution was more uniform throughout the column and cracks were formed at the center. Very few vertical cracks were found in the compressive side of the column with a 2'-4" lap splice length.

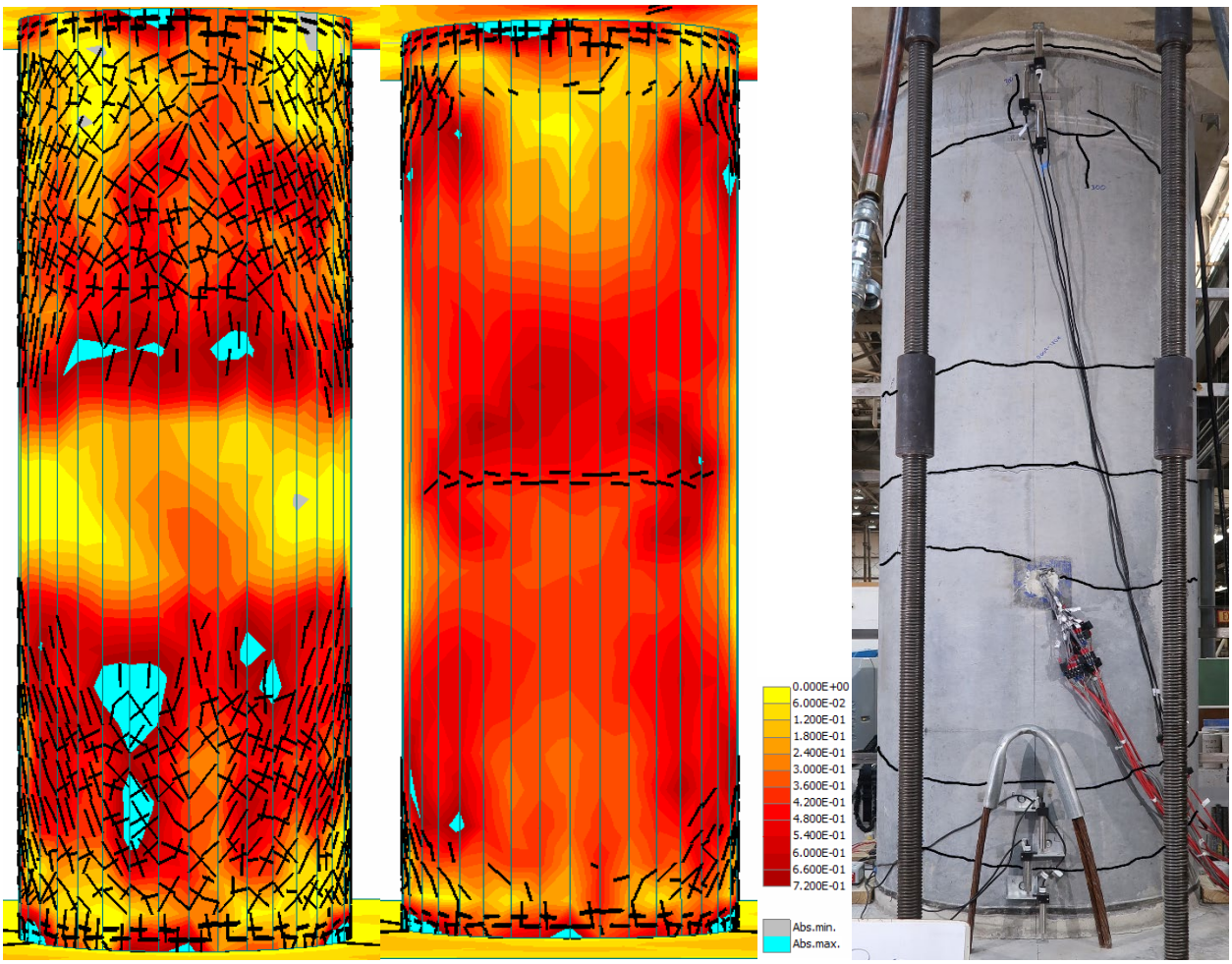

(a) FEA Column (2'-4" length) (b) FEA Column (3'-10") (c) Experimental Column (3'-10")

Figure 6-83: Tensile Region Crack Pattern Comparison for 40.25 in. Eccentricity Analysis at 300 Kips of Axial Load (Kotha, 2024)

6.4.3. Summary of Precast Column Models with Different Parameters

- The precast column with a roughened interface was modeled in the ATENA 3D software, the analysis resulted in a failure load of 430 kips at 40.25 in. eccentricity. The resultant displacements and cracks showed a similar pattern to the experimental results of the precast column with an intentionally roughened interface.

- The model was verified with experimental results, and a difference of only 12.0% was seen at near-failure load. Along with that, crack patterns in tensile, neutral stress, and compressive regions were observed similar to that of experimental analysis.

- The precast column analytical model with 2'-4" lap splice length at top and bottom connections was prepared. Since the shorter length of bars was not enough for complete development, and central regions were void of lap splice, stress was not distributed throughout the column and experienced a premature failure at 310 kips.

6.5. Summary

The Finite Element Analysis in this report involved creating a model for a specimen cast in place and for four precast columns. The analysis included a parametric study to closely represent the performance observed in the experimental specimens. The main conclusions from the analysis are as follows:

- **Shear interface model:** The experimental specimens used for the push-through tests provided data that allowed for creating an accurate interface surface model using ATENA 3D. The results from this model effectively reflect the behavior of the experimental specimens. This modeling step is crucial for analyzing precast columns, as it helped to understand how concrete operates without shear connectors.

- **Meshing size and load rate impact:** An analysis was conducted to examine the influence of meshing size and loading rate. The study revealed that a smaller meshing size leads to longer computational time but provides more accurate capacity for the specimen. Conversely, a coarser mesh size increases the model's stiffness, which has an impact on the final displacement. Additionally, a faster loading rate to achieve the final axial load adversely affects the results, yielding unconservative values for lateral displacement.

- **Bonding model for the connections:** The analysis considered a model with perfect bonding between the precast column and the bent cap, or the footing, at the connections for the precast column models. Under these boundary conditions, we were able to predict behavior similar to the experimental results. In contrast, imperfect bonding between the concrete of the precast column and the other members could result in significant lateral deformations, despite the failure load being closer to the experimental results, with an error percentage of 4.4%.

- **Prestress bond model:** The analysis included a parametric study of the prestress bond in both the bent cap and the precast column. The findings suggested that disregarding prestress in the members could lead to excessively conservative outcomes. Conversely, assuming perfect bonding for the prestress, where the prestressing force is distributed along the entire length of the specimen, resulted in highly unconservative conclusions. Ultimately, the bond model proposed by Bigaj (1999) was considered a suitable representation of the prestressing strands' bond and was utilized in the analysis of the precast columns.

- **Construction sequence in the model:** In order to simulate the prestressing for the specimens in the bent cap or in the precast columns, the model had to incorporate two construction steps: one for prestressing and the second one to apply the load pattern. This approach ensures that the prestressing forces are applied to the specimens without creating stresses in members that are not prestressed.

- **Accuracy of Analytical Results:** Using the established parameters for contact elements, bond properties, prestressing, the finite element models of experimental specimens were found accurate in terms of lateral displacement, crack patterns, and the peak load-carrying capacity with minor disparity, effectively reflecting the behavior.

Chapter 7. Design Guidelines and Recommendations

This chapter presents design recommendations according to the results obtained from testing four precast columns and one control specimen. In addition, construction details are given to be considered by the design engineer. Suggested drawings are presented in Appendix C.

7.1. Design Assumptions for Axial and Moment Capacity

The development of an interaction diagram for a precast column could consider the following approach:

- The maximum compressive strain for concrete at the extreme fiber (ε_u) is considered as 0.003, as ACI-318-19 and AASHTO LRFD 9th Edition suggested.
- A strain-compatibility analysis should be followed to calculate the strain in the concrete and the prestressing strands located on the compressive and tension sides. That is, plane sections remain plane.
- The concrete stress could be calculated using a parabolic shape or a rectangular stress block as suggested by ACI-318-19 and AASHTO LRFD 9th Edition.
- The f'_c used in the calculation should be the average between the f'_c from the precast column and the f'_c from the concrete cast-in-place. The minimum f'_c value of them is acceptable for design.
- The material properties for concrete and prestressing strands should be considered as established by AASHO LRFD 9th Edition.
- Knowing ε_u, axial load capacity should be determined by force equilibrium by taking a value of "c" that represents the depth of the compression zone in the column. To complete a full interaction diagram, the procedure should be repeated using several values of "c" through the entire sectional depth of the column. A minimum of six calculations should be used.
- The moment capacity corresponding to each value "c" should be calculated by establishing moment equilibrium.
- The interaction diagram should not consider the tensile strength of the concrete.
- The prestressing strands should consider the effective stress after prestressing considering losses, f_{pe}.
- The stress f_{ps} of the prestressing strands could reach f_{pu} if the strain compatibility confirms this assumption and the strands can fully develop inside the column.

- The stress f_{ps} of the prestressing strands should be reduced to the corresponding f_{px} according to AASHTO 5.9.4.3.2 considering the embedment length of the connectors.

7.2. P-M Interaction Diagram

For the construction of this diagram, the process is summarized in Figure 7-1. Two design examples are presented in Appendix A and Appendix B, respectively. It is required to check if the factored design loads are inside the constructed design P-M curve.

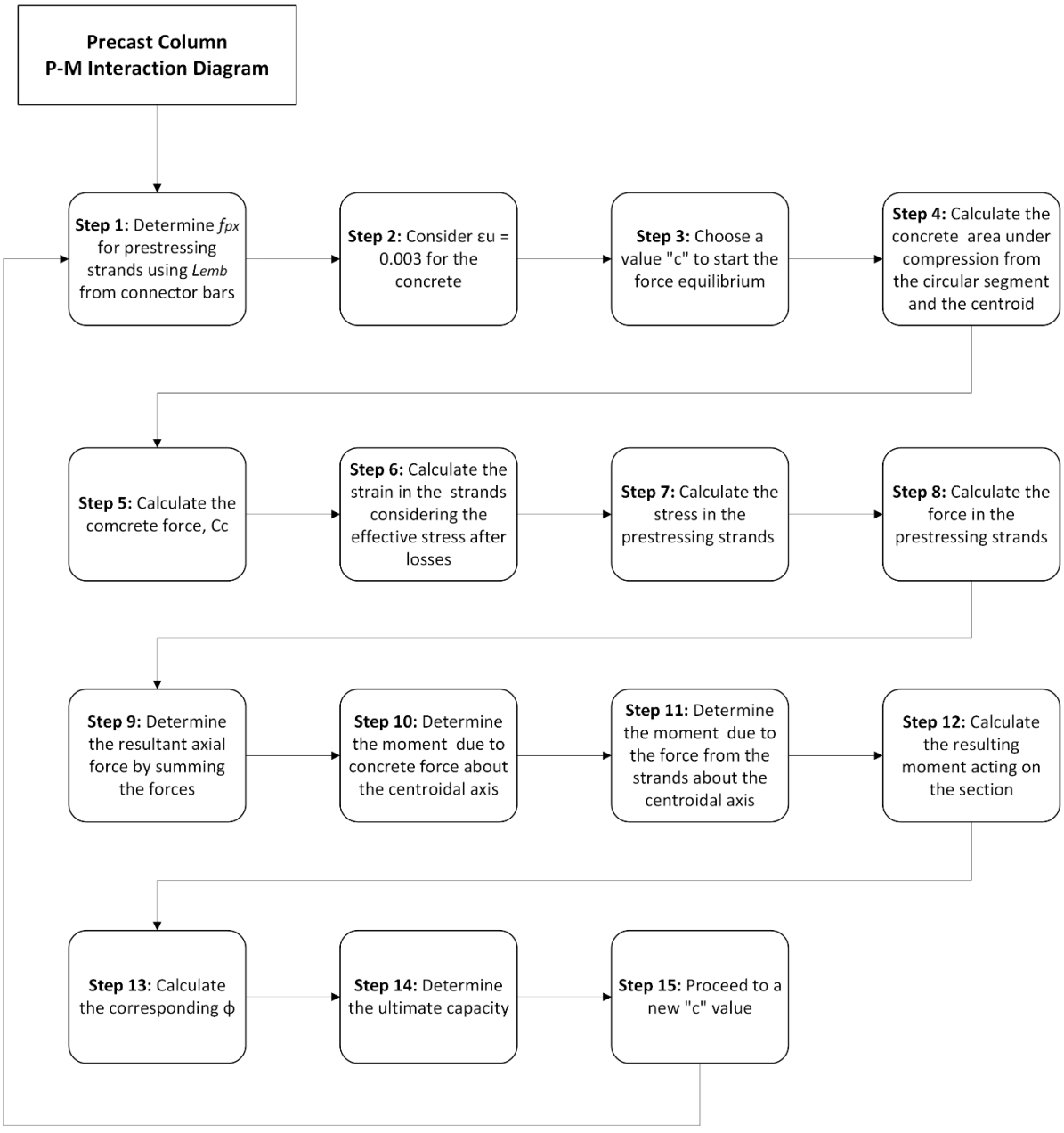

Figure 7-1: P-M interaction diagram design flow chart.

7.3. Suggested Specifications for the Precast Column Solution

7.3.1. Hollow Precast Shell and Sectional Dimensions

The research was focused on round columns with an outer diameter of 36 in. However, other diameters or shapes may be used if the following requirements regarding the cross-section are satisfied:

- Minimum wall thickness of 6 in.
- Prestressing strands should be located at 3 in. from the edge or centered in the precast column.
- Internal void must be circular if a not-round section is used.

In the project, spun-cast shells were used and found several benefits over conventional cast elements. However, as long as the above requirements can be achieved, other precast methods may be viewed as viable alternatives.

7.3.2. Minimum Concrete Strength

The precast column solution should accomplish the following concrete compressive strength:

- TxDOT Class C (3.6 ksi) for the core. TxDOT Class C (3.6 ksi) or S (4.0 ksi) for the voids in the bent cap.
- TxDOT Class H (7 ksi) for the precast prestressed concrete shell.

7.3.3. The Roughness of Internal Face for the Precast Shell

The roughness of the internal face should satisfy the following:

- The internal face of the precast shell should be roughened along the entire height.
- The internal face should be roughened accomplishing a concrete surface preparation of ICRI CSP 6 to CSP 7.
- An alternative solution could be a helical corrugated steel pipe provided inside the precast column. The steel pipe should be 12-gage, Type I, and lock-seam. This was not tested in this research.

7.3.4. Limits on Structural Configuration

The dimension limits for the precast column solution are established by TxDOT Standards for Interior Bents. The maximum column height is 36 ft.

7.3.5. Concrete Cover

The cover specified for this solution should satisfy the following:

- The cover used in the precast column should be at least 1-3/4 in.
- For the CIP concrete inside the void of the precast column, the cover could be reduced to 1.5 in.

7.3.6. Minimum Reinforcement

If applying the precast column solution on round columns with 36 in. in diameter according to the research, the reinforcement configuration should satisfy the following:

- Twenty-four low relaxation prestressing strands with a diameter of 0.5 in. pretensioned at 75% f_{pu}. Larger sizes of low relaxation prestressing strands can be used if similar or higher structural capacity can be achieved per Section 7.2.
- Hoops or spirals should consist of #3 bars with 2 in. pitch. One and a half flat turns at both ends should apply.
- Twelve #9 Grade 60 bars without coating should be used at the connection with the footing and the bent cap.

If applying the precast column solution on other diameters, calculation should be conducted per Section 7.2 to determine the number of the connectors and the strand pattern in the shell in order to achieve the desired structural capacity.

7.3.7. Development Length Inside the Precast Shell

The bars from the footing and the at the top continuing inside the column should accomplish the following:

- The minimum required development length is 3’9’’ for #9 bars inside the column, as per TxDOT Standard “Common foundation details FD”.
- The embedment length of the bars could be increased to have a longer non-contact lap splice with the prestressing strands, potentially resulting in higher sectional capacity

7.3.8. Void of Precast Bent Cap Connection

The connection between the precast column and the precast bent cap should satisfy the following:

- A helical corrugated steel pipe should be provided at the connection. The steel pipe should be 12-gage, Type I, and lock-seam.

- The corrugated steel pipe diameter should be the column's diameter minus 6 in. as established in TxDOT Standard "Prestressed, precast bent cap option for round columns".
- The corrugated steel pipe depth could be the total depth of the bent cap, or it can be reduced to allow horizontal rebar at the top or the bottom of the bent cap. The minimal height of the corrugated pipe should be the depth of the bent cap minus 6 in. at the top and the bottom, as per TxDOT Standard "Prestressed, precast bent cap option for round columns".
- The embedment length of the bars inside the bent cap should be 2'-9'' as per TxDOT Standard "Prestressed, precast bent cap option for round columns".
- The concrete could be specified as Class C (3.6 ksi) or Class S (4 ksi), as per TxDOT Standard "Prestressed, precast bent cap option for round columns".

7.3.9. Mounting Shims

The shims are used to place and align the precast column and to allow the concrete CIP to pass under the column. The shims should follow the next configuration:

- The shim depth should be between 1.5 in. to 2 in.
- The material could be High-Density Polyethylene (HDPE) or steel, determined by the designer.
- The area of all the shims should not be more than 5% of the cross-section of the column.
- The distance from the edge of the column to the shims should be 1.5 in.
- The shims shall not move during the assembling of the precast column and the bent cap.
- The coarse aggregate size should be smaller than the shim height used in the precast column. With this, the concrete could flow between the exterior forms and the shims fully completing the gap generated by the shims.

7.4. Precast Column Assembling

The proposed Design Guidelines are based on the results obtained at the laboratory. For that reason, the assembling process presented in the section 4.2.7 could work as a first iteration for the process followed in the field.

Chapter 8. Conclusions

This project, initiated by the Texas Department of Transportation (TxDOT) under Project #0-7089, sought to bridge the gap in the application of precast bridge substructures, specifically focusing on precast column solutions for multi-column bents in Texas. The research combined experimental and advanced analytical techniques to address several key objectives. Firstly, the research team extensively collected past studies about successfully implemented precast columns. Synthesizing past research, the research team developed innovative design concepts and construction details for precast concrete columns, including precast shell sections with a cast-in-place (CIP) core, utilizing pocket connections with bent caps and reinforcing bars as connectors with footings. Comprehensive experimental investigations were conducted into the interface shear strength between precast elements and CIP concrete cores, exploring different surface preparations and concrete types to ensure optimal composite action. Additionally, the constructability and structural performance of the proposed precast column systems and their connections were evaluated through large-scale laboratory tests and finite element analysis. These efforts culminated in the development of detailed design guidelines for implementing precast columns in Texas bridges. Key findings from each chapter are summarized as follows:

Chapter 2 summarizes relevant studies on precast columns, column connections, interface shear, and the finite element method. The literature review indicates that precast column systems significantly expedite construction but face constraints like lifting weight and transportation, making full-height precast columns impractical. Experimental research shows promise in using a precast concrete shell with a cast-in-place (CIP) core, reducing lifting weight and facilitating installation and transportation, despite that limited studies exist. Connections are crucial, with socket connections proving effective in linking precast columns to footings, offering sufficient resistance through interface shear and ease of construction, requiring proper surface preparation. Interface shear in unreinforced connections primarily arises from shear friction, influenced by factors like differential shrinkage and stiffness, yet limited research characterizes this behavior. Development length for reinforcement bars and prestressing strands is vital for reinforced concrete behavior, with ACI 318-19 and AASHTO LRFD providing estimation procedures, and ongoing research aims to unify these calculations. In finite element modeling, variables like element shape and mesh size affect accuracy and computational time; incorporating reinforcement bonding models can enhance structural performance estimation.

Chapter 3 presents an experimental program including 27 push-off tests and a comprehensive analysis of factors influencing interface shear strength. Recommendations for designing and constructing a hybrid precast column system are as follows: Circular interfaces are preferred over square ones, with circular interfaces showing a 127% strength increase for smooth and a 34.4% increase for roughened interfaces. Hybrid precast columns with a cast-in-place core are viable without altering existing mix designs; lower concrete strength for the shell or the core seemingly leads to ductile failure modes. Shrinkage reducing admixture (SRA) in core concrete reduced interface strengths (61.2% for smooth and 18.7% for rough) but enhanced consistency and post-

peak behavior. Interface roughness is crucial, with modest roughening increasing strengths by 19.4% for circular and 101% for square interfaces; roughening is recommended if feasible. The current AASHTO LRFD interface shear equation is inadequate for unreinforced core-shell interfaces. A modified equation better represents unreinforced confined core-shell interfaces. This program provides substantial data on unreinforced core-shell concrete interfaces, enabling efficient hybrid precast column system designs and numerical models.

Chapters 4 and 5 introduce a large-scale test program that explores a precast column solution combining a prestressed precast hollow section with a cast-in-place (CIP) concrete core. This innovative method aims to reduce installation time and costs by allowing precast columns to serve as both structural members and formwork. The experimental program included one specimen based on TxDOT's standard 36-inch round column and four specimens based on the new precast solution, with variables such as interface roughness and connector embedment length. Key findings include the effectiveness of plastic shims for maintaining vertical alignment. Proper vibration at the column base is crucial to prevent voids, especially as column height increases.

The tests revealed that prestressed precast hollow sections filled with CIP concrete function as composite sections, regardless of internal roughness, leading to a comparable or superior behavior to traditional TxDOT standard columns. However, roughness influenced the yield length of the bars, with smoother interfaces requiring more embedment length. The embedment length for rebar connectors varied, but all tested lengths allowed bars to reach yielding, suggesting that the TxDOT standard embedment length of 2’10” is suitable. Shorter embedment lengths created new critical sections due to the underdeveloped stress in prestressing strands. Precast columns demonstrated greater stiffness and capacity at low eccentricities compared to control specimens, with no cracks observed until testing at higher eccentricities. Precast columns with longer embedment lengths showed similar or higher capacity than control specimens, but capacity decreased with shorter embedment lengths. A strain compatibility model with layered section analysis provided accurate capacity predictions, while a rectangular stress block model with average f'_c proved conservative and close to the predicted load-carrying capacity.

Chapter 6 presents finite element analysis conducted for both the small-scale interface test and the full-scale structural testing, incorporating a parametric study to reflect experimental performance. Key findings include: The shear interface model, developed using ATENA 3D, accurately mirrored experimental behavior, crucial for understanding concrete performance without interface reinforcement. Analysis of meshing size and load rate showed that finer mesh sizes yield more accurate capacities but require longer computation times, while coarser meshes impact final displacement. For the full-scale modeling, the model simulated two construction steps—prestressing and load application—to avoid undesired initial stresses. Results for Specimen S1-CIP were consistent with experimental data, while Specimen S2-R-AASH9-45 (intentionally roughened) demonstrated elastic behavior for small eccentricities but was slightly unconservative for larger eccentricities. Specimen S3-S-AASH9-45 (non-intentionally roughened) matched experimental data for small eccentricities but was 12% unconservative at higher loads. The bonding model indicated that perfect bonding predictions were close to experimental results while

ignoring prestress led to overly conservative outcomes. The Bigaj (1999) model was found suitable for representing prestressing strands. Specimen S5-R-ZABORAC-28, with reduced embedment length, showed a 3% error margin in failure load predictions. In general, the finite element models were successful in predicting the behavior of precast column solution in terms of strength, stiffness, and crack patterns.

Chapter 7 presents design guidelines based on testing four precast columns and one control specimen. For axial and moment capacity, the guidelines include a strain-compatibility analysis and layered sectional analysis using average concrete compressive strength values of the shell and the core. The P-M interaction diagram can be determined per the assumptions for structural designers' convenience. Recommendations for precast column dimensions include a 6-inch minimum thickness and a 24-inch maximum void diameter, with specific concrete strengths and roughness requirements. The design mandates a maximum column height of 36 feet, spacing of 8 feet, and cover of at least 1-3/4 inches. Minimum reinforcement includes 24 prestressing strands and specific bar configurations. Connections should feature helical corrugated steel pipes, and shims should be 1.5 to 2 inches deep. These guidelines aim to streamline precast column assembly and ensure structural performance.

In conclusion, this research project spearheaded by TxDOT has significantly advanced the application of precast bridge substructures in Texas. By integrating experimental results with analytical models, the project has developed robust design guidelines and innovative construction techniques that enhance the efficiency and performance of precast columns. The findings emphasize the benefits of using hybrid precast systems, optimized interface designs, and precise construction details. The project not only improves the feasibility of precast columns but also provides a comprehensive framework for their implementation, ensuring better performance and durability in Texas bridge infrastructure. The detailed recommendations and design guidelines set a new standard for future precast column applications, supporting both practical and theoretical advancements in the field.

Chapter 9. Value of Research

9.1. Introduction

TxDOT Project #0-7089, focused on advancing the application of precast bridge substructures, represents a significant leap forward in bridge engineering. By addressing the unique challenges associated with precast columns, such as lifting weight and transportation constraints, this research has developed innovative design concepts and construction techniques that promise to revolutionize bridge construction in Texas. Through a comprehensive approach that combined experimental investigations with advanced analytical techniques, the project yielded valuable insights and practical guidelines that enhance the feasibility, efficiency, and performance of precast column systems. The following sections discuss the multifaceted value of this research, highlighting its contributions to knowledge, quality of life, customer satisfaction, system reliability, service life, project delivery speed, cost reductions, and engineering design improvements, as summarized in Table 9-1.

Table 9-1. Selected Benefit Area

Benefit	Qualitative	Economic	Both
Level of Knowledge	X		
Quality of Life	X		
Customer Satisfaction	X		
System Reliability		X	
Increased Service Life		X	
Expedited Project Delivery		X	
Reduced User Cost		X	
Reduced Construction, Operations, and Maintenance Cost		X	
Engineering Design Improvement			X

9.2. Level of Knowledge

This research significantly enhances the level of knowledge in the field of precast bridge substructures. By combining experimental and analytical approaches, the study offers in-depth insights into the behavior of hybrid precast column systems. First, it provides valuable data obtained from the push-off test on interface shear strength of unreinforced core-shell concrete interfaces. The data assists in the development of modified equations for the strength of such interfaces. The findings also contribute to the development of the hybrid precast column system. Secondly, the research experimentally validates the constructability and the performance of the hybrid precast column system, as well as proposes an analytical method, filling critical knowledge gaps identified in previous studies. These contributions advance theoretical knowledge and provide practical guidelines for future research and application in bridge engineering.

9.3. Quality of Life and Customer Satisfaction

The implementation of the developed hybrid precast bridge system directly impacts the quality of life by reducing construction time and minimizing disruptions to traffic and local communities. Shorter construction periods mean less inconvenience for commuters and residents, contributing to smoother daily operations and enhanced community well-being. Furthermore, the validated structural performance of bridges constructed using the hybrid precast system ensures safer transportation infrastructure. This fosters a more reliable and efficient transportation network, thereby positively affecting the daily lives of individuals and communities relying on these structures. These improvements align with public expectations for efficient and safe transportation systems; therefore, customer satisfaction is greatly enhanced through the application of the hybrid precast column system. Additionally, the project's success in developing practical design guidelines ensures that future bridge projects can replicate these benefits, continually enhancing user satisfaction over time.

9.4. System Reliability and Increased Service Life

The research findings contribute to increased system reliability by providing a comprehensive understanding of the structural performance and serviceability of the hybrid precast column system. The innovative design and construction techniques also contribute to the increased service life of bridge structures. The experimental and analytical results demonstrated that these columns offer superior stiffness and capacity, particularly at low eccentricities, compared to traditional systems, meaning that the system withstands the stresses of daily use and environmental factors more effectively than traditional methods. This robustness translates to fewer structural damages and maintenance issues over the lifespan of the bridges. The developed design guidelines ensure that these reliable systems can be consistently replicated in future projects, leading to a more dependable transportation infrastructure.

9.5. Expedited Project Delivery

One of the primary benefits of this research is the potential for expedited project delivery. The use of precast components, as demonstrated in the study, significantly reduces on-site construction time. Precast prestressed hollow piles, which serve as both structural members and formwork, streamline the construction process by minimizing the need for extensive on-site formwork and curing times associated with traditional cast-in-place methods. This acceleration in project timelines not only reduces costs but also minimizes the impact on traffic and local communities.

9.6. Reduced User Cost

The adoption of the hybrid precast column system results in reduced user costs in several ways. Firstly, the expedited construction process minimizes the duration of traffic disruptions, reducing fuel consumption and time lost due to delays. Secondly, the increased durability and service life of the precast column system mean fewer repairs and maintenance activities, which often lead to costly detours and extended travel times for users. Lastly, the improved reliability of the transportation infrastructure reduces the likelihood of unexpected closures and the associated costs for alternative routes. These factors collectively lower the overall expenses for daily commuters and commercial vehicles.

9.7. Reduced Construction, Operations, and Maintenance Cost

The research demonstrates significant potential for reducing construction, operations, and maintenance costs through the use of the hybrid precast column system. The efficient construction process, characterized by the use of precast elements, decreases labor and material costs associated with on-site formwork and prolonged curing times. Additionally, the durability and robustness of the precast columns lead to lower maintenance costs over the structure's lifespan. The enhanced structural performance reduces the frequency and extent of repairs, further lowering long-term expenses. These cost savings make the hybrid precast column system an economically viable option for bridge construction and maintenance.

9.8. Engineering Design Improvement

This research contributes to substantial engineering design improvements in bridge construction. The innovative hybrid precast column system, detailed in the study, offers enhanced structural performance. The findings provide a more accurate and reliable basis for designing precast column connections and precast prestressed hollow sections, leading to safer and more efficient structures. The development of comprehensive design guidelines based on experimental and analytical results ensures that these improvements are effectively translated into practice. These advancements not only enhance the quality and safety of bridge designs but also promote the adoption of more innovative and efficient construction techniques in the industry.

References

AASHTO. (2020). “LRFD Bridge Design Specifications, 9th Edition”. Washington, DC: American Association of State Highway and Transportation Officials.

ACI 347-04, “Guide to Formwork for Concrete,” ACI 347, Farmington Hills, MI: American Concrete Institute. 2005.

ACI Committee 318. (2019). “Building Code Requirement for Structural Concrete (ACI 318-19) and Commentary of Building Code Requirements for Structural Concrete (ACI 318R-19)”. Farmington Hills, MI: American Concrete Institute.

Aktan, H., Attanayake, U. (2013). “Improving Bridges with Prefabricated Precast Concrete Systems,” Western Michigan University.

Alirezaei Abyaneh, R. (2017). “Computational modeling of prestress transfer, end-region cracks and shear behavior in prestressed concrete I-girders employing large-diameter strands (Doctoral dissertation)”.

ASTM C31 / C31M-19. (2019). ”Standard Practice for Making and Curing Concrete Test Specimens in the Field”, ASTM International, West Conshohocken, PA, www.astm.org

ASTM C39/C39M (2016). “Standard Test Method for Compressive Strength of Cylindrical Concrete Specimens”. ASTM International, West Conshohocken, PA. www.astm.org

ASTM C878/C878M (2014). “Standard Test Method for Restrained Expansion of Shrinkage-Compensating Concrete”. ASTM International, West Conshohocken, PA. www.astm.org

ASTM Standard C192-15 (2015). “Standard Practice for Making and Curing Concrete Test Specimens in the Laboratory”. ASTM International, West Conshohocken, PA. www.astm.org

Attanyake, U., Abudayyeh, O., Aktan, H., Cooper, J., (2012). “First Fully Prefabricated Full-Depth Deck Panel Bridge System in Michigan: Challenges and Lessons Learned,” TRB 91st Annual Meeting Session 442.

Aziz, R. J. (2010). “Shear Capacity of Concrete Prisms with Interface Joints”. Journal of Engineering, 5084-5097.

Barnoff, R. M., & Orndorff, Jr., J. A. (1974). “An Experimental Prestressed Concrete Bridge”. University Park: The Pennsylvania Transportation Institute.

Bayrak, O. (2023). Approved Changes to the Ninth Edition AASHTO LRFD Bridge Design Specifications: Reinforcing Bar Anchorage. Aspire The Concrete Bridge Magazine (Winter), pp. 46-49.

Bigaj, A. J. (1999). “Structural dependence of rotations capacity of plastic hinges in RC beams and slobs”.

Birkeland, H. W. (1960). “Differential Shrinkage in Composite Beams”. Journal of the American Concrete Institute, 1123-1136.

Birkeland, P. W., & Birkeland, H. W. (1966). “Connections in Precast Concrete Construction”. Journal of the American Concrete Institute, 345-368.

Caluk, N. (2020). “Use of UHPC Stay-In-Place Shells in Bridge Column Construction for Accelerated Bridge Construction”.

Caluk, N., Mantawy, I., & Azizinamini, A. (2019). “Durable bridge columns using stay-in-place UHPC shells for accelerated bridge construction. Infrastructures, 4(2), 25”.

Cervenka Consulting. (2015). “ATENA Program Documentation, Part 1. Theory Manual”. Prague, Czech Republic.

Cervenka Consulting. (2015). “ATENA Program Documentation, Part 2-2, 2015. User’s Manual for ATENA 3D”. Prague, Czech Republic.

Cheng, Z., Sritharan, S., Ashlock, J. (2020). “Design and Performance Verification of a Bridge Column/Footing/Pile System for Accelerated Bridge Construction – Final Report. Iowa Highway Research Board Project No. TR-673”, Iowa Department of Transportation.

Cifuentes, A. O., & Kalbag, A. (1992). “A performance study of tetrahedral and hexahedral elements in 3-D finite element structural analysis. Finite Elements in Analysis and Design, 12(3-4), 313-318”.

City of Auburn (2019). “Accelerated Innovation Deployment (AID) Demonstration Project: Precast Bent Columns, Moore’s Mill Bridge over I-85 in Auburn, Alabama”.

Collins, M., & Mitchell, D. (1991). “Prestress concrete structures”. New Jersey: Prentice-Hall.

Crisafulli, F. J., & Restrepo, J. I. (2003). “Ductile steel connections for seismic resistant precast buildings. Journal of earthquake engineering, 7(04), 541-553”.

Federal Highway Administration (2009). “Connection Details for Prefabricated Bridge Elements and Systems,” Report No. FHWA-IF-09-010.

fib, fib Model Code for Concrete Structures 2010, International Federation of Concrete Wilhelm Ernst & Sohn, Germany, 2013

Fouad, F. H., Rizk, T., Stafford, E.L., Hamby, D. (2006). “A Prefabricated Precast Concrete Bridge System for the State of Alabama,” Report No. 05215, University Transportation Center for Alabama, University of Alabama.

Ghassa Fawaz, Juan Murcia-Delso, Oguzhan Bayrak. “Synthesis of Precast Column Designs for Texas Bridges,” Rep. No. 0-6978, University of Texas at Austin. Center for Transportation Research (CTR), Austin Texas, 2019, 89 pp.

Gribniak, V., Kaklauskas, G., Idnurm, S., & Bačinskas, D. (2010). “Finite element mesh size effect on deformation predictions of reinforced concrete bridge girder”. The Baltic Journal of Road and Bridge Engineering, 5(1), 19-27.

Hanson, N. W. (1960). “Precast-Prestressed Concrete Bridges”. Journal of the PCA Research and Development Laboratories, 38-58.

Haraldsson, O.S., Janes, T.M., Eberhard, M.O., Stanton, J.F. (2013). “Seismic resistance of socket connection between footing and precast column,” Journal of Bridge Engineering 18(9), 910-919.

Hewes, J.T. (2013). “Analysis of the State of the Art of Precast Concrete Bridge Substructure Systems,” Final Report 687, Arizona Laboratory for Applied Transportation Research, Northern Arizona University.

Hewes, J.T., Priestley, M.J.N. (2002). “Seismic Design and Performance of Precast Concrete Segmental Bridge Columns,” Report No. SSRP 2001/25, Department of Structural Engineering, University of California at San Diego.

Hieber, D., Wacker, J., Eberhard, M., and Stanton, J. F. (2005). “Precast Concrete Pier Systems for Rapid Construction of Bridges in Seismic Regions,” Report No. WA-RD-611.1, Washington State Transportation Center, University of Washington.

Hossein Yousefpour, Hyun Su Kim, Rodolfo Bonetti, Roya Alirezaei Abyaneh, Alex Katz, Alistair Longshaw, Jessica Salazar, Trevor Hrynyk, Oguzhan Bayrak (2018). “End-Region Behavior and Shear Strength of Pretensioned Concrete Girders Employing 0.7-in. Diameter Strands”. University of Texas at Austin.

Huria, V., Lee, K. L., & Aktan, A. E. (1993). “Nonlinear finite element analysis of RC slab bridge. Journal of Structural Engineering, 119(1), 88-107”

Khaleghi, B., Schultz, E., Seguirant, S., Marsh, L., Haraldsson, O., Eberhard, M., Stanton, J. (2012). “Accelerated bridge construction in Washington State: from research to practice,” PCI Journal, 57(4), 34-49.

Kim, C., Lim, W., Park, H., Oh, J. (2015). “Cyclic Loading Test for Cast-in-Place Concrete-Filled Hollow Precast Concrete Columns”. ACI Structural Journals, March-April 2016, 205-215.

Korkmaz, H. H., & Tankut, T. (2005). “Performance of a precast concrete beam-to-beam connection subject to reversed cyclic loading. Engineering Structures, 27(9), 1392-1407”.

Kotha, C. (2024). “Analytical Investigation of Precast Columns for Bridge Substructures”. Master's Thesis, The University of Texas at Austin, Texas.

KUPFER, H., HILSDORF, H.K., RÜSCH, H. (1969). “Behavior of Concrete under Biaxial Stress”. Journal ACI, Proc. V.66, No.8, Aug., pp.656-666.

Littleton, P., Mallela, J., (2013). “Iowa Demonstration Project: Accelerated Bridge Construction on US 6 over Keg Creek,” Research Report, Applied Research Associates, Inc.

Small, L. (2022). “Investigation of Vertical Shear Strength in Unreinforced Interfaces Between Concrete Cast at Different Times”. University of Texas at Austin.

Mallela, J., Littleton, P., Hoffman, G., Gokhale, S., Ullman, G. (2013). “U.S. I-85 Interchange Design-Build Project Using Prefabricated Bridge Elements in West Point, GA, Final Report”, Federal Highway Administration.

Mattock, A. K. (1976). “Shear Transfer Under Monotonic Loading, Across an Interface Between Concretes Cast at Different Times”. Seattle: University of Washington.

Mellon, D. (2018). “Owners Perspective on ABC – Spotlight on SHRP2 R04 Fort Goff Creek project and Caltrans Laurel Street Overcrossing Project” (available at https://abc-utc.fiu.edu/mc-events/owner-perspective-on-abc-spotlight-on-shrp2-r04-fort-goff-creek-project-and-caltrans-laurel-street-overcrossing-project/?mc_id=381)

Mondal, T. G., & Prakash, S. S. (2016). “Nonlinear finite-element analysis of RC bridge columns under torsion with and without axial compression”. Journal of Bridge Engineering, 21(2), 04015037.

Nguyen-Hoang, S., Sohn, D., & Kim, H. G. (2017). “A new polyhedral element for the analysis of hexahedral-dominant finite element models and its application to nonlinear solid mechanics problems”. Computer Methods in Applied Mechanics and Engineering, 324, 248-277.

Oh, B. H., Lim, S. N., Lee, M. K., & Yoo, S. W. (2014). “Analysis and prediction of transfer length in pretensioned, prestressed concrete members”. ACI Structural Journal, 111(3), 549.

Olivia, W. (2014). “Rawson Ave Bridge Replacement Using Precast Elements and Systems – An Owner’s Experience” (available at https://abc-utc.fiu.edu).

Pang, J.B.K., Steuck, K.P., Cohagen, L., Pang, J.B.K., Eberhard, M.O., Stanton, J.F. (2008). “Rapidly Constructible Large-Bar Precast Bridge-Bent Seismic Connection,” Report Mo. WA-RD 684.2, Washington State Transportation Center, University of Washington.

Ralls, M., Tang, B., Bhidé, S., Brecto, B., Calvert, E., Capers, H., Dorgan, D., Matsumoto, E., Napier, C., Nickas, W., Russell, H., (2005). “Prefabricated Bridge Elements and Systems in Japan and Europe,” FHWA-PL-05-003. Washington, D.C.

Rejane Martins Fernandes Canha, Daniel Alexander Kuchma, Mounir Khalil El Debs, Rafael Alves de Souza. (2014) “Numerical analysis of reinforced high strength concrete corbels”, Engineering Structures, Volume 74, 2014, Pages 130-144, ISSN 0141-0296, https://doi.org/10.1016/j.engstruct.2014.05.014.

Restrepo, J.I., Tobolski, M.J., Matsumoto, E.E. (2011). “Development of a precast bent cap system for seismic regions,” Report NCHRP-681, National Cooperative Highway Research Program (NCHRP) Report, Transportation Research Board, Washington, D.C.

Santos, P. M., & Eduardo, J. N. (2011). “Factors Affecting Bond between New and Old Concrete”. ACI Materials Journal, July-August 2011, 449-456.

Santos, P. M., & Júlio, E. N. (2014). “Interface Shear Transfer on Composite Concrete Members”. ACI Structural Journals, January-February 2014, 113-122.

Seible, F., Latham, C., & Krishman, K. (1988). “Structural Concrete Overlays in Bridge Deck Rehabilitation”. La Jolla: University of California, San Diego.

Steuck, P., Pang, B.K., Stanton, F., Eberhard, O. (2007) “Anchorage of Large Bars in Grouted Ducts.” Washington State Department of Transportation Report No. WA-RD 684.1, Washington State Transportation Center.

Taghia, P., & Bakar, S. A. (2013). “Mechanical behavior of confined reinforced concrete-CFRP short column-based on finite element analysis”. World Applied Sciences Journal, 24(7), 960-970.

Texas Department of Transportation. (2018). “Bridge Detailing Guide”. TxDOT.

Texas Department of Transportation. (2019). “Common Foundation Detail (FD)”. TxDOT.

Texas Department of Transportation. (2019). “Prestressed, Precast Bent Cap Option for Round Columns (PPBC-RC)”. TxDOT.

Texas Department of Transportation. (2020). “Bridge Design Guide”. TxDOT.

Texas Department of Transportation. (2020). “Bridge Design Manual – LRFD”. TxDOT.

Wight, J. K. (2016). “Reinforced Concrete Mechanics and Design”. 7th Edition. Pearson.

Wolf. L (2005). “Texas DOT Experience with Prefabricated Bridge Construction,” (available at http://mceer.buffalo.edu/education/webcast/Accelerated_Bridge_Construction/01Wolf.pdf).

Xiao, J., Huang, X., & Shen, L. (2012). “Seismic behavior of semi-precast column with recycled aggregate concrete”. Construction and Building Materials, 35, 988-1001.

Yu-Chen Ou (2007). “Precast Segmental Post-tensioned Concrete Bridge Columns for Seismic Regions,” Ph.D. dissertation, Dept. of Civil Engineering, University of New York at Buffalo.

Zaborac, J., & Bayrak, O. (2022). “Unified approach for reinforcement development length using the partly cracked elastic stage for bond strength”. Structural Concrete. Retrieved from https://doi.org/10.1002/suco.202200117

Zilveti, L. (2022). “Design and Conceptual Framework for the Development and Validation of Precast Concrete Column Solutions Through Large-Scale Testing”. University of Texas at Austin.

Appendix A. Design example using a layered section analysis and a parabolic shape for the concrete stress

P-M Interaction Diagram using Collins and Mitchel concrete stress model

Dimensions of the circular column:

$Dc := 36 \cdot in$ Column Diameter

$Rc := Dc \cdot 0.5 = 18\ in$ Column Radio

Use f'c precast column

$f'c1 := 10311 \cdot psi$

Use f'c cast in place (void)

$f'c2 := 4369 \cdot psi$

$h_t := 6 \cdot in$ Precast column thickness

$Ec1 := 40000 \cdot \sqrt{f'c1 \cdot psi} + 1000000 \cdot psi = 5061.72\ ksi$

$Ec2 := 57000 \cdot \sqrt{f'c2 \cdot psi} = 3767.61\ ksi$

Collins and Mitchell concrete parabolic model for precast column

$$n := 0.8 + \frac{f'c1}{2500 \cdot psi} = 4.924$$

$$\varepsilon_o := \frac{f'c1}{Ec1} \cdot \frac{n}{n-1} = 0.00256$$ Strain for the concrete at f'c

Location of the prestressing strand from top to bottom:

$d'1 := 4.142 \cdot in$

$d'2 := 7.393 \cdot in$

$d'3 := 12.26 \cdot in$

$d'4 := 23.74 \cdot in$

$d'5 := 28.606 \cdot in$

$d'6 := 31.858 \cdot in$

Area of the 0.5-in. strands locatead at each layer:

$As'1 := 4 \cdot 0.153 \cdot in^2 = 0.612\ in^2$

$As'2 := 4 \cdot 0.153 \cdot in^2 = 0.612\ in^2$

$As'3 := 4 \cdot 0.153 \cdot in^2 = 0.612\ in^2$

$As'4 := 4 \cdot 0.153 \cdot in^2 = 0.612\ in^2$

$As'5 := 4 \cdot 0.153 \cdot in^2 = 0.612\ in^2$

$As'6 := 4 \cdot 0.153 \cdot in^2 = 0.612\ in^2$

$Ep := 28500 \cdot ksi$ MOE for the prestressing strands

$f_{pu} := 270 \cdot ksi$

$f_{loss} := 30 \cdot ksi$

$f_{pe} := 0.75 \cdot f_{pu} - f_{loss} = 172.5\ ksi$ Effective stress after losses

$$\Delta\varepsilon_p := \frac{f_{pe}}{Ep} = 0.006$$

$d_b := 0.5 \cdot in$ Nominal diameter of the prestressing strands

$L_{emb} := 45 \cdot in$ Embedment length used for the connector bars

$f_{ps} := f_{pu} = 270\ ksi$ Calculated with Strain-Compatibility considering strands fully developed

Using the Ramberg-Osgood function values for the prestressing strands (Low relaxation):

$A := 0.025$
$B := 118$
$C := 10$

Step 1: Determine f_{px} for prestressing strands using L_{emb} from connector bars using AASHTO 5.9.4.3.2:

$tl := 60 \cdot d_b = 30\ \textit{in}$ Transfer length

$l_{px} := L_{emb} = 45\ \textit{in}$ distance from free end of pretensioned strand to section of member under consideration (embedment lenght of the connecting bars).

$k := \frac{1.6}{\textit{ksi}}$ 1.6 for pretensioned members with a depth greater than 24 in.

$l_d := k \cdot \left(f_{ps} - \frac{2}{3} \cdot f_{pe}\right) \cdot d_b = 124\ \textit{in} \qquad l_d = 10.33\ \textit{ft}$

$f_{px} := \textbf{if}\left(l_{px} \le tl, l_{px} \cdot \frac{f_{pe}}{tl}, f_{pe} + \left(\frac{l_{px} - tl}{l_d - tl}\right) \cdot (f_{ps} - f_{pe})\right) = 188.06\ \textit{ksi}$

$f_{px} := \textbf{if}\left(f_{px} \ge f_{ps}, f_{ps}, f_{px}\right) = 188.06\ \textit{ksi}$ Checking that f_{px} is not higher than f_{ps}

Step 2: Select a value of εcu:

$\varepsilon cu := 0.003$

Step 3: Choose "c" (to calculate the complete P-M curve, "c" should start from a small value, find P and M, and then increase "c" until completing the depth of the cross-section):

$c := 18 \cdot \textit{in}$

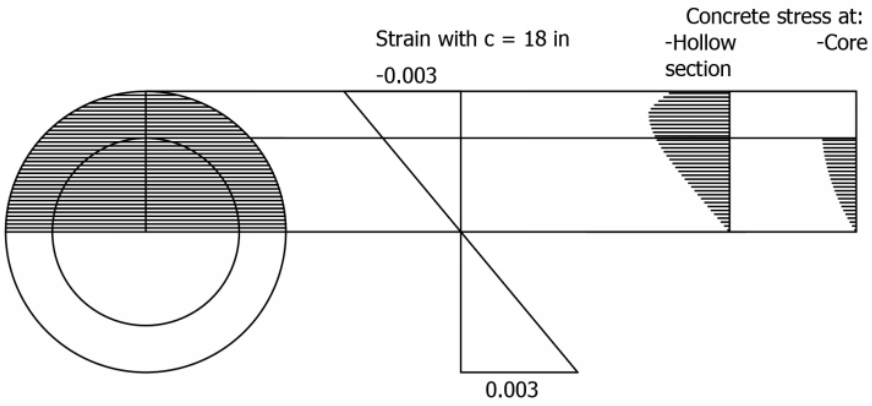

Figure A.1. Layered section for a depth of compression of 18 in.

Step 4: Calculate the concrete compressive area, centroid, effective length and force from each layer:

As this approach is focused on a layered section, the cross-section should be divided into layers to calculate the stress at each point and then multiply it by the area of each layer, as presented in Figure A.1.
The compression zone is divided by 36 in this case to calculate the layer thickness. This number could be modified according to the designer.

Concrete stresses in the precast column (hollow)

$th := \frac{c}{36} = 0.5\ in$ Layer thickness

$L_{n1} := 1$ Layer number (from 1 to 36 in this example)

$L_{l1} := c - (L_{n1} - 0.5) \cdot th = 17.75\ in$ Location of the centroid of Layer #1 measured from the neutral axis

$\varepsilon_{c1} := \frac{\varepsilon cu}{c} \cdot L_{l1} = 0.00296$ Strain at the layer under consideration

$k := \mathbf{if}\left(\varepsilon_{c1} \le \varepsilon_o, 1, 0.67 + \frac{f'c1}{9000 \cdot psi}\right) = 1.816$

$fc_{l1} := f'c1 \cdot \left(\frac{\varepsilon_{c1}}{\varepsilon_o}\right) \cdot \frac{n}{n - 1 + \left(\frac{\varepsilon_{c1}}{\varepsilon_o}\right)^{k \cdot n}} = 7.714\ ksi$ Concrete stress at the location of Layer #1

$C_{1b} := fc_{l1} \cdot th = 3.857\ \frac{kip}{in}$ Force in the layer per unit lenght

$x_1 := Rc - (c - L_{l1}) = 17.75\ in$ Layer location from the column center

$alfa := 2 \cdot \operatorname{acos}\left(\frac{x_1}{Rc}\right) = 0.33\ rad$ Angle measured from the center of the column

$b_1 := 2 \cdot Rc \cdot \sin\left(\frac{alfa}{2}\right) = 5.98\ in$ Length of the layer under consideration considering the circular shape

$b_{1effective} := \mathbf{if}\left(x_1 \le Rc - h_t, b_1 - h_t, b_1\right) = 5.979\ in$ As the precast column has two materials, the effective length of the layer should be checked to consider both materials independently.

$C_1 := C_{1b} \cdot b_{1effective} = 23.06\ kip$ Total compressive force in Layer #1

$M_{C1} := C_1 \cdot x_1 = 34.112\ kip \cdot ft$ Moment from the compressive force in Layer #1

This process should be completed from layer #1 until layer #36 (36 layers in this example). For demonstration, layer #36 is presented:

$th := \frac{c}{36} = 0.5\ in$ Layer thickness

$L_{n36} := 36$ Layer number (from 1 to 36 in this example)

$L_{l36} := c - (L_{n36} - 0.5) \cdot th = 0.25\ in$ Location of the centroid of Layer #36 measured from the neutral axis

$\varepsilon_{c36} := \frac{\varepsilon cu}{c} \cdot L_{l36} = 4.167 \cdot 10^{-5}$ Strain at the layer under consideration

$k := \mathbf{if}\left(\varepsilon_{c36} \le \varepsilon_o, 1, 0.67 + \frac{f'c1}{9000 \cdot psi}\right) = 1$

$fc_{l36} := f'c1 \cdot \left|\frac{\left(\frac{\varepsilon_{c36}}{\varepsilon_o}\right)}{}\right| \cdot \frac{n}{n - 1 + \left|\left(\frac{\varepsilon_{c36}}{\varepsilon_o}\right)\right|^{k \cdot n}} = 0.211\ ksi$ Concrete stress at the location of Layer #36

$C_{36b} := fc_{l36} \cdot th = 0.11\ \frac{kip}{in}$ Force in the layer per unit lenght

$x_{36} := Rc - (c - L_{l36}) = 0.25\ in$ Layer location from the column center

$alfa := 2 \cdot \mathrm{acos}\left(\frac{x_{36}}{Rc}\right) = 3.11\ rad$ Angle measured from the center of the column

$b_{36} := 2 \cdot Rc \cdot \sin\left(\frac{alfa}{2}\right) = 36\ in$ Length of the layer under consideration considering the circular shape

$b_{36internal} := 2 \cdot (Rc - h_i) \cdot \sin\left(\frac{alfa}{2}\right) = 24\ in$ Length of the layer under consideration in the internal material

$b_{36effective} := \mathbf{if}\left(x_{36} \le Rc - h_t, b_{36} - b_{36internal}, b_{36}\right) = 12\ in$ As the precast column has two materials, the effective length of the layer should be checked to consider both materials independently.

$C_{36} := C_{36b} \cdot b_{36effective} = 1.27\ kip$ Total compressive force in Layer #36

$M_{C36} := C_{36} \cdot x_{36} = 0.03\ kip \cdot ft$ Moment from the compressive force in Layer #36

The process should be followed for each layer as presented in Table A.1

Table A.1. Results for the layer section analysis in the precast column (hollow)

Model for Hollow Section												
Layer	Top	Thickness (in)	Location	εcx:	fc layer (psi)	Ci/b (lbs/in)	Angle	b total (in)	b eff. (in)	Ci (kips)	x (in)	Mci (kips-ft)
1	18.00	0.50	17.75	-2.96E-03	7714.03	3857.02	0.33	5.98	5.98	23.06	17.75	34.11
2	17.50	0.50	17.25	-2.88E-03	8416.78	4208.39	0.58	10.28	10.28	43.28	17.25	62.21
3	17.00	0.50	16.75	-2.79E-03	9055.76	4527.88	0.75	13.18	13.18	59.68	16.75	83.31
4	16.50	0.50	16.25	-2.71E-03	9604.13	4802.07	0.89	15.48	15.48	74.35	16.25	100.69
5	16.00	0.50	15.75	-2.63E-03	10041.60	5020.80	1.01	17.43	17.43	87.50	15.75	114.85
6	15.50	0.50	15.25	-2.54E-03	10310.35	5155.18	1.12	19.12	19.12	98.59	15.25	125.29
7	15.00	0.50	14.75	-2.46E-03	10281.42	5140.71	1.22	20.63	20.63	106.07	14.75	130.38
8	14.50	0.50	14.25	-2.38E-03	10209.96	5104.98	1.31	21.99	21.99	112.28	14.25	133.33
9	14.00	0.50	13.75	-2.29E-03	10097.14	5048.57	1.40	23.23	23.23	117.29	13.75	134.40
10	13.50	0.50	13.25	-2.21E-03	9944.77	4972.39	1.49	24.37	24.37	121.16	13.25	133.78
11	13.00	0.50	12.75	-2.13E-03	9755.22	4877.61	1.57	25.41	25.41	123.95	12.75	131.69
12	12.50	0.50	12.25	-2.04E-03	9531.26	4765.63	1.64	26.38	26.38	125.70	12.25	128.32
13	12.00	0.50	11.75	-1.96E-03	9275.96	4637.98	1.72	27.27	22.40	103.88	11.75	101.72
14	11.50	0.50	11.25	-1.88E-03	8992.56	4496.28	1.79	28.10	19.75	88.81	11.25	83.26
15	11.00	0.50	10.75	-1.79E-03	8684.33	4342.16	1.86	28.87	18.21	79.07	10.75	70.83
16	10.50	0.50	10.25	-1.71E-03	8354.48	4177.24	1.93	29.59	17.11	71.49	10.25	61.06
17	10.00	0.50	9.75	-1.63E-03	8006.08	4003.04	2.00	30.26	16.27	65.13	9.75	52.92
18	9.50	0.50	9.25	-1.54E-03	7642.03	3821.01	2.06	30.88	15.59	59.58	9.25	45.93
19	9.00	0.50	8.75	-1.46E-03	7264.93	3632.47	2.13	31.46	15.04	54.62	8.75	39.83
20	8.50	0.50	8.25	-1.38E-03	6877.15	3438.58	2.19	32.00	14.57	50.09	8.25	34.44
21	8.00	0.50	7.75	-1.29E-03	6480.77	3240.38	2.25	32.49	14.17	45.91	7.75	29.65
22	7.50	0.50	7.25	-1.21E-03	6077.56	3038.78	2.31	32.95	13.83	42.01	7.25	25.38
23	7.00	0.50	6.75	-1.13E-03	5669.06	2834.53	2.37	33.37	13.53	38.35	6.75	21.57
24	6.50	0.50	6.25	-1.04E-03	5256.52	2628.26	2.43	33.76	13.27	34.88	6.25	18.17
25	6.00	0.50	5.75	-9.58E-04	4840.98	2420.49	2.49	34.11	13.05	31.58	5.75	15.13
26	5.50	0.50	5.25	-8.75E-04	4423.26	2211.63	2.55	34.43	12.85	28.43	5.25	12.44
27	5.00	0.50	4.75	-7.92E-04	4004.02	2002.01	2.61	34.72	12.68	25.39	4.75	10.05
28	4.50	0.50	4.25	-7.08E-04	3583.74	1791.87	2.66	34.98	12.54	22.47	4.25	7.96
29	4.00	0.50	3.75	-6.25E-04	3162.79	1581.40	2.72	35.21	12.41	19.63	3.75	6.13
30	3.50	0.50	3.25	-5.42E-04	2741.43	1370.72	2.78	35.41	12.31	16.87	3.25	4.57
31	3.00	0.50	2.75	-4.58E-04	2319.83	1159.92	2.83	35.58	12.22	14.17	2.75	3.25
32	2.50	0.50	2.25	-3.75E-04	1898.11	949.05	2.89	35.72	12.14	11.52	2.25	2.16
33	2.00	0.50	1.75	-2.92E-04	1476.33	738.16	2.95	35.83	12.09	8.92	1.75	1.30
34	1.50	0.50	1.25	-2.08E-04	1054.52	527.26	3.00	35.91	12.04	6.35	1.25	0.66
35	1.00	0.50	0.75	-1.25E-04	632.72	316.36	3.06	35.97	12.02	3.80	0.75	0.24
36	0.50	0.50	0.25	-4.17E-05	210.91	105.45	3.11	36.00	12.00	1.27	0.25	0.03
									Cc = ∑ Ci =	2017.16	Mcca = ∑ Mci =	1961.04

Concrete stresses in the concrete cast-in-place (void)

For this material, strain compatibility should be followed to calculate the forces. Recall that as it is a hollow section filled with concrete, this material from the void contributes when "c" is higher than the precast column thickness, which is 6 in. for this example.

$\varepsilon_{ovoid} := \frac{2 \cdot f'c2}{Ec2} = 0.00232$ Strain for the concrete at f'c

$th := \frac{c}{36} = 0.5\ in$ Layer thickness

$L_{n1} := 1$ Layer number (from 1 to 36 in this example)

$L_{l1} := c - (L_{n1} - 0.5) \cdot th = 17.75\ in$ Location of the centroid of Layer #1 measured from the neutral axis

$\varepsilon_{c1} := \frac{\varepsilon cu}{c} \cdot L_{l1} = 0.00296$ Strain at the layer under consideration

$fc_{l1} := 0 \cdot ksi$ Concrete stress at the location of Layer #1. At this location, only the precast column is working.

The material from the void starts contributing when the layer is below the precast column thickness. Thus, Layer #13 is presented to show the behavior of the concrete cast-in-place:

$th := \frac{c}{36} = 0.5\ in$ Layer thickness

$L_{n13} := 13$ Layer number (from 1 to 36 in this example)

$L_{l13} := c - (L_{n13} - 0.5) \cdot th = 11.75\ in$ Location of the centroid of Layer #13 measured from the neutral axis

$\varepsilon_{c13} := \frac{\varepsilon cu}{c} \cdot L_{l13} = 0.00196$ Strain at the layer under consideration

$fc_{l13} := f'c2 \cdot \left[2 \cdot \left(\frac{\varepsilon_{c13}}{\varepsilon_{ovoid}} \right) - \left(\frac{\varepsilon_{c13}}{\varepsilon_{ovoid}} \right)^2 \right] = 4.263\ ksi$ Concrete stress at the location of Layer #13. At this location, both the precast column and the concrete cast-in-place are working.

$C_{13b} := fc_{l13} \cdot th = 2.132\ \frac{kip}{in}$ Force in the layer per unit lenght

$x_{13} := Rc - (c - L_{l13}) = 11.75\ in$ Layer location from the column center

$alfa := 2 \cdot \operatorname{acos}\left(\frac{x_{13}}{Rc - h_t} \right) = 0.41\ rad$ Angle measured from the center of the column

$b_{13} := 2 \cdot (Rc - h_t) \cdot \sin\left(\frac{alfa}{2} \right) = 4.87\ in$ Length of the layer under consideration considering the circular shape

$b_{13effective} := b_{13} = 4.87\ in$ As the precast column is working outside the concrete cast-in-place, the shape used for this is a circle.

$C_{13} := C_{13b} \cdot b_{13effective} = 10.39\ kip$ Total compressive force in Layer #13

$M_{C13} := C_{13} \cdot x_{13} = 10.17\ kip \cdot ft$ Moment from the compressive force in Layer #13

This process should be completed from layer #1 until layer #36 (36 layers in this example). For demonstration, layer #36 is presented:

$th := \frac{c}{36} = 0.5\ in$ Layer thickness

$L_{n36} := 36$ Layer number (from 1 to 36 in this example)

$L_{l36} := c - (L_{n36} - 0.5) \cdot th = 0.25\ in$ Location of the centroid of Layer #36 measured from the neutral axis

$\varepsilon_{c36} := \frac{\varepsilon cu}{c} \cdot L_{l36} = 4.167 \cdot 10^{-5}$ Strain at the layer under consideration

$fc_{l36} := f'c2 \cdot \left[2 \cdot \left(\frac{\varepsilon_{c36}}{\varepsilon_{ovoid}} \right) - \left(\frac{\varepsilon_{c36}}{\varepsilon_{ovoid}} \right)^2 \right] = 0.156\ ksi$ Concrete stress at the location of Layer #36. At this location, both the precast column and the concrete cast-in-place are working.

$C_{36b} := fc_{l36} \cdot th = 0.078\ \frac{kip}{in}$ Force in the layer per unit lenght

$x_{36} := Rc - (c - L_{l36}) = 0.25\ in$ Layer location from the column center

$alfa := 2 \cdot \operatorname{acos}\left(\frac{x_{36}}{Rc - h_t} \right) = 3.1\ rad$ Angle measured from the center of the column

$b_{36} := 2 \cdot (Rc - h_t) \cdot \sin\left(\frac{alfa}{2} \right) = 23.99\ in$ Length of the layer under consideration considering the circular shape

$b_{36effective} := b_{36} = 23.99\ in$ As the precast column is working outside the concrete cast-in-place, the shape used for this is a circle.

$C_{36} := C_{36b} \cdot b_{36effective} = 1.87\ kip$ Total compressive force in Layer #36

$M_{C36} := C_{36} \cdot x_{36} = 0.04\ kip \cdot ft$ Moment from the compressive force in Layer #36

The process should be prepared for each layer as presented in Table A.2

Table A.2. Results for the layer section analysis in the concrete cast-in-place (void)

Model for Void Section												
Layer	Top	Thickness (in)	Location	εcx:	fc layer (psi)	Ci/b (lbs/in)	Angle	b total (in)	b eff. (in)	Ci (kips)	x (in)	Mci (kips-ft)
1	18.00	0.50	17.75	-2.96E-03	0.00	0.00	0.00	0.00	0.00	0.00	17.75	0.00
2	17.50	0.50	17.25	-2.88E-03	0.00	0.00	0.00	0.00	0.00	0.00	17.25	0.00
3	17.00	0.50	16.75	-2.79E-03	0.00	0.00	0.00	0.00	0.00	0.00	16.75	0.00
4	16.50	0.50	16.25	-2.71E-03	0.00	0.00	0.00	0.00	0.00	0.00	16.25	0.00
5	16.00	0.50	15.75	-2.63E-03	0.00	0.00	0.00	0.00	0.00	0.00	15.75	0.00
6	15.50	0.50	15.25	-2.54E-03	0.00	0.00	0.00	0.00	0.00	0.00	15.25	0.00
7	15.00	0.50	14.75	-2.46E-03	0.00	0.00	0.00	0.00	0.00	0.00	14.75	0.00
8	14.50	0.50	14.25	-2.38E-03	0.00	0.00	0.00	0.00	0.00	0.00	14.25	0.00
9	14.00	0.50	13.75	-2.29E-03	0.00	0.00	0.00	0.00	0.00	0.00	13.75	0.00
10	13.50	0.50	13.25	-2.21E-03	0.00	0.00	0.00	0.00	0.00	0.00	13.25	0.00
11	13.00	0.50	12.75	-2.13E-03	0.00	0.00	0.00	0.00	0.00	0.00	12.75	0.00
12	12.50	0.50	12.25	-2.04E-03	0.00	0.00	0.00	0.00	0.00	0.00	12.25	0.00
13	12.00	0.50	11.75	-1.96E-03	4263.27	2131.63	0.41	4.87	4.87	10.39	11.75	10.17
14	11.50	0.50	11.25	-1.88E-03	4208.77	2104.38	0.71	8.35	8.35	17.58	11.25	16.48
15	11.00	0.50	10.75	-1.79E-03	4142.98	2071.49	0.92	10.67	10.67	22.09	10.75	19.79
16	10.50	0.50	10.25	-1.71E-03	4065.92	2032.96	1.09	12.48	12.48	25.37	10.25	21.67
17	10.00	0.50	9.75	-1.63E-03	3977.57	1988.79	1.24	13.99	13.99	27.83	9.75	22.61
18	9.50	0.50	9.25	-1.54E-03	3877.95	1938.97	1.38	15.29	15.29	29.64	9.25	22.85
19	9.00	0.50	8.75	-1.46E-03	3767.04	1883.52	1.51	16.42	16.42	30.94	8.75	22.56
20	8.50	0.50	8.25	-1.38E-03	3644.85	1822.42	1.63	17.43	17.43	31.76	8.25	21.84
21	8.00	0.50	7.75	-1.29E-03	3511.38	1755.69	1.74	18.32	18.32	32.17	7.75	20.78
22	7.50	0.50	7.25	-1.21E-03	3366.63	1683.31	1.84	19.12	19.12	32.19	7.25	19.45
23	7.00	0.50	6.75	-1.13E-03	3210.60	1605.30	1.95	19.84	19.84	31.85	6.75	17.92
24	6.50	0.50	6.25	-1.04E-03	3043.28	1521.64	2.05	20.49	20.49	31.18	6.25	16.24
25	6.00	0.50	5.75	-9.58E-04	2864.69	1432.34	2.14	21.07	21.07	30.17	5.75	14.46
26	5.50	0.50	5.25	-8.75E-04	2674.81	1337.40	2.24	21.58	21.58	28.86	5.25	12.63
27	5.00	0.50	4.75	-7.92E-04	2473.65	1236.83	2.33	22.04	22.04	27.26	4.75	10.79
28	4.50	0.50	4.25	-7.08E-04	2261.21	1130.61	2.42	22.44	22.44	25.38	4.25	8.99
29	4.00	0.50	3.75	-6.25E-04	2037.49	1018.75	2.51	22.80	22.80	23.23	3.75	7.26
30	3.50	0.50	3.25	-5.42E-04	1802.49	901.25	2.59	23.10	23.10	20.82	3.25	5.64
31	3.00	0.50	2.75	-4.58E-04	1556.21	778.10	2.68	23.36	23.36	18.18	2.75	4.17
32	2.50	0.50	2.25	-3.75E-04	1298.64	649.32	2.76	23.57	23.57	15.31	2.25	2.87
33	2.00	0.50	1.75	-2.92E-04	1029.80	514.90	2.85	23.74	23.74	12.23	1.75	1.78
34	1.50	0.50	1.25	-2.08E-04	749.67	374.84	2.93	23.87	23.87	8.95	1.25	0.93
35	1.00	0.50	0.75	-1.25E-04	458.26	229.13	3.02	23.95	23.95	5.49	0.75	0.34
36	0.50	0.50	0.25	-4.17E-05	155.57	77.79	3.10	23.99	23.99	1.87	0.25	0.04
									Cc = ∑ Ci =	540.72	Mcca = ∑ Mci =	302.24

Step 5: Calculate the concrete compressive force: Cc

By summing all the forces from each layer, the total compressive force from the precast column (Table A.1) and the concrete cast-in-place (Table A.2) are added to get the total compressive force.

$C_{pc} := 2017.16 \cdot kip$ Precast column compressive force

$C_{void} := 540.72 \cdot kip$ Concrete cast-in-place compressive force

$Cc := C_{pc} + C_{void} = 2557.88\ kip$ Total compressice force

Step 6: Calculate the strain in the prestressing strands considering the effective stress after losses:

$$\varepsilon s1 := \varepsilon cu \cdot \frac{(c - d'1)}{c} - \Delta\varepsilon_p = -3.74 \cdot 10^{-3}$$

$$\varepsilon s2 := \varepsilon cu \cdot \frac{(c - d'2)}{c} - \Delta\varepsilon_p = -4.28 \cdot 10^{-3}$$

$$\varepsilon s3 := \varepsilon cu \cdot \frac{(c - d'3)}{c} - \Delta\varepsilon_p = -5.1 \cdot 10^{-3}$$

$$\varepsilon s4 := \varepsilon cu \cdot \frac{(c - d'4)}{c} - \Delta\varepsilon_p = -7.01 \cdot 10^{-3}$$

$$\varepsilon s5 := \varepsilon cu \cdot \frac{(c - d'5)}{c} - \Delta\varepsilon_p = -7.82 \cdot 10^{-3}$$

$$\varepsilon s6 := \varepsilon cu \cdot \frac{(c - d'6)}{c} - \Delta\varepsilon_p = -8.36 \cdot 10^{-3}$$

Step 7: Calculate the stress in the prestressing strands with the Ramberg-Osgood function:

$$fs1 := \mathbf{if}\left(\left|\varepsilon s1 \cdot Ep \cdot \left(A + \frac{1-A}{\left(1 + (B \cdot \varepsilon s1)^C\right)^{\frac{1}{C}}}\right)\right| > f_{px}, -f_{px}, \varepsilon s1 \cdot Ep \cdot \left(A + \frac{1-A}{\left(1 + (B \cdot \varepsilon s1)^C\right)^{\frac{1}{C}}}\right)\right) = -106.67 \ \textit{ksi}$$

$$fs2 := \mathbf{if}\left(\left|\varepsilon s2 \cdot Ep \cdot \left(A + \frac{1-A}{\left(1 + (B \cdot \varepsilon s2)^C\right)^{\frac{1}{C}}}\right)\right| > f_{px}, -f_{px}, \varepsilon s2 \cdot Ep \cdot \left(A + \frac{1-A}{\left(1 + (B \cdot \varepsilon s2)^C\right)^{\frac{1}{C}}}\right)\right) = -122.1 \ \textit{ksi}$$

$$fs3 := \mathbf{if}\left(\left|\varepsilon s3 \cdot Ep \cdot \left(A + \frac{1-A}{\left(1 + (B \cdot \varepsilon s3)^C\right)^{\frac{1}{C}}}\right)\right| > f_{px}, -f_{px}, \varepsilon s3 \cdot Ep \cdot \left(A + \frac{1-A}{\left(1 + (B \cdot \varepsilon s3)^C\right)^{\frac{1}{C}}}\right)\right) = -145.15 \ \textit{ksi}$$

$$fs4 := \mathbf{if}\left(\left|\varepsilon s4 \cdot Ep \cdot \left(A + \frac{1-A}{\left(1 + (B \cdot \varepsilon s4)^C\right)^{\frac{1}{C}}}\right)\right| > f_{px}, -f_{px}, \varepsilon s4 \cdot Ep \cdot \left(A + \frac{1-A}{\left(1 + (B \cdot \varepsilon s4)^C\right)^{\frac{1}{C}}}\right)\right) = -188.06 \ \textit{ksi}$$

$$fs5 := \mathbf{if}\left(\left|\varepsilon s5 \cdot Ep \cdot \left(A + \frac{1-A}{\left(1 + (B \cdot \varepsilon s5)^C\right)^{\frac{1}{C}}}\right)\right| > f_{px}, -f_{px}, \varepsilon s5 \cdot Ep \cdot \left(A + \frac{1-A}{\left(1 + (B \cdot \varepsilon s5)^C\right)^{\frac{1}{C}}}\right)\right) = -188.06 \ \textit{ksi}$$

$$fs6 := \mathbf{if}\left(\left|\varepsilon s6 \cdot Ep \cdot \left(A + \frac{1-A}{\left(1 + (B \cdot \varepsilon s6)^C\right)^{\frac{1}{C}}}\right)\right| > f_{px}, -f_{px}, \varepsilon s6 \cdot Ep \cdot \left(A + \frac{1-A}{\left(1 + (B \cdot \varepsilon s6)^C\right)^{\frac{1}{C}}}\right)\right) = -188.06 \ \textit{ksi}$$

Step 8: Calculate the force in the prestressing strands:

$Fs1 := As'1 \cdot fs1 = -65.28\ \textbf{kip}$

$Fs2 := As'2 \cdot fs2 = -74.73\ \textbf{kip}$

$Fs3 := As'3 \cdot fs3 = -88.83\ \textbf{kip}$

Negative = Tension

$Fs4 := As'4 \cdot fs4 = -115.09\ \textbf{kip}$

$Fs5 := As'5 \cdot fs5 = -115.09\ \textbf{kip}$

$Fs6 := As'6 \cdot fs6 = -115.09\ \textbf{kip}$

Step 9: Determine resultant axial force, P:

$P := Fs1 + Fs2 + Fs3 + Fs4 + Fs5 + Fs6 + Cc = 1983.76\ \textbf{kip}$

Step 10: Determine the moment due to concrete force about the centroidal axis:

By summing all the moments from each layer, the total moment from the precast column (Table A.1) and the concrete cast-in-place (Table A.2) are added to get the total moment.

$M_{pc} := 1961.04 \cdot \textbf{kip} \cdot \textbf{ft}$ Precast column moment

$M_{void} := 302.24 \cdot \textbf{kip} \cdot \textbf{ft}$ Concrete cast-in-place moment

$M_{Cca} := M_{pc} + M_{void} = 2263.28\ \textbf{kip} \cdot \textbf{ft}$ Total moment

Step 11: Determine moment due to the force in the prestressing strands about the centroidal axis:

$Ms1 := Fs1 \cdot (Rc - d'1) = -904.69\ \textbf{kip} \cdot \textbf{in}$

$Ms2 := Fs2 \cdot (Rc - d'2) = -792.63\ \textbf{kip} \cdot \textbf{in}$

$Ms3 := Fs3 \cdot (Rc - d'3) = -509.89\ \textbf{kip} \cdot \textbf{in}$

$Ms4 := Fs4 \cdot (Rc - d'4) = 660.63\ \textbf{kip} \cdot \textbf{in}$

$Ms5 := Fs5 \cdot (Rc - d'5) = 1220.66\ \textbf{kip} \cdot \textbf{in}$

$Ms6 := Fs6 \cdot (Rc - d'6) = 1594.94\ \textbf{kip} \cdot \textbf{in}$

Negative because of their location, they are up the centroid and down "c". For that reason when you take moments from the centroid they will be negative. The others will be positive because their location is under the centroid.

Step 12: Determine the resulting moment acting on the section:

$M' := M_{Cca} + Ms1 + Ms2 + Ms3 + Ms4 + Ms5 + Ms6 = 2369.03\ \textit{kip} \cdot \textit{ft}$

Step 13: Calculate the corresponding ϕ:

$\varepsilon t := \mathrm{abs}(\varepsilon s6) = 0.008$

$\phi_A := \mathbf{if}\left(\varepsilon t \le 0.002, 0.65, \mathbf{if}\left(\varepsilon t \le 0.005, \frac{1.0-0.75}{0.005-0.002} \cdot \varepsilon t + \left(0.75 - \frac{1.0-0.75}{0.005-0.002} \cdot 0.002\right), 1\right)\right)$

$\phi_A = 1$ According to AASHTO 5.6.2.1

Considering that the strands are not fully developed in the transfer zone as ACI 318-19 21.2.3:

$l_{tr} := \left(\frac{f_{pe}}{3000 \cdot \textit{psi}}\right) d_b = 28.75\ \textit{in}$

$l_{px} = 45\ \textit{in}$

$\phi := \mathbf{if}\left(l_{px} \le l_{tr}, 0.75, \mathbf{if}\left(l_{px} \le l_d, \frac{\phi_A - 0.75}{l_d - l_{tr}} \cdot l_{px} + 0.75 - \frac{1-0.75}{l_d - l_{tr}} \cdot l_{tr}, \phi_A\right)\right)$

$\phi = 0.793$

Step 14: Determine the ultimate capacity:

$\phi Pn := \phi \cdot P = 1572.43\ \textit{kip}$

$\phi Mn := \phi \cdot M' = 1877.82\ \textit{kip} \cdot \textit{ft}$

Pure compression

$\varepsilon cu := 0.003 \qquad \varepsilon s := \varepsilon cu - \Delta\varepsilon_p = -0.003$

$A_{cpc} := 0.25 \cdot \left(Dc^2 - (Dc - 2 \cdot h_t)^2\right) \cdot \pi = 565.49\ \textit{in}^2$ Precast Concrete area

$A_{cvoid} := 0.25 \cdot (Dc - 2 \cdot h_t)^2 \cdot \pi = 452.39\ \textit{in}^2$ Concrete cast-in-place area

$fs := \mathbf{if}\left(\mathrm{abs}\left(\varepsilon s \cdot Ep \cdot \left(A + \frac{1-A}{\left(1 + (B \cdot \varepsilon s)^C\right)^{\frac{1}{C}}}\right)\right) > f_{px}, -f_{px}, \varepsilon s \cdot Ep \cdot \left(A + \frac{1-A}{\left(1 + (B \cdot \varepsilon s)^C\right)^{\frac{1}{C}}}\right)\right) = -87\ \textit{ksi}$

$As := 24 \cdot 0.153 \cdot \textit{in}^2 = 3.672\ \textit{in}^2 \qquad Fs := As \cdot fs = -319.46\ \textit{kip}$

$P_{oc} := 0.85 \cdot f'c1 \cdot (A_{cpc} - As) + 0.85 \cdot f'c2 \cdot A_{cvoid} + Fs = 6284.49\ \textit{kip}$

Pure Tension

$As = 3.672\ \textit{in}^2$

$fs := -f_{px} = -188.06\ \textit{ksi}$

$Fs := As \cdot fs = -690.55\ \textit{kip}$

$P_{ot} := Fs = -690.55\ \textit{kip}$

The complete P-M Interaction Diagram is presented below:

Comp (*in*)	*Load* (*kip*)	*Moment* (*kip · ft*)
0	−690.55	0
1.50	−601.49	116.75
3.00	−455.83	314.33
4.50	−256.87	564.31
6.00	−29.07	830.81
7.50	224.33	1103.03
8.59	409.83	1289.11
9.00	479.66	1356.22
10.50	734.61	1586.61
12.00	991.10	1792.87
13.50	1244.84	1974.34
15.00	1495.96	2130.73
16.50	1743.78	2261.18
18.00	1990.60	2367.91
19.50	2234.85	2449.48
21.00	2480.38	2505.81
22.50	2730.99	2544.19
24.00	2967.77	2548.24
25.50	3214.40	2536.01
27.00	3450.46	2493.87
28.50	3698.14	2440.18
30.00	3923.55	2347.93
31.50	4160.16	2249.66
33.00	4397.58	2138.87
34.50	4606.29	1990.28
36.00	6284.49	0.00

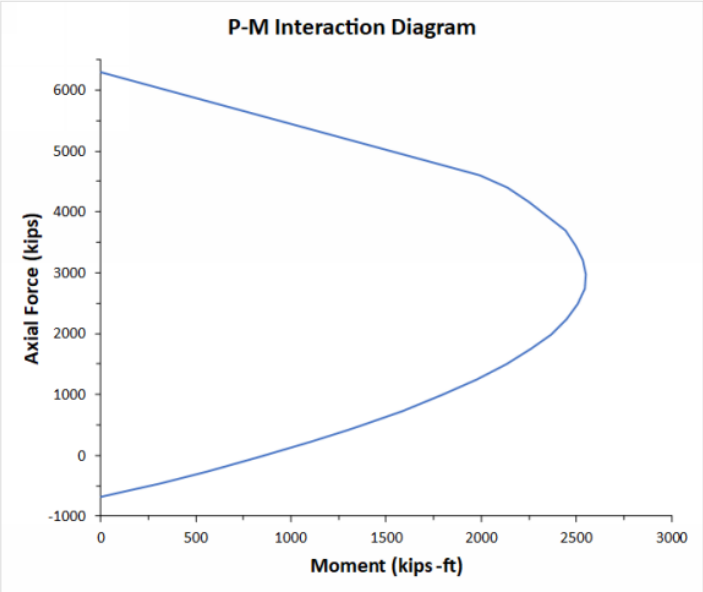

Appendix B. Design example using rectangular stress block for the concrete

P-M Interaction Diagram using Rectangular Stress Block

Dimensions of the circular column:

$Dc := 36 \cdot in$ Column Diameter

$Rc := Dc \cdot 0.5 = 18\ in$ Column Radio

Use f'c average

$f'c := 7340 \cdot psi$

$\alpha := 0.85$

$\beta 1 := \mathbf{if}\left(f'c \le 4000 \cdot psi, 0.85, \mathbf{if}\left(f'c \le 8000 \cdot psi, 0.85 - \left(\frac{(0.05 \cdot (f'c - 4000 \cdot psi))}{1000 \cdot psi}\right), 0.65\right)\right) = 0.68$

Location of the prestressing strand from top to bottom:

$d'1 := 4.142 \cdot in$

$d'2 := 7.393 \cdot in$

$d'3 := 12.26 \cdot in$

$d'4 := 23.74 \cdot in$

$d'5 := 28.606 \cdot in$

$d'6 := 31.858 \cdot in$

Area of the 0.5-in. strands locatead at each layer:

$As'1 := 4 \cdot 0.153 \cdot in^2 = 0.612\ in^2$

$As'2 := 4 \cdot 0.153 \cdot in^2 = 0.612\ in^2$

$As'3 := 4 \cdot 0.153 \cdot in^2 = 0.612\ in^2$

$As'4 := 4 \cdot 0.153 \cdot in^2 = 0.612\ in^2$

$As'5 := 4 \cdot 0.153 \cdot in^2 = 0.612\ in^2$

$As'6 := 4 \cdot 0.153 \cdot in^2 = 0.612\ in^2$

$Ep := 28500 \cdot ksi$ MOE for the prestressing strands

$f_{pu} := 270 \cdot ksi$ $f_{loss} := 30 \cdot ksi$

$f_{pe} := 0.75 \cdot f_{pu} - f_{loss} = 172.5\ ksi$ Effective stress after losses $\Delta\varepsilon_p := \frac{f_{pe}}{Ep} = 0.006$

$d_b := 0.5 \cdot in$ Nominal diameter of the prestressing strands

$L_{emb} := 45 \cdot in$ Embedment length used for the connector bars

$f_{ps} := f_{pu} = 270\ ksi$ Calculated with Strain-Compatibility

Using the Ramberg-Osgood function values for the prestressing strands (Low relaxation):

$A := 0.025$
$B := 118$
$C := 10$

Step 1: Determine f_{px} for prestressing strands using L_{emb} from connector bars using AASHTO 5.9.4.3.2:

$tl := 60 \cdot d_b = 30\ in$ Transfer length

$l_{px} := L_{emb} = 45\ in$ distance from free end of pretensioned strand to section of member under consideration (embedment lenght of the connecting bars).

$k := \frac{1.6}{ksi}$ 1.6 for pretensioned members with a depth greater than 24 in.

$l_d := k \cdot \left(f_{ps} - \frac{2}{3} \cdot f_{pe}\right) \cdot d_b = 124\ in \qquad l_d = 10.33\ ft$

$f_{px} := \text{if}\left(l_{px} \le tl, l_{px} \cdot \frac{f_{pe}}{tl}, f_{pe} + \left(\frac{l_{px} - tl}{l_d - tl}\right) \cdot (f_{ps} - f_{pe})\right) = 188.06\ ksi$

$f_{px} := \text{if}(f_{px} \ge f_{ps}, f_{ps}, f_{px}) = 188.06\ ksi$ Checking that f_{px} is not higher than f_{ps}

Step 2: Select a value of εcu:

$\varepsilon cu := 0.003$

Step 3: Choose "c" (to calculate the complete P-M curve, "c" should start from a small value, find P and M, and then increase "c" until completing the depth of the cross-section):

$c := 18 \cdot in$

Step 4: Calculate the concrete compressive area from the circular segment and the centroid:

$a := \beta 1 \cdot c = 12.29\ in$

$h := Rc - a = 5.71\ in$

$alfa := 2 \cdot \text{acos}\left(\frac{h}{Rc}\right) = 2.5\ rad$

$Aseg := \frac{Rc^2}{2} \cdot (alfa - \sin(alfa)) = 307.02\ in^2$

$y_{Aseg} := \frac{4 \cdot Rc \cdot (\sin(alfa \cdot 0.5))^3}{3 \cdot (alfa - \sin(alfa))} = 10.8\ in$

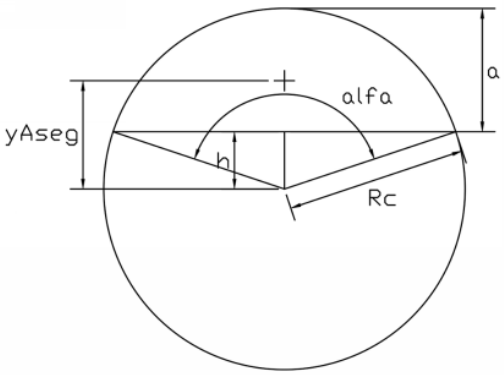

Step 5: Calculate the concrete compressive force: Cc

$Cc := \alpha \cdot Aseg \cdot f'c = 1915.47\ kip$

Step 6: Calculate the strain in the prestressing strands considering the effective stress after losses:

$$\varepsilon s1 := \varepsilon cu \cdot \frac{(c - d'1)}{c} - \Delta\varepsilon_p = -3.74 \cdot 10^{-3}$$

$$\varepsilon s2 := \varepsilon cu \cdot \frac{(c - d'2)}{c} - \Delta\varepsilon_p = -4.28 \cdot 10^{-3}$$

$$\varepsilon s3 := \varepsilon cu \cdot \frac{(c - d'3)}{c} - \Delta\varepsilon_p = -5.1 \cdot 10^{-3}$$

$$\varepsilon s4 := \varepsilon cu \cdot \frac{(c - d'4)}{c} - \Delta\varepsilon_p = -7.01 \cdot 10^{-3}$$

$$\varepsilon s5 := \varepsilon cu \cdot \frac{(c - d'5)}{c} - \Delta\varepsilon_p = -7.82 \cdot 10^{-3}$$

$$\varepsilon s6 := \varepsilon cu \cdot \frac{(c - d'6)}{c} - \Delta\varepsilon_p = -8.36 \cdot 10^{-3}$$

Step 7: Calculate the stress in the prestressing strands with the Ramberg-Osgood function:

$$fs1 := \mathbf{if}\left(\left|\varepsilon s1 \cdot Ep \cdot \left(A + \frac{1 - A}{\left(1 + (B \cdot \varepsilon s1)^C\right)^{\frac{1}{C}}}\right)\right| > f_{px}, -f_{px}, \varepsilon s1 \cdot Ep \cdot \left(A + \frac{1 - A}{\left(1 + (B \cdot \varepsilon s1)^C\right)^{\frac{1}{C}}}\right)\right) = -106.67 \ \textit{ksi}$$

$$fs2 := \mathbf{if}\left(\left|\varepsilon s2 \cdot Ep \cdot \left(A + \frac{1 - A}{\left(1 + (B \cdot \varepsilon s2)^C\right)^{\frac{1}{C}}}\right)\right| > f_{px}, -f_{px}, \varepsilon s2 \cdot Ep \cdot \left(A + \frac{1 - A}{\left(1 + (B \cdot \varepsilon s2)^C\right)^{\frac{1}{C}}}\right)\right) = -122.1 \ \textit{ksi}$$

$$fs3 := \mathbf{if}\left(\left|\varepsilon s3 \cdot Ep \cdot \left(A + \frac{1 - A}{\left(1 + (B \cdot \varepsilon s3)^C\right)^{\frac{1}{C}}}\right)\right| > f_{px}, -f_{px}, \varepsilon s3 \cdot Ep \cdot \left(A + \frac{1 - A}{\left(1 + (B \cdot \varepsilon s3)^C\right)^{\frac{1}{C}}}\right)\right) = -145.15 \ \textit{ksi}$$

$$fs4 := \mathbf{if}\left(\left|\varepsilon s4 \cdot Ep \cdot \left(A + \frac{1 - A}{\left(1 + (B \cdot \varepsilon s4)^C\right)^{\frac{1}{C}}}\right)\right| > f_{px}, -f_{px}, \varepsilon s4 \cdot Ep \cdot \left(A + \frac{1 - A}{\left(1 + (B \cdot \varepsilon s4)^C\right)^{\frac{1}{C}}}\right)\right) = -188.06 \ \textit{ksi}$$

$$fs5 := \mathbf{if}\left(\left|\varepsilon s5 \cdot Ep \cdot \left(A + \frac{1 - A}{\left(1 + (B \cdot \varepsilon s5)^C\right)^{\frac{1}{C}}}\right)\right| > f_{px}, -f_{px}, \varepsilon s5 \cdot Ep \cdot \left(A + \frac{1 - A}{\left(1 + (B \cdot \varepsilon s5)^C\right)^{\frac{1}{C}}}\right)\right) = -188.06 \ \textit{ksi}$$

$$fs6 := \text{if}\left(\left|\varepsilon s6 \cdot Ep \cdot \left(A + \frac{1-A}{\left(1+(B\cdot\varepsilon s6)^{C}\right)^{\frac{1}{C}}}\right)\right| > f_{px}, -f_{px}, \varepsilon s6 \cdot Ep \cdot \left(A + \frac{1-A}{\left(1+(B\cdot\varepsilon s6)^{C}\right)^{\frac{1}{C}}}\right)\right) = -188.06 \ \textbf{\textit{ksi}}$$

Step 8: Calculate the force in the prestressing strands:

$Fs1 := As'1 \cdot fs1 = -65.28$ ***kip***

$Fs2 := As'2 \cdot fs2 = -74.73$ ***kip***

$Fs3 := As'3 \cdot fs3 = -88.83$ ***kip***

Negative = Tension

$Fs4 := As'4 \cdot fs4 = -115.09$ ***kip***

$Fs5 := As'5 \cdot fs5 = -115.09$ ***kip***

$Fs6 := As'6 \cdot fs6 = -115.09$ ***kip***

Step 9: Determine resultant axial force, P:

$P := Fs1 + Fs2 + Fs3 + Fs4 + Fs5 + Fs6 + Cc = 1341.36$ ***kip***

Step 10: Determine moment due to concrete force about the centroidal axis:

From step 3 and 4:

$M_{Cca} := Cc \cdot y_{Aseg} = 20694.31$ ***kip·in***

Step 11: Determine moment due to the force in the prestressing strands about the centroidal axis:

$Ms1 := Fs1 \cdot (Rc - d'1) = -904.69$ ***kip·in***

$Ms2 := Fs2 \cdot (Rc - d'2) = -792.63$ ***kip·in***

$Ms3 := Fs3 \cdot (Rc - d'3) = -509.89$ ***kip·in***

$Ms4 := Fs4 \cdot (Rc - d'4) = 660.63$ ***kip·in***

$Ms5 := Fs5 \cdot (Rc - d'5) = 1220.66$ ***kip·in***

$Ms6 := Fs6 \cdot (Rc - d'6) = 1594.94$ ***kip·in***

Negative because of their location, they are up the centroid and down "c". For that reason when you take moments from the centroid they will be negative. The others will be positive because their location is under the centroid.

Step 12: Determine the resulting moment acting on the section:

$M' := M_{Cca} + Ms1 + Ms2 + Ms3 + Ms4 + Ms5 + Ms6 = 1830.28\ \textit{kip} \cdot \textit{ft}$

Step 13: Calculate the corresponding ϕ:

$\varepsilon t := \mathrm{abs}(\varepsilon s6) = 0.008$

$\phi_A := \mathbf{if}\left(\varepsilon t \le 0.002, 0.65, \mathbf{if}\left(\varepsilon t \le 0.005, \frac{1.0-0.75}{0.005-0.002} \cdot \varepsilon t + \left(0.75 - \frac{1.0-0.75}{0.005-0.002} \cdot 0.002\right), 1\right)\right)$

$\phi_A = 1$ According to AASHTO 5.6.2.1

Considering that the strands are not fully developed in the transfer zone as ACI 318-19 21.2.3:

$l_{tr} := \left(\frac{f_{pe}}{3000 \cdot \textit{psi}}\right) d_b = 28.75\ \textit{in}$

$l_{px} = 45\ \textit{in}$

$\phi := \mathbf{if}\left(l_{px} \le l_{tr}, 0.75, \mathbf{if}\left(l_{px} \le l_d, \frac{\phi_A - 0.75}{l_d - l_{tr}} \cdot l_{px} + 0.75 - \frac{1-0.75}{l_d - l_{tr}} \cdot l_{tr}, \phi_A\right)\right)$

$\phi = 0.793$

Step 14: Determine the ultimate capacity:

$\phi Pn := \phi \cdot P = 1063.23\ \textit{kip}$

$\phi Mn := \phi \cdot M' = 1450.77\ \textit{kip} \cdot \textit{ft}$

Pure compression

$\varepsilon cu := 0.003$ $A_c := 0.25 \cdot Dc^2 \cdot \pi = 1017.88\ \textit{in}^2$ Concrete area

$\varepsilon s := \varepsilon cu - \Delta\varepsilon_p = -0.003$

$fs := \mathbf{if}\left(\mathrm{abs}\left(\varepsilon s \cdot Ep \cdot \left(A + \frac{1-A}{\left(1 + (B \cdot \varepsilon s)^C\right)^{\frac{1}{C}}}\right)\right) > f_{px}, -f_{px}, \varepsilon s \cdot Ep \cdot \left(A + \frac{1-A}{\left(1 + (B \cdot \varepsilon s)^C\right)^{\frac{1}{C}}}\right)\right) = -87\ \textit{ksi}$

$As := 24 \cdot 0.153 \cdot \textit{in}^2 = 3.672\ \textit{in}^2$ $Fs := As \cdot fs = -319.46\ \textit{kip}$

$P_{oc} := 0.85 \cdot f'c \cdot (A_c - As) + Fs = 6008.16\ \textit{kip}$

Pure Tension

$As = 3.672\ \textbf{\textit{in}}^2$

$fs := -f_{px} = -188.06\ \textbf{\textit{ksi}}$

$Fs := As \cdot fs = -690.55\ \textbf{\textit{kip}}$

$P_{ot} := Fs = -690.55\ \textbf{\textit{kip}}$

The complete P-M Interaction Diagram is presented below:

Comp (***in***)	*Load* (***kip***)	*Moment* (***kip·ft***)
0	−690.56	0
1.50	−639.24	74.35
3.00	−546.69	201.11
4.50	−413.80	369.97
6.00	−264.24	548.95
7.50	−91.89	738.78
11.08	356.21	1170.58
9.00	88.47	923.90
10.50	279.04	1103.14
12.00	481.95	1275.63
13.50	690.33	1436.37
15.00	903.82	1583.72
16.50	1121.94	1716.23
18.00	1344.10	1832.60
19.50	1569.72	1931.74
21.00	1802.30	2010.75
22.50	2036.52	2071.16
24.00	2273.02	2111.32
25.50	2512.10	2130.05
27.00	2752.46	2127.26
28.50	2992.87	2103.64
30.00	3231.21	2061.05
31.50	3466.85	1999.82
33.00	3699.12	1920.47
34.50	3927.29	1823.76
36.00	6008.16	0.00

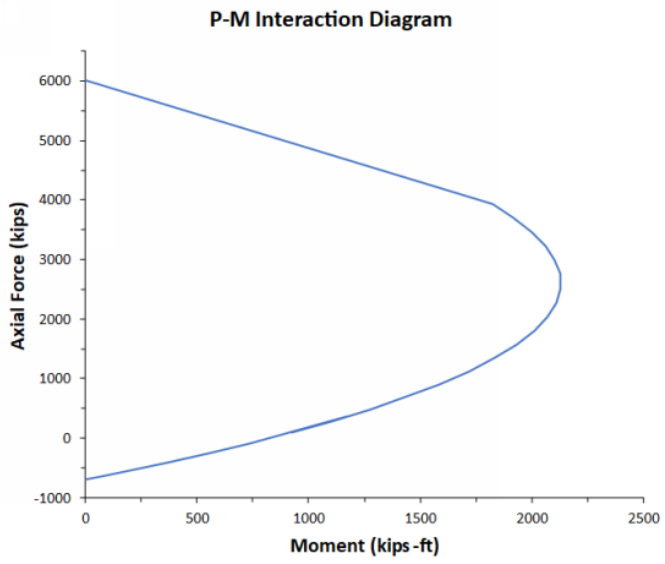

Appendix C. Drawings for the Precast Column Solution